

This file is part of the following reference:

Johnson, Kate (2005) *Load-Deformation Behaviour of Foundations Under Vertical and Oblique Loads*. PhD thesis, James Cook University.

Access to this file is available from:

<http://eprints.jcu.edu.au/1313>

The author has certified to JCU that they have made a reasonable effort to gain permission and acknowledge the owner of any third party copyright material included in this document. If you believe that this is not the case, please contact ResearchOnline@jcu.edu.au and quote <http://eprints.jcu.edu.au/>

THESIS

JAMES COOK UNIVERSITY

SCHOOL OF ENGINEERING

www.eng.jcu.edu.au

**LOAD-DEFORMATION BEHAVIOUR
OF FOUNDATIONS
UNDER VERTICAL AND OBLIQUE LOADS**

Kate Johnson

Thesis submitted to the School of Engineering in
fulfilment of the requirements for the degree of

**Doctor of Philosophy
(Civil Engineering)**

May 2005

ABSTRACT

The work in this thesis explores the load-deformation behaviour of shallow and pile foundations under axial and oblique loads.

- A statistical review was performed on five popular shallow foundation settlement methods, which showed that different prediction methods could give highly variable results for the same foundation and soil conditions. The probability of failure charts allowing direct comparison between methods is presented, based on the statistical work.

There are 40+ settlement methods available for predicting the settlement of shallow foundations in granular soil. There is no way to account for the differences between settlement methods, other than assume one specific design criterion for every method. For example, limiting the settlement of a shallow foundation to 25 mm is a design criterion that is commonly used. From previous statistical work, it is shown that the Terzaghi and Peck method is more conservative than the method developed by Berardi and Lancellotta. The work in this thesis produced ‘probability of failure charts’, and the charts give the probability that the settlement for the commonly used methods will exceed an actual design value in the field. These charts allow users to design shallow foundations on the basis of an acceptable failure probability, instead of using one settlement criterion for every settlement method.

- A finite element analysis was performed on obliquely loaded piles. The analysis showed that the axial and lateral load components, and moment capacity of a pile is reduced if multiple load types act in unison. Combination loading also affects the pile head displacement. The oblique interaction charts herein allow the ultimate capacity and pile head displacement for a pile under combination loading to be estimated.

From the literature review of pile foundations, it is found that the influence due to combination loading is not well defined (i.e. axial loads, lateral loads and moments all acting at once). Previous work has shown that combination loading reduces the ultimate capacity of a pile, and the influence on pile head displacement has not been quantified. The influence of combination loading on pile capacity and settlement was explored, with the use of a finite element computer package entitled ABAQUS. The results from the numerical modelling are summarised into easy-to-use design charts, allowing the user to quantify the reduction in ultimate capacity and influence in settlement.

ELECTRONIC COPY AND STATEMENT ON SOURCES DECLARATION

I, the undersigned, the author of this work, declare that the electronic copy of this thesis provided to the James Cook University Library is an accurate copy of the print thesis submitted, within the limits of the technology available.

I declare that this thesis is my own work and has not been submitted in any form for another degree or diploma at any university or other institution of tertiary education. Information derived from the published or unpublished work of other has been acknowledged in the text and a list of references is given.

 -----
Kate Johnson

1st August 2005

Date

STATEMENT OF ACCESS

I, the undersigned, the author of this thesis, understand that James Cook University will make available for use within the University Library and, by microfilm or other means, allow access to other users in other approved libraries. All users consulting this thesis will have to sign the following statement:

In consulting this thesis I agree not to copy or closely paraphrase it in whole or in part without the written consent of the author, and to make proper public written acknowledgement for any assistance, which I have obtained from it.

Beyond this, I do not wish to place any restriction on access to this thesis.



Kate Johnson

1st August 2005

Date

ACKNOWLEDGEMENTS

The journey has been filled with many challenges and personal tests of will. I had the pleasure of working with some interesting people along the way. Firstly, I would like to extend my warm thanks to my supervisor Dr. W. Karunasena. His kind and approachable manner was much appreciated. Karu's patience and ability to reason through problems provided a platform for me to move towards my aims.

I would also like to thank my second supervisor Dr. N. Sivakugan. Siva allowed me many opportunities to enhance my skills as a teacher and a consultant. His questioning mind made me pay attention to fine detail. I chose Siva as a supervisor, because he was enthusiastic about the discipline of geotechnical engineering at James Cook University.

I liked working with the technical support people at James Cook University. A thank-you to Mr Stuart Petersen, Mr Curt Arrowsmith, Mr Warren O'Donnell, Mr John Ellis, and all the technicians in the laboratory. Year after year, the technicians make equipment to help the PhD and undergraduate students in their experimental work. They are inspiring and hard working members of the JCU community.

During the course of my research I enlisted the help of two undergraduate students who worked under my direction. The two undergraduate students were:

- Mr Andrew Guazzo worked with me for the experimental pile phase (Chapter 6). Andrew and I spent a great deal of time setting up apparatuses, testing the small-scale piles and analysing the results. Andrew had a very good attitude even when we were shovelling 7 tonne of sand back and forth.
- Mr Paul Lemcke worked with me exploring the influence of pile shape on the capacity of a pile. Paul was patient while we worked some long days and late nights to obtain a numerical ABAQUS model, which would be suitable for the pile shape research.

A thank-you to Dr J Eckersley (Coffey). I thank John for his council and guidance, and I liked being challenged by his inquisitive mind. He gave me some good ideas when I have needed them most.

My final acknowledgement is to my parents. I thank them for their support during the high and low points throughout the years. I have memories of working through the nights trying to solve problems with the numerical modelling. My mother sat in my office to offer support, and my father rang to see if I was successful. They made me feel part of a team and never gave up on me. THANK-YOU. I think we can have a vacation now...

Finally, I have chosen two poems to close the acknowledgement section of this thesis.

Does the road wind up-hill all the way?

Yes, to the very end.

Will the day's journey take the whole long day?

From morn to night, my friend.

Christina Rossetti

“Over the Mountains

Of the Moon

Down the Valley of the Shadow,

Ride, boldly ride,”

The shade replied,

“If you seek for Eldorado!”

Edgar Allan Poe

CONTENTS

Abstract	II
Statement of Sources Declaration	IV
Statement of Access	V
Acknowledgements	VI
Table of Contents	VIII
List of Tables	XIII
List of Figures	XV
Notations	XXI
Chapter 1: Introduction	1
1.1 General	1
1.2 History of Shallow and Pile Foundations	3
1.3 Research Objectives and Aims	4
1.4 Thesis Overview	8
Chapter 2: Literature Review – Shallow Foundations	10
2.1 General	10
2.2 Accuracy and Reliability	10
2.3 Shallow Foundation Settlement Prediction Methods	11
2.3.1 Terzaghi and Peck Method	12
2.3.2 Burland and Burbidge Method	12
2.3.3 Berardi and Lancellotta Method	13
2.3.4 Schmertmann Method	13
2.4 Results from the Reliability Analysis	13
2.5 Soil Variability	15
2.6 Statistical Review of Settlement for Shallow Footings	17
Chapter 3: Settlement Predictions in Granular Soil: A Probabilistic Approach	23
3.1 General	23
3.2 Statistical Analysis	23
3.2.1 Settlement Ratio Probability Density Function	24

3.2.2	Probabilistic Design Charts	27
Chapter 4:	Soil Strength and Constitutive Behaviour	34
4.1	General	34
4.2	Constitutive Models	34
4.2.1	General Background	34
4.2.2	Types of Constitutive Models	36
4.2.3	Linear Elastic Constitutive Model	37
4.2.4	Non-Linear Elastic Constitutive Model	38
4.2.5	Mohr-Coulomb's Model	39
4.2.6	Drucker Prager Model	41
4.3	Determination of Sand Constitutive Properties	42
4.3.1	Correlations for Friction Angle of Sand	42
4.3.2	Correlations for Dilatancy of Sand	55
4.3.3	Correlations for Elastic Modulus of Sand	58
4.3.4	Poisson's Ratio (ν) of Sand	64
Chapter 5:	Estimating Shallow Foundation Behaviour using Numerical Models	66
5.1	General	66
5.2	Behaviour Criteria and Numerical Model Development	69
5.2.1	Shallow Foundation Failure Mechanism	69
5.2.2	Development of Shallow Foundation ABAQUS Model	70
5.2.2.1	Shallow Foundation Model Types	71
5.2.2.2	General Model Characteristics	74
5.3	Prediction of Shallow Foundation Behaviour	77
5.3.1	Symposium Footing Size and Soil Profiles	77
5.3.2	Prediction of Symposium Footing Behaviour	80
5.4	Comparison of Symposium Results	87
Chapter 6:	Literature Review – Piles	94
6.1	General	94
6.2	Piles Subjected to Oblique Loading	95

6.3	Pile Installation Techniques	101
6.4	Current Design Techniques	103
6.4.1	Piles subjected to Axially Compressive Loading in Sand	104
6.4.2	Piles subjected to Axially Uplift Loading	106
6.4.3	Piles subjected to Lateral Loading	110
6.5	Finite Element Method (FEM)	114
Chapter 7:	Small-Scale Model Pile Tests	120
7.1	General	120
7.2	Apparatuses Used for Small-Scale Pile Testing	120
7.2.1	Model Piles	121
7.2.2	Tank	121
7.2.3	Main Loading Frame	122
7.2.4	Pile Jacking Frame	123
7.2.5	Pile Loading Equipment	124
7.2.6	Measuring Devices	127
7.3	Methodology for Model Pile Testing	128
7.3.1	Experimental Sand Properties and Sand Placement	129
7.3.2	Sand Bed Properties	132
7.3.3	Model Pile Placement	133
7.3.4	Load-Displacement Testing	134
7.4	Load Settlement Results for Model Piles	134
7.4.1	Compressive Axial Load Test Results	135
7.4.2	Compressive Oblique Load Test Results	137
7.4.3	Horizontal Load Results	139
7.5	Experimental Observations	141
7.5.1	Surface Displacement Prior to Loading	141
7.5.2	Surface Displacement Post Loading	143
Chapter 8:	Numerical Pile Model Development and Verification	145
8.1	General	145
8.2	Numerical Model Algorithms and Behaviour Criteria	145
8.2.1	General Finite Element Algorithms	146

8.2.2	Implementation of Constitutive Model into Finite Element Model	149
8.2.3	Implementation of Interface Frictional Criteria in Finite Element Model	152
8.2.3.1	Surface-Based Contact	153
8.2.3.2	Contact Elements	155
8.2.3.3	Models of Interaction	155
8.2.4	Initial Stress States	158
8.3	Construction of Finite Element Model in ABAQUS	161
8.3.1	Problem Geometry and Boundary Conditions	161
8.3.2	Finite Element Pile Mesh	164
8.4	Verification of ABAQUS Pile Model	166
8.4.1	Predictions for Cast-In-Place Piles	166
8.4.2	Predictions for Impact Driven Piles	169
8.4.3	Discussion of Verification Results	171
Chapter 9:	Oblique Interaction Charts for Piles	178
9.1	General Introduction	178
9.2	Numerical Model Cases	178
9.3	Results from Numerical Analysis	188
9.4	Comparison of FEM Results with Other Theoretical Methods	195
9.5	Development of Three Dimensional Oblique Charts	198
9.5.1	General	198
9.5.2	Cast-in-Place Pile with Free and Fixed Head, and Up Thrust Combination Loading	199
9.5.3	Cast-in-Place Pile with Free and Fixed Head, and Compression Combination Loading	203
9.5.4	Impact Driven Pile with Free Head and Uplift Combination Loading	206
9.5.5	Impact Driven Pile with Free Head and Compression Combination Loading	209
9.5.6	Three-Dimensional Oblique Interaction Charts	210
9.6	Influence of Oblique Load on Displacement	216

Chapter 10: Discussion of Numerical Results for Piles	219
10.1 General	219
10.2 Oblique Interaction Charts and Comparison with Experimental Data	219
10.3 Comparison between Numerical and Theoretical Results	227
10.4 Influential Factors on Design Charts	230
10.4.1 Soil Properties	230
10.4.2 Influence of Pile Installation Technique	231
10.4.3 Influence of Vertical Stress Fields	232
10.4.4 Pile Head Fixity	233
10.5 Influence of Pile Shape	234
10.6 Design Examples	235
10.6.1 Determining the Ultimate Load of an Example Pile	235
10.6.2 Determining the Pile Head Displacement of an Example Pile	237
 Chapter 11: Conclusions and Recommendations	 239
11.1 Conclusions and Recommendations for Shallow Foundations	239
11.2 Conclusions and Recommendations for Pile Foundations	240
 REFERENCES	 243
 APPENDIXES	
Appendix A: Probability of Failure - Shallow Foundations	253
Appendix B: Texas '94 Symposium SPT Results and Interpretation	266
Appendix C: Small Scale Model Test Pile Procedures	272
Appendix D: Laboratory Testing Results for Experimental Sand	278
Appendix E: Experimental Results from Model Piles	292
Appendix F: Mesh Configuration of Constructed Pile	304
Appendix G: ABAQUS Code	307
Appendix H: Verification Results	320
Appendix I: ABAQUS Case Results	332
Appendix J: Sample Calculations	401
Appendix K: Pile Article	406

LIST OF TABLES

<u>Table</u>	<u>Description</u>	<u>Page</u>
1.1	Current techniques for pile design in granular soil	6
2.1	Reliability results by Tan and Duncan (1991)	13
2.2	Reliability results by Berardi and Lancellotta (1994)	14
2.3	Reliability results by Sivakugan and Johnson (2002)	14
2.4	Recommended coefficients of variation (Harr, 1987)	16
2.5	Summary of statistical parameters (Johnson, 1999)	22
3.1	The probability of exceeding 25mm settlement in field	32
4.1	Standard field-testing procedure	43
4.2	Some selected correlations for sand friction angles in terms of blow counts	48
4.3	Commonly used correlations to determine friction angle of experimental sand	54
4.4	Dilation angle for experimental sand	57
4.5	Popular correlations for Young's modulus (E) of sand using SPT results	59
4.6	Final correlations for E_s based on a study of available popular correlations	64
4.7	Typical ranges for Poisson's ratio of sand	65
5.1	Footing and general soil characteristics for symposium	66
5.2	Footing dimensions and assumed soil profile under footings	78
5.3	Author's FEM results for symposium footings	88
5.4	Prediction comparison for individual predictors	89
5.5	FEM Comparison	92
6.1	Ultimate loads for Prideaux (1998) model piles in dense sand	98
6.2	Ultimate loads for Prideaux (1998) model piles in saturated loose sand	98
6.3	Advantages/disadvantages of various settlement prediction methods	107
7.1	Number of tests for each load case	129
7.2	Grain size distribution	129

7.3	Sand characteristics	130
7.4	Experimental sand bed properties	133
7.5	Sand material properties	133
8.1	Case study results.	175
9.1	Results from the numerical modelling of free head, cast-in-place, and uplift combination-loaded piles	189
9.2	Results from the numerical modelling of free head, cast-in-place, and compression combination-loaded piles	191
9.3	Results from the numerical modelling of fixed head, cast-in-place, and uplift/compression combination-loaded piles	192
9.4	Results from the numerical modelling of free head, impact driven, and uplift combination-loaded piles	193
9.5	Results from the numerical modelling of free head, impact driven, and compression combination-loaded piles	194
9.6	Comparison of numerical results against existing techniques	196
9.7	Design ratios for uplift cast-in-place free head piles	200
9.8	Design ratios for uplift cast-in-place fixed head pile	202
9.9	Design ratios for compression cast-in-place free head piles	204
9.10	Design ratios for compression cast-in-place fixed head piles	205
9.11	Design ratios for uplift impact driven free head piles	207
9.12	Design ratios for down thrust impact driven free head piles	209
10.1	Experimental small-scale test pile results conducted as part of current research	221
10.2	Experimental small-scale test pile results conducted by Prideaux (1998)	222

LIST OF FIGURES

<u>Figure</u>	<u>Description</u>	<u>Page</u>
1.1a	Typical failure mechanism for shallow footing (Craig, 1992)	1
1.1 b	Typical construction layout for shallow footing (http://www.ce.washington.edu/~liquefaction/selectpiclique/kobe95/foundation1.jpg)	1
1.2	Typical cast-in-place pile layout (http://www.valpo.edu/clir/images/construction/092602/092602-2.jpg)	2
1.3	Bunces Pile Enginer (left) and Vaulone's Pile Engine (right) (http://www.geoengineer.org/oldpiles.html)	4
2.1	Reliability	11
2.2	Actual settlement versus predicted settlement using Terzaghi and Peck	18
2.3	Actual settlement versus predicted settlement using Burland and Burbidge	18
2.4	Actual settlement versus predicted settlement using Berardi and Lancellotta	19
2.5	Actual settlement versus predicted settlement using Schmertmann	19
2.6	Space of Pearson's probability distributions	21
2.7	Schematic representations of probability distributions	21
3.1	The histogram and beta distribution of settlement ratios for Terzaghi and Peck (1967) method	25
3.2	The histogram and beta distribution of settlement ratios for Burland and Burbidge (1985) method	26
3.3	The histogram and beta distribution of settlement ratios for Schmertmann et al. (1978) method	26
3.4	The histogram and beta distribution of settlement ratios for Berardi and Lancellotta (1994) method	27
3.5	The design chart for Terzaghi and Peck (1967) method	28
3.6	The design chart for Schmertmann et al. (1978) method	29
3.7	The design chart for Burland and Burbidge (1985) method	30

3.8	The design chart for Berardi and Lancellotta (1994) method	31
4.1	Ideal stress-strain material assumed for most structural materials	35
4.2	Stress-strain relationship for elasto-plastic material	35
4.3	Typical linear elastic and non-linear elastic soil response	38
4.4	Mohr-Coulomb failure line	39
4.5	Mohr-Coulomb failure surface (Chen and Saleeb, 1983)	40
4.6	Drucker-Prager failure surface (Chen and Saleeb, 1983)	41
4.7	Typical shear stress (τ) vs. effective normal stress (σ') relation for sand (Craig, 1992)	46
4.8	Typical shear stress (τ) vs. axial strain (ϵ_a) for a sand (Craig, 1992)	47
4.9	Shear stress vs. axial strain for experimental sand	50
4.10	Shear stress vs. effective normal stress for experimental sand	50
4.11	Typical plot of void ratio vs. horizontal displacement for sand (Craig, 1992)	51
4.12	Void ratio vs. axial strain for experimental sand	51
4.13	Relationship between vertical effective stress and field blow count N (Alpan, 1967)	53
4.14	Typical vertical displacement vs. horizontal displacement plot for sand (Yasufuku et al., 2004)	56
4.15	Horizontal displacement vs. vertical displacement for experimental sand	56
4.16	Approximation of dilation, ψ (Bolton, 1987)	57
4.17	Typical stress-strain relationship for sand	58
4.18	Non-dimensional Young's modulus vs. field blow count for normally consolidated sand	62
4.19	Non-dimensional Young's modulus vs. field blow count for preloaded sand or sand exposed to driving forces	62
4.20	Line of best fit for non-dimensional Young's modulus vs. field blow count of normally consolidated sand	63
4.21	Line of best fit for non-dimensional Young's modulus vs. field blow count of preloaded sand or sand exposed to pile driving forces	63

5.1a	Cross-section A-A	67
5.1b	Layout of test footings for Federal Highway Administration Symposium	68
5.2	The bearing capacity failure diagram from Terzaghi (Cernica, 1995)	70
5.3	The domain example for finite element problem	71
5.4	Idealized sensitivity plot	72
5.5	Shallow footing coarse mesh	72
5.6	Shallow footing medium mesh	73
5.7	Shallow footing fine mesh	73
5.8	Shallow footing quadratic mesh	74
5.9	Lines of symmetry for square footing	75
5.10	Final model boundary conditions	75
5.11	Displacement of rigid footing under load	76
5.12	Footing 1 load-displacement prediction	81
5.13	Footing 2 load-displacement prediction	82
5.14	Footing 3 load-displacement prediction	83
5.15	Footing 4 load-displacement prediction	84
5.16	Footing 5 load-displacement prediction	85
5.17	Frequency histogram for techniques in symposium	87
5.18	Footing 1 comparative histogram	90
5.19	Footing 2 comparative histogram	90
5.20	Footing 3 comparative histogram	91
5.21	Footing 4 comparative histogram	91
5.22	Footing 5 comparative histogram	92
6.1	Vertically installed pile subjected to oblique loading	96
6.2 a)	Experimental results from Eckersley et al. (1996)	99
6.2 b)	Interaction diagram for horizontal and vertical components	99
6.3	In-plane and out-of-plane loading of a pile	100
6.4	Cast-in-place pile installation process	101
6.5	Impact driven pile installation process	102
6.6	Forces acting on a single axially loaded pile	104
6.7	Pile subjected to uplift forces	110
6.8	Generalized forces acting on a laterally loaded short rigid pile	111

6.9	Typical meshed problem domain for FEM	116
7.1	Experimental model pile	121
7.2	Influence zone for a typical driven pile	122
7.3 (a)	Photo of axial loading arrangement	
7.3 (b)	Schematic of axial loading arrangement	124
7.4	Oblique loading cap, axial loading cap, horizontal loading saddle, respectively	125
7.5 (a)	Photo of lateral loading arrangement	125
7.5 (b)	Schematic of lateral loading arrangement	126
7.6 (a)	Photo of oblique loading arrangement	
7.6 (b)	Schematic of oblique loading arrangement	127
7.7	Sieve analysis of experimental sand	130
7.8	Vibrating plate for compaction	132
7.9	Plan view of sand tank and pile layout	
	Note: All dimensions have units of mm	134
7.10	Load-displacement curve for axial load in loose soil	136
7.11	Load-displacement curve for axial load in dense soil	136
7.12	Load-displacement curve for axial load in layered soil	137
7.13	Load-displacement curve for oblique load in loose soil	138
7.14	Load-displacement curve for oblique load in dense soil	138
7.15	Load-displacement curve for oblique load in layered soil	139
7.16	Load-displacement curve for horizontal load in loose soil	140
7.17	Load-displacement curve for horizontal load in dense soil	140
7.18	Load-displacement curve for horizontal load in layered soil	141
7.19	Surface disturbance from placement in loose soil	142
7.20	Surface disturbance from placement in dense soil	143
7.21	Horizontal load on pile with failed pile in foreground	144
7.22	Average surface indentations after pile removal	144
8.1 (a)	Linear elements	147
8.1 (b)	Quadratic elements	148
8.2	Bending nature of linear elements	148
8.3	Penetration restriction between slave and master surfaces (Hibbett et al., 2001)	155
8.4	Interaction between contact pressure and shear stress at	

	interface surface	156
8.5	Relative movement between pile and soil due to surface-based contact	157
8.6	Influence of initial stress in Mohr-Coulomb failure criterion	158
8.7	Initial stress field due to self weight of system	160
8.8	Plan view of axially loaded pile showing line of symmetry	161
8.9	Plan view of obliquely loaded circular pile showing	162
8.10	Boundary conditions for obliquely loaded pile	163
8.11(a)	Plan view of problem	163
8.11(b)	Elevation view of pile-soil problem	163
8.12	Illustrative view of mesh adopted	164
8.13	Case study 1 - large scale, cast-in-place, axial compression loading	167
8.14	Case study 2 - large scale, cast-in-place, axial compression loading	168
8.15	Case study 3 - large scale, cast-in-place, axial uplift loading	168
8.16	Case study 4 - smaller scale, placed in tank, lateral loading	169
8.17	Case study 5 - large scale, impact driven, compression loading	170
8.18	Case study 6 - large scale, impact driven, compression loading	170
8.19	Case study 7 - large scale, impact driven, lateral loading (Hage-Chehade ,1991)	172
8.20	Load-displacement curve for typical pile	173
9.1	The chosen hypothetical numerical modelling cases	180
9.2	Example of pile head fixity	181
9.3	Pile loading (a) Compression load combination (b) Uplift load combination	182
9.4	Typical pile response	183
9.5	Graphical representation of load ratio	185
9.6	Example of load-displacement curve for pure axial uplift of case pile	185
9.7	Example of applied moment	186
9.8	Example of non-dimensional behaviour for Case 18	187
9.9	Example of how failure loads were approximated from numerical results	188

9.10	3D design ratio plot for cast-in-place piles with uplift loading scenarios	199
9.11	3D design ratio plot for cast-in-place piles with compression loading scenarios	206
9.12	3D design ratio plot for impact driven piles with uplift loading scenarios	208
9.13	3D design ratio plot for impact driven piles with compression loading scenarios	210
9.14	2D ratio plots for uplift combination loading scenarios	211
9.15	2D ratio plots for compression combination loading scenarios	212
9.16	2D plot of a cast-in-place lateral pile ratio vs. axial uplift pile ratio	215
9.17	Relationship between load ratios and displacement ratios for uplift combination, free/fixed head CIP and ID piles	217
9.18	Relationship between load ratios and displacement ratios for compression combination, free head CIP and ID piles	218
10.1	Comparison between experimental and design surface for uplift combination loading	224
10.2	Comparison between experimental and design surface for compression combination loading	224
10.3	Estimated point of contraflexure for a $L/d=3$ pile in sand, with $N=5$ based on works by Poulos and Davis (1980)	228
10.4	Estimated point of contraflexure for a $L/d=3$ pile in sand, with $N=5$ based on numerical modelling	228
10.5	Estimated point of contraflexure for a $L/d=10$ pile in sand, with $N=30$ based on works by Poulos and Davis (1980)	229
10.6	Estimated point of contraflexure for a $L/d=10$ pile in sand, with $N=30$ based on numerical modelling	229
10.7	Influence of initial stress in Mohr-Coulomb failure criteria	233

NOTATIONS

The following symbols have been used in multiple locations throughout the document.

<u>Symbol</u>	<u>Definition</u>	<u>Units</u>
a	minimum possible value for x	[-]
b	maximum possible value for x	[-]
B	width of footing	[m]
c	cohesion	[kPa]
C	axial compression component of oblique load	[kN]
C_{ER}	hammer efficiency factor	[-]
CIP	cast-in-place pile	[-]
C_N	overburden correction factor	[-]
d	pile diameter	[m]
D_r	relative density	[%]
e	void ratio (used in Chapter 4)	[-]
e	load eccentricity (used in Chapter 6)	[m]
e_{cv}	critical void ratio	[-]
E_s	Young's modulus for sand	[MPa]
FOS	factor of safety	[-]
H_u	ultimate lateral capacity under combined uplift and lateral load	[kN]
H_{ult}	ultimate horizontal load	[kN]
H_{uo}	ultimate lateral capacity under pure lateral load (used by Eckersley et al.(1996))	[kN]
ID	impact driven pile	[-]
K_o	at rest earth coefficient	[-]
L	lateral load	[kN]
L_b	embedment length of pile	[m]
M	applied moment	[kN.m]
M_{ult}	ultimate moment capacity of the pile	[kN.m]
N	uncorrected blow count or field blow count	[blows/100mm]
N_{60}	blow count corrected for hammer efficiency	[blows/100mm]

$(N_1)_{60}, N_{\text{corr}}$	blow count corrected for hammer efficiency and overburden	[blows/100mm]
p_a	atmospheric pressure	[kPa]
p_f	probability of failure	[-]
p_u	soil pressure at depth z	[kPa]
q_f	ultimate failure pressure on footing	[kPa]
q_o	surcharge on soil surface	[kPa]
Q_b	end bearing load	[kN]
Q_f	shaft friction load	[kN]
Q_{ult}	ultimate bearing load	[kN]
S_x	standard deviation	[-]
T_{un}	net uplift capacity	[kN]
T_{ug}	gross uplift capacity	[kN]
u	pore water pressure	[kPa]
u_x	displacement of the centre of the pile head in x-direction	[mm]
u_y	displacement of the centre of the pile head in y-direction	[mm]
u_z	displacement of the centre of the pile head in z-direction	[mm]
U	axial uplift	[kN]
W	effective weight of the pile	[kN]
x	settlement ratio	[-]
\bar{x}	average settlement ratio	[-]
z	depth from soil surface	[m]
Z_r	depth of rotation point	[m]
$\beta(1)$	coefficient of skewness	[-]
$\beta(2)$	coefficient of kurtosis	[-]
ε_a	axial strain	[-]
ε_x	normal strain in x direction	[-]
ε_y	normal strain in y direction	[-]
ε_z	normal strain in z direction	[-]
ϕ	friction angle	[°]

ϕ'_{cv}	effective friction angle at critical void \approx residual effective friction angle	[°]
ϕ'_{max}	peak effective friction angle	[°]
σ	normal stress	[kPa]
σ_f	failure normal stress	[kPa]
σ'_v	effective vertical stress Overburden Pressure	[kPa]
σ_x	normal stress in x direction	[kPa]
σ_y	normal stress in y direction	[kPa]
σ_z	normal stress in z direction	[kPa]
σ_1	major principle stress	[kPa]
σ_2	intermediate principle stress	[kPa]
σ_3	minor principle stress	[kPa]
τ	shear stress	[kPa]
τ_f	failure shear stress	[kPa]
ρ	density of sand and pile	[kg/m ³]
μ	coefficient of friction	[-]
ψ	dilation angle (ψ)	[°]

CHAPTER 1: Introduction

1.1 General

Foundations are structural components that enable loads to be transferred into the subsoil. The type of foundation required depends on a number of factors including soil strength, soil type, load magnitude and costing. Foundations are generally categorised as deep and shallow and are described below:

- Shallow foundations are structural elements that tend to be wider than deep. Examples of shallow foundations include strip and pad footings. Shallow footings transfer the load primarily via bearing at the footing soil interface, as presented in Figure 1.1a. A photo of a strip footing is also presented in Figure 1.1b.

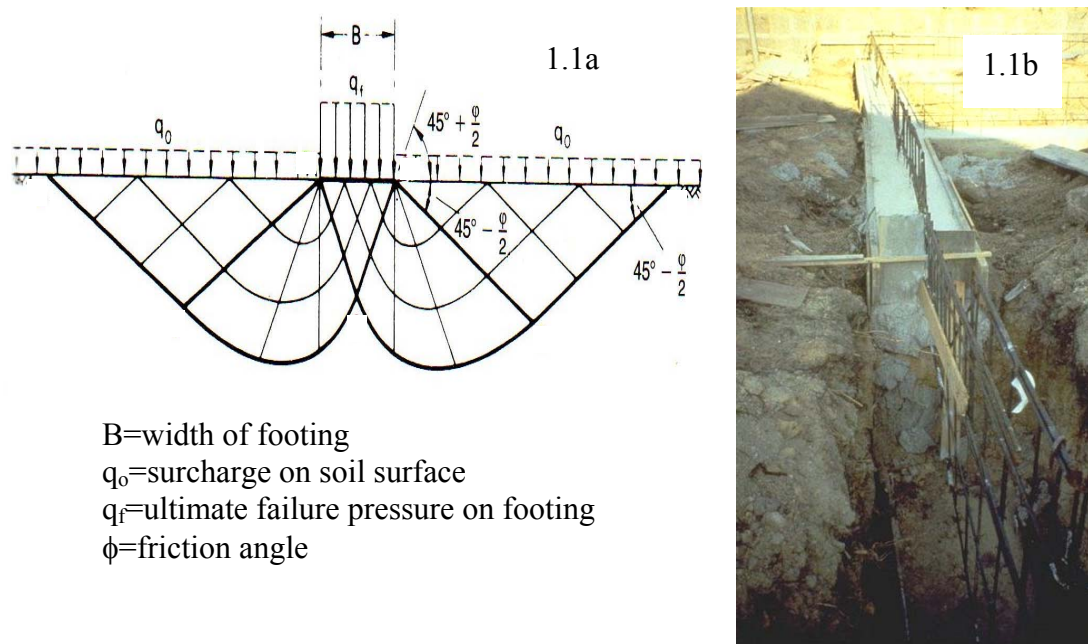


Figure 1.1 a: Typical failure mechanism for shallow footing (Craig, 1992)

1.1 b: Typical construction layout for shallow footing

(<http://www.ce.washington.edu/~liquefaction/selectpiclique/kobe95/foundation1.jpg>)

- As a general rule deep foundations are considered to be deeper than wide. Examples of deep foundations are piles, piers and barrettes. The installation, loading direction and construction of deep foundations such as piles vary with project and location. As the loading direction on the pile changes so too does the

failure mechanism within the soil. A typical pile layout for a tall building is depicted in Figure 1.2.



Figure 1.2: Typical cast-in-place pile layout

(<http://www.valpo.edu/clir/images/construction/092602/092602-2.jpg>)

When designing shallow and deep foundations in granular soil two aspects are considered:

1. Bearing capacity and skin friction capacity of the soil surrounding the foundation.
2. Predicted settlement/displacement of the foundation within the granular soil.

The loading capacity of the soil and the displacement under load are functions of a foundation's geometry, and the granular soil properties.

For a shallow foundation in sand, the settlement criterion usually governs the design where footings are larger than 1.5 m (Beradi and Lancellotta 1994; Jeyapalan and Boehm 1986; Tan and Duncan 1991). Design engineers aim at ensuring excessive settlement does not occur beneath the footing, while at the same time producing a cost efficient foundation design. Then the choice of the settlement prediction model is very important, as the predicted settlement usually governs the size of the shallow foundation. There are a number of techniques available for predicting the settlement of

a shallow foundation in granular soil. This makes the task of estimating the settlement of a shallow foundation difficult for many engineers.

In the case of deep foundations, the load transfer mechanism between the deep foundation and surrounding soil is more complex than their shallow counterpart. Deep foundations such as piles tend to transfer structural loads through a series of interactions at the pile-soil interface. Due to the depth and complexities of deep foundations, it is difficult to accurately define the interactions that take place when the pile is under a load. Various researchers have used a number of assumptions regarding the true interactions between the pile and soil. The assumptions have been based on limited observations made from test and instrumented model piles. Like shallow foundations, numerous methods have been derived to assess the behaviour of a pile under pure axial, lateral and moment loads.

1.2 History of Shallow and Pile Foundations

Since the start of civilisation buildings of varying size and geometry were constructed. Many of the buildings were founded on soil and hence foundations were used. The science involved in designing foundations has evolved with the march of time and technology. Shallow foundations were constructed out of materials such as rock in ancient times, or steel and concrete in more recent times. The range of pile installation techniques required researchers to explore the pile-soil interaction to greater depths.

The use of deep foundations such as piles can be traced back to the Romans, who used piers and piles to support roads and structures. The Roman piles were typically made out of stones and timber. The use of cedar oil was common to prolong the functional life of the timber piles. Some evidence of pile construction in past civilisations can still be seen in various regions throughout the world.

The design of Roman piles was linked to the technology available at that time. As civilisation progressed into the industrial age, it allowed for new innovative approaches in pile design and installation. Some early devices to improve the pile installation process for timber piles include the Bunces Pile Enginer and Vaulone's Pile Engine, which are shown in Figure 1.3. These machines were developed before

the 1800s and work on a similar principle to the modern day pile driving rigs. The Bunces Pile Engine and Vulone's Pile Engine allow a man to winch a rope, thus elevating a weight above the timber pile. Then the weight is released and hammers the pile into the ground.

Modern day piles are often made of steel, timber, concrete or a combination of these materials. There are currently several ways to install pile foundations, and two of the most common techniques are cast-in-place and impact-driven. These methods are reviewed in more detail in Chapter 5.

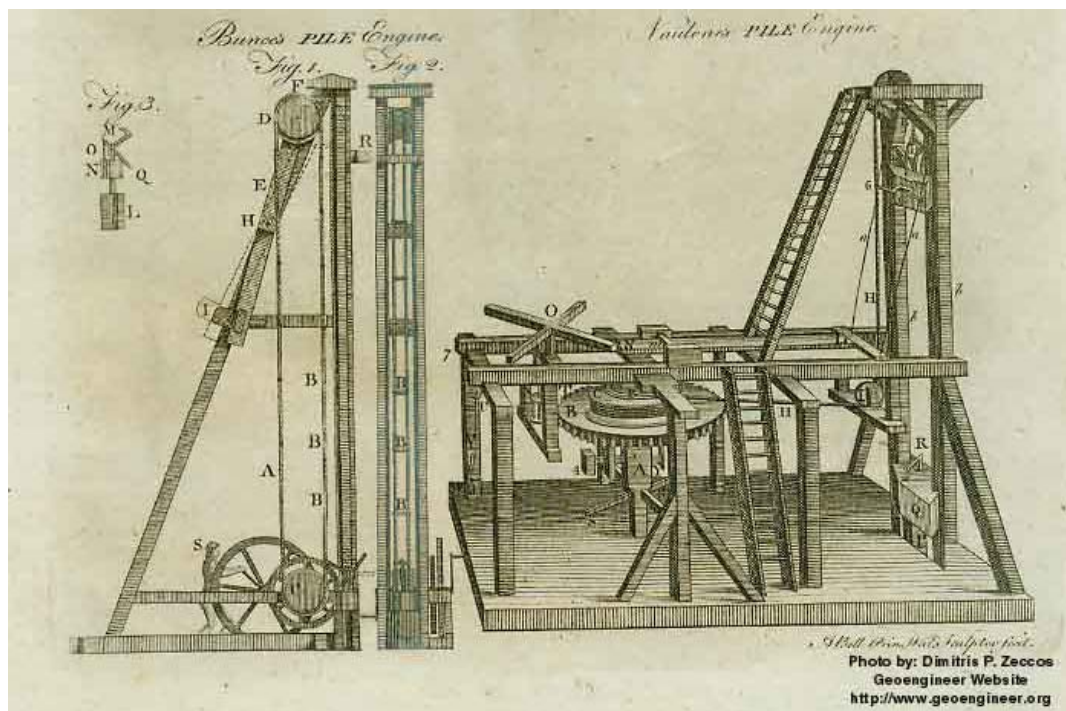


Figure 1.3: Bunces Pile Enginer (left) and Vaulone's Pile Engine (right)

(<http://www.geoengineer.org/oldpiles.html>)

1.3 Research Objectives and Aims

As a general rule, piles are used when the bearing capacity and settlement criteria cannot be satisfied with shallow foundations. Designers choose pile foundations over shallow foundations under the following conditions:

- Predicted settlement of a shallow foundation is expected to exceed serviceability limit state.

- Differential settlement under a structure is excessive.
- The bearing capacity of the soil is not sufficient to support shallow foundations.
- When faced with possible scour problems in creeks, rivers and coastal belts.

Therefore, the question one has to ask is what techniques are appropriate to use for predicting the bearing capacity and settlement of a foundation design? The procedures associated with bearing capacity tend to be better documented and defined than the settlement prediction methods. Some recent works discussing bearing capacity under combined loading can be found in an article by Poulos et al. (2001).

The settlement prediction for shallow foundations can be more of a challenge, as there are 40+ methods available to estimate shallow foundation settlements (Douglas 1986). One possible way of comparing the differing methods for predicting shallow foundation settlement is to use a probabilistic approach.

As part of this work, a probabilistic analysis of four common shallow foundation settlement techniques has been investigated. These techniques include Terzaghi and Peck's method, Burland and Burbidge's method, Berardi and Lancellotta's method and Schmertmann's method. All the mentioned methods have been described in more detail in Chapter 2. The final results show the estimation of probability that the actual field settlements will exceed the design criteria. The probability of failure for each of the settlement techniques has been given in an easy-to-use design chart.

The literature review of shallow foundations and foundations in general led to the second and major focus of this research. The design techniques for a pile in granular soil subjected to varying load combinations were not well developed. An overview of the design techniques to predict pile bearing capacity and settlement is presented in Table 1.1.

Some typical applications for pile foundations can be seen under large buildings, portal frames, sheds, pontoons and oil platforms. These types of structures can place a range of loading combinations on the pile including axial (tension/compression) forces, lateral loads and moments as shown in Table 1.1. The current design techniques can account for any of the above individual loading scenarios. However, in the field these loads

rarely exist individually and they often act in unison. The exact influence an axial load, lateral load or moment has on each other's failure mechanism is not clearly understood, as discussed in Chapter 5. Investigations by some researchers have indicated that when a lateral component is added to an axial load, the ultimate vertical load carrying capacity of the pile can decrease dramatically.

Table 1.1: Current techniques for pile design in granular soil

Load Type	Are there techniques available to determine ultimate capacity?	Are there techniques available to determine pile head displacement?
Axial compression	Yes	Yes
Axial uplift	Yes	Yes
Lateral	Yes	Yes
Moment	Yes	Yes
Combined axial compression and lateral loads	Some semi-empirical data available based on small-scale modelling.	No
Combined axial uplift and lateral loads	No (some limited field and laboratory test data available)	No
Combined lateral and moment loads	Yes	Yes
Combined axial compression, lateral and moment	No	No
Combined axial uplift, lateral and moment	No	No

Finite Element Method (FEM) is a rational tool to analyse the complex nature of pile foundations under loading. However, the computational method is limited by input data available and idealised algorithms, such as constitutive models that describe the behaviour of soil and pile once loaded. The method requires experimental work to verify output, and a realistic input for the constitutive properties and in situ stresses.

Structure failures from combined loading in sand can lead to collapses, and excessive pile head displacement. As the knowledge of the failure mechanisms for combined loading increases, an improved factor of safety can be achieved.

Finite Element Method (FEM) was used to study the effects of combined loads on pile capacity and settlement. Three-dimensional interaction diagrams were developed for the bearing capacity of a combined loaded pile. The displacement of the pile head from axial and lateral loads acting together was also investigated. The results from the displacement analysis were summarised into an easy-to-use design chart.

A brief summary of the work covered in this thesis is as follows:

- A statistical analysis was used to formulate a set of probabilistic design charts for shallow foundations. The charts allow design engineers to estimate the probability that the predicted settlement using Terzaghi and Peck's method, Schmertmann's method, Burland and Burbidge's method, and Berardi and Lancellotta's method will exceed the actual field settlement. The charts show that using one design settlement criterion for every method may not be a suitable assumption, unless the criterion is conservative.
- The Federal Highway Administration in 1994 held a symposium to compare techniques for predicting the settlement of five shallow foundations. Thirty-one predictors took part in the study and provided estimates for the shallow foundations. In this thesis, the five foundations were modelled using the finite element computer software package entitled ABAQUS (Hibbitt et al., 2001). The results from the modelling have been compared against the predictions made by the 31 participants in the symposium, and the actual test results.
- The major focus of this research was on the influence of combined loading for piles. It is noted that the term 'combined loading' refers to the presence of axial compression/uplift loads, lateral forces and moments all acting on the pile head at the same time. In Table 1.1, it is shown that there has been little investigation into the effects of combined loading on the pile capacity and pile head

displacement. The work in this thesis explores this apparent gap in the pile literature. Three-dimensional ultimate capacity diagrams have been developed to aid in predicting the ultimate load components that may be placed simultaneously on a pile. This includes allowances for uplift and compression axial components.

- The influence on pile head displacement under combined axial and lateral loads is also provided in the form of easy-to-use design charts. The pile section of this thesis was completed using a verified finite element model in the computer package ABAQUS. The ABAQUS model had to be constructed in three-dimensional space given the geometry and loading scenarios to be explored. The model also allowed for elastic and plastic deformations in conjunction with a complicated pile-soil interface. This resulted in many difficulties as a converged solution using implicit formulations became a challenge, but an outcome was achieved by taking into consideration vertical and horizontal stresses due to the gravity field in the sand body.

1.4 Thesis Overview

The work on the shallow foundations is discussed in Chapters 1 to 5, and Chapter 11. A brief literature review of five popular shallow foundation settlement techniques is given in Chapter 2, plus the definitions of some common statistical terms that are used in various sections of the document. An easy-to-use design chart developed from a statistical analysis can be found Chapter 3. The design chart allows users to assign a probability of failure that a shallow footing will exceed an actual settlement in the field.

The variances between the five shallow foundation methods in Chapters 2 and 3 are partially due to assumptions on the constitutive behaviour, as shown in Chapter 4. In this chapter some of the available constitutive relations and correlations to determine the constitutive properties were explored. A set of empirical correlations based on the work of several researchers was chosen to estimate the constitutive properties.

These empirical correlations are given in Chapter 4, and they are used to define the constitutive behaviour of the sand in the numerical models of the document. The

empirical correlations were placed into a numerical model that estimated the response of square shallow foundations, to explore the validity of the empirical correlations chosen in Chapter 4.

The shallow foundation numerical model in Chapter 5 was developed as part of the work of this thesis. The solutions given by the numerical model for the settlement of five full-scale footings from a prediction symposium were compared against actual results. After comparing the actual test data with the numerical model output, conclusions were reached regarding the suitability of the assumed empirical correlations and the model used. The conclusions are also discussed in Chapter 5.

The work associated with the pile research can be seen in Chapters 6 to 11. A pile literature review is also given in Chapter 6, which reviews common methods for predicting pile bearing capacity and displacement. In this chapter some key issues that influence pile behaviour under load is discussed. From the pile literature review, it was decided by the author to explore the impact of combined loading on pile response. The pile research was completed using small scale modelling given in Chapter 7, and numerical modelling shown in Chapters 8 to 10.

A pile numerical model was developed in a finite element computer software package ABAQUS, as shown in Chapter 8. The model was compared against actual results for a range of piles under a variety of loading conditions, to define the accuracy of the model. The results from the verification exercise can be seen in Chapter 8. The verified pile model was used to examine the influence of combined loading on pile behaviour, with the help of a series of hypothetical cases chosen by the author. The results from the pile numerical analysis is shown in Chapters 9 and 10, along with a discussion regarding trends on the impact of pile ultimate capacity and pile head displacement.

The conclusions based on the work from the research, and recommendations for further research are presented in Chapter 11.

CHAPTER 2: Literature Review – Shallow Foundations

2.1 General

There are numerous techniques available for predicting the settlement of shallow foundations as discussed in Chapter 1. The developers of each method have based their theories on theoretical and semi-empirical correlations, and this results in differences between the individual methods. Hence the estimated settlement of a footing may differ significantly from method to method. What settlement prediction technique is more appropriate to use becomes a key issue for designers. Tan and Duncan (1991) said:

‘It is important that engineers who design footings on sand understand the accuracy with which settlements can be estimated, and the reliability of the estimates they make’.

This work gives charts to predict the probability of a method exceeding the pre-defined settlement criterion. The study has been founded and expanded on probabilistic research completed by Tan and Duncan (1991), and by this author (Sivakugan and Johnson, 2002). Tan and Duncan compared twelve shallow foundation settlement techniques by determining the accuracy and reliability of each method, as discussed further in Section 2.2.

2.2 Accuracy and Reliability

Tan and Duncan (1991) completed a reliability study on twelve settlement prediction methods. They compared methods by determining the ‘accuracy’ and ‘reliability’ of each technique. The terms ‘accuracy’ and ‘reliability’ as defined by Tan and Duncan (1991) are as follows:

Accuracy: the average value of calculated settlement divided by measured settlement.

Reliability: the percentage of the cases for which the calculated settlement is greater than or equal to the measured settlement. This is shown in Figure 2.1.

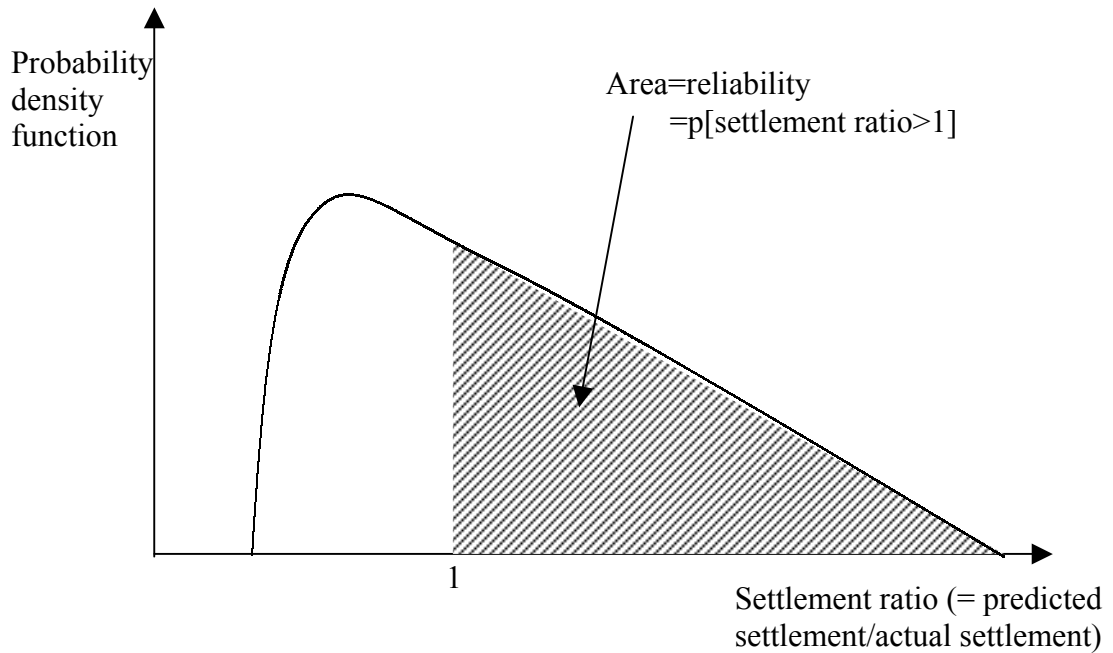


Figure 2.1: Reliability

A settlement prediction method that has accuracy equal to one and reliability equal to 100% is ideal. The method predicts the exact settlement which occurs in the field. Tan and Duncan (1991), and Berardi and Lancellotta (1994) did reliability studies on various methods for settlement prediction. This author also completed a reliability study of four popular settlement techniques developed by the following researchers:

- Terzaghi and Peck
- Burland and Burbidge
- Berardi and Lancellotta
- Schmertmann

It is important to review the four methods before comparing the reliability results from Tan and Duncan (1991), Berardi and Lancellotta (1994), and Sivakugan and Johnson (2002).

2.3 Shallow Foundation Settlement Prediction Methods

An overview of the four settlement techniques is given in the following sections.

2.3.1 *Terzaghi and Peck Method*

Terzaghi and Peck (1948) developed an empirical method for determining the settlement of a shallow foundation in granular soil. This empirical method is one of the oldest techniques used for settlement prediction.

Terzaghi and Peck set up a number of load tests on an experimental 300*300 mm square plate. The plate was loaded a number of times and the settlement for each load was recorded. This experiment was performed in three types of sand. Each type of sand had a constant relative density, i.e. each type of sand should have a constant standard penetration test blow count (N).

An empirical correlation was established between the settlement of the experimental plate and the settlement of a footing under the same load. The final equation shows the settlement of the footing is a function of the settlement from the 300*300 mm experimental plate, and the geometry of the footing.

2.3.2 *Burland and Burbidge Method*

Burland and Burbidge's empirical method for settlement prediction was based on a statistical analysis of 200 plus full-scale load tests (Craig, 1992). Burland and Burbidge treat sand in a similar way as to cohesive soils, and this resulted in a procedure based on the consolidation concept.

Relationships were found between the compressibility of the foundation subgrade (a_f), the width of the foundation (B), and the average value for the standard penetration (\bar{N}). The final settlement equation is based on the above relationships, and whether the sand is considered to be normally or over consolidated. Other factors may be incorporated into the Burland and Burbidge method, such as the shape of the footing, and the presence of bedrock within the influence zone below the footing.

2.3.3 Berardi and Lancellotta Method

Berardi and Lancellotta (1994) developed a settlement prediction model based on elastic analysis. They argue that it is incorrect to assume a single value for the stress-strain modulus for any one granular soil type. When considering the stress-strain curve for sand there is no linear region. This means the Young's modulus (E_s) of granular soil cannot be determined easily, unlike steel. Berardi and Lancellotta found a way to determine the 'exact' Young's modulus (E_s) value, corresponding to the strain level under the predicted loads. This method uses an iterative procedure resulting in a high calculation time compared with other methods.

2.3.4 Schmertmann Method

Schmertmann (1970) used model tests, elastic analysis and finite element analysis to obtain an equation for the vertical strain beneath the centre of a shallow footing. Schmertmann predicts that the vertical strain is a function of the applied pressure, Young's modulus of the soil and the strain influence factor.

Schmertmann (1970) related a homogenous Young's modulus for the soil to the cone penetration resistance of the sand.

2.4 Results from the Reliability Analysis

The results from the reliability studies conducted by Tan and Duncan (1991), Berardi and Lancellotta (1994), and Sivakugan and Johnson (2002) are displayed in Tables 2.1 to 2.3.

Table 2.1: Reliability results by Tan and Duncan (1991)

Method	Reliability (%)	Average Settlement Ratio (\bar{x})
Terzaghi and Peck	86	3.2
Schmertmann	70	2
Burland and Burbidge	52	1.45

Note: values in Table 2.1 obtained from accuracy and reliability plot.

Table 2.2: Reliability results by Berardi and Lancellotta (1994)

Method	Average Settlement Ratio (\bar{x})	Standard Deviation (S_x)	Coefficient of Skewness $\beta(1)$	Coefficient of Kurtosis $\beta(2)$
Terzaghi and Peck	2.79	1.93	0.8	2.94
Burland and Burbidge	1.56	0.88	0.74	3.04
Berardi and Lancellotta	0.94	0.58	0.72	2.94

Note: values extracted from Berardi and Lancellotta's data tables.

Table 2.3: Reliability results by Sivakugan and Johnson (2002)

Method	Reliability (%)	Average Settlement Ratio (\bar{x})	Standard Deviation (S_x)
Terzaghi and Peck	80.25	3.515	3.127
Burland and Burbidge	58.85	1.509	1.102
Berardi and Lancellotta	44.2	0.999	0.862
Schmertmann	71.36	2.656	2.085

A close examination of the above tables lead to the following conclusions:

1. The results for Terzaghi and Peck's method determined by Tan and Duncan (1991), and Sivakugan and Johnson (2002) were consistent with each other. Berardi and Lancellotta (1994) found that the average settlement ratio was lower for Terzaghi and Peck's method when compared to Tan and Duncan (1991), and Sivakugan and Johnson (2002). The difference in Berardi and Lancellotta's results could be due to the initial database chosen for their reliability study. Also the correction factors that Berardi and Lancellotta used such as the depth correction factor in the Terzaghi and Peck method may lead to different results.

2. The probabilistic parameters determined for Schmertmann, Burland and Burbidge, and Berardi and Lancellotta's settlement prediction methods were in reasonably close agreement, as shown in Tables 2.1 to 2.3.

From the four techniques listed in Tables 2.1 to 2.3, the review indicated that Terzaghi and Peck, and Schmertmann have developed methods that are more reliable than accurate. This may result in unnecessarily large shallow footings that are not cost efficient. Berardi and Lancellotta, and Burland and Burbidge have settlement prediction models that tend to be more accurate than reliable. The footings designed using less reliable models run a higher risk of settling more than the pre-decided settlement criteria in the field.

One possible reason for the variation could be the way researchers account for sand stiffness and sand properties in general. From the discussion in Section 2.5, it was noted that the predicted sand properties could be considered to be random variables due largely to the non-homogenous nature of the soil. This means that footing settlement must also be a random variable as it is a function of the sand property and geometry of the footing.

The possible variations seen between the methods leads to a question: is it appropriate to use the same settlement criterion for every settlement technique? For example, 25 mm is typically used as the maximum settlement limit regardless of the settlement technique used. The work in this thesis explores the probability of exceeding a particular settlement criterion for each of the four footing displacement techniques above. The results from the study are displayed in an easy-to-use design chart in Chapter 3.

2.5 Soil Variability

The settlement of a shallow foundation in granular soil is a function of the footing's geometry and the soil properties. Some variations in the predictions of settlement techniques could result from how a designer takes into account the sand stiffness parameters. The sand properties could be subject to variability, and this can affect the way researchers develop their methods. The potential for soil variability to impact on

the performance of a shallow footing increases as the footing size increases, i.e. the footing covers more ground surface. Also, if a series of shallow footings are connected via a suspended slab or beams, the variability of soil may result in the footings settling at different rates. Hence this causes stresses in the connecting components from the differential movement.

Sand properties cannot be determined precisely due to a number of reasons (Ang and Tang, 1975):

- Soil is not a homogenous material.
- Soil has a multi-layered structure.
- When taking field samples for laboratory testing, the orientation and sample size affects the values obtained for the soil parameters.
- It is difficult to obtain undisturbed samples from field investigations. This point applies more so to granular soil.
- Budget restraints dictate a limited number of field samples being taken from the investigation site and tested in the laboratory. As the number of field samples tested decreases, more uncertainty is introduced into the soil parameter values.

In reality soil properties are random variables each having a mean and standard deviation. The variability within soil properties are often much greater than those seen in other engineering materials, such as steel.

Harr (1987) recommends coefficients of variation for some soil parameters as given in Table 2.4. The coefficient of variation is defined as the standard deviation divided by the mean multiplied by 100%. The coefficient of variation describes the spread of the distribution. For example, when the coefficient of variation from the soil parameter increases there is more uncertainty introduced into the soil parameter.

Table 2.4: Recommended coefficients of variation (Harr, 1987)

Property	Symbol	Coefficient of Variation (%)
<u>Soil</u>		
Friction Angle (sand)	ϕ'	12
Cohesion	c	40
Unit Weight	γ	3
Cone Penetration	q_c	37
Standard Penetration	N	26
Porosity	n	10
Specific Gravity	G_s	2
Degree of Saturation	S	10
Coefficient of Permeability	K	90-240
Preconsolidation Pressure	σ'_p	19
<u>Load</u>		
Dead Load	DL	10
Live Load	LL	25
Wind Load	WL	37
Earthquake Load	EQ	100+

2.6 Statistical Review of Settlement for Shallow Footings

Statistical analyses are a good way of determining how accurate or reliable a prediction may be, and provide a platform where methods may be compared against each other. In previous work, this author conducted a statistical analysis on a set of data for 118 full-scale shallow foundations (Johnson, 1999). For each of the 118 cases, the actual settlements were known and compared against the four settlement prediction methods discussed in Section 2.3. A graphical representation of the scatter between the predicted settlement and the actual settlement is shown in Figures 2.2 to 2.5.

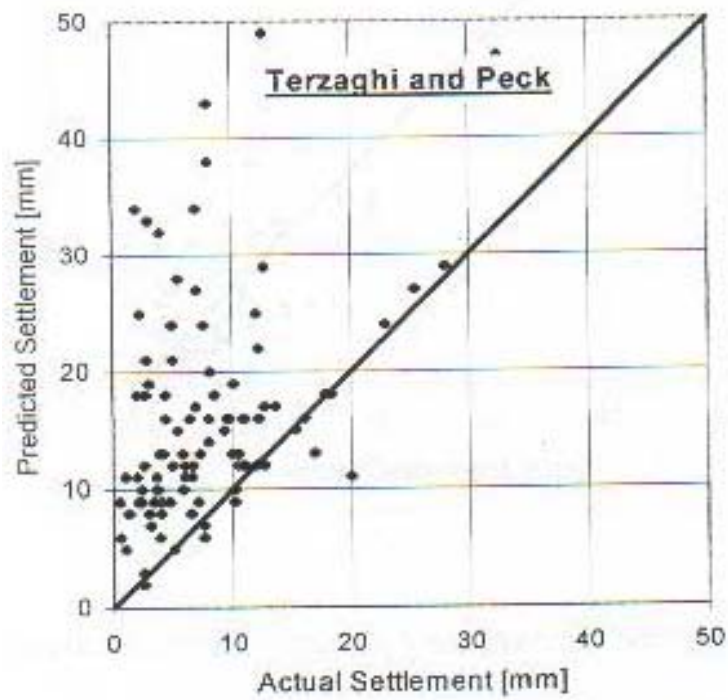


Figure 2.2: Actual settlement versus predicted settlement using Terzaghi and Peck

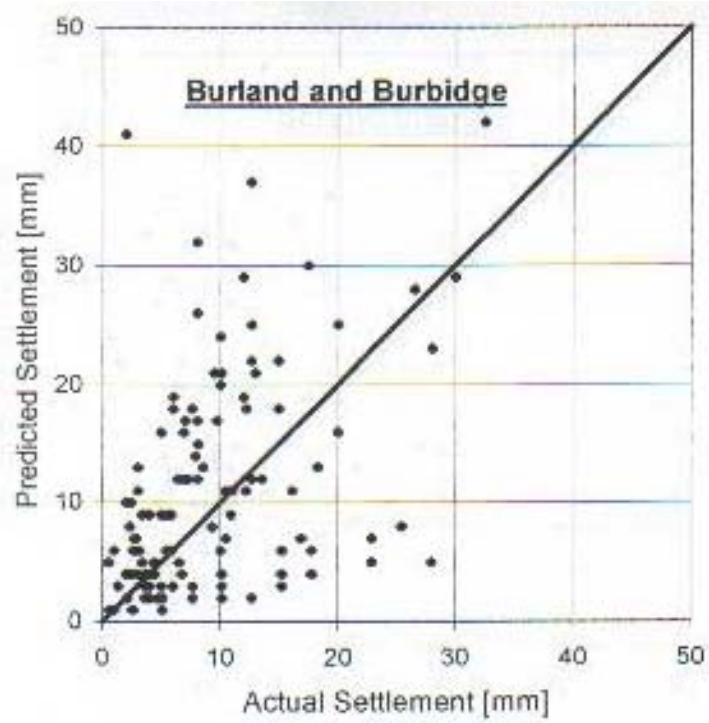


Figure 2.3: Actual settlement versus predicted settlement using Burland and Burbidge

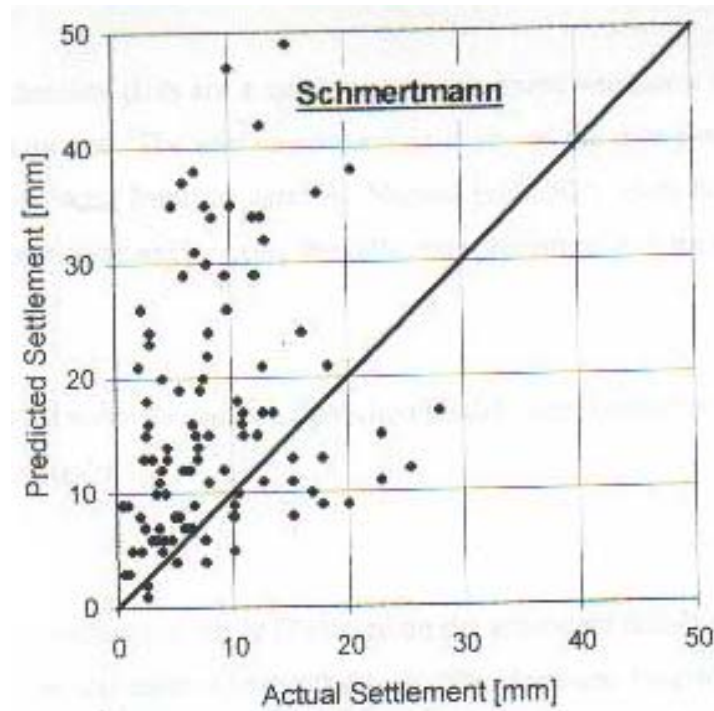


Figure 2.4: Actual settlement versus predicted settlement using Schmertmann

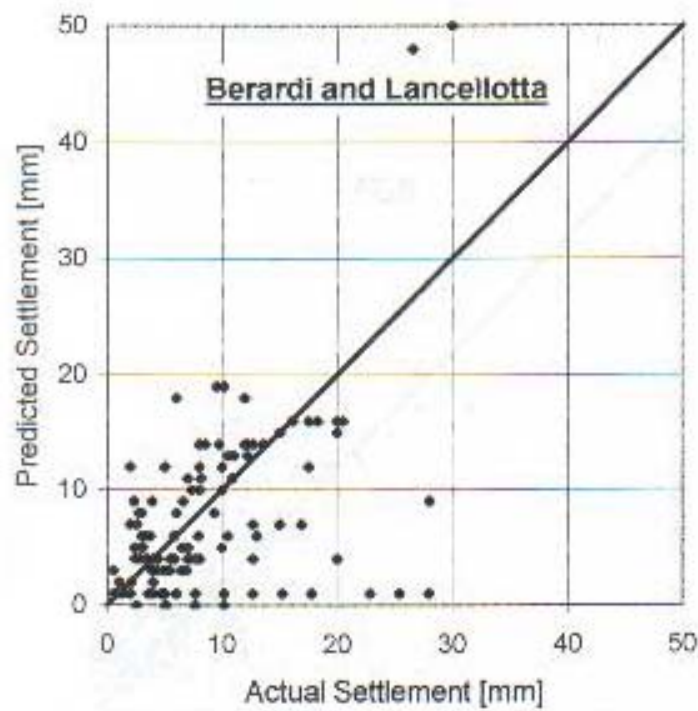


Figure 2.5: Actual settlement versus predicted settlement using Berardi and Lancellotta

The solid diagonal line in Figures 2.2 to 2.5 shows where the actual and estimated settlements are equal to each other. The points above the diagonal line represent the number of times the prediction method overestimated the settlement. The points below the line represent the number of times the estimated settlement underestimated the settlement.

A comparison between the individual points in Figures 2.2 to 2.5 in their present form could not be achieved. The predicted and actual settlements within the database were a function of the footing's geometry and soil properties. Direct comparison could only be made if the footings had the same geometry and soil properties. However, no two cases contained within the database were identical.

The settlement ratio (x) used in the current and previous works by the author is defined as the predicted settlement divided by the actual settlement. Settlement ratios are non-dimensional and can be compared directly against each other. The settlement ratios for each settlement technique were grouped together to form a data set. The following statistical parameters were determined for the data:

- Mean (\bar{x})
- Standard deviation (S_x)
- Minimum settlement ratio (a)
- Maximum settlement ratio (b)
- Coefficient of skewness ($\beta(1)$) – defined by Harr (1897)
- Coefficient of kurtosis ($\beta(2)$) – defined by Harr (1987)
- Distribution type

The distribution type was determined by using one of the two charts from Harr (1987), and shown in Figures 2.6 and 2.7.

A summary of the statistical parameters of the settlement ratio data sets for each prediction method reviewed is given in Table 2.5.

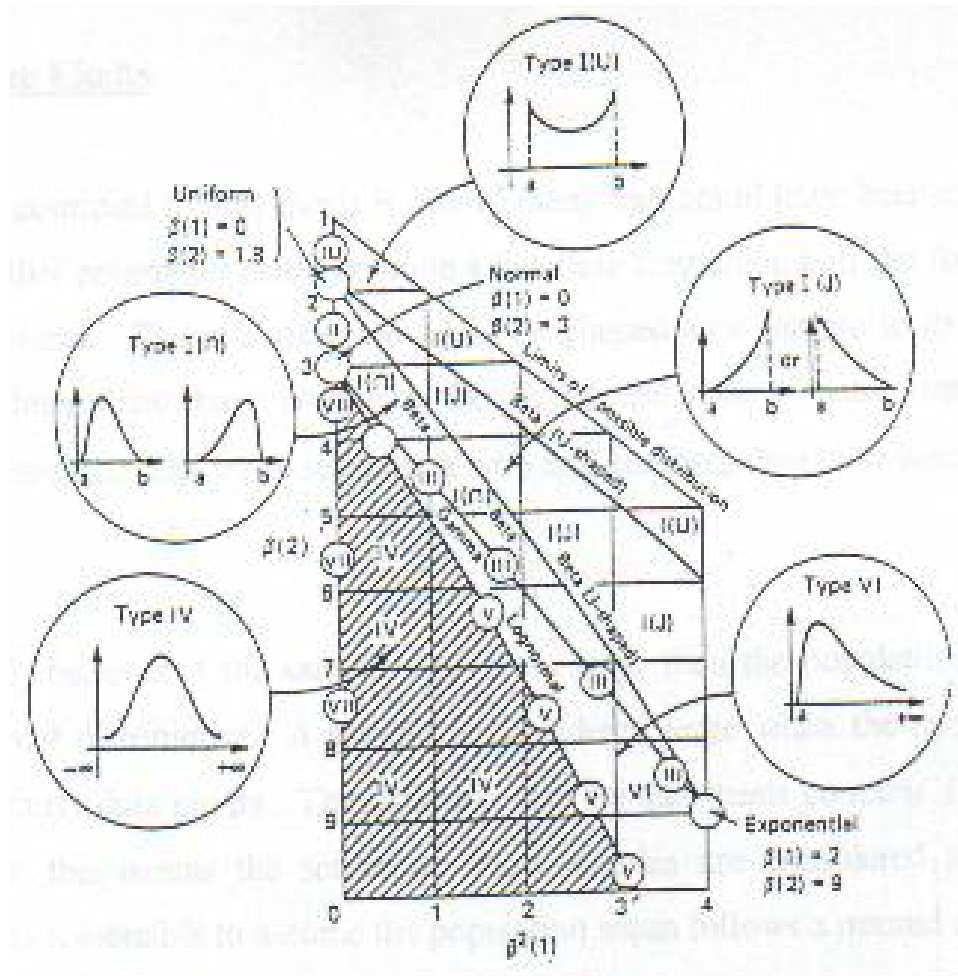
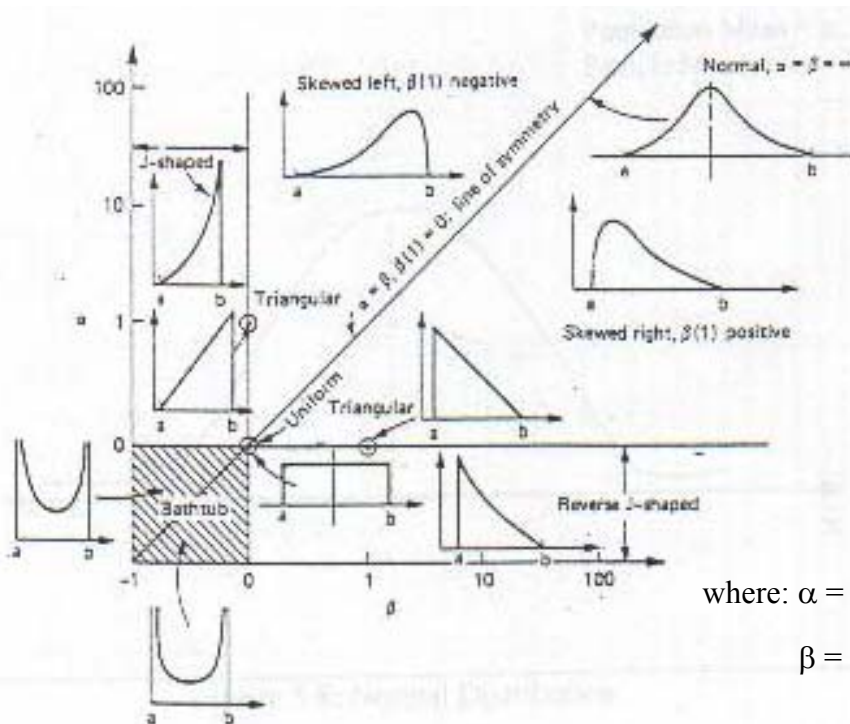


Figure 2.6: Space of Pearson's probability distributions



where: $\alpha = f(\bar{x}, S_x, a \text{ and } b)$

$\beta = f(\alpha, \bar{x}, a \text{ and } b)$

Figure 2.6: Schematic representations of probability distributions

Table 2.5: Summary of statistical parameters (Johnson, 1999)

Method	\bar{x}	S_x	a	b	$\beta(1)$	$\beta(2)$	Distribution Type*
Terzaghi and Peck	3.515	3.127	0.550	14.286	1.171	3.523	Reverse J shape
Burland and Burbidge	1.509	1.102	0.157	6.000	0.956	3.273	Reverse J shape
Berardi and Lancellotta	0.999	0.862	0.000	4.331	0.989	3.308	Reverse J shape
Schmertmann	2.656	2.085	0.394	11.304	1.121	3.659	Reverse J shape

* Figures 2.6 and 2.7 indicate the probability functions follow a J-shaped distributions.

This statistical analysis of the data sets indicated that the four methods reviewed have distinctive but differing spreads to the probability functions. This previous work indicated that the methods would estimate settlement differently for the same given footing. Using single settlement criteria such as 25 mm that is currently used today may be a risky or conservative criteria depending on the prediction method chosen. Therefore, a probabilistic approach as discussed in Chapter 3 may be employed to develop an alternative design approach which would standardise the various prediction methods.

CHAPTER 3: Settlement Predictions in Granular Soil: A Probabilistic Approach

3.1 General

The settlement of shallow foundations in granular soil is more critical than the bearing capacity, especially when the foundation width is greater than 1.5 m (Beradi and Lancellotta 1994; Jeyapalan and Boehm 1986; Tan and Duncan 1991). The settlement prediction exercise in Texas, U.S.A. in 1994 clearly demonstrated the inadequacy in the current state-of-the-art for settlement prediction (Briaud and Gibbens 1994). In spite of having abundant soil data through extensive laboratory and in situ tests, the predictions for settlement of shallow foundations were quite poor. For a design situation where the engineer has access to limited soil data, the problem of which prediction method to use can be very difficult.

Risk assessments and probabilistic/reliability studies have become increasingly popular in geotechnical engineering over the past few decades. While the geotechnical engineers will continue to use their preferred settlement prediction methods, some guidance on the risk associated with the predictions would be valuable. The work in this chapter presents a simple probabilistic model with design charts for four settlement prediction methods, which enable a designer to quantify the probability that the settlement will exceed a specific limiting value. The settlement predictions can be quite different depending on the method employed for the same input data. At present there is no rational procedure for comparing these different prediction methods. The probabilistic design charts herein will provide a base-line, from which all settlement prediction methods can be compared against each other.

3.2 Statistical Analysis

As discussed in Chapter 2, the author completed a preliminary statistical analysis on the reliability and accuracy of four popular settlement techniques. Also a brief study of the probability that one of the four methods would exceed a field footing settlement of 25 mm was explored (Sivakugan and Johnson, 2002). The settlement ratio defined as the

ratio of predicted to actual settlements follows a beta distribution, and led to histograms along with the beta distribution parameters.

After reviewing the preliminary work completed by Sivakugan and Johnson (2002), it was evident that further clarification of the probability density functions for the settlement ratio could be more decisively defined. If the shape of the settlement ratio density function for a particular method could be determined as a rational function, it would allow for a more precise examination of each method reviewed.

3.2.1 Settlement Ratio Probability Density Function

The probability density function of a random variable x following a beta distribution is given by:

$$f(x) = \frac{\Gamma(\alpha + \beta)}{\Gamma(\alpha)\Gamma(\beta)} \frac{1}{(b-a)^{\alpha+\beta-1}} (x-a)^{\alpha-1} (b-x)^{\beta-1}, \text{ for } a \leq x \leq b \quad (3.1)$$

where Γ is Gamma function defined as $\Gamma(\beta) = \int_0^{\infty} x^{\beta-1} e^{-x} dx$ (3.2)

a = minimum possible value for x

b = maximum possible value for x

Here, x , is the value taken by the settlement ratio, x , which is a random variable.

The advantage of the beta distribution is that it allows for lower and upper limits, and skewness to be associated with the random variable X . This enables a more realistic distribution to be fitted to a given set of data. Previous studies by Berardi and Lancellotta (1994) showed that settlement ratios are better modelled by beta distribution than log normal or other distributions.

The following probability density functions were determined for the four settlement prediction methods, using parameters given by Sivakugan and Johnson (2002), and the procedures described by Harr (1977) for computing Gamma functions.

Berardi and Lancellotta: $f(x) = 0.0499 x^{-0.21} (4.33 - x)^{1.65}$ for $0 \leq x \leq 4.33$ (3.2)

Burland and Burbidge: $f(x) = 0.0142 (x - 0.16)^{-0.09} (6 - x)^{2.03}$ for $0.16 \leq x \leq 6.00$ (3.3)

Terzaghi and Peck: $f(x) = 0.0251 (x - 0.55)^{-0.51} (14.29 - x)^{0.77}$ for $0.55 \leq x \leq 14.29$ (3.4)

Schmertmann et al: $f(x) = 0.0046 (x - 0.39)^{-0.29} (11.3 - x)^{1.72}$ for $0.39 \leq x \leq 11.3$ (3.5)

The lower and upper bounds (a and b) are simply the minimum and maximum settlement ratios observed within the settlement records. These probability density functions were plotted along with the histograms in Figures 3.1 to 3.4. All four probability distributions are reverse-J shape and strongly skewed to the right, taking the maximum value of ∞ at $x = a$.

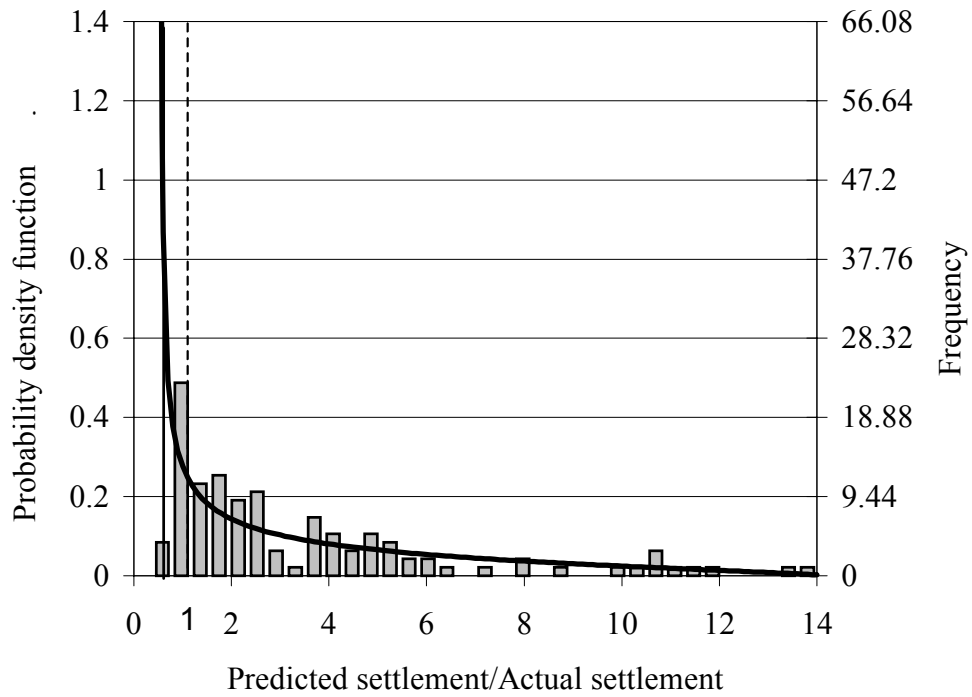


Figure 3.1: The histogram and beta distribution of settlement ratios for Terzaghi and Peck (1967) method

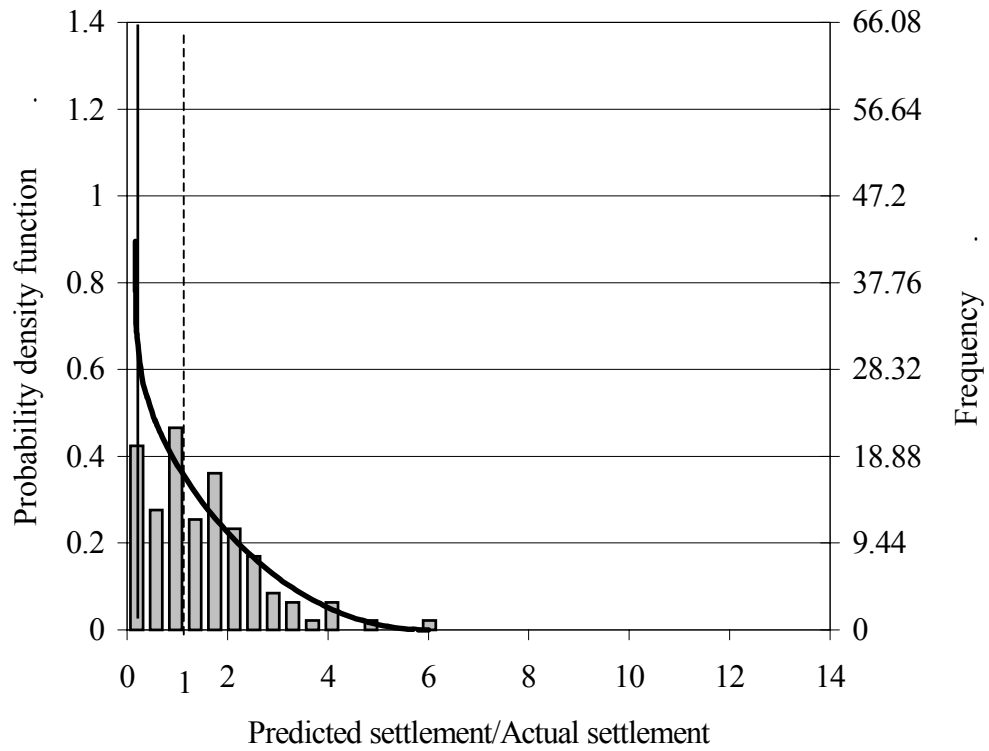


Figure 3.2: The histogram and beta distribution of settlement ratios for Burland and Burbidge (1985) method

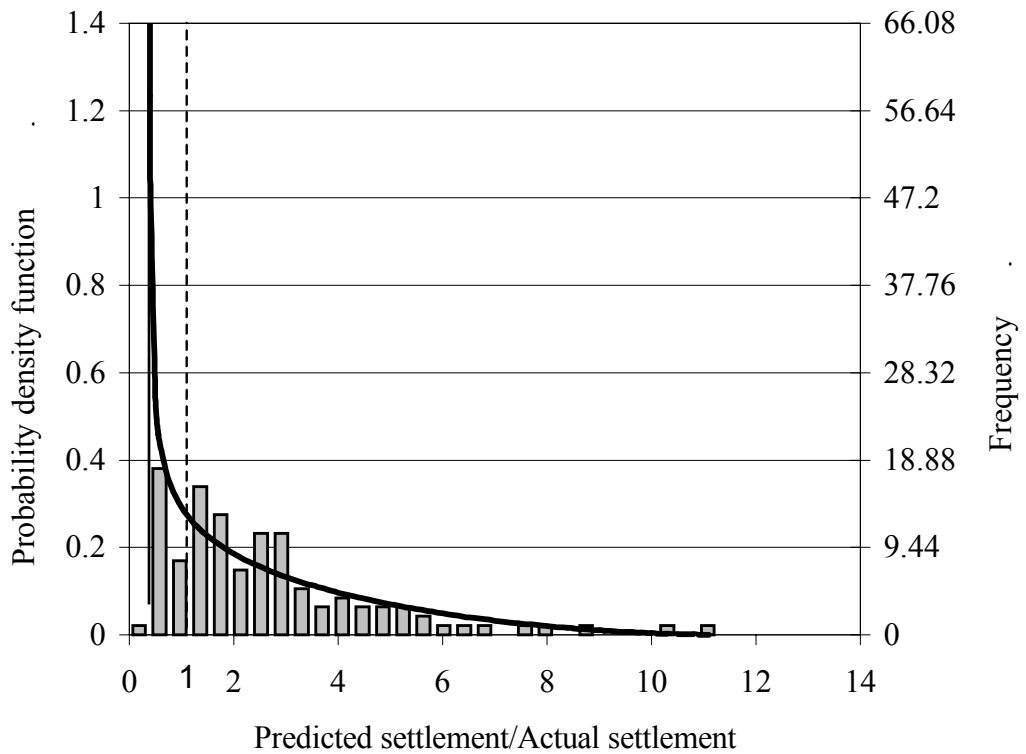


Figure 3.3: The histogram and beta distribution of settlement ratios for Schmertmann et al. (1978) method

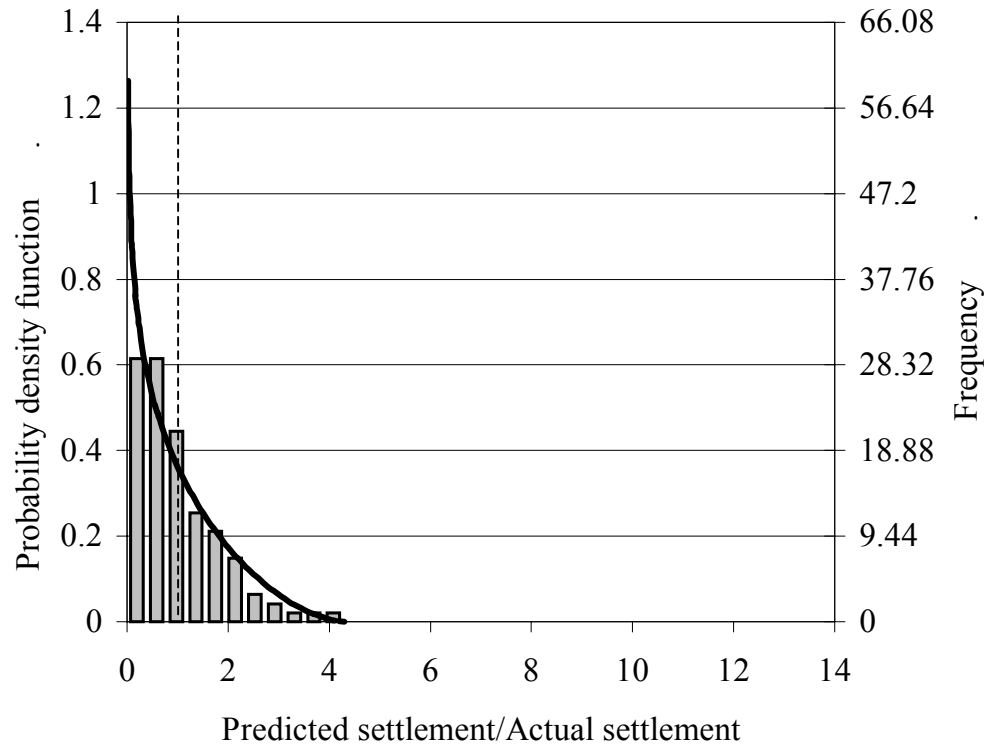


Figure 3.4: The histogram and beta distribution of settlement ratios for Berardi and Lancellotta (1994) method

3.2.2 Probabilistic Design Charts

The probability of failure p_f can be defined as the probability that the actual settlement will exceed the specified limiting value. When predicted settlement is S and measured settlement is Y , then the settlement ratio $X (= S/Y)$ is a random variable modelled by the probability distributions (Equations 3.2 to 3.5). If the limiting value is 25 mm then the probability of failure p_f is given by:

$$p_f = p[Y \geq 25] = p[S/X \geq 25] = p[X \leq S/25]$$

For example, the settlement prediction using the Terzaghi & Peck method is 35 mm, $p_f = p[X \leq 35/25] = p[X \leq 1.4]$. From the BETADIST function in EXCEL (2000), with beta distribution parameters for the Terzaghi and Peck method given in Sivakugan and Johnson (2002), $p_f = 0.35$. Here, BETADIST function gives the probability of X being less than the specified value, which is 1.4.

The p_f values were determined for a series of different values of S and different limiting settlement values. This was repeated for the four settlement prediction methods, shown in Appendix A. The values of p_f were plotted against the predicted settlement in Figures 3.5 to 3.8. From the charts of the four methods, one can obtain the probability (p_f) that the actual settlement will be greater than a limiting value. The limiting values in a wide range of 15 mm to 40 mm were considered when developing the design charts. The 25 mm limit is the most common so this curve is shown as darker on the plot below. Most of the following discussion is based solely on the limiting settlement of 25 mm, unless stated otherwise.

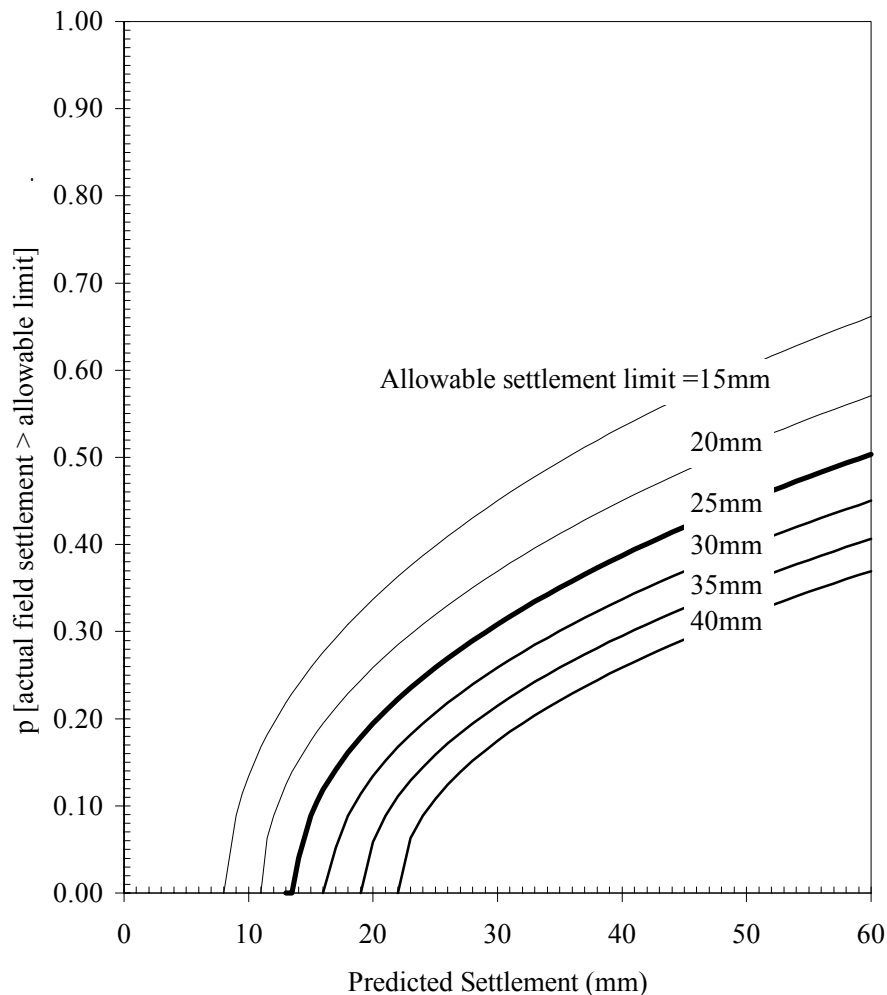


Figure 3.5: The design chart for Terzaghi and Peck (1967) method

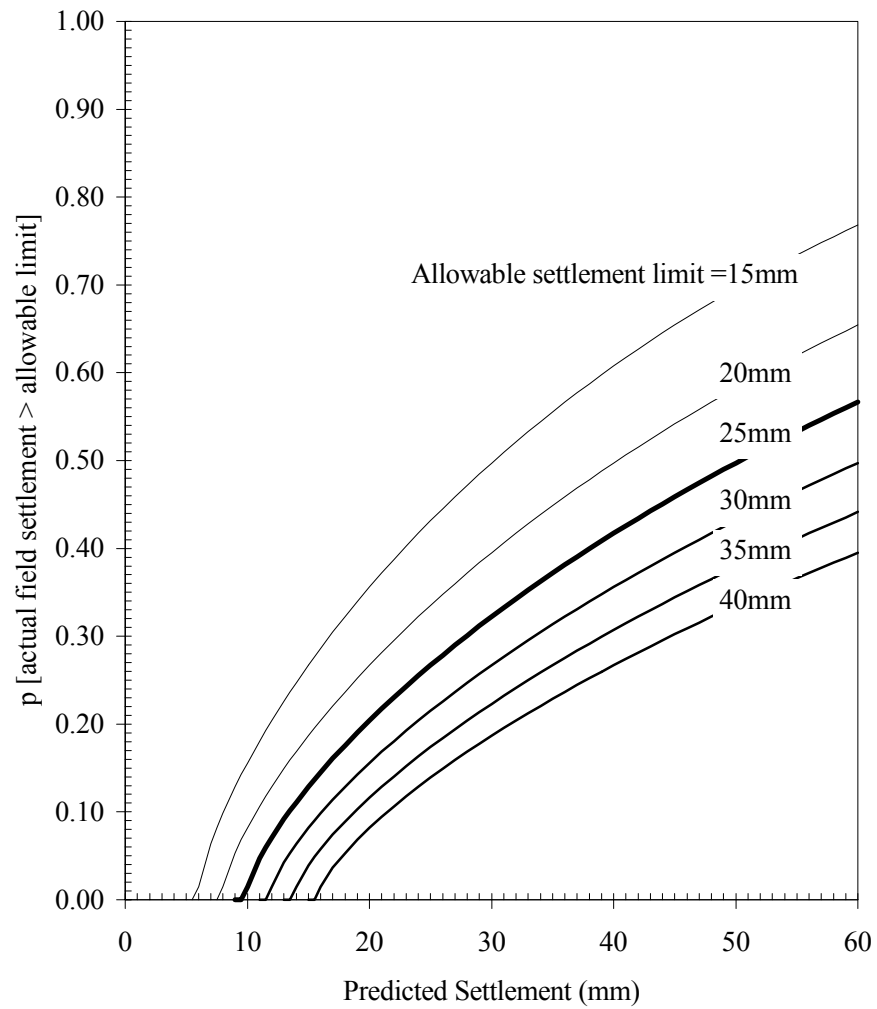


Figure 3.6: The design chart for Schmertmann et al. (1978) method

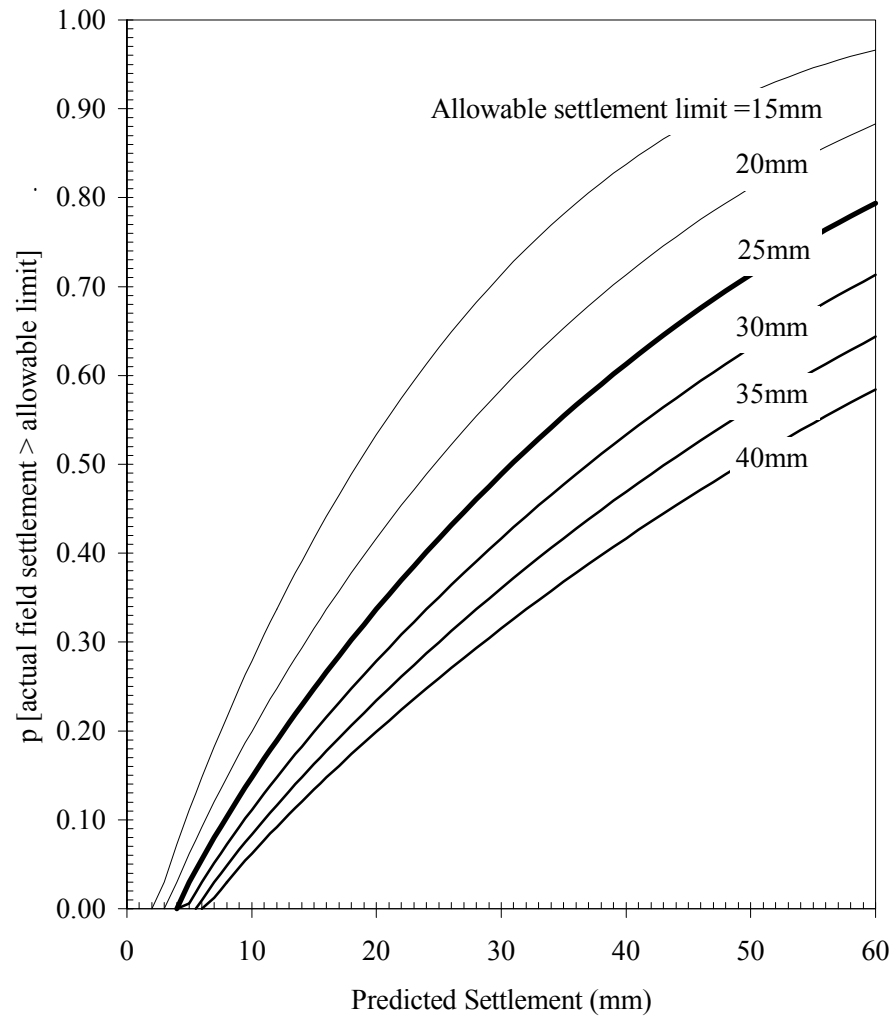


Figure 3.7: The design chart for Burland and Burbidge (1985) method

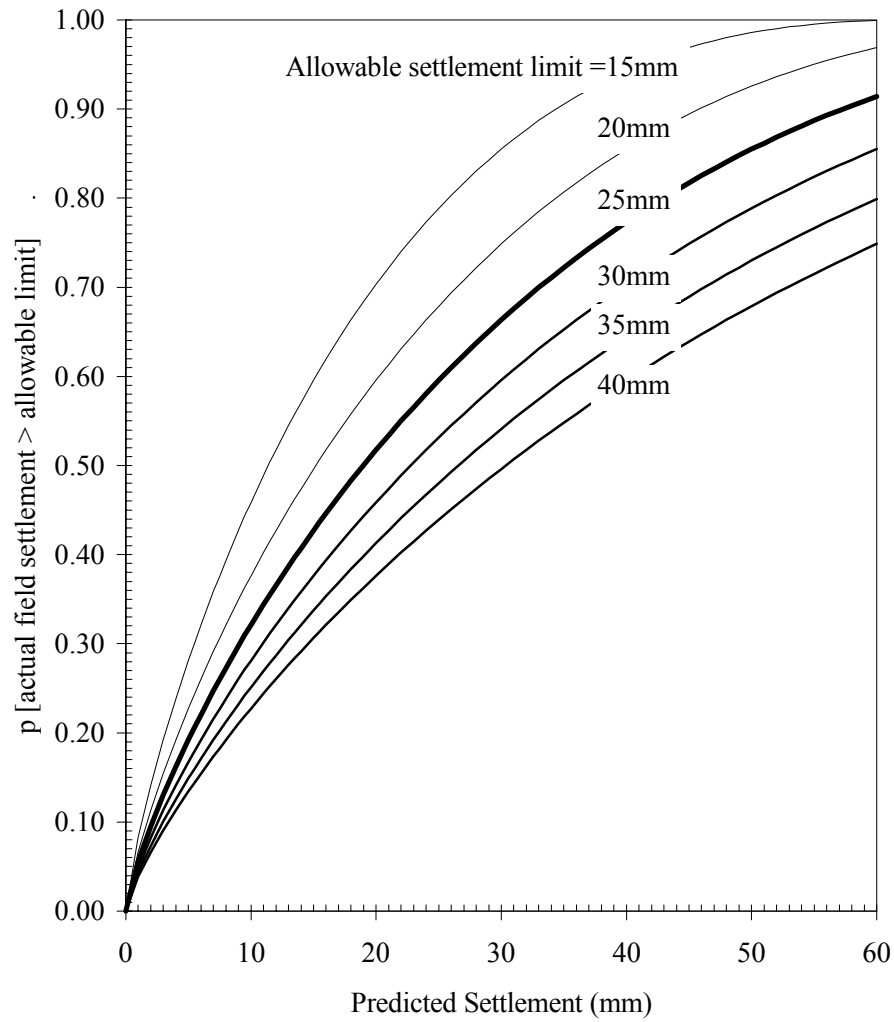


Figure 3.8: The design chart for Berardi and Lancellotta (1994) method

The computed settlement value can have a quite different meaning depending on the settlement prediction method used. For the same predicted settlement, the probability of exceeding the limiting settlement can vary greatly depending on the method selected. This can be seen in Table 3.1, where the probability values of field settlement exceeding 25 mm are shown for the four methods. For example, a 20 mm settlement computed by the Terzaghi and Peck or Schmertmann et al. methods implies a 0.20 (20%) probability that the actual settlement is more than 25 mm in the field. If the same settlement of 20 mm was estimated using the Berardi & Lancellotta method, there is a 0.52 (52%) probability that the actual settlement will exceed 25 mm in the field.

Table 3.1: The probability of exceeding 25mm settlement in field

Predicted Settlement (mm)	Probability of Exceeding 25 mm Settlement in Field			
	Terzaghi and Peck	Schmertmann et al.	Burland and Burbidge	Berardi and Lancellotta
1	0	0	0	0.06
5	0	0	0.03	0.19
10	0	0.02	0.15	0.32
15	0.09	0.13	0.25	0.43
20	0.20	0.20	0.34	0.52
25	0.26	0.27	0.42	0.60
30	0.31	0.32	0.49	0.66
35	0.35	0.37	0.55	0.72
40	0.387	0.42	0.61	0.77

It is seen from Figures 3.5 to 3.8 that the Terzaghi and Peck method is the most conservative of all four methods. For example, when the Terzaghi and Peck method predicts a 25 mm settlement, there is only a 0.26 (26%) probability that the actual settlement will exceed 25 mm. On the other hand, the more sophisticated Berardi & Lancellotta method gives predictions closer to the actual values. Here, a 25 mm prediction implies there is a 0.60 (60%) probability the actual settlement will exceed 25 mm. For predicted settlements up to about 40 mm, the Terzaghi and Peck and Schmertmann et al. methods have a similar probability that the actual settlement will exceed 25 mm in the field.

The proposed design charts above are based on settlement records representing a wide range of footings, well documented in the literature. When using the design charts, it can be assumed that the reliability and uncertainty associated with the current input

parameters, including the field data, are comparable to the settlement records. The uncertainties associated with the different settlement methods have been built into the design chart, which would become a valuable tool in the design of shallow foundations. The probabilistic approach proposed herein can be extended to include other settlement prediction methods as well.

CHAPTER 4: Soil Strength and Constitutive Behaviour

4.1 General

Most pile design procedures were developed assuming an elastic response for the stress-strain relationship within the sand and pile material. However, when sand and clay are subjected to relatively small loads they undergo both elastic and plastic deformation. Once the load is released the soil rebounds only partially.

Some researchers have characterized soil as an elasto-plastic material and made attempts at defining constitutive models to describe the stress-strain response (Chen and Saleeb, 1983). There has been no firm agreement on which constitutive model is the best to use. A popular constitutive model used to represent sand response under loads is the linear elastic model during loading, with either Mohr-Coulomb or Drucker-Prager failure cap models to define the failure state (Wang and Sitar, 2004; Potts and Zdravkovic, 1999 and 2001). As an alternative, a non-linear elastic response with failure cap models may also be employed.

This research used a finite element computer package ABAQUS to model the response for a set of actual piles in the field, and a series of hypothetical pile cases. The numerical pile analysis is shown in Chapters 8 to 9. The results from ABAQUS are dependent on the choice of constitutive model to idealize the material behaviour of sand, and the correlations used to determine the constitutive parameters. The following sections will discuss the various constitutive models most commonly used, and the possible correlations to determine the constitutive parameters. A limited parametric analysis to examine the reliability of the available parameters is also presented.

4.2 Constitutive Models

4.2.1 General Background

The increase in technology of recent years has made it possible for more complex soil problems to be solved using numerical methods, such as the finite element method. This has resulted in a higher demand for researchers to develop more comprehensive constitutive models for soil behaviour.

Prevost and Popescu (1996) state that for a constitutive model to be satisfactory it must be able to:

- 1) Make a statement about the material behaviour for all stress and strain paths;
- 2) Identify model parameters by means of standard material tests; and
- 3) Physically represent the material response to changes in applied stress or strain.

From standard tests researchers have determined that sand behaves elasto-plastically when loaded, as shown in Figures 4.1 and 4.2 (Chen and Saleeb, 1983).

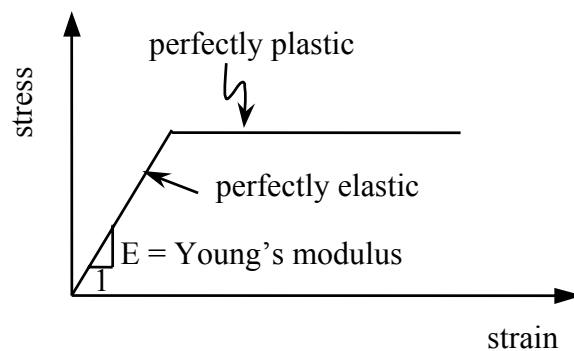


Figure 4.1: Ideal stress-strain relation assumed for most structural materials

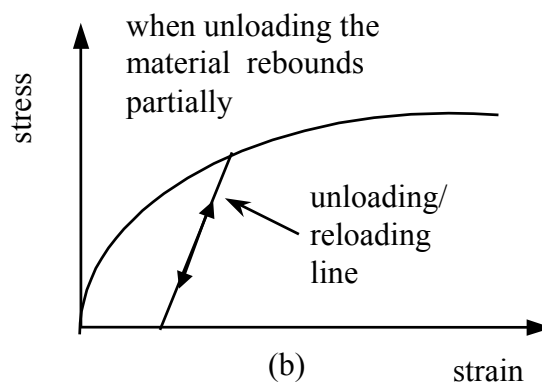


Figure 4.2: Stress-strain relation for elasto-plastic material

4.2.2 Types of Constitutive Models

The constitutive models available for describing the stress-strain behaviour of sand fall into one of two categories (Chen and Saleeb, 1983). The first category of constitutive models was derived under the assumption that the soil material behaves in an isotropic manner, in which the mechanical behaviour of the material is identical in all directions. The second category of soil constitutive models falls under anisotropic behaviour, in which the material behaviour in at least two directions is different.

The common constitutive models available for sand in each category are listed below:

1) isotropic constitutive models

⇒ elastic

- linear elastic (i.e. Hooke's law)
- non-linear elastic

⇒ elasto-plastic

- Mohr-Coulomb
- Drucker Prager



2) anisotropic constitutive models

All of the above constitutive models have been placed in order of complexity. The most complex models are anisotropic, which require a vast amount of input data from laboratory testing. The increase in accuracy using an anisotropic constitutive model could be lost due to crude soil testing and laboratory procedures. A rigorous amount of soil tests can lead to a substantial increase of costs for geotechnical engineers in the field. Therefore, the anisotropic constitutive models are difficult to employ resulting in them rarely being used.

Many researchers have explored constitutive models and found the use of isotropic models, such as linear elastic with Mohr-Coulomb or Drucker-Prager is sufficiently accurate (Chen and Saleeb, 1983; Hibbitt et al., 2001). In the past, linear elastic constitutive models without the use of a cap model have been commonly used in developing pile design methods (Vesic, 1977). The differences between pure linear

elastic and non-linear elastic constitutive models are discussed below, along with each of the respective cap models.

4.2.3 Linear Elastic Constitutive Model

Various researchers have explored the stress-strain behavior of soil and found it undergoes elastic strain under small stresses. As the stress level increases the soil will develop plastic strains until ultimate shearing capacity is attained. The elastic stress-strain behaviour may be represented by one of two approaches, linear-elastic as discussed in this section or non-linear elastic as presented in Section 4.2.4.

In the engineering world, the linear elastic constitutive model (Hooke's law) is probably the most common model used to approximate the stress-strain relationship of a material. Hooke's law relates the stresses as a linear function of strains in three-dimensional space through two constants, Young's modulus (E) and Poisson's ratio (ν), in the following manner:

$$\sigma_x = \left(\frac{E}{(1+\nu)(1-2\nu)} \right) (\epsilon_x (1-\nu) + \nu(\epsilon_y + \epsilon_z)) \quad (4.1a)$$

$$\sigma_y = \left(\frac{E}{(1+\nu)(1-2\nu)} \right) (\epsilon_y (1-\nu) + \nu(\epsilon_x + \epsilon_z)) \quad (4.1b)$$

$$\sigma_z = \left(\frac{E}{(1+\nu)(1-2\nu)} \right) (\epsilon_z (1-\nu) + \nu(\epsilon_x + \epsilon_y)) \quad (4.1c)$$

where $\sigma_x, \sigma_y, \sigma_z$ = normal stress in x, y and z directions respectively, and

$\epsilon_x, \epsilon_y, \epsilon_z$ = normal strain in x, y and z directions respectively.

These equations can be simplified for two and one dimensional stress-strain problems. The form of the final equations depends on the type of problem, e.g. whether the problem is plane stress, plane strain or axisymmetrical.

4.2.4 Non-Linear Elastic Constitutive Model

Non-linear elastic models are more complex to define than their linear elastic counterparts. This is because the relationship between the stress and strain at various stress levels is not constantly proportional. Some typical linear elastic and non-linear elastic stress-strain plots are shown in Figure 4.3.

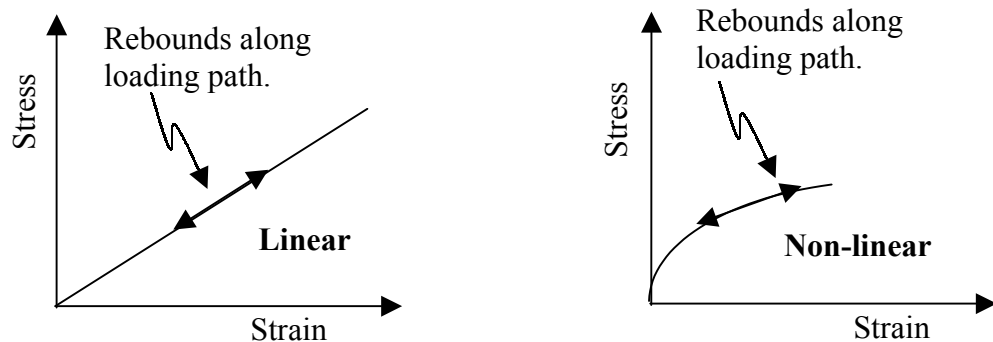


Figure 4.3: Typical linear elastic and non-linear elastic soil response

As seen in the diagram above, if a material is purely elastic it will undergo elastic strains only, and will rebound along the same stress-strain path once unloaded.

Two of the more popular approaches for estimating a non-linear elastic stress-strain relationship are to use a hypoelastic or hyperelastic model. Hypoelastic models are only valid for small elastic strains and hyperelastic models can be used for large strain problems (i.e. stretching of rubber). When using these models additional parameters from laboratory testing (e.g. triaxial testing) are required as opposed to the traditional linear elastic model. A computational approach is necessary due to the complexity of such models. This makes the application of non-linear elastic models difficult to employ in everyday calculations by practicing engineers.

The use of non-linear elastic models were considered for this research (hypoelastic). However, it was found that the input parameters to define the models needed good quality results from undisturbed samples in the laboratory. Due to the crudeness of field-testing techniques and the less than perfect laboratory testing procedures, it was decided that the benefit of using non-linear elastic models would be negated by the

inaccuracies associated with the input parameters. Therefore, a linear elastic model was considered sufficient to model the elastic response for the current research. It is noted that other researchers have adopted linear elastic models to define soil behaviour (e.g. Chen and Saleeb, 1983). The use of a specific constitutive model is governed by the soil type and complexity of the problem, and is chosen at the discretion of the predictor.

4.2.5 Mohr-Coulomb's Model

Soil behaves elasto-plastically as discussed in Section 5.2.1, and when sand is subjected to loads the displacement will contain both a recoverable and non-recoverable component. Hence a failure criterion needs to be included in the elastic models to define the stress states that cause plastic deformation. One possible failure criterion is the Mohr-Coulomb line shown in Figure 4.4.

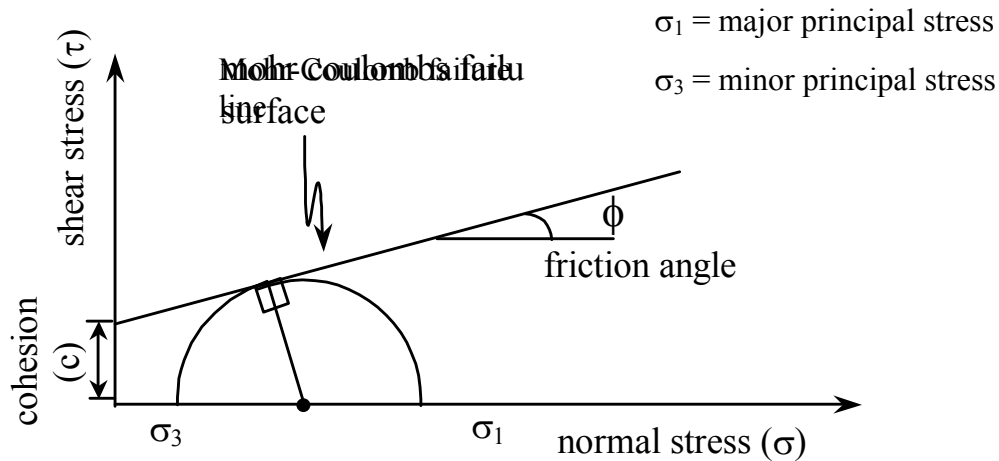


Figure 4.4: Mohr-Coulomb failure line

The Mohr-Coulomb failure surface in τ - σ space is defined by:

$$\tau_f = c + \sigma_f \tan \phi \quad (4.2)$$

where τ_f = failure shear stress,

σ_f = failure normal stress,

ϕ = friction angle, and

c = cohesion.

The failure surface is only dependent on the major and minor principle stresses (σ_1 , σ_3), and is independent of the intermediate principle stress (σ_2). Mohr-Coulomb criterion resolves into an irregular hexagonal pyramid once mapped into three-dimensional stress space, as shown in Figure 4.5.

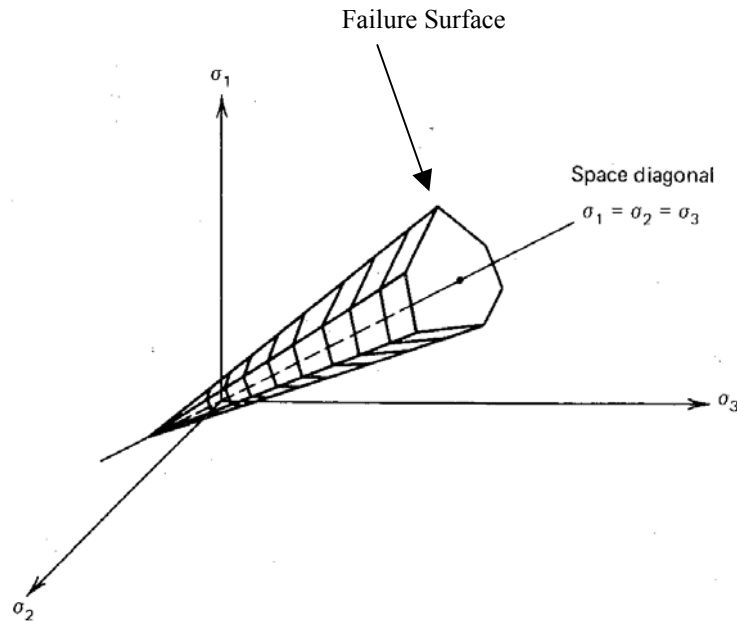


Figure 4.5: Mohr-Coulomb failure surface (Chen and Saleeb, 1983)

The above pyramid forms the failure/yield surface that in turn governs how the soil will behave. The material will behave either linear or non-linear elastically if the stress point lies within the failure envelope. However, if the stress point reaches the yield surface the material will undergo a degree of plastic deformation.

It is noted that several researchers have utilized Mohr-Coulomb failure criterion, and found it to be sufficiently accurate for most geotechnical applications (Chen and Saleeb, 1983).

4.2.6 Drucker Prager Model

The Drucker-Prager model is similar in concept to the Mohr-Coulomb model, with one major difference being this model incorporates the intermediate principal stress. There

are commonly three forms of the Drucker-Prager model. These forms are the linear, hyperbolic and exponent Drucker-Prager models that describe the shape of the failure surface (Hibbitt et al., 1998).

There are techniques available to map parameters between Mohr-Coulomb and Drucker-Prager linear failure lines, as discussed by Hibbitt et al. (2001), and Wang and Sitar (2004). The mapping techniques depend on the loading conditions and geometry of the problem (i.e. plain stress, plain strain, etc). Some further discussion on mapping parameters from Mohr-Coulomb to Drucker-Prager is given in Chapter 8.

Drucker-Prager criterion resolves into a cone when mapped into three-dimensional stress space, as shown in Figure 4.6.

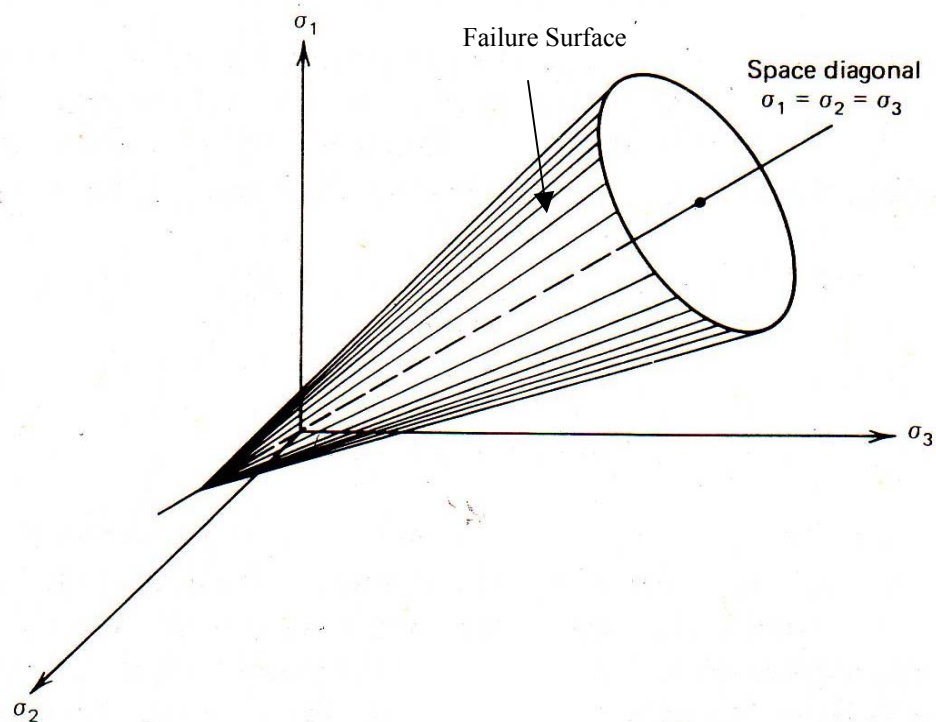


Figure 4.6: Drucker-Prager failure surface (Chen and Saleeb, 1983)

4.3 Determination of Sand Constitutive Properties

The accuracy and reliability of estimating a foundation and sand (or any soil) response are dependent on the constitutive and failure models used to represent the stress-strain behaviour (see Chapters 5). Several models have been developed for estimating the stress-strain behaviour of sands and soils in general, as mentioned in Section 4.2.

Constitutive and failure models are dependent on a number of variables, which have to be estimated from standard field and laboratory testing of soils. The correlations used to estimate the constitutive parameters have largely been based on empirical relationships, and developed from experience in the field and laboratory testing.

However, it is important to obtain undisturbed samples from the field, and strength parameters are dependent on the in situ conditions of soil. In the case of sand it is extremely difficult to collect undisturbed samples. Sand samples have to be reconstituted in the laboratory or frozen in the field, then cut and brought back to the laboratory. Geotechnical engineers often rely on empirical correlations based on standard field tests, due to large costs from laboratory testing. Laboratory testing is usually limited to classification tests to confirm soil types in field engineering logs.

Some of the standard field-testing used today is presented in Table 4.1.

4.3.1 *Correlations for Friction Angle of Sand*

Soil in real life is a collection of discrete particles that interact with each other to form an overall continuum. Sand particles interact with surrounding particles via friction at particle surface. This friction in effect forms interlocking along shear lines that result from loads being placed onto the sand. The roughness, particle shape, particle density and overburden pressure of sand influences its shearing capacity.

Table 4.1: Standard field-testing procedure

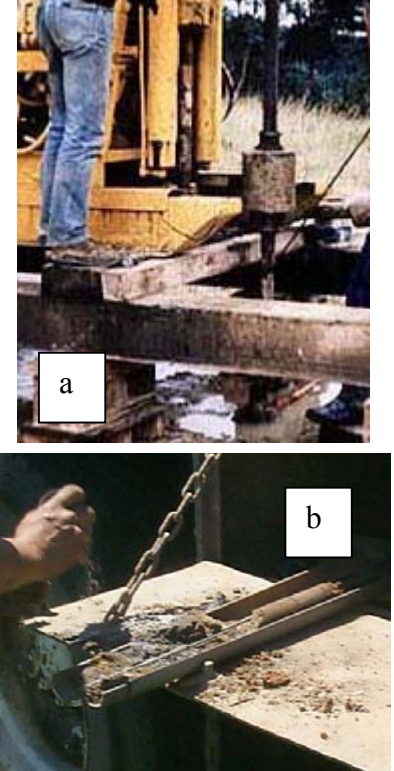
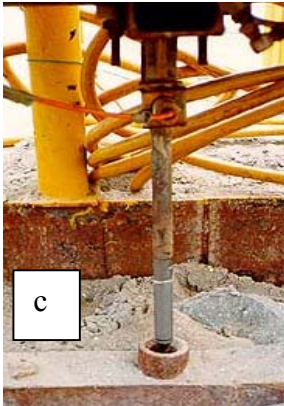

Test Type	Test Procedure	Advantages/ Disadvantages	Example of Testing Rig <i>(see note at bottom of page 40 for photo reference)</i>
Standard Penetration Test (SPT)	A hole is generally bored by an auger, and a split sampler connected to a rod is lowered to the base of the hole. The rod is connected to a hammer, which is usually driven by the hydraulics from the drilling rig. The hammer is approximately 63.5 kg and is dropped a distance of 0.76 m. The spilt sampler is driven down in three increments of 150 mm, with the number of blows required for each 150 mm increment being recorded. The first 150 mm of sample may have been disturbed due to the auger, and therefore is considered to be a seating interval. The number of blows required to drive the spilt tube the final 300 mm is commonly referred to as the blow count.	<p>SPT allows the sand density and strength to be estimated at deep depths below the ground surface. Also the spilt tube sampler allows disturbed samples to be collected at the same time as testing, enabling visual and laboratory soil classification to be performed.</p> <p>One disadvantage of the SPT test is that the testing is limited to the depth at which it was tested. The soil between testing depths has to be classified based on the experience of the field operative.</p>	 <p>The figure consists of two photographs. Photograph 'a' shows a person in blue jeans operating a yellow drilling rig. A vertical rod with a hammer at the top is being lowered into a hole in the ground. Photograph 'b' is a close-up of the spilt tube sampler, which is a metal tube with a split design, containing a sample of soil. A chain is attached to the top of the tube.</p>

Table 4.1 Continued: Standard field-testing procedure

Test Type	Test Procedure	Advantages/ Disadvantages	Example of Testing Rig (see note at bottom of page 40 for photo reference)
Static Cone Penetration Test (CPT)	The CPT penetrates the soil using a Dutch cone assembly, which has a cone tip approximately 36 mm in diameter. The cone is linked to a outer rod with an inner rod assembly inside. The cone is pushed into the ground at a constant rate, and continuous measurements are made of the resistance to penetration of the cone, the friction of the outer surface of a sleeve and pore pressure.	CPT tests allow for continuous readings through the soil profile. It also allows pore pressure to be monitored. One distinct disadvantage is soil samples cannot be retrieved for visual and laboratory classification. Also the cone is sensitive and can be damaged in hard dense soils and gravel.	
Dynamic Cone Penetrometer Test (DCP)	The DCP apparatus is a combination of the SPT hammer apparatus, CPT rod and cone assembly. The DCP contains a 9 kg hammer connected to a series of thin rods with a solid cone tip. This particular apparatus is operated by hand. The hammer is dropped over a standard distance. The number of blows required to drive the cone 100 mm through the soil profile is recorded continuously.	Like the CPT, the cone can be used to take continuous readings through the soil profile. Unlike the SPT and CPT, the DCP is operated by hand and therefore is not suitable for great depths. Also like the CPT, samples of soil below the ground surface cannot be collected.	

* Photo (a) obtained from: <http://civcal.media.hku.hk/airport/investigation/fieldwork/spt/default.htm>

Photo (b) obtained from: <http://physics.uwstout.edu/geo/images/library10.jpg>

Photo (c) obtained from: http://civcal.media.hku.hk/airport/investigation/fieldwork/cpt/_hidden/cpt2.htm

Photo (d) obtained from: <http://www.dynatest.com/hardware/CSIR/dcp.htm>

The interlocking capacity or shear strength of sand is represented by an angle of internal friction, which is commonly referred to as effective friction angle, ϕ' . This friction angle effectively represents the inclination of the ultimate shear stress failure line, as defined by Mohr-Coulomb and shown in Figure 4.7. It is noted that the ultimate shear stress line is usually approximated to be linear (Craig, 1992). Researchers have found this assumption is generally valid unless the sand is exposed to exceptionally high stresses. However such high stresses can be difficult to achieve in real life.

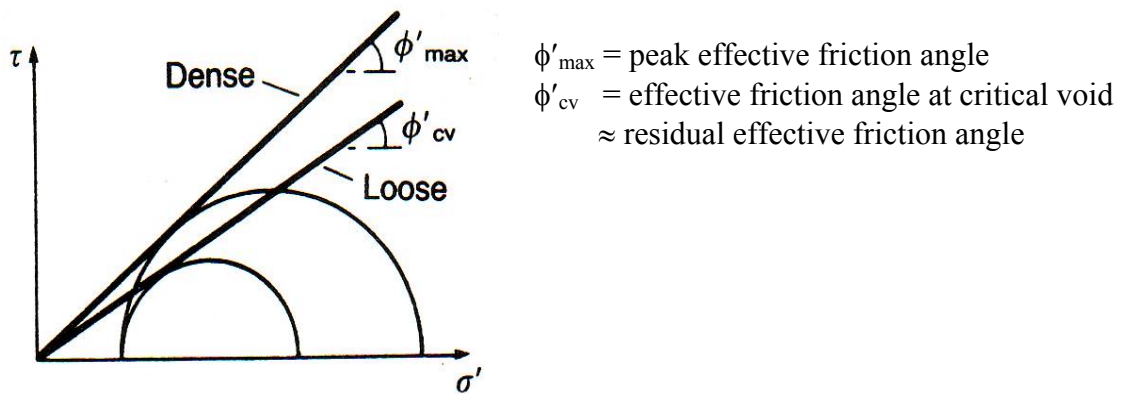


Figure 4.7: Typical shear stress (τ) vs. effective normal stress (σ') relation for sand (Craig, 1992)

When determining the friction angle one of two methods may be employed. The first method involves determining the friction angle directly from laboratory testing. This requires the use of a direct shear apparatus designed specifically to determine the friction angle of sand, or the use of a triaxial machine. In practice laboratory testing for friction angle is only sought where unusual sands are encountered, and if the project is large scale or the client requests the test. This is due to the significant cost associated with laboratory testing.

Craig (1992) shows the typical relationship between the shearing stress (τ) and axial strain (in direction of applied load) from laboratory tests. The relationship can be seen in Figure 4.8.

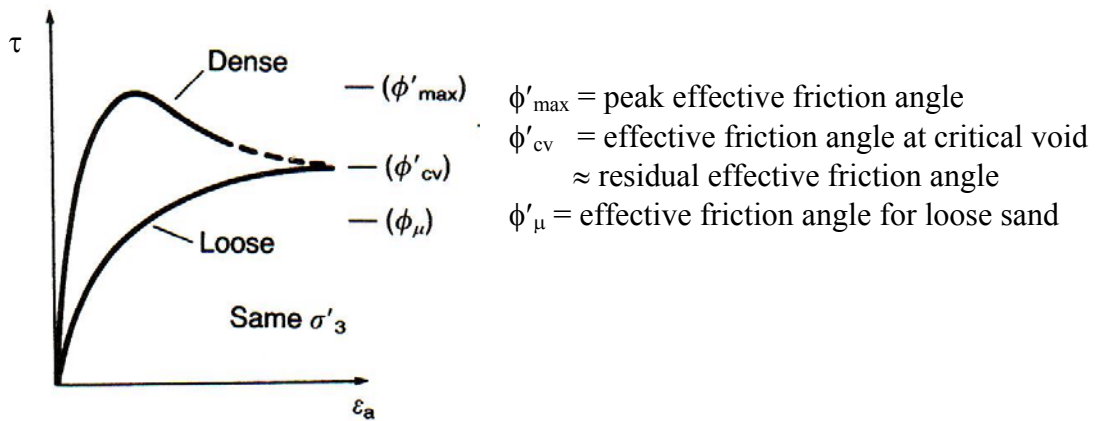


Figure 4.8: Typical shear stress (τ) vs. axial strain (ϵ_a) for sand (Craig, 1992)

From the above figure the following characteristics were noted:

- In the dense case the sand particles interlocked before shearing commenced. The shearing load had to overcome the initial interlocking of the sand particles to shear through the specimen. This process is reflected in the ascending part of the curve for the dense case. The shear stress capacity for the dense case increased significantly to a peak value at a relatively low axial strain. After the maximum shear stress was reached, the interlocking resistance was progressively overcome until ultimate frictional resistance of the sand was achieved. The ultimate frictional resistance for sand occurs when the material reaches a constant shearing stress with increased axial strain. This process happens when the sand body is at its critical void ratio, thus allowing particles to move over and around adjacent particles with no net change in the volume.
- For the loose case the shearing stress increased steadily until an ultimate shearing stress was reached at critical void ratio. It is noted that the loose case reached the ultimate shear stress state without a prior peak, because the loose sand was not manually packed together and no interlocking resistance was present.

From the above processes, it can be stated that the behavior of sand under shearing load is dependent on its density and confining stresses. The sand particle shape can also influence its frictional resistance capability, as the rougher the particle the higher the ability to resist shearing loads.

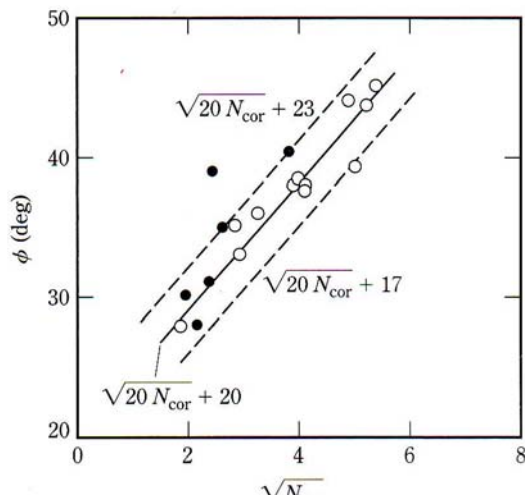
Given the sand characteristics under shearing load, the friction angle for clean sand falls between the loose friction angle (approximately equal to critical void friction angle) and the dense peak angle. For purposes of design the friction angle is generally taken as the peak value for that particular sand density. Sometimes the loading situation or nature of the soil (i.e. very soft clays) requires careful consideration, and it may be more prudent to use the critical friction angle for critical void ratio.

The second approach used for estimating the friction angle is to employ an existing empirical correlation, based primarily on field test data obtained from either standard penetration or cone penetration tests. To date several friction angle correlations have been derived. Some of the more popular correlations are summarized in Table 4.2.

Table 4.2: Some selected correlations for sand friction angles in terms of blow counts

Researcher	Correlation
Schmertmann (1975)	
Wolff (1989) Based on work by Peck et al. (1974)	$\phi \text{ (deg)} = 27.1 + (0.3) (N_1)_{60} - 0.00054(N_1)_{60}^2$ <p>where, $(N_1)_{60}$ = blow count corrected for hammer efficiency and overburden.</p>

Table 4.2 Continued: Some selected correlations for sand friction angles in terms of blow counts

Researcher	Correlation
Hatanaka and Uchida (1996)	 <p>Where, $N_{corr} = (N_1)_{60}$ = blow count corrected for hammer efficiency and overburden – see Table 4.3.</p>

Note: there are more correlations available based on work from various researchers.

There are a number of methods available to estimate the friction angle of sand, as seen from the previous table. This is one of the greatest challenges facing geotechnical engineers today. There is no current standard method, and geotechnical engineers depend on field experience and on suggestions by others. A brief comparison between the above empirical correlations was explored using test data given from sand used for experimental work in this thesis. The details on the experimental sand are shown in Chapter 7 as part of the small scale pile laboratory testing.

From the direct shear test, the shear stress (τ) versus axial strain (ϵ_a) for three separate normal stress (σ) states was determined for the experimental sand, and the results are presented in Figure 4.9. The σ - τ relationship for the loose and dense state of the experimental sand was also produced and shown in Figure 4.10.

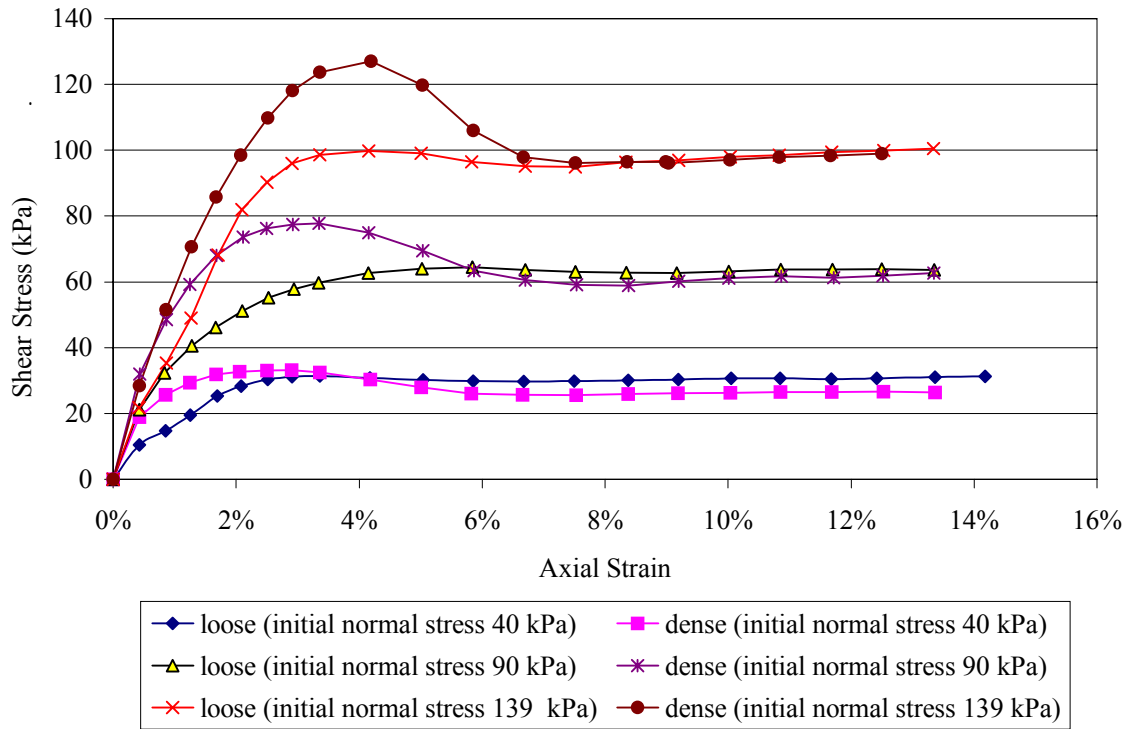


Figure 4.9: Shear stress vs. axial strain for experimental sand

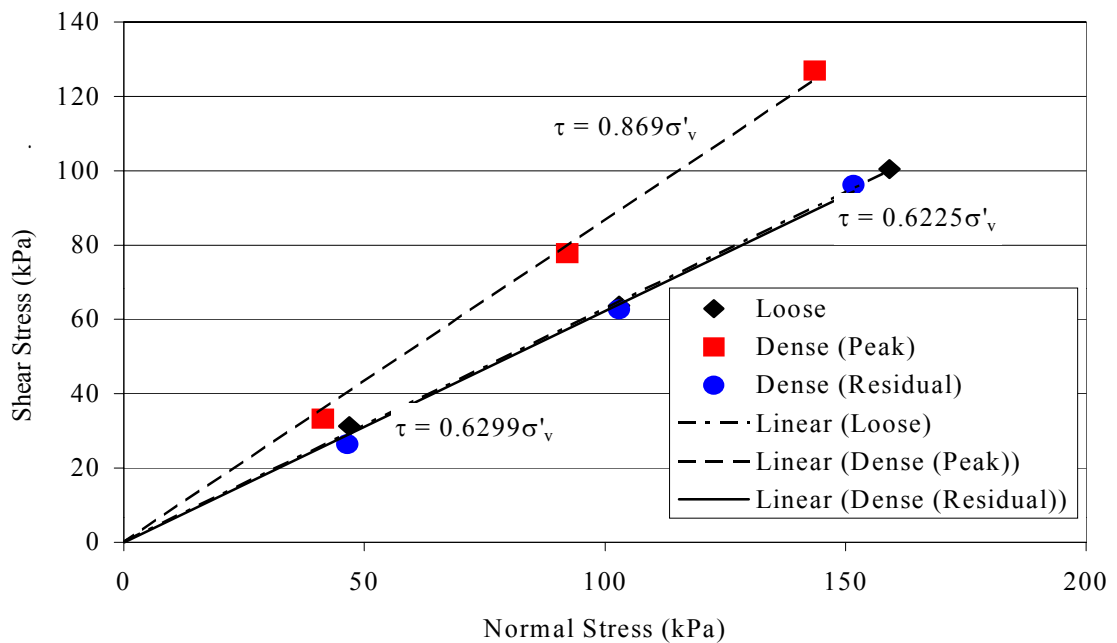


Figure 4.10: Shear stress vs. effective normal stress for experimental sand

Figures 4.9 to 4.10 show similar trends as those portrayed in Figures 4.7 to 4.8. The trends from the experimental sand cases agree with observations by other researchers. The loose and dense sands should return to a critical void ratio (e_{cv}) for a given normal stress, and this is shown in Figure 4.11. The experimental void ratio (e) vs. horizontal displacement for a normal stress of 323 N is plotted in Figure 4.12. Again this plot agrees with typical trends experienced by other researchers.

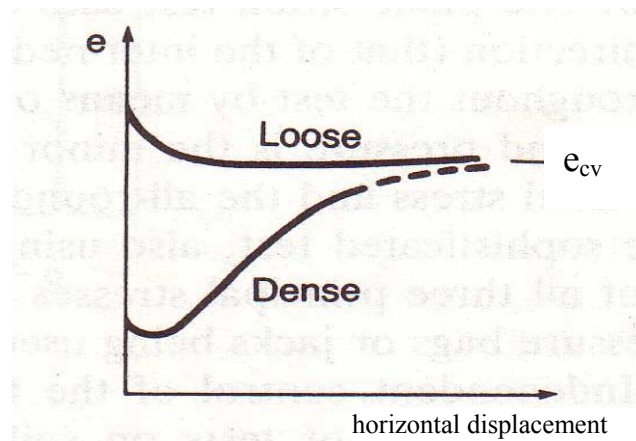


Figure 4.11: Typical plot of void ratio vs. horizontal displacement for sand (Craig, 1992)

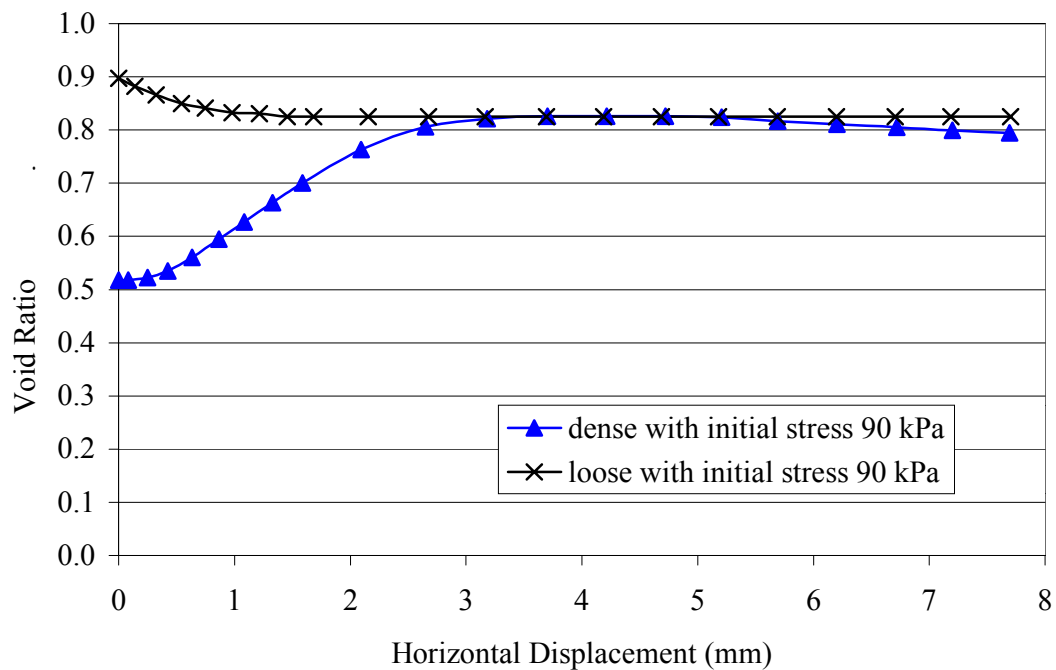


Figure 4.12: Void ratio vs. horizontal displacement for experimental sand

As discussed previously, the friction angle of sand can be estimated using correlations relating the friction angle to field test data such as standard penetration test (Table 4.2). The standard penetration test gives an indication of the density for sand as shown in Figure 4.13. From the direct shear results, a small limited parametric study was conducted to explore the validity of friction angle correlations given in Table 4.2. A further comparison with field test data is shown in Chapter 5.

An equivalent overburden pressure can be estimated for each direct shear specimen using the initial load (i.e. load corresponding to no shear load), and the corresponding load area of the direct shear specimen. An approximate uncorrected blow count may be assumed from the overburden pressure and the D_r (relative density) of the direct shear specimens (Table 4.3). The corrected blow count can then be calculated using the formulae presented in Section 5.3.1. The friction angle for the experimental sand based on the direct shear results is given in Table 4.3, along with the predicted friction angle from the correlations in Table 4.2.

It was noted that estimates from the method developed by Wolff (based on works by Peck et al., 1974) tended to be conservative for the denser sands, and Schmertmann's method tended to be conservative for the looser sands. Hatanaka and Uchinda method tended to produce the overall most accurate results for the experimental sand. The differences in methods may lie with the sand types employed to formulate the correlations, i.e. grain size of sand, experimental differences, or approximations of relationships for other sand properties such as density, etc.

The correlation formulated by Hatanaka and Uchinda was used for the numerical modelling research in this document. However, it was found by several researchers that sand typically has a maximum upper bound friction angle of 50° that should not be exceeded. Therefore, one has to use caution when only equations are employed to determine sand/soil properties. The equation to determine soil parameters should be within realistic bounds, and for sand the friction angle should typically be in the bounds of 25° to 50° . In this research an upper bound of 50° for the friction angle of sand has been adopted.

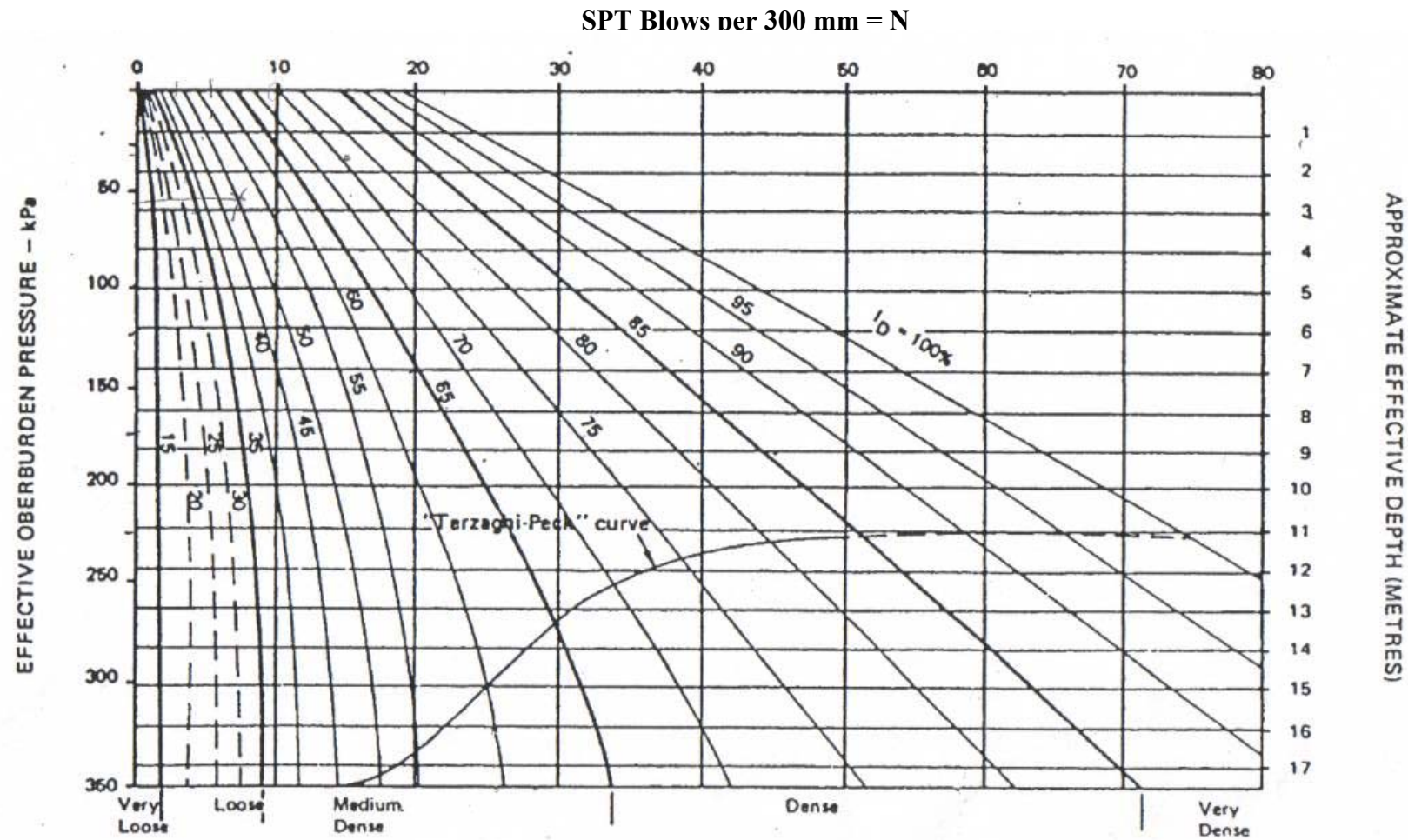


Figure 4.13: Relationship between vertical effective stress and field blow count N (Alpan, 1964)

Table 4.3: Commonly used correlations to determine friction angle of experimental sand

Sand Condition	Overburden Pressure (kPa)	Direct shear Friction Angle (°)	Uncorrected Blow Count* (N_f)	Corrected Blow Count (N_1) ₆₀	Schmertmann (1975) ϕ [°]	Wolff (1989) ϕ [°]	Hatanaka and Uchinda (1996) ϕ (°)
Very Loose	40	31	2	3	25	28	28
	90	31	2	2.2	25	28	27
	140	31	2	1.6	25	28	26
Very Dense	40	41	20	30	45	36	44
	90	41	20	22	41	34	41
	140	41	20	16	38	32	38

*Estimated uncorrected blow counts were obtained using blow count vs. overburden pressure in Alpan (1964).

The lower bound blow count for the given overburden pressure was adopted.

Summary:

Schmertmann (1975): gave an estimate 6° less than the direct shear result for the very loose sand, and within $\pm 4^\circ$ for the very dense sand.

Wolff (1989): gave an estimate of 3° less than the direct shear result for the very loose sand, and within -9° for the very dense sand.

Hatanaka and Uchinda (1996): gave an estimate of 5° less than the direct shear result for the very loose sand, and within $\pm 3^\circ$ for the very dense sand.

4.3.2 Correlations for Dilatancy of Sand

As discussed in the above section, the way sand reacts under shearing load depends on the density, normal stress and angularity of the sand grains. When the experimental sand was packed densely the shearing had to overcome initial interlocking of the sand particles. This means the sand grains in the dense case were packed tightly together so the grains were effectively restrained. Yet once the shearing started to overcome this interlocking, the sand particles started to roll up onto each other pushing against the normal load.

This resulted in a negative volume change (i.e. increase in volume) that is represented by a negative volumetric strain. The increase in volume shows the potential dilation property of the sand in question. Therefore, to achieve critical void ratio dense sand has to loosen so particle interlocking was overcome in the shear failure zone. This action of the dense sand becoming lower in density when approaching ultimate shear failure is referred to as ‘shear softening’.

In the case of loose sand, the particles tend to compact under shear loads so the density is increased. Then the volumetric strain for loose sand under shear load is generally positive, i.e. decrease in volume. This means that loose sand tends not to exhibit dilation. To reach critical void ratio loose sand needs to increase in density, and this is commonly referred to as ‘shear hardening’ (Craig, 1992).

Some typical volumetric trends for loose and dense sands determined from direct shear tests are shown in Figure 4.14.

The vertical displacement verses the lateral displacement for the experimental sand is plotted in Figure 4.15. When comparing Figures 4.14 and 4.15, the experimental direct shear test data agrees with trends indicated by other researchers.

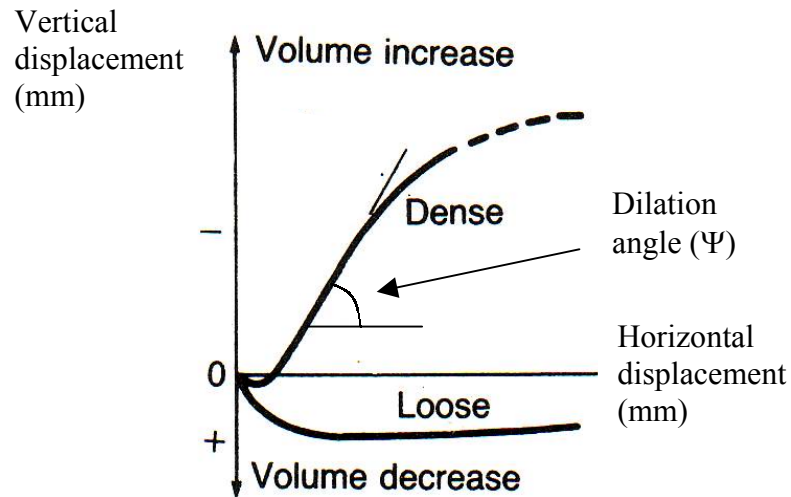


Figure 4.14: Typical vertical displacement vs. horizontal displacement plot for sand (Yasufuku et al., 2004)

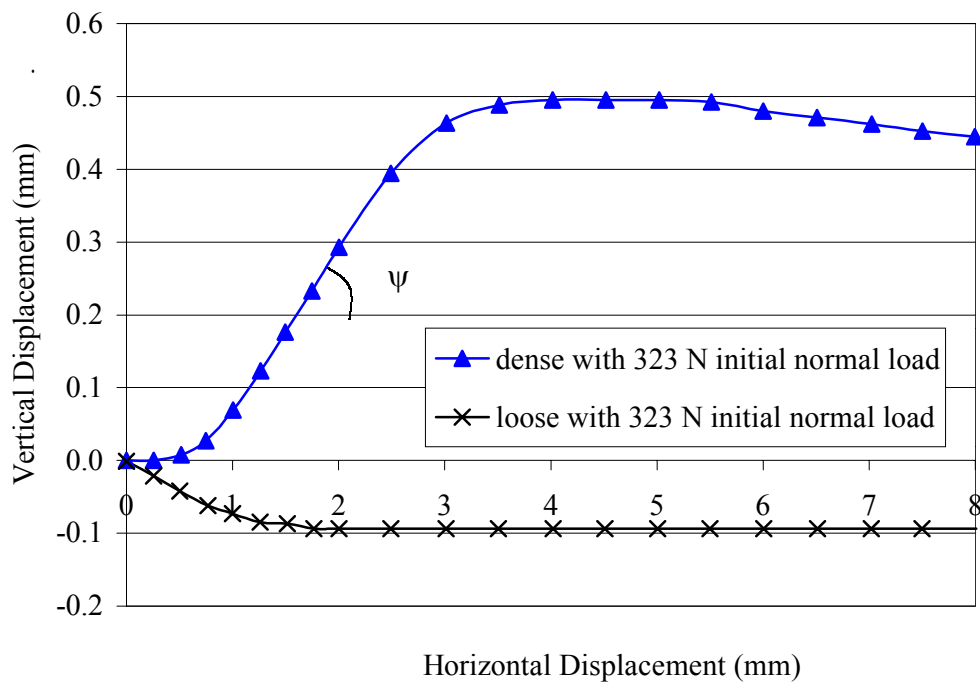


Figure 4.15: Horizontal displacement vs. vertical displacement for experimental sand

From Figure 4.15, the dilation angle (ψ) for the experimental sand can be approximated as (Yasufuku et al, 2004; and Craig, 1992):

$$\psi = \tan^{-1}(\text{vertical displacement/horizontal displacement}) \quad (4.1)$$

In the field geotechnical engineers don't usually have access to direct shear test data and rely on semi-empirical correlations. One such correlation for the dilation angle is given by Bolton (1986), and shown in Figure 4.16.

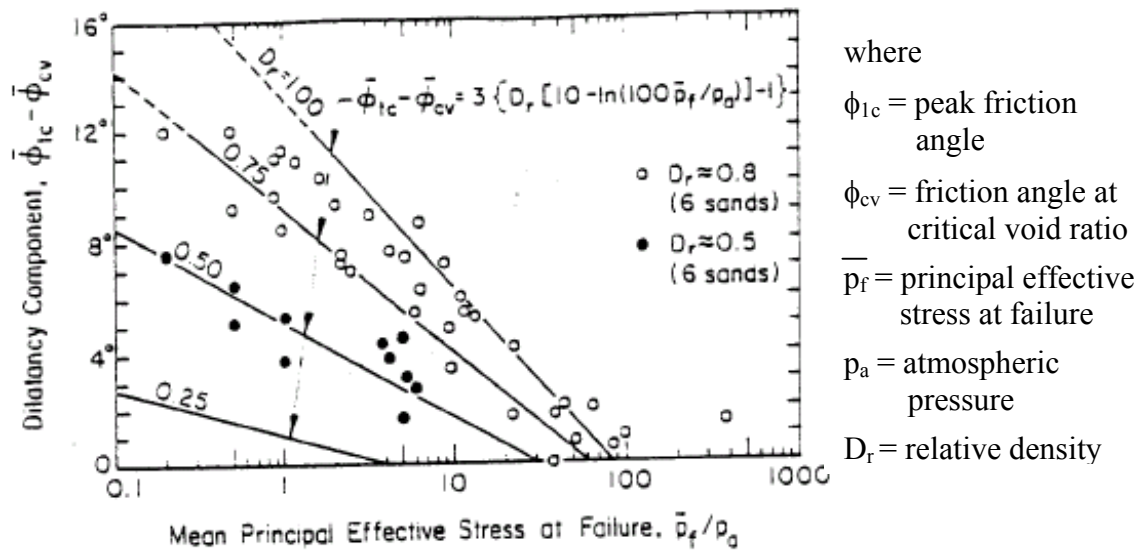


Figure 4.16: Approximation of dilation, ψ (Bolton, 1986)

The dilation angle determined from the direct shear test, and the predicted dilation angle from Equation 4.1 are given in Table 4.4.

Table 4.4: Dilation angle for experimental sand

Sand Condition	Experimental Dilation using Equation 4.1 (°)	Predicted Dilation using Bolton's Method $[\phi_{1c} - \phi_{cv}]$ (°)
Very Loose	0	0
Very Dense	12	11

*where $\phi_{1c} = 41^\circ$ for the very dense experimental sand, and $\phi_{cv} = 30^\circ$ for the dense residual state and very loose state – see Table 4.3.

From Table 4.4, it can be concluded that the correlation provided by Bolton (1986) provides a reasonable estimate for the dilation angle. This correlation is used for the subsequent work in this thesis.

It is noted by Bolton that the friction angle at critical void ratio rarely tends to be outside a range of 30° to 33° , except when a significant portion of silt is present resulting in a critical friction angle as low as 27° . Therefore, a conservative approach for determining the dilation angle of sand is to adopt a critical friction angle of 33° (i.e. $\psi = \phi_{\text{peak at a given density}} - 33^\circ$).

4.3.3 Correlations for Elastic Modulus of Sand

Sand is made from a countless number of small particles typically between the size of 0.075 mm and 2.36 mm. When in contact with each other the particles can transfer load from one to another, and deform until a new equilibrium state is achieved. The sand acts as a continuum and its stiffness may be estimated, using similar principles as for other homogenous engineering materials. One such strength parameter is Young's modulus that is equal to the gradient of the stress-strain curve (Figure 4.17).

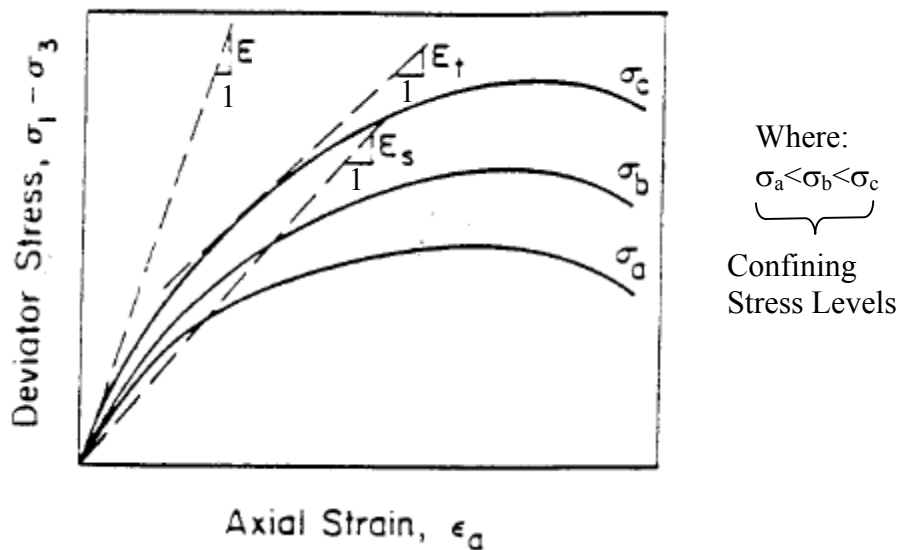


Figure 4.17: Typical stress-strain relationship for sand

Sand or soil usually exhibits a non-linear response under load as seen from the above figure. Several ways to represent the Young's modulus for sand are listed below:

- Initial tangent modulus (E)

- Tangent modulus (E_t) at a particular stress level
- Secant modulus (E_s) at a particular stress level

It is important to note that the elastic modulus of sand is dependent on the confining stress levels indicated as σ_a , σ_b and σ_c in Figure 4.17. Therefore, the soil is commonly said to be a non-linear elasto-plastic material that is stress history dependent. For example, if a pile is embedded in sand and loaded at a stress level then discrete plastic strains would occur. Sand acts as an elasto-plastic material where a percentage of strains would not be recoverable upon load release. If the pile load were increased shear failure zones would eventually occur along with areas of plastic strain.

Given the above, it is clear that the constitutive behaviour of sand or soil in general is very complex. Therefore, approximations and simplifications have to be made when estimating constitutive parameters such as Young's modulus (E) for sand. Many researchers have provided empirical correlations for predicting Young's modulus due to this uncertainty. Three of the more popular correlations are shown in Table 4.5.

Table 4.5: Popular correlations for Young's modulus (E) of sand using SPT results

Researcher	Correlation for Young's modulus		
Poulos (1975)	Consistency	Normalised Elastic Modulus E/p_a	
		Typical	Driven Piles
	Loose	100 to 200	275 to 550
	Medium	200 to 500	550 to 700
	Dense	500 to 1000	700 to 1100
	Where the sand condition can be related generally to the field blow count as follows (Craig, 1992):		

Table 4.5 Continued: Popular correlations for Young's modulus (E) of sand
using SPT results

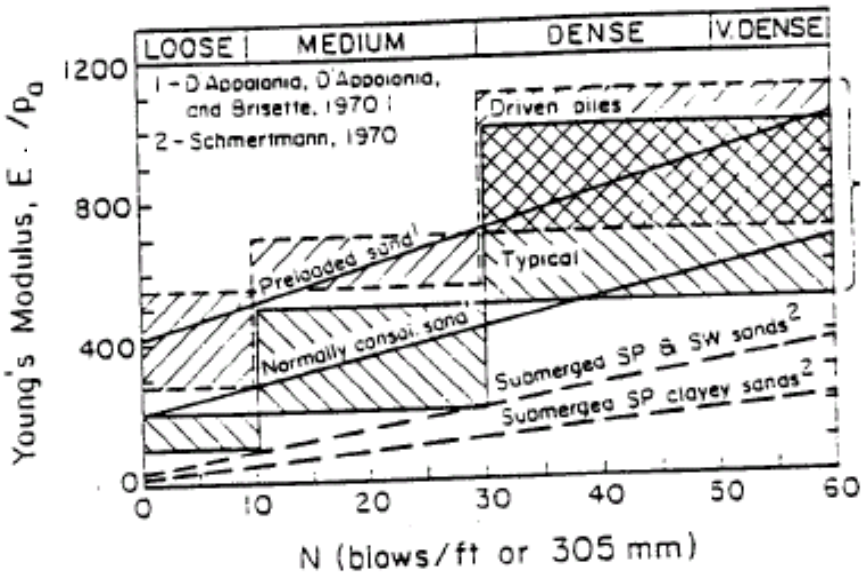
Researcher	Correlation for Young's modulus																								
Poulos (1975)	<table><tr><th>N Value</th><th>Classification</th><th>D_r (%)</th><th>(N₁)₆₀</th></tr><tr><td>0-4</td><td>Very Loose</td><td>0-15</td><td>0-3</td></tr><tr><td>4-10</td><td>Loose</td><td>15-35</td><td>3-8</td></tr><tr><td>10-30</td><td>Medium Dense</td><td>35-65</td><td>8-25</td></tr><tr><td>30-50</td><td>Dense</td><td>65-85</td><td>25-42</td></tr><tr><td>>50</td><td>Very Dense</td><td>85-100</td><td>42-58</td></tr></table>	N Value	Classification	D _r (%)	(N ₁) ₆₀	0-4	Very Loose	0-15	0-3	4-10	Loose	15-35	3-8	10-30	Medium Dense	35-65	8-25	30-50	Dense	65-85	25-42	>50	Very Dense	85-100	42-58
N Value	Classification	D _r (%)	(N ₁) ₆₀																						
0-4	Very Loose	0-15	0-3																						
4-10	Loose	15-35	3-8																						
10-30	Medium Dense	35-65	8-25																						
30-50	Dense	65-85	25-42																						
>50	Very Dense	85-100	42-58																						
Schmertmann (1970) – based on statistical comparisons between CPT and SPT.	$E \approx 766N \text{ (kPa)}$ <p>where: N is the uncorrected blow count.</p>																								
Miscellaneous as shown in adjacent diagram. Extracted from Callanan and Kulhawy (1985)																									
Mitchell and Gardner (1975)	$E/p_a = 5N_{60} \text{ (for sands with fines)}$ $E/p_a = 10N_{60} \text{ (for clean normally consolidated sands)}$ $E/p_a = 15N_{60} \text{ (for clean overconsolidated sands)}$ <p>Where: N₆₀ is the blow count corrected for hammer efficiency.</p>																								

Table 4.5 Continued: Popular correlations for Young's modulus (E) of sand using SPT results

Researcher	Correlation for Young's modulus	
Das (1999)	Type of soil	Elastic Modulus E (MPa)
	Loose sand	10.35-24.15
	Medium dense sand	17.25-27.60
	Dense sand	34.50-55.20
	Silty sand	10.35-17.25
	Sand and Gravel	69-172.50

Young's modulus is also dependent on the confining stresses, foundation type and different loading scenarios. Then it is expected that the method of pile installation would have a vast impact on the soil properties. For example, when piles are driven into sand driving stresses are imposed on the sand body around the pile. It is anticipated that the values for the soil modulus would become higher than previous in situ values. This increase in sand modulus has been examined by Poulos (1975).

A comparison plot for non-dimensional Young's modulus vs. field blow count has been prepared for normally consolidated in situ sand, and for preloaded sand or sand exposed to pile driving loads. The blow counts explored corresponded to $N_{60} = 0$ (very loose state), $N_{60} = 5$ (loose to medium dense state), $N_{60} = 30$ (dense to very dense state), and $N_{60} = 50$ (very dense state, possibly highly to moderately weathered rock or cemented soil). These plots are shown in Figures 4.18 and 4.19.

It is noted that some correlations such as the ones developed by Poulos (1975) give a range of Young's modulus for any one particular blow count. The upper and lower range for Young's modulus of sand from each of the explored blow counts discussed above is represented as a single point on the plots.

It can be seen from Figures 4.18 and 4.19 there is a degree of scatter in the prediction correlation used for the Young's modulus of sand. Therefore, a set of data for Young's modulus vs. blow count was assembled from correlations suggested by various researchers. A line of best fit was then used to represent this set of data, as the line of best fit would be influenced by all the correlations. It is also noted that three points on

the upper range of Poulos's correlation have been excluded in the formulation of the line of best fit. This exclusion gave an additional realm of conservatism to the line of best fit. The final data set and best fit correlation for normally consolidated sand, and preloaded sand or sand exposed to pile driving forces is presented in Figures 4.20 and 4.21.

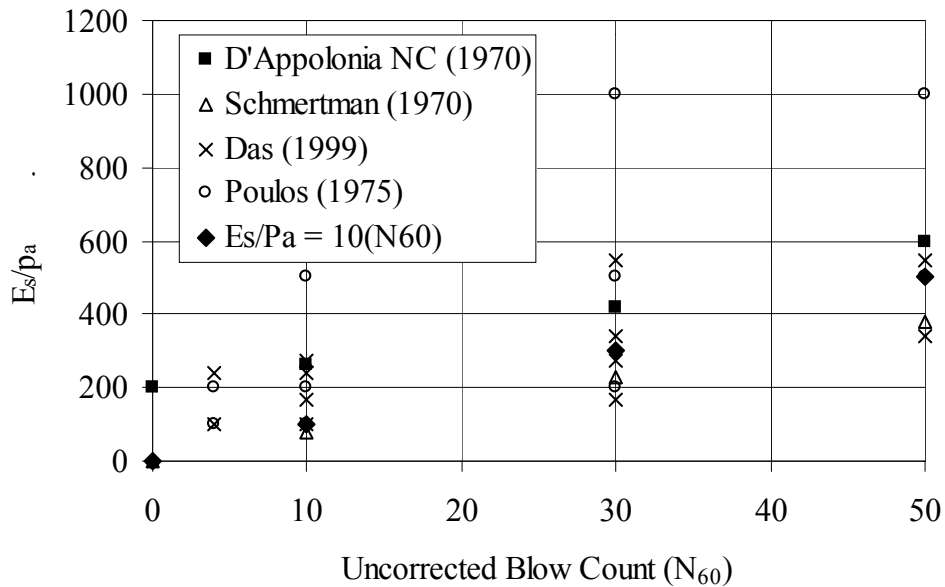


Figure 4.18: Non-dimensional Young's modulus vs. field blow count for normally consolidated sand

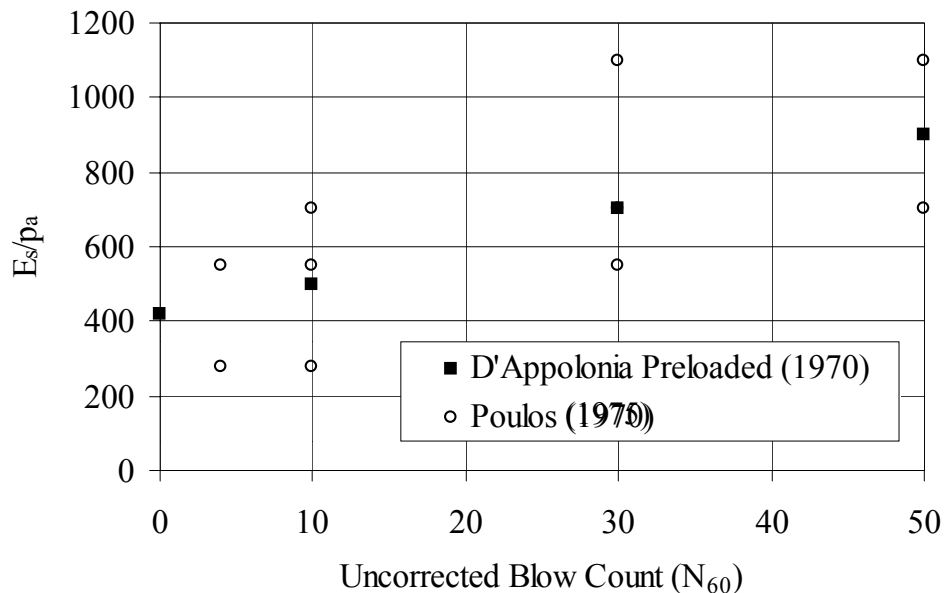


Figure 4.19: Non-dimensional Young's modulus vs. field blow count for preloaded sand or sand exposed to driving forces

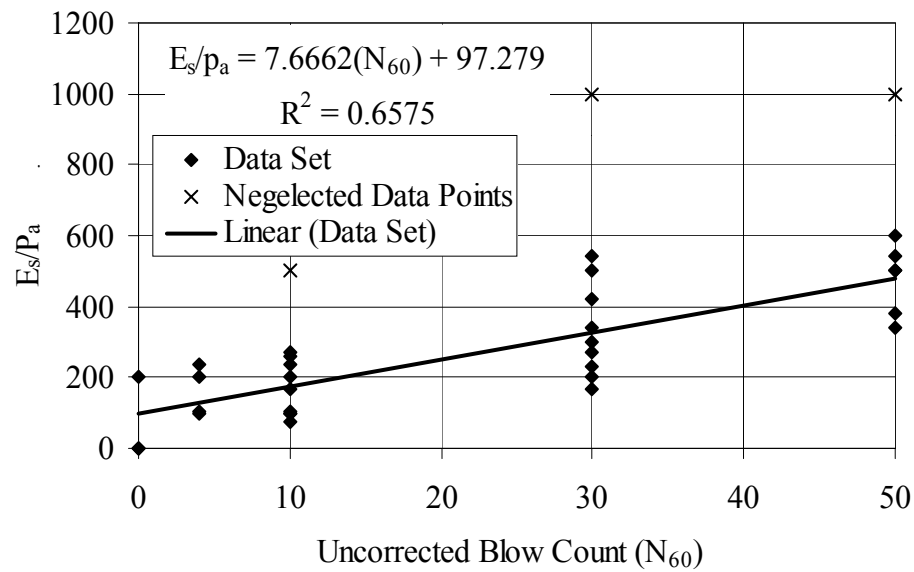


Figure 4.20: Line of best fit for non-dimensional Young's modulus vs. field blow count of normally consolidated sand

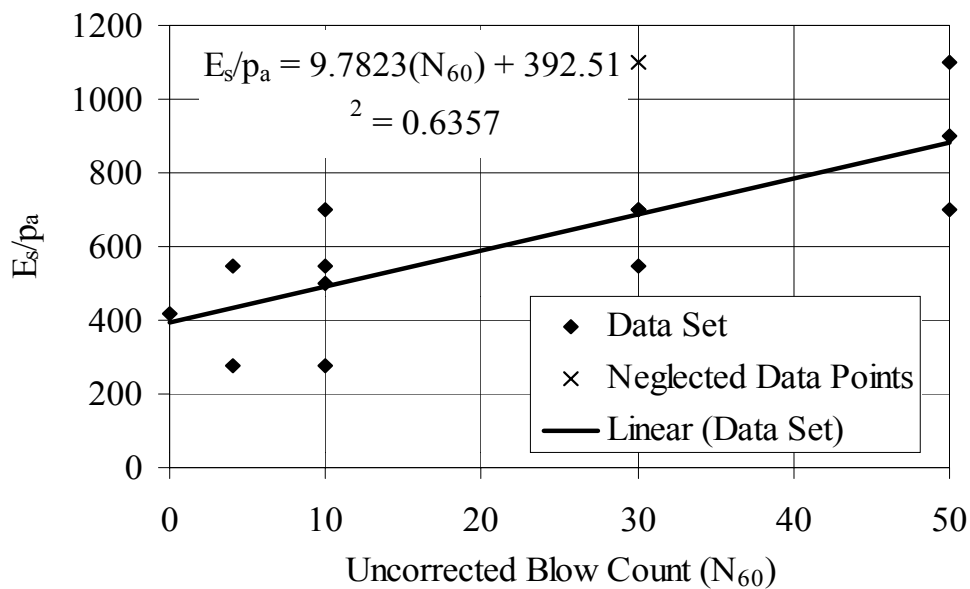


Figure 4.21: Line of best fit for non-dimensional Young's modulus vs. field blow count of preloaded sand or sand exposed to pile driving forces

The line of best-fit correlation for Young's modulus is used in the subsequent computational sections of this research. The final correlations employed to determine the line of best fit are given in Table 4.6. It is also noted that the sand surrounding bored piles is assumed to be unaffected by the pile installation process. It has been assumed that the in situ sand is normally consolidated as opposed to overconsolidated, as the preconsolidation pressure is difficult to calculate accurately in the field. Then assuming the sand to be normally consolidated in its natural state will add a realm of conservatism when predicting settlement in natural sand conditions, i.e. in the case of bored cast-in-place piles.

Table 4.6: Final correlations for E_s based on a study of some available correlations

Sand condition	Proposed correlations for sand Young's modulus
Normally consolidated sand	$E/p_a = 7.7N_{60} + 97.3$
Overconsolidated sand	$E/p_a = 15N_{60}$
Preloaded sand or sand exposed to pile driving	$E/p_a = 9.7N_{60} + 392.5$

4.3.4 Poisson's Ratio (ν) of Sand

Soils in real life generally exhibit anisotropic behaviour. However, as discussed previously assumptions and simplifications are required to achieve a closed form solution that can be used to estimate footing and soil response. For this reason many researchers have idealized soil behaviour as an elastic isotropic material, which allows approximations for the footing's displacement behaviour to be determined. Young's modulus and Poisson's ratio are needed to define the sand behaviour under load, when assuming the soil is an elastic medium.

Poisson's ratio typically represents the relationship between axial and lateral strain components. As a general rule Poisson's ratio, ν , for an elastic isotropic material is given by the following equation.

$$\nu = - \epsilon_{\text{lateral}} / \epsilon_{\text{axial}} \quad (4.3)$$

where $\epsilon_{\text{lateral}}$ = lateral strain

ϵ_{axial} = axial strain

This equation is complicated further if the material is considered to be anisotropic.

Poisson's ratio does not vary greatly for sands as noted by researchers such as Trautmann and Kulhawy (1987). For isotropic elastic material Poisson's ratio varies from 0 to 0.5, and for dilatant soils experiencing inelastic behaviour Poisson's ratio may exceed 0.5.

Typical ranges for Poisson's ratio of sands is shown in Table 4.7.

Table 4.7: Typical ranges for Poisson's ratio of sand

Source	Poisson's Ratio (ν)	
Das (1999)	Consistency	Poisson's Ratio
	Loose Sand	0.2-0.4
	Medium Sand	0.25-0.4
	Dense Sand	0.3-0.45
Trautmann and Kulhawy (1987)	Consistency	Poisson's Ratio
	Loose Sand	0.1-0.3
	Dense Sand	0.3-0.4

Given the above ranges, a Poisson's ratio of 0.3 has been adopted for the research in this thesis.

CHAPTER 5: Estimating Shallow Foundation Behaviour using Numerical Models

5.1 General

A symposium was held in 1994 by the Federal Highway Administration to evaluate current standards in industry and academic practice for predicting shallow foundation settlement (Briaud and Gibbens, 1994). The results were published so that designers could gain a better understanding of their prediction tools. This symposium attracted 31 participants from nine different countries, and some of the countries were Japan, France, Australia, and United States of America. The information supplied by the symposium and discussed in this chapter will be used to help calibrate the numerical models developed as part of the current works.

The task of the symposium was to estimate the loads for five footings with settlements of 25 mm and 150 mm. The five square footings constructed in sandy soil ranged in size from 1 m to 3 m, and were loaded vertically at their centers. The participants received the results from a detailed geotechnical investigation that was undertaken at the site. A general soil profile and testing from the site plus footing geometry are shown in Table 5.1. A site plan showing the general site layout is provided in Figures 5.1a and 5.1b.

Table 5.1: Footing and general soil characteristics for symposium

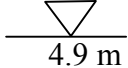
Footing	Footing Dimensions	Soil Profile (Common to all footings)	Soil Tests Available (Common to all footings)
1	3 m x 3 m	0 m Medium dense silty fine sand	<ul style="list-style-type: none"> • Borehole shear test • Cross hole wave test • Piezo-Cone penetration test
2	1.5 m x 1.5 m	3.5 m Medium dense silty sand with clay and gravel 	<ul style="list-style-type: none"> • Dilation test • Dilatometer test w/thrust measurement

Table 5.1 Continued: Footing and general soil characteristics for symposium

Footing	Footing Dimensions	Soil Profile (Common to all footings)	Soil Tests Available (Common to all footings)
3	3 m x 3 m	7 m Medium dense silty sand to sandy clay and gravel	<ul style="list-style-type: none"> • Pressure meter test • Step blade test • Standard penetration test • Water content and unit weight • Atterberg limits • Relative density • Triaxial test • Resonant column test
4	2.5 m x 2.5 m	11 m Medium dense silty sand to sandy clay and gravel	
5	1 m x 1 m	33 m	

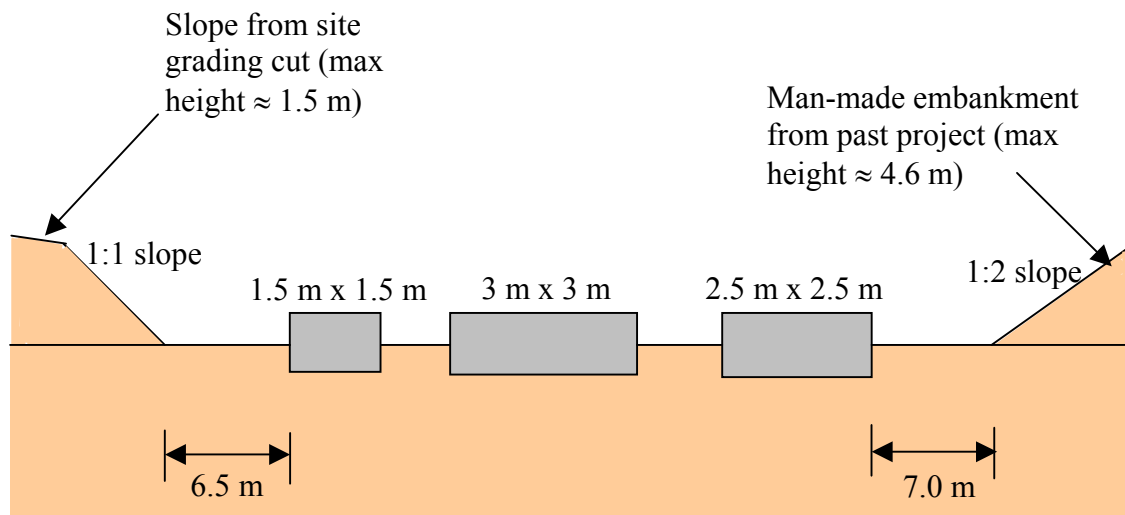


Figure 5.1 a): Cross-section A-A (see Figure 5.1b for location of cross-section)

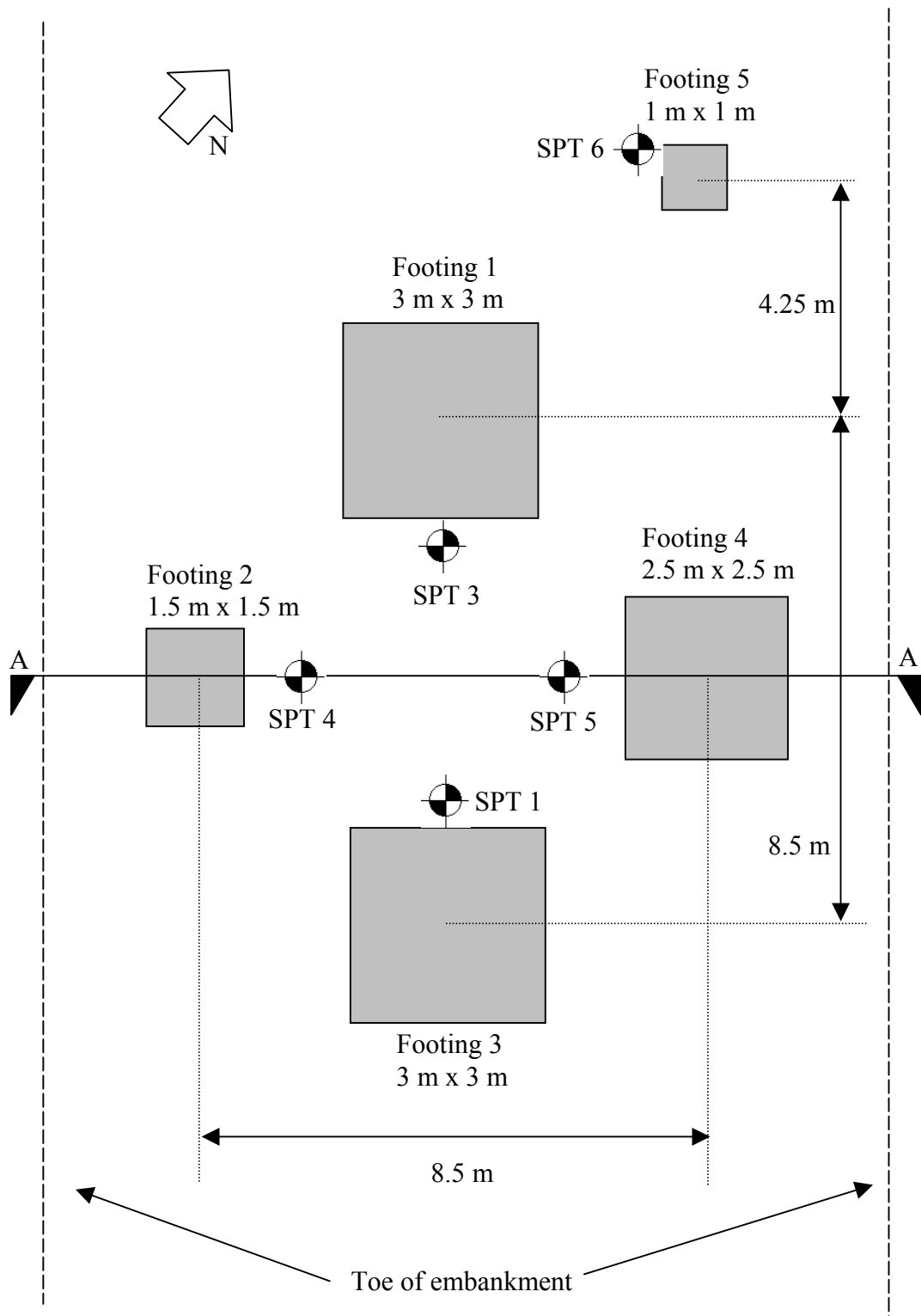


Figure 5.1 b): Layout of test footings for Federal Highway Administration Symposium

The exercise was used to evaluate numerical modelling for predicting foundation behaviour. The appropriate constitutive relationships and constitutive parameters were chosen for the study, and more discussion about constitutive parameters can be seen in Chapter 4.

This chapter also presents a numerical model of a shallow foundation as part of the work. The estimations were made by the model for the five footings, and the estimates were compared with the predictions made by the 31 participants of the symposium. The predictions from this work and estimates by the participants will also be compared to actual experimental results.

The research in this thesis uses the finite element computer package, ABAQUS, to explore shallow foundation behaviour under loads. ABAQUS is a multi-purpose computer package that allows a user to investigate mechanical, structural, and geotechnical problems under static and dynamic loadings. It is an ideal package due to its capability in modelling complex interactions between several bodies, and the available constitutive models for both geotechnical and structural materials. The package also allows for initial residual stress fields to be defined.

5.2 Behaviour Criteria and Numerical Model Development

5.2.1 *Shallow Foundation Failure Mechanism*

A variety of models have been developed to characterize the constitutive relationship and the failure behaviour of soils as discussed in Chapter 4. The constitutive models are expected to describe all types of soils realistically, and are easily calibrated (Chen, 1988). It is difficult to characterize the stress-strain relationship due to the complexity of soil under loads. The soil will undergo an elastic response at low loads. Some localized failure will occur resulting in plastic strain in the immediate area as the load increases. This results in the sand body under the foundation acting as an elasto-plastic material, and the localized plastic regions will extend as the load approaches its ultimate limit. Once the ultimate capacity of the sand is reached the foundation will undergo a large settlement.

Failure mechanism for a shallow foundation after reaching the ultimate capacity of the underlying soil is shown in Figure 5.2.

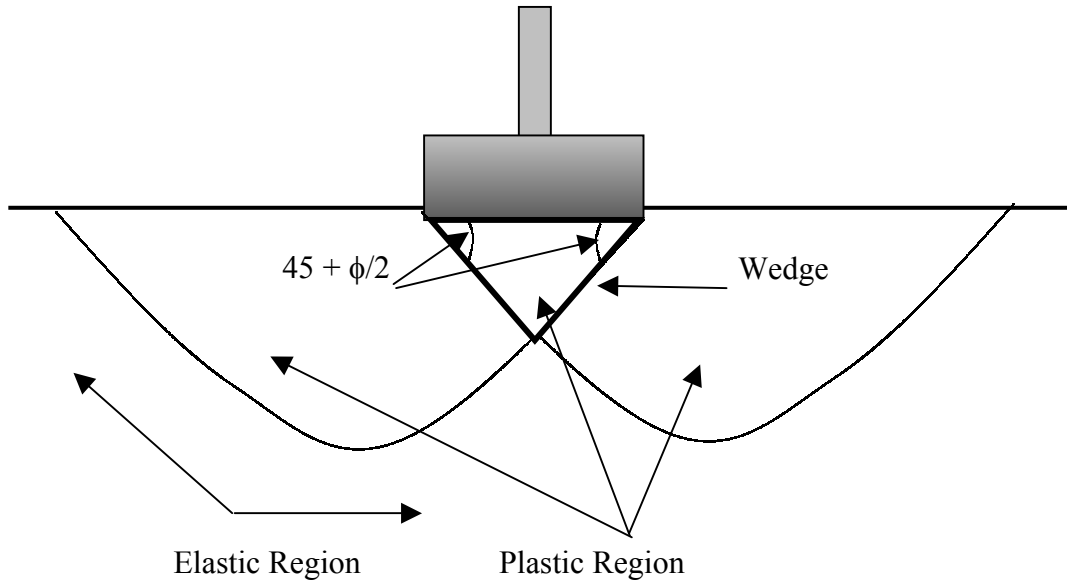


Figure 5.2: The bearing capacity failure diagram from Terzaghi (Cernica, 1995)

The footing will be pushed downwards into the soil mass when the applied load becomes equal to the ultimate bearing capacity, giving a state of plastic equilibrium below the footing at an angle of $45 + \phi/2$. The downward movement of the wedge pushes the adjoining soil sideways, and thus produces lateral forces on both sides of the wedge. The transition between the downward force and the lateral movement of the wedges takes place through regions of radial shear known as 'slip planes'. A state of plastic equilibrium will exist above the influence zone, and the remaining soil mass is in a state of elastic equilibrium. Therefore, any numerical model constructed must be able to account for elastic and plastic strains, and produce a similar failure mechanism to the one observed under an actual footing.

5.2.2 Development of Shallow Foundation ABAQUS Model

When formulating the problem an element type has to be chosen. ABAQUS has a broad range of element types available to simulate one, two and three-dimensional

problems. This section explores the feasibility of using a finite element model to predict the behaviour of shallow foundations. This was achieved by constructing a shallow foundation in ABAQUS, and comparing the output from the model against actual test results from the field. The input parameters (eg. constitutive parameters) were determined using correlations given in Chapter 4 and Section 6.5, and the field and laboratory test data. Since the shallow foundation used in the symposium was square in shape, it was considered appropriate that the soil-footing system be modelled using three-dimensional elements. A further discussion on the element types can be found in Chapter 8.

5.2.2.1 Shallow Foundation Model Types

When constructing a finite element model the problem space is discretized into a series of elements connected by nodes, as shown in Figure 5.3.

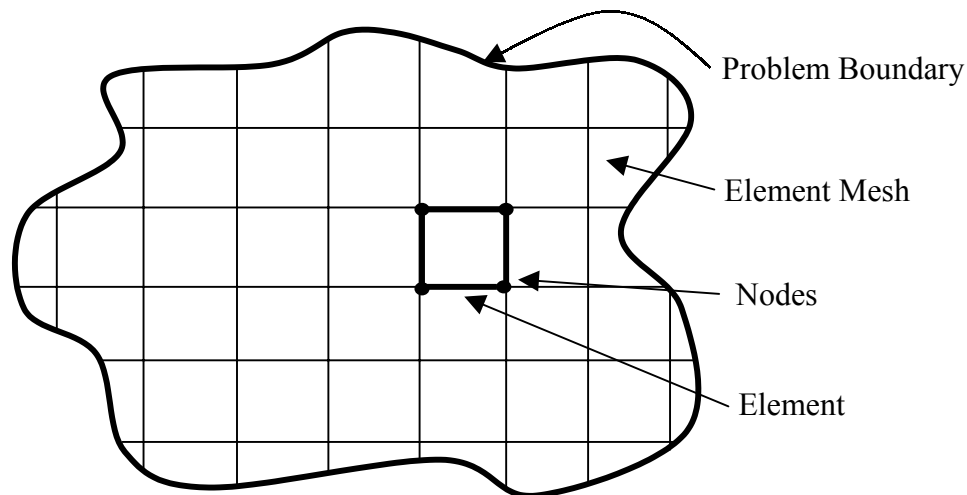


Figure 5.3: The domain example for finite element problem

The sensitivity analysis is vital for development of a reliable model. A sensitivity analysis involves refining element sizes at the cost of computational time, until the estimated values converge towards the exact model value (Figure 5.4). The solution from the model may not be entirely the same as the measured value in the field. Difference between the solution from the model and the field value could be due to assumed constitutive parameters (often based on limited field test data), assumed constitutive relationships, model geometry and errors associated with field measuring.

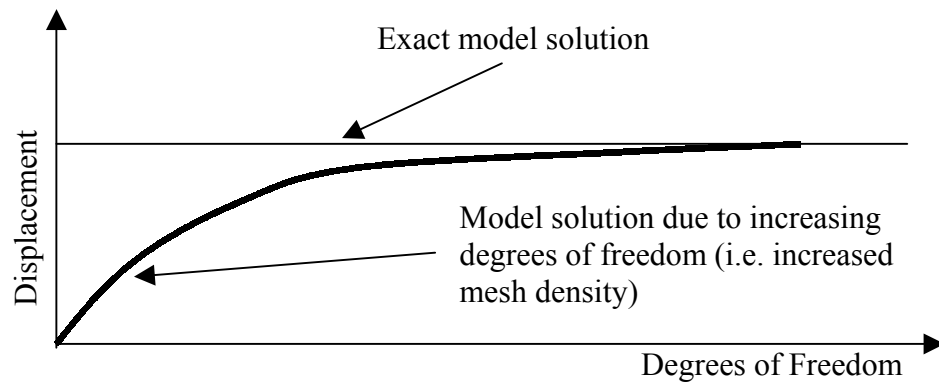


Figure 5.4: Idealized sensitivity plot

Further refinement of the mesh comes at a high computational cost with marginal gains in accuracy beyond the converged value. Four separate models were constructed to explore sensitivity. These models are as follows:

1. Coarse mesh: contains 409 active nodes connected through a series of linear elements. The general boundary conditions and model characteristics are discussed in Section 5.2.2.2. The coarse mesh is shown in Figure 5.5.

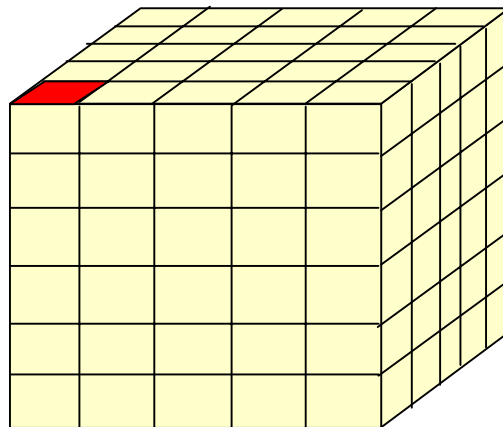


Figure 5.5: Shallow footing coarse mesh

2. Medium mesh: contains 1041 active nodes connected through a series of linear elements. The general boundary conditions and model characteristics are discussed in Section 5.2.2.2. The medium mesh is shown in Figure 5.6.

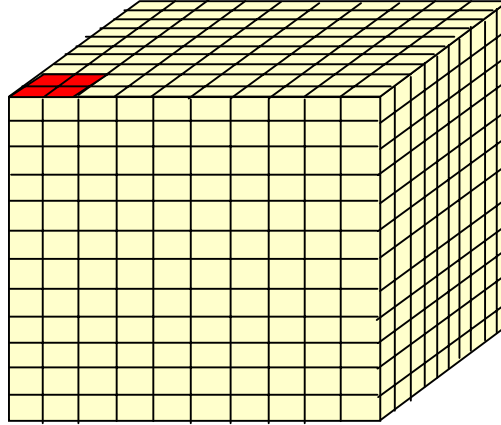


Figure 5.6: Shallow footing medium mesh

3. Fine mesh: contains 11161 active nodes connected through a series of linear elements. The general boundary conditions and model characteristics are discussed in Section 5.2.2.2. The fine mesh is shown in Figure 5.7.

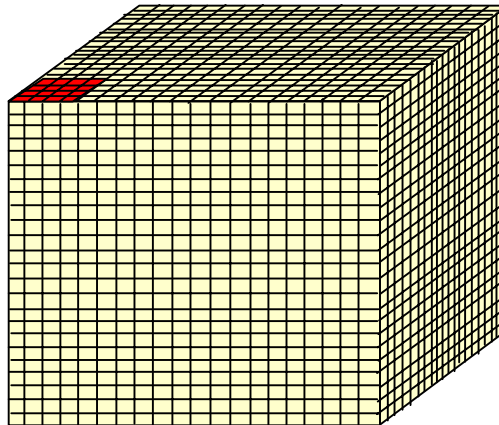


Figure 5.7: Shallow footing fine mesh

4. Quadratic mesh: contains 1041 active nodes connected through a series of quadratic elements. The number of active nodes in the quadratic mesh is the same as the medium mesh, but has the same amount of elements as the coarse

mesh. The general boundary conditions and model characteristics are discussed in Section 5.2.2.2. The quadratic mesh is shown in Figure 5.8.

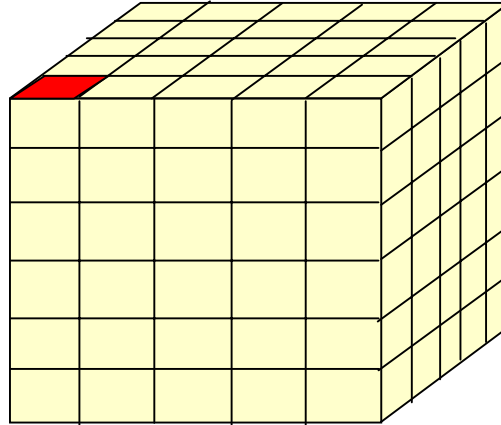


Figure 5.8: Shallow footing quadratic mesh

5.2.2.2 General Model Characteristics

The four shallow foundation models above were generally constructed from the following inputs:

- **Geometry:** The depth and width of the models were designed using the Boussinesq pressure bulbs (isobars) for stresses in a semi-infinite elastic soil. An influence zone of four times the width (B) of the footing was used based on the pressure bulbs. Beyond this zone it is assumed the displacement is equal to zero, without any effects occurring.
- **Boundary Conditions:** The square footings in this work were modelled in 3D. As a result, boundary conditions and loading symmetry were used to reduce the problem space. Figure 5.9 shows a square footing with two lines of symmetry, and each of the quadrants are equal in both geometry and loading. The problem can then be reduced down to a quarter of its original size. The displacements on the lines of symmetry (i.e. line a-a and b-b) are equal to zero, and roller supports may be used to restrain the soil along the lines of symmetry (Hibbitt et al., 2001).

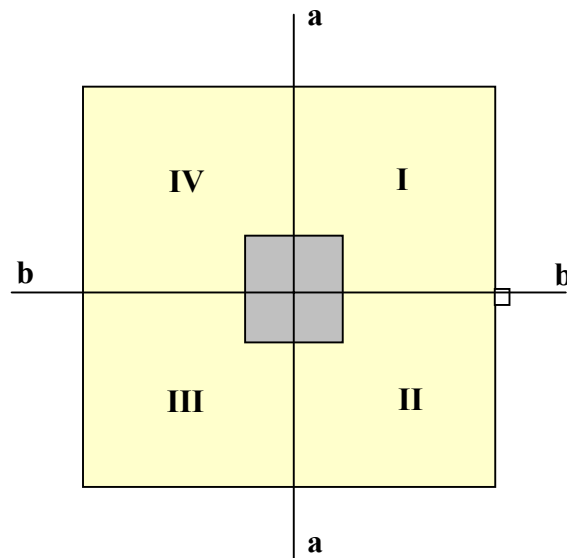


Figure 5.9: Lines of symmetry for square footing

The final model and the associated boundary conditions are shown in Figure 5.10. The model represents quadrant I of Figure 5.9.

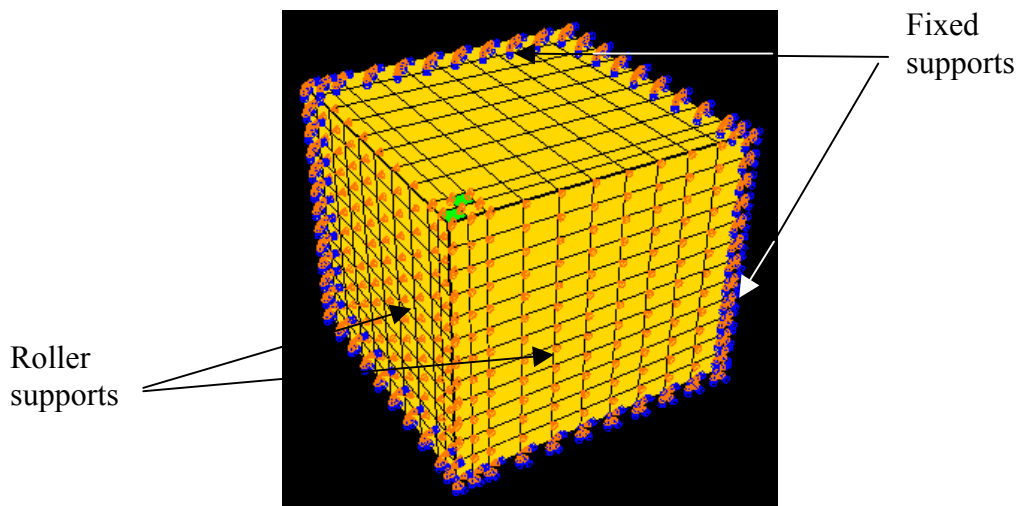


Figure 5.10: Final model boundary conditions

- **Elements:** four separate models were constructed for sensitivity purposes as discussed in Section 5.2.1.1. Three of these models were the coarse, medium and fine mesh models constructed from linear 3D elements. The fourth quadratic mesh

consisted of 20 noded 3D elements. This was for a comparison between the linear and quadratic elements to represent the sand body. For more information on the differences between these element types refer to Chapter 8.

- **Input Data:** a detailed table showing the soil parameters that were entered into the models is given Appendix A. The use of a linear elastic model in conjunction with a Mohr-Coulomb failure criterion controlled the constitutive behaviour of the model. The footings were constructed of reinforced concrete slabs, and for the purposes of these predictions are assumed to be sufficiently rigid. Hence the displacement of the sand directly below a footing is anticipated to be the same at every location. To simulate a rigid footing in the model the nodes from the footing were tied together. This meant that the tied nodes acted as a single object once displaced by the load (Figure 5.11), and therefore the footing itself did not need to be modelled.

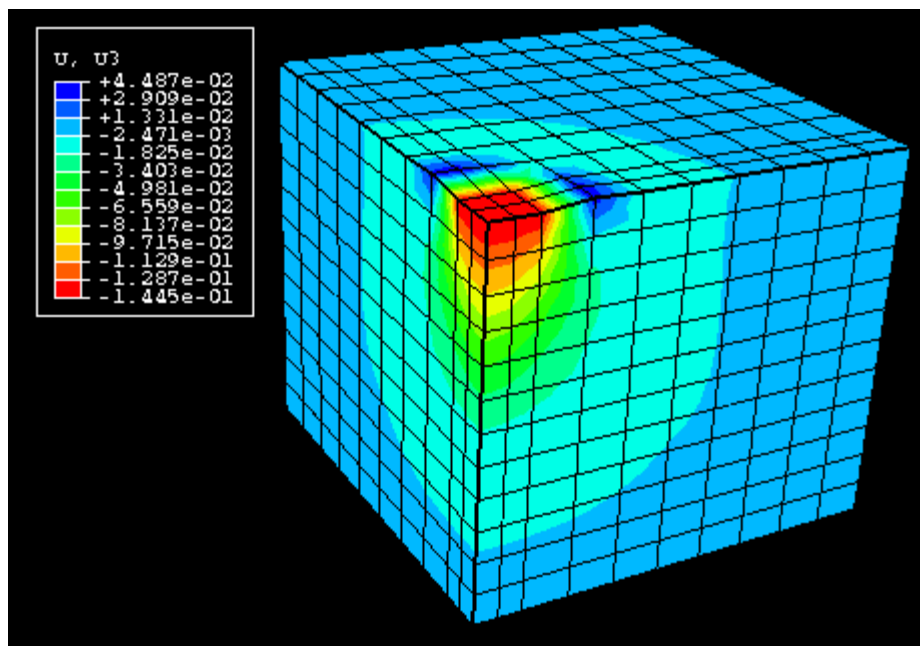


Figure 5.11: Displacement of rigid footing under load (vertical displacement contour)

- **Initial Stress State:** in most geotechnical problems a non-zero stress state exists in the soil profile, and the vertical stress increases linearly with depth. When the load is applied to soil it is applied on the initial stress state. Therefore, it is clear that the response of the system would be different with a different initial stress state. For a

non-linear analysis, the response from external loading depends on the state of the system once the loading sequence begins. The initial stress conditions for the soil profiles were established in the models with the use of ABAQUS GEOSTATIC command. A more detailed discussion on the influence of initial stress state on foundation behaviour is provided in Chapter 8.

5.3 Prediction of Shallow Foundation Behaviour

The shallow foundation constructed in ABAQUS was used to predict foundation behaviour under load. By studying the behaviour of shallow foundations with numerical modelling, it is possible to explore whether the constitutive correlations used to predict constitutive parameters in Chapter 4 are valid.

5.3.1 Symposium Footing Size and Soil Profiles

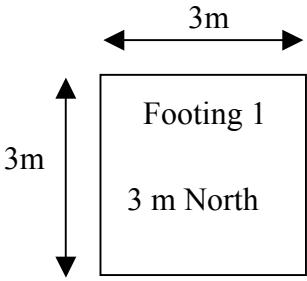
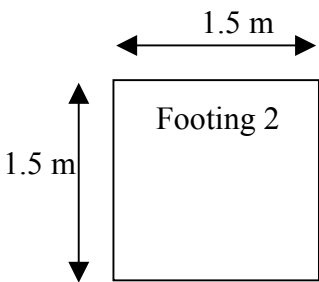
The standard penetration test (SPT) was chosen as the primary source of test data rather than the cone penetration test (CPT) data. The reason for this being that the blow count information and the associated correlations were based on SPT data (Chapter 4). In general practice, SPT may be conducted in loose to very dense sand deposits. CPT may be employed in regions where very soft to stiff clays are encountered, but the clay must be soft enough to ensure the CPT tip is not damaged during the testing process.

The five footings and soil characteristics tested for the Federal Highway Administration Prediction Symposium are presented in Table 5.2 and in Section 5.1.

For a profile of the soil layering and properties refer to Appendix A. The first layer of each set of soil test data was neglected (approximately 1m). This is done regularly in general practice, as the first layer of soil can often yield inaccurate characteristics of the soil profile below. The friction angle and elastic modulus of the sand was calculated using the correlations outlined in Chapter 4. The blow counts from the test data were separated into layers and a weighted average value was obtained for each of the soil layers. In order to determine ϕ' , the Hatanaka and Uchida (1996) correlation was used and is described in Chapter 4. This correlation uses $(N_1)_{60}$, which is the blow count corrected for overburden (C_N) and hammer efficiency (C_{ER}). The hammer efficiency is

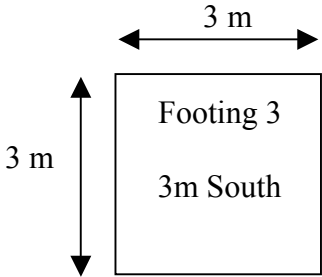
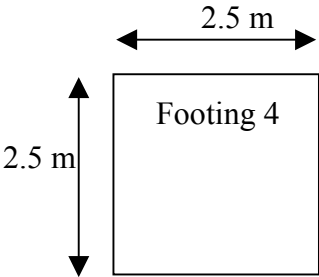
assumed to be 60% that results in C_{ER} being equal to 1. From this the following correlation was used to convert the field blow count (N) to the corrected blow count $(N_1)_{60}$.

Table 5.2: Footing dimensions and assumed soil profile under footings

Footing Dimensions and Characteristics	Soil Profile and Values
 <p>Embedment depth = 0.762 m Footing thickness = 1.219 m Bulk unit weight = 18 kN/m³</p>	<div data-bbox="810 616 1334 913" style="background-color: #ffffcc; padding: 10px; border: 1px solid black;"> <p style="text-align: center;">Layer 1</p> <p>Depth of soil layer = 8 m Average blow count $N_{ave} = 19$ Young modulus of soil $E_s = 25$ MPa Friction angle of soil $\phi = 40^\circ$</p> </div> <div data-bbox="810 920 1334 1218" style="background-color: #ffcc99; padding: 10px; border: 1px solid black;"> <p style="text-align: center;">Layer 2</p> <p>Depth of soil layer = 4 m Average blow count $N_{ave} = 42$ Young modulus of soil $E_s = 43$ MPa Friction angle of soil $\phi = 43^\circ$</p> </div>
 <p>Embedment depth = 0.762 m Footing thickness = 1.219 m Bulk unit weight = 18 kN/m³</p>	<div data-bbox="804 1395 1327 1697" style="background-color: #ffffcc; padding: 10px; border: 1px solid black;"> <p style="text-align: center;">Layer 1</p> <p>Depth of soil layer = 4 m Average blow count $N_{ave} = 17$ Young modulus of soil $E_s = 23$ MPa Friction angle of soil $\phi = 38^\circ$</p> </div>

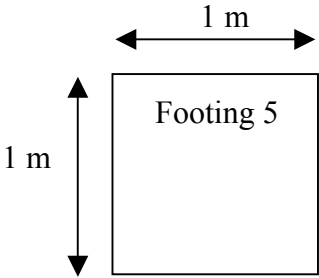
Note: the average blow count for each layer was obtained using a weighted average of each individual blow count within the layer.

Table 5.2 Continued: Footing dimensions and assumed soil profile under footings

Footing Dimensions and Characteristics	Soil Profile and Values
 <p>Embedment depth = 0.889 m Footing thickness = 1.346 m Bulk unit weight = 18 kN/m³</p>	<div data-bbox="810 387 1334 689" style="background-color: #ffffcc; padding: 10px; border: 1px solid black;"> <p>Layer 1</p> <p>Depth of soil layer = 8 m Average blow count $N_{ave} = 23$ Young modulus of soil $E_s = 28$ MPa Friction angle of soil $\phi = 42^\circ$</p> </div> <div data-bbox="810 689 1334 992" style="background-color: #ffcc99; padding: 10px; border: 1px solid black;"> <p>Layer 2</p> <p>Depth of soil layer = 4m Average blow count $N_{ave} = 49$ Young modulus of soil $E_s = 48$ MPa Friction angle of soil $\phi = 44^\circ$</p> </div>
 <p>Embedment depth = 0.762 m Footing thickness = 1.219 m Bulk unit weight = 18 kN/m³</p>	<div data-bbox="817 1162 1340 1464" style="background-color: #ffffcc; padding: 10px; border: 1px solid black;"> <p>Layer 1</p> <p>Depth of soil layer = 8 m Average blow count $N_{ave} = 24$ Young modulus of soil $E_s = 29$ MPa Friction angle of soil $\phi = 39^\circ$</p> </div> <div data-bbox="817 1464 1340 1767" style="background-color: #ffcc99; padding: 10px; border: 1px solid black;"> <p>Layer 2</p> <p>Depth of soil layer = 2 m Average blow count $N_{ave} = 44$ Young modulus of soil $E_s = 44$ MPa Friction angle of soil $\phi = 45^\circ$</p> </div>

Note: the average blow count for each layer was obtained using a weighted average of each individual blow count within the layer.

Table 5.2 Continued: Footing dimensions and assumed soil profile under footings

Footing Dimensions and Characteristics	Soil Profile and Values
 <p>Embedment depth = 0.711 m Footing thickness = 1.168 m Bulk unit weight = 18 kN/m³</p>	<div style="border: 1px solid black; padding: 10px; background-color: #ffffcc; margin: 10px auto; width: 80%;"> <p style="text-align: center;">Layer 1</p> <p>Depth of soil layer = 4 m Average blow count $N_{ave} = 19$ Young modulus of soil $E_s = 25$ MPa Friction angle of soil $\phi = 40^\circ$</p> </div>

Note: the average blow count for each layer was obtained using a weighted average of each individual blow count within the layer.

$$(N_1)_{60} = (C_{ER}) * (C_N) * (N) \quad (5.1)$$

where: C_N = overburden correction factor = $9.78 \sqrt{\frac{1}{\sigma'_{v0} \text{ (kPa)}}}$, and

C_{ER} = hammer efficiency factor (standard hammer used) = 1.

5.3.2 Prediction of Symposium Footing Behaviour

The 31 predictors who took part in the symposium had to predict the load that would correspond to a footing settlement of 25 mm and 150 mm (documented by Briaud and Gibbens, 1994). In the present work, the actual (measured) load-displacement curves for the four shallow foundation tested at the symposium were compared with the predictions from ABAQUS. A direct comparison against the estimates made by the 31 predictors is also given in subsequent sections.

From the footing dimensions and soil properties shown in Section 5.3.1, the following load-displacement curves were produced for each of the five footings tested at the symposium (Figures 5.12 to 5.16).

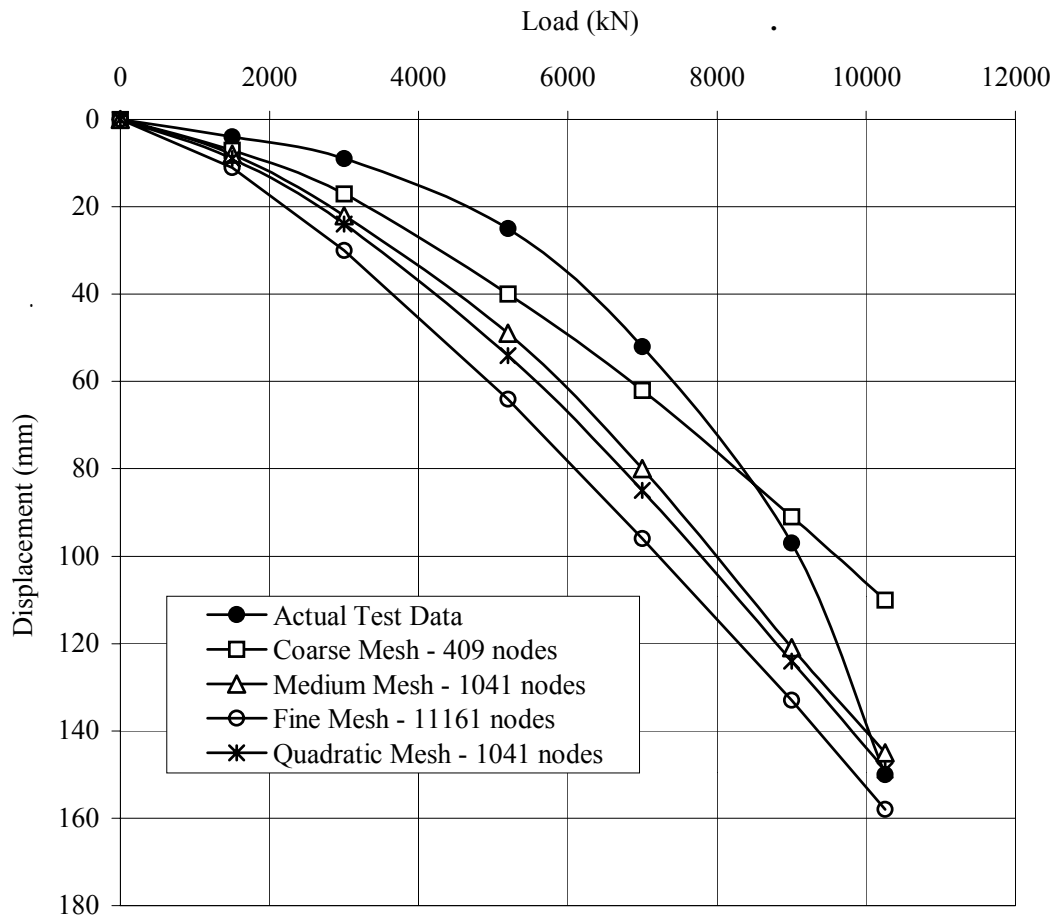


Figure 5.12: Footing 1 load-displacement prediction

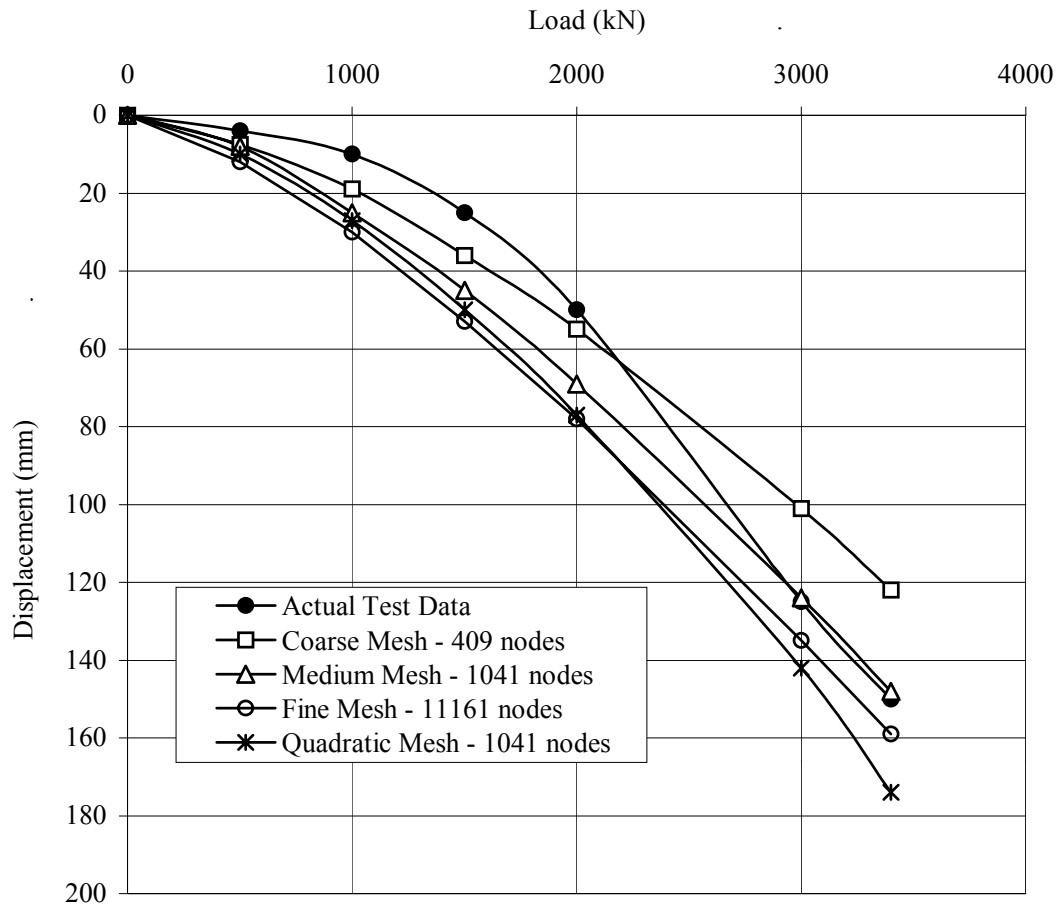


Figure 5.13: Footing 2 load-displacement prediction

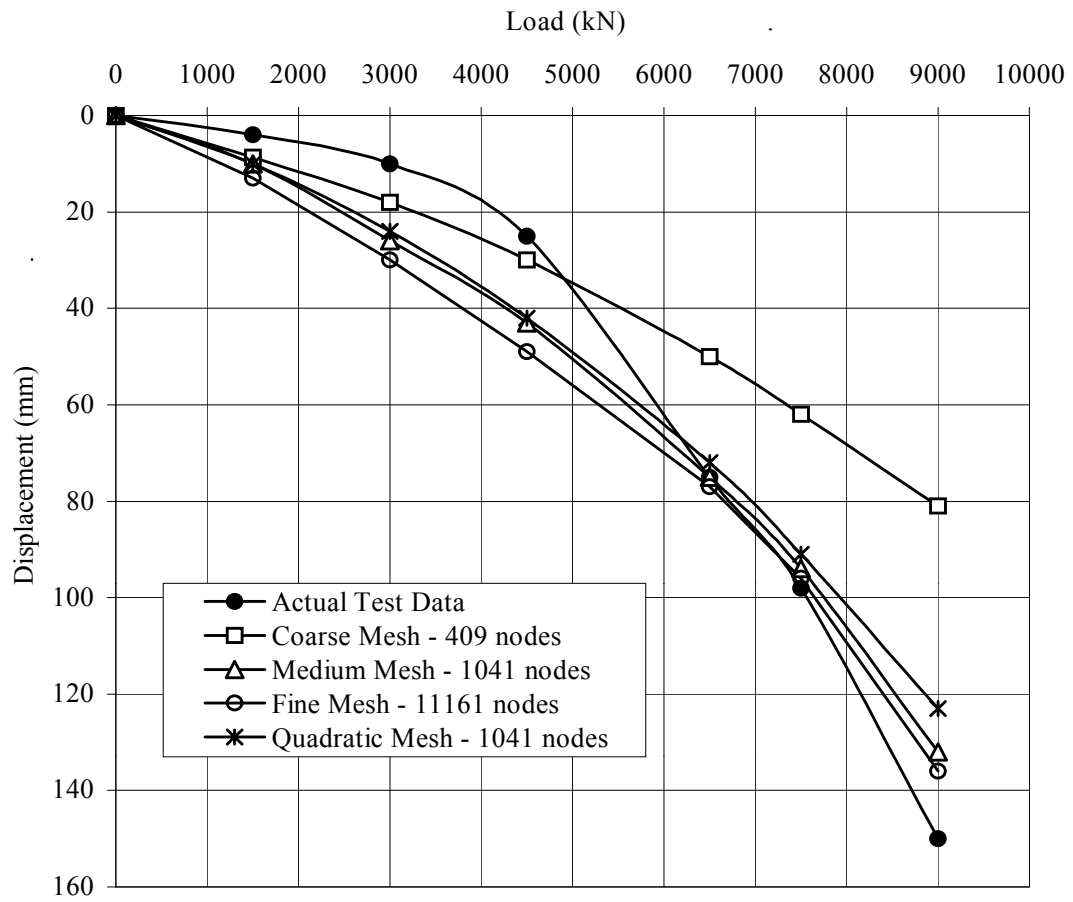


Figure 5.14: Footing 3 load-displacement prediction

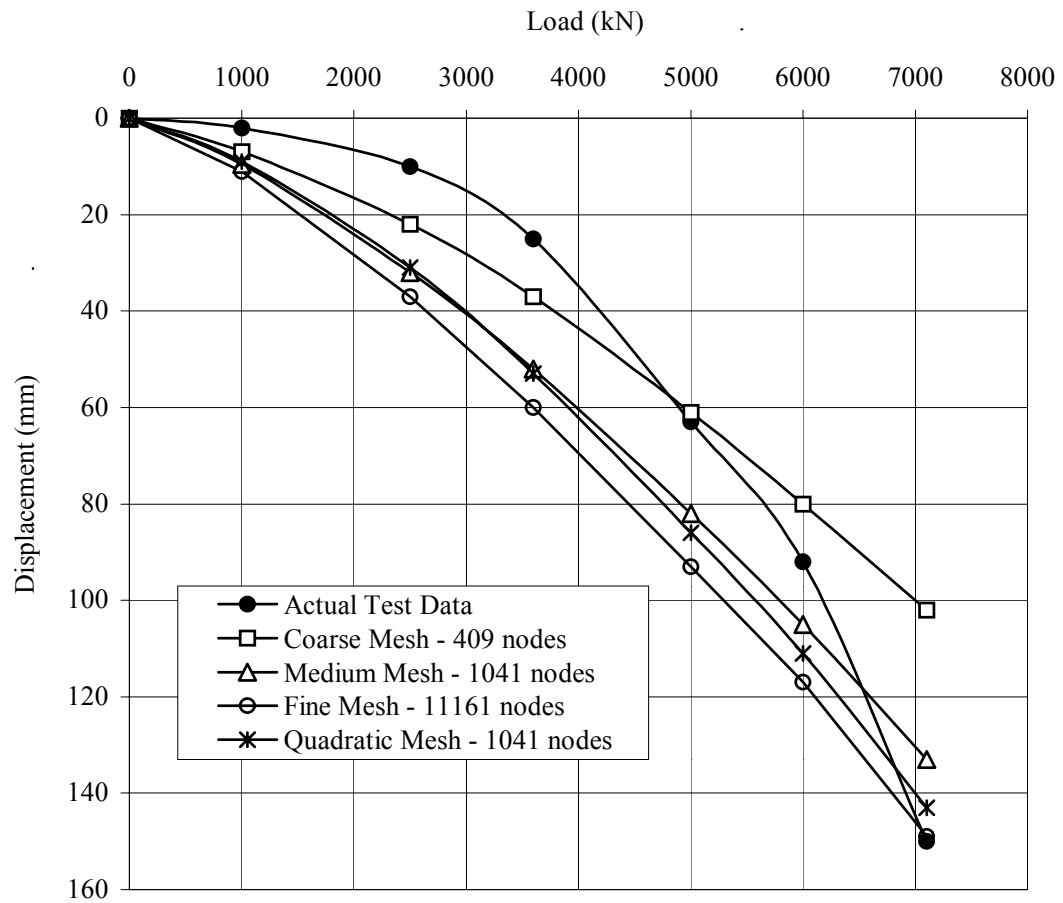


Figure 5.15: Footing 4 load-displacement prediction

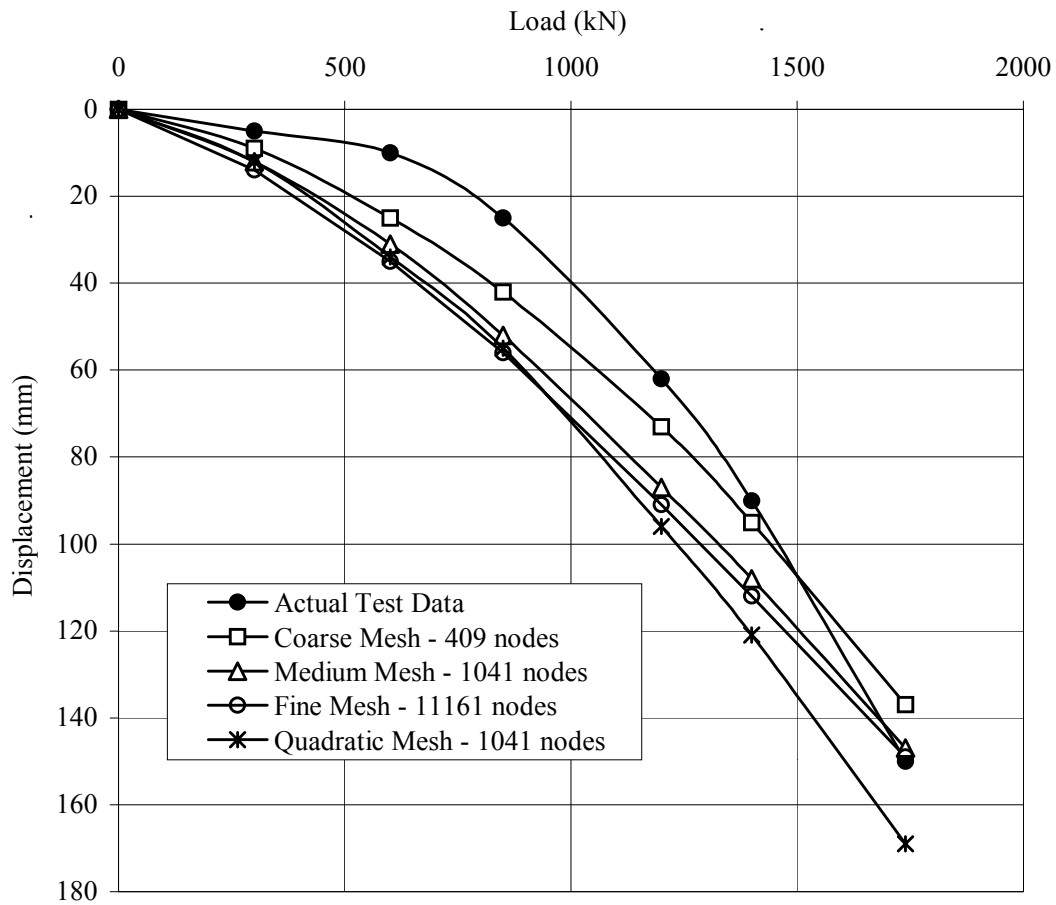


Figure 5.16: Footing 5 load-displacement prediction

The numerical modeling showed the following trends:

- The meshes with increased active nodes tended to converge towards a single converged solution as discussed in Section 5.2.2.1.
- The linear and quadratic meshes containing the same amount of active nodes produced close results, with the quadratic mesh having slightly higher displacements than its linear counterpart. The linear mesh may be slightly more 'rigid' due to the linear shape function used to approximate the displacement between the nodes. It is anticipated that the numerical models will generally converge to a similar result regardless of the mesh type (e.g. linear or quadratic), provided a converged mesh solution is achieved.
- The meshes with increased node number (i.e. higher mesh density) produced higher displacements for each given load. This is due to the mesh with increased node

density being able to ‘bend’ more realistically under load. For example, the displacement of the coarse mesh with a linear shape function approximation does not allow a higher bending action to occur between nodes when compared to a higher node density mesh. It was also noted that meshes with differing node densities produced results that were similar in the elastic range, but became more significantly different once the load induced elasto-plastic to plastic strain range.

- The meshes tended to converge away from the actual results in the elastic region, but tended to converge towards the actual curve in the plastic range. It is anticipated that the meshes with varying node densities will converge towards one single exact model solution. The exact solution is dependent on the soil properties, constitutive behaviour models chosen to represent the sand, the sand stress history, and the assumption that the sand is a continuum. The sand in the field forms discrete slip planes that may result in some differences between the real footing, and the finite element footing behaviour. It is such factors that result in differences between the models (Section 5.2.1).

To examine the performance of a model, it is good practice to compare against actual test data, predictions made by other well-known researchers, and popular prediction methods. If the model is behaving with some accuracy compared to popular methods, it is believed that the soil constitutive models and the semi-empirical correlations used for the sand parameters are applicable (see Chapter 4).

Overall, the medium linear element mesh with 1041 active nodes produced sufficient converged results, and was employed to model the five shallow foundations.

The data measurements for the symposium were made in the wet season. The water table laid approximately 4.9 m below the ground level, indicating a degree of saturation in the soil. The SPT data was used to calculate the stiffness of the sand. The SPT measurements taken from the field would be influenced by the water, which would reduce the blow count and then reduce the stiffness (E) of the sand. For example, the stiffness of the soil (E) is proportional to the moisture content within the soil. This may have led to conservative estimations by some participants as seen in Section 5.4.

5.4 Comparison of Symposium Results

A majority of the 31 predictors used a combination of four techniques, and then chose the most appropriate technique based on engineering judgment and experience. A frequency graph showing the methods used in the symposium is given in Figure 5.17. As seen from this figure, the more common methods of analysis used were Schmertmann, Burland and Burbidge, and FEM.

The numerical analysis performed by this author for the footings investigated at the symposium is given in Table 5.3. The loads in this table are for the load corresponding to 25 mm settlement (Q_{25}), and the load corresponding to 150 mm settlement (Q_{150}).

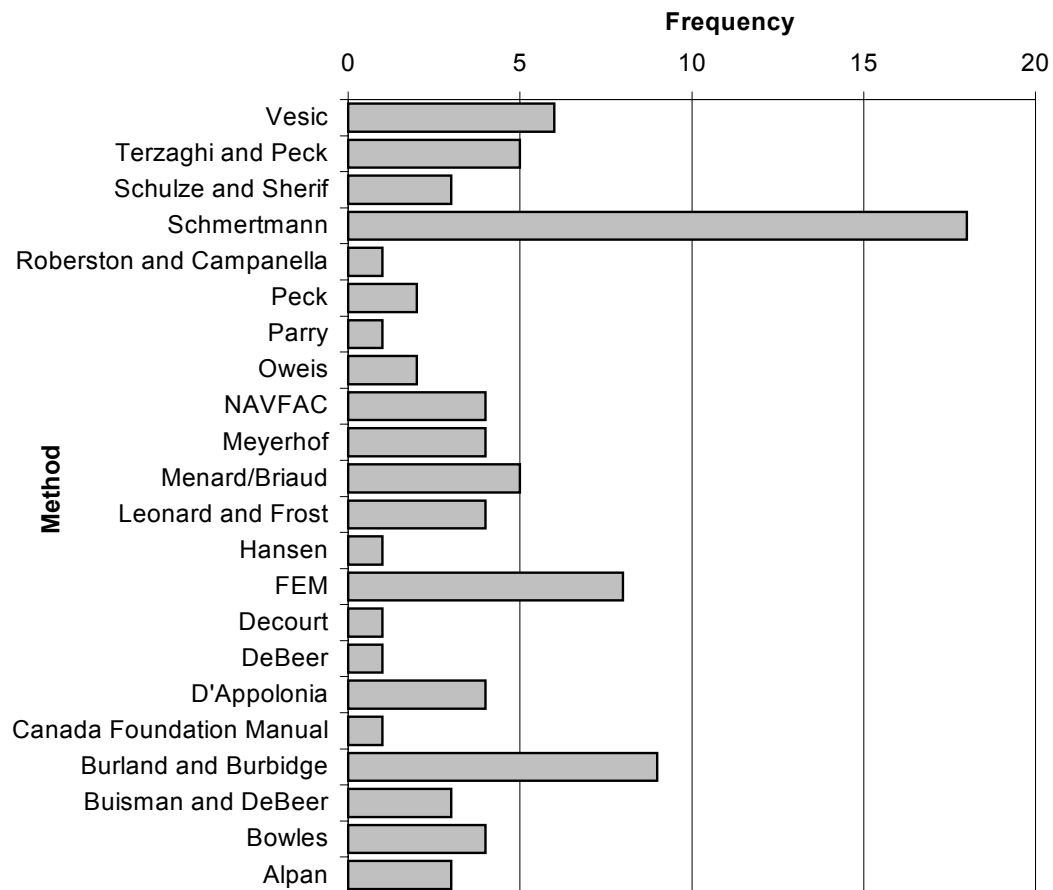


Figure 5.17: Frequency histogram for techniques in symposium

Table 5.3: Author's FEM results for symposium footings

Footing	Settlement 25 mm		Settlement 150 mm	
	Predicted Load (kN)	Actual Field Load (kN)	Predicted Load (kN)	Actual Field Load (kN)
1	3300	5200	10500	10250
2	1000	1500	3450	3400
3	3000	4500	9700	9000
4	2200	3600	7700	7100
5	510	850	1850	1740

A comparison of the ratio $Q_{\text{actual}} / Q_{\text{predicted}}$ for the loads corresponding to 25 mm and 150 mm for each of the predictors can be seen in Table 5.4. It was attempted to discover what method was the most consistent for predicting the loads at 25 and 150 mm settlement. From an observation of the top 5 prediction ratios, it was not clear what method yielded the more reliable results (Table 5.4). This springs from a majority of participants modifying existing methods to incorporate their engineering judgment and experience.

The performance by symposium predictors for each footing is shown in the histograms of Figures 5.18 to 5.22.

Eight participants in the symposium used FEM analysis as one of their predicting tools (mainly academics), and this is shown from the plot in Figure 5.17. One possible reason why academics chose to use FEM rather than consultants is because of the increased complexity and programming time. Generally, for predictions of settlement in industry numerical models would rarely be adopted because of the above reasons.

All FEM users employed an axi-symmetric analysis. This simplifies the problem into a two-dimensional working plane that in turn assumes the footing is circular. From the participants who used FEM, it was mostly found that the predictions for the FEM Q_{150} were submitted as their final estimates. The FEM Q_{25} predictions were usually averaged with other traditional methods or even excluded. This suggests that the participants were not confident in the results obtained for their FEM Q_{25} , i.e. the results

were not as reliable as current techniques. An overall average ratio for all FEM predictions can be seen in Table 5.5.

Table 5.4: Prediction comparison for individual predictors

Q₂₅ Predictions		Q₁₅₀ Predictions	
Predictor	Ave Ratio	Predictor	Ave Ratio
Siddiquee (A)	12.63	Siddiquee (A)	7.38
Chang (C)	3.87	Thomas (A)	3.82
Shahrour (A)	3.53	Chang (C)	3.59
Foshee (C)	3.48	Chua (A)	3.16
Chua (A)	3.15	Kuo (C)	2.64
Thomas (A)	2.63	Mayne (A)	2.15
Silverstri (A)	2.26	Diyaljee (C)	1.8
Kuo (C)	2.03	Shahrour (A)	1.57
Brahma (A)	1.94	Foshee (C)	1.56
Diyaljee (C)	1.93	Silverstri (A)	1.48
Altaee (C)	1.78	Cooksey (A)	1.38
Boone (C)	1.72	Boone (C)	1.36
Bhowmik (C)	1.71	Tand (C)	1.35
Johnson (Author)	1.57	Funegard (C)	1.35
Ariemma (C)	1.51	Surendra (C)	1.27
Cooksey (A)	1.51	Utah State (A)	1.17
Abid (C)	1.45	Brahma (A)	1.15
Scott (C)	1.43	Floess (C)	1.15
Mayne (A)	1.42	Wiseman (A)	1.09
Wiseman (A)	1.25	Scott (C)	1.08
Mesri (A)	1.23	Deschamps (A)	1.05
Tand (C)	1.16	Bhowmik (C)	1.01
Poulos (A)	1.16	Johnson (Author)	0.95
Decourt (C)	1.15	Abid (C)	0.95
Townsend (A)	1.11	Gottardi (A)	0.89
Horvath (A)	1.06	Altaee (C)	0.86
Funegard (C)	1.04	Poulos (A)	0.8
Utah State (A)	1.02	Ariemma (C)	0.75
Deschamps (A)	1	Horvath (A)	0.66
Floess (C)	0.93	Townsend (A)	0.62
Surendra (C)	0.91	Decourt (C)	0.53
Gottardi (A)	0.85	Mesri (A)	
Risky	9%	Risky	28%
Conservative	91%	Conservative	69%
		No Prediction	3%

Note: Ave ratio = $Q_{\text{predicted}} / Q_{\text{actual}}$

C = consultant

A =academic

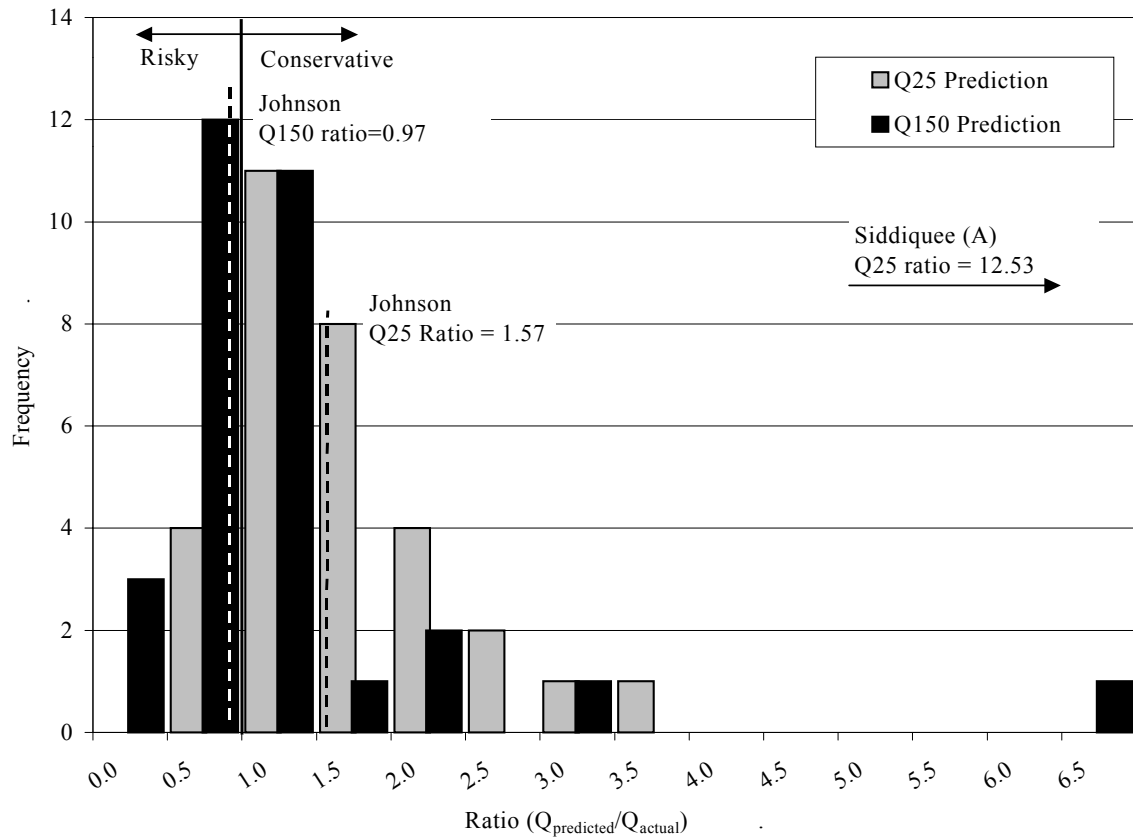


Figure 5.18: Footing 1 comparative histogram

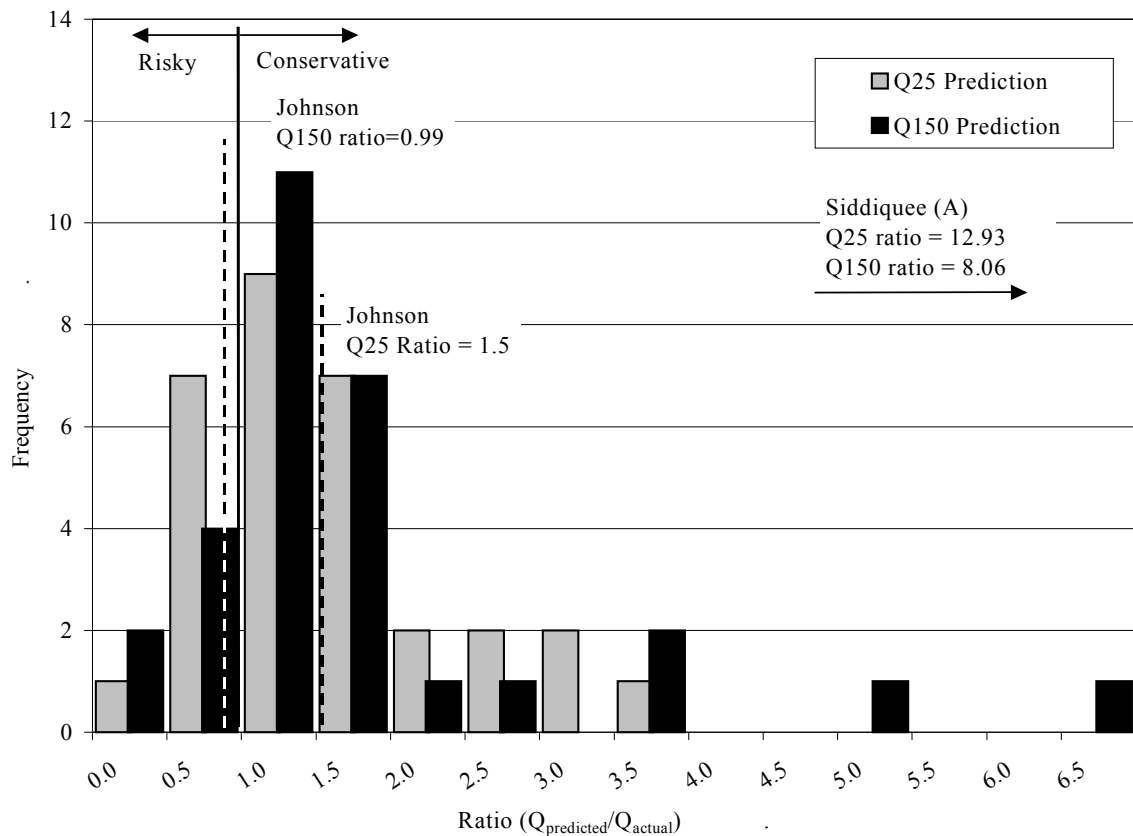


Figure 5.19: Footing 2 comparative histogram

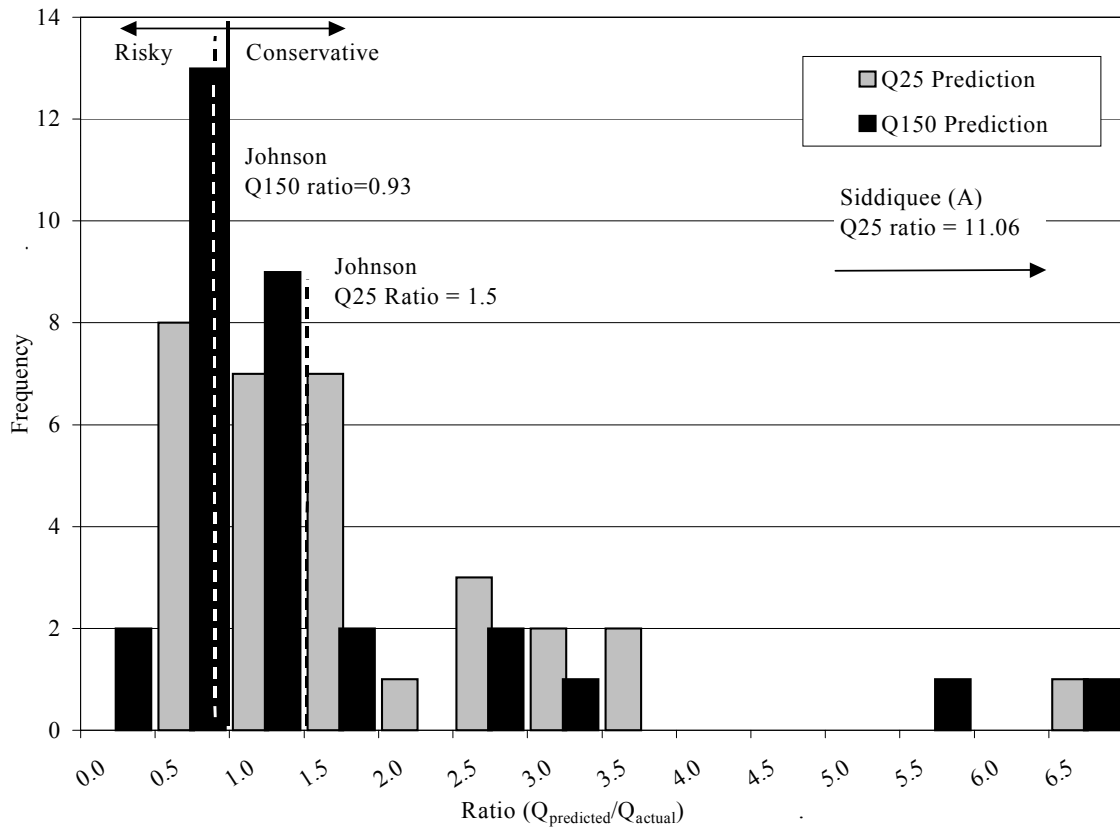


Figure 5.20: Footing 3 comparative histogram

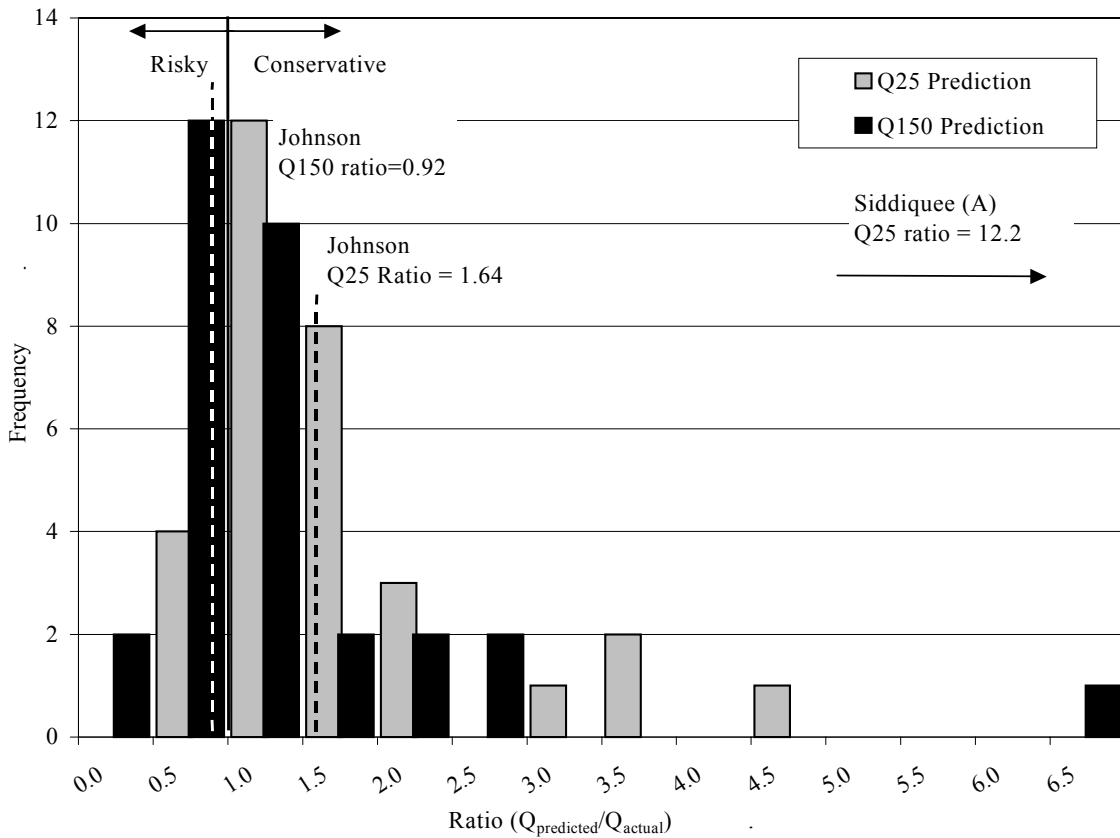


Figure 5.21: Footing 4 comparative histogram

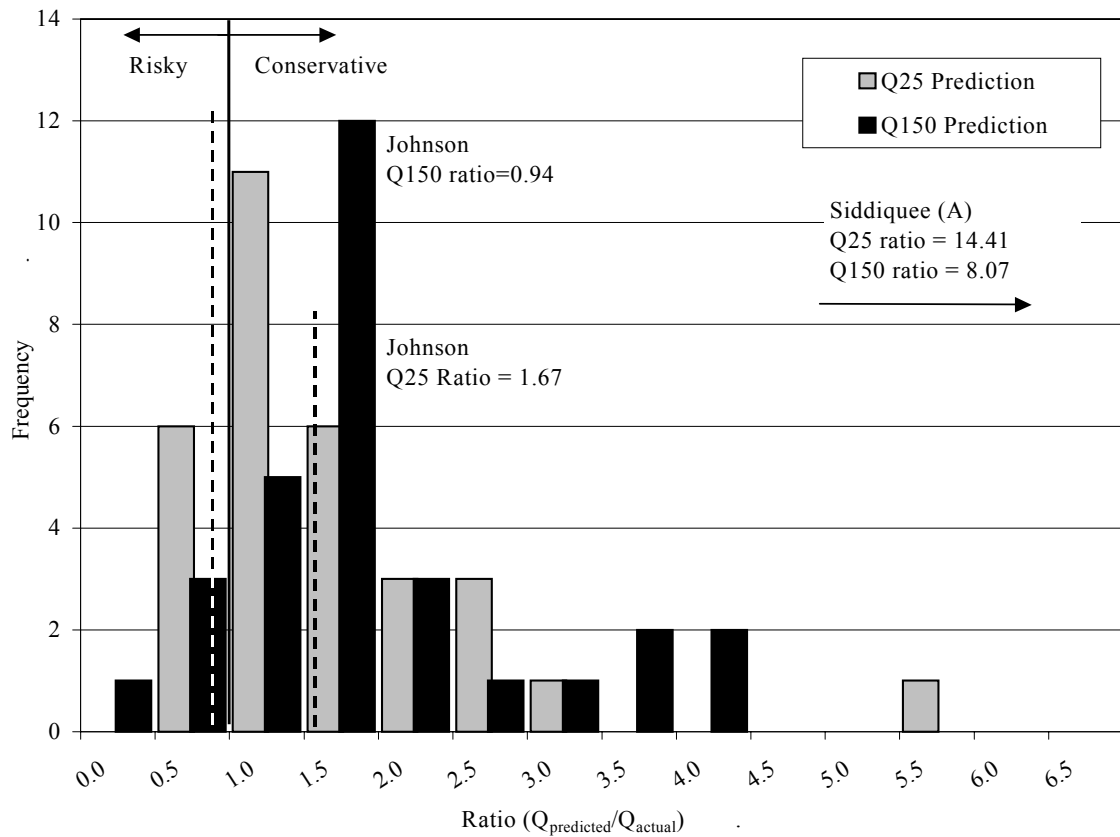


Figure 5.22: Footing 5 comparative histogram

Table 5.5: FEM Comparison

Predictor	Ratio ($Q_{\text{predicted}}/Q_{\text{actual}}$) For settlement = 25mm*	Ratio ($Q_{\text{predicted}}/Q_{\text{actual}}$) For settlement = 150mm*
Chang	3.87	3.59
Siddiquee	12.63	7.38
Cooksey	1.75	1.42
Townsend	0.97	1.46
Deschamps	2.22	1.20
Shahrour	3.53	1.57
Utah State	N/A	1.17
Chua	3.15	3.16
Johnson (Author)	1.57	0.95
Average	3.71	2.33

*Note: results for the above FEM analysis were obtained directly from the predictor's articles, and may not have been the final prediction used in the exercise.

From Tables 5.4 and 5.5, the shallow foundation finite element model constructed as part of this work performed well when compared with the other predictions. It tended to produce the 16th most conservative estimate out of 31 for the Q_{25} prediction, and was the second closest to the actual ratio for the Q_{150} prediction. Table 5.5 shows the direct comparison between the predictors who attempted to predict the footing behaviour using FEM. The model developed by this author and the constitutive parameter correlations defined in Chapter 4 produced estimates, which were within the top two most accurate out of a total of 9 predictors (some of which are well known researchers such as Deschamps). This suggests that the model and correlations determined in this chapter and in Chapter 4 are adequate, and may be applied with some confidence to other geotechnical FEM applications or problems.

It was observed that Q_{150} predictions performed with higher accuracy as opposed to the Q_{25} predictions. One possible reason for this could be the effect of cohesion. In the case of clean sands the effective cohesion is zero. After examining the borehole logs, it was found the influence zone contained small amounts of clay especially for the 3 m footings. The presence of clay would induce cohesion between the particles, and with this increase in cohesion the failure envelope of the Mohr-coulomb analysis would extend. This means that the area under the failure envelope would spread, which in turn would increase the elastic region of deformation. After this it would take a higher load to displace the footing a certain distance.

Other factors that may have affected the accuracy of some predictions were the times at which field testing and load testing were conducted. The field testing was performed during a relative wet season, whereas the load testing was conducted in a dry period. For this reason the field test data may indicate wetter-weaker conditions than would be seen in a dry soil profile. It is normal for engineers to take into account seasonal changes when designing shallow foundations. However, the purpose of this exercise was to predict as accurately as possible, and seasonal fluctuations would impact on the accuracy of results.

CHAPTER 6: Literature Review - Piles

6.1 General

As discussed in Chapter 1, it was found from an extensive foundation literature review that pile design techniques are mostly limited to the loading scenarios where only pure axial, lateral loads, and moments act on the pile. Some researchers also found that the individual failure mechanisms acting together produce a reduction in the net capacity of the pile (Section 6.2).

However, the effect of combined loads acting on a pile was mostly limited to small scale testing and a few large scale field experiments. The experimental piles were mainly tested in cohesive soil with axial uplift and lateral loads. In reality piles can be exposed to axial compression, lateral loads, and moments, or axial uplift, lateral loads, and moments all acting together, e.g. as in the case of transmission towers, portal frames, pontoons and large skyscrapers. Also the pile can be placed into clay, silt, sand, gravel or a combination of these soil types.

It was decided to study this particular problem in more depth, given the lack of design information on piles in granular soil under a variety of loading combinations. Therefore, the aim for the pile research is to explore the effect of combined loading on the ultimate capacity of a pile and the pile head displacement. There are three possible paths that could be followed to achieve the aim of the pile study. The paths are discussed below:

1. Small scale laboratory modelling may be employed to explore the effect of combined loading acting on a pile in granular soil. However, the use of small scale modelling to develop pile design techniques may present difficulties. Small scale modelling may not portray the same characteristics as full scale testing due to the scaling effects. Therefore, it was concluded that small scale modelling would help verify results and to aid in trend setting.

2. Full scale experiments could be used. However, such a venture would be costly to gather enough data to develop a design procedure. Full scale testing requires a large field area that needs to be modified so a controlled environment can be established. Many factors can affect the overall capacity of the pile as discussed in Section 6.4. These factors include pile head fixity, the way a pile is installed, and the length to diameter ratio of the pile. Then given the limited amount of funds available at the time of this work meant that full scale testing was not an option.
3. The third option that may be used to achieve the aims of the pile research was to use numerical modelling techniques. The use of numerical modelling to investigate pile behaviour has been attempted by a number of researchers as shown in Section 6.5. At the time of this research only one computer package 'ABAQUS' was available to the author at James Cook University, which had enough capability to achieve the aims of the pile research.

From the above options, it was considered that finite element modelling was the most viable option and hence would be employed. Some small scale modelling was also done to help verify the trends from the numerical study, as shown in Chapter 7.

To construct a reliable numerical pile model it was essential the influences that could impact on the results of the model (e.g. pile installation technique) be understood. Therefore, a literature review of the existing techniques used to predict the capacity and displacement of a single pile under axial, lateral, and moment loads was carried out. The literature associated with each prediction method gives valuable insight into what affects the behaviour of a pile. The existing techniques have been discussed in Section 6.4.

6.2 Piles Subjected to Oblique Loading

Piles subjected to oblique loading (Figure 6.1) are currently designed by assuming the lateral and axial components act independently from each other (Poulos and Davis, 1980; Anagnostopoulos and Georgiadis, 1993). The ultimate oblique capacity is then found to be the lesser of the oblique loads calculated from the ultimate axial and lateral

loads. Broms (1965) acknowledged that the axial and lateral components do influence each other to some extent. Therefore, Broms extended the above method to include the influence of the lateral component of the load on the axial uplift capacity for a pile in granular soil. Yet he still assumed that the vertical load has no influence on the lateral capacity. Similarly, the settlement of the pile can be predicted by using existing techniques for lateral and axial displacement assuming no interaction occurs between the load components.

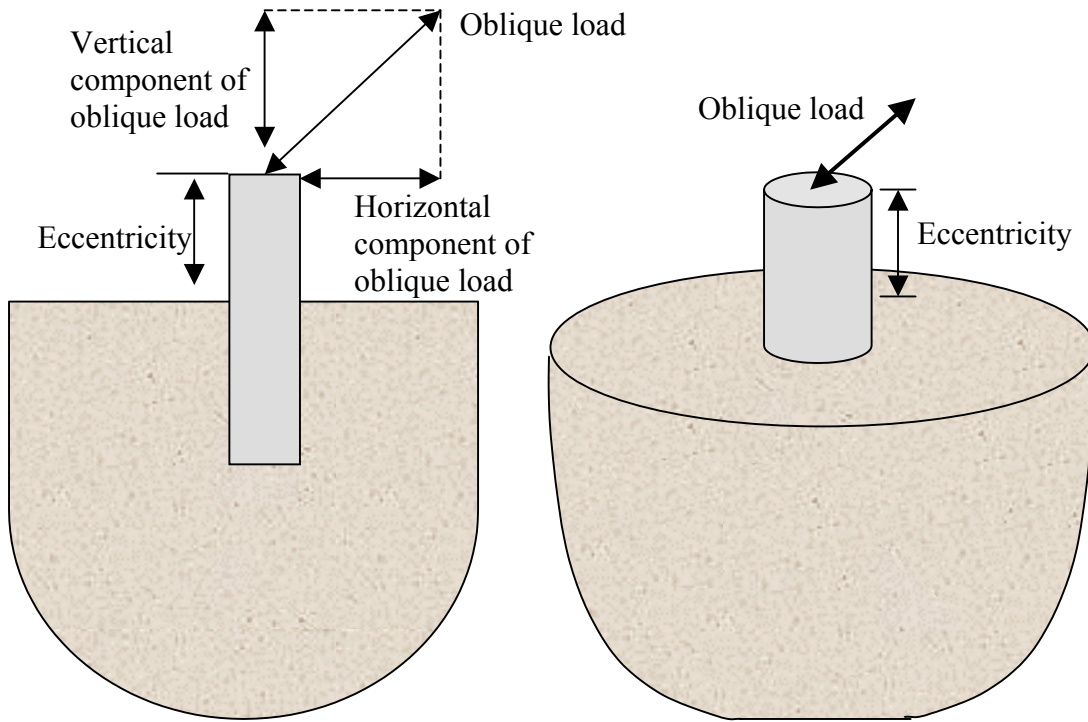


Figure 6.1: Vertically installed pile subjected to oblique loading

Meyerhof et al. (1983) conducted small-scale testing on a series of small-scale steel pipe piles under compression and lateral loads in sand. Meyerhof showed that, for a central inclined load at the head of a rigid fully embedded pile, an approximate semi-empirical relationship could be used to estimate the capacity of the pile. For the horizontal and vertical compression load components, Q_h and Q_c , respectively, and the ultimate capacities under lateral and axial compression loads, Q_{uh} and Q_{uc} , respectively, Meyerhof's equation is:

$$\left(\frac{Q_c}{Q_{uc}} \right)^n + \left(\frac{Q_h}{Q_{uh}} \right)^n = 1 \quad (6.1)$$

where n is an unknown power.

However, the value of n is not confidently known at present. With little data available the designers have suggested this value is 2 (Meyerhof et al., 1983). For a pile under pure axial compression and moment load Meyerhof (1983) has recommended:

$$\left(\frac{Q_c}{Q_{uc}}\right)^2 + \left(\frac{M}{M_{ult}}\right) = 1 \quad (6.2)$$

where Q_c = applied compression load,

Q_{uc} = ultimate compression capacity of the pile,

M = applied moment, and

M_{ult} = ultimate moment capacity of the pile.

It is noted that Meyerhof's work did not explore the influence of combined loads that include axial uplift forces. He did not address the influence of pile installation, pile head fixity, or the change in length to diameter ratio on the proposed failure curves. Also he did not discuss the impact of combined loads on the pile head displacement.

Prideaux (1998) also conducted a series of small-scale testing on hollow steel piles in loose, dense and saturated loose sand at James Cook University. In the testing Prideaux placed four load combinations on the pile. The loading scenarios explored a combination of both axial uplift and lateral loads. A summary of the pile test results from Prideaux (1998) is given in Tables 6.1 and 6.2.

The small-scale testing done by Prideaux (1998) showed that the axial uplift and lateral capacities are reduced when both loads act in unison on a pile.

Anagnostopoulos and Georgiadis (1993) conducted a series of tests on instrumented model piles in clay to investigate the effects of combined axial compression and lateral response. They found the lateral load significantly increased the axial pile displacement and caused a small reduction of the axial pile stresses near the ground. There appeared to be a limited effect on the ultimate axial load. Anagnostopoulos and Georgiadis's

findings differ greatly from Meyerhof on whether the presence of a lateral load affects the ultimate axial load, and this aspect should be investigated further.

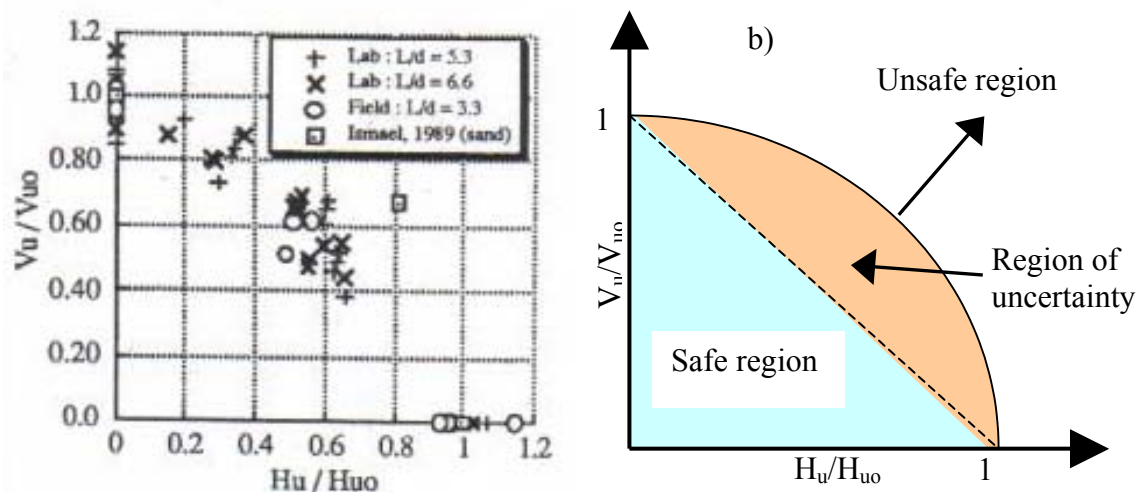
Table 6.1: Ultimate loads for Prideaux (1998) model piles in dense sand

Load Direction Angle (to the vertical) (°)	Ultimate Load (N)	Mean (N)	Variation (above or below mean) (N)	Variation (above or below mean) (%)
0°	242.32	272.01	-29.69	-10.92
	275.87		+3.86	+1.42
	297.84		+25.83	+9.50
22.5°	271.16	298.43	-27.27	-9.14
	325.70		+27.27	+9.14
45°	310.20	312.82	2.62	-0.84
	313.34		+0.52	+0.17
	314.91		+2.09	+0.67
67.5°	392.61	404.71	-12.10	-2.99
	406.34		+1.64	+0.40
	415.17		+10.46	+2.59
90°	437.34	459.58	-22.24	-4.84
	442.64		-16.94	-3.69
	498.75		+39.17	+8.52

Table 6.2: Ultimate loads for Prideaux (1998) model piles in saturated loose sand

Load Direction Angle (to the vertical) (°)	Ultimate Load (N)	Mean (N)	Variation (above or below mean) (N)	Variation (above or below mean) (%)
0°	126.17	133.69	-7.52	-5.62
	126.36		-7.33	-5.48
	148.53		+14.84	+11.10
22.5°	118.32	119.10	+0.78	+0.66
	119.89		-0.78	-0.66
45°	135.58	141.18	-5.59	-3.96
	146.77		+5.59	+3.96
67.5°	165.21	165.80	-0.59	-0.36
	166.39		+0.59	+0.36
90°	216.42	226.33	-9.91	-4.38
	236.23		+9.91	+4.38

Eckersley et al. (1996), based on the works by Greensill (1990) and Graham (1991), showed for piers embedded in clay with a length to diameter ratio less than 5, the axial uplift and lateral loads had an effect upon each other. It was discovered that the true ultimate uplift and lateral capacities were substantially less than their predicted counterparts. Then Eckersley et al. recommends the use of interaction diagrams like the one displayed in Figure 6.2. As a conservative measure, a linear relationship can be assumed between the ultimate uplift and lateral loads if there is no other accurate data available. There is no current procedure for predicting the true relationship between the vertical and horizontal load components.



where: V_u = ultimate uplift capacity under combined uplift and lateral loads,
 V_{uo} = ultimate uplift capacity under pure uplift load,
 H_u = ultimate lateral capacity under combined uplift and lateral loads, and
 H_{uo} = ultimate lateral capacity under pure lateral load.

Figure 6.2: a) Experimental results from Eckersley et al. (1996)

b) Interaction diagram for horizontal and vertical components

It is noted that the proposed interaction diagrams were based on experimental test data for piles in clayey material. Also the current interaction diagrams do not include a reduction in components due to moments acting on the pile. The moments are induced on the pile from structural loading or eccentricity of the horizontal or axial load component. Broms method indicates that coexisting lateral and moment loads induced in the pile at ground surface influence each other. Then based on the above research it

is anticipated that piles with combined loads will experience capacity reductions, due to interaction of the separate loading failure mechanisms.

Obliquely installed piles subjected to oblique loads are often referred to as batter or raking piles. The oblique loads on the batter pile can either be 'in-plane' or 'out-of-plane' as shown in Figure 6.3. The load is considered to be in-plane when the pile and load angle lie in the same plane. Similarly, when the inclination angle of the pile and load lie on a different plane the pile is said to be subjected to out-of-plane loading.

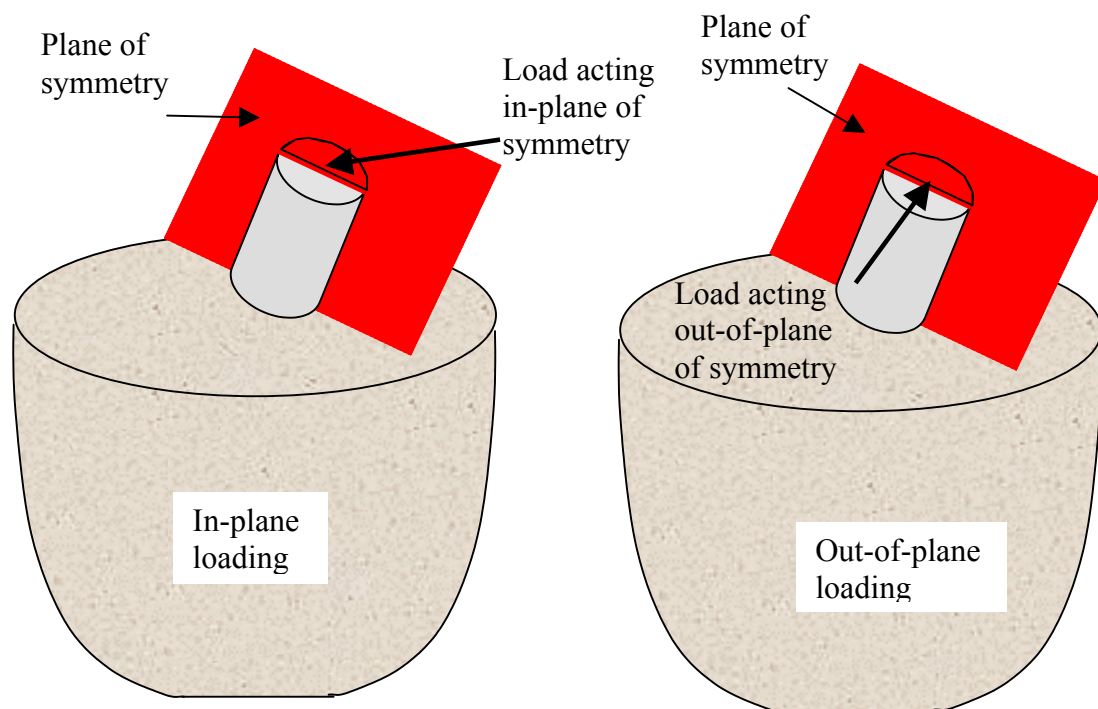


Figure 6.3: In-plane and out-of-plane loading of a pile

The ultimate load can be determined for in-plane loading by assuming the inclination does not affect the ultimate axial or lateral capacity of a pile, as stated by Poulos and Davis (1980). Then the pile is converted to an equivalent vertical pile and ultimate load, and the settlement is estimated using the same procedures as the vertically installed pile under oblique loading. There are no prediction methods for determining the ultimate load of an obliquely installed pile subjected to out-of-plane loading.

6.3 Pile Installation Techniques

The method of pile installation can change the in situ soil properties and residual stress profile within the soil body. There are several pile installation techniques available for pile construction and these include cast-in-place and vibratory piles. Two of the common older techniques are cast-in-place and impact driven, and they will be discussed in this review.

Cast-in-place piles are installed by excavating a hole commonly done with an auger (controlled by hydraulic machinery). A reinforcement cage is placed in the hole and then concrete is poured into the hole. Some examples of the cast-in-place installation process can be seen in Figure 6.4.



Figure 6.4: Cast-in-place pile installation process

The impact driven pile technique has been used since at least the mid 1700's. The procedure used in the 1700's is generally the same method as used today. However, the sophistication of the driving apparatus has been advanced through the industrial age, and some modern installation processes are shown in Figure 6.5.

When an impact driven pile installation technique is chosen, a prefabricated pile consisting of concrete, steel, timber or combination of these materials is transported to site via trucks. The pile is placed into a driving rig (Figure 6.5) that supports the pile while it is hammered into the ground using a dropping weight.



Figure 6.5: Impact driven pile installation process

The choice of pile installation technique depends largely on the geology of the site, equipment available, time constraints of the project, and construction budget. Cast-in-place and impact driven installation methods have definite advantages and disadvantages, which are discussed below:

The major advantages/disadvantages of impact driven pile foundations are listed below.

- + Material of pile can be inspected before it goes into the ground
- + Construction procedure unaffected by ground water
- + Can be readily carried above ground level, especially in marine structures
- + Can be driven in very long lengths
- Pile may suffer unseen damage in hard driving conditions
- Noise and vibration while driving may cause nuisance or damage
- Displacement of soil during driving piles in groups may damage adjacent structures, or cause lifting by ground heave of adjacent piles
- Cannot be driven in very large diameters

The major advantages/ disadvantages of cast-in-place piles are listed below.

- + Length can be varied to suit ground conditions
- + Can be installed in very large diameters

- + Can be installed without appreciable noise or vibration
- + Can be installed in conditions of very low head-room
- + No risk of ground heave
- Concrete is not placed under ideal conditions and cannot be subsequently inspected
- Water under artesian pressure may rise up pile shaft and wash out cement
- Cannot be readily extended above ground level as in river and marine structures
- Boring methods may loosen sandy or gravely soils

The choice of installation technique can influence the in situ soil properties, and affect the prediction methods used to estimate the capacities and deflection of the pile. For instance, the cast-in-place piles once drilled may allow the soil at the excavation surface (pile-soil interface) to loosen, hence residual stresses will relax. When the hole is filled with concrete the soil is returned to an equilibrium stress state assumed to be similar to the original in situ condition. As opposed to their cast-in-place counterparts, impact driven piles induce driving stresses into the immediate soil-pile from the hammer energy transferred to the pile during driving. The response of the soil under driving varies depending on the soil type, soil density and several other factors.

6.4 Current Design Techniques

When designing piles there are two criteria that must be addressed: (a) the allowable bearing capacity of the soil surrounding the pile must not be exceeded, (b) the serviceability limit state design deflection criterion should be satisfied. The limiting deflection is generally defined as a magnitude of 10% of the pile diameter (Budhu, 2000).

Piles are usually categorised into two separate groups and these are friction and end-bearing piles. Piles that transfer a majority of the load via friction at the pile-soil interface are known as friction piles. There are also end-bearing piles where the bottom of the pile is sitting on stiff strata. This results in most of the load being transferred into the soil via bearing at the pile base. Floating piles are friction piles and it is assumed

the entire load is carried by friction at the pile-soil interface, and no end-bearing occurs. Piers are concrete piles that have a low length to diameter ratio and are used in sheds, bridge abutments, and various other structures.

Several methods have been developed to estimate bearing capacities and deflections of single piles. The methods depend on soil type, pile geometry, pile installation method, magnitude and direction of applied load, etc. The advancement of pile prediction techniques has evolved with technology and the invention of modern pile installation techniques. A brief summary of common pile installation techniques and methods used in pile design today are discussed in the following sections.

6.4.1 Piles Subjected to Axial Compressive Loading in Sand

Bearing Capacity

Ultimate bearing load (Q_{ult}) for a single pile subjected to axial loading can be determined using statics or dynamics, depending on the pile installation technique. The statics approach is based on soil mechanics and requires the input of soil properties, as described by Poulos and Davis (1980). The dynamic approach is used to estimate the load capacity of a driven pile provided the pile-driving data is available. The dynamic approach is highly unreliable and generally factors of safety in the order of 5-6 are applied to the predicted loads.

The statics approach is commonly used and requires the estimation of the ultimate shaft friction and end bearing loads a pile can carry, as shown in Figure 6.6.

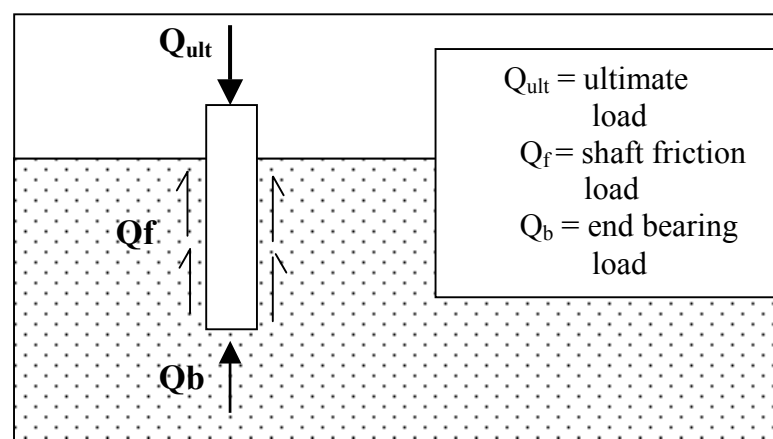


Figure 6.6: Forces acting on a single axially loaded pile

Often the weight of a pile is neglected, and it is assumed the pile's weight equals the weight of the displaced or removed soil (Craig, 1992). The equation given by Budhu (2000) is:

$$Q_{ult} = Q_f + Q_b \quad (6.3)$$

The shaft friction load (Q_f) is a product of the shaft surface area and skin friction (f_s). There are a number of methods to determine f_s depending on soil type and pile geometry, as reported in the literature by Poulos and Davis (1980), Craig (1995) and Budhu (2000). The method to determine the end bearing resistance of a pile is based on the same technique used to estimate the ultimate bearing capacity of a shallow foundation.

All of the above methods used to approximate the ultimate capacity (Q_{ult}), are based on the assumption that the skin friction and end bearing resistance have been fully mobilised. The effects of pile driving combined with the heterogenous nature of soil can have a profound influence on the soil properties around the pile. This makes the estimation of the pile's bearing capacity difficult. Then many researchers often include empirical corrections to help account for a range of external factors. A design engineer will also divide the ultimate load by a factor of safety (FOS) usually equal to 3, to reduce the risk of failure (Equation 6.4). This enables an allowable design-working load (Q_{all}) to be determined for a working pile.

$$Q_{all} = \frac{Q_{ult}}{FOS} \quad (6.4)$$

Vertical Pile Displacement

There are several approaches for predicting the vertical displacement of a pile subjected to axial compressive loading. The initial settlement prediction calculations were based on empirical correlations found through experimental data. Numerous investigators have developed empirical correlations that account for variations in soil properties and testing procedures. These researchers include Meyerhof (1959), Focht (1967) and more recently Tomlinson (1994). Empirical correlations are limited in their use as they cannot provide load-settlement curves and are highly unreliable.

The advances in technology led to the development of more reliable solutions for predicting pile settlement. Poulos and Davis (1980) noted that settlement theories are based on one of the following three categories: -

1. Load-transfer methods, which use measured relationships between pile resistance and pile movement at various points along the pile.
2. Methods based on elastic theory that utilise Mindlin's (1936) equations for sub surface loading within a semi-infinite mass.
3. Numerical methods that use either finite element method (FEM) or finite difference method (FDM).

The advantages and disadvantages of the three settlement prediction categories are listed in Table 6.3.

6.4.2 Piles Subjected to Axial Uplift Loading

It is possible for some piles to be subjected to axial uplift forces. Examples of piles subjected to axial uplift forces include piers supporting transmission towers with large turning moments, and piles anchoring water structures. Researchers have become interested in predicting the uplift behaviour of a pile, and methods have been developed for approximating the ultimate pullout resistance. However, there has been little attempt to formulate models for predicting the deflection of piles subjected to uplift loading.

Meyerhof and Adams (1968), and Das (1999) have shown the ultimate pullout resistance (T_{ug}) for uplift piles. They demonstrate that ultimate pullout resistance can be approximated using equilibrium of vertical forces. This is shown in Equation 6.5 and Figure 6.7.

$$T_{ug} = T_{un} + W \quad (6.5)$$

where T_{ug} = gross uplift capacity

T_{un} = net uplift capacity

W = effective weight of the pile

Table 6.3: Advantages/disadvantages of various settlement prediction methods

Category	Popular Researchers	Basic principles of methods	Advantages	Disadvantages
Load-Transfer Methods	Coyle and Reese (1966) Coyle and Sulaiman (1967) Reese and Cox (1969)	Involves iterative calculations in which the pile is broken into a number of segments. The displacement of the base segment is calculated using the load-transfer curve obtained from a pile load test. The segment displacement is then compared with a previous assumed displacement. Once convergence is reached between the calculated and assumed segment displacement, the designer will move up to the next segment and repeat the above steps until the last pile segment is reached.	Methods based on load-transfer analysis allow design engineers to formulate a load- settlement curve. Depending on computational time, engineers can increase the accuracy of the load-settlement curve by increasing the number of segments the pile is separated into.	Some of the major disadvantages as noted by Poulos and Davis (1980) are as follows: <ul style="list-style-type: none"> • Assume that the movement at any point is related only to the shear stress at that point, and independent of the stresses elsewhere on the pile. • To obtain load-transfer curves more instrumentation is required in the pile-load test at the site. Also, extrapolation between one site and another is not always successful, resulting in more pile-load tests needing to be performed. This increases the cost considerably.

Table 6.3 Continued: Advantages/disadvantages of various settlement prediction methods

Category	Popular Researchers	Basic principles of methods	Advantages	Disadvantages
Elastic Theory Methods	Vesic (1977) Poulos and Davis (1980)	<p>Elastic methods involve dividing the pile into elements all uniformly loaded. A solution is obtained by imposing compatibility between the pile and soil elements. A brief summary of two popular methods is:</p> <ol style="list-style-type: none"> (1) Vesic's method is clearly explained by Das (1999). Vesic predicts that the total settlement is equal to the sum of the elastic shorting of the pile, and the settlement of the pile caused by load at the pile tip and along the pile shaft. (2) Poulos & Davis's method is similar to Vesic's method. The main differences being the absence of the settlement due to the load along the pile shaft, and the way they predict the settlement components. 	<ul style="list-style-type: none"> • Compared to the load-transfer method, elastic prediction methods are easier and clearer to apply. • Poulos and Davis (1980) found that piles with a length to diameter ratio greater than 20 had load-settlement curves almost linear, until at least a load of 50% of the failure load is reached. Therefore, Poulos concludes that linear elastic analysis is an adequate assumption to predict the settlement of piles under working loads. • A load-settlement curve can be obtained for each new pile design. 	<p>The following is a list of assumptions that may result in limitations within the elastic methods:</p> <ul style="list-style-type: none"> • Soil is assumed to be a homogenous isotropic half-space. It will have elastic properties (E_s, ν_s), which are not influenced by the presence of the pile. • Piles undergo uniform compression (ie uniform axial stress). The pile is also assumed to act elastically at all times. • Poulos and Davis assume the shear stress is distributed uniformly around the circumference of the pile. This assumption has been widely accepted. • The accuracy of Vesic's method depends on the ability of the design engineer to predict the percentage of load taken by the shaft and base.

Table 6.3 Continued: Advantages/disadvantages of various settlement prediction methods

Category	Popular Researchers	Basic principles of methods	Advantages	Disadvantages
Numerical Modelling	See Section 6.5.	<p>One of the more popular techniques used in numerical modelling is the finite element method (FEM). FEM is a procedure in which the pile and surrounding soil continuum is discretized into a number of elements. Each of the elements is assigned properties. The stresses, strains and deflections of the soil-pile are calculated by solving a number of equations. To obtain a solution in FEM the following criteria must be satisfied:</p> <ul style="list-style-type: none"> • Differential equations of equilibrium • Strain/displacement and compatibility differential equations • Stress/strain or material constitutive laws 	<p>FEM has some major benefits as opposed to the load-transfer and elastic methods. Instead of using simple linear elastic stress-strain properties, FEM can accommodate more complex models, such as non-linear elastic and hyperbolic stress-strain functions. The slip at the pile surface can also be accounted for by including special joint elements at the pile-soil interface. There are no limits to complexity of the FEM models as shown by a number of researchers.</p>	<p>Numerical models such as FEM involve the solving of a vast number of equations, often going into the thousands. This makes it almost impossible to solve numerical models by hand, and computer input is necessary. Then the use of numerical modelling is not very practical for design engineers, as computational expenses and time become a major drawback.</p>

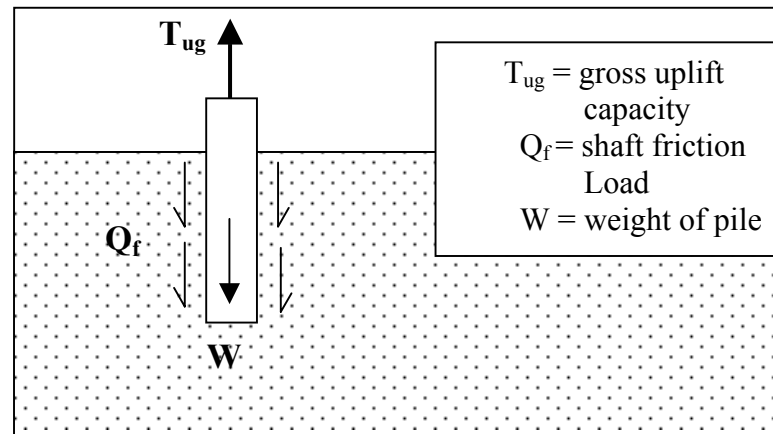


Figure 6.7: Pile subjected to uplift forces

The differences between methods lie in determining the net uplift capacity (T_{un}). The net uplift capacity is dependant on estimating the adhesion/friction at the pile-soil interface. Experimental observations and empirical correlations have been used in both methods to approximate the shearing force at the interface.

Descourt (1995) explained that frictional pressure at the interface of a pile varies from compression to uplift loading. When piles are placed under compressive loads they expand around the circumference slightly, causing some additional stresses at the pile-soil surface. Once the pile is subjected to uplift loading the pile elongates and the circumference decreases, resulting in loosening and stress relaxing at the pile-soil interface. Therefore, Descourt (1995) recommends that the skin friction estimated for compression be reduced by 20% for uplift loading.

6.4.3 Piles subjected to Lateral Loading

A pile subjected to lateral loading has to satisfy the same design criteria as a pile under axial loading. The criteria are: (1) an adequate factor of safety against ultimate failure, (2) acceptable deflection at working loads. Generally each of the above criterion is analysed separately and should satisfy their individual safety margins. A brief overview of current methods used to approximate the ultimate lateral resistance and deflection is given below.

Ultimate Lateral Resistance

There are two popular methods used to determine the ultimate lateral resistance of a pile. The two prediction methods are based on a statical approach, which is described in Section 6.4.1, and depends on soil mechanics and requires an input of soil properties. Poulos and Davis (1980) found that the ultimate lateral resistance is given by the lesser of:

1. Horizontal load required to cause failure of the soil along the whole length of the pile (i.e. pile is considered to be short and rigid).
2. The horizontal load required to produce a maximum moment that is equal to the yield moment of the pile section.

The first prediction method known as the conventional statical approach is considered the simplest. The conventional statical approach the magnitude of the ultimate lateral load (H_u), by considering equilibrium of horizontal forces and moments. A diagram (Figure 6.8) of forces acting on an unrestrained short rigid pile under lateral loading is shown from Poulos and Davis (1980).

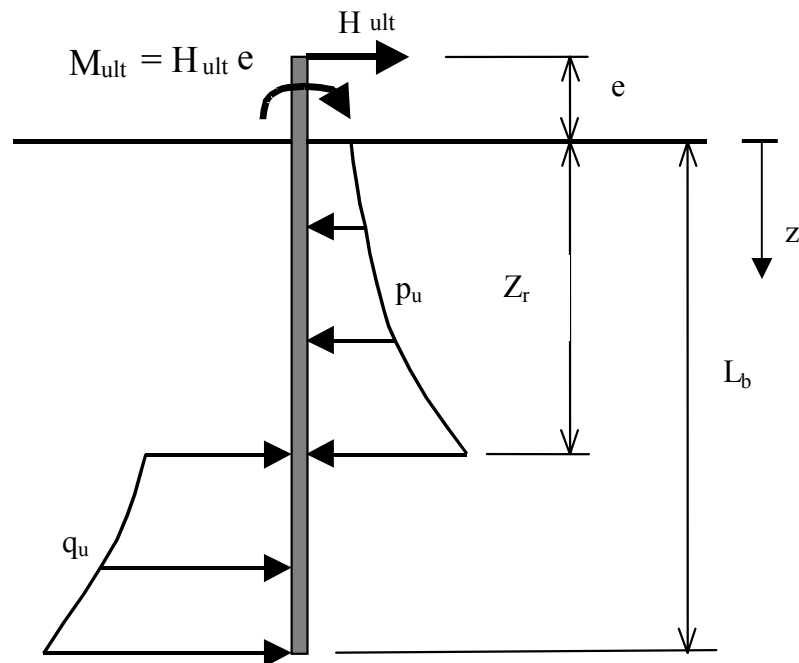


Figure 6.8: Generalized forces acting on a laterally loaded short rigid pile

In Figure 6.8: M_{ult} = ultimate moment; H_{ult} = horizontal load; e = load eccentricity; L_b = embedment length of pile; d = diameter; z = depth from soil surface; p_u = soil pressure at depth z ($z \leq Z_r$), q_u = soil pressure at depth z ($z \geq Z_r$), and Z_r = depth of rotation point.

Therefore, the ultimate horizontal load (H_{ult}) and moment (M_{ult}) can be found using the following equations:

$$H_{ult} = \int_0^{Z_r} p_u \cdot d \cdot dz - \int_{Z_r}^L q_u \cdot d \cdot dz \quad (6.7)$$

$$M_{ult} = H_{ult}e = - \int_0^{Z_r} p_u \cdot d \cdot z \cdot dz + \int_{Z_r}^L q_u \cdot d \cdot z \cdot dz \quad (6.8)$$

Equations 6.7 and 6.8 can be further simplified by assuming the distribution of ultimate lateral pressure along the pile shaft. The above method will be further complicated for non-rigid piles.

Broms's (1964) method is also based on the statical approach. The major difference between other methods and Brom's method lies in the way Broms simplifies the distribution of the ultimate soil resistance along the pile shaft. Some allowances have been made for different restraint types at the pile head. Broms has tested his method by collecting experimental data from various literature sources, and predicting the pile's lateral capacity. He found for cohesive soil the ratio of the calculated to measured values ranged from 0.88 to 1.19, with an average ratio of 1.06. For granular soil the calculated to measured ratio varied from 0.54 to 1.61, with an average of 0.93. The variations between predicted and measured results may result from a number of assumptions Broms made to derive the method.

Lateral Pile Displacement

Listed below are two common approaches used to determine the lateral deflection for laterally loaded piles.

1. ***Subgrade-Reaction Approach*** is a method that characterises the soil as a set of unconnected linear elastic springs. Therefore, the prediction methods based on

this approach disregard the continuous nature of the soil. Poulos and Davis (1980) assume that to neglect the fact soil is a continuum may lead to inaccuracies, as the displacements within the pile-soil are influenced by stresses and forces at surrounding locations.

Winkler's work in 1867 showed the pressure (p) at any point along the pile can be linearly related to the displacement (ρ) via the horizontal modulus of subgrade (k_h), i.e. $p=k_h\rho$. The pile is also assumed to behave according to simple beam theory. Winkler's linear relationship can then be substituted into the beam equation to yield a governing equation for the pile's behaviour. The governing equation relates the pile stiffness to the displacement and horizontal modulus of subgrade-reaction.

The numerical techniques such as finite difference method have been employed to determine solutions for the governing equation of piles. Researchers such as Palmer and Thompson (1948), and Gleser (1953) transform the governing equation into finite difference form and then use boundary conditions to obtain solutions.

Later researchers argued that for real soils the pressure and deflection are related non-linearly as opposed to Winkler's original linear model. Therefore, Reese (1974) developed the 'p-y' approach commonly used today. Reese starts with a more universal form of the governing equation that takes into account axial load and variations in pile stiffness. Then the finite difference method is used to obtain solutions for the governing equation. The final solution depends on an iterative procedure between sets of 'p-y' curves for various points along the pile, i.e. 'p-y' curves can be developed using methods by Frydman et al. (1975), and Sullivan et al. (1979).

2. **Elastic Approach** is a method that describes the soil as an elastic continuum, and the numerous settlement prediction methods based on the elastic approach are quite similar. The major differences lie in the assumption made in regard to

pile action under horizontal loading. Poulos (1971) developed one of the more popular elastic methods.

Poulos assumes that pile behaviour is governed by simple beam theory, like methods based on subgrade-reaction models. The displacements of the pile (ρ_p) can then be obtained using the differential equation for bending of a thin beam, and the soil displacements (ρ_s) for all points along the pile can be approximated using Mindlin's equations. For the purpose of predicting soil displacements it is assumed the soil is an ideal, isotropic, semi-infinite elastic material with a uniform Young's modulus.

Both the pile and soil behave elastically in the elastic approach, and this results in pile-soil displacements along the pile shaft being identical (i.e. $\rho_p = \rho_s$). Poulos was able to develop solutions for predicting the load-settlement curve for a pile under horizontal loading using the above equality, boundary conditions and equilibrium constraints.

Poulos and Davis (1980) show comparisons between Poulos's (1971) elastic method and the subgrade-reaction method to be in reasonable agreement until a length to diameter ratio (L/d) of 25 is reached. When L/d becomes greater than 25 the subgrade-reaction method tends to over predict the moments, displacements and rotations within the pile.

6.5 Finite Element Method (FEM)

The advancement in technology has led to computers with increased CPU power. This has allowed for complex solving techniques such as finite element method (FEM) to become a readily available tool for solving highly complex problems. The direct form of the FEM numerical algorithm is dependent on the problem at hand as discussed by Cook et al. (1989). In real life the way an object reacts under load depends on several factors, and some of the factors are listed below:

- The material needs to be classified as a discrete or continuum material. Discrete material can be made from millions of particles that transfer loads via contact. However, material classed as a continuum is assumed to act as a single body allowing stress to propagate through the medium.
- The constitutive behavior or stress-strain relationship of the material from which the object of interest has been constructed. The constitutive behavior of a material type can be a highly complex relationship that can be dependent on several variables, such as time and temperature.
- Interaction between the object of interest and other surrounding bodies. Contact algorithms ranging in various degrees of complexity can represent the interaction.
- The load type and direction. For example, static loads are not a function of time, as opposed to dynamic loads that fluctuate with time often with a damping effect.
- External factors acting on the object of interest. An example of this may be a pile subjected to additional loading from underground water pressure or flow.

Finite element modelling can allow researchers to study the interactions between various objects, and estimate the response of the objects under a range of loading conditions and material strengths.

As discussed in Section 6.1, finite element modelling is a good tool to examine the behaviour of piles provided the model is properly verified. Rajashree and Sitharam (2001), Ashour and Norris (2000), Zhang et al. (1999), Chen and Poulos (1997), Simonini (1996), Mabsout et al. (1995), De Nicola and Randolph (1993), Trochanis et al. (1991), Phoon et al. (1990), Wu et al. (1989), and Poulos and Davis (1980) are some of the researchers using numerical modelling to explore the behaviour of piles. The models constructed by each of the researchers varied significantly in complexity. The form of the models was dependant on load type, soil type, pile installation technique, and problem symmetry.

When using FEM to estimate the response of an object the first step is to define the problem domain. The problem domain usually includes all the material enclosed by a set of restraints known as boundary conditions. For example, all the material between locations at which the displacement or external forces are known can be defined as the domain. Then the problem domain can be broken (discretized) into a series of

continuum elements to form a mesh. The elements in the problem domain are connected together by nodes that transfer forces and displacements between elements. An illustrative diagram showing a typical problem domain is presented in Figure 6.9.

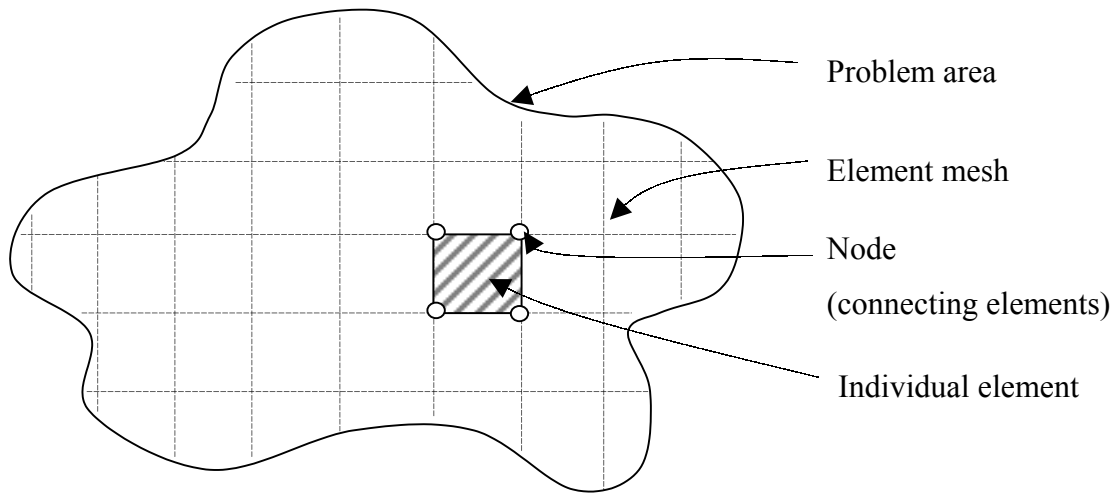


Figure 6.9: Typical meshed problem domain for FEM

The problem domain for a pile is often dependent on the load direction and pile geometry. For axially loaded circular piles, the problem domain may be reduced into a two dimensional problem using axisymmetric elements due to the soil and pile symmetry (Wang and Sitar, 2004; Johnson et al., 2001; De Nicola and Randolph, 1993). However, circular piles subjected to lateral load cannot be modelled using simplistic axisymmetric elements to reduce the problem size. Some researchers simplified the lateral loaded pile into a one dimensional problem. Then it is modelled using beam elements with the reaction force from the soil given by a series of springs (Rajashree and Sitharam, 2001; Trochanis et al., 1991; Poulos and Davis, 1980).

Circular piles subjected to oblique loads are more complex than their pure axial and lateral loaded counterparts. Given the geometry of the pile and load symmetry, the use of two dimensional axisymmetric elements or one dimensional elements is not appropriate once the pile is subjected to oblique loading. Therefore, a three-dimensional model may be a viable option for the pile and load symmetry of a circular pile subjected to oblique loads. When compared to one and two dimensional models, three-dimensional models require additional time to construct and additional computational time to solve. A further discussion on circular piles subjected to oblique loads is given in Chapters 8 to 10.

Once the problem domain is known and the element type is chosen, the elements in the individual element matrices can be formed. The individual elements have an element property matrix, a vector of unknown degrees of freedom, and a resultant vector of element nodal forcing parameters, commonly denoted as:

$$[k^e]\{d^e\} = \{f^e\} \quad (6.9)$$

where: $[k^e]$ = element property matrix, commonly a stiffness or general property matrix

$\{d^e\}$ = vector of unknown degrees of freedom (e.g. nodal displacements)

$\{f^e\}$ = vector of element nodal forcing parameters

When relating the nodal forces to corresponding nodal displacements in stress analyses, a constitutive model has to be assumed, where the forces are related to the displacements by using material strength parameters. This constitutive relationship effectively represents the stiffness of the continuum material and is given in the above equation as the $[k^e]$ matrix. Common constitutive relationships used for geotechnical analyses can be found in Chapters 4, 5 and 8. The selection of a constitutive model is a source of debate between many researchers.

When sand is exposed to load transferred through the pile it initially may undergo elastic deformation. As the load increases the strain in the sand starts to experience localised discrete plastic failure zones. This results in the sand acting as an elasto-plastic material. At ultimate load, the sand will undergo excessive plastic strain and the pile displaces by large magnitudes with little to no load increase. The source of debate stems from the relationship between the stress corresponding to strain levels. Some researchers (Wang and Sitar, 2004; Johnson et al., 2001; Chen and Poulos, 1997; De Nicola and Randolph, 1993) have used either linear or hyperelastic constitutive models along with failure models to predict the sand response. The load type such as the static load or dynamic load, and the practicality of obtaining parameters may impact on the selection of the model. A discussion on the more common models used for static loading is given in Chapter 8.

The displacement field within an element can be approximated by using shape functions. For example, linear elements assume a linear displacement relationship between the adjoining nodes, whereas quadratic elements use a quadratic relation to estimate the displacement between nodes.

In general the displacement field with a multi-noded element can be expressed in matrix form as:

$$\begin{Bmatrix} u \\ v \\ w \end{Bmatrix} = [N] \cdot \{d^e\} \quad (6.10)$$

where: u, v, w = displacement components in the x, y and z local directions, respectively,

$[N]$ = shape function between nodes – dependent on element type (i.e. linear, quadratic, etc.), and

$\{d^e\}$ = vector of unknown nodal displacements.

It is noted that shape functions must observe the following criteria to achieve a convergent FEM solution for the displacement field.

1. $N_i = 1$ at Node i , while $N_i = 0$ at all other nodes.
2. Element should be able to undergo rigid body motions. For example,
 $u = N_1 \cdot u_1 + N_2 \cdot u_2 + \dots + N_p \cdot u_p$, where $N_1 + N_2 + \dots + N_p = 1$.
3. Shape functions should be continuous within the element.
4. Shape functions should have the ability to produce a constant strain field.

The elemental equations can be assembled in an overall global matrix after the shape functions are chosen for a stress analysis, and a representative constitutive model is assumed. The assembly of the global matrix can be achieved by using several methods such as superposition (utilizing compatibility equations), or an energy approach where the potential energy is minimized.

Researchers have to make assumptions to provide enough information to build even a simplistic model, as shown by basic finite element algorithms (Equations 6.9 and 6.10). Pile foundations are complex and to model them realistically the finite element model has to include the following:

- The elasto-plastic constitutive behaviour for the soil, which can react to a range of loading scenarios (Wang and Sitar, 2004).
- The pile-soil interaction (Wang and Sitar, 2004; Hoback and Rujipakorn, 2004; Johnson et al., 2001; De Nicola and Randolph, 1993).
- The constitutive behaviour of the pile (Wu et al., 1989).
- The initial stress fields due to gravity and installation (De Nicola and Randolph, 1993). The constitutive behaviour is dependent on the stress level in the sand.

From the literature review on pile foundations it was found that some debate surrounds the exact performance of a pile subjected to combined loading. No literature was found for combined axial (uplift and compression), lateral loads and moments acting together to form one definite failure criterion. No literature was found that could help designers to estimate the pile head displacement due to combined axial (uplift/compression) and lateral loads. Then the aim of this research is to explore the effects of combined loading on a pile, including axial (compression and uplift), lateral loads and moments acting together on the pile. The influence of combined axial and lateral loads on the pile head displacement is of interest as well. To complete the pile section of this work each of the basic properties listed in point form above will need to be addressed.

CHAPTER 7: Small-Scale Model Pile Tests

7.1 General

It is difficult to conduct extensive experiments on full-scale piles due to the pile size and associated costs. Small-scale modelling of piles can be used as an alternative to full-scale testing. However small-scale experimental work is prone to scaling effects, but it does allow for trends and behaviour patterns to be observed. The trends and behaviour patterns will help to verify the numerical modelling results in Chapter 9.

A number of small-scale piles were tested in the laboratory under static axial compression, oblique 45° (compression) and lateral loads in various sand conditions. The tests were to compliment small-scale testing performed by Prideaux (1998). Laboratory testing performed included the loading of small-scale piles in sand. The loading directions used by Prideaux included axial tensile, oblique uplift and lateral loads.

The apparatus and testing procedure is presented in the following sections. The test piles were made of hollow metal tubes with an end plug at the base of the pile. Each pile was installed using a mounted hydraulic ram.

7.2 Apparatuses Used for Small-Scale Pile Testing

The basic items for the experimental work included model piles, tank, pile placement mechanism, pile loading apparatus and measuring devices. Separate loading devices had to be employed for each case as there were three different load cases to be performed. The other equipment had to be designed and fabricated except for the lateral pullout apparatus.

7.2.1 Model Piles

The model piles are the focal point of the experimental work in this research. The model piles were fabricated from thin walled tubular steel with an internal diameter of 48 mm, external diameter (d) of 51 mm, and length (L) of 300 mm. This resulted in a length to diameter (L/d) ratio of approximately six. Each model pile was fitted with a solid metal plug in the base and welded in place securely, and this simulated a small-scale closed ended pile. The pile head was left open ended to allow a specialized loading cap to fit on the top of the pile. For theoretical calculation purposes, the assumed material properties for the pile material elastic modulus and Poisson's ratio are 200 GPa and 0.3, respectively.

The piles were embedded to a depth of 250 mm, and the lower 250 mm of each pile was roughened by means of knurling. A photo of a model pile used for the experiments is shown below in Figure 7.1.



Figure 7.1: Experimental model pile

7.2.2 Tank

The sand for the small-scale pile testing was contained in a tank. Given that the loads were in compression, the influence zone for each pile required at least 2-5 pile diameter

zones (Meyerhof, 1961). A typical influence zone around a driven pile in sand was drawn from information given by Meyerhof (1961), and is shown in Figure 7.2.

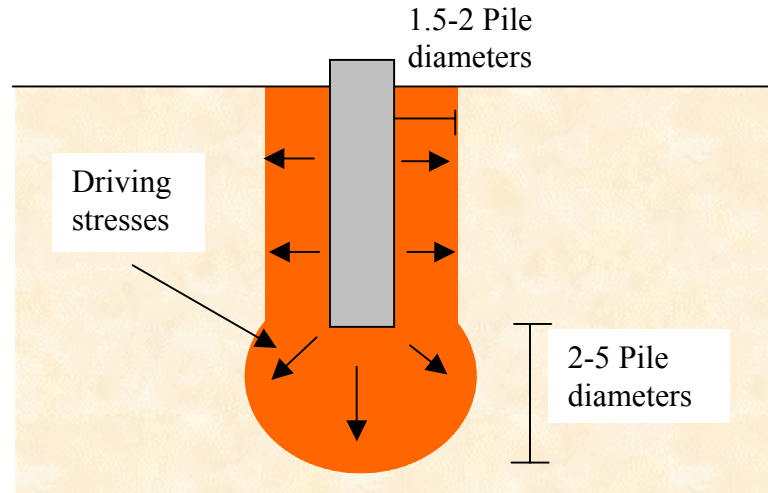


Figure 7.2: Influence zone for a typical driven pile

It is assumed that the movement of the pile or loading does not impact largely on the soil outside the influence zone. This means the pile loading mechanism does not influence the strain and stress profile in the soil past the influence zone.

The most cost effective measure was to hire a refuse removal bin to act as the experimental tank. The final tank (i.e. the hired refuse bin) chosen had been fabricated from 5 mm thick mild steel and had been reinforced around the top edge. The internal dimensions of the tank were 3 m long, 1.8 m wide and 0.7 m deep. The tank was large enough to facilitate the installation of ten model piles, at sufficient spacing to reduce the disturbance effects during the testing (Section 7.3.3).

7.2.3 Main Loading Frame

The main loading frame was constructed from four pieces of mild steel angle welded together to form a rectangular structure. The loading frame was a heavy structure that provided a rigid platform to aid the placement and loading of the model piles. The frame straddled the width of the tank and was clamped securely onto the edge of the

tank. This kept the loading apparatus from resting on the surface of the soil, and this minimized possible disturbance from external loading apparatus in the testing environment.

The axial loading hydraulic ram and the oblique loading equipment for this research were designed to sit on the frame, shift laterally and then clamp into position. Four hooks were welded onto the side of the main loading frame, enabling the frame to be lifted with an overhead crane.

7.2.4 *Pile Jacking Frame*

The method used for placement will ultimately affect the capacity of the model pile under load. The pile installation method chosen for the testing had to allow for high repeatability, and full control of alignment and depth of embedment.

Two common methods of pile installation include impact-driven and cast-in-place, as discussed in Chapter 6. The pile installation method required some driving as the model piles were prefabricated. The methods available to drive the model piles into the sand were hand installation, hammer apparatus or the use of a hydraulic ram. Hand installation was not acceptable as depth of embedment could not be controlled, and repeatability of driving conditions would be difficult to achieve. The use of a hammer to drive the piles would present difficulties in repeatability.

The frequency of the hammer drop and the hammer weight along with friction in the apparatus would impact on the results. The reliability of the pile installation direction due to possible eccentricity from the hammer load had also to be considered. Given the scale of the available test piles, it was inappropriate to hammer them into the sand, as the methods involved would be too crude and hard to quantify. Therefore, a hydraulic ram was considered to be the most viable option for driving. The hydraulic ram would allow for maximum control, minimum disturbance and control over pile alignment. The hydraulic ram was positioned to ensure clearance between the jacking frame and sand, which eliminated loads being placed onto the sand due to the installation apparatus.

7.2.5 Pile Loading Equipment

Three loading conditions were explored during the model pile testing for this research. These were axial compression, oblique 45° (compressive) and horizontal loading. Each loading situation required a different apparatus to be used.

Axial Loading

The axial compressive loading apparatus employed was the same as the installation apparatus presented in Figures 7.3 (a) and 7.3 (b). The hydraulic ram was lowered onto the tank and fastened in place with “G” clamps to the main loading frame. An extensometer was fitted using magnets for displacement measurement.

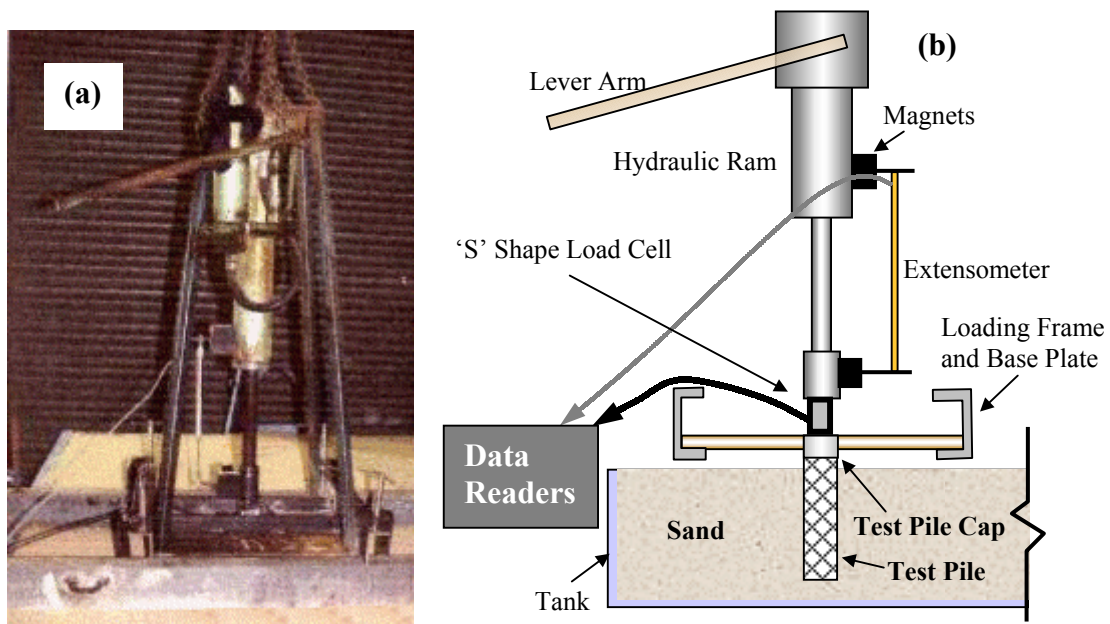


Figure 7.3 (a): Photo of axial loading arrangement

(b): Schematic of axial loading arrangement

A special loading cap was pushed onto the pile head before placement and axial loading. The cap consisted of a solid metal plug that fitted neatly into the pile (i.e. thin walled tube), and a 15 mm hole was bored out of the plug to join the loading extension. This arrangement controlled the vertical alignment for the pile loading. A photo of the vertical loading cap for a test pile is shown in Figure 7.4.



Figure 7.4: Oblique loading cap, axial loading cap and horizontal loading saddle, respectively

Horizontal Loading

The horizontal loading was achieved by pulling the head of the model pile, as shown in Figures 7.5 (a) and 7.5 (b). The force is applied through a cable and pulley system attached to the loading bin. The frame of the cable and pulley system was made from a square section of mild steel and has three pulleys. A cable was attached to the head of the pile with the saddle arrangement, and is shown in Figure 7.4.

Two holes were drilled 50 mm below the top rim of the pile, which allowed for the pin and saddle to be attached. The horizontal loading frame straddled the tank and applied the pulling load parallel to the soil surface. A load cell determined the applied load and was connected in series between the cable and the loading bin. The displacement was evaluated with an extensometer attached from the frame to the cable.



Figure 7.5 (a): Photo of lateral loading arrangement

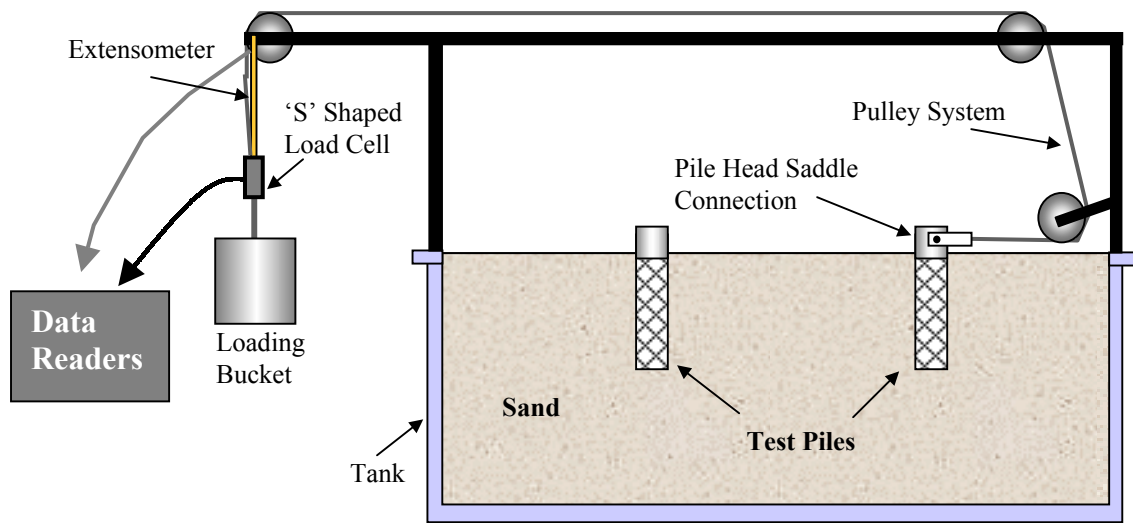


Figure 7.5 (b): Schematic of lateral loading arrangement

Compressive Oblique Loading

Various options were considered for the oblique loading apparatus. The oblique load was to be applied at an angle of 45° from the soil surface, and one option was to apply simultaneous axial and horizontal loads. This loading option was difficult to control, because as the pile shifted horizontally the axial loading mechanism would shift as well. The loading option chosen incorporated the use of a threaded rod mounted onto a frame, which could be clamped onto the main loading frame. A nut was welded to a piece of square hollow section at an angle of 45° , and the rod was threaded through it. This arrangement gave full control of displacement and alignment, and is shown in Figures 7.6 (a) and 7.6 (b).

The load was applied to the pile head with a rod rounded at the end, and fitted into the specially made pile cap. A load cell was positioned in series between the rounded rod and the threaded rod as mentioned in the previous paragraph. A device containing three bearings was also placed between the load cell and the threaded rod. The device allowed the load cell and rounded rod to remain stationary as the threaded rod was turned, thus allowing an extensometer to be attached to the apparatus.

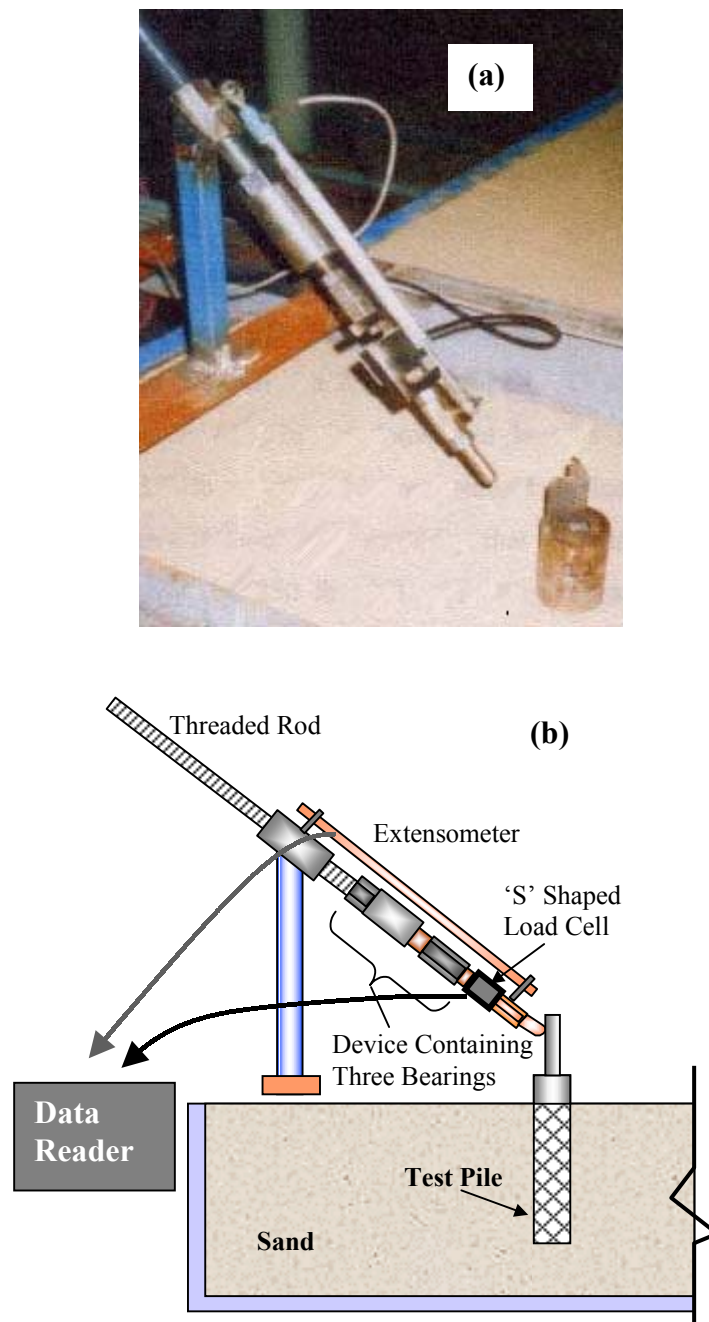


Figure 7.6 (a): Photo of oblique loading arrangement

(b): Schematic of oblique loading arrangement

7.2.6 Measuring Devices

Load Cells

Three different load cells were used at various times during the experiments. The largest load cell was a ten tonne (98100 N) cell used to weigh bags of sand as the tank

was filled. The bags were weighed and then emptied, and then weighed again to find the mass of the empty bag. This procedure allowed the net amount of sand in the tank to be determined.

Two small “s” shaped load cells were used to measure the load on the piles during loading. The smallest of the two load cells was a 250 lb (1115 N) load cell. This cell was used in all tests except for the axial loading in the dense and layered sand cases (Section 5.3), where the estimates for the ultimate load exceeded the capacity of the 250 lb load cell. The load cells were used in conjunction with a three-channel amplifier that in turn was serviced by a multimeter. This process resulted in a voltage output reading. The 250 lb load cell was calibrated for tension and compression using an Instron loading machine, and thus the voltage reading was converted into an equivalent force in Newtons.

The third load cell used was a 750 kg (7358 N) capacity cell. This cell was also calibrated using the Instron testing machine. A digital reading of the load was achieved with the use of a Kyowa read-out.

Extensometer

An extensometer was used to measure the displacement of the pile head in all loading situations. The device was attached to each loading apparatus and this made the task of experimental data recording much simpler. The extensometer was capable of measuring displacement to an accuracy of 0.1 mm.

7.3 Methodology for Model Pile Testing

To achieve a level of confidence in the experimental results a repeatable procedure must be followed in each test. Three different cases were explored - compressive axial, compressive oblique 45° and lateral. Each of the loading cases was performed in three different sand densities, and the densities were loose, dense, and a layered profile of half-loose and half-dense. This resulted in a total of nine different loading cases, and for each loading case three model piles were tested to ensure repeatability of similar results.

Twenty-seven model piles were subjected to a steadily increasing load during the laboratory testing. A summary of the load testing is given in Table 7.1.

Table 7.1: Number of tests for each load case

Load Action	Soil Condition		
	Loose	Dense	Layered
Compressive Axial	3	3	3
Compressive Oblique	3	3	3
Horizontal Pull-Out	3	3	3

A detailed testing procedure has been provided in Appendix C. The information for sand characteristics, sand placement and model pile layout are discussed in subsequent sections.

7.3.1 Experimental Sand Properties and Sand Placement

The sand used for the experimental work was sourced from R. Townsend and Co., in Townsville, Queensland. Seven tonnes of sand was supplied in seven one tonne bags all with identical grading. However, for quality assurance particle size distribution tests were performed on four of the seven bags in the soil laboratory at James Cook University. A summary of the sieve analysis results are given in Table 7.2 and Figure 7.7.

Table 7.2: Grain size distribution

Sieve Size (mm)	Sample 1	Sample 2	Sample 3	Sample 4	Grading from Distributor (Actual)
	(% Passing Sieve)				
1.180	100	100	100	100	100
0.600	72	71	68	69	69
0.425	56	57	56	51	56

Table 7.2 Continued: Grain size distribution

Sieve Size (mm)	Sample 1	Sample 2	Sample 3	Sample 4	Grading from Distributor (Actual)
	(% Passing Sieve)				
0.425	56	57	56	51	56
0.300	46	45	42	42	42
0.150	8	9	7	10	9
0.075	3	1	2	2	3

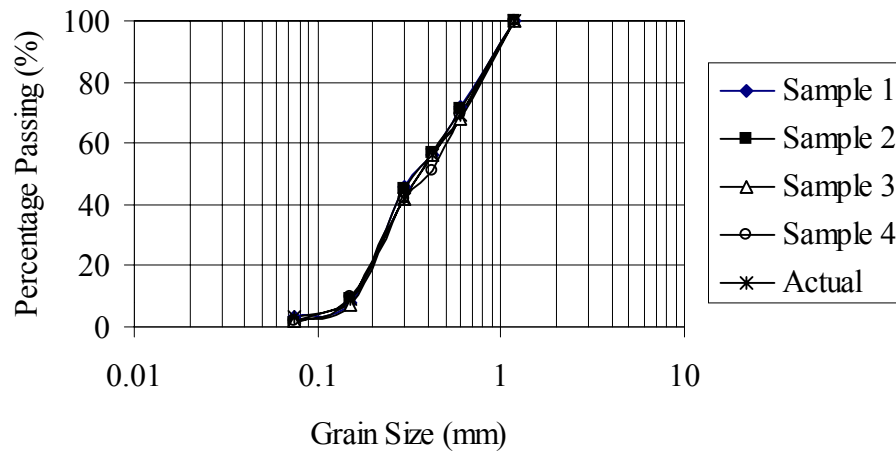


Figure 7.7: Sieve analysis of experimental sand

The sand characteristics were established based on the above results, and presented in Table 7.3.

Table 7.3: Sand characteristics

Particles Size Range	1.18-0.075mm
Coefficient of Uniformity C_u	3
Coefficient of Curvature C_z	0.9
Coefficient of Roughness R (Das, 1999)	0.25, angular

The results indicate poorly-graded uniform sand with an angular particle shape. Testing was carried out on the experimental sand to determine its characteristics, and the testing included the following information:

- Particle Size Distribution (AS 1289 3.3.1 – 1995)
- Minimum/Maximum Density (AS 1289 5.5.1 – 1998)
- Direct Shear (AS1289.0-2000)

The raw test data from the above tests is given in Appendix D.

Loose State Placement

The first sand density case considered was the placing of sand in its loosest form that could be achieved in the laboratory. When sand is in its loosest state (i.e. relative density 0%) then its strength (e.g. friction angle) and deformation (e.g. Young's modulus) properties are at a minimum. The loose sand state was achieved by allowing the sand to free-fall (approximately 0.5 m) out of a one tonne holding-bag from a uniform height. The bag was steadily moved around the tank with the overhead crane, and this achieved a homogenous sand bed.

The weight of the sand was measured and the volume of the tank was known, therefore the bulk density of the sand could be calculated (Section 7.3.2). The tank was filled and levelled using a piece of timber. The levelling board slid along the top-edge of the tank, so that no downwards pressure was applied to the sand surface.

Dense State Placement

The second sand density case considered was the placing of sand in its densest form that could be achieved in the laboratory. When sand is in its densest state (i.e. relative density 100%) then its strength and deformation characteristics are at a maximum. The method adopted for dense state placement was aimed at producing the maximum density possible by dry compaction.

The tank was loaded with successive layers of sand approximately 150 mm – 200 mm thick. Sand layers were compacted with a vibrating plate compactor, until the tank was

filled with sand (Figure 7.8). The sand surface was levelled using a timber board as mentioned for the loose sand placement.

The weight and density of the sand was estimated using the same procedure as the placement method for the loose state.



Figure 7.8: Vibrating plate for compaction

Layered State Placement

The purpose of using a layered soil profile is to simulate a natural soil stratum, where the layers of different types of soil have different properties. A model pile had the bottom half of its embedded length in dense sand, and the top half of its embedded length in loose sand. This resulted in the tank containing 575 mm of compacted sand on the bottom layer, and 125 mm of loose sand in the surface layer.

7.3.2 Sand Bed Properties

The test sand was prepared for three different soil profiles consisting of two separate sand density states. The bulk densities were calculated by measuring the sand weight being placed into the known volume of the tank. In addition, samples were taken and the water contents calculated for each test stratum. All the sands were sufficiently dry with a moisture content less than 0.25%. A summary of the results is provided in Table 7.4.

Table 7.4: Experimental sand bed properties

Sand Condition	Moisture Content (%)	Bulk Density (t/m ³)
Loose	0.15	1.44
Dense	0.22	1.74
Layered	0.13, 0.16	1.49, 1.72

A summary table of sand material properties is given Table 5.5.

Table 7.5: Sand material properties

Soil Condition	ρ_{\min} (t/m ³)	ρ_{\max} (t/m ³)	ϕ (Deg.)	D_r (%)
Loose	1.39	1.78	30.6*	14.6
Dense	1.39	1.78	40.7**	92.6
Layered	1.39	1.78	30.6*, 40.7**	30.6, 87.6

* It is assumed the looser layers of sand (i.e. $D_r \leq 31\%$) have approximately the same friction angle as the loose sand tested in the shear box.

** It is assumed the denser layers of sand (i.e. $D_r \geq 87\%$) have approximately the same friction angle as the dense sand tested in the shear box.

The constitutive parameters are discussed in Chapter 4.

7.3.3 Model Pile Placement

The tank had sufficient surface area to place the ten model piles, as shown in the schematic drawing in Figure 7.9. Each pile had approximately 300 mm (i.e. minimum of 6*diameter) clearance from the walls of the tank, and centre to centre spacing of the piles was no less than 600 mm. The layout of the tank simulated a semi-infinite homogeneous sand bed. This is based on the influence zones recommended by Meyerhof (1961), and discussed in Section 7.2.2.

The three piles used in each load direction scenario were tested after being placed, and then removed. The model piles were embedded to a depth of 250 mm, and this was achieved by employing a hydraulic ram as described in Section 7.2.4.

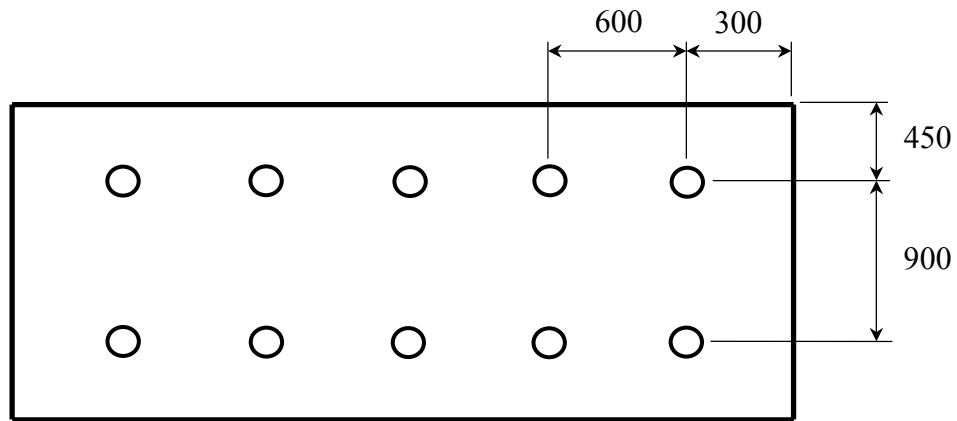


Figure 7.9: Plan view of sand tank and pile layout

Note: All dimensions have units of mm.

The embedment length was controlled with a digital vernier gauge, which is accurate to 0.01 mm. The gauge measured the distance from the pile head to the loading frame. Once the model pile was driven to an adequate depth the placement apparatus was removed, and the sand indentations from placement were smoothed. Thereafter, the small model pile was tested.

7.3.4 Load-Displacement Testing

The model piles were subjected to a steadily increasing load until a predetermined settlement was reached. The applied load and displacement were recorded, along with pertinent information such as sand settlement. The procedure was followed strictly each time a pile was tested to ensure quality results.

7.4 Load Settlement Results for Model Piles

The ultimate capacity of a pile in sand is dependent on several factors, as discussed in previous chapters. The factors fit basically into one of four categories mentioned below:

- Problem geometry – this includes pile shape, presence of embankments, etc.
- Sand properties – the relative density, particle size and shape, and the water content has an impact on the ability of the sand to resist load.

- Pile material properties – the material from which a pile is constructed influences the rigidity and performance of the pile under load.
- Load direction – the combination of loading scenarios and load direction has an impact on the ultimate capacity of a pile. The work in this thesis examines the influence of different load combinations.

The three different load cases considered consisted of axial compressive load, compressive oblique load at 45° and a horizontal load. The tabulated results for the load tests can be found in Appendix E.

7.4.1 *Compressive Axial Load Test Results*

The model piles were subjected to a controlled compressive axial load. The piles in the dense and layered sand bed were loaded to 10 mm settlement and released. The piles in the dense sand bed were then loaded to 20 mm settlement and released again. The piles in the loose sand bed were loaded to 5 mm settlement and released, then loaded to 10 mm settlement and released again. The readings for load and displacement were recorded during the loading actions. The load-displacement curves for the loose state, dense state, and layered state are shown in Figures 7.10 to 7.12.

The loose sand case was loaded to 5 mm before being released. The pile in the loose sand had a lower ultimate load compared to the dense sand that was loaded to 10 mm. Loading in the dense sand remained in the elastic strain range at higher stress levels. The load was mostly transferred and supported by bearing at the base, due to the small-scale testing and rigid pile material.

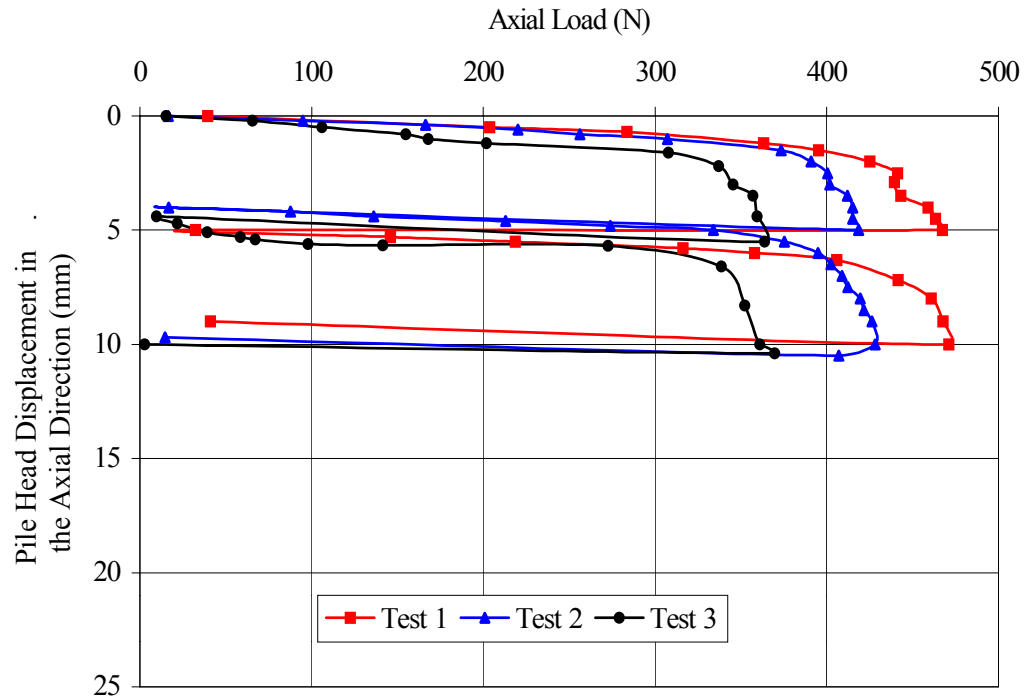


Figure 7.10: Load-displacement curve for axial load in loose sand

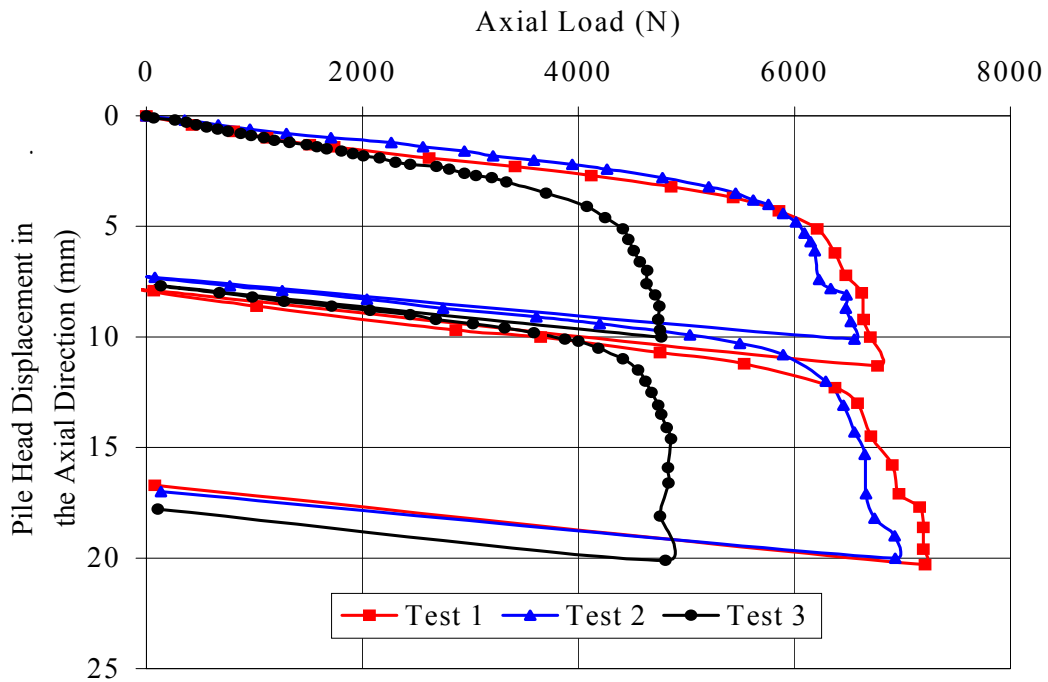


Figure 7.11: Load-displacement curve for axial load in dense sand

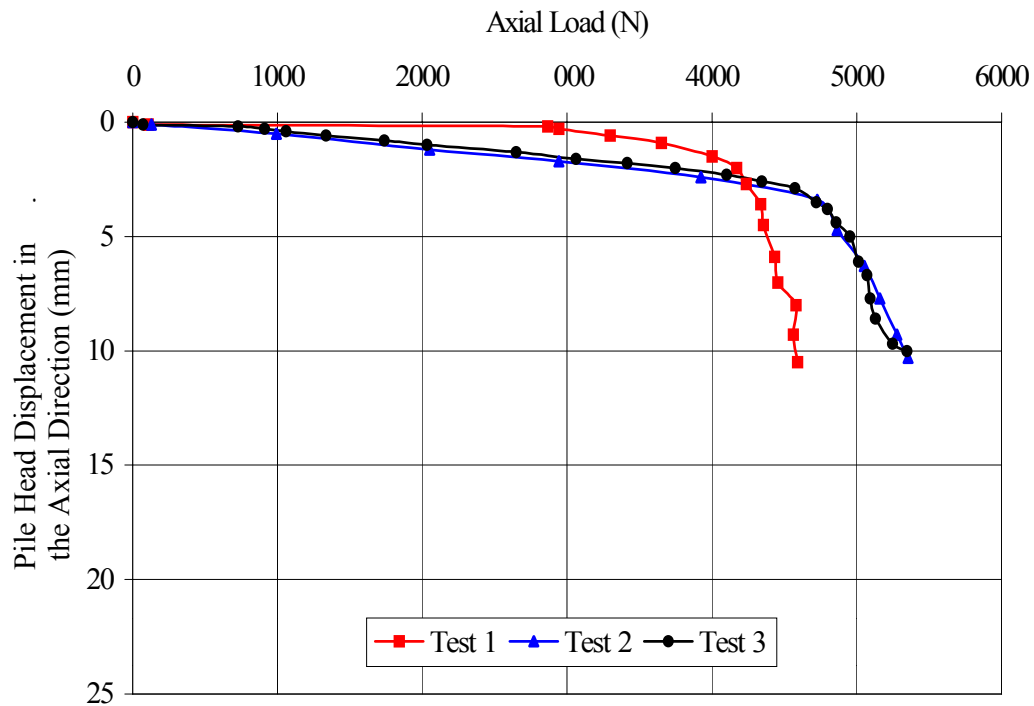


Figure 7.12: Load-displacement curve for axial load in layered sand

7.4.2 Compressive Oblique Load Test Results

The pile head displacement along the direction of the load was measured with an extensometer attached to the loading apparatus. It was assumed for the 45° compressive oblique loading, the major movement of the pile head was in the direction of the load.

However some movement may appear perpendicular to the direction of the load. The movement could not be measured reliably due to the limitations of the apparatus and sensitivity. It was thought the above assumption would be adequate for the purpose of this work. The experimental results were used to establish trends for the numerical analysis. The trends for the oblique load case will also be compared with other researchers' work where possible.

Graphical results for load-deformation of oblique loading in loose, dense, and layered soils are shown in Figures 7.13 to 7.15. The displacement magnitude of the pile head was in the direction of the load (i.e. 45° towards the soil surface).

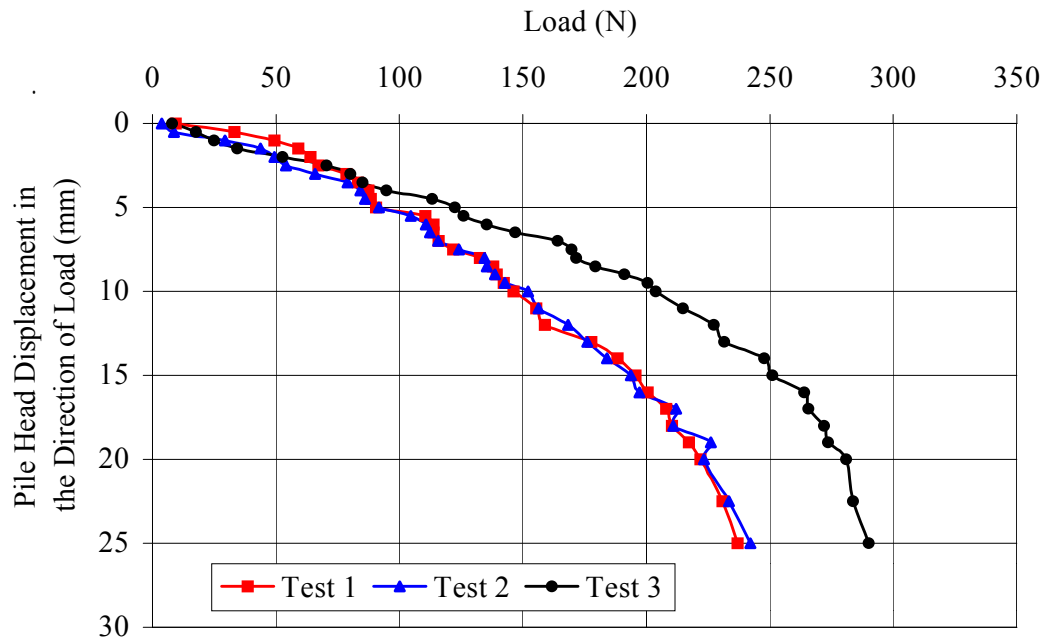


Figure 7.13: Load-displacement curve for oblique load in loose sand

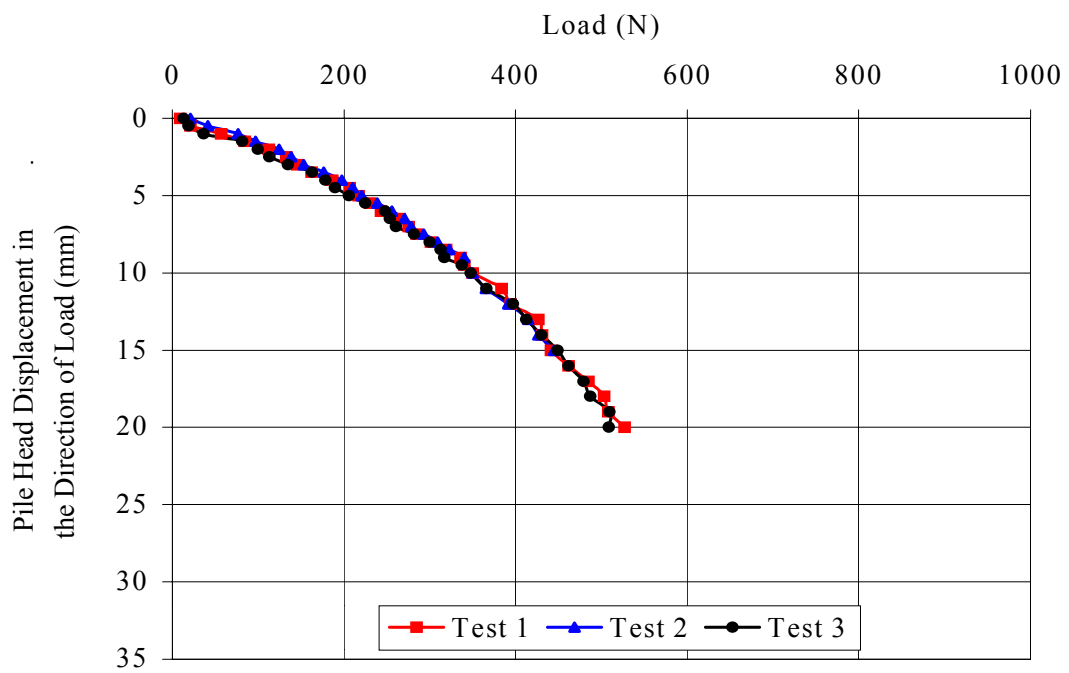


Figure 7.14: Load-displacement curve for oblique load in dense sand

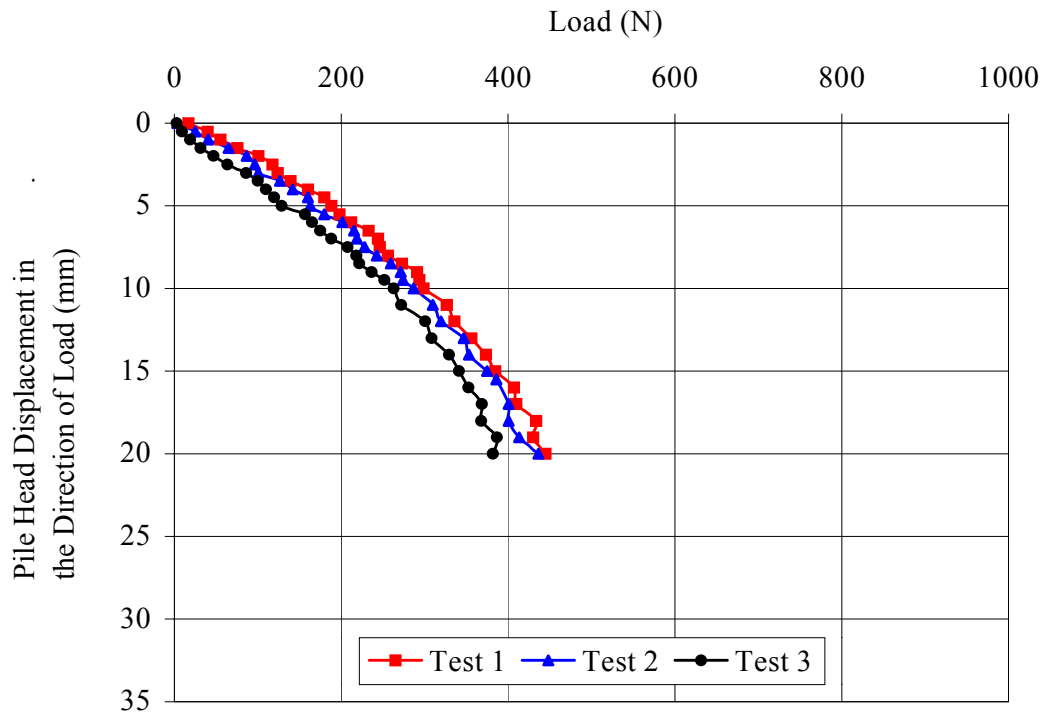


Figure 7.15: Load-displacement curve for oblique load in layered sand

7.4.3 Horizontal Load Test Results

A steadily increasing load was applied to the model piles during horizontal loading until the load caused the piles to be pulled out from the sand bed. The applied load and displacement in the lateral direction were recorded during loading, until the ultimate load was attained.

The pile head displacement was observed to be almost parallel to the soil surface towards the origin of the load. Load-displacement relations for different states of sand considered are shown in Figures 7.16 to 7.18.

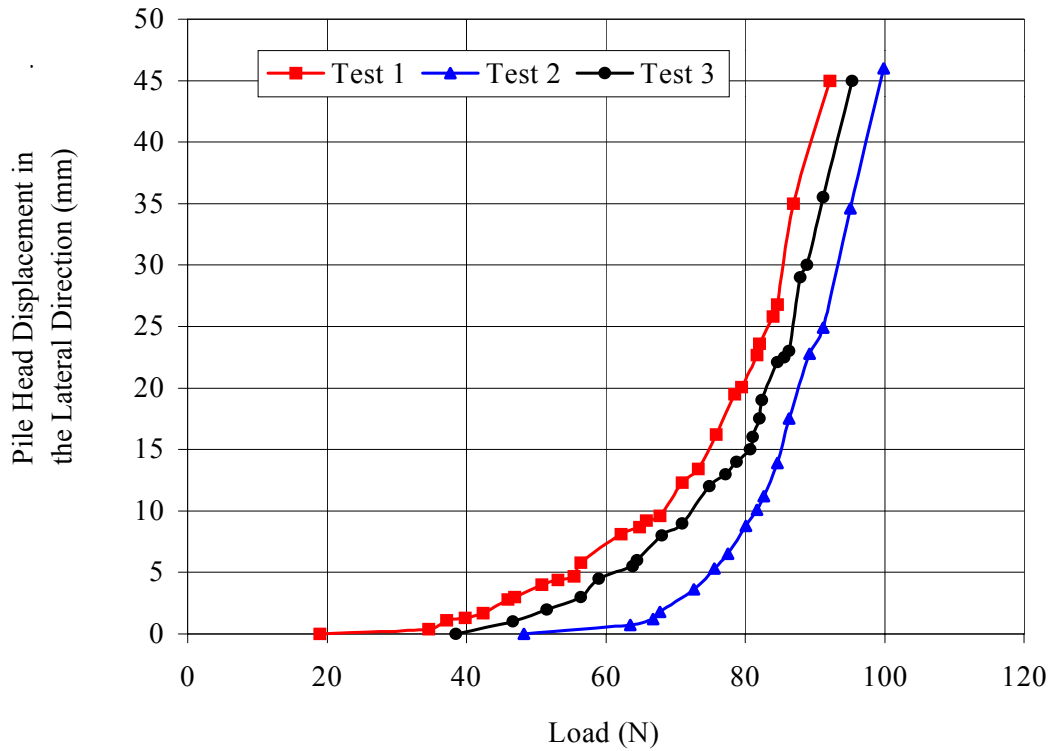


Figure 7.16: Load-displacement curve for horizontal load in loose sand

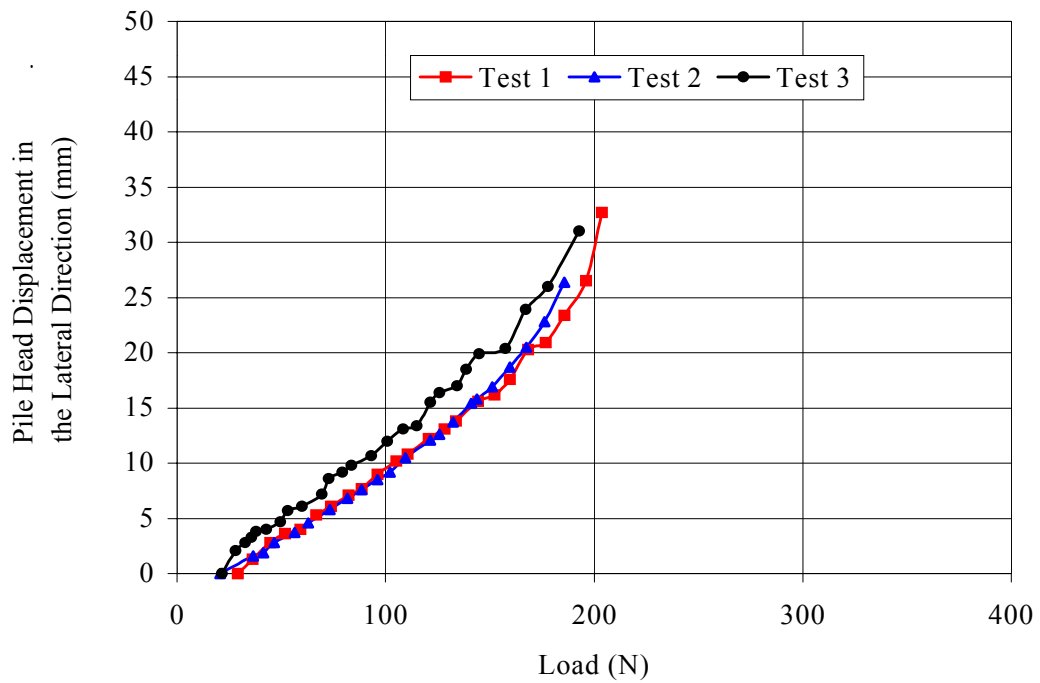


Figure 7.17: Load-displacement curve for horizontal load in dense sand

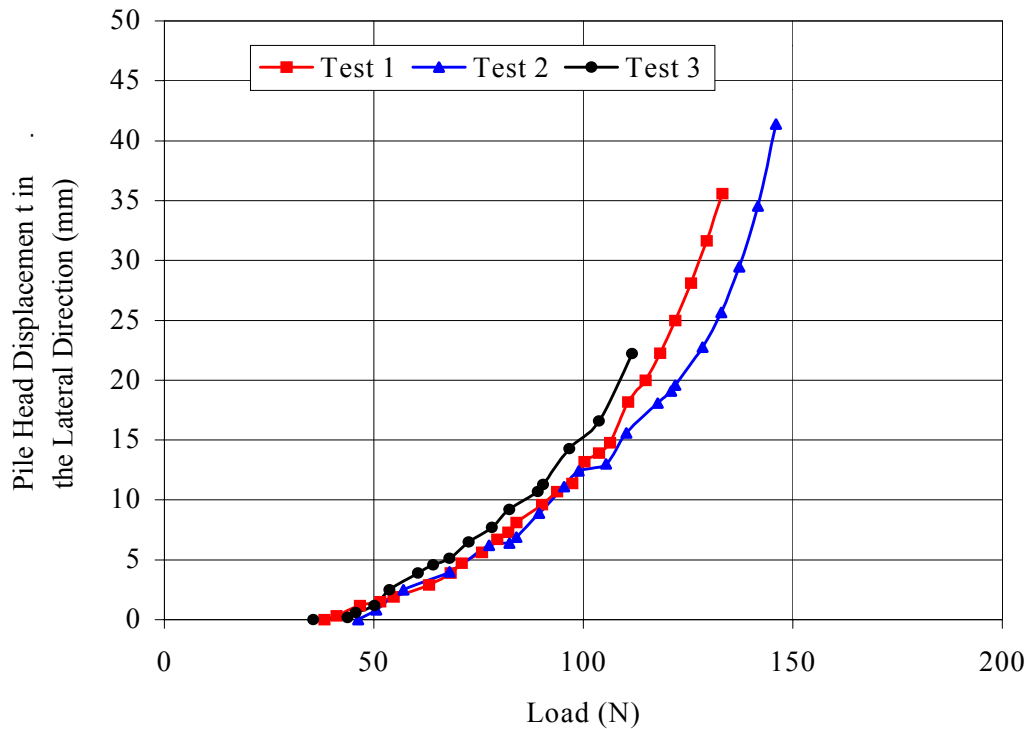


Figure 7.18: Load-displacement curve for horizontal load in layered sand

7.5 Experimental Observations

During the loading it was noted that the test piles in Figures 7.11 to 7.13 generally had two piles that were in relatively good agreement, and one remaining pile that varied from the other two. The reason behind the variation may be due to disturbance during placement, i.e. the soil loosening or becoming more dense. Given the small scale of the test piles, any change in conditions may lead to significantly varied results. When two test piles gave similar results, the results were averaged and used to represent the test piles' response to load. A review of the test pile response and trends under loading have been explored in Chapter 10.

Some observations were made throughout the experimental testing. The visual characteristics observed were surface profiling, driving effects, etc. The observations for the experimental testing are presented in the following sections.

7.5.1 Surface Displacement Prior to Loading

Pile driving can create large residual stresses along the pile shaft and at the pile base. In the loose case, the sand surface around the pile caved in towards the pile. It would be unrealistic to assume that the soil remained homogeneous after placement of the model piles.

An indentation appeared around the pile indicating a sign of compaction (Figure 7.19). This produced an increase in density, which would change the elastic modulus of the soil within the disturbed zone.

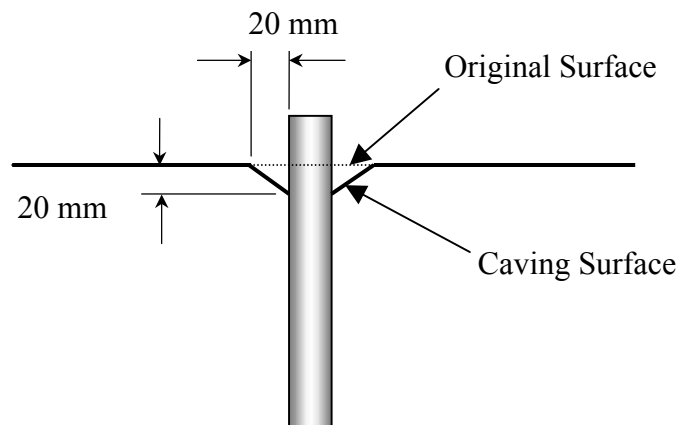


Figure 7.19: Surface disturbance from placement in loose sand

The sand was almost at maximum compaction in the dense state, where the relative density was 92.6%. This led to surface swelling during placement. The sand particles could not pack closely together and the sand was pushed upwards. This caused a symmetrical swelling about the axis of the pile (i.e. dilation). The upheaval of the soil surface extended out to approximately one embedded length (250 mm) horizontal from the pile. Some caving of the sand in the immediate vicinity of the pile-soil interface was also observed (Figure 7.20).

Surface swelling indicated a change in soil properties. The swelling changed the soil volume around the pile and effectively lowered the density. The driving stresses also have an impact on the sand strength and are discussed in the next chapter.

The bottom half of the pile was embedded in dense sand for the layered case, and the top half in loose sand. The soil response was observed to be somewhere between loose and dense state. Swelling occurred around the pile but not to the extent of the dense case, i.e. partial dilation. It is noted that some caving occurred around the pile as well.

After placement the sand was levelled with a small straight edge, and this returned the soil surface to its previous profile. However, it is noted that the soil properties would no longer be the same especially in the immediate vicinity of the pile-soil interface.

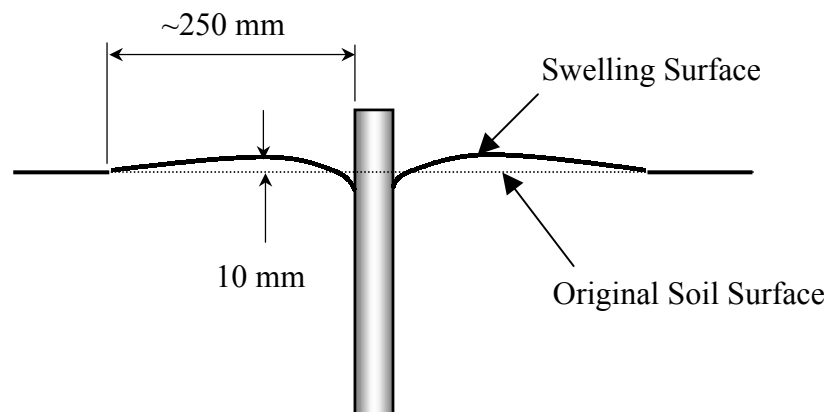


Figure 7.20: Surface disturbance from placement in dense sand

Another observation noted was the slight consolidation of the loose state sand bed. The surface of the sand bed was seen to settle about 2 mm to 3 mm over 7 days. This led to small changes in the density of the sand bed, which in turn marginally affected the elastic modulus. External vibrations or simply the self-weight of the sand may have caused this consolidation.

7.5.2 Surface Displacement Post Loading

The sand was levelled to make a smooth surface around the pile before loading commenced. No major surface displacements occurred during axial loading. This was expected considering the piles only settled 20 mm after loading, compared to 250 mm during placement. Slight caving occurred approximately 5 mm around the pile shaft to a depth of about 4 mm.

The pure lateral loading produced sand heave in front of the pile, and sand caving behind the pile (Figure 7.21). This form of pattern in the failed sand indicates that the pile is possibly rotating beneath the surface (Brom's Method, Chapter 6). Hence the top of the pile is pulling away at the back of the pile, and sand is collapsing in behind. The sand at the front of the pile is being compacted and shunted forward, resulting in heave up of the sand surface.



Figure 7.21: Horizontal load on pile with failed pile in foreground

The piles were manually removed after loading was completed, and various indentations were observed in the sand after removal. The indentations were typically conically shaped pits symmetrical around the axis of the pile. It was found that the denser the sand the smaller the indentation. Again, the layered soil showed results in between the two extremes of dense and loose conditions. The average indentations for the loose and dense case are shown below in Figure 7.22.

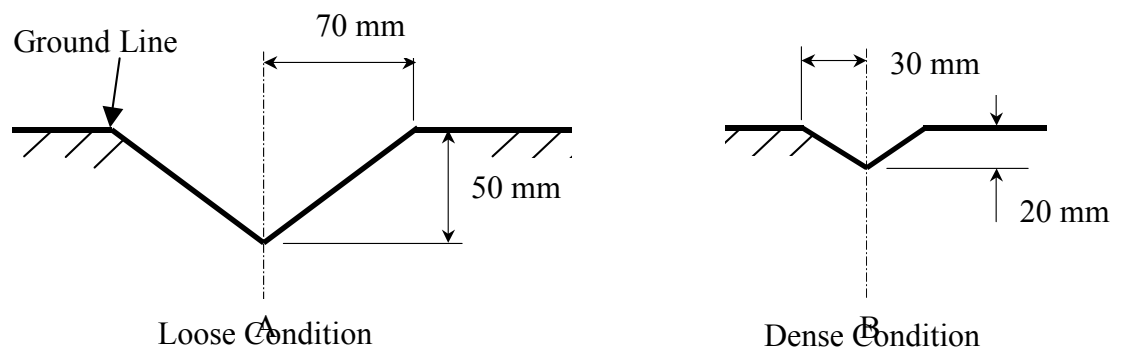


Figure 7.22: Average surface indentations after pile removal

CHAPTER 8: Numerical Pile Model Development and Verification

8.1 General

The use of numerical models to simulate complex problems has become more popular due to advances in technology and computer speed (CPU power). Numerical models allow for multiple simulations to be explored, and they also allow researchers to gain a better understanding of the mechanisms involved.

The researching of piles through full-scale testing can be a difficult task due to their size and cost. Researchers can explore the interaction of both pile and soil under various loading scenarios and sand properties by using numerical methods, such as finite element method or finite difference method. The research presented in this thesis uses the finite element computer package, ABAQUS, to explore the interaction between different pile load combinations.

ABAQUS is a multi-purpose computer package that allows users to investigate mechanical, structural, and geotechnical problems under static and dynamic loadings. It is an ideal package due to its capability in modelling complex interactions between several bodies, and the available constitutive models for both structural and geotechnical materials. The package also allows for initial residual stress fields to be defined.

It is important to verify a numerical model to ensure its predictions are within an acceptable limit when compared to a real life situation. The following sections show the finite element model and algorithms used to achieve the aims of this work, along with the verification cases used to test the developed pile model.

8.2 Numerical Model Algorithms and Behaviour Criteria

This section explores some of the available numerical model algorithms and constitutive behaviour models, which may be used to predict sand and pile behaviour.

8.2.1 General Finite Element Algorithms

The general algorithms associated with the finite element method are discussed in Chapter 9. In addition to the information provided in Chapter 9, it is noted that the assembled matrix may be solved implicitly or explicitly. The differences between these solving techniques are discussed in point form below.

- **Implicit Algorithm:** these algorithms assume a constant average acceleration over each time step, between t_n and t_{n+1} . Herein, t_n is the time at the beginning of n^{th} time step and t_{n+1} is time at the end of the n^{th} time step. The governing equation is evaluated and the resulting accelerations and velocities at t_{n+1} are calculated. Then the unknown displacements at t_{n+1} are determined.
- **Explicit Algorithm:** explicit integration schemes assume a linear change in displacement over each time step. The governing equation is evaluated and the resulting accelerations and velocities at t_n are calculated. Then the unknown displacements at t_{n+1} are determined.

The major difference between implicit and explicit techniques lies in the equations that are used to solve for displacements at t_{n+1} . The implicit solution method requires matrix inversion of the structural stiffness matrix and the explicit solution does not. However, unlike the implicit solution scheme that is unconditionally stable for large time steps, the explicit scheme is stable only if the time step size is smaller than the critical time step size for the structure being simulated.

Given that this research is to explore pile response under oblique loading, it was considered desirable the solution should be in a state of equilibrium. Therefore the finite element mesh was solved implicitly. This introduced a series of complications where non-convergence problems occurred. The complications were eliminated by modelling as close to the real in situ state as humanly possible. One such example of adapting the mesh to be more realistic was the inclusion of initial gravity stresses, due to the self-weight of the system to overcome plastic strain non-convergence problems. This particular aspect of the model has been discussed in Section 8.2.4.

When formulating the problem an element type has to be chosen. ABAQUS has a broad range of available element types to simulate one, two and three-dimensional problems. The research herein explores the interaction of different load combinations acting on a pile. Since the pile problem has loads in various directions it was considered appropriate that the pile-soil system be modelled using three-dimensional elements. A further discussion on the element types used for the pile and sand is given below.

The three dimensional elements that can be used to simulate the response of a pile under load include:

- Linear elements – these elements assume a linear shape function between adjoining nodes. Two examples are shown in Figure 8.1 (a).
- Quadratic elements – these elements assume a quadratic shape function between two adjoining nodes. This is achieved by including secondary nodes between the two primary nodes located at the element boundary as shown in Figure 8.1 (b).

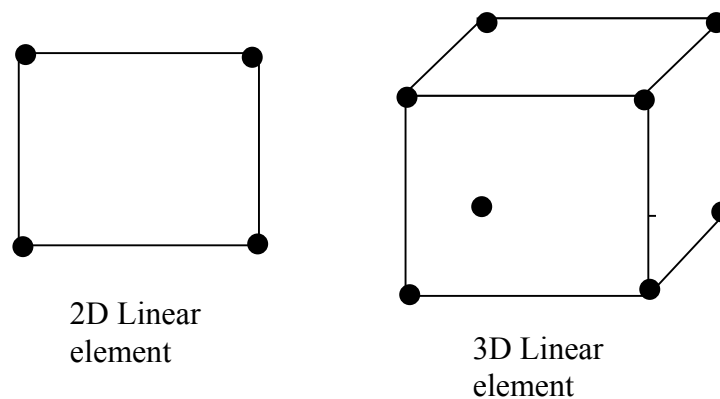


Figure 8.1 (a): Linear elements

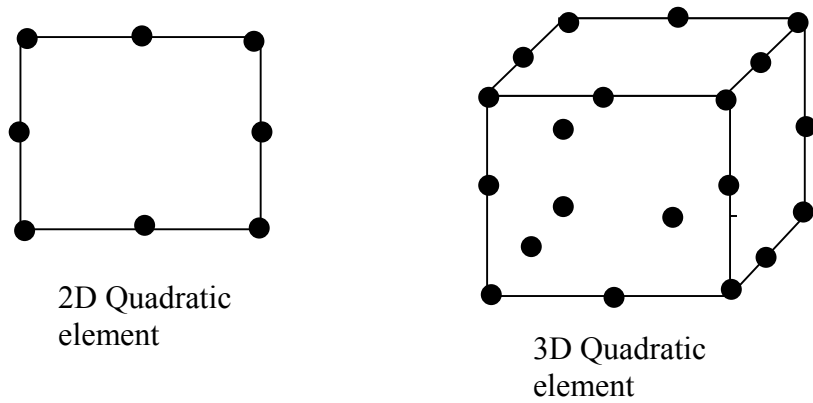


Figure 8.1 (b): Quadratic elements

When the displacement shape function between the nodes is assumed to be linear, it can cause problems for materials subjected to large bending stresses. This means the linear elements have a problem in bending and can't flex to suit loading, as shown in Figure 8.2.

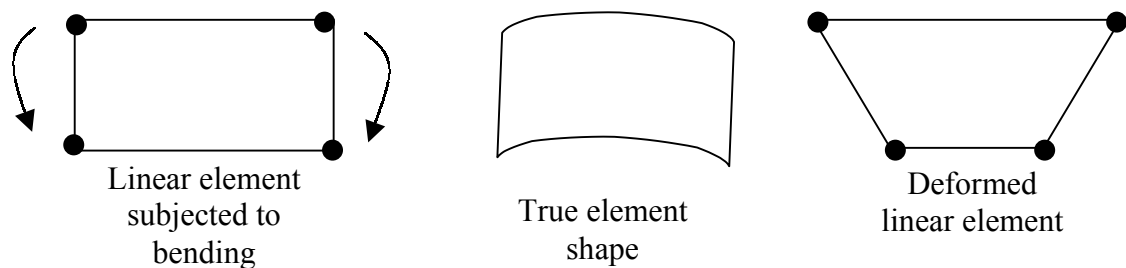


Figure 8.2: Bending nature of linear elements

However, the rigidity may be reduced by using smaller elements so the linearity is occurring over a smaller span (e.g. distance between nodes), and this allows for the overall mesh to deform more realistically. As an alternative, quadratic elements may be used as they are more flexible in movement.

In the past geotechnical researchers have used one or both of the element types discussed above to discretize the soil mass. In an ideal situation quadratic elements allow the mesh to bend more realistically. When modelling deep foundations such as piles, the quadratic elements hamper the use of surface based interaction between the pile-soil interface, as discussed in Section 8.2.3. It is noted that the pile to soil interaction has a large impact on the pile reaction and must be included in the model to

gain a realistic response (Wang and Sitar, 2004; Johnson et al., 2001). Then in the case of deep foundations, such as piles subjected to various loading scenarios, linear elements had to be employed. This was considered satisfactory provided a sensitivity analysis was completed, so the movement of the overall model was not restricted from the linear element approximation. The use of linear elements still allowed for reasonable approximations as shown in the verification section. This indicated linear elements are suitable for modelling pile response, provided they are used appropriately.

8.2.2 Implementation of Constitutive Model into Finite Element Model

Several constitutive and failure models can be used to describe the behaviour of soil or more specifically sand (Chapter 4.2). There are many benefits and disadvantages in using each of the various models. The following questions must be addressed when choosing a constitutive model to describe the behaviour of sand:

- Does the constitutive model and failure model combination give a realistic representation of the stress-strain states in the sand, under various loading conditions and problem geometry?
- Can the constitutive model and failure model's parameters be determined readily from standard field and laboratory testing?
- What are the limitations of the constitutive/failure models when used to represent a particular soil type? For example, when the constitutive/failure models are derived several simplifications are needed to obtain usable criteria. These simplifications are based on the soil type, problem geometry and whether the soil is considered isotropic or anisotropic.

For this research the interaction between an obliquely loaded vertical pile and sand is being explored. The in situ state of the sand is often assessed by using field tests, such as standard penetration test (SPT), cone penetration test (CPT), or dynamic cone penetrometer (DCP). The in situ method of testing is preferred as undisturbed samples of sand are very difficult to obtain. One method of collecting undisturbed samples of in situ sand is to freeze the sand sample in the ground before collecting and returning it to the laboratory. Yet this form of sampling is expensive and often not practical to implement. Therefore, the assessment of the in situ properties of sand (i.e. Young's

modulus) is based on correlations from the standard field tests. When determining the constitutive parameters of sand such as the friction and dilation angle, again correlations from standard tests are employed. Laboratory testing is then restricted to classification such as grain size distributions on disturbed samples.

From the above, it is anticipated that predicting the variables needed to define non-linear elastic models would be a time consuming, profitably non-feasible and a difficult exercise to accurately achieve. Unless the problem being explored is considered to be high-risk and sensitive, the benefits achieved by performing more expensive testing might be outweighed by the cost feasibility of the job. It was concluded by this author that the use of a linear elastic model to represent the elastic response would be sufficient for the purpose of this research. Other researchers also agree with such an assumption (De Nicola and Randolph, 1993; Trochanis et al., 1991; and Wu et al., 1989).

The decision to use a linear elastic model to estimate the elastic response was further reinforced, based on the verification results of the final pile FEM model. The choice of a failure surface to model the response of the sand was reduced to two popular models, Mohr-Coulomb and Drucker-Prager. The Drucker-Prager model has three main failure surface types, linear, hyperbolic and exponent (Chapter 4). The hyperbolic and exponent Drucker-Prager failure surfaces require detailed laboratory testing such as triaxial tests on non-disturbed samples. Therefore, these two surface types were not explored due to the impracticality of obtaining the input parameters.

The choice of the failure surface was then reduced to either Mohr-Coulomb or the linear Drucker-Prager model. It is noted that the linear Drucker-Prager model also requires triaxial test parameters in order to define the failure surface. As discussed by Hibbett et al. (2001), the parameters required for the Drucker-Prager model may be correlated to the friction angle and cohesion of the soil (equal to zero for sand). Hibbett et al. (2001) also indicate that this method of parameter mapping between Mohr-Coulomb and linear Drucker-Prager models is valid, when the friction angle is less than or equal to 22° . When the friction angle is less than 22° the linear Drucker-Prager model remains convex and compares well with the Mohr-Coulomb parameters. Sand in its loosest state generally has a friction angle greater than 25° , and the friction angle increases to

approximately 50° in its densest state (Chapter 4). Then parameter mapping for sand to enable the use of the linear Drucker-Prager model is considered to be inappropriate. Hibbett et al. (2001) suggest that if the friction angle of the material (in this case sand) is significantly greater than 22° the Mohr-Coulomb model should be employed. From the strength of the above argument, it was decided that the use of the Mohr-Coulomb model is the most appropriate for this work.

The Mohr-Coulomb elasto-plastic model consists of an elastic constitutive model together with a defined failure surface (Chapter 4). In this work the Mohr-Coulomb model is used to define the stress state at which plastic failure occurs at an integration point within the finite element mesh (De Nicola and Randolph, 1993). Once plastic failure occurs the strain-deformation no longer is governed solely by elastic constitutive relationships, but rather a more complex elasto-plastic strain model. The elasto-plastic strain model adopted uses a non-associate flow rule. Therefore, the total strain rate at any integration point is as follows:

$$\dot{\varepsilon} = \dot{\varepsilon}^{el} + \dot{\varepsilon}^{pl} \quad (8.1)$$

where $\dot{\varepsilon}$ = total strain rate

$\dot{\varepsilon}^{el}$ = elastic strain rate

$\dot{\varepsilon}^{pl}$ = plastic strain rate

Like many engineering theories, there are several variations proposed by different researchers for determining the elastic and plastic strain potential components. The variations are often a focal point when choosing a finite element computer package for modelling real-life engineering problems.

In this case ABAQUS is being used to model the pile and surrounding sand. ABAQUS generally uses traditional Mohr-Coulomb plasticity theory but instead of using the irregular hexagonal section in the deviatoric plane, it uses a completely smooth flow potential. The flow potential used by ABAQUS is hyperbolic in the meridional plane and the programme has a smooth deviatoric section (Hibbett et al., 2001).

The plastic strain rate is, therefore, defined as follows (Hibbett et al., 2001):

$$\dot{\varepsilon}^{pl} = \frac{\left(\dot{\varepsilon}^{pl} \right) (\partial G)}{(g)(\partial \sigma)} \quad (8.2)$$

where G = flow potential

$$= \sqrt{(\varepsilon_m c|_0 \tan \psi)^2 + (R_{mw} q)^2} - p \tan \psi \quad (8.3)$$

$$g = \frac{1}{c} \sigma : \frac{\delta G}{\delta \sigma} \quad (8.4)$$

σ = normal stress

q = Mises equivalent stress

p = mean normal stress

$c|_0$ = initial cohesion yield stress

= 0 kPa for clean sand

ε_m = meridional eccentricity

(defines the rate at which the function approaches asymptote)

ψ = dilation angle

R_{mw} = deviatoric elliptic function

$$= \frac{4(1 - e^2)\cos^2 \Theta + (2e - 1)^2}{2(1 - e^2)\cos \Theta + (2e - 1)\sqrt{4(1 - e^2)\cos^2 \Theta + 5e^2 - 4e}} R_{mc}\left(\frac{\Pi}{3}, \phi\right) \quad (8.5)$$

e = deviatoric eccentricity (describes out of roundness for the deviatoric section)

$$= \frac{3 - \sin \phi}{3 + \sin \phi} \quad (8.6)$$

Θ = deviatoric polar angle

$$R_{mc}\left(\frac{\Pi}{3}, \phi\right) = \frac{3 - \sin \phi}{6 \cos \phi} \quad (8.7)$$

ϕ = friction angle

8.2.3 Implementation of Interface Frictional Criteria in Finite Element Model

Sometimes in geotechnical engineering problems it is necessary to simulate the interaction between two material types. A classical example of this is a loaded pile in

soil. As the load on the pile is increased the shear stress at the pile-soil interface will reach a critical mobilizing value. Once the critical shear stress is exceeded the pile will move relative to the soil. Other interface problems exist when pore fluid is present, and this results in flow across contact surfaces. Therefore, the continuity of pore pressure between materials must be maintained.

ABAQUS has a vast range of interaction models available. The models include:

- 1) Mechanical (e.g. friction)
- 2) Thermal
- 3) Coupled Thermal-Mechanical
- 4) Coupled Pore Fluid-Mechanical (mainly used in geotechnical problems)
- 5) Coupled Thermal-Electrical

There are two ways to model the interaction between materials. The first is surface-based interaction using contact nodes employed in this research. The second is contact elements. Surface-based contact simulations are common and can be applied to a large number of problems, because they are simple to use. In the case of modelling the pile-soil interaction surface-based contact allows for great versatility and control.

8.2.3.1 Surface-Based Contact

Surface-based interactions are dependent on the master and slave concept. The nodes on the two contacting surfaces are grouped together to form master and slave surfaces. This concept is an interaction model that governs the transfer of stresses from one surface to another. Some typical examples of surface-based interactions are:

- a) Contact between two deformable bodies (e.g. pile-soil interaction).
- b) Contact between rigid and deformable bodies.
- c) Self contact.
- d) Problems where two separate surfaces need to be tied together, so no relative motion occurs between the bodies. This is helpful when the user wants to join together two dissimilar meshes.

- e) Coupled-pore fluid-mechanical interaction between two bodies. For example, interfaces between layered soil material at a waste disposal site.

ABAQUS defines the contact conditions between two bodies using a master and slave algorithm. Firstly, the user must make a decision as to which surface should be defined as master or slave. The choice between master and slave surfaces is an important one, and ABAQUS determines the normal stress directions and penetration constraints based on surface type. Some useful guidelines for determining which surface is the master or slave are given below:

- Slave node surfaces must always be attached to deformable bodies.
- Rigid surfaces should always be defined as the master surface.
- When both surfaces are deformable, the master surface represents the interface of the stiffer material. In this case, the pile should be selected as the master and the sand as the slave, unless the pile is socketed into rock then more consideration would be needed.

The two surfaces on either side of the interface form a contact pair. For each of the slave surface nodes, ABAQUS attempts to find the closest master surface node, whose normal vector direction has to pass through the slave node. An interaction model then describes the reaction between the slave and master node.

ABAQUS imposes restraints and relationships onto master and slave surfaces. These conditions are listed below:

- 1) The slave nodes are not permitted to penetrate into the master surface. However, the master surface nodes can penetrate into the slave surface. This is illustrated in Figure 8.3.
- 2) Contact direction is always normal to master surface.
- 3) Only the master surface is used as a surface, where its geometry and orientation are taken into consideration. The data retained from the slave surface is restricted to the slave node locations and the area associated with each node. Hence a slave surface can be defined as a group of nodes.

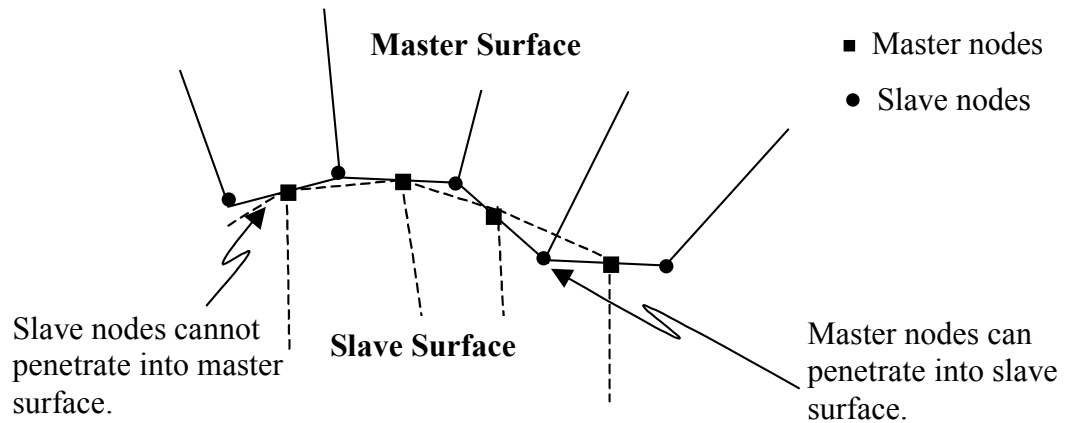


Figure 8.3: Penetration restriction between slave and master surfaces
(Hibbett et al., 2001)

8.2.3.2 Contact Elements

Sometimes it is impossible to use surface-based interactions, and therefore the use of contact elements is imperative. Various examples of real-life applications that would require the use of contact elements are listed below:

- Contact between an external and internal tube.
- Contact in coupled soil mechanics simulations such as seepage of fluid into a back-filled trench. In the above problem the material is no longer continuous at the interface, and the pore fluid in the material flows across and possibly along the material interface.
- Pile-soil interaction.

Where interface contact elements are generated they are created in a similar fashion to normal elements. Additional interaction variables are assigned to the elements properties to govern their behaviour.

8.2.3.3 Models of Interaction

There are several interaction models available in ABAQUS to model the response between surfaces. The type of model chosen depends on the form of interaction required. The following section briefly outlines some of the basic interaction models.

Mechanical Contact Interaction: When surfaces come into contact they transmit both shear and normal stresses across their interface. ABAQUS employs the use of a basic Coulomb friction model to relate the shear stress (τ) to contact pressure (p).

$$\tau = \mu p \quad (8.8)$$

where μ = coefficient of friction.

If the shear stress is less than the critical shear stress then the surfaces are said to stick together. This means there is no relative motion between the contact nodes. However, once the critical shear is achieved slip will occur between the contact nodes at the interface. This is shown graphically below:

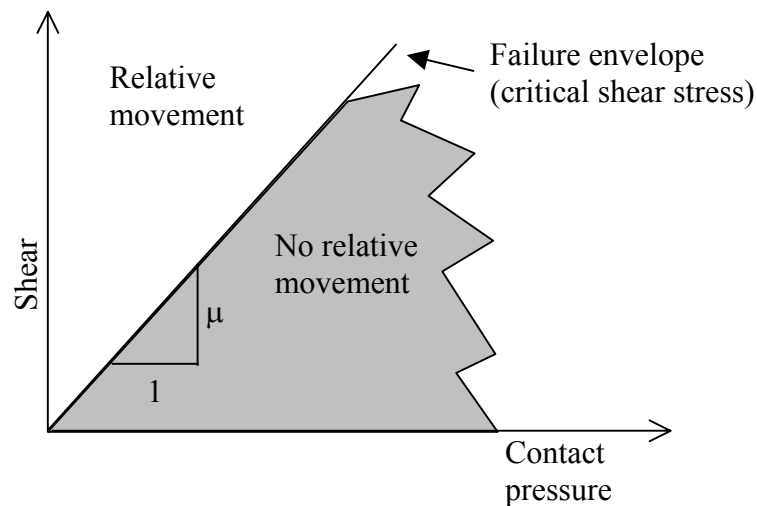


Figure 8.4: Interaction between contact pressure and shear stress at interface surface

Note: the basic Coulomb friction model in ABAQUS assumes the frictional behaviour is isotropic. However, with the use of additional variables ABAQUS can also model anisotropic friction behaviour.

Additional Interaction Models: there are additional interaction models to simulate thermal, pore fluid and coupled analyses. The choice of model depends on the field variables affecting the response between the surfaces. The interaction model chosen

will ultimately lead to whether a surface-based interaction analysis, or contact elements based analysis is needed.

Given the above, it was considered appropriate that a surface-based interaction with mechanical contact be used to represent the interaction at the pile-soil interface. The representation of the pile-soil interface by surface-based contact has many distinct advantages. One such advantage found in the case of lateral and axial uplift loads is that sand is allowed to separate from the pile rather than impose tension forces. For example, lateral loads result in the pile thrusting forward in the direction of the load, and this resulted in a bearing reaction from the sand in front of the pile and separation of the sand at the back of the pile. The typical response under lateral loads occurs when using surface-based contact. If a continuous mesh was adopted the element behind the pile would stretch and then generate tensile stress, pulling the pile back and not give a realistic response.

Therefore, surface-based contact was adopted in the models developed for this research. An example of the relative movement between pile-soil under uplift loads after critical mobilizing shear stress is presented in Figure 8.5.

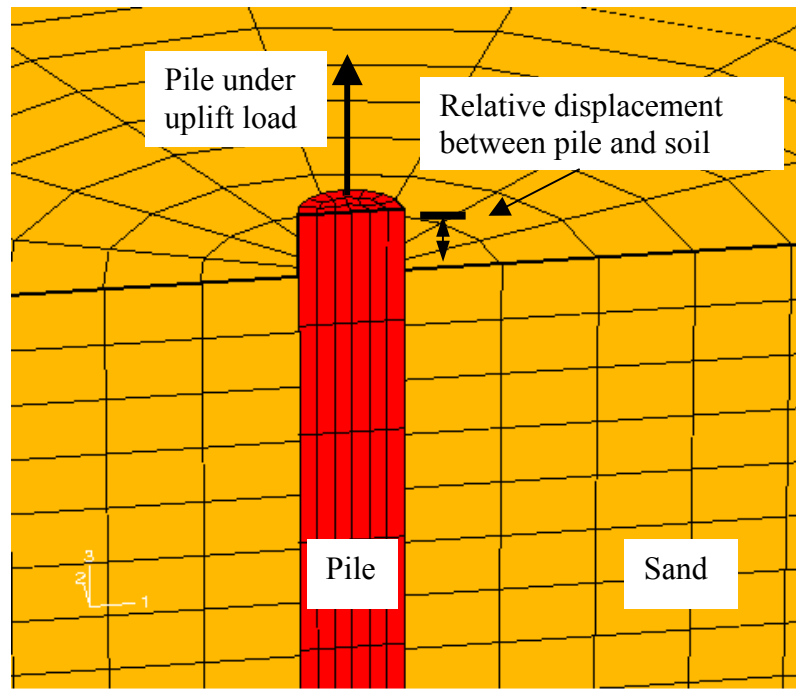


Figure 8.5: Relative movement between pile and soil due to surface-based contact

8.2.4 Initial Stress States

The stress state in the sand-pile before a static or dynamic load is placed on the pile head can have a significant effect on a pile's response under load. The Mohr-Coulomb diagram shown again in Figure 8.6 can be used as an illustrative example of how initial stresses can affect the response of a pile.

The initial stress state causes a shift along the normal stress axis as shown in Figure 8.6. Hence the Mohr-Coulomb failure circle has an increase in radius, and then larger loads are required to induce shear failure within the sand mass.

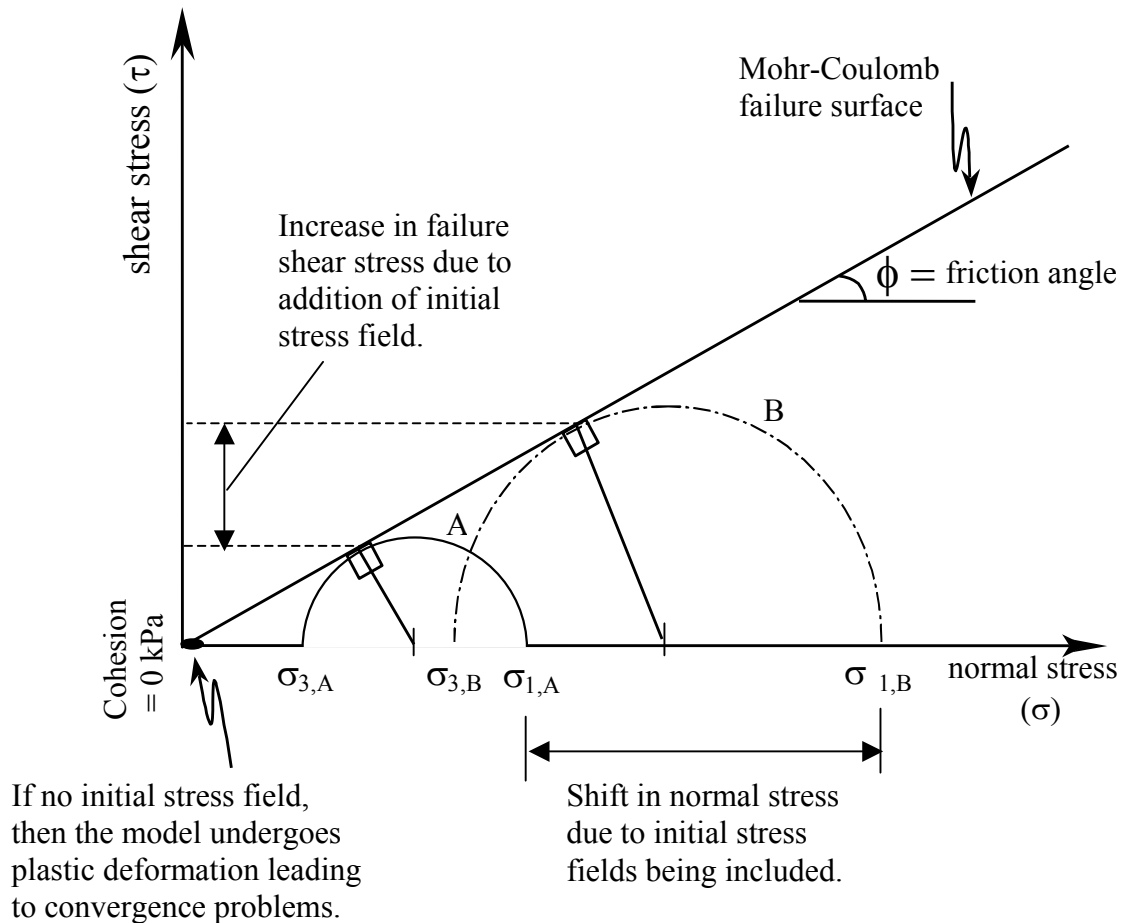


Figure 8.6: Influence of initial stress in Mohr-Coulomb failure criterion

The initial stress state within the sand depends upon many factors. Sand and soil in general is said to have a memory of past events such as preloading, vibration and

compaction. The pile installation technique can also have an impact on the stress field surrounding the pile. In the case of an impact driven pile, the pile is hammered into the ground causing loosening and dilation in the dense sand, and densifying in the case of loose sand. Cast-in-place piles tend to allow some loosening of sand around the bored hole.

The initial stress state for cast-in-place piles modelled in this research generally consist of a normal gravity field from the self-weight of sand and pile. The initial vertical stress in the cast-in-place model is given by:

$$\sigma'_v = \rho gh - u \quad (8.9)$$

where σ'_v = effective vertical stress (it is noted that this work is based on an effective stress analysis).

ρ = density of sand and pile (it is assumed the soil and pile has approximately the same density = 2 t/m³)

g = gravity

h = depth below the ground surface (i.e. in z direction)

u = pore water pressure (the influence of the water table was not investigated as part of this research)

= 0 kPa

An example of an initial vertical stress field for a cast-in-place pile model is shown in Figure 8.7.

For the given effective vertical stress field there is an effective horizontal stress field. The horizontal stress at any depth can be approximated as equal to the vertical stress at the same depth times by the effective earth coefficient (K). For piles constricted in a region where the ground surface is relatively flat the earth coefficient at rest (K_o) may be employed. The inclusion of the horizontal stress field is important, as it is these stresses that resist movement in the horizontal direction. As shown by Das (1999), the effective at rest earth coefficient may be approximated by $K_o = 1 - \sin\phi'$ for bored and cast-in-place piles, or $K_o = 1.8*(1 - \sin\phi')$ for high displacement driven piles.

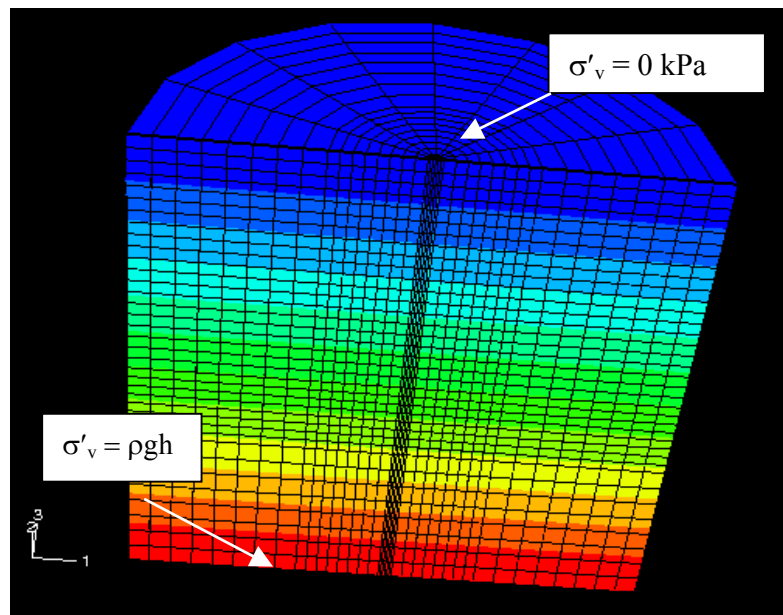


Figure 8.7: Initial stress field due to self weight of system

The initial stress state for an impact driven pile includes a gravity field as for the cast-in-place case, plus a stress field induced by the pile driving. Some researchers have noted that it is difficult to include the driving stresses in numerical models (Lehane and Randolph, 2002). Due to recent developments in numerical modelling packages it is now possible to simulate driving of the pile into soil. However, the variables associated with such a programme would be numerous. For example, the hammer type, drop height, and loading frequency are just a few of the more prominent variables. To obtain generic design charts each of the variables would need to be examined to determine the impact they have on the pile's response.

The additional stresses imposed by driving result in an additional shift along the normal stress axis as shown in Figure 8.6. Unlike the gravitational stress field that increases with depth (i.e. in the z -axis direction), the stress field in the sand surrounding a driven pile tends to radiate away from the pile and hence affect the stress in the x , y , and z axes. For example, the driving stresses are radial along the shaft and transpose into being normal to the pile base (Meyerhof, 1961).

This research will endeavour to explore the trends in load capacity and displacement for cast-in-place and impact driven piles. However, this work will not investigate the driving process or attempt to include the driving stresses. The influence from pile driving can be accounted for by in situ soil properties and is discussed in Chapter 4. The overall trends for the driven piles examined in this document will be based on a model with a gravity stress field, and suitably modified soil characteristics as discussed in Chapter 5.

8.3 Construction of Finite Element Model in ABAQUS

The following section will discuss the finite element ABAQUS model constructed specifically for the purpose of this research.

8.3.1 Problem Geometry and Boundary Conditions

The identification of the line of symmetry in the loading, geometry and material conditions within a problem space allow for modellers to reduce the size of the problem. For example, a circular pile under pure axial loading (compression or tension) can be modelled using axisymmetric elements as shown in Figure 8.8.

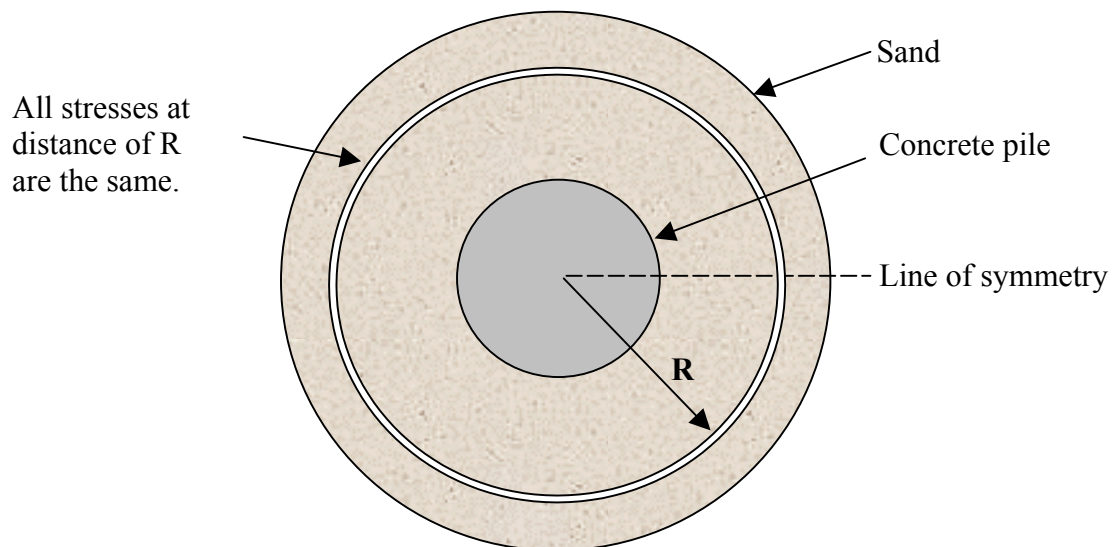


Figure 8.8: Plan view of axially loaded pile showing line of symmetry

In the case of an axially loaded pile the stresses at a radial distance of R (Figure 8.8) are identical for each given line of symmetry rotated through 360° . However, the current work is examining combined loading that has a horizontal component. Therefore, the use of axisymmetric elements will only be applicable in pure axially loaded cases.

For a pile under combined loading one plane of symmetry is available to reduce the problem size as depicted in Figure 8.9. Once the plane of symmetry was identified boundary conditions were used to eliminate one half of the problem size, as shown in Figure 8.10.

Given that displacement normal to the plane of symmetry is zero, forces are equal and opposite in the normal direction to the plane of symmetry, and the displacements parallel to the symmetry are not equal to zero. Then the use of roller supports was deemed appropriate. It was also assumed that the displacement at the outer edge of the model is zero (problem limit). This assumption is reasonable if sufficient distance is provided between the loading area and the outer boundary. As an alternative, infinite elements may be used to help reduce the problem space. It is noted that infinite elements were not used in this research. Yet if reasonable estimation of the outer edge of the model were performed, the two possible boundary conditions (fixed boundary with sufficient distance and elastic boundary with infinite elements) would yield similar results. This is shown in subsequent sections.

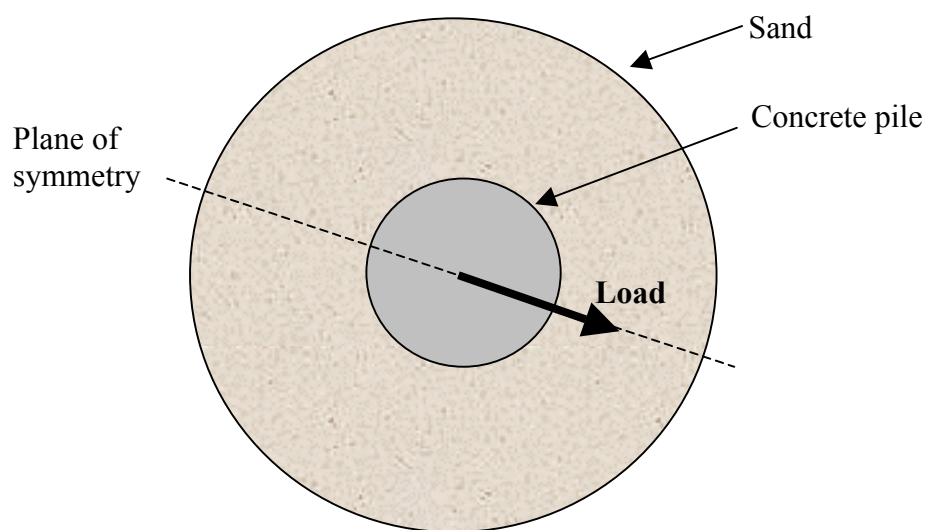


Figure 8.9: Plan view of obliquely loaded circular pile showing plane of symmetry

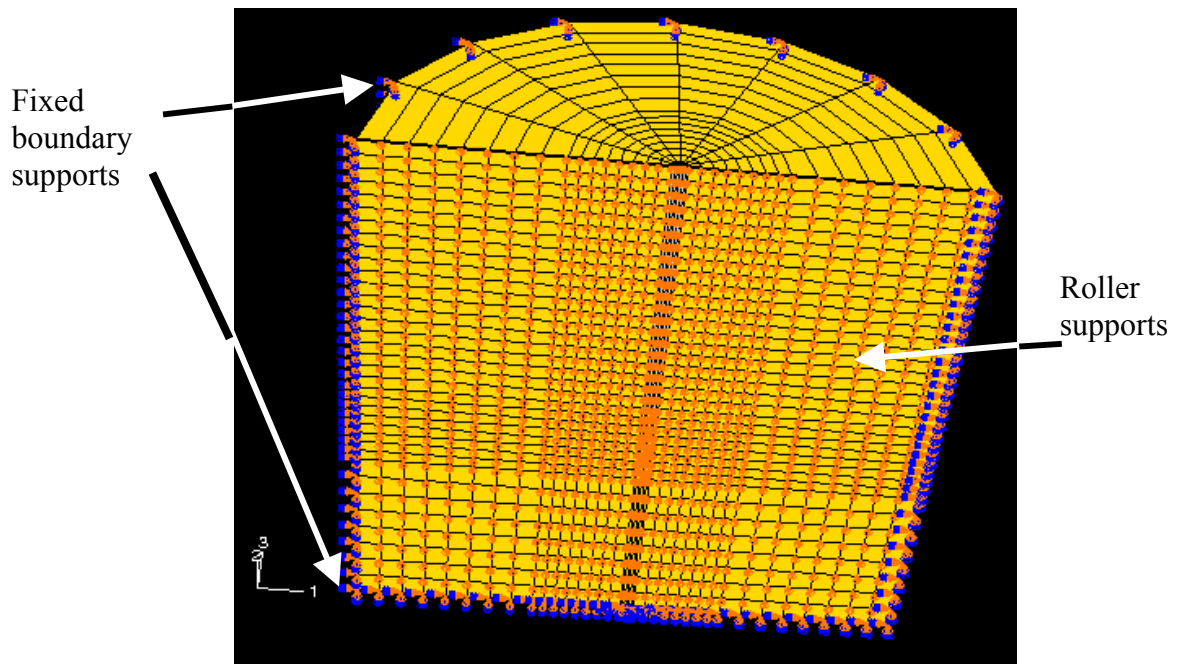


Figure 8.10: Boundary conditions for obliquely loaded pile

Boundary conditions in the plane of symmetry and outer cylindrical surface are also shown in 2-D representation in Figure 8.11.

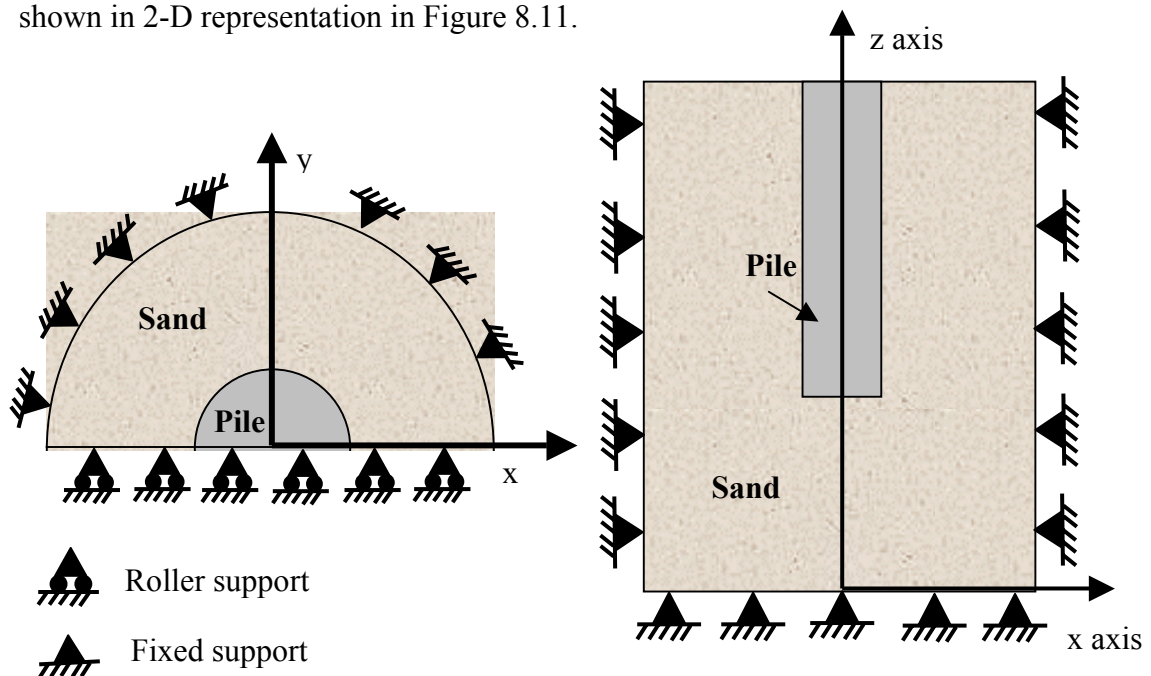


Figure 8.11 (a): Plan view of problem **(b)** Elevation view of pile-soil problem

As well as choosing appropriate boundary conditions, it is important to choose appropriate element types. The simplifications chosen to reduce the problems size have a significant impact on the performance of the model to behave realistically, and give an estimation within a tolerable limit.

8.3.2 Finite Element Pile Mesh

Several models were developed during the course of this research project. The initial models ranged from simple linear elastic two-dimensional models, to intricate linear elastic three-dimensional models with contact surfaces and elasto-plastic constitutive behaviour. Also varying mesh densities and distances from the loading area to the outer edge of the model were explored for sensitivity analysis. Each variation required a new mesh to be prepared from the beginning and constructed again in ABAQUS.

At the commencement of this work no pre-processor (ABAQUS CAE) was available at James Cook University, so each mesh was drawn and constructed initially by hand. More detailed information on the mesh used can be found in Appendix F. The author then prepared the pile input data file in ABAQUS code to achieve the aims of the thesis (Appendix G). The final mesh used is shown in Figure 8.12.

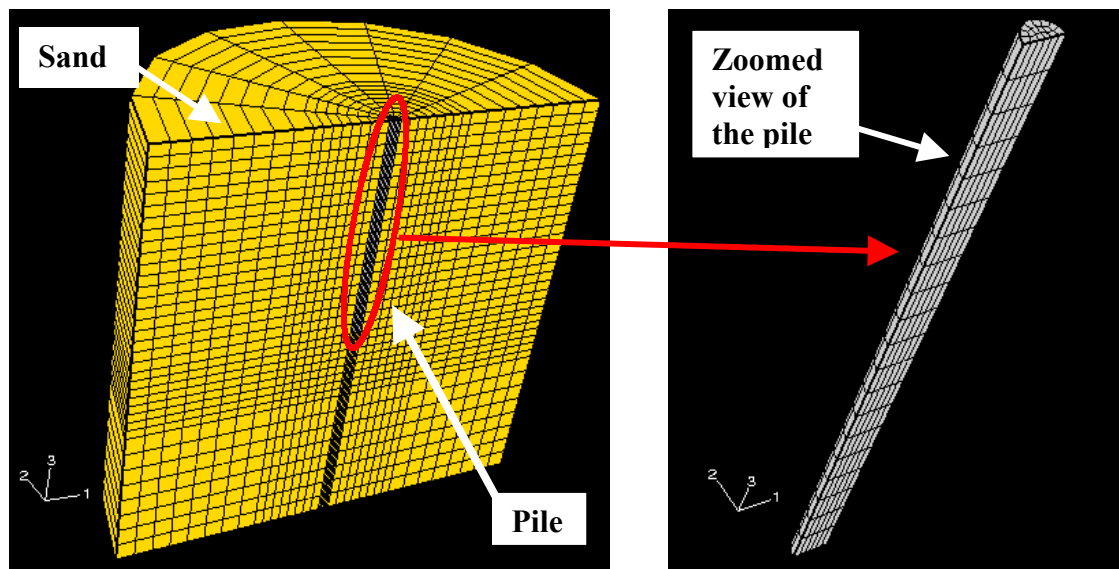


Figure 8.12: Illustrative view of mesh adopted

The final numerical model used in the analysis contained 6917 nodes and 5388 elements.

The general characteristics of each mesh are as follows:

- *Element Type:* the problem was discretized using 3-D finite elements due to the pile shape and load being oblique. Eight noded rectangular prisms were utilised. These rectangular prisms have linear shape functions to approximate the displacement pattern between nodes.
- *Boundary Conditions:* two separate boundary conditions were imposed onto the models. Due to the symmetry, the problem space could be reduced into half of its original size. The nodes at the base of the mesh and far bounds are fixed against all displacements. The nodes on the plane of symmetry are restrained from moving normal to the plane of symmetry, but can move along the plane symmetry (Figure 8.10).
- *Contact Interface:* the interaction at the pile-soil interface was modelled by using surface-based contact as discussed in Section 8.2.3. The co-efficient of friction used for cast-in-place was equal to $\tan \phi$ (i.e. rough) where ϕ is the friction angle of sand in contact with the pile, and for impact driven equal to 0.2 (Das, 1999; Kulhawy, 1984). The interface allows for relative motion between the pile and soil to occur, and in the case of lateral loading the sand can separate from the back of the pile as the interface separates. Then the pile can pull away from the soil. This in turn prohibits tensile stresses from forming behind the pile.
- *Input Data:* the pile and soil properties given in Chapter 4 were used in the numerical analysis. It was assumed that the sand behaved linear elastically until a Mohr-Coulomb plastic failure envelope was reached. Once the stress state at any location reaches the failure surface it will undergo plastic deformation. The constitutive parameters and initial stress state were imposed onto the model before the analysis was started. The initial stress accounted for the in situ stresses due to the self-weight of the system before the load is applied.

As stated previously, some additional adaptations of the mesh were also explored for convergence checking. The results presented in Section 8.4 correspond to two distinct

mesh densities that consisted of 6917 active nodes (medium mesh), and 47829 active nodes (fine mesh).

8.4 Verification of ABAQUS Pile Model

To verify the reliability of the developed FEM pile meshes, the load-deflection response prediction from the numerical models was compared against a number of full-scale pile test data. The test data used was obtained from the electronic deep foundation load test database established by the Federal Highway Administration in U.S.A. [<http://www.fhrc.gov/structur/agids/agids.htm>]. Several individual piles were selected where the sand and pile properties were given. The final cases chosen for verification are shown in the following Sections 8.4.1 to 8.4.2.

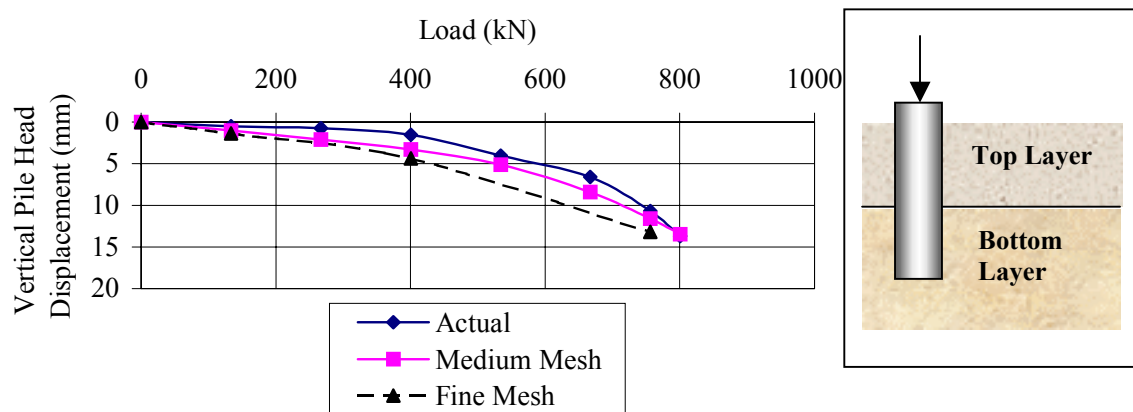
8.4.1 Predictions for Cast-In-Place Piles

To help verify the performance of the cast-in-place pile model results, these were compared against several actual cast-in-place pile results obtained from the Federal Highway Administration database. It is noted that the pile cases available on the database tended to be axial compression cases with one uplift case. To aid in the verification of lateral load cases, a 0.5 m long concrete pile was cast as part of this research and placed under lateral load. The final cast-in-place cases shown in this section include:

- 2 axial compressive loading cases obtained from the Federal Highway Administration database.
- 1 axial uplift loading case obtained from the Federal Highway Administration database.
- 1 lateral loading case that was conducted as part of this research at James Cook University. It is noted that the lateral pile tested was prefabricated before placement into the experimental tank. The sand was placed loosely into the tank (assumed to be $D_r \approx 0\%$), and the pile was placed by excavating the sand and putting the pile into the hole, and then replacing the sand loosely back around the pile. Therefore, it is anticipated that the soil properties can be obtained using correlations for the cast-in-place scenario, except that the co-

efficient of friction at the soil-pile interface will be taken as the driven pile scenario. This is due to the experimental pile being prefabricated and hence the pile had a relatively smooth surface. It is also noted that the horizontal load was placed on the pile at a distance of approximately 300 mm above the sand surface. The finite element pile model developed by the author was extended above the sand to simulate the experimental case as close as possible.

The results of the cast-in-place verification models are shown in the Figures 8.13 to 8.16. The full version of each case including the raw data used to predict the soil properties is given in Appendix H.



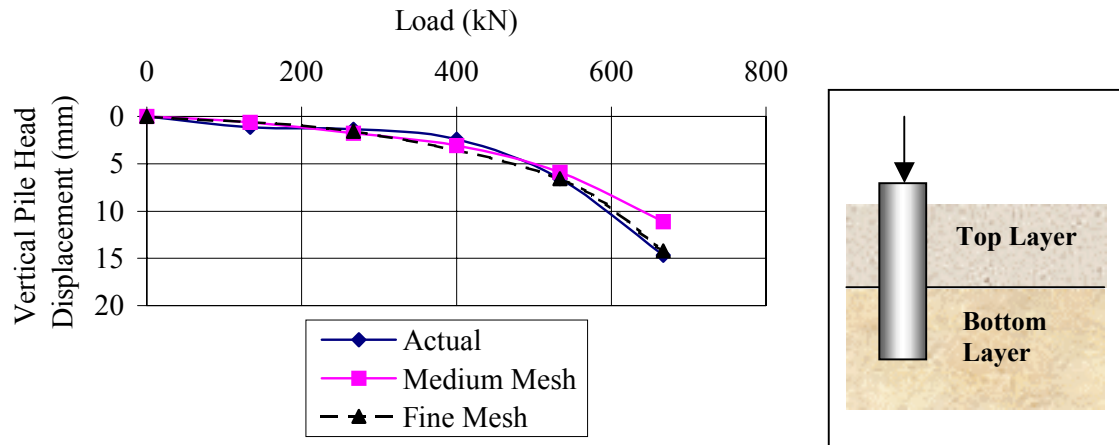
Circular Pile Characteristics

Length (m)	8.53
Diameter (m)	0.406
Area (m ²)	0.129
E (MPa)	30

Soil Characteristics

Homogenous Top Layer		Homogenous Bottom Layer	
E (MPa)	24.5	E (MPa)	65.2
ϕ'	41	ϕ'	50
c (kPa)	2	c (kPa)	0.1
Height (m)	9.6	Height (m)	7.46
N(average)	19	N(average)	71
Dilation ψ	8	Dilation ψ	17
K_o	0.3	K_o	0.2

Figure 8.13: Case study 1 - large scale, cast-in-place, axial compression loading



Circular Pile Characteristics

Length (m)	7.32
Diameter (m)	0.457
Area (m ²)	0.164
E (MPa)	30

Soil Characteristics

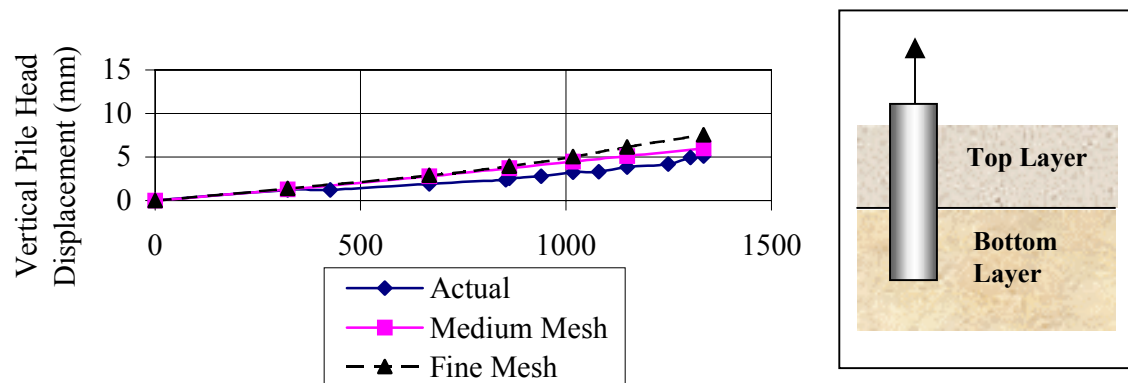
Homogenous Top Layer

E (MPa)	28.8
ϕ'	43
c (kPa)	0.1
Height (m)	10.67
N(average)	24
Dilation ψ	10
K_o	0.3

Homogenous Bottom Layer

E (MPa)	61.3
ϕ'	50
c (kPa)	0.1
Height (m)	3.97
N(average)	66
Dilation ψ	17
K_o	0.2

Figure 8.14: Case study 2 - large scale, cast-in-place, axial compression loading



Circular Pile Characteristics

Length (m)	13.72
Diameter (m)	0.610
Area (m ²)	0.292
E (MPa)	30

Soil Characteristics

Homogenous Top Layer

E (MPa)	32.1
ϕ'	43
c (kPa)	0.1
Height (m)	15.85
N(average)	29
Dilation ψ	10
K_o	0.3

Homogenous Bottom Layer

E (MPa)	88
ϕ'	50
c (kPa)	0.1
Height (m)	11.59
N(average)	100
Dilation ψ	17
K_o	0.2

Figure 8.15: Case study 3 - large scale, cast-in-place, axial uplift loading

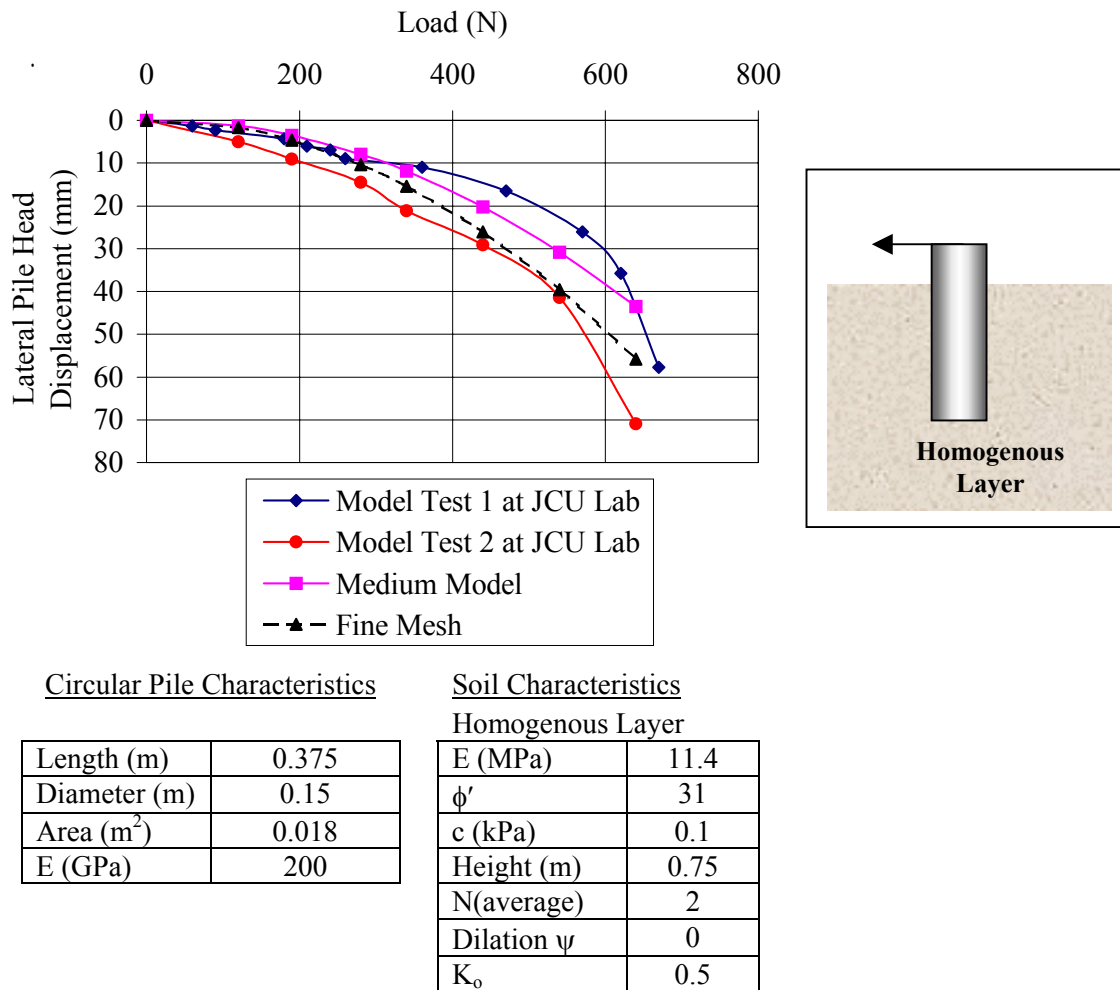
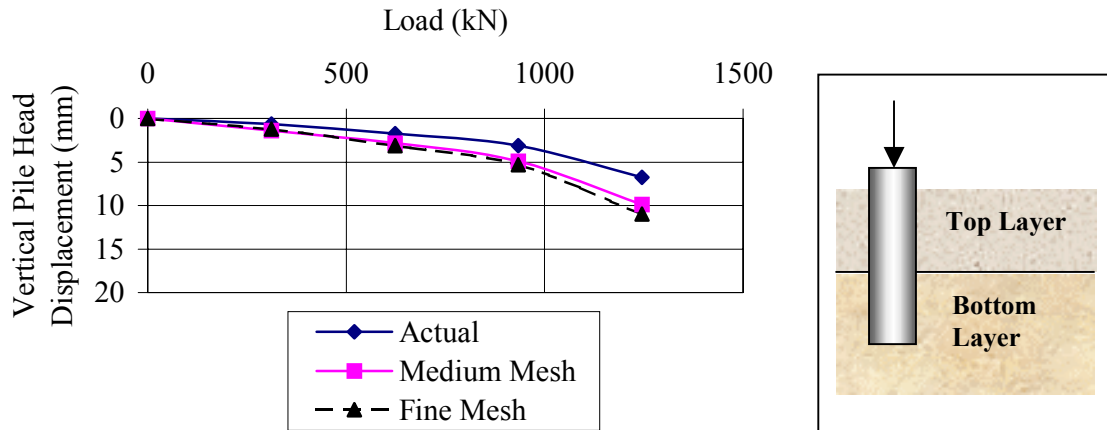


Figure 8.16: Case study 4 - smaller scale, placed in tank, lateral loading

8.4.2 Predictions for Impact Driven Piles

To help verify the performance of the driven pile model it was compared against a limited number of available results obtained from the Federal Highway Administration database, and Hage-Chehade et al. (1991). It is noted that the pile cases available on the database were mostly piles with square cross-sections under axial compression loading. Given the limited available data, the results from the axial and lateral loading cases in the parametric study for the design charts in Chapter 9 were compared against results from existing techniques. These additional verification checks are also discussed in Chapter 9. The final driven cases shown in this section includes two axial compressive loading cases obtained from the database, and one lateral case obtained from Hage-Chehade et al. (1991). The results from the axial compression driven verification models are shown in the Figures 8.17 to 8.18.



Circular Pile Characteristics

Length (m)	14.81
Diameter (m)	0.305
Area (m ²)	0.073
E (GPa)	30

Soil Characteristics

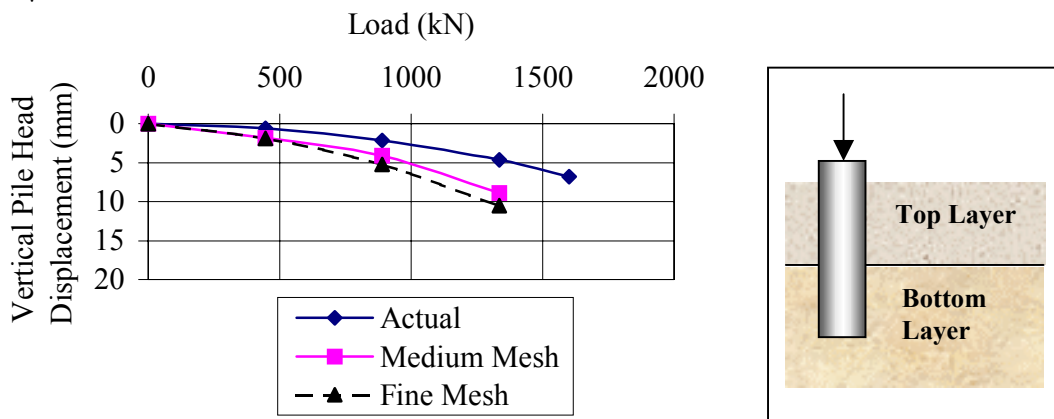
Homogenous Top Layer

E (MPa)	62.9
ϕ'	40
c (kPa)	0.1
Height (m)	15.85
N(average)	24
Dilation ψ	7
K_o	0.6

Homogenous Bottom Layer

E (MPa)	92.8
ϕ'	45
c (kPa)	1
Height (m)	13.77
N(average)	54
Dilation ψ	10
K_o	0.3

Figure 8.17: Case study 5 - large scale, impact driven, compression loading



Circular Pile Characteristics

Length (m)	12.46
Diameter (m)	0.406
Area (m ²)	0.130
E (GPa)	30

Soil Characteristics

Homogenous Top Layer

E (MPa)	74.8
ϕ'	46
c (kPa)	0.1
Height (m)	10.67
N(average)	36
Dilation ψ	13
K_o	0.5

Homogenous Bottom Layer

E (MPa)	89.9
ϕ'	47
c (kPa)	0.1
Height (m)	14.25
N(average)	51
Dilation ψ	14
K_o	0.5

Figure 8.18: Case study 6 - large scale, impact driven, compression loading

The lateral case obtained from Hage-Chehade et al. (1991) is an impact driven, square cross-section pile. From modelling Hage-Chehade et al. (1991) found that a circular pile model with equivalent cross sectional area gave similar results to the square mesh model. For the purposes of verification, the output from the model developed in this work will be compared against the circular numerical model and experimental results given by Hage-Chehade et al. (1991). The pile deflection versus pile depth for 10 kN and 20 kN static lateral loads is shown in Figure 8.19.

It is noted that the experimental pile test conducted by Hage-Chehade et al. (1991) was in an area where the pile and soil were submerged in water (i.e. had an elevated water table). Therefore, for this case an effective stress analysis taking into account pore pressure was conducted (Equation 8.9). Also the material properties such as Young's modulus were given directly by Hage-Chehade et al. (1991), and are not based on SPT correlations used in previous verification cases.

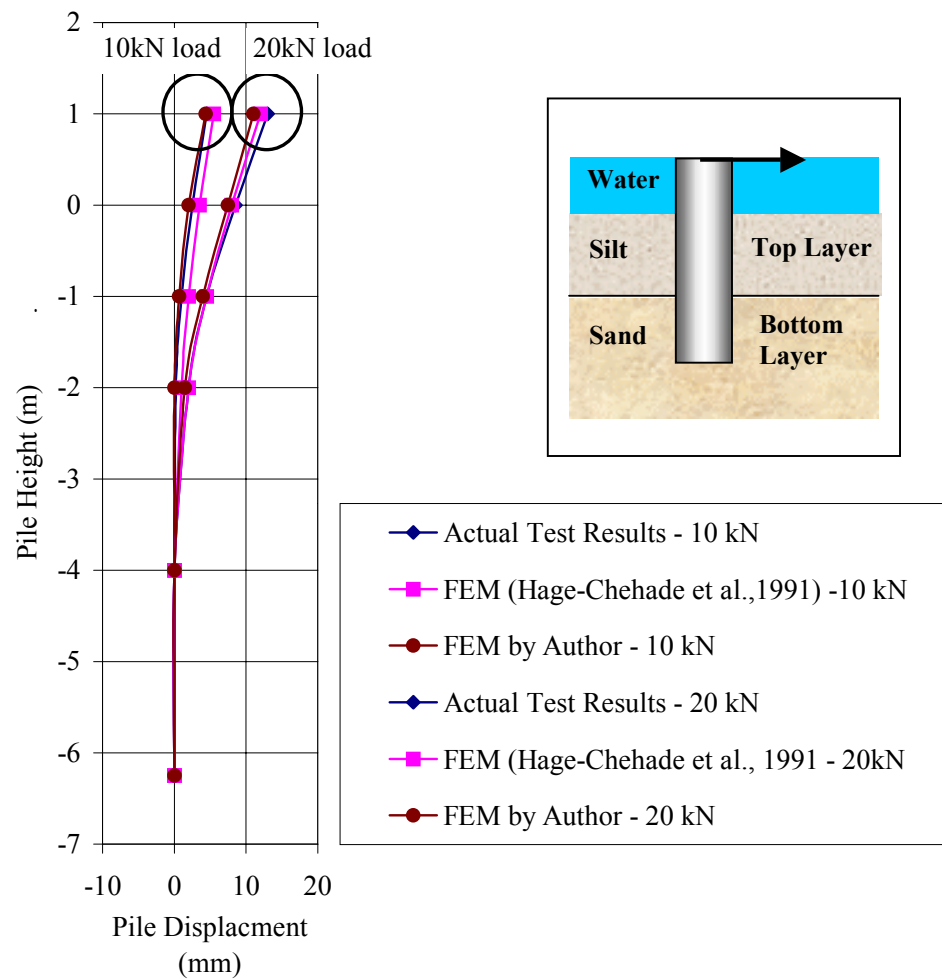
Figure 8.19 shows close agreement between the model outputs and experimental results, indicating that the basic model structure is performing adequately.

8.4.3 Discussion of Verification Results

In the case of geotechnical predictions the level of accuracy is never exact due to the non-homogeneity of soil, and the constitutive relationships used to approximate the behaviour. Therefore, the reliability and accuracy of the prediction method varies from model to model. A preliminary study of the accuracy and reliability of common models used to predict the displacement of shallow foundations was done by the author (Sivakugan and Johnson, 2002).

This research showed in the case of less complicated shallow foundation prediction, the accuracy and reliability is variable and can be represented statistically by a skewed left beta distribution. Then it is anticipated the variance and performance of the pile prediction techniques, including the numerical model developed in this study, may be subjected to similar variances. The elasto-plastic pile numerical models have one distinct advantage over other settlement and bearing capacity techniques for predicting

pile behaviour. The advantage being that they can be used to portray the relationship between load and displacement, enabling trends and design charts to be estimated.



Circular Pile Characteristics

Length (m)	7.25
Diameter (m)	0.284
EI (MNm ²)	30

Soil Characteristics

Homogenous Top Layer

E (MPa)	15
ϕ'	38
c (kPa)	0.1
Height (m)	4
Dilation ψ	5
K_o	0.4

Homogenous Bottom Layer

E (MPa)	15
ϕ'	40
c (kPa)	0.1
Height (m)	5
Dilation ψ	7
K_o	0.4

Figure 8.19: Case study 7 - large scale, impact driven, lateral loading
(Hage-Chehade et al.,1991)

The ultimate bearing capacity was defined as the approximate point where the pile no longer undergoes predominately elastic strains, but rather the plastic failure zone governs the response, i.e. irrecoverable strain and failure occurring. The ultimate bearing capacities and linear elastic displacement response for piles were defined, as shown in Figure 8.20. The ultimate bearing capacity can be estimated by extending the straight line through the elastic region of the load-displacement curve, so that it intersects a straight line extending back from the plastic region of the curve. The corresponding load at the intersection point is defined as the ultimate capacity of the pile. It is noted that the straight line extending through the elastic region of the curve is referred to as the linear elastic displacement response, and only represents the displacement response in the elastic region of the curve. It is often assumed by researchers such as Craig, (1992) that the elastic region extends from zero load to approximately 1/3 of the ultimate load (Figure 8.20).

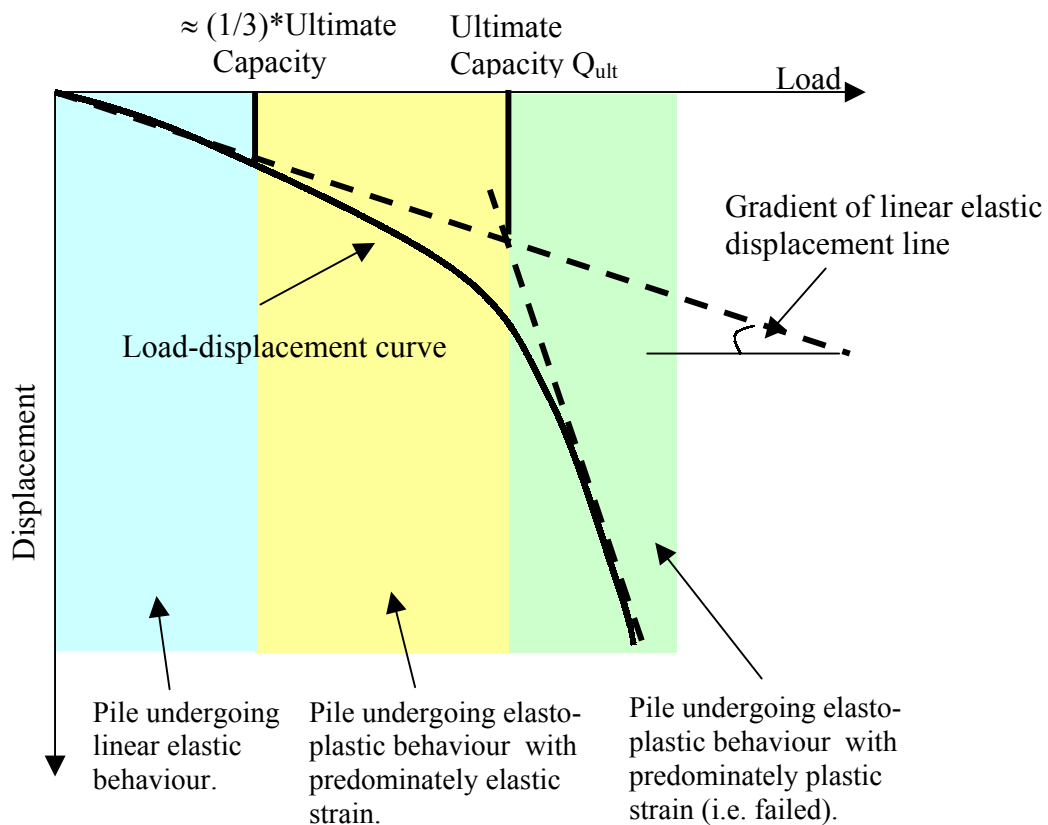


Figure 8.20: Load-displacement curve for a typical pile

The loads at a particular displacement magnitude and displacement gradients for the verification cases in Sections 8.4.1 to 8.4.2 are shown in Table 8.1, along with the

accuracy between the actual and numerical model results for the medium mesh. It is noted that the load test data generally did not extend to the ultimate capacity. Hence the load with the largest difference between the model prediction and actual data at a particular pile head displacement was used for purposes of comparison. As stated previously, additional checks were performed between existing techniques for estimating ultimate capacity and the model results given in Chapter 9.

Table 8.1 shows the accuracy of the developed model when predicting the ultimate capacity of the pile, which tended to be in the range of 0.8 – 1.4 with an average of 1.27. The accuracy for the predicted displacement gradient of the pile was typically in the range of 0.79 – 2.95 with an average value of 1.61. This indicates that the numerical model tends to be more on the conservative side based on the limited parametric verification study.

The relative error from the limited number of available verification cases in the database shows that the accuracy for the load estimates and displacement gradient is typically 0.79 to 2.95. Also, the maximum difference in linear elastic settlement between the actual and predicted data is less than 5 mm. From a statistical study on settlements of shallow foundations by the author (Johnson, 1999), the settlement ratio (predicted settlement/actual settlement) generally lied within the bounds of 0.7 to 3.5. The load ratio (actual loads/predicted loads) generally lied within the bounds of 0.53 to 3.87, as in Chapter 5. The error in the numerical model developed as part of this research lies within the bounds observed in shallow foundations. Given the complexity of deep foundations, pile foundations would have a higher error range than noted in shallow foundations. From these observations, it was considered that the numerical model developed for this work is performing within tolerable bounds and is adequate.

Table 8.1: Case study results.

Case No.	Description	Load (kN) - units in kN unless marked otherwise				Linear Elastic Displacement Gradient (mm/kN)		
		Comment	Actual	Predicted	Accuracy ³	Actual	Predicted	Accuracy ⁴
1	CIP ¹ Compression	Loads correspond to a pile head displacement of 7.5 mm.	700	650	1.08	0.004	0.008	2
2	CIP ¹ Compression	Loads correspond to a pile head displacement of 5 mm.	500	500	1.00	0.0051	0.0048	0.93
		Loads correspond to a pile head displacement of 10 mm.	650	700	0.93			
3	CIP ¹ Uplift	Loads correspond to a pile head displacement of 3 mm.	940	667	1.4	0.0029	0.004	1.4
4	CIP ¹ Lateral	Loads correspond to a pile head displacement of 25 mm.	Predicted ± 100 N ⁵	500 N	1.0 ± 0.2 ⁶	0.022 ⁵	0.017	0.79 ⁶
5	ID ² Compression	Loads correspond to a pile head displacement of 5 mm.	1110	935	1.19	0.0028	0.0045	1.6
6	ID ² Compression	Loads correspond to a pile head displacement of 5 mm.	1300	1000	1.3	0.0013	0.004	2.95

1. CIP = cast-in-place pile.

2. ID = impact driven pile.

3. Accuracy for load estimate = actual/predicted (if > 1 predicted is conservative).
4. Accuracy for displacement = predicted/actual (if > 1 predicted is conservative).
5. Load and displacement gradient chosen represents the range or average value of the two smaller-scale test cases.
6. Scaling effect due to smaller scale modelling may have resulted in this larger variation.

The model based on the verification plots was considered to be acceptable, given the range of the displacement gradient in the linear range was less than 5 mm.

It was concluded that the mesh with a node number of 6917 is sufficient for the purpose of this research, based on the verification cases. It is noted that some variation did occur between the results especially after yielding had occurred in the soil mass. Also the far boundary (i.e. fixed boundary) located at a vertical and horizontal distance of L (L = length of the pile) away from the outer edge of the pile was deemed to be adequate based on the works by Meyerhof (1961). Meyerhof indicates that the influence zone is approximately 2-5 times the diameter surrounding the pile when the pile is driven into the sand. The loads to drive the pile result in the bearing capacity of the sand to be exceeded and excessively high pile displacements occur. It was assumed that the influence zone around a driven pile is likely to be significantly higher than those under static load. After some thought, it was considered that the current mesh is adequate for cases where the pile length is greater than 3 times the diameter of the pile. Maharaj (2003) also found for laterally loaded piles that distances to the fixed boundary of at least $3/4 L$ below the base of the pile and a horizontal distance L from the side of pile were adequate for modelling purposes. The work in this document supports Maharaj's (2003) conclusions regarding these distances to the fixed boundaries on the outer edge of the model. This influence zone may be greater while pile driving is occurring and the pile is pushed a large distance into the ground.

CHAPTER 9: Oblique Interaction Charts for Piles

9.1 General

The main objective of this research was to explore the influence of load combinations on the pile load carrying capacity and displacement. As shown in Chapter 8, an ABAQUS model has been developed to investigate the pile response under combined loading.

Non-dimensional approaches showing trends of the pile behaviour under various loading scenarios can provide a good platform for comparison, and allow design charts to be developed. It is necessary that the methods can be used on a broad scale when formulating design charts or figures. Therefore, the numerical model cases chosen to produce the non-dimensional design charts as part of this research needed some careful consideration. For instance, pile and soil properties that impact on the pile-soil reaction need to be varied, to explore sensitivity of the developed design techniques.

This chapter presents a set of hypothetical numerical cases used to develop the non-dimensional pile design charts. It also discusses the final results from the numerical analysis and shows the apparent trends observed.

9.2 Numerical Model Cases

The following factors affect the pile response under loading, as shown in Chapters 4 ,6 and 8.

- Length to diameter ratio (L/d) of the pile;
- Young's modulus of the pile (E_p) and soil (E_s);
- Friction angle of the sand (ϕ);
- Dilation of the sand (ψ);
- Initial effective stress before loading; and,
- Technique used to install the pile.

The model cases chosen need to explore and incorporate the sensitivity of each of the above characteristics. The final cases selected for the purpose of this work are given in Figure 9.1.

Sand properties such as friction angle, dilation angle, and Young's modulus can be approximated directly or indirectly from the standard penetration blow count (N) of the sand (Chapter 4). The correlations used for the sand properties also depend on the pile installation method. Blow counts of $N=5$ and $N=30$ were chosen as they represent the lower and upper density ranges for sand (Figure 9.1), as given by Alpan (1967). The pile installation methods explored were limited to two popular techniques, cast-in-place and impact driven.

The length to diameter ratio (L/d) was set to 3 and 10 (Figure 9.1). In the field L/d can be significantly higher. However, as the L/d ratio increases so does the likelihood that the pile will act as a slender element. This means that piles with a large L/d ratio may tend to have the maximum design governed by pile crushing or bending strength, rather than the ultimate soil capacity. The pile response due to the soil failure mechanisms was also investigated as part of this research. It was assumed the pile acted elastically and the ultimate failure of the system is due to the sand reaching a plastic strain state. Piles with $L/d=3$ (rigid pile) and $L/d=10$ (rigid-intermediate pile) were chosen for this work, as it is anticipated that piles with L/d ratios less than 10 will fail due to sand characteristics rather than the pile strength. It is anticipated that the charts developed may be used with caution for higher L/d ratios provided the ultimate strength of the pile is not exceeded. If a detailed analysis is required for the pile, a concrete cracking model and reinforcement bars will need to be added to the model in this thesis.

The diameter chosen for the purposes of this work was 0.6 m. This means the pile size was in the range of typical pile sizes used for cast-in-place and impact driven piles. It was assumed that smaller and larger pile sizes would exhibit similar trends to those observed for the 0.6 m diameter pile.

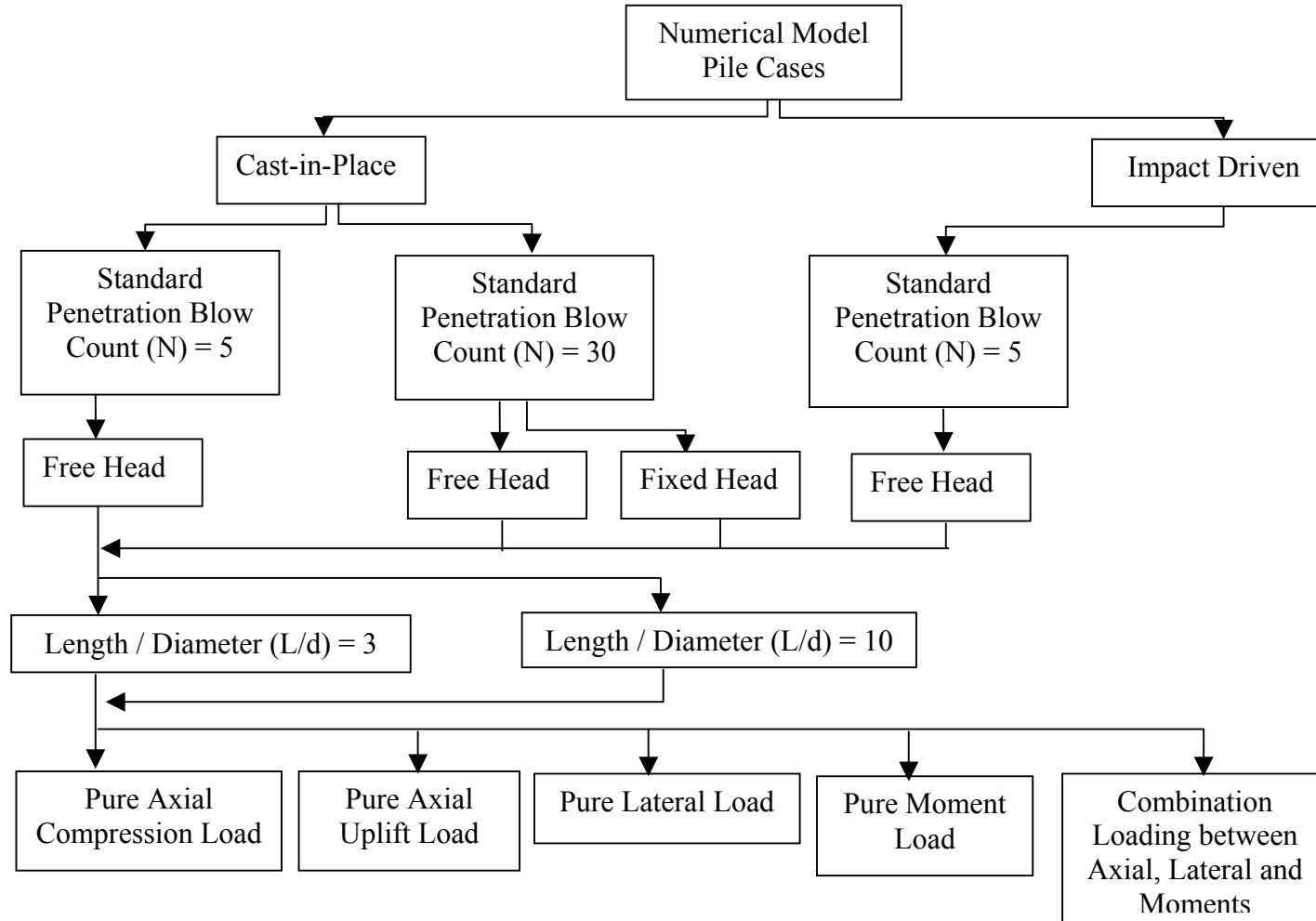


Figure 9.1: The chosen hypothetical numerical modelling cases

Also note that the fixity of the pile head can have a significant effect on the lateral capacity of the pile. The work in this chapter deals with free and fixed head piles that are allowed to translate into three dimensional space. In the case of free head piles, the nodes on the top of the pile can have different displacements in the horizontal and vertical directions (i.e. the pile head can rotate). It was found that the fixed head pile does not allow the top of the pile to rotate, so that all areas on the pile head move by the same amount in three dimensional space. Examples of free head and fixed head piles are shown in Figure 9.2.

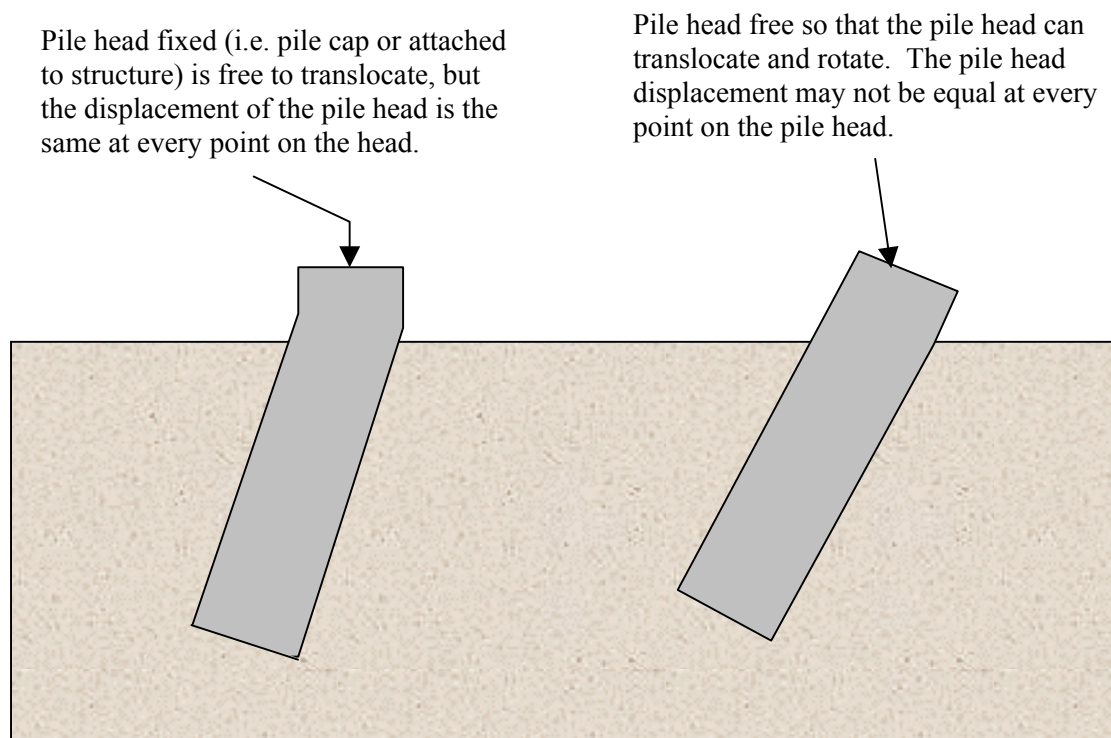


Figure 9.2: Example of pile head fixity

The loading combinations chosen explored forces and moments acting simultaneously. These combinations were basically separated into two broad categories - uplift load combination and compression load combination. Examples of these two loading combinations are given in Figure 9.3 (a) and (b).

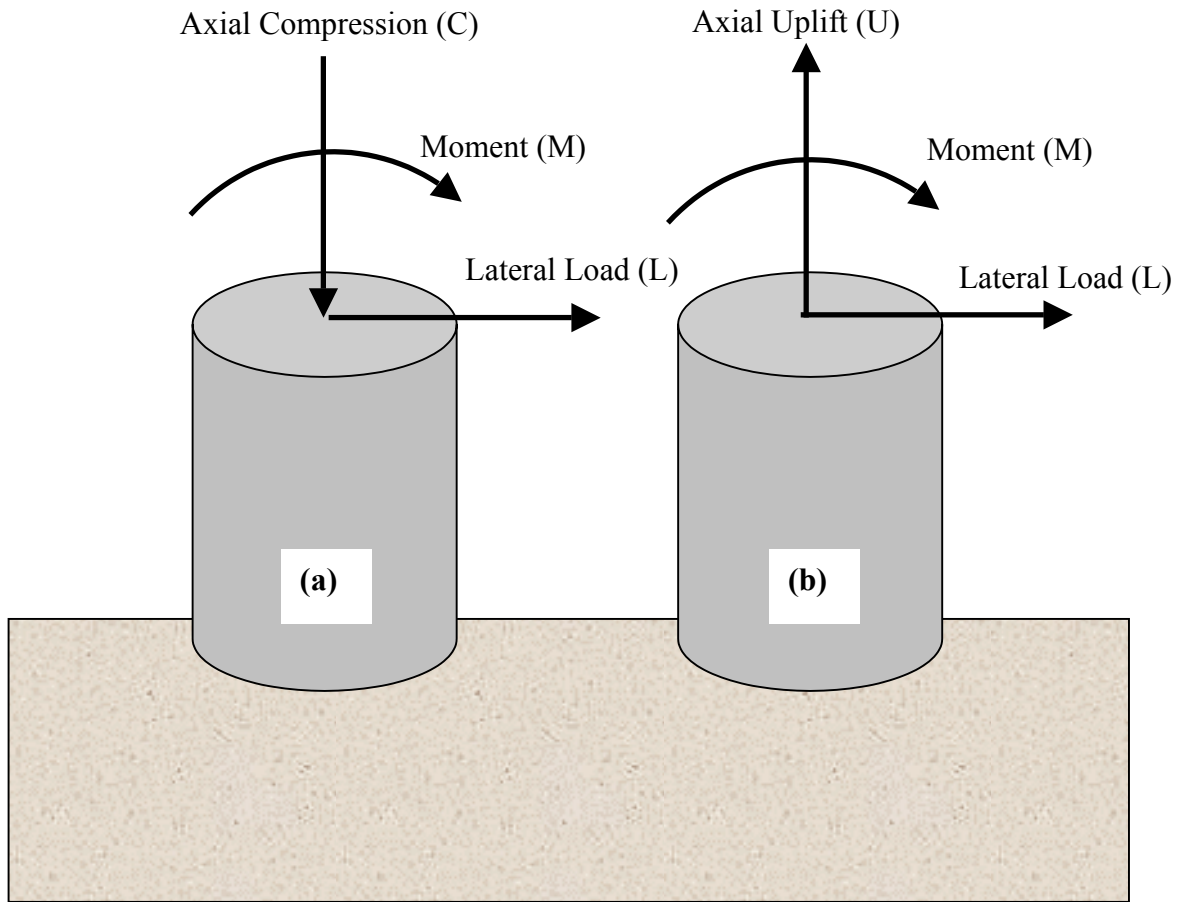


Figure 9.3: (a) Compression load combination
(b) Uplift load combination

The linear elastic response of each model was approximated by extending the linear line through the initial section of the load-displacement curve, assuming little to no plastic strains had occurred. This was done to investigate the influence of load combinations on the horizontal and vertical displacement components. Current theory assumes the displacement response of a pile is linear, when the applied load on the pile is approximately equal to or less than the ultimate load divided by 3. An example of a typical pile response under loads is shown in Figure 9.4.

The net reduction and increase in the gradient of the load-displacement curves in the linear elastic range was explored using the linear elastic ABAQUS pile simulations. Each of the ABAQUS cases given in Figure 9.1 (flow chart) were solved using elasto-

plastic soil properties to obtain the ultimate load of the pile, and linear elastic displacement of the pile head approximated from the first section of each curve.

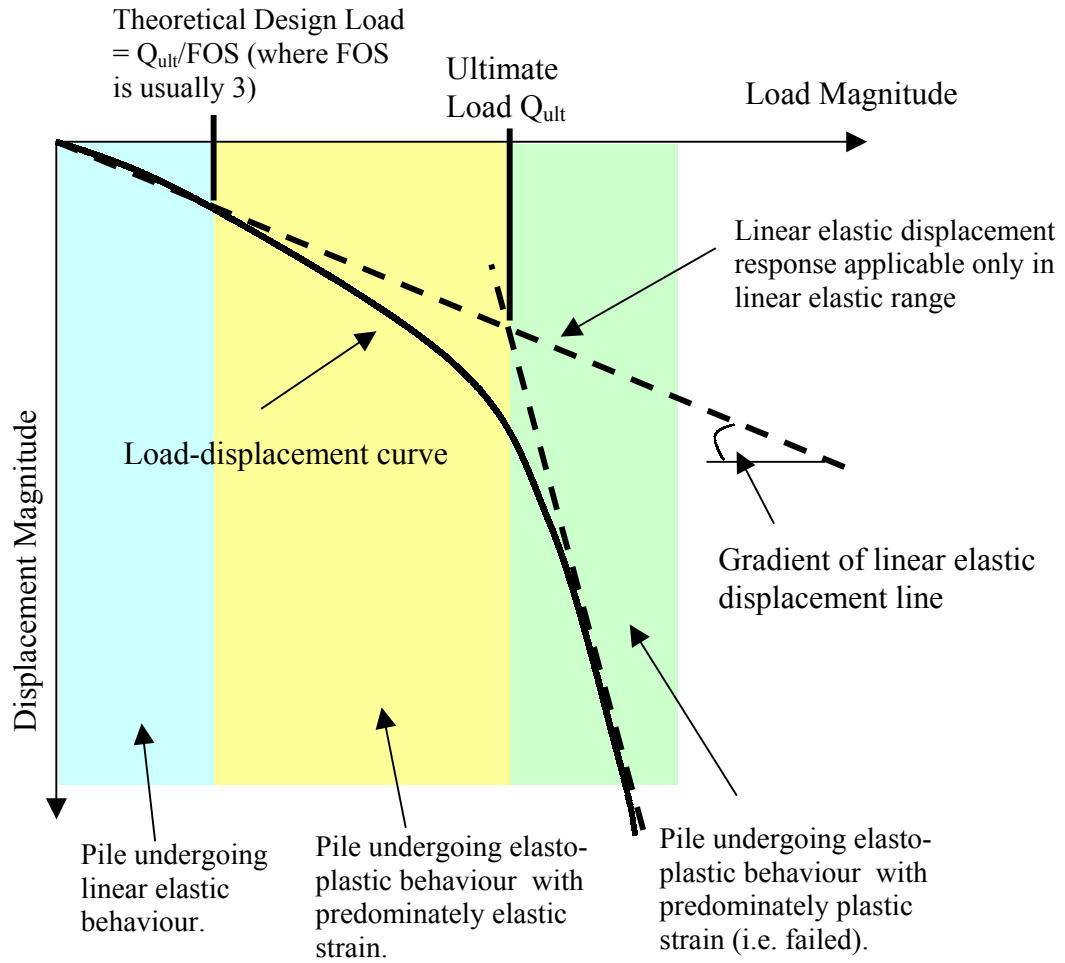


Figure 9.4: Typical pile response

The overall failure of the system was based on all the loads, which in the case of combined loading can result in displacements in all three dimensional space. As part of this work, a method had to be chosen to produce a plot similar to the pile response (Figure 9.4) that can take into account both forces and moments. Then it was decided by this author to represent the force and moment combinations by using a single load ratio defined as:

$$\text{Load ratio} = \sqrt{\left(\frac{A}{A_{ult}}\right)^2 + \left(\frac{L}{L_{ult}}\right)^2 + \left(\frac{M}{M_{ult}}\right)^2} \quad (9.1)$$

A = ultimate axial uplift (U) or compression (C) load at failure

L = ultimate lateral load at failure

M = ultimate moment at failure

A_{ult} = ultimate axial uplift (U) or compression (C) load due to the pile being subjected to pure axial loads

L_{ult} = ultimate lateral load due to the pile being subjected only to lateral loading

M_{ult} = ultimate moment due to the pile being subjected only to moment loading

The displacement magnitude can be defined as:

$$\text{Displacement magnitude} = \sqrt{u_x^2 + u_y^2 + u_z^2} \quad (9.2)$$

where: u_x = displacement of the centre of the pile head in x-direction

u_y = displacement of the centre of the pile head in y-direction

$= 0 \text{ mm}$

u_z = displacement of the centre of the pile head in z-direction

Each of the individual components in the load ratio equation (e.g. L/L_{ult}) basically represents the fraction of either the axial, lateral or moment load due to the loading combination. For example, if $L/L_{ult} = 0.6$ then the lateral component of the combination load resulting in failure of the pile and soil system is approximately 60% of the ultimate lateral load the pile can withstand, if no other load types are present. The load ratio defined by Equation 9.1 is graphically shown in Figure 9.5.

The load ratio represents the combination of up to three separate loads acting together, which can be plotted against the displacement magnitude (Equation 9.2) of the pile head. The resulting curve is similar in form to that shown in Figure 9.4, except that the load magnitude is replaced by the single load ratio.

To illustrate the process an example case is presented below. The example case chosen is Case 18 of the numerical models presented in Appendix I.

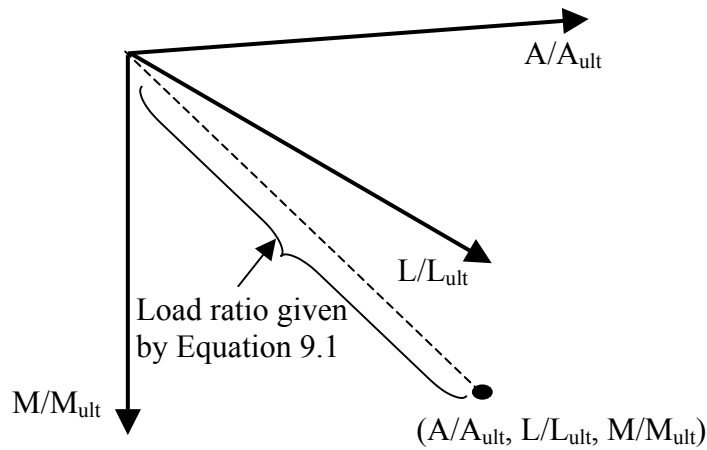


Figure 9.5: Graphical representation of load ratio

Case 18 is a 1.8 m long cast-in-place pier with a 0.6 m diameter and the sand has a blow count of $N=5$. Before determining the ultimate combination load that this hypothetical pile can handle, the pure ultimate axial uplift load, lateral load and moment have first to be determined. To achieve this a load-displacement curve was constructed for each of the pure loading cases as shown in the example of Figure 9.6. For Case 18 the pure ultimate axial uplift = 14 kN, ultimate lateral capacity = 20 kN, and the ultimate moment capacity = 35 kN.

Once the pure ultimate loads are known then the combination load may then be applied to the pier. A series of combination loads with increasing magnitude were placed on the pier and the resulting pile head displacement was numerically determined.

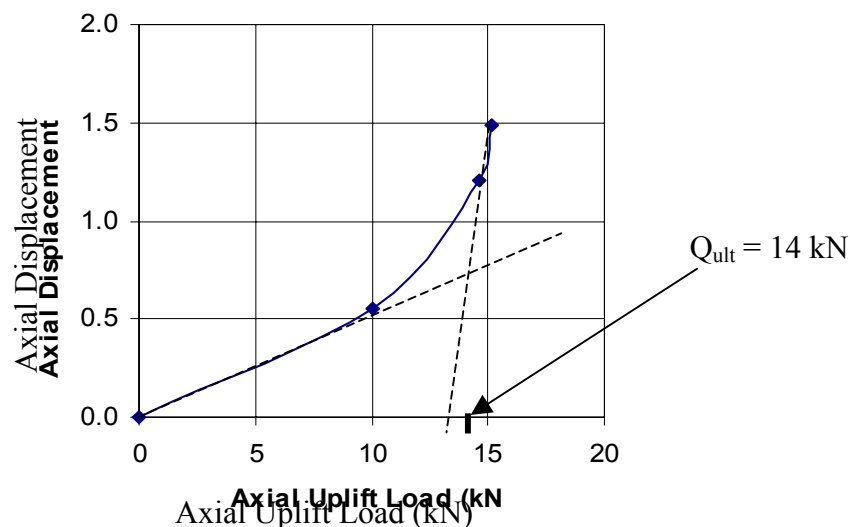
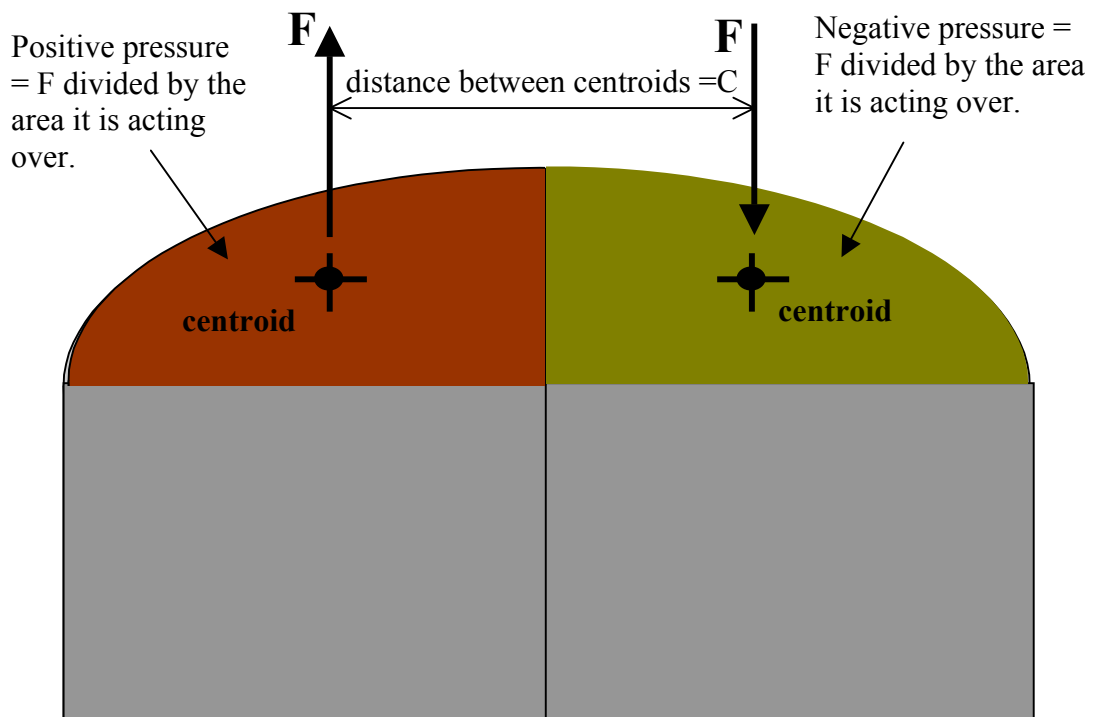


Figure 9.6: Example of load-displacement curve for pure axial uplift of case pile

The final load ratio-displacement curve for example Case 18 is shown in Figure 9.8 along with all the model data. It is noted that the moment was applied to the pile by using a couple force. The nodes on the model pile head were divided into two regions as shown in Figure 9.7. The applied moment was converted into a couple force with a magnitude as shown in Diagram 9.7. This force was then converted to a positive and negative pressure across the nodes to create the moment needed (using the tributary area of the nodes).

The failure point may be obtained by extending a linear line from the elastic region to cross over a linear line extended back through the elasto-plastic region (Figure 9.4). The intersection where the elastic line meets the elasto-plastic line is considered to be the failure point. Therefore, the load ratio at failure for the combination load can be determined as shown in Figure 9.8. From the load table the ultimate axial load, lateral load and moment resulting in failure of the system was approximated using linear interpolation (Figure 9.9).



Model Moment = $C * F$

Note: total moment = model moment *2

Figure 9.7: Example of applied moment

Model Results

Load Magnitudes and Combinations

Vertical Load (kN)	Horizontal Load (kN)	Moment (kN.m)	Load Ratio
0	0	0	0
2	2.8	2	0.208
4	5.6	4	0.416
6	8.4	6	0.624
8	11.2	8	0.832
10	14	10	1.040

Pile Head Displacement

Displacement Magnitude (mm)	Vertical Displacement (mm)	Horizontal Displacement (mm)
0	0	0
0	0.11	0.350
1	0.29	0.98
2	0.56	1.95
4	1.04	3.43
7	2.28	7.07

Soil Details

E (MPa)	14
phi (°)	36
c (kPa)	0.1
height (m)	3.6
Nave	5
(N1ave)	12
dilation (°)	3
earth press, K	0.4

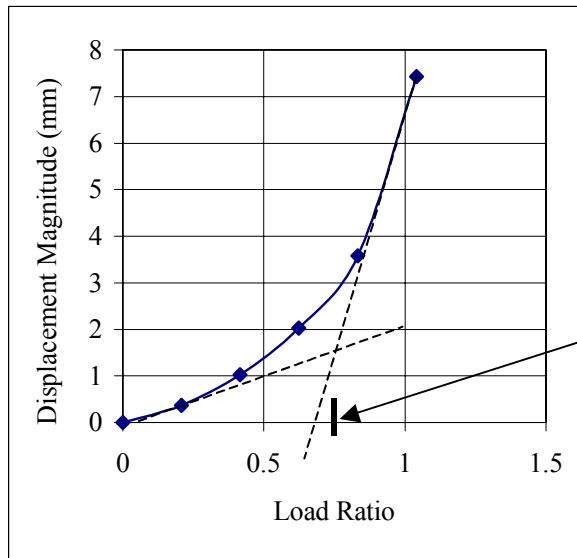
Pile Details

Length(m)	1.8
Dia (m)	0.6
Area (m^2)	0.283
L/d	3

Sample calculation of the load ratio for Case 18

$$\text{Load Ratio} = \sqrt{\left(\frac{A}{A_{\text{ult}}}\right)^2 + \left(\frac{L}{L_{\text{ult}}}\right)^2 + \left(\frac{M}{M_{\text{ult}}}\right)^2}$$

$$0.832 = \sqrt{\left(\left(\frac{8}{14}\right)^2 + \left(\frac{11.2}{20}\right)^2 + \left(\frac{8}{35}\right)^2\right)}$$



Approximate Ultimate Ratio

Load Ratio = 0.7

Ultimate Load

Axial Uplift = 7 kN

Lateral = 9.5 kN

Moment = 7 kN.m

Figure 9.8: Example of non-dimensional behaviour curve for Case 18

Load Magnitudes and Combinations

Vertical Load (kN)	Horizontal Load (kN)	Moment (kN.m)	Load Ratio
0	0	0	0
2	2.8	2	0.208
4	5.6	4	0.416
6	8.4	6	0.624
8	11.2	8	0.832
10	14	10	1.040

⇒ failure ratio
⇒ ≈ 0.7

Therefore, $(0.7 - 0.624) / (0.832 - 0.624) = 0.365$

Vertical uplift load at failure (using linear interpolation) = $(8 - 6) * 0.365 + 6 \approx 7$ kN.

Horizontal load at failure (using linear interpolation) = $(11.2 - 8.4) * 0.365 + 8.4 \approx 9.5$ kN.

Moment at failure (using linear interpolation) = $(8 - 6) * 0.365 + 6 \approx 7$ kN.

Figure 9.9: Example of how failure loads were approximated from numerical results

Failure loads for each of the chosen load cases were determined using the same approach adopted for the example Case 18. The load fractions corresponding to the ultimate failure of the system were then used in the design charts presented in Section 9.4.

9.3 Results from Numerical Analysis

The pile geometry, soil properties and results for each of the cases are shown in Appendix I. Where possible additional comparison of the FEM results with accepted theoretical methods used today are given in Section 9.4. This information provides a good checkpoint enabling further verification of the FEM results. From these results the ultimate failure load of the pile as defined in Section 9.2 was determined, along with the linear elastic gradient of the initial section of the load-displacement curve.

A summary of the ultimate load results from the FEM analysis is given in Tables 9.1 to 9.5. A full version of each case is given in Appendix I.

Tables 9.1: Results from the numerical modelling of free head, cast-in-place, and uplift combination-loaded piles

Comment	Uncorrected Blow Count N=5							
	L/d=3, L=1.8 m, d=0.6 m				L/d=10, L=6 m, d=0.6 m			
	Case No.*	Ultimate Uplift Load (kN)	Ultimate Lateral Load (kN)	Ultimate Moment (kN.m)	Case No.*	Ultimate Uplift Load (kN)	Ultimate Lateral Load (kN)	Ultimate Moment (kN.m)
Pure Axial Uplift Load	2	14	0	0	42	75	0	0
Axial Uplift + Lateral Load	4	13.2	3	0	44	64	40	0
Axial Uplift + Lateral Load	6	12	7.5	0	46	50	86	0
Axial Uplift + Lateral Load	8	8	14.5	0	48	25	112	0
Pure Lateral Load	9	0	20	0	49	0	125	0
Pure Moment	10	0	0	35	50	0	0	730
Axial Uplift + Moment	12	10	0	23	52	10	0	699
Axial Uplift + Moment	14	12	0	6	54	60	0	480
Lateral Load + Moment	15	0	5	30	55	0	65	500
Lateral Load + Moment	16	0	12	21	56	0	105	191
Axial Uplift + Lateral Load +Moment	18	7	9.5	7	58	21	98	172
Axial Uplift + Lateral Load +Moment	20	12	3	3	60	55	48	185

Tables 9.1 Continued: Results from the numerical modelling of free head, cast-in-place, and uplift combination-loaded piles

Comment	Uncorrected Blow Count N=30			
	L/d=10, L=6 m, d=0.6 m			
	Case No.*	Ultimate Uplift Load (kN)	Ultimate Lateral Load (kN)	Ultimate Moment (kN.m)
Pure Axial Uplift Load	62	160	0	0
Axial Uplift + Lateral Load	64	145	71	0
Axial Uplift + Lateral Load	66	122	81	0
Axial Uplift + Lateral Load	68	100	150	0
Pure Lateral Load	69	0	290	0
Pure Moment	70	0	0	1250
Axial Uplift + Moment	72	125	0	735
Axial Uplift + Moment	74	140	0	276
Lateral Load + Moment	76	0	227	377
Axial Uplift + Lateral Load +Moment	78	71	198	280
Axial Uplift + Lateral Load +Moment	80	109	127	185

Tables 9.2: Results from the numerical modelling of free head, cast-in-place, and compression combination-loaded piles

Comment	Uncorrected Blow Count N=5				Uncorrected Blow Count N=30			
	L/d=3, L=1.8 m, d=0.6 m				L/d=10, L=6 m, d=0.6 m			
	Case No.*	Ultimate Compression Load (kN)	Ultimate Lateral Load (kN)	Ultimate Moment (kN.m)	Case No.*	Ultimate Compression Load (kN)	Ultimate Lateral Load (kN)	Ultimate Moment (kN.m)
Pure Axial Compression Load	1	220	0	0	61	1200	0	0
Axial Compression + Lateral Load	3	200	5	0	63	535	168	0
Axial Compression + Lateral Load	5	110	14	0				
Pure Lateral Load	9	0	20	0	69	0	290	0
Pure Moment	10	0	0	35	70	0	0	1250
Axial Compression + Moment	11	85	0	21	71	826	0	358
Lateral Load + Moment	15	0	5	30	75	0	227	377
Lateral Load + Moment	16	0	12	21				
Axial Compression + Lateral Load + Moment	17	65	12	8	77	309	188	268

Tables 9.3: Results from the numerical modelling of fixed head, cast-in-place, and uplift/compression combination-loaded piles

Comment	Uncorrected Blow Count N=30			
	L/d=10, L=6 m, d=0.6 m			
	Case No.*	Ultimate Uplift Load (kN)	Ultimate Lateral Load (kN)	Ultimate Moment (kN.m)
Pure Axial Uplift Load	82	160	0	0
Axial Uplift + Lateral Load	84	145	69	0
Axial Uplift + Lateral Load	86	138	96	0
Axial Uplift + Lateral Load	88	100	183	0
Pure Lateral Load	89	0	275	0

Comment	Uncorrected Blow Count N=30			
	L/d=10, L=6 m, d=0.6 m			
	Case No.*	Ultimate Compression Load (kN)	Ultimate Lateral Load (kN)	Ultimate Moment (kN.m)
Pure Axial Compression Load	81	1200	0	0
Axial Compression + Lateral Load	83	544	170	0
Pure Lateral Load	89	0	275	0

Tables 9.4: Results from the numerical modelling of free head, impact driven, and uplift combination-loaded piles

Comment	Uncorrected Blow Count N=5							
	L/d=3, L=1.8 m, d=0.6 m				L/d=10, L=6 m, d=0.6 m			
	Case No.*	Ultimate Uplift Load (kN)	Ultimate Lateral Load (kN)	Ultimate Moment (kN.m)	Case No.*	Ultimate Uplift Load (kN)	Ultimate Lateral Load (kN)	Ultimate Moment (kN.m)
Pure Axial Uplift Load	102	15	0	0	142	100	0	0
Axial Uplift + Lateral Load	104	14.4	2	0	144	96	20	0
Pure Lateral Load	109	0	35	0	149	0	180	0
Pure Moment	110	0	0	60	150	0	0	1150
Axial Uplift + Moment	112	14.5	0	2				
Lateral Load + Moment	115	0	20	35	155	0	90	800
Axial Uplift + Lateral Load +Moment	118	8	2	0.4	158	90	20	50

Tables 9.5: Results from the numerical modelling of free head, impact driven, and compression combination-loaded piles

Comment	Uncorrected Blow Count N=5			
	L/d=3, L=1.8 m, d=0.6 m			
	Case No.*	Ultimate Compression Load (kN)	Ultimate Lateral Load (kN)	Ultimate Moment (kN.m)
Pure Axial Compression Load	101	300	0	0
Axial Compression + Lateral Load	103	174	18	0
Pure Lateral Load	109	0	35	0
Pure Moment	110	0	0	60
Axial Compression + Moment	111	250	0	10
Lateral Load + Moment	115	0	20	35
Axial Compression + Lateral Load +Moment	117	130	21	5

9.4 Comparison of FEM Results with Other Theoretical Methods

To provide additional verification where possible the FEM results were compared against results from existing methods of prediction. As discussed in Chapter 6, several methods are available to estimate axial, lateral and moment capacity of a pile when loads are acting individually. The FEM results were compared with results from the following methods:

- The ultimate axial compression capacity of the hypothetical pile case was determined using methods proposed by Decourt (1995), Poulos and Davis (1980), Vesic (1977), and Meyerhof (1976).
- The ultimate axial uplift capacity of the hypothetical pile case was estimated using Decourt (1995) work, which shows that the uplift capacity is approximately equal to 0.8 times the shaft capacity for a pile under compression loading. The compression shaft capacities were determined as part of the approximation of the compression capacity of the pile.
- The ultimate lateral capacity of the hypothetical pile case was determined by adopting the methods of Meyerhof (1995), Broms (1965), and Poulos and Davis (1980).
- The elastic displacement of the pile head under axial compression and lateral loads was determined using the techniques described by Das (1999), based on works by Vesic (1977), and Broms (1965).

Estimates of pile capacity and displacement under axial loads, lateral loads and moments for each of the hypothetical pile cases are given in Table 9.6. A sample calculation for each of the ultimate capacity prediction methods listed in Table 9.6 is presented in Appendix J.

Tables 9.6: Comparison of present numerical results against existing techniques

Pile and Sand Parameters	Method	Load Type	Ultimate Capacity (kN)	Pile Head Displacement* (mm)
Pile: L/d = 3, d=0.6 m, L = 1.8 m, free head, cast-in-place. Sand: N=5	Author's FEM model	Compression	220	7
	Other existing techniques.		149-273	6-10
	Author's FEM model	Uplift	14	
	Other existing techniques.		9-33	
	Author's FEM model	Lateral	20	1.5
	Other existing techniques.		25-50	2
Pile: L/d = 3, d=0.6 m, L = 1.8 m, free head, impact driven. Sand: N=5	Author's FEM model	Compression	300	3.5
	Other existing techniques.		169-540	3-7
	Author's FEM model	Uplift	15	
	Other existing techniques.		12-65	
	Author's FEM model	Lateral	35	2
	Other existing techniques.		34-73	4-5

* The pile head displacement was determined using the maximum and minimum predicted ultimate capacities. The capacities were determined at working loads, which were estimated to be equal to the ultimate capacity / Factor of Safety (FOS) that has been taken as 3.

Tables 9.6 Continued: Comparison of present numerical results against existing techniques

Pile and Sand Parameters	Method	Load Type	Ultimate Capacity (kN)	Pile Head Displacement* (mm)
Pile: $L/d = 10$, $d=0.6$ m, $L = 6$ m, free head, cast-in-place. Sand: $N=30$	Author's FEM model	Compression	1200	20
	Other existing techniques.		1603-3073	26-49
	Author's FEM model	Uplift	160	
	Other existing techniques.		160-425	

* The pile head displacement was determined using the maximum and minimum predicted ultimate capacities. The capacities were determined at working loads, which were estimated to be equal to the ultimate capacity / Factor of Safety (FOS) that has been taken as 3.

Table 9.6 shows that there is a degree of scatter between one prediction technique to the next. This degree of scatter between prediction methods was similar to that observed during the statistical analysis of shallow foundations, as shown in Chapters 3 and 5. The FEM results obtained using the pile model developed for this research tended to be within the bounds formed by other existing techniques. The FEM results also tended to be closer to or form the conservative bound of all the methods reviewed. From the verification provided in Chapter 8, and the brief comparison between the FEM results and other existing techniques, the developed model seems to be yielding reasonable results and may be used for the remainder of the research.

It is noted that a non-dimensional approach is being used as the basis of any design charts being developed as part of this work.

9.5 Development of Three Dimensional Oblique Charts

9.5.1 General

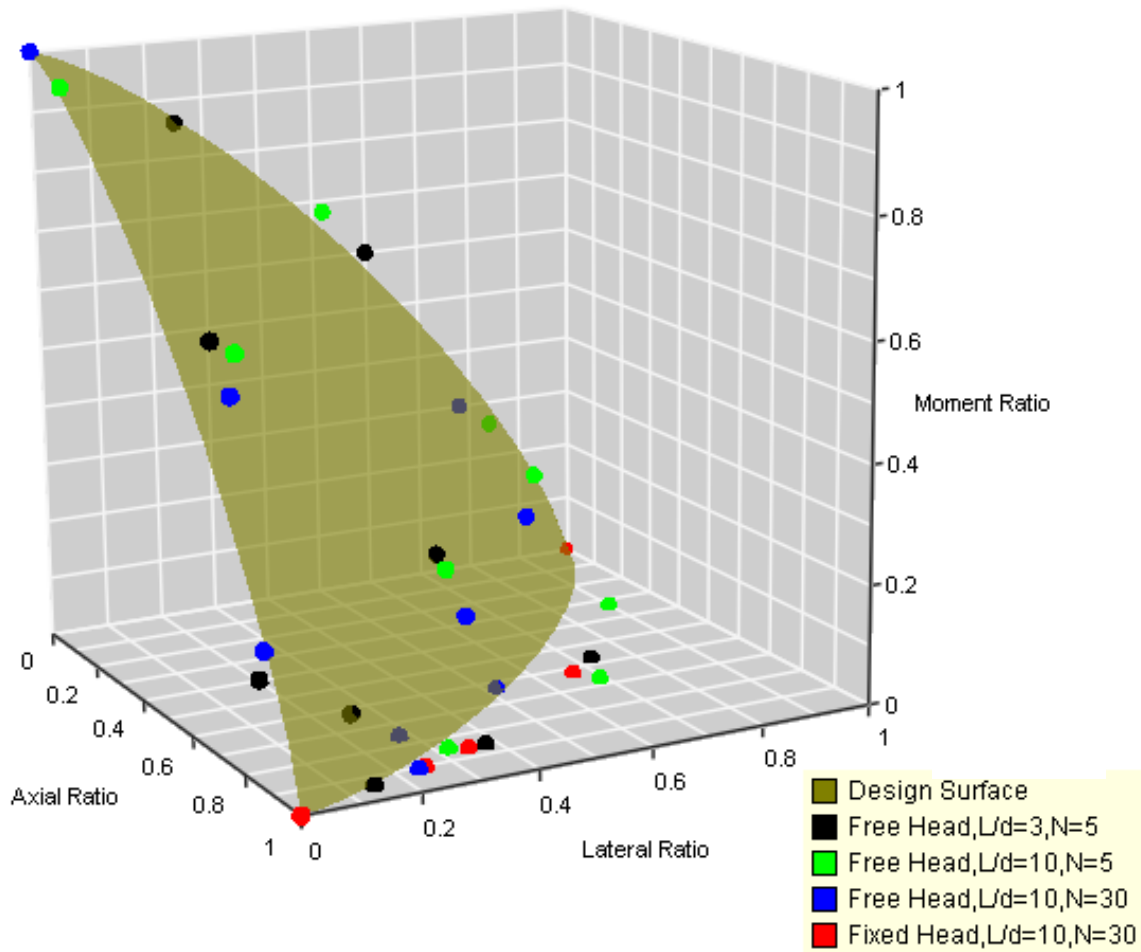
A good way to compare the impact of combined loading on the ultimate capacity of a pile is to construct a non-dimensional chart, as shown by researchers such as Meyerhof et al. (1983), Poulos and Davis (1980), and Eckserley et al (1996). The non-dimensional approach allows trends to be determined between different loading scenarios and soil properties, without having to include several variables to define the pattern. Each unique combination of pile geometry, loading combination and soil properties forms a discrete point on the non-dimensional plot and allows results to be analysed. A non-dimensional analysis is given in subsequent sections for each of the following loading scenarios:

1. Cast-in-place, free and fixed head pile with uplift, horizontal and moment loading combinations.
2. Cast-in-place, free and fixed head pile with compression, horizontal and moment loading combinations.
3. Impact driven, free head pile with uplift, horizontal and moment loading combinations.

4. Impact driven, free head pile with compression, horizontal and moment loading combinations.

9.5.2 Cast-in-Place Pile with Free and Fixed Head, and Uplift Combination Loading

The non-dimensional ratios for the cast-in-place pile under uplift, horizontal and moment loading combination are given in Tables 9.7 and 9.8. From the ratios in Tables 9.7 and 9.8, a three dimensional plot was constructed and is shown in Figure 9.10.



Note: Axial Ratio = design axial load component (U)/pure ultimate axial load (U_{ult})
 Lateral Ratio = design lateral load component (L)/pure ultimate lateral load (L_{ult})
 Moment Ratio = design moment component (M)/pure ultimate moment load (M_{ult})

Figure 9.10: 3D design ratio plot for cast-in-place piles with uplift loading scenarios

Tables 9.7: Design ratios for cast-in-place, free head piles with uplift combination loads

Comment	Uncorrected Blow Count N=5							
	L/d=3, L=1.8 m, d=0.6 m				L/d=10, L=6 m, d=0.6 m			
	Case No.	Uplift Ratio*	Lateral Ratio*	Moment Ratio*	Case No.	Uplift Ratio*	Lateral Ratio*	Moment Ratio*
Pure Axial Uplift Load	2	1.00	0.00	0.00	42	1.00	0.00	0.00
Axial Uplift + Lateral Load	4	0.94	0.15	0.00	44	0.85	0.32	0.00
Axial Uplift + Lateral Load	6	0.86	0.38	0.00	46	0.67	0.69	0.00
Axial Uplift + Lateral Load	8	0.57	0.73	0.00	48	0.33	0.90	0.00
Pure Lateral Load	9	0.00	1.00	0.00	49	0.00	1.00	0.00
Pure Moment	10	0.00	0.00	1.00	50	0.00	0.00	1.00
Axial Uplift + Moment	12	0.71	0.00	0.66	52	0.13	0.00	0.96
Axial Uplift + Moment	14	0.86	0.00	0.17	54	0.80	0.00	0.66
Lateral Load + Moment	15	0.00	0.25	0.86	55	0.00	0.52	0.68
Lateral Load + Moment	16	0.00	0.60	0.60	56	0.00	0.84	0.26
Axial Uplift + Lateral Load +Moment	18	0.50	0.48	0.20	58	0.28	0.78	0.24
Axial Uplift + Lateral Load +Moment	20	0.86	0.15	0.09	60	0.73	0.38	0.25

* The ratio is equal to the ultimate component in either axial, lateral or moment/ultimate capacity under pure axial, lateral or moment.

Tables 9.7 Continued: Design ratios for cast-in-place, free head piles with uplift combination loads

Comment	Uncorrected Blow Count N=30			
	L/d=10, L=6 m, d=0.6 m			
	Case No.	Uplift Ratio*	Lateral Ratio*	Moment Ratio*
Pure Axial Uplift Load	62	1.00	0.00	0.00
Axial Uplift + Lateral Load	64	0.91	0.24	0.00
Axial Uplift + Lateral Load	66	0.76	0.28	0.00
Axial Uplift + Lateral Load	68	0.63	0.52	0.00
Pure Lateral Load	69	0.00	1.00	0.00
Pure Moment	70	0.00	0.00	1.00
Axial Uplift + Moment	72	0.78	0.00	0.59
Axial Uplift + Moment	74	0.88	0.00	0.22
Lateral Load + Moment	76	0.00	0.78	0.30
Axial Uplift + Lateral Load +Moment	78	0.44	0.68	0.22
Axial Uplift + Lateral Load +Moment	80	0.68	0.44	0.15

* The ratio is equal to the ultimate component in either axial, lateral or moment/ultimate capacity under pure axial, lateral or moment.

Tables 9.8: Design ratios for cast-in-place, fixed head piles with uplift combination loads

Comment	Uncorrected Blow Count N=30			
	L/d=10, L=6 m, d=0.6 m			
	Case No.	Uplift Ratio*	Lateral Ratio*	Moment Ratio*
Pure Axial Uplift Load	82	1.00	0.00	0.00
Axial Uplift + Lateral Load	84	0.91	0.25	0.00
Axial Uplift + Lateral Load	86	0.86	0.35	0.00
Axial Uplift + Lateral Load	88	0.63	0.67	0.00
Pure Lateral Load	89	0.00	1.00	0.00

*Under pure axial, lateral or moment.

The ratio is equal to the ultimate component in either axial, lateral or moment/ultimate capacity under pure axial, lateral or moment.

The design surface in Figure 9.10 is given by:

$$\left(\frac{U}{U_{ult}}\right)^{1.3} + \left(\frac{L}{L_{ult}}\right)^{1.3} + \left(\frac{M}{M_{ult}}\right)^{1.3} \leq 1 \quad (9.2)$$

The reasoning and theory for the form of the design surface are presented in Section 9.5.5. The non-dimensional plot in Figure 9.10 indicates that a definite relationship exists between the ultimate load of the pile, and the loading combination used to achieve that ultimate load. A discussion on trends and final deductions is given in Section 9.5.6, and in Chapter 10.

9.5.3 Cast-in-Place Pile with Free and Fixed Head, and Compression Combination Loading

The non-dimensional ratios for the cast-in-place pile under compression, horizontal and moment loading combination are given in Tables 9.9 and 9.10. From the ratios in Tables 9.9 and 9.10 a three dimensional plot was constructed and is shown in Figure 9.11.

The design surface in Figure 9.11 is given by:

$$\left(\frac{C}{C_{ult}}\right)^{1.2} + \left(\frac{L}{L_{ult}}\right)^{1.2} + \left(\frac{M}{M_{ult}}\right)^{1.2} \leq 1 \quad (9.3)$$

The reasoning and theory for the form of the design surface are presented in Section 9.5.6. A discussion on trends and final deductions is also given in Section 9.5.6, and in Chapter 10.

Table 9.9: Design ratios for cast-in-place, free head piles with compression combination loads

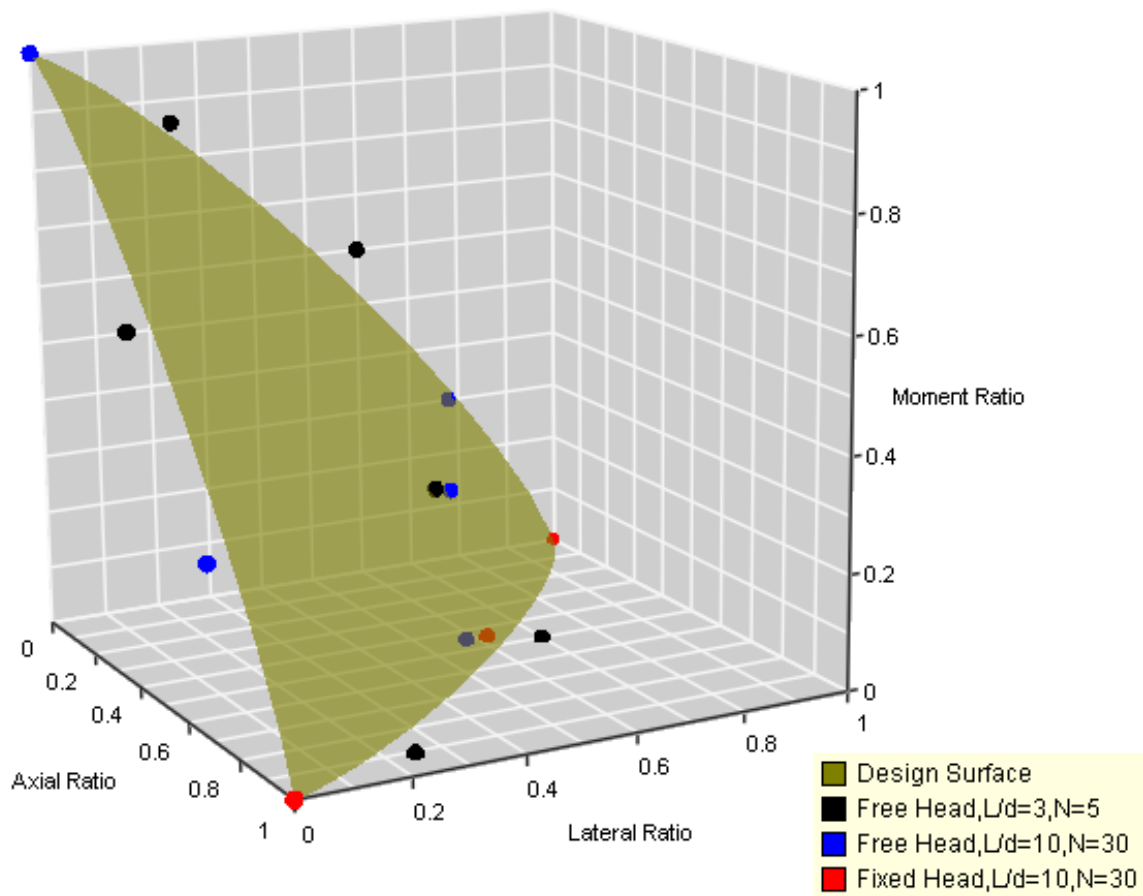
Comment	Uncorrected Blow Count N=5				Uncorrected Blow Count N=30			
	L/d=3, L=1.8 m, d=0.6 m				L/d=10, L=1.8 m, d=0.6 m			
	Case No.	Compression Ratio*	Lateral Ratio*	Moment Ratio*	Case No.	Compression Ratio*	Lateral Ratio*	Moment Ratio*
Pure Axial Compression Load	1	1.00	0.00	0.00	61	1.00	0.00	0.00
Axial Compression + Lateral Load	3	0.91	0.25	0.00	63	0.45	0.58	0.00
Axial Compression + Lateral Load	5	0.50	0.70	0.00				
Pure Lateral Load	9	0.00	1.00	0.00	69	0.00	1.00	0.00
Pure Moment	10	0.00	0.00	1.00	70	0.00	0.00	1.00
Axial Compression + Moment	11	0.39	0.00	0.60	71	0.69	0.00	0.29
Lateral Load + Moment	15	0.00	0.25	0.86	75	0.00	0.78	0.30
Lateral Load + Moment	16	0.00	0.60	0.60				
Axial Compression + Lateral Load + Moment	17	0.30	0.60	0.23	77	0.26	0.65	0.21

* The ratio is equal to the ultimate component in either axial, lateral or moment/ultimate capacity under pure axial, lateral or moment.

Table 9.10: Design ratios for cast-in-place, fixed head piles with compression combination loads

Comment	Uncorrected Blow Count N=30			
	L/d=10, L=6 m, d=0.6 m			
	Case No.	Compression Ratio*	Lateral Ratio*	Moment Ratio*
Pure Axial Compression Load	81	1.00	0.00	0.00
Axial Compression + Lateral Load	83	0.45	0.62	0.00
Pure Lateral Load	89	0.00	1.00	0.00

* The ratio is equal to the ultimate component in either axial, lateral or moment/ultimate capacity under pure axial, lateral or moment.



Note: Axial Ratio = design axial load component (C) / pure ultimate axial load (C_{ult})
 Lateral Ratio = design lateral load component (L) / pure ultimate lateral load (L_{ult})
 Moment Ratio = design moment component (M) / pure ultimate moment load (M_{ult})

Figure 9.11: 3D design ratio plot for cast-in-place piles with compression loading scenarios

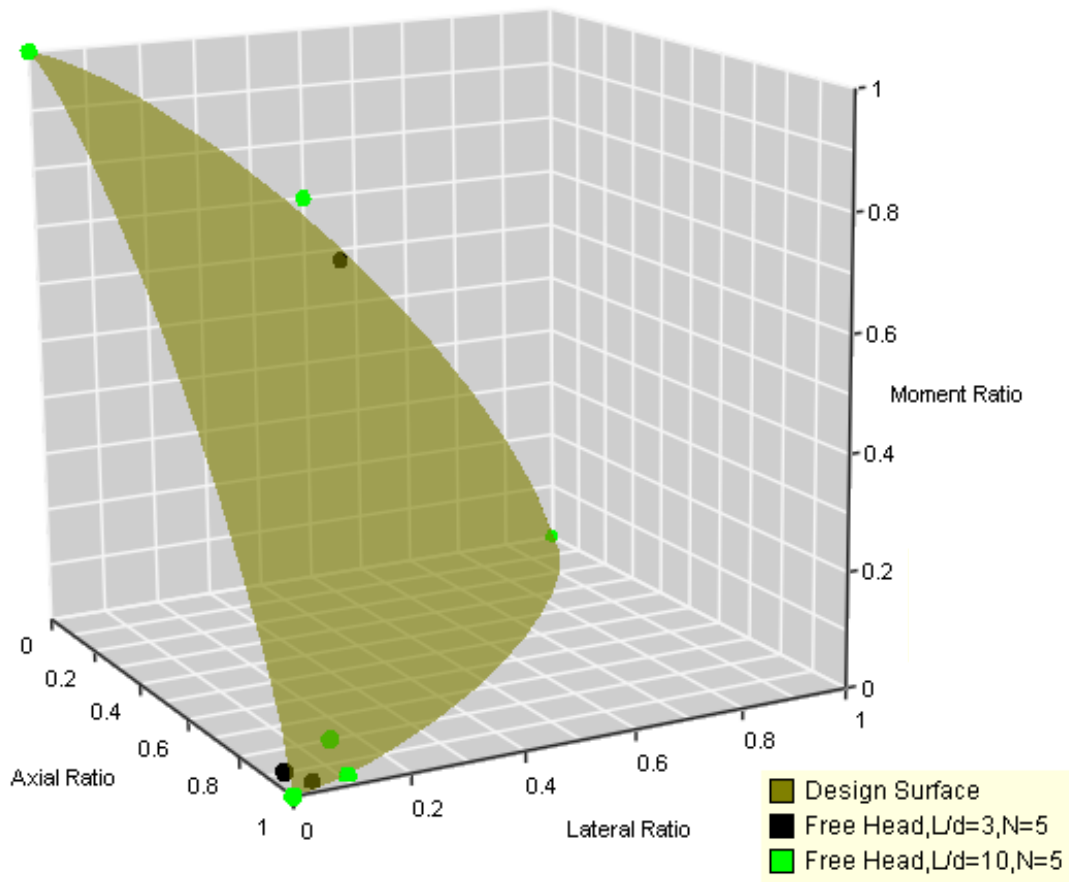
9.5.4 Impact Driven Pile with Free Head and Uplift Combination Loading

The non-dimensional ratios for an impact driven pile under uplift, horizontal and moment loading combination are presented in Table 9.11. From the ratios in Table 9.11, a three dimensional plot was constructed and is shown in Figure 9.12.

Table 9.11: Design ratios for impact driven, free head piles with uplift combination loads

Comment	Uncorrected Blow Count N=5							
	L/d=3, L=1.8 m, d=0.6 m				L/d=10, L=6 m, d=0.6 m			
	Case No.	Uplift Ratio*	Lateral Ratio*	Moment Ratio*	Case No.	Uplift Ratio*	Lateral Ratio*	Moment Ratio*
Pure Axial Uplift Load	102	1.00	0.00	0.00	142	1.00	0.00	0.00
Axial Uplift + Lateral Load	104	0.96	0.05	0.00	144	0.96	0.11	0.00
Pure Lateral Load	109	0.00	1.00	0.00	149	0.00	1.00	0.00
Pure Moment	110	0.00	0.00	1.00	150	0.00	0.00	1.00
Axial Uplift + Moment	112	0.97	0.00	0.03				
Lateral Load + Moment	115	0.00	0.57	0.58	155	0.00	0.50	0.70
Axial Uplift + Lateral Load +Moment	118	0.53	0.06	0.01	158	0.90	0.11	0.04

* The ratio is equal to the ultimate component in either axial, lateral or moment/ultimate capacity under pure axial, lateral or moment.



Note: Axial Ratio = design axial load component (U) / pure ultimate axial load (U_{ult})
 Lateral Ratio = design lateral load component (L) / pure ultimate lateral load (L_{ult})
 Moment Ratio = design moment component (M) / pure ultimate moment load (M_{ult})

Figure 9.12: 3D design ratio plot for impact driven piles with uplift loading scenarios

The design surface in Figure 9.12 is given by:

$$\left(\frac{U}{U_{ult}}\right)^{1.3} + \left(\frac{L}{L_{ult}}\right)^{1.3} + \left(\frac{M}{M_{ult}}\right)^{1.3} \leq 1 \quad (9.4)$$

The reasoning and theory for the form of the design surface are presented in Section 9.5.6. A discussion on trends and final deductions is also given in Section 9.5.6, and in Chapter 10.

9.5.5 Impact Driven Pile with Free Head and Compression Combination Loading

The non-dimensional ratios for an impact driven pile under compression, horizontal and moment loading combination are given in Table 9.12.

Table 9.12: Design ratios for impact driven, free head piles with compression combination loads.

Comment	Uncorrected Blow Count N=5			
	L/d=3, L=1.8 m, d=0.6 m			
	Case No.	Compression Ratio*	Lateral Ratio*	Moment Ratio*
Pure Axial Compression Load	101	1.00	0.00	0.00
Axial Compression + Lateral Load	103	0.58	0.51	0.00
Pure Lateral Load	109	0.00	1.00	0.00
Pure Moment	110	0.00	0.00	1.00
Axial Compression + Moment	111	0.83	0.00	0.17
Lateral Load + Moment	115	0.00	0.57	0.58
Axial Compression + Lateral Load + Moment	117	0.43	0.60	0.08

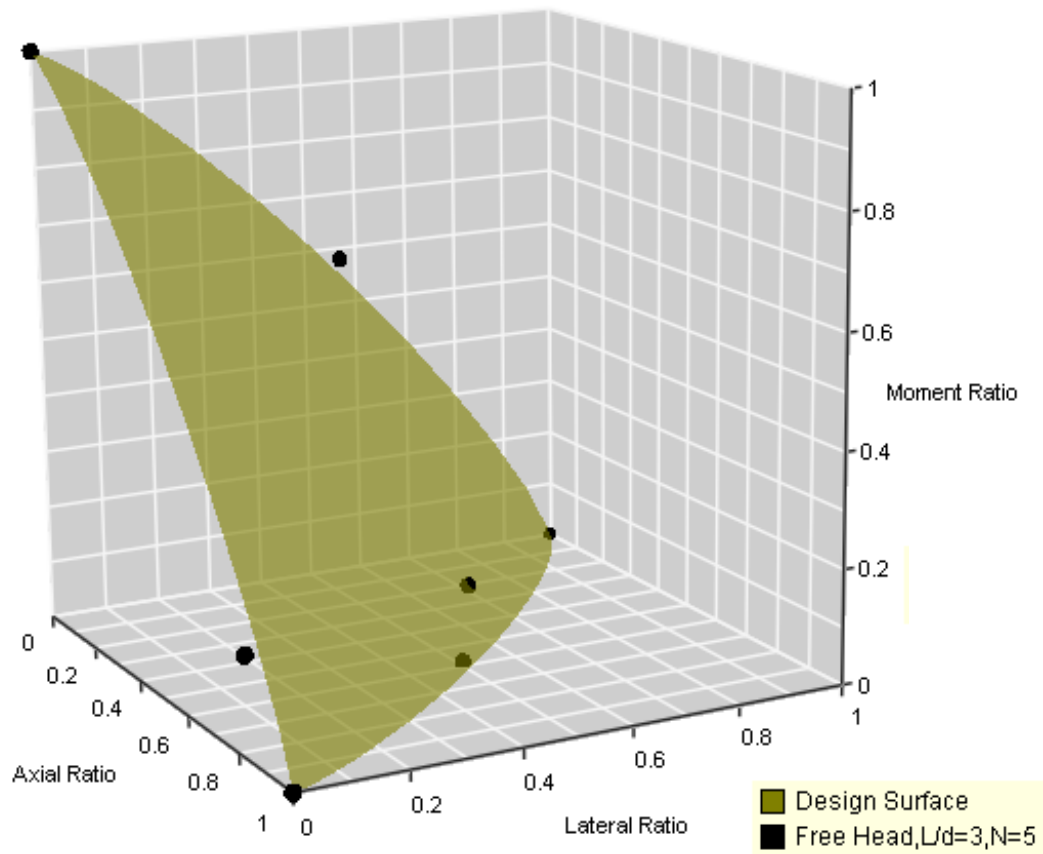
* The ratio is equal to the ultimate component in either axial, lateral or moment/ultimate capacity under pure axial, lateral or moment.

The three dimensional plot shown in Figure 9.13 was developed using the load ratios in Table 9.12.

The design surface in Figure 9.13 is given by:

$$\left(\frac{C}{C_{ult}}\right)^{1.2} + \left(\frac{L}{L_{ult}}\right)^{1.2} + \left(\frac{M}{M_{ult}}\right)^{1.2} \leq 1 \quad (9.5)$$

The reasoning and theory for the form of the design surface are presented in Section 9.5.6. A discussion on trends and final deductions is also given in Section 9.5.6, and in Chapter 10.



Note: Axial Ratio = design axial load component (C) / pure ultimate axial load (C_{ult})
 Lateral Ratio = design lateral load component (L) / pure ultimate lateral load (L_{ult})
 Moment Ratio = design moment component (M) / pure ultimate moment load (M_{ult})

Figure 9.13: 3D design ratio plot for impact driven piles with compression loading scenarios

9.5.6 Three-Dimensional Oblique Interaction Charts

Figures 9.10 to 9.13 show a design curve that was developed as part of these works. To determine the design surface the non-dimensional ratios were first plotted in a two dimensional space. This is shown in Figure 9.14 for uplift combination loading, and Figure 9.15 for compression combination loading.

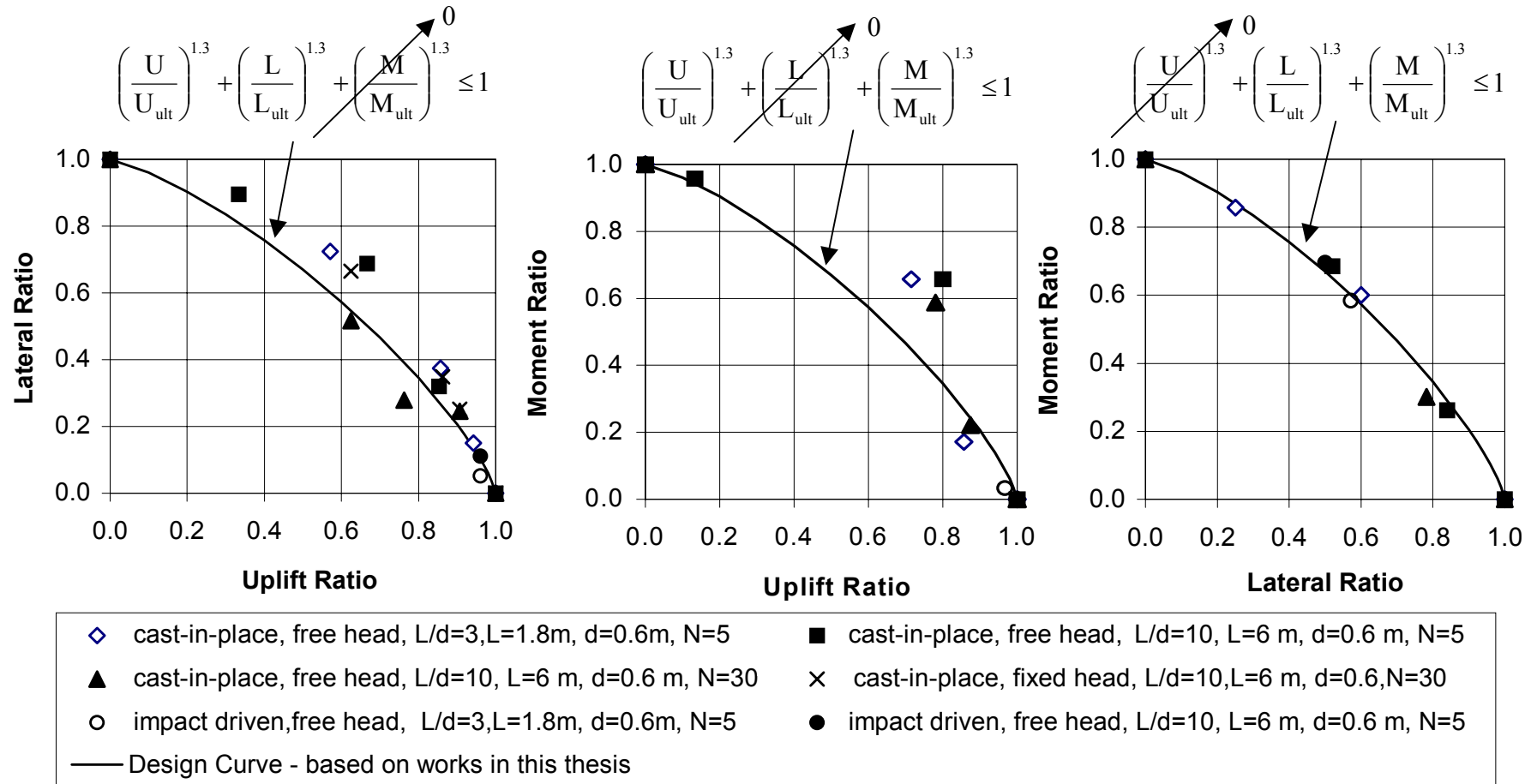


Figure 9.14: 2D ratio plots for uplift combination loading scenarios

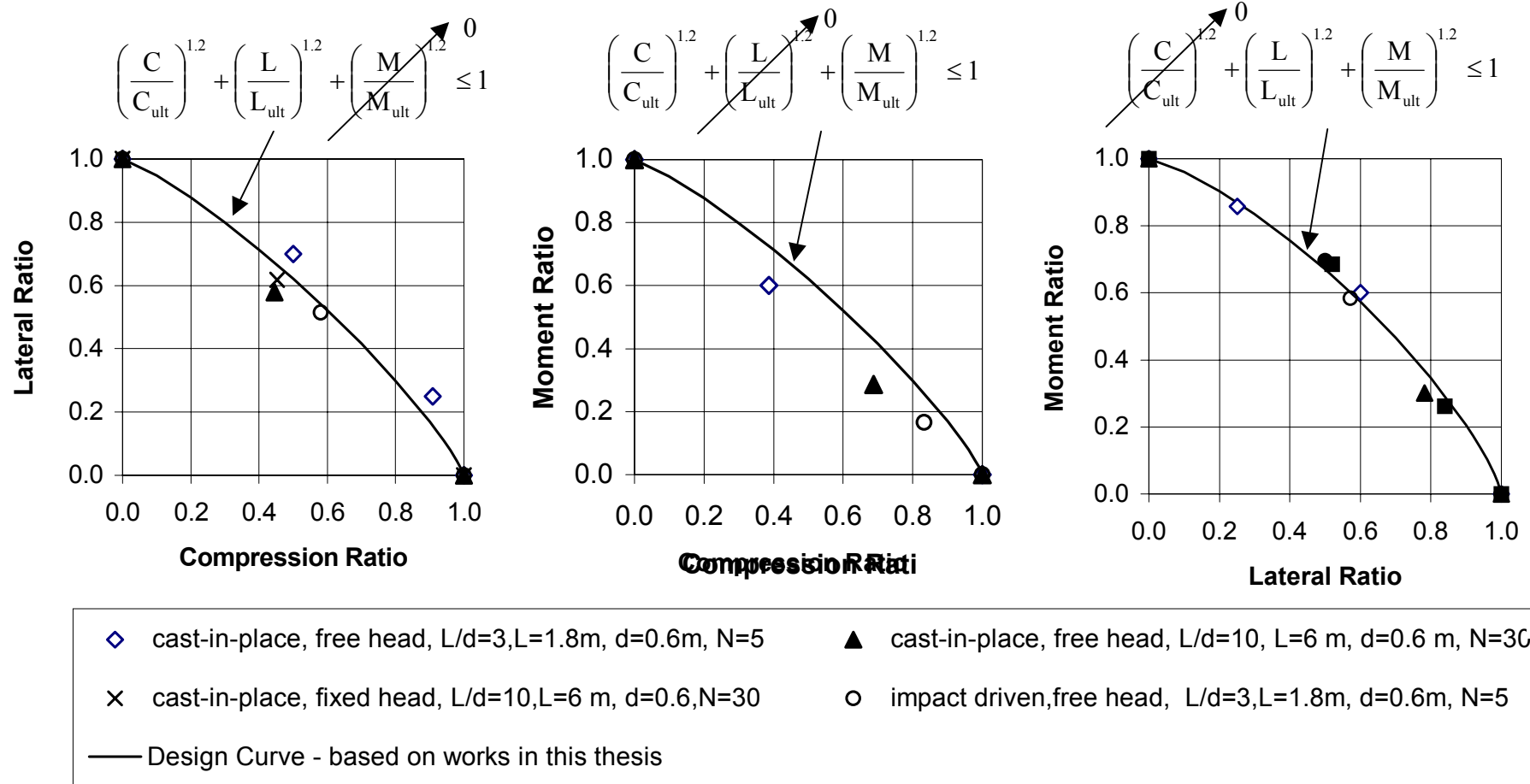


Figure 9.15: 2D ratio plots for compression combination loading scenarios

From the two-dimensional plots, it can be seen that the design surface has been chosen to represent the average of all three views of the two dimensional plots for the uplift and compression combination loading scenarios (see Figures 9.14 and 9.15). It is noted that the additional points with an axial ratio, lateral ratio and moment ratio have also been obtained through the numerical modelling, and are plotted in the three-dimensional views in Figures 9.10 to 9.13. These additional points lie outside the three-dimensional surface, and this means that the surface lies on the conservative side of the point.

The final surfaces were chosen so that the number of numerically determined data points lying outside the surface (i.e. on the conservative side) was greater than the points on the inside of the surface (i.e. on the risky side). This means the surface was chosen such that it generally represented the conservative side of the average of points. The surface was determined through a process of trial and error, where the following general equation was used in which the power n was varied, until the conservative side of the data cluster was determined:

$$\left(\frac{A_{\text{design}}}{A_{\text{ult}}} \right)^n + \left(\frac{L_{\text{design}}}{L_{\text{ult}}} \right)^n + \left(\frac{M_{\text{design}}}{M_{\text{ult}}} \right)^n \leq 1 \quad (9.6)$$

where Axial Ratio = design axial load component (A_{design}) / pure ultimate axial load (A_{ult}),

Lateral Ratio = design lateral load component (L_{design}) / pure ultimate lateral load (L_{ult}), and

Moment Ratio = design moment component (M_{design}) / pure ultimate moment load (M_{ult}).

The above basic form of the equation is an extension onto previous works by Meyerhof et al. (1983), Poulos and Davis (1980) and Eckserley et al (1996), who used this form of equation but only in a two-dimensional sense.

From the Figures 9.10 to 9.13, a failure envelope function may be fitted to the data that represents each of the respective data sets. The final interaction formula for each of the failure envelopes is as follows:

- For uplift combination loading:

$$\left(\frac{U_{\text{design}}}{U_{\text{ult}}} \right)^{1.3} + \left(\frac{L_{\text{design}}}{L_{\text{ult}}} \right)^{1.3} + \left(\frac{M_{\text{design}}}{M_{\text{ult}}} \right)^{1.3} \leq 1. \quad (9.7)$$

- For compression combination loading:

$$\left(\frac{C_{\text{design}}}{C_{\text{ult}}} \right)^{1.2} + \left(\frac{L_{\text{design}}}{L_{\text{ult}}} \right)^{1.2} + \left(\frac{M_{\text{design}}}{M_{\text{ult}}} \right)^{1.2} \leq 1. \quad (9.8)$$

If a factor of safety (FOS) is incorporated, Equations 9.7 and 9.8 are modified to the following form:

- For uplift combination loading:

$$\left(\frac{U_{\text{design}} * \text{FOS}}{U_{\text{ult}}} \right)^{1.3} + \left(\frac{L_{\text{design}} * \text{FOS}}{L_{\text{ult}}} \right)^{1.3} + \left(\frac{M_{\text{design}} * \text{FOS}}{M_{\text{ult}}} \right)^{1.3} \leq 1. \quad (9.9)$$

- For compression combination loading:

$$\left(\frac{C_{\text{design}} * \text{FOS}}{C_{\text{ult}}} \right)^{1.2} + \left(\frac{L_{\text{design}} * \text{FOS}}{L_{\text{ult}}} \right)^{1.2} + \left(\frac{M_{\text{design}} * \text{FOS}}{M_{\text{ult}}} \right)^{1.2} \leq 1. \quad (9.10)$$

The major trends shown by the numerical modelling indicate the following:

- Figures 9.10 to 9.13 show that the free head connection is comparable to the lower conservative bound, and this failure surface has been used to define the average to lower conservative bound.
- The load combinations on piles affect both compression and uplift loading scenarios.

- The final failure envelopes as defined above are more conservative than the failure envelope suggested by Meyerhof et al. (1983). As a matter of interest, the uplift cast-in-place numerical model results for the simultaneous axial and lateral loaded piles are plotted along with the failure envelope suggested by this research and by Meyerhof et al. (1983). An example plot is shown in Figure 9.16.

From Figure 9.16 and based on this study, Meyerhof's failure criterion for axial uplift and lateral loading combination tends to be on the upper bound and 'risky' side. All the numerical points obtained by this work indicate that failure may have occurred before the Meyerhof's failure criterion has been reached. The failure envelope in this study tends to be on the conservative side of the points, in this case for the lateral-axial uplift interaction. However the failure curve extends to three dimensions and includes moments. This additional dimension also plays an important role and has been chosen so that all three dimensions are satisfied (Figures 9.14 and 9.15).

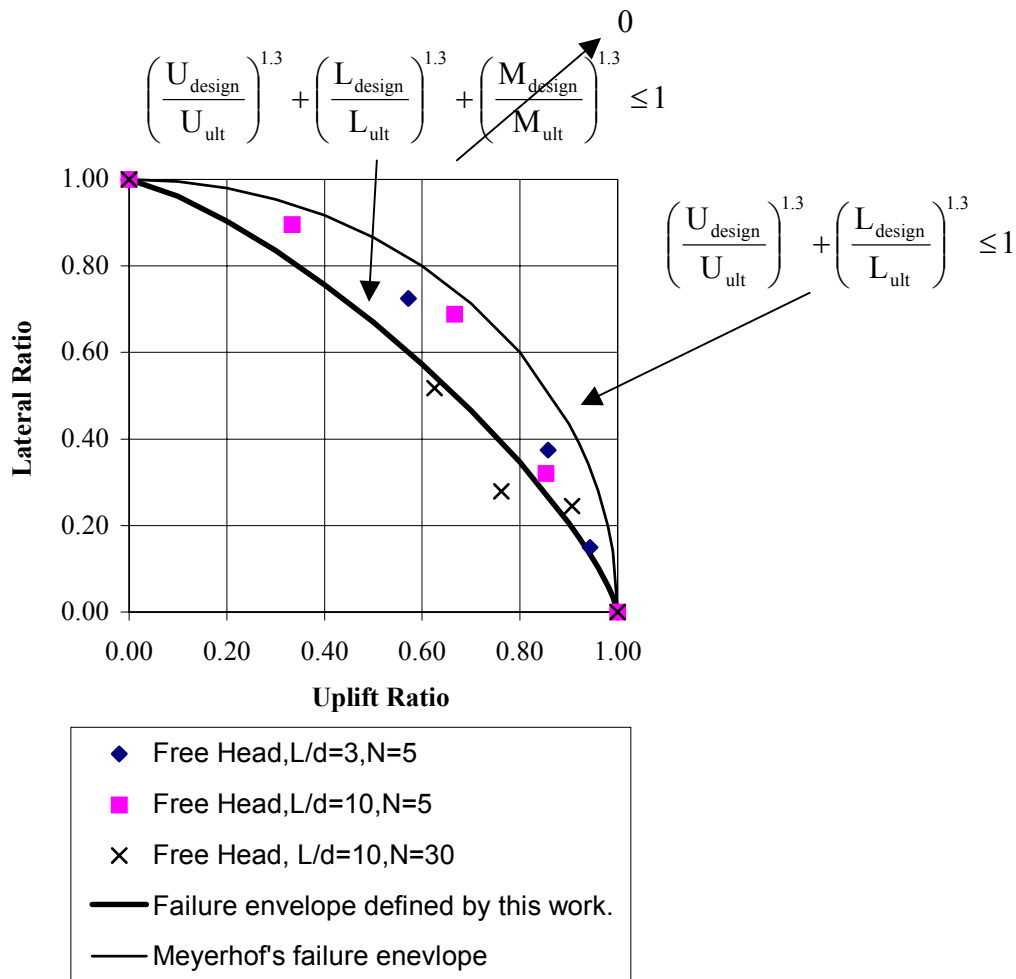


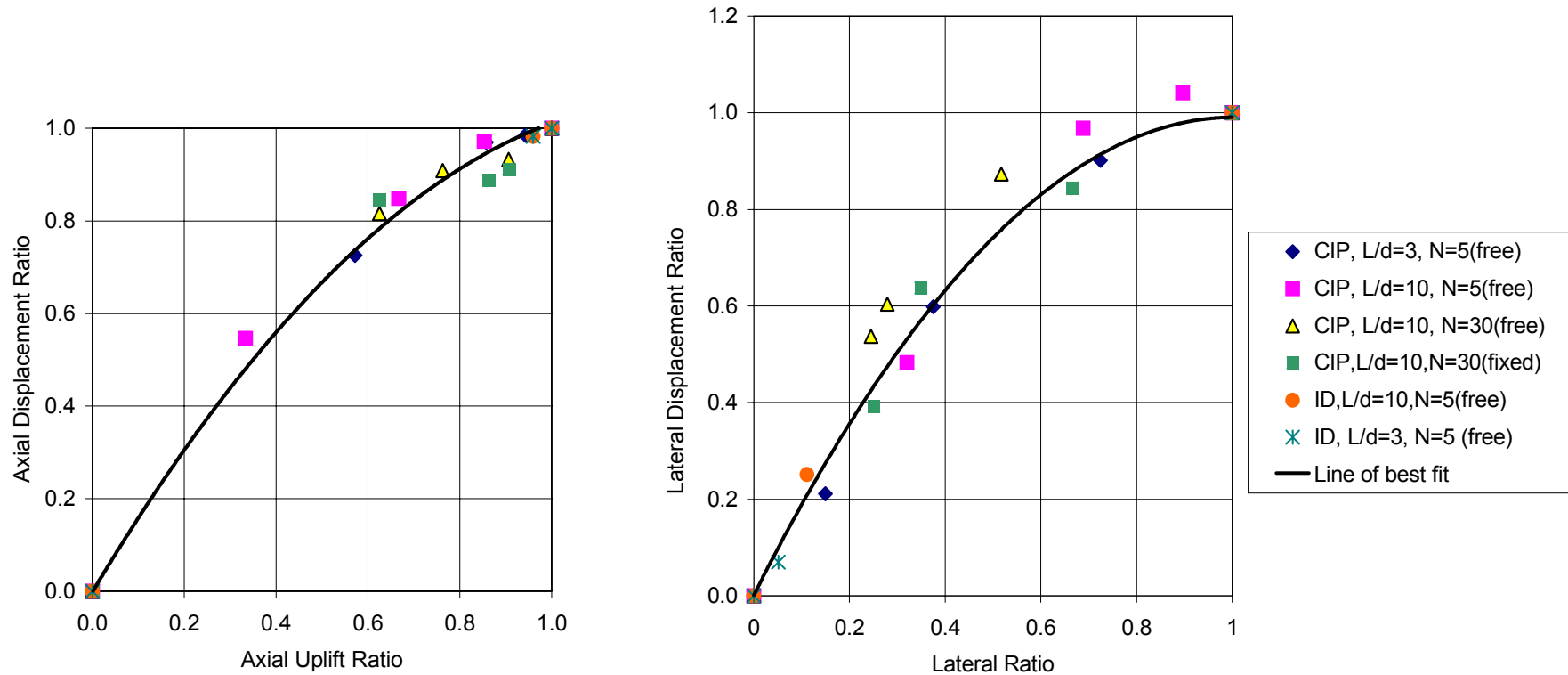
Figure 9.16: 2D plot of lateral ratio vs. axial uplift ratio for a cast-in-place pile

Some additional discussion on the results from this chapter is given in Chapter 10. The discussion includes worked examples of how to use the charts, limitations of the plots and in what ground conditions they are suitable for application. Comparisons between the laboratory results in Chapter 7 and the numerical results are also shown in Chapter 10.

9.6 Influence of Oblique Load on Displacement

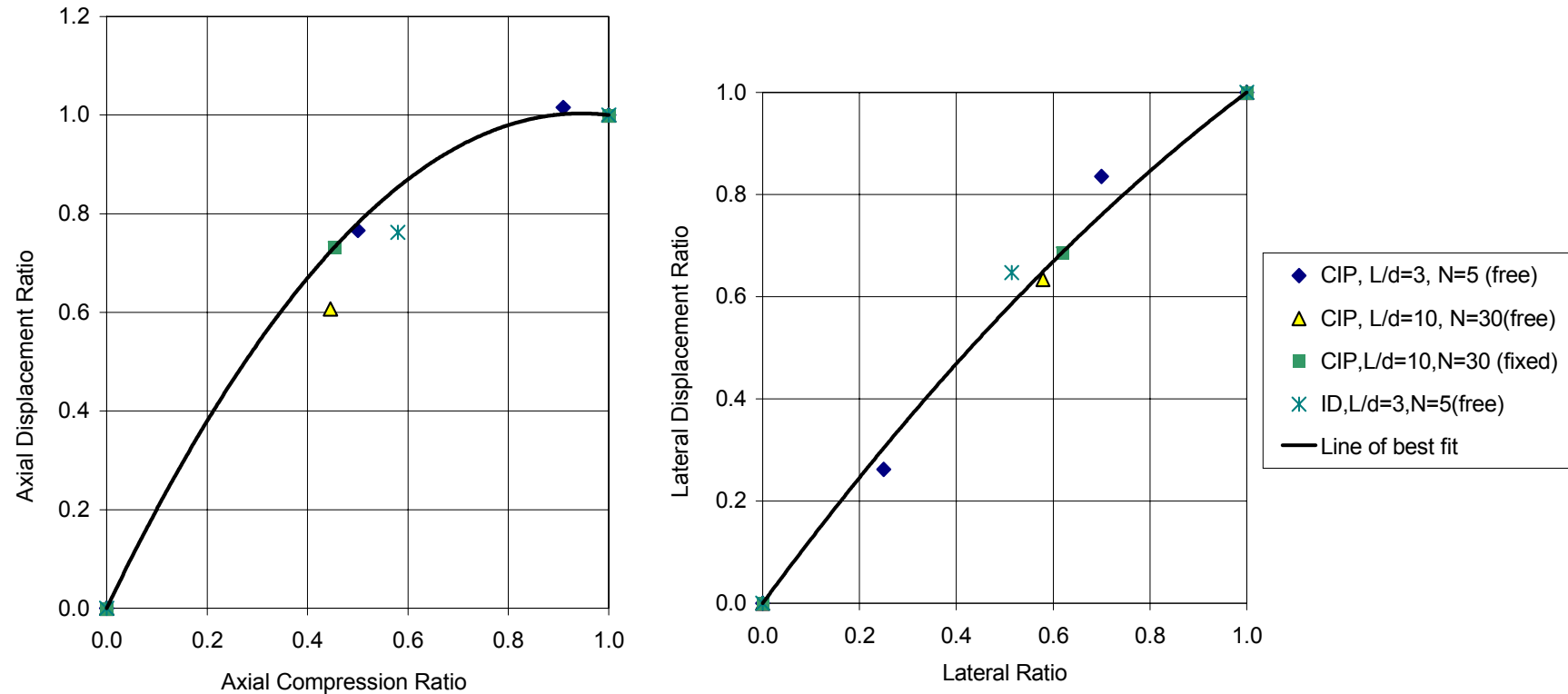
The increase or decrease in the gradient (or stiffness of the system) of the linear elastic response at the centre of the pile head under axial and horizontal oblique loading was compared to the pure axial and horizontal load displacement gradient. The change in normalized displacement magnitude of both the horizontal and vertical directions for the axial and lateral ratios are shown in Figures 9.17 and 9.18.

The plots given in Figures 9.17 and 9.18 show an estimated line of best fit that relates the pure pile head displacement under lateral and axial loads to the pile head displacement under oblique load. For instance, if the axial uplift load ratio (=design axial load due to interaction/pure ultimate uplift load) is equal to 0.5 the displacement ratio from Figure 9.16 is equal to approximately 0.62. This means that the axial pile head displacement for the obliquely loaded pile is approximately equal to 0.62 times the predicted pile head displacement under pure axial load. The plots given in this chapter allow estimates for both uplift and compression loading combination scenarios. The working and plots associated with the displacement equations can be found in Appendix I. A further discussion on these plots can be found in Chapter 10.



where: Axial displacement ratio = predicted axial pile head displacement/pile head displacement due to pure axial load.
 Axial uplift ratio = design axial load due to oblique interaction/pure ultimate axial load.
 Lateral displacement ratio = predicted lateral pile head displacement/pile head displacement due to pure lateral load.
 Lateral ratio = design lateral load due to oblique interaction/pure ultimate lateral load.
 CIP = cast in place
 ID = impact driven

Figure 9.17: Relationship between load ratios and displacement ratios for uplift combination, free/fixed head CIP and ID piles



where: Axial displacement ratio = predicted axial pile head displacement/pile head displacement due to pure axial load.
 Axial down thrust ratio = design axial load due to oblique interaction/pure ultimate axial load.
 Lateral displacement ratio = predicted lateral pile head displacement/pile head displacement due to pure lateral load.
 Lateral ratio = design lateral load due to oblique interaction/pure ultimate lateral load.
 CIP = cast in place
 ID = impact driven

Figure 9.18: Relationship between load ratios and displacement ratios for compression combination, free head CIP and ID piles

CHAPTER 10: Discussion of Numerical Results for Piles

10.1 General

The numerical results in Chapter 9 indicate that the interaction between various loading combinations have a definite impact on the capacity and displacement of a pile. The work in this study has formed a design criterion by means of numerical modelling. As stated in previous chapters, the numerical models were developed in a finite element-modelling package entitled ABAQUS. This chapter discusses the pros and cons of the oblique interaction charts for the ultimate capacity, and the displacement of a pile subjected to combination loading (see Chapter 9). The final results have been compared with small-scale tests modelled in Chapter 7, and to the estimates from other researchers' methods. Some design examples using the oblique interaction charts are also presented in this chapter.

10.2 Oblique Interaction Charts and Comparison with Experimental Data

The numerical modelling in Chapter 9 showed that the application of combination loading on a pile in sand results in a reduction in axial, lateral and moment capacity of the pile. This reduction in the axial, lateral and moment capacity of the pile can be represented by a three-dimensional surface, as shown in Chapter 9 (Equations 9.7 and 9.8). This surface referred to as the oblique interaction chart is expressed in the equation form as:

- For uplift combination loading:

$$\left(\frac{U_{\text{design}}}{U_{\text{ult}}}\right)^{1.3} + \left(\frac{L_{\text{design}}}{L_{\text{ult}}}\right)^{1.3} + \left(\frac{M_{\text{design}}}{M_{\text{ult}}}\right)^{1.3} \leq 1. \quad (10.1)$$

- For compression combination loading:

$$\left(\frac{C_{\text{design}}}{C_{\text{ult}}}\right)^{1.2} + \left(\frac{L_{\text{design}}}{L_{\text{ult}}}\right)^{1.2} + \left(\frac{M_{\text{design}}}{M_{\text{ult}}}\right)^{1.2} \leq 1. \quad (10.2)$$

where U_{design} = design axial uplift load component,
 C_{design} = design compression load component,
 L_{design} = design lateral load component,
 M_{design} = design moment component,
 U_{ult} = pure ultimate axial uplift load,
 C_{ult} = pure ultimate axial compression load,
 L_{ult} = pure ultimate lateral load, and
 M_{ult} = pure ultimate moment.

The proposed design surface is based on a parametric numerical study for a series of pile cases chosen by the author. These pile cases include a sensitivity analysis of the following factors:

- Uplift and compression combination loading
- Length (L) to diameter (d) ratios $L/d = 3$ and 10
- Standard penetration blow counts for the sand $N=5$ and $N=30$

To a lesser degree the following aspects were also explored:

- Differences between cast-in-place and impact driven pile non-dimensional ratios
- Pile head fixity, in particular free head and fixed head piles

The numerical modelling indicated that the influence from changing the above parameters was not significant when using a non-dimensional approach (Figures 9.9 to 9.12 in Chapter 9). A further discussion on each of the above parameters is given in subsequent sections.

To explore the reliability of the results from the numerical analysis, the non-dimensional charts have been compared with small-scale experimental test data completed in this work, and by Prideaux (1998). The results from the small-scale modelling are shown in Tables 10.1 and 10.2.

Table 10.1: Experimental small-scale test pile results conducted as part of current research

Ultimate Loads and Error Range of Results between Identical Test Piles								
Pure Compression Load			Pure Lateral Load		Oblique Load with Axial Compression and Lateral Loads (inclination angle = 45 deg)			
Sand Condition	Ultimate Compression Load (N)	Error Range +/- (N)	Ultimate Lateral Load (N)	Error Range +/- (N)	Load Magnitude at Failure (N)	Compression Component at Failure (N)	Ultimate Lateral Component at Failure (N)	Error Range +/- (N)
Loose	400	50	90	10	120	85	85	100
Dense	5500	1000	175	10	240	170	170	10
Layered	4500	300	130	20	185	131	131	20

Load Ratios		
Sand Condition	Ultimate Compression Component Ratio	Ultimate Lateral Component Ratio
Loose	0.21	0.94
Dense	0.03	0.97
Layered	0.03	1.01

Table 10.2: Experimental small-scale test pile results conducted by Prideaux (1998)

Sand Condition	Ultimate Loads				
	Pure Uplift Load	Pure Lateral Load	Oblique Load with Axial Uplift and Lateral Loads (inclined to vertical at 22.5 deg)		
	Ultimate Compression Load (N)	Ultimate Lateral Load (N)	Load Magnitude at Failure (N)	Uplift Component at Failure (N)	Lateral Component at Failure (N)
Dense - dry	272	460	298	276	114
Dense - saturated	134	226	119	110	46
Load Ratios					
	Ultimate Compression Component Ratio	Ultimate Lateral Component Ratio			
Dense - Dry	1.01	0.25			
Dense - Saturated	0.82	0.20			

	Ultimate Loads					
	Oblique Load with Axial Uplift and Lateral Loads (inclined to vertical at 45 deg)			Oblique Load with Axial Uplift and Lateral Loads (inclined to vertical at 67.5 deg)		
Sand Condition	Load Magnitude at Failure (N)	Axial Uplift Component at Failure (N)	Lateral Component at Failure (N)	Load Magnitude at Failure (N)	Axial Uplift Component at Failure (N)	Lateral Component at Failure (N)
Dense - Dry	313	221	221	405	155	374
Dense - Saturated	141	100	100	166	63	153
		Load Ratios			Load Ratios	
Sand Condition		Ultimate Compression Component Ratio	Ultimate Lateral Component Ratio		Ultimate Compression Component Ratio	Ultimate Lateral Component Ratio
Dense - Dry		0.81	0.48		0.57	0.81
Dense - Saturated		0.75	0.44		0.47	0.68

The final failure surface for the uplift and compression axial loads with added lateral loads (i.e. moments assumed to be = 0) have been plotted along with the experimental data, as shown in Figures 10.1 and 10.2. For further comparison, Meyerhof's curve for the axial compression and lateral load domain has also been plotted.

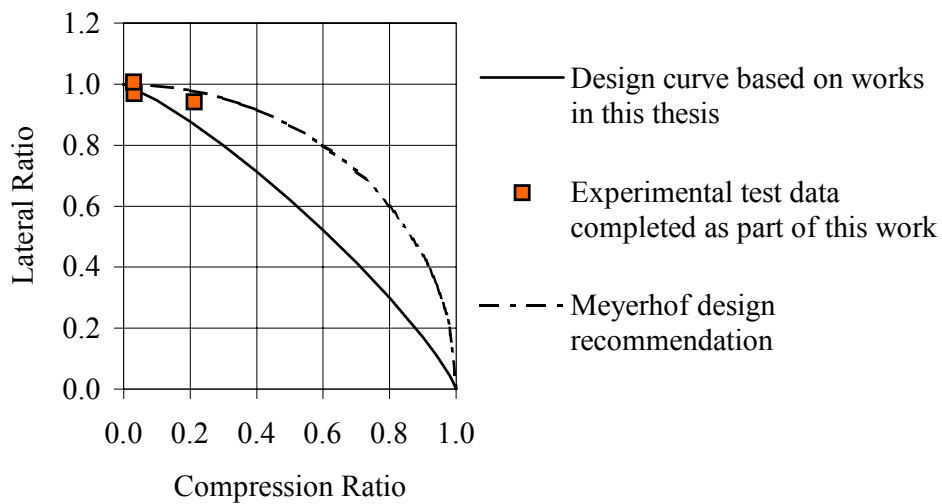


Figure 10.1: Comparison between experimental and design surface for compression combination loading

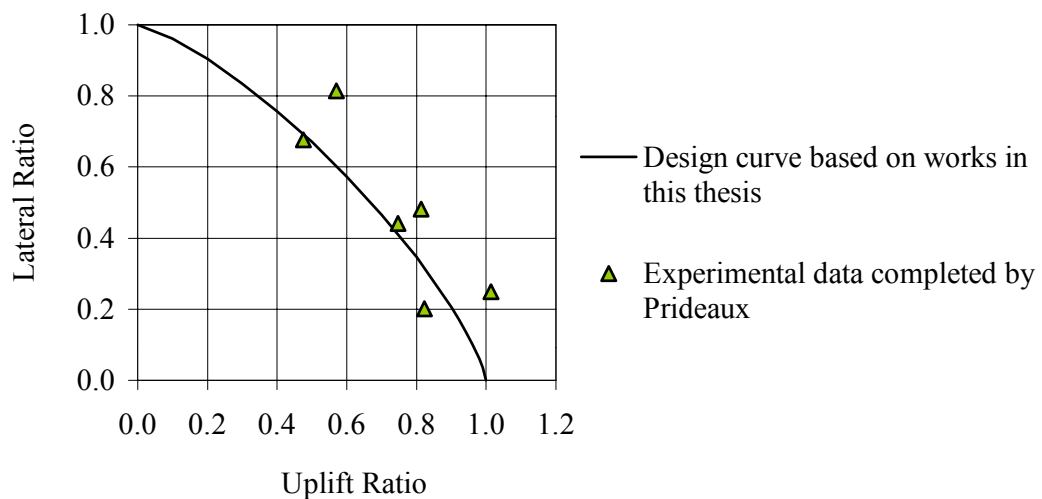


Figure 10.2: Comparison between experimental and design surface for uplift combination loading

The following was concluded for the failure surfaces developed as part of this work and Meyerhof's curve, when comparing the experimental data with numerical results.

- Uplift combination loading: the design curve from the numerical model developed as part of this work was generally located on the conservative side of the scatter (Figure 10.2). This indicates that the curve proposed by this work should provide a relatively safe method of estimating the ultimate capacity of a pile under uplift combination oblique loads. It is also important to note that the three points lying directly on or within proximity to the proposed curve were for a small-scale pile in saturated dense sand (Prideaux, 1998). As suggested previously, the influence of changing the stiffness of a material (i.e. impact driven to cast-in-place comparison) indicates that the change in stiffness did not cause an extreme change in shape of the non-dimensional curve. This means that the overall trend or percentage change in the pile capacity could be represented by a single curve. When developing the curve it was determined that the curve lied on the conservative side of the scatter. The proposed curve could then represent a range of sand and pile characteristics and conditions. It can be seen that the proposed curve fits the data closely when compared with the saturated small-scale test data. This indicates that the proposed design curve may be applied to systems where water is present.
- Compression combination loading: when comparing the limited experimental work by this research and the proposed design curve, it can be seen from Figure 10.1 that the curve formed the lower conservative bound of the scatter plot. This suggests that the proposed design curve may be applied with some degree of confidence that the design load will be slightly less than the actual ultimate load. This is important and a good trait for a design technique to have. If the design curve was plotted on the more risky upper bound of the scatter plot there would be an increased risk of the pile failing before the design ultimate load is reached. From the limited verification provided by the small-scale compression oblique piles, it is anticipated that the design curve proposed in this research is adequate for the purpose of design.

From the comparison between the numerical and experimental results mentioned above, it is anticipated that the design criteria for the ultimate capacity in this study forms a conservative lower bound. Meyerhof's relationship based on the results appears to be on the upper unconservative (risky) bound. The analysis was chosen such that length (L) to diameter (d) ratios were less than or equal to $L/d \leq 10$. Given the absence of better data, it is anticipated higher values of L/d should be designed using a reduced capacity criteria. As Meyerhof's formula may be slightly on the risky side, it is then recommended that a conservative ultimate capacity failure surface be employed for cases where $L/d \geq 10$ (i.e. slender piles). It is anticipated that the failure surface developed in this work may be used as a guide for ultimate capacity of the soil surrounding slender piles. If a more conservative approach is sought due to variable or uncertain conditions, a linear failure surface given in Equation 10.3 for the ultimate capacity may be adopted. This conservative failure criteria has also been recommended by Poulos and Davis (1980) and Eckersley et al. (1996) in the form of a linear failure line between the lateral and axial components. It is also recommended that the failure line be extended into a failure surface including lateral, axial, and moment loads if a conservative approach due to uncertainty is needed.

$$\left(\frac{A_{\text{design}}}{A_{\text{ult}}} \right) + \left(\frac{L_{\text{design}}}{L_{\text{ult}}} \right) + \left(\frac{M_{\text{design}}}{M_{\text{ult}}} \right) \leq 1 \quad (10.3)$$

where A_{design} = design axial load component,
 L_{design} = design lateral load component,
 M_{design} = design moment component,
 U_{ult} = pure ultimate axial load,
 L_{ult} = pure ultimate lateral load, and
 M_{ult} = pure ultimate moment.

The charts in Figures 9.9 and 9.12 may be used when predicting displacements of the pile head once the pile is under combination loading. It is anticipated that these charts are applicable for cast-in-place and impact driven for piles with $L/d \leq 10$. However, if conditions are highly variable or some uncertainty surrounds the in situ conditions, it is recommended that the displacement under pure axial, lateral and moment loads is

determined. A displacement magnitude of the pile head may be determined using the pure case values. The displacement magnitude will form the upper conservative bound for pile head displacement. It is anticipated that the true pile head displacement is likely to be less than this value. It is also noted that linear interpolation between a pure case and oblique component is not recommended. For example, if the maximum axial uplift load that can be applied to a pile from the oblique interaction is 50%, it does not mean that the resulting axial displacement is 50% of the pure axial displacement case. As seen in the results of this study, the axial displacement is likely to be greater than 60% of the pure axial displacement case, i.e. the relationship between the load ratio and displacement ratio is not linear and linear interpolation should be avoided. Therefore, the pile head displacement with a $L/d \leq 10$ (e.g. rigid piles or intermediate slender piles) may be estimated using Figures 9.16 and 9.17. For piles with greater L/d ratios, it is anticipated that the true pile head displacement is likely to be between the value obtained from the Figures 9.16 and 9.17, and the pile head displacement magnitude from the combined displacements from the pure axial, lateral, and moment cases.

10.3 Comparison between Numerical and Theoretical Results

The comparisons between numerical results and other theoretical results are given in Section 9.4. Two further observations were noted during the course of the numerical modelling. The first observation was the comparison between the numerical modelling and theoretical estimate for the cast-in-place point of contraflexure for a pile below the ground. Based on the theory for piles in sand with a standard penetration blow count $N=5$ and $L/d=3$, the rotation point for the pile under pure moment and horizontal loading is shown in Figure 10.3. From the analysis of the resulting displacement field within the pile, the numerical model gave a point of contraflexure as shown in Figure 10.4.

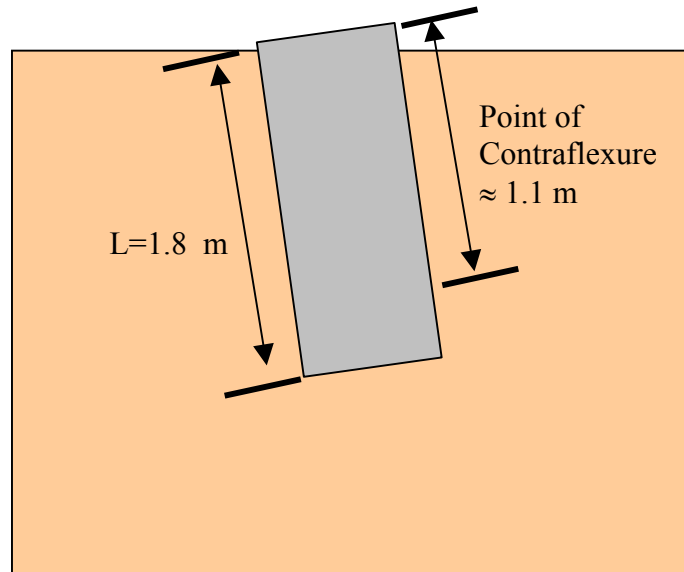


Figure 10.3: Estimated point of contraflexure for a $L/d=3$ pile in sand, with $N=5$ based on works by Poulos and Davis (1980)

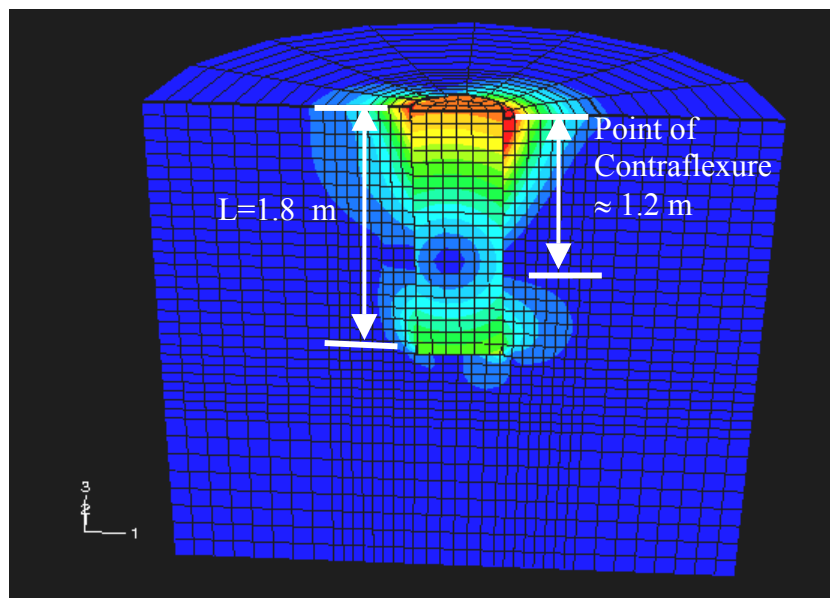


Figure 10.4: Estimated point of contraflexure for a $L/d=3$ pile in sand, with $N=5$ based on numerical modelling

Similarly, for the cast-in-place pile case with $N=30$ and $L/d \leq 10$, the theoretical and numerical points of contraflexure are shown in Figures 10.5 and 10.6.

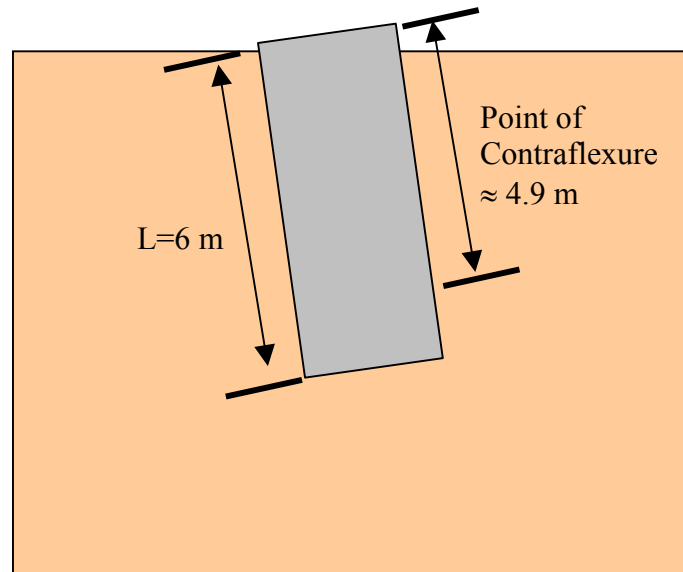


Figure 10.5: Estimated point of contraflexure for a $L/d=10$ pile in sand, with $N=30$ based on works by Poulos and Davis (1980)

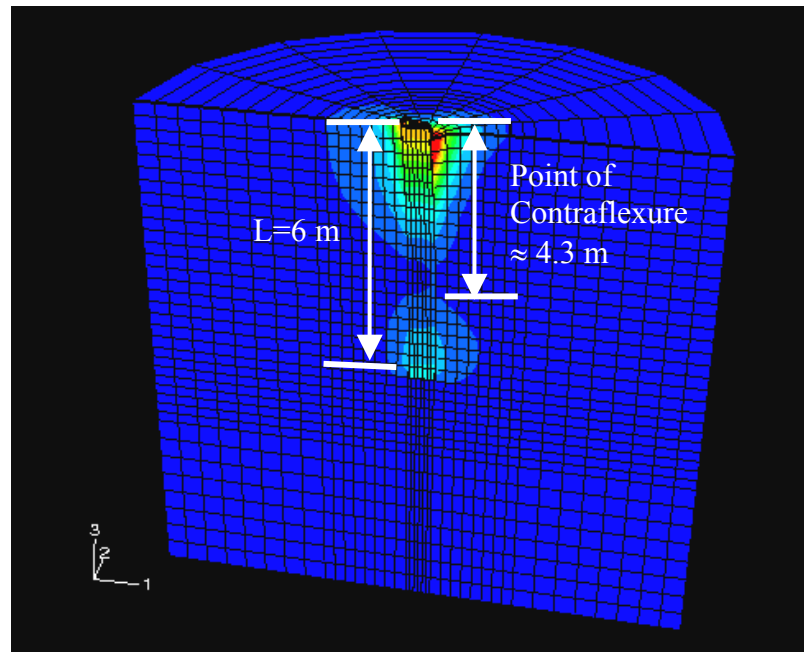


Figure 10.6: Estimated point of contraflexure for a $L/d=10$ pile in sand, with $N=30$ based on numerical modelling

The points of contraflexure in Figures 10.3 to 10.6 indicate that the numerical model compared reasonably well with theory, and the pile behaviour below the ground surface to a certain extent was predicted realistically.

10.4 Influential Factors on Design Charts

As part of the numerical modelling the influence of several parameters on the pile-soil behaviour was explored to a limited degree, and this allowed trends to be approximated. A brief summary of the variables explored and the influence they had on the overall trends is given in the following sections.

10.4.1 Sand Properties

To explore the impact that sand properties have on the combination loading trends, the author changed the standard penetration blow count (N) of sand from N=5 to N=30. The blow count in Chapter 4 can be linked to the Young's modulus, friction angle and dilatancy angle of sand.

The numerical analysis in Chapter 9 indicates that the variation in soil properties for the cast-in-place and impact driven piles had a minimal impact on the oblique ratios or trends. While the capacities and displacements for each pile were affected significantly by the variation of the soil properties, any advantage or disadvantage in capacity was ultimately cancelled out when determining the oblique ratio. This suggests that the soil parameters cause an approximate multiple increase or decrease in capacities and displacements, which is similar in the oblique case and pure load direction cases. The factor of increase or decrease will later cancel out when dividing the oblique component by the pure load component. This indicated that the trends due to the load combination are similar with the variation of sand properties. The scatter in Figures 9.9 to 9.12 for the cases where the standard blow count changed from N=5 to N=30, is partially due to interpretation or approximation of ultimate capacities from the load-displacement curves (Appendix I). The overall minimal scatter between the plots in Figures 9.9 to 9.12 suggests that the sand properties are unlikely to cause significant shifts in the non-dimensional design charts.

10.4.2 Influence of Pile Installation Technique

When modelling the impact driven pile cases it was assumed that the effects of driving could be accounted for by using elevated soil parameters with a normal effective stress gravity field, and an accompanying effective horizontal stress field. Based on these assumptions, a limited analysis was carried out to determine the influence of driving on the non-dimensional capacity charts. From the results of the numerical analysis in Figures 9.9 to 9.12, it was noted that the failure surfaces from the cast-in-place analysis is still applicable for the impact driven cases. When inspecting the cast-in-place and impact driven results it can be concluded (as in the case of varying sand properties) that the advantages and disadvantages of driving has a great impact on the load magnitude, which the pile can withstand but a minimal influence on the load ratios. This meant that the pros and cons between cast-in-place and impact driving of a pile resulted in multiples lower or higher in pile capacity, which are cancelled out when working out the load ratios.

The assumption that driving is the only stress acting on the impact driving system is not entirely correct but considered appropriate for this research. The true impact driven system would include additional driving stresses as discussed in Chapters 6 and 8. To attempt to include the driving stresses researchers will have to either model the actual driving process, or find a way of accounting for the stresses such as putting a stress field in the model. Some attempts at putting in a driving stress field were made during the modelling phase of this work. While a tentative driving stress field could be incorporated, ABAQUS requires the use of a loading stress field as the first load step, and then the imposed stresses can be balanced and referenced as a zero displacement state. However, the loading scenarios that would include the incorporated driving stress field could not be achieved without simulating the actual driving process.

The modelling of the actual driving process is difficult to achieve as a discrete slip occurs below the pile (bearing capacity failure zone), and this enables the pile to be impacted into the ground. Then using continuum packages may present some difficulties so an adaptive mesh would need to be employed. Also when modelling the process additional variables such as hammer drop height, hammer weight, pile

configuration (i.e. slenderness and reinforcement) need to be examined, which will introduce several additional variables. This research aimed to explore the static response of the pile and did not attempt to model a pile being hammered into the ground.

It was thought by this author that the trends from the analysis would be sufficient for the purposes of the research. As stated in the first paragraph, it is anticipated that the benefits of pile driving definitely increases the pile capacity and reduces displacements when compared to their cast-in-place counterparts. Hence this multiple increase is likely to be similar in the axial, lateral, and moment capacities as the loading combination is changed. When the interaction component is divided by the pure loading case, the multiple is cancelled out and comes back to a similar trend as seen in the cast-in-place cases. The capacity failure surface proposed in this work was based on the lower bound of the numerical modelling data, and is anticipated to give a good basis for estimation of loads in impact driven cases. However, if conditions are difficult and little data is available it is recommended that a linear plane failure surface be adopted (Equation 10.3).

10.4.3 Influence of Vertical Stress Fields

When modelling the pile response using an elasto-plastic criteria it is important that at least an effective vertical stress field and accompanying effective horizontal stress field be implemented. If no effective vertical stress field is implemented then the model will achieve plastic failure with only small increments of load, and a converged solution may not be achieved. This is shown in the diagram of Figure 10.7.

As shown in Figure 10.7, the Mohr-Coulomb failure circle resorts to a dot and plastic failure will occur with any increment of load. The displacement strains are then in the plastic strain region with any increments of load. This results in a large displacement with little increase in load and convergence problems will occur relatively quickly. Convergence problem can occur when the load increment is unchanged but has an infinite number of possible strain solutions (i.e. pure plastic failure and pile displaces with little to no increase in load). This can be avoided and the load-displacement curve

can be achieved realistically by implementing the effective stresses, which will allow for Mohr-Coulomb failure circle to be achieved and allow some elastic response to be modelled.

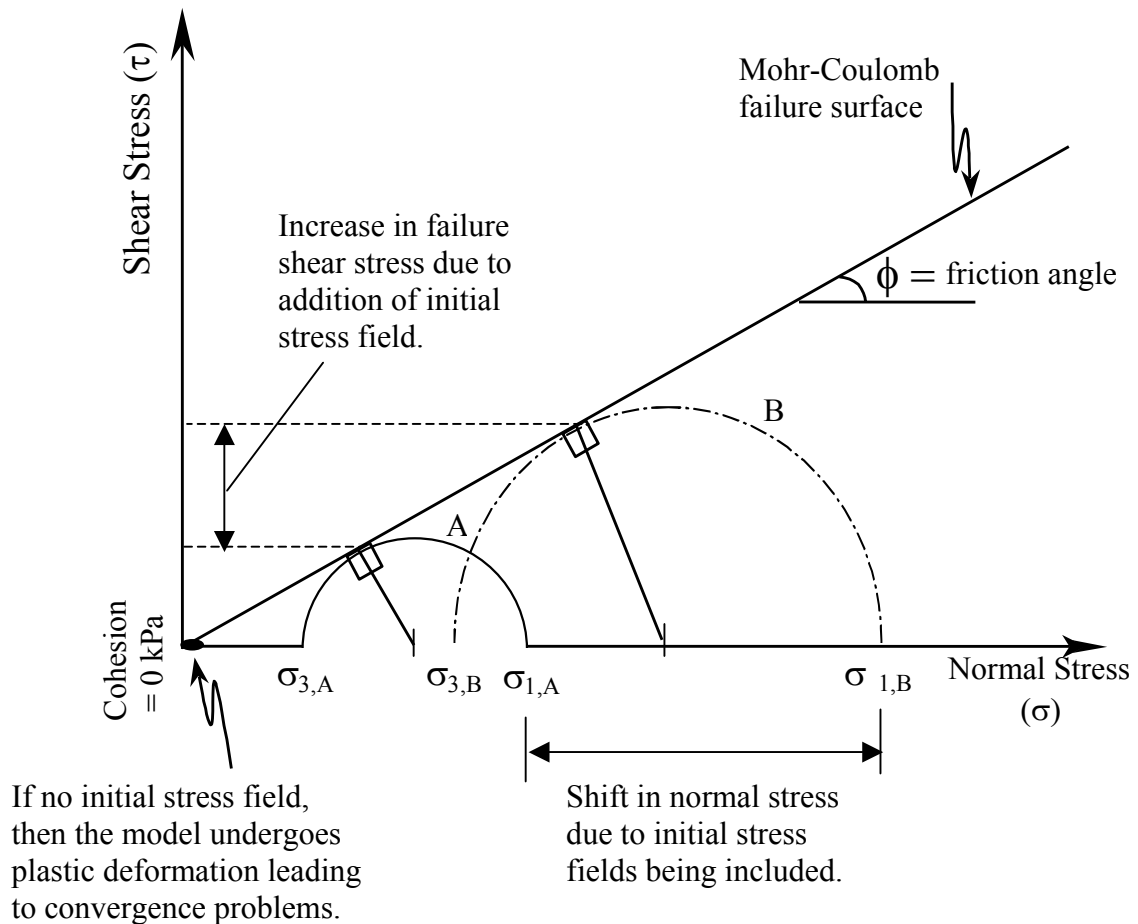


Figure 10.7: Influence of initial stress in Mohr-Coulomb failure criteria

10.4.4 Pile Head Fixity

To explore the influence of pile head fixity on the capacity and displacement design ratios, a preliminary numerical model investigation was undertaken to study fixed head and free head piles. The results from the numerical models are shown in Figures 9.9 to 9.12. The preliminary analysis indicated that the results from the fixed head piles tended to give less conservative ratios than their free head counterparts. The difference

between the results from both head fixity methods was observed to be very small. Therefore, it was considered appropriate to use a single failure surface to represent both head fixity methods. The final failure surfaces are given in Section 10.2.

10.5 Influence of Pile Shape

As an offshoot from the research in this thesis, the author assisted by Mr Paul Lemcke explored the influence that pile shape has on the capacity of a pile under lateral and axial combined loading. This research was completed using two verified models, one with a square cross-sectional shape and the other with a traditional circular shape. The findings from the study at the time of the writing of this thesis had been accepted for publication in a Journal. A copy of this paper is given in Appendix K.

The major finding from the cross-sectional analysis indicated that trends existed between the square and circular piles with various lateral and axial loading combinations. The study explored in-plane loaded square piles compared against circular piles. From this comparison, it was seen that surface shape and sand density could induce different failure profiles.

It was found that the sand density and L/d ratio of the pile could have a significant impact on the percentage difference between the capacity of a square and circular pile. For example, a square and circular pile with the same cross-sectional area and L/d ratio was numerically loaded to failure in loose and dense sand conditions. It was found that when comparing the lateral capacity of a square and circular pile in loose sand conditions, the ratio between the ultimate load of the square pile to the circular pile was 1 for $L/d=10$ and 1.2 for $L/d=20$. When the density was increased to medium dense, the ratio of the square pile to circular pile ultimate lateral capacity was 1.1 for $L/d=10$ and 1.3 for $L/d=20$. This means that the increase in capacity between the square pile and circular pile is not just a function of the surface area (i.e. not a constant multiple). These trends were also observed in limited test data given by Ashour and Norris (2000).

It is also thought by this author that the pile shape and loading direction can impact on the pile capacity as well. For example, it is anticipated that an in-plane loaded square

pile may have a slightly higher capacity than a square pile loaded out-of-plane. The in-plane loaded square pile induces a bearing failure similar in pattern to that experienced below the base of a shallow foundation when axially loaded. Whereas an out-of-plane loaded square pile may act more like a wedge cutting through the sand body. In-plane and out-of-plane loading was not explored as part of the additional research but may provide an interesting small-scale research topic.

10.6 Design Examples

Oblique interaction charts were developed by this research. Two examples have been chosen to demonstrate the use of the oblique interaction charts for ultimate capacity and pile head displacement. The examples are shown in Sections 10.6.1 and 10.6.2.

10.6.1 Determining the Ultimate Load of an Example Pile

To demonstrate how to use the oblique interaction chart for ultimate load failure the following example pile has been chosen.

The pile in question is to support a 20 m light pole that has to provide light in a train car park. The pile case has the following characteristics:

- The light pole is made from concrete and has an inner diameter of 200 mm and an outer diameter of 400 mm. Therefore, the pole has an approximate factored dead load of 55 kN.
- Pile installation = bored pier
- Length = 6 m
- Diameter = 0.6 m

The pile is to be placed into a clayey sand soil with 80-90% sand and 10-20% clay. Given the presence of the clay, it is anticipated that the augered hole should stay open and allow the pier to be cast-in-place. The water level based on a single borehole is approximated to be at approximately 10 m below ground surface. The clayey sand had a average blow count of $N=30$.

From the above information it is assumed that the soil characteristics are as follows:

- Predominant soil type = sand
- Average blow count (N) = 30
- Assume the cohesion $c = 0$ kPa

Based on the constitutive correlations in Chapter 4, the sand has an approximate friction angle of 48° and Young modulus of 33 MPa.

Therefore, one would question what is the maximum horizontal load that may be applied to the pole, given the light pole is to be constructed in a cyclonic region?

It is assumed that the horizontal load due to wind forces acts through the centroid of the pole (i.e. at a distance of $20 \text{ m}/2 = 10 \text{ m}$ above the ground).

The ultimate failure of the pile is governed by the following equation:

$$\left(\frac{C_{\text{design}} * \text{FOS}}{C_{\text{ult}}} \right)^{1.2} + \left(\frac{L_{\text{design}} * \text{FOS}}{L_{\text{ult}}} \right)^{1.2} + \left(\frac{M_{\text{design}} * \text{FOS}}{M_{\text{ult}}} \right)^{1.2} \leq 1 \quad (10.4)$$

Assume : C_{design} = design compression load component = 55 kN

L_{design} = design lateral load component = H

M_{design} = design moment component = $10 \text{ m} * H$

C_{ult} = pure ultimate axial load = 1730 kN

L_{ult} = pure ultimate lateral load = 933 kN

M_{ult} = pure ultimate moment = 1250 kNm

FOS = 3

It is noted that the ultimate loads given above are estimated using traditional prediction methods.

Substituting the above into Equation 10.4 and allowing for a factor of safety of 3 gives:

$$\left(\frac{55 * 3}{1730}\right)^{1.2} + \left(\frac{H * 3}{933}\right)^{1.2} + \left(\frac{10 * H * 3}{1250}\right)^{1.2} \leq 1 \quad (10.5)$$

Solving Equation 10.5 results in:

$$H_{\text{design}} \leq 37 \text{ kN (including a FOS} = 3)$$

This means that if the design wind loads are greater than 37 kN the bored pier is insufficient and needs to be redesigned.

10.6.2 Determining the Pile Head Displacement of an Example Pile

In this example a pile has to support a working compression load of 400 kN and working lateral load of 131 kN. If we assume the pile and sand characteristics are the same as those given in Section 10.6.1, the estimation of pile head displacement under axial compression and lateral loads is as follows.

Firstly, the pile head displacement under pure compression load needs to be determined. It is assumed that the working load for the pure axial compression case is equal to the ultimate axial compression load divided by 3, i.e. this load should be in the linear elastic region of the load-displacement curve (Figure 9.4).

Therefore, the working load for the pure axial compression case is equal to $1730 \text{ kN}/3 = 577 \text{ kN}$. It was assumed that 88% of this working load is supported by the tip of the pile, and the skin friction along the shaft of the pile supports the remaining 12% of the load. Then it is estimated that the pile head displacement under these pure compression working loads is approximately 26 mm using traditional estimation techniques.

The lateral pile head deflection under pure lateral working loads needs to be determined as well. Again the working load for the pure lateral load case is assumed to be equal to $933 \text{ kN}/3 = 311 \text{ kN}$. The lateral pile head displacement under this working load is estimated to be approximately 16 mm using traditional methods.

Using the charts in Section 9.6, the pile head displacement due to the combination of the design loads can be estimated. The axial compression and lateral ratios need to be calculated using Figure 9.17. The axial and lateral ratio is equal to the design component divided by the pure case component. For example, the axial compression ratio is equal to $400/577 = 0.69$, and the lateral ratio is equal to $131/311 = 0.42$.

Using Figure 9.17, the axial displacement ratio is equal to 0.92 and the lateral displacement ratio is equal to 0.52. This means that the axial displacement of the pile head is approximately 0.92 times the pure axial case displacement. Similarly, the lateral pile head displacement is approximately 0.52 times the pure lateral case displacement. Hence the axial pile head displacement is $0.92 \times 26 \text{ mm} = 24 \text{ mm}$, and the lateral pile head displacement is $0.52 \times 16 \text{ mm} = 8 \text{ mm}$. The magnitude of the pile head displacement is, therefore, estimated to be $\sqrt{(24)^2 + (8)^2} \approx 26 \text{ mm}$.

CHAPTER 11: Conclusions and Recommendations

11.1 Conclusions and Recommendations for Shallow Foundations

The work in Chapters 2, 3 and 5 show that the techniques for predicting shallow foundation settlement may vary significantly from one technique to another. There are 40+ methods for predicting shallow foundation settlements, and this means several estimates are available for any given problem. This results in inconsistency from one predictor to the next predictor.

This research shows that the estimated settlements for four popular methods of shallow foundation prediction methods can be converted to a probability of failure. The probability of failure being the probability a method will exceed a design criterion. A statistical approach where the estimated settlement can be converted to a probability of failure provides a platform from which settlement techniques can be directly compared against each other.

Some recommendations for further research in this area include the following:

- Researchers have modified or added correction factors to existing settlement prediction methods to form hybrid methods. The reliability of a prediction model will depend on the correction factors used. A reliability study should be carried out on the hybrid methods to determine how corrections factors perform.
- A reliability study should be conducted on common methods used for the settlement prediction of a shallow foundation in granular soil. A booklet can then be made available to the geotechnical community to make them aware of the accuracy and reliability of settlement estimates.
- Reliability studies can be conducted on other geotechnical problems, such as slope stability, bearing capacity and predicted settlements in clay. This research can also be extended to review deep foundations (i.e. pile foundations) to allow conformity between predictions to be achieved.

The work in Chapters 4 and 5 shows that finite element modelling may be used as a tool for predicting the behaviour of shallow foundations. A numerical model for a stiff shallow footing was constructed in ABAQUS, which allowed a load-displacement curve to be estimated for 5 individual footings. The footings modelled were based on actual data from a symposium held by the Federal Highway Administration (Briaud and Gibbens, 1994). The comparisons between the model behaviour by this work and the models by 8 other participants of the symposium, showed the model constructed by the author was within the two top most accurate models. The results confirmed that the approach and correlations in Chapter 4 to define sand and footing characteristics were at least on the correct path, and may be applied with some confidence.

The numerical section of this research allowed the author to make conclusions regarding element type and sand characteristic correlations. The basic modelling techniques could then be applied in the numerical modelling of pile foundations, as discussed in Section 11.2.

11.2 Conclusions and Recommendations for Pile Foundations

The pile foundation section of this thesis focuses on defining the influence of multiple load combinations acting simultaneously on the response of a pile. Given the limitations of small scale laboratory testing of piles and the expense of large scale testing, numerical modelling using a verified model was considered to be a viable option. A numerical pile model was constructed in ABAQUS, which allowed the simulation of various piles under different loading scenarios, pile head fixity, pile installation technique, and changes in sand stiffness.

The first step of numerical modelling the simulated piles meant constructing the pile in ABAQUS code, and verifying its output against actual test data obtained from an external database. It was found during the construction of the model that the initial stress state, installation technique, pile-soil interface, and pile head fixity all influence the output of the model significantly. It is also noted that the initial stress field can have an impact on whether a converged solution can be obtained. The overall response of the pile head given by the developed model (Chapters 8 and 9) compared well against actual test data, and other prediction techniques. The work showed that the use of finite

element modelling for foundation response is a viable option provided the user knows the limitations of the model.

The results from the numerical modelling of the pile foundations under various load combinations (Chapter 9) showed the following trends:

- The ultimate axial lateral and moment capacity of the pile is reduced when axial, lateral and moment loads all act on a pile simultaneously. The resulting reduction due to the combination loads can be represented by a three-dimensional failure surface that gives limiting values for the design of axial, lateral, and moment loads acting on a pile. The failure surface is given in equation form in Chapters 9 and 10.
- From the numerical modelling where axial and lateral loads were present on the pile, it was found that the pile deflection in the axial direction increased as the ratio of axial load ratio (design axial load / ultimate axial load of pile) to lateral load ratio (design lateral load / ultimate lateral load of pile) increased. It was also found that the increase in the axial displacement did not increase linearly with the axial ratio. For example, when the axial ratio is 50% the pile head displacement was greater than 60% of the possible axial displacement once the pile is subjected to pure axial load. Similar trends were observed for the lateral pile head displacement when the lateral ratio was increased.
- From the modelling it was found that the benefits and disadvantages of changing the pile head fixity and pile installation technique didn't influence the overall trend of the non-dimensional failure plot for a pile under combined axial, lateral and moment loads. A discussion on this trend is given in Chapters 9 and 10.

Some recommendations for further research of piles include the following:

- Review the assumptions involved in the impact driven piles and confirm conclusions using a numerical model and actual test data, which simulates the pile being driven. This simulation should include investigating the impact of different hammers and pile shapes.

- Explore the impact on the proposed oblique interaction chart for piles with L/d ratios greater than 10, i.e. use other diameters apart from the 0.3m adopted for this research.
- Extend the research of pile response under combination loading into clay material. Some correlations are available for the reduction of the ultimate axial and lateral capacity of a pile installed in clay, due to a combination of loads acting in unison. However, the influence on the pile head displacement is still not clearly defined and requires further investigation.
- The influence of pile batter angle on the non-dimensional failure surface could also be further investigated. If the change in the pile batter angle has an impact on the overall non-dimensional failure surface, it may be possible to account for this using the influence factors in conjunction with the non-dimensional failure equation in this research.
- The work explored in this research may also be expanded to include pile groups.

Overall, this section of the research showed that the response of piles under combination loading is a complex problem. When modelling pile foundations it is important to model the pile-soil system as close to the real situation as possible. It is impossible to include all facets of the real life system into the model and the model itself is only an approximation. Yet it is considered necessary that the pile-soil interface, installation technique, pile head fixity, gravity field/initial stress field, and appropriate boundary conditions be accounted for in the model.

REFERENCES

- Alpan, I. (1964), "Estimating the Settlements of Foundations on Sands", Civil Engineering and Public Works Review, Grampian Ltd., Woolwich, London, SE18 6QH, England, Vol. 59, pp. 1415-1418.
- Anagnostopoulos, C. and Georgiadis, M. (1993), "Interaction of Axial and Lateral Pile Responses", Journal of Geotechnical Engineering, Vol. 119, No. 4, pp. 793-798.
- Ang and Tang (1975), Probability Concepts in Engineering Planning and Design, John Wiley and Sons Inc, New York, USA.
- Ashour, M. and Norris, G. (2000), "Modeling Lateral Soil-Pile Response Based on Soil-Pile Interaction", Journal of Geotechnical and Geoenvironmental Engineering, ASCE, Vol. 126, No. 5, pp. 420-428.
- Berardi, R. and Lancellotta, R. (1994), "Prediction of Settlements of Footings on Sand: Accuracy and Reliability", Proceedings of Settlement '94, Texas, ASCE, Geotechnical Special Publication 40, pp. 640-651.
- Bolton, M. D. (1986), "The Strength and Dilatancy of Sands", Geotechnique, Vol. 36, No. 1, pp. 65-78.
- Briaud, J. L. and Gibbens, R. M. (1994), Predicted and Measured Behaviour of Five Spread Footings on Sand, Geotechnical Special Publication 41, Texas, ASCE.
- Broms, B. B. (1964), "Lateral Resistance of Piles in Cohesionless Soils", Journal of Soil Mechanics and Foundation Division, ASCE, Vol. 90, pp. 123-156.
- Broms, B. B. (1965), Discussion to paper by Y. Yoshimi, Journal of Soil Mechanics and Foundation Division, ASCE, Vol. 91, No. 4, pp. 199-205.

- Budhu, M. (2000), *Soil Mechanics and Foundations*, John Wiley and Sons Inc, New York, USA.
- Burland, J. B. and Burbidge, M. C. (1985), "Settlement of Foundations on Sand and Gravel", *Proceedings Institution of Civil Engineers*, U.K., Vol. 78, No. 1, pp. 1325-1381.
- Callanan, J. F. and Kulhawy, F. H. (1985), "Evaluation of Procedures for Predicting Foundation Uplift Movements", Report EL4107, Electric Power Research Institute, Palo Alto, pp. 124.
- Cernica, J. N. (1995), *Geotechnical Engineering: Foundation Design*, John Wiley and Sons Inc, New York, USA.
- Chen, F. H. (1988), *Foundations on Expansive Soils*, Elsevier, Amsterdam.
- Chen, L. T. and Poulos, H. G. (1997), "Piles Subjected to Lateral Soil Movements", *Journal of Geotechnical and Geoenvironmental Engineering*, Vol. 123, No. 9, pp. 802-811.
- Chen, W. and Saleeb, A. (1983), *Constitutive Equations for Engineering Materials, Volume 1: Elasticity and Modeling*, John Wiley and Sons, Canada.
- Cook, R. D., Malkus, S. D., and Plesha, M. E., (1989), *Concepts and Applications of Finite Element Analysis*, 3rd Edition, John Wiley and Sons, New York.
- Coyle, H. M. and Reese, L. C. (1966), "Load Transfer for Axially Loaded Piles in Clay", *Journal of Soil Mechanics and Foundation Division*, ASCE, Vol. 92, pp. 1-26.
- Coyle, H. M. and Sulaiman, I. H. (1967), "Skin Friction for Steel Piles in Sand", *Journal of Soil Mechanics and Foundation Division*, ASCE, Vol. 93, pp. 261-278.
- Craig, R. F. (1992), *Soil Mechanics*, 5th Edition, E and FN Spon, London.

- D'Appolonia, D. J., D'Appolonia, E. and Brisette, R. F. (1970), "Settlement of Spread Footings in Sands", Journal of Soil Mechanics and Foundations Division, ASCE, Vol. 96, No. 2, pp.754-761.
- Das, B. (1999), Principles of Foundation Engineering, 4th Edition, PWS Publishing, Melbourne.
- Decourt, L. (1995), "Prediction of Load-Settlement Relationships for Foundations on the Basis of the SPT-T", Ciclo de Conference Intern, Leonardo Zeevaert, UNAM, Mexico, pp. 85-104.
- De Nicola, A. D. and Randolph, M. F. (1993), "Tensile and Compressive Shaft Capacity of Piles in Sand", Journal of Geotechnical Engineering, Vol. 119, No. 12, pp. 1952-1964.
- Douglas, D. J. (1986), "State-of-the-art," Ground Engineering, Vol. 19, No. 2, U.K., pp. 2-6.
- Eckersley, J. D., Graham, K. G. and Greensill, B. N. (1996), "Pullout Capacity of Short Piers with Oblique Loading – Experimental Results", Australian Geomechanics, Technical Paper 9607, pp. 71-79.
- Focht, J.A. (1967), Discussion to paper by Coyle and Reese, Journal of Soil Mechanics and Foundation Division, ASCE, Vol. 93, pp. 133-138.
- Frydman, S., Sha'al, B. and Mazurik, A. (1975), "Analysis of an Instrumented Laterally Loaded Pile", Proceedings of the 5th Regional Conference of Soil Mechanics and Foundation Engineering, Bangalore, India.
- Gleser, S. M. (1953), "Lateral Load Tests on Vertical Fixed-head and Free-Head Piles", ASTM, STP 154, pp.75-93.

- Graham, K. J. (1991), B.E. Thesis, An Investigation of Combined Uplift and Lateral Load Resistance of Short Bored Piers, James Cook University.
- Greensill, B. N. (1990), M.Eng.Sc. Thesis, An Investigation of Short Bored Piers Subjected to Combined Uplift and Lateral Loads, James Cook University.
- Hage-Chehade, F., Meimon, Y. and Shahrour, I. (1991), "Validation of FEM Calculations for Piles Under Lateral Loading", Computers and Structures, Vol. 41, No. 3, pp. 475-482.
- Harr, M. E. (1987), Reliability Based Design in Civil Engineering, McGraw-Hill, Inc.
- Harr, M. E. (1977), Mechanics of Particulate Media, McGraw- Hill.
- Hatanaka, M. and Uchinda, A. (1996), "Empirical Correlations Between Penetration Resistance and Internal Friction Angle of Sandy Soils", Soils and Foundations, Vol. 36, No. 4, pp. 1-10.
- Hibbitt, Karlsson and Soreson Inc. (2001), ABAQUS / Standard User's Manual, United States (Pawtucket), Hibbitt, Karlsson and Soreson Inc.
- Hoback, A. S. and Rujipakorn, D. E. (2004), "Prediction of Bearing Capacity of Large Drilled Piles in Nonhomogeneous Soil by Using 3D Finite Element Method", Electronic Journal Geotechnical Engineering, <http://www.ejge.com/2004/Ppr0464/Ppr0464.htm>.
- Ismael, N. F., (1989), "Field Tests on Bored Piles Subjected to Axial and Oblique Pull", Journal of Geotechnical Engineering, Vol. 15, No. 11, pp. 1588-1598.
- Jeyapalan, J. K. and Boehm, R. (1986), "Procedures for Predicting Settlements in Sands", Settlements of Shallow Foundations on Cohesionless Soils: Design and Performance, ASCE, pp. 1-22.

- Johnson, K. (1999), B.E. Thesis, Reliability Studies on the Settlement of a Shallow Foundation in Granular Soil, James Cook University.
- Johnson, K., Karunasena, W. and Sivakugan, N. (2001), "Modelling Pile-Soil Interaction Using Contact Surfaces", Proceedings First Asian Pacific Congress on Computational Mechanics, Sydney, pp. 375-380.
- Kulhawy, F. H. (1984), "Limiting Tip and Side Resistance: Fact or Fallacy?", Proceedings of the Symposium on the Analysis and Design of Pile Foundations, ASCE, San Francisco, pp. 80-98.
- Lehane, B. M. and Randolph, M. F. (2002), "Evaluation of a Minimum Base Resistance for Driven Pipe Piles in Siliceous Sand", Journal of Geotechnical and Geoenvironmental Engineering, Vol. 128, No. 3, pp. 198-205.
- Mabsout, M. E., Reese, L. C. and Tassoulas, J. L. (1995), "Study of Pile Driving by Finite-Element Method", Journal of Geotechnical Engineering, Vol. 121, No. 7, pp. 535-543.
- Maharaj, D. K. (2003), "Load-Deflection Response of Laterally Loaded Single Pile by Nonlinear Finite Element Analysis", Electronic Journal for Geotechnical Engineering, <http://www.ejge.com/2003/Ppr0342/Ppr0342.htm>.
- Meyerhof, G. G. (1959), "Compaction of Sands and Bearing Capacity of Piles", Journal of Soil Mechanics and Foundation Division, ASCE, Vol 85, No. 6, pp. 1-29.
- Meyerhof, G. G. (1961), "Compaction of Sands and Bearing Capacity of Piles", Transactions, ASCE, Vol. 126, No. 1, pp. 1292-1323.
- Meyerhof, G. G., and Adams J. I. (1968), "The Ultimate Uplift Capacity of Foundations", Canadian Geotechnical Engineering Division, ASCE, Vol. 5, pp. 225-244.

- Meyerhof, G. G. (1976), "Bearing Capacity and Settlement of Pile Foundations", Canadian Geotechnical Engineering Division, ASCE, Vol. 102, pp. 195-228.
- Meyerhof, G. G., Yalcin, A. S. and Marthur, S. K. (1983), "Ultimate Pile Capacity for Eccentric Inclined Load.", Journal of Geotechnical Engineering, ASCE, Vol. 109, No.3, pp. 408-423.
- Meyerhof, G. G. (1995), "Behaviour of Pile Foundations Under Special Loading Conditions: 1994 R. M. Hardy Keynote Address", Candian Geotechnical Journal, Vol. 32, No. 2, pp. 204-222.
- Mindlin, R. D. (1936), "Force at a Point in the Interior of a Semi-Infinite Solid", Physics 7, pp. 195.
- Mitchell, J. K. and Gardner, W. S. (1975), "Insitu Measurement of Volume Change Characteristics", Proceedings, Speciality Conference, ASCE, Vol. 2, pp. 279-345.
- Palmer, L. A. and Thompson, J. B. (1948), "The Earth Pressure and Deflection Along the Embedded Lengths of Piles Subjected to Lateral Thrusts", Proceedings 2nd International Conference of Soil Mechanics and Foundation Engineering, Rotterdam, Vol. 5, pp. 156-161.
- Peck, R. B., Hansen, W. E., and Thorburn, T. H. (1974), Foundations Engineering, 2nd Edition, New York, Wiley.
- Phoon, K. K., Quek, S. T., Chow, Y. K. and Lee, S. L. (1990), "Reliability Analysis of Pile Settlement", Journal of Geotechnical Engineering, Vol. 116, No. 11, pp. 1717-1735.
- Potts, D. M. and Zdravkovic, L. (1999), Finite Element Analysis in Geotechnical Engineering, Vol. 1:Theory, Thomas Telford Publishing.

- Potts, D. M. and Zdravkovic, L. (2001), *Finite Element Analysis in Geotechnical Engineering*, Vol. 2: Application, Thomas Telford Publishing.
- Poulos, H. G., (1971), "Behaviour of Laterally Loaded Piles – Single Piles", *Journal of Soil Mechanics and Foundation Division*, ASCE, Vol. 97, pp. 711-731.
- Poulos, H. G. (1975), "Settlement of Isolated Foundations", *Soil Mechanics Recent Developments*, Eds S. Viliappan, S Hain, I.K. Lee, William H Sellen, Pty, Zetland, pp. 181-212.
- Poulos, H.G., Carter J.P. and Small J.C., (2001), "Foundations and retaining structures – research and practice", *Proceedings of the 15th International Conference SMGE*, Istanbul, Vol. 4, pp. 2527-2606.
- Poulos, H. G. and Davis, E. H. (1975), "Prediction of Down Drag Forces in End-Bearing Piles", *Journal of Geotechnical Engineering Division*, ASCE, Vol. 101, pp. 189-204.
- Poulos, H. G. and Davis, E. H. (1980), *Pile Foundation Analysis and Design*, John Wiley and Sons, Inc, Toronto.
- Prideaux, M. L. (1998), B.E. Thesis, "An Investigation of Short Piles in a Sand Bed Subjected to Inclined Loading", James Cook University.
- Prevost, J. H., and Popescu, R. (1996), "Constitutive Relations for Soil Materials", *Electronic Journal of Geotechnical Engineering*.
<http://geotech.civen.okstate.edu/ejge/ppr9609/part11.htm>.
- Rajashree, S. S. and Sitharam, T. G. (2001), "Nonlinear Finite-Element Modelling of Batter Piles Under Lateral Load", *Journal of Geotechnical and Geoenvironmental Engineering*, Vol. 127, No. 7, pp. 604-612.

- Reese, L. C. and Cox, W. R. (1969), "Soil Behaviour from Analysis of Tests on Uninstrumented Piles under Lateral Loading", ASTM, STP444, pp. 160-176.
- Reese, L. C., Cox, W. R. and Koop, W. D. (1974), "Analysis of Laterally Loaded Piles in Sand", Offshore Technology Conference, Paper No OTC 2080, Houston, pp. 473-482.
- Schmertmann, J. H. (1970), "Static Cone to Compute Static Settlement over Sand", Journal of Soil Mechanics and Foundations Division, ASCE, Vol. 96, No. 3, pp. 1011-1043.
- Schmertmann, J. H. (1975), "Measurement of Insitu Shear Strength", Proceedings of Conference on Insitu Measurement of Soil Properties, ASCE, Vol. 2, pp. 57-138.
- Schmertmann, J. H., Hartmann, J. P. and Brown, P. R. (1978), "Improved Strain Influence Factor Diagrams," Journal of the Geotechnical Engineering Division, ASCE, Vol. 104, No. 8, pp. 1131-1135.
- Simonini, P. (1996), "Analysis of Behaviour of Sand Surrounding Pile Tips", Journal of Geotechnical Engineering, Vol. 122, No. 11, pp. 897-905.
- Sivakugan, N. and Johnson, K. (2002), "Probabilistic Design Chart for Settlements of Shallow Foundations in Granular Soils," Australian Civil Engineering Transactions, CE 43, pp. 19-24.
- Sullivan, W. R., Reese, L. C. and Fenske, C.W. (1979), "Unified Method for Analysis of Laterally Loaded Piles in Clay", Conference on Numerical Methods in Offshore Piling, London, Institution Civil Engineers, Paper No. 17.
- Tan, C. K. and Duncan, J. M. (1991), "Settlement of Footings on Sands – Accuracy and Reliability", Geotechnical Engineering Congress, Colorado, ASCE, Vol. 1, pp. 446-455.

- Terzaghi and Peck (1948), *Soil Mechanics in Engineering Practice*, John Wiley and Sons Inc, New York, USA.
- Terzaghi, K. and Peck, R. B. (1967), *Soil Mechanics in Engineering Practice*, 2nd Edition, John Wiley and Sons, New York, USA.
- Tomlinson, M. J. (1994), *Pile Design and Construction Practice*, 4th Edition, John Wiley and Sons Inc, Toronto.
- Trautmann, C. H. and Kulhawy, F. H. (1987), “CUFAD-A Computer Program for Compression and Uplift Foundation Analysis and Design”, Report EL-4540-CCM, Vol. 16, Electric Power Research Institute, Palo Alto, pp. 148.
- Trochanis, A., Bielak J. and Christiano, P. (1991), “Three-Dimensional Nonlinear Study of Piles”, *Journal of Geotechnical Engineering*, Vol. 117, pp. 429-447.
- Vesic, A. S. (1977), *Design of Pile Foundations*, National Conservative Highway Research Program Synthesis of Practice No. 42, Transportation Research Board, Washington, D.C.
- Wang, G. and Sitar, N. (2004), “Numerical Analysis of Piles in Elasto-Plastic Soils Under Axial Loading”, 17th ASCE Engineering Mechanics Conference, University of Delaware, Newark, D.E.
- Wolff, T. F. (1989), “Pile Capacity Prediction Using Parameter Functions”, Predicted and Observed Axial Behaviour of Piles - Results of a Pile Prediction Symposium, sponsored by the Geotechnical Engineering Division, ASCE, Evanston, IL, Special Publication, No.23, pp. 96-106.
- Wu, A. H., Kuhlemeyer, R. L. and To, C. W. (1989), “Validity of Smith Model in Pile Driving Analysis”, *Journal of Geotechnical Engineering*, Vol. 115, No. 9, pp. 1285-1301.

Yasufuku, N., Ochiai, H., Kaneshige, M., Kawamura, T. and Hirai, T. (2004), “Confining Effect in Geogrid-Reinforced Soil Related to Soil Dilatancy”, 3rd Asian Regional Conference on Geosynthetics,

http://www.geosynthetica.net/tech_docs/GeoAsia04Yasufuku.pdf

Zhang, L., McVay, M. C. and Lai, P. (1999), “Numerical Analysis of Laterally Loaded 3x3 to 7x3 Pile Group in Sands”, Journal of Geotechnical Geoenvironmental Engineering, Vol. 125, No. 11, pp. 936-946.

APPENDIX A: Probability of Failure - Shallow Foundations

---oooOOOooo---

This appendix is referred to in Chapter 3. It contains the tabulated results for the probabilistic analysis of four popular shallow foundation settlement methods. These tables represent the data sets used for the shallow foundation design charts, displayed in Figures 3.5 to 3.8.

Table A1: Statistical Parameters

	Terzaghi and Peck (1967)	Schmertmann et al. (1978)	Burland and Burbridge (1985)	Berardi and Lancellotta (1994)
α	0.49	0.71	0.91	0.79
β	1.77	2.72	3.03	2.65
a = minimum ratio	0.55	0.39	0.16	0
b = maximum ratio	14.29	11.3	6	4.33

The statistical parameters were determined by the author based on comparisons between predicted and actual values from real constructed shallow footings.

Table A2: Probability of failure for a design criterion of 15 mm settlement

Predicted Settlement (mm)	Settlement Ratio (Predicted Settlement/15mm)	p[actual settlement > 15 mm]			
		Terzaghi and Peck (1967)	Schmertmann et al. (1978)	Burland and Burbridge (1985)	Berardi and Lancellotta (1994)
0	0.000	0.000	0.000	0.000	0.000
1	0.067	0.000	0.000	0.000	0.083
2	0.133	0.000	0.000	0.000	0.141
3	0.200	0.000	0.000	0.030	0.192
4	0.267	0.000	0.000	0.072	0.238
5	0.333	0.000	0.000	0.111	0.281
5.5	0.367	0.000	0.000	0.130	0.301
6	0.400	0.000	0.015	0.148	0.321
7	0.467	0.000	0.063	0.182	0.358
7.5	0.500	0.000	0.082	0.199	0.376
8	0.533	0.000	0.098	0.216	0.394
9	0.600	0.089	0.129	0.248	0.427
9.5	0.633	0.114	0.142	0.263	0.443
10	0.667	0.134	0.156	0.279	0.459
11	0.733	0.167	0.181	0.308	0.489
11.5	0.767	0.182	0.193	0.323	0.503
12	0.800	0.195	0.204	0.337	0.517
13	0.867	0.218	0.226	0.364	0.545
13.5	0.900	0.229	0.237	0.378	0.558
14	0.933	0.239	0.247	0.391	0.571
15	1.000	0.259	0.267	0.417	0.596
15.5	1.033	0.268	0.277	0.429	0.607
16	1.067	0.276	0.286	0.442	0.619
17	1.133	0.293	0.305	0.466	0.642
18	1.200	0.308	0.322	0.489	0.663
19	1.267	0.323	0.339	0.511	0.684
20	1.333	0.337	0.356	0.533	0.703

Table A2 Continued: Probability of failure for a design criterion of 15 mm settlement

Predicted Settlement (mm)	Settlement Ratio (Predicted Settlement/15mm)	p[actual settlement > 15 mm]			
		Terzaghi and Peck (1967)	Schmertmann et al. (1978)	Burland and Burbidge (1985)	Berardi and Lancellotta (1994)
21	1.400	0.350	0.372	0.554	0.722
22	1.467	0.363	0.387	0.574	0.740
23	1.533	0.375	0.403	0.594	0.757
24	1.600	0.387	0.417	0.613	0.773
25	1.667	0.399	0.431	0.631	0.789
26	1.733	0.410	0.445	0.649	0.803
27	1.800	0.420	0.459	0.666	0.817
28	1.867	0.430	0.472	0.682	0.830
29	1.933	0.440	0.485	0.698	0.843
30	2.000	0.450	0.497	0.713	0.855
31	2.067	0.460	0.510	0.728	0.866
32	2.133	0.469	0.521	0.742	0.877
33	2.200	0.478	0.533	0.756	0.887
34	2.267	0.486	0.545	0.769	0.897
35	2.333	0.495	0.556	0.782	0.906
36	2.400	0.503	0.567	0.794	0.914
37	2.467	0.511	0.577	0.806	0.922
38	2.533	0.519	0.588	0.817	0.929
39	2.600	0.527	0.598	0.827	0.936
40	2.667	0.535	0.608	0.838	0.943
41	2.733	0.542	0.617	0.848	0.949
42	2.800	0.550	0.627	0.857	0.954
43	2.867	0.557	0.636	0.866	0.960
44	2.933	0.564	0.645	0.875	0.964
45	3.000	0.571	0.654	0.883	0.969
46	3.067	0.578	0.663	0.891	0.973
47	3.133	0.584	0.672	0.898	0.977
48	3.200	0.591	0.680	0.905	0.980
49	3.267	0.597	0.688	0.912	0.983
50	3.333	0.604	0.696	0.919	0.986
51	3.400	0.610	0.704	0.925	0.988
52	3.467	0.616	0.712	0.930	0.990
53	3.533	0.622	0.719	0.936	0.992
54	3.600	0.628	0.727	0.941	0.994
55	3.667	0.634	0.734	0.946	0.995
56	3.733	0.639	0.741	0.951	0.996
57	3.800	0.645	0.748	0.955	0.997
58	3.867	0.651	0.755	0.959	0.998
59	3.933	0.656	0.762	0.963	0.999
60	4.000	0.662	0.768	0.966	0.999

Table A3: Probability of failure for a design criterion of 20 mm settlement

Predicted Settlement (mm)	Settlement Ratio (Predicted Settlement/20mm)	p[actual settlement > 20 mm]			
		Terzaghi and Peck (1967)	Schmertmann et al. (1978)	Burland and Burbidge (1985)	Berardi and Lancellotta (1994)
0	0.000	0.000	0.000	0.000	0.000
1	0.050	0.000	0.000	0.000	0.066
2	0.100	0.000	0.000	0.000	0.113
3	0.150	0.000	0.000	0.000	0.154
4	0.200	0.000	0.000	0.030	0.192
5	0.250	0.000	0.000	0.062	0.227
5.5	0.275	0.000	0.000	0.077	0.244
6	0.300	0.000	0.000	0.092	0.260
7	0.350	0.000	0.000	0.120	0.291
7.5	0.375	0.000	0.000	0.134	0.306
8	0.400	0.000	0.015	0.148	0.321
9	0.450	0.000	0.053	0.174	0.349
9.5	0.475	0.000	0.068	0.187	0.363
10	0.500	0.000	0.082	0.199	0.376
11	0.550	0.000	0.106	0.224	0.402
11.5	0.575	0.063	0.118	0.236	0.415
12	0.600	0.089	0.129	0.248	0.427
13	0.650	0.125	0.149	0.271	0.451
13.5	0.675	0.139	0.159	0.282	0.463
14	0.700	0.152	0.168	0.293	0.474
15	0.750	0.175	0.187	0.315	0.496
15.5	0.775	0.185	0.195	0.326	0.507
16	0.800	0.195	0.204	0.337	0.517
17	0.850	0.213	0.221	0.358	0.538
18	0.900	0.229	0.237	0.378	0.558
19	0.950	0.244	0.252	0.398	0.577
20	1.000	0.259	0.267	0.417	0.596
21	1.050	0.272	0.281	0.435	0.613
22	1.100	0.285	0.295	0.454	0.631
23	1.150	0.297	0.309	0.472	0.647
24	1.200	0.308	0.322	0.489	0.663
25	1.250	0.320	0.335	0.506	0.679
26	1.300	0.330	0.348	0.522	0.694
27	1.350	0.341	0.360	0.538	0.708
28	1.400	0.350	0.372	0.554	0.722
29	1.450	0.360	0.384	0.569	0.736
30	1.500	0.369	0.395	0.584	0.749
31	1.550	0.378	0.406	0.599	0.761
32	1.600	0.387	0.417	0.613	0.773
33	1.650	0.396	0.428	0.627	0.785
34	1.700	0.404	0.438	0.640	0.796
35	1.750	0.412	0.449	0.653	0.807
36	1.800	0.420	0.459	0.666	0.817
37	1.850	0.428	0.469	0.678	0.827
38	1.900	0.436	0.478	0.690	0.837

Table A3 Continued: Probability of failure for a design criterion of 20 mm settlement

Predicted Settlement (mm)	Settlement Ratio (Predicted Settlement/20mm)	p[actual settlement > 20 mm]			
		Terzaghi and Peck (1967)	Schmertmann et al. (1978)	Burland and Burbidge (1985)	Berardi and Lancellotta (1994)
39	1.950	0.443	0.488	0.702	0.846
40	2.000	0.450	0.497	0.713	0.855
41	2.050	0.457	0.507	0.725	0.863
42	2.100	0.464	0.516	0.735	0.872
43	2.150	0.471	0.524	0.746	0.880
44	2.200	0.478	0.533	0.756	0.887
45	2.250	0.484	0.542	0.766	0.894
46	2.300	0.491	0.550	0.775	0.901
47	2.350	0.497	0.558	0.785	0.908
48	2.400	0.503	0.567	0.794	0.914
49	2.450	0.509	0.575	0.803	0.920
50	2.500	0.515	0.582	0.811	0.926
51	2.550	0.521	0.590	0.819	0.931
52	2.600	0.527	0.598	0.827	0.936
53	2.650	0.533	0.605	0.835	0.941
54	2.700	0.539	0.613	0.843	0.946
55	2.750	0.544	0.620	0.850	0.950
56	2.800	0.550	0.627	0.857	0.954
57	2.850	0.555	0.634	0.864	0.958
58	2.900	0.560	0.641	0.870	0.962
59	2.950	0.566	0.648	0.877	0.966
60	3.000	0.571	0.654	0.883	0.969

Table A4: Probability of failure for a design criterion of 25 mm settlement

Predicted Settlement (mm)	Settlement Ratio (Predicted Settlement/25 mm)	p[actual settlement > 25 mm]			
		Terzaghi and Peck (1967)	Schmertmann et al. (1978)	Burland and Burbidge (1985)	Berardi and Lancellotta (1994)
0	0.000	0.000	0.000	0.000	0.000
1	0.040	0.000	0.000	0.000	0.055
2	0.080	0.000	0.000	0.000	0.095
3	0.120	0.000	0.000	0.000	0.130
4	0.160	0.000	0.000	0.000	0.162
5	0.200	0.000	0.000	0.030	0.192
5.5	0.220	0.000	0.000	0.043	0.206
6	0.240	0.000	0.000	0.056	0.220
7	0.280	0.000	0.000	0.080	0.247
7.5	0.300	0.000	0.000	0.092	0.260
8	0.320	0.000	0.000	0.103	0.273
9	0.360	0.000	0.000	0.126	0.297
9.5	0.380	0.000	0.000	0.137	0.309
10	0.400	0.000	0.015	0.148	0.321
11	0.440	0.000	0.047	0.169	0.344
11.5	0.460	0.000	0.059	0.179	0.355
12	0.480	0.000	0.071	0.189	0.366
13	0.520	0.000	0.092	0.209	0.387
13.5	0.540	0.000	0.102	0.219	0.397
14	0.560	0.040	0.111	0.229	0.407
15	0.600	0.089	0.129	0.248	0.427
15.5	0.620	0.105	0.137	0.257	0.437
16	0.640	0.118	0.145	0.266	0.446
17	0.680	0.142	0.161	0.285	0.465
18	0.720	0.161	0.176	0.302	0.483
19	0.760	0.179	0.190	0.320	0.500
20	0.800	0.195	0.204	0.337	0.517
21	0.840	0.209	0.217	0.353	0.534
22	0.880	0.223	0.230	0.370	0.550
23	0.920	0.235	0.243	0.386	0.566
24	0.960	0.247	0.255	0.401	0.581
25	1.000	0.259	0.267	0.417	0.596
26	1.040	0.269	0.279	0.432	0.610
27	1.080	0.280	0.290	0.447	0.624
28	1.120	0.290	0.301	0.461	0.637
29	1.160	0.299	0.312	0.475	0.650
30	1.200	0.308	0.322	0.489	0.663
31	1.240	0.317	0.333	0.503	0.676
32	1.280	0.326	0.343	0.516	0.688
33	1.320	0.334	0.353	0.529	0.700
34	1.360	0.343	0.362	0.542	0.711
35	1.400	0.350	0.372	0.554	0.722
36	1.440	0.358	0.381	0.566	0.733
37	1.480	0.366	0.390	0.578	0.743
38	1.520	0.373	0.400	0.590	0.754
39	1.560	0.380	0.408	0.602	0.764

Table A4 Continued: Probability of failure for a design criterion of 25 mm settlement

Predicted Settlement (mm)	Settlement Ratio (Predicted Settlement/25 mm)	p[actual settlement > 25 mm]			
		Terzaghi and Peck (1967)	Schmertmann et al. (1978)	Burland and Burbidge (1985)	Berardi and Lancellotta (1994)
40	1.600	0.387	0.417	0.613	0.773
41	1.640	0.394	0.426	0.624	0.783
42	1.680	0.401	0.434	0.635	0.792
43	1.720	0.407	0.443	0.645	0.800
44	1.760	0.414	0.451	0.656	0.809
45	1.800	0.420	0.459	0.666	0.817
46	1.840	0.426	0.467	0.676	0.825
47	1.880	0.432	0.475	0.686	0.833
48	1.920	0.438	0.482	0.695	0.841
49	1.960	0.444	0.490	0.704	0.848
50	2.000	0.450	0.497	0.713	0.855
51	2.040	0.456	0.505	0.722	0.862
52	2.080	0.461	0.512	0.731	0.868
53	2.120	0.467	0.519	0.740	0.875
54	2.160	0.472	0.526	0.748	0.881
55	2.200	0.478	0.533	0.756	0.887
56	2.240	0.483	0.540	0.764	0.893
57	2.280	0.488	0.547	0.772	0.898
58	2.320	0.493	0.553	0.779	0.904
59	2.360	0.498	0.560	0.787	0.909
60	2.400	0.503	0.567	0.794	0.914

Table A5: Probability of failure for a design criterion of 30 mm settlement

Predicted Settlement (mm)	Settlement Ratio (Predicted Settlement/30 mm)	p[actual settlement > 30 mm]			
		Terzaghi and Peck (1967)	Schmertmann et al. (1978)	Burland and Burbidge (1985)	Berardi and Lancellotta (1994)
0	0.000	0.000	0.000	0.000	0.000
1	0.033	0.000	0.000	0.000	0.048
2	0.067	0.000	0.000	0.000	0.083
3	0.100	0.000	0.000	0.000	0.113
4	0.133	0.000	0.000	0.000	0.141
5	0.167	0.000	0.000	0.006	0.167
5.5	0.183	0.000	0.000	0.018	0.180
6	0.200	0.000	0.000	0.030	0.192
7	0.233	0.000	0.000	0.052	0.216
7.5	0.250	0.000	0.000	0.062	0.227
8	0.267	0.000	0.000	0.072	0.238
9	0.300	0.000	0.000	0.092	0.260
9.5	0.317	0.000	0.000	0.102	0.271
10	0.333	0.000	0.000	0.111	0.281
11	0.367	0.000	0.000	0.130	0.301
11.5	0.383	0.000	0.000	0.139	0.311
12	0.400	0.000	0.015	0.148	0.321
13	0.433	0.000	0.042	0.165	0.340
13.5	0.450	0.000	0.053	0.174	0.349
14	0.467	0.000	0.063	0.182	0.358
15	0.500	0.000	0.082	0.199	0.376
15.5	0.517	0.000	0.090	0.208	0.385
16	0.533	0.000	0.098	0.216	0.394
17	0.567	0.052	0.114	0.232	0.411
18	0.600	0.089	0.129	0.248	0.427
19	0.633	0.114	0.142	0.263	0.443
20	0.667	0.134	0.156	0.279	0.459
21	0.700	0.152	0.168	0.293	0.474
22	0.733	0.167	0.181	0.308	0.489
23	0.767	0.182	0.193	0.323	0.503
24	0.800	0.195	0.204	0.337	0.517
25	0.833	0.207	0.215	0.351	0.531
26	0.867	0.218	0.226	0.364	0.545
27	0.900	0.229	0.237	0.378	0.558
28	0.933	0.239	0.247	0.391	0.571
29	0.967	0.249	0.257	0.404	0.583
30	1.000	0.259	0.267	0.417	0.596
31	1.033	0.268	0.277	0.429	0.607
32	1.067	0.276	0.286	0.442	0.619
33	1.100	0.285	0.295	0.454	0.631
34	1.133	0.293	0.305	0.466	0.642
35	1.167	0.301	0.313	0.477	0.653
36	1.200	0.308	0.322	0.489	0.663
37	1.233	0.316	0.331	0.500	0.674
38	1.267	0.323	0.339	0.511	0.684
39	1.300	0.330	0.348	0.522	0.694

Table A5 Continued: Probability of failure for a design criterion of 30 mm settlement

Predicted Settlement (mm)	Settlement Ratio (Predicted Settlement/30 mm)	p[actual settlement > 30 mm]			
		Terzaghi and Peck (1967)	Schmertmann et al. (1978)	Burland and Burbidge (1985)	Berardi and Lancellotta (1994)
40	1.333	0.337	0.356	0.533	0.703
41	1.367	0.344	0.364	0.544	0.713
42	1.400	0.350	0.372	0.554	0.722
43	1.433	0.357	0.380	0.564	0.731
44	1.467	0.363	0.387	0.574	0.740
45	1.500	0.369	0.395	0.584	0.749
46	1.533	0.375	0.403	0.594	0.757
47	1.567	0.381	0.410	0.604	0.765
48	1.600	0.387	0.417	0.613	0.773
49	1.633	0.393	0.424	0.622	0.781
50	1.667	0.399	0.431	0.631	0.789
51	1.700	0.404	0.438	0.640	0.796
52	1.733	0.410	0.445	0.649	0.803
53	1.767	0.415	0.452	0.657	0.810
54	1.800	0.420	0.459	0.666	0.817
55	1.833	0.425	0.465	0.674	0.824
56	1.867	0.430	0.472	0.682	0.830
57	1.900	0.436	0.478	0.690	0.837
58	1.933	0.440	0.485	0.698	0.843
59	1.967	0.445	0.491	0.706	0.849
60	2.000	0.450	0.497	0.713	0.855

Table A6: Probability of failure for a design criterion of 35 mm settlement

Predicted Settlement (mm)	Settlement Ratio (Predicted Settlement/35 mm)	p[actual settlement > 35 mm]			
		Terzaghi and Peck (1967)	Schmertmann et al. (1978)	Burland and Burbidge (1985)	Berardi and Lancellotta (1994)
0	0.000	0.000	0.000	0.000	0.000
1	0.029	0.000	0.000	0.000	0.043
2	0.057	0.000	0.000	0.000	0.073
3	0.086	0.000	0.000	0.000	0.100
4	0.114	0.000	0.000	0.000	0.125
5	0.143	0.000	0.000	0.000	0.149
5.5	0.157	0.000	0.000	0.000	0.160
6	0.171	0.000	0.000	0.010	0.171
7	0.200	0.000	0.000	0.030	0.192
7.5	0.214	0.000	0.000	0.039	0.202
8	0.229	0.000	0.000	0.049	0.213
9	0.257	0.000	0.000	0.066	0.232
9.5	0.271	0.000	0.000	0.075	0.242
10	0.286	0.000	0.000	0.084	0.251
11	0.314	0.000	0.000	0.100	0.269
11.5	0.329	0.000	0.000	0.108	0.278
12	0.343	0.000	0.000	0.116	0.287
13	0.371	0.000	0.000	0.132	0.304
13.5	0.386	0.000	0.000	0.140	0.313
14	0.400	0.000	0.015	0.148	0.321
15	0.429	0.000	0.039	0.163	0.337
15.5	0.443	1.000	0.049	0.170	0.345
16	0.457	0.000	0.058	0.178	0.353
17	0.486	0.000	0.074	0.192	0.369
18	0.514	0.000	0.089	0.206	0.384
19	0.543	0.000	0.103	0.220	0.399
20	0.571	0.059	0.116	0.234	0.413
21	0.600	0.089	0.129	0.248	0.427
22	0.629	0.111	0.141	0.261	0.441
23	0.657	0.129	0.152	0.274	0.454
24	0.686	0.145	0.163	0.287	0.468
25	0.714	0.159	0.174	0.300	0.480
26	0.743	0.172	0.184	0.312	0.493
27	0.771	0.183	0.194	0.325	0.505
28	0.800	0.195	0.204	0.337	0.517
29	0.829	0.205	0.214	0.349	0.529
30	0.857	0.215	0.223	0.360	0.541
31	0.886	0.224	0.232	0.372	0.552
32	0.914	0.234	0.241	0.383	0.563
33	0.943	0.242	0.250	0.395	0.574
34	0.971	0.251	0.259	0.406	0.585
35	1.000	0.259	0.267	0.417	0.596
36	1.029	0.266	0.275	0.428	0.606
37	1.057	0.274	0.283	0.438	0.616
38	1.086	0.281	0.291	0.449	0.626
39	1.114	0.288	0.299	0.459	0.635

Table A6 Continued: Probability of failure for a design criterion of 35 mm settlement

Predicted Settlement (mm)	Settlement Ratio (Predicted Settlement/35 mm)	p[actual settlement > 35 mm]			
		Terzaghi and Peck (1967)	Schmertmann et al. (1978)	Burland and Burbidge (1985)	Berardi and Lancellotta (1994)
40	1.143	0.295	0.307	0.469	0.645
41	1.171	0.302	0.315	0.479	0.654
42	1.200	0.308	0.322	0.489	0.663
43	1.229	0.315	0.330	0.499	0.672
44	1.257	0.321	0.337	0.508	0.681
45	1.286	0.327	0.344	0.518	0.690
46	1.314	0.333	0.351	0.527	0.698
47	1.343	0.339	0.358	0.536	0.706
48	1.371	0.345	0.365	0.545	0.714
49	1.400	0.350	0.372	0.554	0.722
50	1.429	0.356	0.379	0.563	0.730
51	1.457	0.361	0.385	0.572	0.737
52	1.486	0.367	0.392	0.580	0.745
53	1.514	0.372	0.398	0.588	0.752
54	1.543	0.377	0.405	0.597	0.759
55	1.571	0.382	0.411	0.605	0.766
56	1.600	0.387	0.417	0.613	0.773
57	1.629	0.392	0.423	0.621	0.780
58	1.657	0.397	0.429	0.629	0.786
59	1.686	0.402	0.435	0.636	0.793
60	1.714	0.406	0.441	0.644	0.799

Table A7: Probability of failure for a design criterion of 40 mm settlement

Predicted Settlement (mm)	Settlement Ratio (Predicted Settlement/40 mm)	p[actual settlement > 40 mm]			
		Terzaghi and Peck (1967)	Schmertmann et al. (1978)	Burland and Burbidge (1985)	Berardi and Lancellotta (1994)
0	0.000	0.000	0.000	0.000	0.000
1	0.025	0.000	0.000	0.000	0.038
2	0.050	0.000	0.000	0.000	0.066
3	0.075	0.000	0.000	0.000	0.090
4	0.100	0.000	0.000	0.000	0.113
5	0.125	0.000	0.000	0.000	0.134
5.5	0.138	0.000	0.000	0.000	0.144
6	0.150	0.000	0.000	0.000	0.154
7	0.175	0.000	0.000	0.012	0.174
7.5	0.188	0.000	0.000	0.021	0.183
8	0.200	0.000	0.000	0.030	0.192
9	0.225	0.000	0.000	0.046	0.210
9.5	0.238	0.000	0.000	0.054	0.219
10	0.250	0.000	0.000	0.062	0.227
11	0.275	0.000	0.000	0.077	0.244
11.5	0.288	0.000	0.000	0.085	0.252
12	0.300	0.000	0.000	0.092	0.260
13	0.325	0.000	0.000	0.106	0.276
13.5	0.338	0.000	0.000	0.113	0.284
14	0.350	0.000	0.000	0.120	0.291
15	0.375	0.000	0.000	0.134	0.306
15.5	0.388	0.000	0.000	0.141	0.314
16	0.400	0.000	0.015	0.148	0.321
17	0.425	0.000	0.036	0.161	0.335
18	0.450	0.000	0.053	0.174	0.349
19	0.475	0.000	0.068	0.187	0.363
20	0.500	0.000	0.082	0.199	0.376
21	0.525	0.000	0.094	0.212	0.389
22	0.550	0.000	0.106	0.224	0.402
23	0.575	0.063	0.118	0.236	0.415
24	0.600	0.089	0.129	0.248	0.427
25	0.625	0.108	0.139	0.259	0.439
26	0.650	0.125	0.149	0.271	0.451
27	0.675	0.139	0.159	0.282	0.463
28	0.700	0.152	0.168	0.293	0.474
29	0.725	0.164	0.178	0.305	0.485
30	0.750	0.175	0.187	0.315	0.496
31	0.775	0.185	0.195	0.326	0.507
32	0.800	0.195	0.204	0.337	0.517
33	0.825	0.204	0.212	0.347	0.528
34	0.850	0.213	0.221	0.358	0.538
35	0.875	0.221	0.229	0.368	0.548
36	0.900	0.229	0.237	0.378	0.558
37	0.925	0.237	0.244	0.388	0.568
38	0.950	0.244	0.252	0.398	0.577

Table A7 Continued: Probability of failure for a design criterion of 40 mm settlement

Predicted Settlement (mm)	Settlement Ratio (Predicted Settlement/40 mm)	p[actual settlement > 40 mm]			
		Terzaghi and Peck (1967)	Schmertmann et al. (1978)	Burland and Burbidge (1985)	Berardi and Lancellotta (1994)
39	0.975	0.252	0.260	0.407	0.586
40	1.000	0.259	0.267	0.417	0.596
41	1.025	0.265	0.274	0.426	0.605
42	1.050	0.272	0.281	0.435	0.613
43	1.075	0.278	0.288	0.445	0.622
44	1.100	0.285	0.295	0.454	0.631
45	1.125	0.291	0.302	0.463	0.639
46	1.150	0.297	0.309	0.472	0.647
47	1.175	0.303	0.316	0.480	0.655
48	1.200	0.308	0.322	0.489	0.663
49	1.225	0.314	0.329	0.497	0.671
50	1.250	0.320	0.335	0.506	0.679
51	1.275	0.325	0.341	0.514	0.686
52	1.300	0.330	0.348	0.522	0.694
53	1.325	0.335	0.354	0.530	0.701
54	1.350	0.341	0.360	0.538	0.708
55	1.375	0.346	0.366	0.546	0.715
56	1.400	0.350	0.372	0.554	0.722
57	1.425	0.355	0.378	0.562	0.729
58	1.450	0.360	0.384	0.569	0.736
59	1.475	0.365	0.389	0.577	0.742
60	1.500	0.369	0.395	0.584	0.749

APPENDIX B: Texas '94 Symposium SPT Results and Interpretation

---oooOOOooo---

This appendix is referred to in Chapter 5. It contains the SPT results and constitutive properties used in the ABAQUS shallow foundation FEM models, constructed as part of this work. The SPT locations are shown in Figure 5.1(b).

The symbols used in this Appendix are as follows:

C_{ER} = hammer efficiency factor

C_N = overburden correction factor

N_{60} = blow count corrected for hammer efficiency

N_1 = blow count corrected for overburden

$(N_1)_{60}$ = blow count corrected for hammer efficiency and overburden

APPENDIX B: Texas '94 Symposium SPT Results and Interpretation

Footing 1 3 m * 3 m
SPT 3

Depth (m)	Layer Depth (m)	Blow Count (1st 150 mm)	Blow Count (2nd 150 mm)	Blow Count (3rd 150 mm)	Blow Count (N)	Energy Correction (C_{er})	Overburden Correction (C_N)	N_{60}	N_1	$(N_1)_{60}$
0.3	0.3	5	5	8	13	1	4.0	13	52	52
0.9	0.6	4	8	10	18	1	2.3	18	41	41
1.5	0.6	6	11	14	25	1	1.8	25	45	45
2.1	0.6	6	9	8	17	1	1.5	17	26	26
2.7	0.6	6	8	10	18	1	1.3	18	24	24
3.6	0.9	4	9	10	19	1	1.2	19	22	22
4.8	1.2	6	12	14	26	1	1.0	26	26	26
5.7	0.9	7	11	11	22	1	0.9	22	20	20
7.2	1.5	6	9	10	19	1	0.8	19	15	15
8.7	1.5	3	5	5	10	1	0.7	10	7	7
10.2	1.5	11	20	24	44	1	0.7	44	30	30
11.7	1.5	43	48	51	99	1	0.6	99	63	63
13.2	1.5	14	18	28	46	1	0.6	46	28	28
14.7	1.5	13	15	21	36	1	0.6	36	21	21

Layer 1	N_1	19	average	Layer 2	N_1	42	average	<div style="background-color: #cccccc; width: 20px; height: 10px; display: inline-block;"></div> Neglected Layer
	$(N_1)_{60}$	20	average		$(N_1)_{60}$	26	average	
	E (MPa)	25			E (MPa)	43		
	ϕ (deg)	40			ϕ (deg)	43		
	ψ (deg)	7			ψ (deg)	10		

Note: a list of symbols for this appendix is given on the Appendix B title page (pp. 260)

APPENDIX B: Texas '94 Symposium SPT Results and Interpretation

Footing 2 1.5 m * 1.5 m

SPT 4

Depth (m)	Layer Depth (m)	Blow Count (1st 150 mm)	Blow Count (2nd 150 mm)	Blow Count (3rd 150 mm)	Blow Count (N)	Energy Correction (C_{er})	Overburden Correction (C_N)	N_{60}	N_1	$(N_1)_{60}$
0.3	0.3	3	4	7	11	1	4.0	11	44	44
0.9	0.6	5	8	7	15	1	2.3	15	35	35
1.5	0.6	5	8	10	18	1	1.8	18	32	32
2.1	0.6	5	8	9	17	1	1.5	17	26	26
2.7	0.6	5	8	8	16	1	1.3	16	21	21
3.6	0.9	6	8	7	15	1	1.2	15	17	17
4.8	1.2	8	7	7	14	1	1.0	14	14	14
5.7	0.9	6	8	9	17	1	0.9	17	16	16
7.2	1.5	8	8	8	16	1	0.8	16	13	13
8.7	1.5	5	9	11	20	1	0.7	20	15	15
10.2	1.5	11	23	27	50	1	0.7	50	34	34
11.7	1.5	21	31	39	70	1	0.6	70	45	45
13.2	1.5	14	21	32	53	1	0.6	53	32	32
14.7	1.5	17	23	37	60	1	0.6	60	34	34

Layer 1	N_1	17	average	Layer 2	N_1	54	average	Neglected Layer
	$(N_1)_{60}$	17			$(N_1)_{60}$	33		
	E (MPa)	23			E (MPa)	52		
	ϕ (deg)	38			ϕ (deg)	46		
	ψ (deg)	5			ψ (deg)	13		

Note: a list of symbols for this appendix is given on the Appendix B title page (pp. 260)

APPENDIX B: Texas '94 Symposium SPT Results and Interpretation

Footing 3 3 m * 3 m

SPT 1

Depth (m)	Layer Depth (m)	Blow Count (1st 150 mm)	Blow Count (2nd 150 mm)	Blow Count (3rd 150 mm)	Blow Count (N)	Energy Correction (C_{er})	Overburden Correction (C_N)	N_{60}	N_1	$(N_1)_{60}$
0.3	0.3	4	5	6	11	1	4.0	11	44	44
0.9	0.6	7	9	14	23	1	2.3	23	53	53
1.5	0.6	13	18	12	30	1	1.8	30	54	54
2.1	0.6	6	10	11	21	1	1.5	21	32	32
2.7	0.6	8	10	13	23	1	1.3	23	31	31
4.2	1.5	11	14	14	28	1	1.1	28	30	30
5.7	1.5	9	15	19	34	1	0.9	34	31	31
7.2	1.5	8	8	9	17	1	0.8	17	14	14
8.7	1.5	4	5	8	13	1	0.7	13	10	10
10.2	1.5	10	20	34	54	1	0.7	54	37	37
11.7	1.5	19	29	47	76	1	0.6	76	49	49
13.2	1.5	14	19	21	40	1	0.6	40	24	24
14.7	1.5	15	22	31	53	1	0.6	53	30	30

Layer 1	N_1	23	average	Layer 2	N_1	49	average	Neglected Layer
	$(N_1)_{60}$	25	average		$(N_1)_{60}$	30	average	
	E (MPa)	28			E (MPa)	48		
	ϕ (deg)	42			ϕ (deg)	44		
	ψ (deg)	9			ψ (deg)	11		


Note: a list of symbols for this appendix is given on the Appendix B title page (pp. 260)

APPENDIX B: Texas '94 Symposium SPT Results and Interpretation

Footing 4 2.5 m * 2.5 m

SPT 5

Depth (m)	Layer Depth (m)	Blow Count (1st 150 mm)	Blow Count (2nd 150 mm)	Blow Count (3rd 150 mm)	Blow Count (N)	Energy Correction (C_{er})	Overburden Correction (C_N)	N_{60}	N_1	$(N_1)_{60}$
0.3	0.3	4	5	6	11	1	4.0	11	44	44
0.9	0.6	5	7	8	15	1	2.3	15	35	35
1.5	0.6	6	10	10	20	1	1.8	20	36	36
2.1	0.6	4	8	11	19	1	1.5	19	29	29
2.7	0.6	4	7	9	16	1	1.3	16	21	21
3.6	0.9	4	7	9	16	1	1.2	16	18	18
4.8	1.2	8	12	15	27	1	1.0	27	27	27
5.7	0.9	6	7	11	18	1	0.9	18	16	16
7.2	1.5	4	9	7	16	1	0.8	16	13	13
8.7	1.5	4	12	13	25	1	0.7	25	19	19
10.2	1.5	12	33	31	64	1	0.7	64	44	44
11.7	1.5	11	17	21	38	1	0.6	38	24	24
13.2	1.5	10	14	22	36	1	0.6	36	22	22
14.7	1.5	11	12	27	39	1	0.6	39	22	22

Layer 1	N_1	24	average	 Neglected Layer
	$(N_1)_{60}$	19	average	
	E (MPa)	29		
	ϕ (deg)	39		
	ψ (deg)	6		

Note: a list of symbols for this appendix is given on the Appendix B title page (pp. 260)

APPENDIX B: Texas '94 Symposium SPT Results and Interpretation

Footing 5 1.5 m * 1.5 m

SPT 6

Depth (m)	Layer Depth (m)	Blow Count (1st 150 mm)	Blow Count (2nd 150 mm)	Blow Count (3rd 150 mm)	Blow Count (N)	Energy Correction (C_{er})	Overburden Correction (C_N)	N_{60}	N_1	$(N_1)_{60}$
0.3	0.3	6	6	7	13	1	4.0	13	52	52
0.9	0.6	6	8	11	19	1	2.3	19	44	44
1.5	0.6	5	9	9	18	1	1.8	18	32	32
2.1	0.6	4	7	6	13	1	1.5	13	20	20
2.7	0.6	4	7	7	14	1	1.3	14	19	19
3.6	0.9	11	11	15	26	1	1.2	26	30	30
4.8	1.2	5	9	14	23	1	1.0	23	23	23
5.7	0.9	5	9	11	20	1	0.9	20	18	18
7.2	1.5	7	13	15	28	1	0.8	28	23	23
8.7	1.5	3	4	4	8	1	0.7	8	6	6
10.2	1.5	9	20	29	49	1	0.7	49	34	34
11.7	1.5	12	20	31	51	1	0.6	51	33	33
13.2	1.5	16	18	35	53	1	0.6	53	32	32
14.7	1.5	17	21	33	54	1	0.6	54	31	31

Layer 1	N_1	19	average	Layer 2	N_1	52	average	Neglected Layer
	$(N_1)_{60}$	20	average		$(N_1)_{60}$	32	average	
	E (MPa)	25			E (MPa)	50		
	ϕ (deg)	40			ϕ (deg)	45		
	ψ (deg)	7			ψ (deg)	12		

Note: a list of symbols for this appendix is given on the Appendix B title page (pp. 260)

APPENDIX C: Small-Scale Model Test Pile Procedures

---oooOOOooo---

This appendix is referred to in Chapter 7. It contains a detailed test procedure used for the small-scale pile testing conducted as part of these works. The testing was performed in the structures/hydrology laboratory at James Cook University.

Table C1: Small-scale model pile test procedure for axial loads

Loading Scenario	Procedure Used
<p>Summary of Axial Load Test</p>	<p><i>Step 1.</i></p> <p>The main loading frame was placed on the tank so that it was straddling the pile to be tested. The frame was clamped securely to the tank using four ‘G’ clamps, and this in turn restrained the loading apparatus making it rigid with the tank. An overhead crane positioned the hydraulic jack above the tank. The hydraulic ram was then clamped onto the main loading frame in four places using ‘G’ clamps, thus restraining any vertical and horizontal movement. This resulted in a fully rigid loading mechanism with the only moving part being the actual ram. The jack was fitted with the loading attachment that slotted into the axial loading cap and put on the pile.</p> <p><i>Step 2.</i></p> <p>The extensometer was fitted to the side of the hydraulic ram, and the ram lowered so that it was only touching the pile cap. The extensometer was then zeroed and the initial readings of load and displacement recorded. The model piles were subjected to a steadily increasing load until 10 mm displacement was reached. The readings were recorded at every 0.1 mm to 0.5 mm settlement.</p> <p><i>Step 3.</i></p> <p>The load was released when 10 mm settlement was reached, and the pile was allowed to stand free for a minimum of 15 minutes so residual stresses could ease. Thereafter, the ram was lowered onto the pile cap and readings taken before the load was re-applied. The pile was loaded until 20 mm settlement was reached, and the load was released for a minimum of 15 minutes once 20 mm was attained. The ram was lowered and final readings taken.</p>

Table C1 Continued: Small-scale model pile test procedure for axial loads

Loading Scenario	Procedure Used
Summary of Axial Load Test	<i>Step 4.</i> The main loading frame and hydraulic ram were unclamped and removed. The surrounding sand and model pile were inspected for any peculiarities and sand movements. The model pile was removed by hand and the resulting indentation in the sand was recorded before proceeding onto the next model pile test.

Table C2: Small scale model pile test procedure for oblique loads

Loading Scenario	Procedure Used
<p>Summary of Oblique Load Test</p>	<p><i>Step 1.</i></p> <p>The main loading frame was clamped securely in place as described in the axial loading test. The fully assembled oblique loading apparatus with extensometer was positioned and clamped to the loading frame. The special oblique loading cap was fitted to the pile head.</p> <p><i>Step 2.</i></p> <p>The bolt at the end of the loading mechanism was placed neatly into the pile cap, and the extensometer was zeroed and initial readings recorded. Loading commenced by turning the handle at the end of the threaded rod, that in turn displaced the pile head. The pile was loaded in displacement increments of 0.5 mm until 10 mm was reached, then 1 mm increments until 20 mm was reached, then 2.5 mm increments and stopping at 30 mm total displacement.</p> <p><i>Step 3.</i></p> <p>The loaded pile and surrounding soil were examined for any irregularities and movements. The load was released by turning the handle in the opposite direction to loading. Then the load was completely released and the loading apparatus removed. The pile was removed manually and the resulting indentation measurements recorded before the next pile was loaded.</p>

Table C3: Small scale model pile test procedure for lateral loads

Loading Scenario	Procedure Used
<p>Summary of Horizontal Load Test</p>	<p>The horizontal load was applied by a cable and pulley system attached to a loading bin, as opposed to previous loading scenarios. Neither the load nor displacement could be increased in regular increments, due to the limitations in the apparatus. The consistency in increment was attempted by dropping similar amounts of lead shot into the load bin, and this method was considered adequate and therefore adopted. The following procedure was reproduced for each horizontal load test in all three-soil cases.</p> <p><i>Step 1.</i></p> <p>The pulley frame was placed over the model pile to be tested, and the frame was secured to the tank with two ‘G’ clamps. The special loading saddle was attached to the head of the pile, and the bottom pulley was positioned so that the pulling angle was parallel to the sand surface.</p> <p><i>Step 2.</i></p> <p>The cable loading system was assembled. This system included a load bin, load cell, 5 mm stainless steel cable, clip, and all were attached in series. The cable was put on each of the three pulleys and clipped to the pile saddle, and the extensometer was placed to measure the net displacement of the pile head. The extensometer was zeroed and initial load and displacement readings recorded. A drum was placed underneath the loading bin to stop the loading bin falling to the ground, possibly causing damage to the extensometer. A horizontal load about to be applied to the model pile is shown in Figure 7.5 (a).</p>

Table C3 Continued: Small scale model pile test procedure for lateral loads

Loading Scenario	Procedure Used
<p>Summary of Horizontal Load Test</p>	<p><i>Step 3.</i></p> <p>The displacement and load readings were recorded after each load increment, and the pile was loaded until ultimate failure was reached. Failure for this test was defined at the point where the model pile was fully pulled out of the sand bed.</p> <p><i>Step 4.</i></p> <p>The load bin was removed and the failed pile was inspected after ultimate failure was reached. The loading apparatus was then unclamped and removed as well. The pile was manually lifted out and the resulting sand indentation was examined before commencing to test the next model pile.</p>

APPENDIX D: Laboratory Testing Results for Experimental Sand

---oooOOOooo---

This appendix is referred to in Chapter 7. It contains the shear box test results conducted on the experimental sand used for the small-scale pile testing.

APPENDIX D: Laboratory Testing Results for Experimental Sand

Table D1: Shear box results for loose sand under a normal load of 40.4 kPa

Test :-	<u>Direct shear</u>			Sample No. Nominal Size <u>60x60</u> mmxmm Specific Gravity (Gs) meas./assumed <u>2.65</u>				
Location	<u>JCU Geomechanics Laboratory</u>							
Operator	<u>K.Johnson</u>							
Type of Test								
Soil Description								
Type of specimen	<u>undisturbed/ remoulded/ compacted</u>							
Specimen preparation								
Initial Measurement	Length (L)	<u>60.00</u>	<u>mm</u>	Area (A)	<u>3595.2</u>	<u>mm²</u>		
	Breadth (B)	<u>59.92</u>	<u>mm</u>	Volume (V _o)	<u>87.26</u>	<u>cm³</u>		
	Height (H _o)	<u>24.27</u>	<u>mm</u>	Bulk Density (ρ)	<u>1.40</u>	<u>g/cm³</u>		
	Mass (m)	<u>122.00</u>	<u>g</u>	Dry Density (ρ _d)	<u>1.40</u>	<u>g/cm³</u>		
	Moisture (w)	<u>0.00</u>	<u>%</u>	Voids Ratio (e _o)	<u>0.895</u>			
<u>SHEARING</u>				<u>AFTER CONSOLIDATION</u>				
Machine No.	<u>1</u>	Proving Ring No.	<u>A-100 lbs</u>	Settlement (Rdg1)	<u>0</u>	<u>mm</u>		
Mean Calibration C _R	<u>1.328</u>	N/div		Settlement (Rdg2)	<u>0.058</u>	<u>mm</u>		
Proving Ring conversion	<u>0.002</u>	mm/div		Height (H ₁)	<u>24.21</u>	<u>mm</u>		
Rate of displacement	<u>0.900</u>	mm/min		Dry Density (ρ _{d1})	<u>1.40</u>	<u>g/cm³</u>		
Vertical Dial Gauge conversion	<u>0.01</u>	mm/div		Voids Ratio (e ₁)	<u>0.891</u>		Relative Density, Dr (%)	<u>3.6512</u>
Hanging Wt. - Apparatus			<u>5.72</u>	Kg				
Hanging Wt. - Weights	<u>20.00</u>	lbs	<u>9.07</u>	Kg				
Normal Load			<u>145.13</u>	N	Initial Normal Stress (kPa) =		<u>40.4</u>	

APPENDIX D: Laboratory Testing Results for Experimental Sand

Table D1 Continued: Shear box results for loose sand under a normal load of 40.4 kPa

Horizontal Displacement Reading (mm)	Proving Ring Dial Reading (mm)	Relative Shear Displacement δh (mm)	Horizontal Load (N)	Shear Surface Area (mm ²)	Shear Stress τ (kPa)	Vertical Movement			Normal Stress σ_n (kPa)	Axial Strain (ϵ_o)
						dial reading (div)	Vertical Movement (mm)	expansion - settlement + (mm)		
Initial Proving Ring Reading										
0	0	0.00	0.00	0.00	0.00	0	0.000	0.000	#DIV/0!	0.00%
0.255	0.058	0.20	37.76	3588.18	10.52	-0.03	-0.300	-0.300	40.45	0.43%
0.51	0.081	0.43	52.73	3574.26	14.75	-0.06	-0.600	-0.600	40.60	0.85%
0.751	0.107	0.64	69.66	3561.36	19.56	-0.08	-0.800	-0.800	40.75	1.25%
1.016	0.138	0.88	89.84	3547.32	25.33	-0.1	-1.000	-1.000	40.91	1.69%
1.25	0.154	1.10	100.25	3534.24	28.37	-0.11	-1.100	-1.100	41.06	2.08%
1.508	0.164	1.34	106.76	3519.36	30.34	-0.115	-1.150	-1.150	41.24	2.51%
1.745	0.168	1.58	109.37	3505.38	31.20	-0.12	-1.200	-1.200	41.40	2.91%
2.016	0.168	1.85	109.37	3489.12	31.35	-0.115	-1.150	-1.150	41.59	3.36%
2.505	0.164	2.34	106.76	3459.54	30.86	-0.11	-1.100	-1.100	41.95	4.18%
3.025	0.159	2.87	103.51	3428.04	30.19	-0.1	-1.000	-1.000	42.34	5.04%
3.514	0.156	3.36	101.56	3398.52	29.88	-0.09	-0.900	-0.900	42.70	5.86%
4.005	0.154	3.85	100.25	3368.94	29.76	-0.08	-0.800	-0.800	43.08	6.68%
4.5	0.153	4.35	99.60	3339.18	29.83	-0.07	-0.700	-0.700	43.46	7.50%
5.026	0.153	4.87	99.60	3307.62	30.11	-0.06	-0.600	-0.600	43.88	8.38%
5.515	0.153	5.36	99.60	3278.28	30.38	-0.06	-0.600	-0.600	44.27	9.19%
6.028	0.153	5.88	99.60	3247.50	30.67	-0.06	-0.600	-0.600	44.69	10.05%
6.506	0.152	6.35	98.95	3218.76	30.74	-0.06	-0.600	-0.600	45.09	10.84%
7.006	0.149	6.86	97.00	3188.58	30.42	-0.06	-0.600	-0.600	45.52	11.68%
7.449	0.149	7.30	97.00	3162.00	30.68	-0.06	-0.600	-0.600	45.90	12.42%
8.021	0.149	7.87	97.00	3127.68	31.01	-0.06	-0.600	-0.600	46.40	13.37%
8.507	0.149	8.36	97.00	3098.52	31.30	-0.06	-0.600	-0.600	46.84	14.18%

APPENDIX D: Laboratory Testing Results for Experimental Sand

Table D2: Shear box results for dense sand under a normal load of 40.4 kPa

Test :-	Direct shear			Sample No.	Nominal Size	60x60	mmxmm	Specific Gravity (Gs) meas./assumed	2.65
Location	JCU Geomechanics Laboratory								
Operator	K.Johnson								
Type of Test									
Soil Description									
Type of specimen	undisturbed/ remoulded/ compacted								
Specimen preparation									
Initial Measurement	Length (L)	60.00	mm	Area (A)	3595.2	mm ²			
	Breadth (B)	59.92	mm	Volume (V _o)	87.26	cm ³			
	Height (H _o)	24.27	mm	Bulk Density (ρ)	1.76	g/cm ³			
	Mass (m)	154.00	g	Dry Density (ρ _d)	1.76	g/cm ³			
	Moisture (w)	0.00	%	Voids Ratio (e _o)	0.501				
<u>SHEARING</u>				<u>AFTER CONSOLIDATION</u>					
Machine No.	1	Proving Ring No.	A-100 lbs	Settlement (Rdg1)	0	mm			
Mean Calibration C _R	1.328	N/div		Settlement (Rdg2)	0.042	mm			
Proving Ring conversion	0.002	mm/div		Height (H ₁)	24.23	mm			
Rate of displacement	0.900	mm/min		Dry Density (ρ _{d1})	1.77	g/cm ³			
Vertical Dial Gauge conversion	0.01	mm/div		Voids Ratio (e ₁)	0.499		Relative Density (Dr)	97.6316	
Hanging Wt. - Apparatus			5.72	Kg					
Hanging Wt. - Weights	20.00	lbs	9.07	Kg					
Normal Load			145.13	N	Initial Normal Stress (kPa) = 40.4				

APPENDIX D: Laboratory Testing Results for Experimental Sand

Table D2 Continued: Shear box results for dense sand under a normal load of 40.4 kPa

Horizontal Displacement Reading (mm)	Proving Ring Dial Reading (mm)	Relative Shear Displacement δh (mm)	Horizontal Load (N)	Shear Surface Area (mm ²)	Shear Stress τ (kPa)	Vertical Movement			Normal Stress σ_n (kPa)	Axial Strain (ϵ_o)
						dial reading (div)	Vertical Movement (mm)	expansion - settlement + (mm)		
0.00	0.00									
0	0	0.00	0.00	0.00	0.00	0	0.000	0.000	#DIV/0!	0.00%
0.255	0.104	0.15	67.70	3590.94	18.85	-0.01	-0.100	-0.100	40.42	0.43%
0.511	0.141	0.37	91.79	3577.80	25.66	0.04	0.400	0.400	40.56	0.85%
0.747	0.161	0.59	104.81	3564.84	29.40	0.11	1.100	1.100	40.71	1.25%
1.003	0.174	0.83	113.27	3550.26	31.91	0.18	1.800	1.800	40.88	1.67%
1.235	0.178	1.06	115.88	3536.58	32.77	0.28	2.800	2.800	41.04	2.06%
1.501	0.179	1.32	116.53	3520.68	33.10	0.37	3.700	3.700	41.22	2.50%
1.74	0.179	1.56	116.53	3506.34	33.23	0.45	4.500	4.500	41.39	2.90%
2.015	0.174	1.84	113.27	3489.54	32.46	0.51	5.100	5.100	41.59	3.36%
2.509	0.161	2.35	104.81	3459.12	30.30	0.56	5.600	5.600	41.96	4.18%
3.007	0.147	2.86	95.70	3428.40	27.91	0.57	5.700	5.700	42.33	5.01%
3.493	0.136	3.36	88.54	3398.58	26.05	0.59	5.900	5.900	42.70	5.82%
3.994	0.133	3.86	86.58	3368.34	25.70	0.59	5.900	5.900	43.09	6.66%
4.516	0.131	4.39	85.28	3336.90	25.56	0.595	5.950	5.950	43.49	7.53%
5.024	0.132	4.89	85.93	3306.48	25.99	0.6	6.000	6.000	43.89	8.37%
5.51	0.132	5.38	85.93	3277.32	26.22	0.6	6.000	6.000	44.28	9.18%
6.021	0.131	5.89	85.28	3246.60	26.27	0.6	6.000	6.000	44.70	10.04%
6.512	0.131	6.38	85.28	3217.14	26.51	0.6	6.000	6.000	45.11	10.85%
7.012	0.13	6.88	84.63	3187.08	26.55	0.6	6.000	6.000	45.54	11.69%
7.514	0.129	7.39	83.98	3156.90	26.60	0.6	6.000	6.000	45.97	12.52%
8.021	0.127	7.89	82.68	3126.36	26.45	0.6	6.000	6.000	46.42	13.37%

APPENDIX D: Laboratory Testing Results for Experimental Sand

Table D3: Shear box results for loose sand under a normal load of 89.9 kPa

Test :-			<u>Direct shear</u>			Sample No. Nominal Size <u>60x60</u> mmxmm Specific Gravity (Gs) meas./assumed <u>2.65</u>					
Location			<u>JCU Geomechanics Laboratory</u>								
Operator			<u>K.Johnson</u>								
Type of Test											
Soil Description											
Type of specimen			<u>undisturbed/ remoulded/ compacted</u>								
Specimen preparation											
Initial Measurement	Length (L)	<u>60.00</u>	<u>mm</u>	Area (A)	<u>3595.2</u>	<u>mm²</u>					
	Breadth (B)	<u>59.92</u>	<u>mm</u>	Volume (V _o)	<u>87.26</u>	<u>cm³</u>					
	Height (H _o)	<u>24.27</u>	<u>mm</u>	Bulk Density (ρ)	<u>1.41</u>	<u>g/cm³</u>					
	Mass (m)	<u>123.00</u>	<u>g</u>	Dry Density (ρ _d)	<u>1.41</u>	<u>g/cm³</u>					
	Moisture (w)	<u>0.00</u>	<u>%</u>	Voids Ratio (e _o)	<u>0.880</u>						
<u>SHEARING</u>						<u>AFTER CONSOLIDATION</u>					
Machine No.	<u>1</u>	Proving Ring No.	<u>A-100 lbs</u>	Settlement (Rdg1)	<u>0</u>	<u>mm</u>					
Mean Calibration C _R	<u>1.328</u>	N/div		Settlement (Rdg2)	<u>0.233</u>	<u>mm</u>					
Proving Ring conversion	<u>0.002</u>	mm/div		Height (H ₁)	<u>24.04</u>	<u>mm</u>					
Rate of displacement	<u>0.900</u>	mm/min		Dry Density (ρ _{d1})	<u>1.42</u>	<u>g/cm³</u>					
Vertical Dial Gauge conversion	<u>0.01</u>	mm/div		Voids Ratio (e ₁)	<u>0.862</u>		Relative Density (Dr)	<u>10.5882</u>			
Hanging Wt. - Apparatus			<u>5.72</u>	Kg							
Hanging Wt. - Weights	<u>60.00</u>	lbs	<u>27.22</u>	Kg							
Normal Load			<u>323.12</u>	N	Initial Normal Stress (kPa) =	<u>89.9</u>					

APPENDIX D: Laboratory Testing Results for Experimental Sand

Table D3 Continued: Shear box results for loose sand under a normal load of 89.9 kPa

Horizontal Displacement Reading (mm)	Proving Ring Dial Reading (mm)	Relative Shear Displacement δh (mm)	Horizontal Load (N)	Shear Surface Area (mm ²)	Shear Stress τ (kPa)	Vertical Movement			Normal Stress σ_n (kPa)	Axial Strain (ϵ_o)
						dial reading (div)	Vertical Movement (mm)	expansion - settlement + (mm)		
0.00	0.00									
0	0	0.00	0.00	0.00	0.00	-0.001	-0.010	0.000	#DIV/0!	0.00%
0.255	0.117	0.14	76.17	3591.72	21.21	-0.021	-0.210	-0.200	89.96	0.43%
0.502	0.178	0.32	115.88	3580.56	32.36	-0.042	-0.420	-0.410	90.24	0.84%
0.766	0.222	0.54	144.52	3567.36	40.51	-0.062	-0.620	-0.610	90.58	1.28%
1	0.252	0.75	164.05	3555.12	46.15	-0.073	-0.730	-0.720	90.89	1.67%
1.259	0.278	0.98	180.98	3541.14	51.11	-0.085	-0.850	-0.840	91.25	2.10%
1.516	0.299	1.22	194.65	3526.98	55.19	-0.087	-0.870	-0.860	91.61	2.53%
1.766	0.312	1.45	203.11	3512.76	57.82	-0.094	-0.940	-0.930	91.99	2.94%
2.005	0.321	1.68	208.97	3498.96	59.72	-0.094	-0.940	-0.930	92.35	3.34%
2.491	0.334	2.16	217.43	3470.58	62.65	-0.094	-0.940	-0.930	93.10	4.15%
3.014	0.338	2.68	220.04	3439.44	63.97	-0.094	-0.940	-0.930	93.95	5.02%
3.505	0.338	3.17	220.04	3409.98	64.53	-0.094	-0.940	-0.930	94.76	5.84%
4.022	0.33	3.69	214.83	3378.48	63.59	-0.094	-0.940	-0.930	95.64	6.70%
4.511	0.324	4.19	210.92	3348.78	62.99	-0.094	-0.940	-0.930	96.49	7.52%
5.007	0.32	4.69	208.32	3318.78	62.77	-0.094	-0.940	-0.930	97.36	8.35%
5.498	0.317	5.18	206.37	3289.14	62.74	-0.094	-0.940	-0.930	98.24	9.16%
6.005	0.316	5.69	205.72	3258.66	63.13	-0.094	-0.940	-0.930	99.16	10.01%
6.514	0.316	6.20	205.72	3228.12	63.73	-0.094	-0.940	-0.930	100.10	10.86%
7.02	0.313	6.71	203.76	3197.58	63.72	-0.094	-0.940	-0.930	101.05	11.70%
7.499	0.311	7.19	202.46	3168.72	63.89	-0.094	-0.940	-0.930	101.97	12.50%
8.01	0.307	7.70	199.86	3137.82	63.69	-0.094	-0.940	-0.930	102.98	13.35%

APPENDIX D: Laboratory Testing Results for Experimental Sand

Table D4: Shear box results for dense sand under a normal load of 89.9 kPa

Test :-	<u>Direct shear</u>			<div>Sample No.</div> <div>Nominal Size <u>60x60</u> mmxmm</div> <div>Specific Gravity (Gs) meas./assumed <u>2.65</u></div>
---------	---------------------	--	--	---

APPENDIX D: Laboratory Testing Results for Experimental Sand

Table D4 Continued: Shear box results for dense sand under a normal load of 89.9 kPa

Horizontal Displacement Reading (mm)	Proving Ring Dial Reading (mm)	Relative Shear Displacement δh (mm)	Horizontal Load (N)	Shear Surface Area (mm ²)	Shear Stress τ (kPa)	Vertical Movement			Normal Stress σ_n (kPa)	Axial Strain (ϵ_o)
						dial reading (div)	Vertical Movement (mm)	expansion - settlement + (mm)		
0.00	0.00									
0	0	0.00	0.00	0.00	0.00	0	0.000	0.000	#DIV/0!	0.00%
0.258	0.177	0.08	115.23	3595.14	32.05	0	0.000	0.000	89.88	0.43%
0.518	0.267	0.25	173.82	3584.94	48.49	0.08	0.008	0.008	90.13	0.86%
0.747	0.325	0.42	211.58	3574.68	59.19	0.27	0.027	0.027	90.39	1.25%
1.005	0.372	0.63	242.17	3562.02	67.99	0.69	0.069	0.069	90.71	1.68%
1.266	0.401	0.87	261.05	3548.10	73.57	1.23	0.123	0.123	91.07	2.11%
1.496	0.414	1.08	269.51	3535.08	76.24	1.76	0.176	0.176	91.40	2.50%
1.75	0.419	1.33	272.77	3520.14	77.49	2.33	0.233	0.233	91.79	2.92%
2.005	0.419	1.59	272.77	3504.84	77.83	2.93	0.293	0.293	92.19	3.35%
2.492	0.4	2.09	260.40	3474.48	74.95	3.94	0.394	0.394	93.00	4.16%
3.016	0.367	2.65	238.92	3441.06	69.43	4.63	0.463	0.463	93.90	5.03%
3.516	0.332	3.18	216.13	3408.96	63.40	4.88	0.488	0.488	94.79	5.87%
4.016	0.314	3.70	204.41	3377.88	60.52	4.95	0.495	0.495	95.66	6.70%
4.517	0.304	4.21	197.90	3347.22	59.12	4.95	0.495	0.495	96.53	7.54%
5.022	0.3	4.72	195.30	3316.68	58.88	4.95	0.495	0.495	97.42	8.38%
5.512	0.304	5.21	197.90	3287.52	60.20	4.92	0.492	0.492	98.29	9.20%
5.999	0.306	5.69	199.21	3258.42	61.14	4.8	0.480	0.480	99.17	10.01%
6.509	0.306	6.20	199.21	3227.82	61.72	4.71	0.471	0.471	100.11	10.86%
7.022	0.301	6.72	195.95	3196.74	61.30	4.62	0.462	0.462	101.08	11.72%
7.501	0.301	7.20	195.95	3168.00	61.85	4.52	0.452	0.452	102.00	12.52%
7.996	0.302	7.69	196.60	3138.36	62.64	4.45	0.445	0.445	102.96	13.34%

APPENDIX D: Laboratory Testing Results for Experimental Sand

Table D5: Shear box results for loose sand under a normal load of 139.4 kPa

Test :-		<u>Direct shear</u>		Sample No.	
Location		<u>JCU Geomechanics Laboratory</u>			
Operator		<u>K.Johnson</u>			
Type of Test					
Soil Description					
Type of specimen		<u>undisturbed/ remoulded/ compacted</u>		Nominal Size	
Specimen preparation				<u>60x60</u> mmxmm	
				Specific Gravity (Gs)	
				meas./assumed	
				<u>2.65</u>	
Initial Measurement	Length (L)	<u>60.00</u>	<u>mm</u>	Area (A)	<u>3595.2</u> mm ²
	Breadth (B)	<u>59.92</u>	<u>mm</u>	Volume (V _o)	<u>87.26</u> cm ³
	Height (H _o)	<u>24.27</u>	<u>mm</u>	Bulk Density (ρ)	<u>1.40</u> g/cm ³
	Mass (m)	<u>122.00</u>	<u>g</u>	Dry Density (ρ _d)	<u>1.40</u> g/cm ³
	Moisture (w)	<u>0.00</u>	<u>%</u>	Voids Ratio (e _o)	<u>0.895</u>
<u>SHEARING</u>				<u>AFTER CONSOLIDATION</u>	
Machine No.	<u>1</u>	Proving Ring No.	<u>A-100 lbs</u>	Settlement (Rdg1)	<u>0</u> mm
Mean Calibration C _R	<u>1.328</u>	N/div		Settlement (Rdg2)	<u>0.422</u> mm
Proving Ring conversion	<u>0.002</u>	mm/div		Height (H ₁)	<u>23.85</u> mm
Rate of displacement	<u>0.900</u>	mm/min		Dry Density (ρ _{d1})	<u>1.42</u> g/cm ³
Vertical Dial Gauge conversion	<u>0.01</u>	mm/div		Voids Ratio (e ₁)	<u>0.862</u>
				Relative Density (Dr)	
				<u>10.4679</u>	
Hanging Wt. - Apparatus			<u>5.72</u>	Kg	
Hanging Wt. - Weights	<u>100.00</u>	lbs	<u>45.36</u>	Kg	
Normal Load			501.11	N	
				Initial Normal Stress (kPa) =	
				<u>139.4</u>	

APPENDIX D: Laboratory Testing Results for Experimental Sand

Table D5 Continued: Shear box results for loose sand under a normal load of 139.4 kPa

Horizontal Displacement Reading (mm)	Proving Ring Dial Reading (mm)	Relative Shear Displacement δh (mm)	Horizontal Load (N)	Shear Surface Area (mm ²)	Shear Stress τ (kPa)	Vertical Movement			Normal Stress σ_n (kPa)	Axial Strain (ϵ_o)
						dial reading (div)	Vertical Movement (mm)	expansion - settlement + (mm)		
0.00	0.00									
0	0	0.00	0.00	0.00	0.00	0	0.000	0.000	#DIV/0!	0.00%
0.253	0.12	0.13	78.12	3592.02	21.75	0	0.000	0.000	139.51	0.42%
0.52	0.194	0.33	126.29	3580.44	35.27	-0.01	-0.100	-0.100	139.96	0.87%
0.758	0.269	0.49	175.12	3570.66	49.04	-0.06	-0.600	-0.600	140.34	1.26%
1.023	0.373	0.65	242.82	3561.00	68.19	-0.1	-1.000	-1.000	140.72	1.71%
1.257	0.447	0.81	291.00	3551.40	81.94	-0.12	-1.200	-1.200	141.10	2.10%
1.501	0.491	1.01	319.64	3539.40	90.31	-0.135	-1.350	-1.350	141.58	2.50%
1.745	0.52	1.23	338.52	3526.50	95.99	-0.14	-1.400	-1.400	142.10	2.91%
2.016	0.532	1.48	346.33	3510.96	98.64	-0.15	-1.500	-1.500	142.73	3.36%
2.495	0.534	1.96	347.63	3482.34	99.83	-0.16	-1.600	-1.600	143.90	4.16%
3.006	0.525	2.48	341.78	3451.14	99.03	-0.16	-1.600	-1.600	145.20	5.01%
3.499	0.507	2.99	330.06	3420.48	96.49	-0.16	-1.600	-1.600	146.50	5.83%
4.021	0.495	3.53	322.25	3388.44	95.10	-0.16	-1.600	-1.600	147.89	6.70%
4.511	0.49	4.02	318.99	3358.74	94.97	-0.16	-1.600	-1.600	149.20	7.52%
5.002	0.493	4.51	320.94	3329.46	96.39	-0.16	-1.600	-1.600	150.51	8.34%
5.518	0.491	5.03	319.64	3298.38	96.91	-0.16	-1.600	-1.600	151.93	9.20%
6.022	0.492	5.53	320.29	3268.20	98.00	-0.16	-1.600	-1.600	153.33	10.04%
6.501	0.49	6.01	318.99	3239.34	98.47	-0.16	-1.600	-1.600	154.70	10.84%
7.01	0.49	6.52	318.99	3208.80	99.41	-0.16	-1.600	-1.600	156.17	11.68%
7.517	0.488	7.03	317.69	3178.26	99.96	-0.16	-1.600	-1.600	157.67	12.53%
8.003	0.486	7.52	316.39	3148.98	100.47	-0.16	-1.600	-1.600	159.14	13.34%

APPENDIX D: Laboratory Testing Results for Experimental Sand

Table D6: Shear box results for dense sand under a normal load of 139.4 kPa

Test :-	<u>Direct shear</u>			Sample No. _____ Nominal Size <u>60x60</u> mmxmm Specific Gravity (Gs) <u>2.65</u> meas./assumed _____		
Location	<u>JCU Geomechanics Laboratory</u>					
Operator	<u>K.Johnson</u>					
Type of Test	_____					
Soil Description	_____					
Type of specimen	<u>undisturbed/ remoulded/ compacted</u>			Area (A) <u>3595.2</u> mm ² Volume (V _o) <u>87.26</u> cm ³ Bulk Density (ρ) <u>1.76</u> g/cm ³ Dry Density (ρ _d) <u>1.76</u> g/cm ³ Voids Ratio (e _o) <u>0.501</u>		
Specimen preparation	_____					
Initial Measurement	Length (L)	<u>60.00</u>	<u>mm</u>			
	Breadth (B)	<u>59.92</u>	<u>mm</u>			
	Height (H _o)	<u>24.27</u>	<u>mm</u>			
	Mass (m)	<u>154.00</u>	<u>g</u>			
	Moisture (w)	<u>0.00</u>	<u>%</u>			
<u>SHEARING</u>				<u>AFTER CONSOLIDATION</u>		
Machine No.	<u>1</u>	Proving Ring No.	<u>A-100 lbs</u>	Settlement (Rdg1)	<u>0</u>	<u>mm</u>
Mean Calibration C _R	<u>1.328</u>	N/div		Settlement (Rdg2)	<u>0.184</u>	<u>mm</u>
Proving Ring conversion	<u>0.002</u>	mm/div		Height (H ₁)	<u>24.09</u>	<u>mm</u>
Rate of displacement	<u>0.900</u>	mm/min		Dry Density (ρ _{d1})	<u>1.78</u>	<u>g/cm³</u>
Vertical Dial Gauge conversion	<u>0.01</u>	mm/div		Voids Ratio (e ₁)	<u>0.490</u>	Relative Density (Dr) <u>99.7383</u>
Hanging Wt. - Apparatus			<u>5.72</u>	Kg		
Hanging Wt. - Weights	<u>100.00</u>	lbs	<u>45.36</u>	Kg		
Normal Load			<u>501.11</u>	N	Initial Normal Stress (kPa) =	139.4

APPENDIX D: Laboratory Testing Results for Experimental Sand

Table D6 Continued: Shear box results for dense sand under a normal load of 139.4 kPa

Horizontal Displacement Reading (mm)	Proving Ring Dial Reading (mm)	Relative Shear Displacement δh (mm)	Horizontal Load (N)	Shear Surface Area (mm ²)	Shear Stress τ (kPa)	Vertical Movement			Normal Stress σ_n (kPa)	Axial Strain (ϵ_o)
						dial reading (div)	Vertical Movement (mm)	expansion - settlement + (mm)		
0.00	0.00									
0	0	0.00	0.00	0.00	0.00	0	0.000	0.000	#DIV/0!	0.00%
0.254	0.157	0.10	102.21	3594.18	28.44	0	0.000	0.000	139.42	0.42%
0.517	0.284	0.23	184.88	3586.02	51.56	0	0.000	0.000	139.74	0.86%
0.765	0.388	0.38	252.59	3577.38	70.61	-0.02	-0.200	-0.200	140.08	1.28%
1.005	0.47	0.54	305.97	3567.90	85.76	-0.01	-0.100	-0.100	140.45	1.68%
1.245	0.538	0.71	350.24	3557.58	98.45	-0.01	-0.100	-0.100	140.86	2.08%
1.508	0.598	0.91	389.30	3545.40	109.80	-0.01	-0.100	-0.100	141.34	2.51%
1.749	0.641	1.11	417.29	3533.52	118.09	0.04	0.400	0.400	141.82	2.92%
2.016	0.669	1.35	435.52	3519.18	123.76	0.11	1.100	1.100	142.40	3.36%
2.515	0.681	1.83	443.33	3489.96	127.03	0.25	2.500	2.500	143.59	4.19%
3.018	0.636	2.38	414.04	3457.08	119.76	0.37	3.700	3.700	144.95	5.03%
3.514	0.557	2.96	362.61	3422.58	105.95	0.43	4.300	4.300	146.41	5.86%
4.002	0.51	3.49	332.01	3390.48	97.92	0.43	4.300	4.300	147.80	6.67%
4.51	0.496	4.01	322.90	3359.16	96.12	0.43	4.300	4.300	149.18	7.52%
5.015	0.493	4.52	320.94	3328.68	96.42	0.43	4.300	4.300	150.54	8.36%
5.392	0.49	4.90	318.99	3305.88	96.49	0.43	4.300	4.300	151.58	8.99%
5.419	0.488	4.93	317.69	3304.14	96.15	0.43	4.300	4.300	151.66	9.03%
6.018	0.487	5.53	317.04	3268.14	97.01	0.43	4.300	4.300	153.33	10.03%
6.498	0.487	6.01	317.04	3239.34	97.87	0.43	4.300	4.300	154.70	10.83%
7.001	0.485	6.52	315.74	3209.04	98.39	0.43	4.300	4.300	156.16	11.67%
7.5	0.483	7.02	314.43	3178.98	98.91	0.43	4.300	4.300	157.63	12.50%

Table D7: Summary of results for Mohr-Coulomb analysis

	Dr (%)	Initial Normal Stress (kPa)	Peak		Residual	
			Normal Stress σ_n (kPa)	Shear Stress τ (kPa)	Normal Stress σ_n (kPa)	Shear Stress τ (kPa)
Loose	4	40.4	46.8	31.3		
	10.6	89.9	103.0	63.7		
	10.5	139.4	159.1	100.5		
Dense	97	40.4	41.4	33.2	46.4	26.4
	96	89.9	92.2	77.8	103.0	62.6
	97	139.4	143.6	127.0	151.7	96.1

Table D8: Friction angles for experimental sand

		Equations	Gradient	Friction angle (ϕ) (rads)	Friction angle (ϕ) (deg)	Average (ϕ) (deg)
		$\tau = 0.6299\sigma$	0.6299	0.562	32.2	32.2
Dense	Peak	$\tau = 0.869\sigma$	0.869	0.715	41.0	41.0
	Residual	$\tau = 0.6479\sigma$	0.6479	0.575	32.9	32.9

APPENDIX E: Experimental Results from Model Piles

---oooOOOooo---

This appendix is referred to in Chapter 7. It contains the raw and interpreted load-displacement data in tabular form for the small-scale model piles, tested as part of these works.

Table E1: Test results for axial compression loading in loose sand

Test 1			Test 2			Test 3		
Pile Head Displacement (mm)	Load		Pile Head Displacement (mm)	Load		Pile Head Displacement (mm)	Load	
	(Volts)	(N)		(Volts)	(N)		(Volts)	(N)
0.00	0.22	39.54	0.00	0.14	16.45	0.00	0.14	15.14
0.50	0.72	203.78	0.20	0.39	94.83	0.20	0.30	65.55
0.70	0.97	283.46	0.40	0.61	166.38	0.50	0.42	105.88
1.20	1.21	363.14	0.60	0.77	220.04	0.80	0.57	154.99
1.50	1.31	395.34	0.80	0.88	256.14	1.00	0.61	168.00
2.00	1.40	424.93	1.00	1.04	307.20	1.20	0.71	201.83
2.50	1.45	441.20	1.50	1.24	373.55	1.60	1.04	307.85
2.90	1.44	439.24	2.00	1.30	390.78	2.20	1.13	337.12
3.50	1.46	443.15	2.50	1.33	400.54	3.00	1.16	345.58
4.00	1.51	459.08	3.00	1.33	401.84	3.50	1.19	356.96
4.50	1.52	463.31	3.50	1.36	411.92	4.40	1.20	359.56
5.00	1.53	467.21	4.00	1.37	415.18	5.50	1.21	363.79
5.00	0.19	32.38	4.50	1.37	415.18	4.40	0.12	9.62
5.30	0.54	145.89	5.00	1.38	418.43	4.70	0.16	21.65
5.50	0.77	218.74	4.00	0.15	16.77	5.10	0.21	39.21
5.80	1.07	316.31	4.20	0.36	87.67	5.30	0.27	58.40
6.00	1.19	357.94	4.40	0.51	136.13	5.40	0.30	67.18
6.30	1.34	405.75	4.60	0.75	212.88	5.60	0.40	98.08
7.20	1.45	441.52	4.80	0.94	274.03	5.65	0.53	141.33
8.00	1.51	460.71	5.00	1.12	333.87	5.70	0.93	272.73
9.00	1.53	467.54	5.50	1.25	375.17	6.60	1.14	338.75
10.00	1.54	471.12	6.00	1.31	395.01	8.30	1.18	352.41
9.00	0.22	41.16	6.50	1.33	402.49	10.00	1.20	360.86
			7.00	1.35	409.00	10.40	1.23	369.64
			7.50	1.36	412.25	10.00	0.10	2.79
			8.00	1.38	419.41			
			8.50	1.39	421.68			
			9.00	1.40	426.23			
			10.00	1.41	428.19			
			10.50	1.35	407.05			
			9.70	0.14	14.49			

Table E2: Test results for axial compression loading in dense sand

Test 1			Test 2			Test 3		
Pile Head Displacement (mm)	Load		Pile Head Displacement (mm)	Load		Pile Head Displacement (mm)	Load	
	(Volts)	(N)		(Volts)	(N)		(Volts)	(N)
0	0	0	0	0	0	0	0	0
0.4	43	421.83	0.2	36	353.16	0.1	7	68.67
0.7	82	804.42	0.4	68	667.08	0.2	27	264.87
1	114	1118.3	0.6	98	961.38	0.3	38	372.78
1.3	154	1510.7	0.8	132	1294.9	0.4	47	461.07
1.4	177	1736.4	1	174	1706.9	0.5	57	559.17
1.9	267	2619.3	1.2	231	2266.1	0.6	67	657.27
2.3	348	3413.9	1.4	261	2560.4	0.7	77	755.37
2.7	420	4120.2	1.6	300	2943	0.8	89	873.09
3.2	495	4856	1.8	327	3207.9	0.9	99	971.19
3.7	554	5434.7	2	366	3590.5	1	111	1088.9
4.3	597	5856.6	2.2	402	3943.6	1.1	121	1187
5.1	633	6209.7	2.4	435	4267.4	1.2	135	1324.4
6.2	650	6376.5	2.8	487	4777.5	1.3	151	1481.3
7.2	660	6474.6	3.2	531	5209.1	1.4	161	1579.4
8	675	6621.8	3.5	556	5454.4	1.5	170	1667.7
9.2	677	6641.4	3.8	573	5621.1	1.6	184	1805
10	683	6700.2	4	587	5758.5	1.7	195	1913
11.3	690	6768.9	4.4	601	5895.8	1.8	205	2011.1
7.9	7	68.67	4.8	613	6013.5	1.9	220	2158.2
8.6	104	1020.2	5.3	621	6092	2.1	235	2305.4
9.7	292	2864.5	5.7	627	6150.9	2.2	249	2442.7
10	372	3649.3	6.1	631	6190.1	2.3	274	2687.9
10.7	485	4757.9	7.4	635	6229.4	2.4	286	2805.7
11.2	564	5532.8	7.8	646	6337.3	2.6	300	2943
12.3	650	6376.5	8.1	661	6484.4	2.7	311	3050.9
13	671	6582.5	8.7	660	6474.6	2.8	326	3198.1
14.5	684	6710	9.3	665	6523.7	3	340	3335.4
15.8	704	6906.2	10.1	668	6553.1	3.5	377	3698.4
17.1	710	6965.1	7.3	8	78.48	4.1	416	4081
17.7	730	7161.3	7.7	79	774.99	4.6	433	4247.7
18.6	733	7190.7	7.9	128	1255.7	5.1	450	4414.5
19.6	733	7190.7	8.3	208	2040.5	5.6	455	4463.6
20.3	735	7210.4	8.7	280	2746.8	6.1	460	4512.6
16.7	8	78.48	9.1	368	3610.1	6.6	466	4571.5
			9.4	428	4198.7	7	473	4640.1
			9.9	513	5032.5	7.6	472	4630.3
			10.3	560	5493.6	8.1	480	4708.8
			10.8	601	5895.8	8.6	484	4748
			12	641	6288.2	9.2	483	4738.2
			13.1	658	6455	9.7	485	4757.9
			14.3	668	6553.1	10	486	4767.7
			15.3	678	6651.2	7.7	14	137.34
			17.1	679	6661	8	69	676.89

Table E2 Continued: Test results for axial compression loading in dense sand

Test 1			Test 2			Test 3		
Pile Head Displacement (mm)	Load		Pile Head Displacement (mm)	Load		Pile Head Displacement (mm)	Load	
	(Volts)	(N)		(Volts)	(N)		(Volts)	(N)
			18.2	687	6739.5	8.2	100	981
			19	706	6925.9	8.4	130	1275.3
			20	707	6935.7	8.6	175	1716.8
			17	14	137.34	8.8	211	2069.9
						9	249	2442.7
						9.2	273	2678.1
						9.4	308	3021.5
						9.6	338	3315.8
						9.8	366	3590.5
						10.1	395	3875
						10.2	408	4002.5
						10.5	427	4188.9
						11	450	4414.5
						11.5	464	4551.8
						12	471	4620.5
						12.5	477	4679.4
						13.1	483	4738.2
						13.5	486	4767.7
						14.1	491	4816.7
						14.6	495	4856
						15.9	492	4826.5
						16.6	493	4836.3
						18.1	485	4757.9
						20.1	490	4806.9
						17.8	11	107.91

Table E3: Test results for axial compression loading in layered sand

Test 1			Test 2			Test 3		
Pile Head Displacement (mm)	Load		Pile Head Displacement (mm)	Load		Pile Head Displacement (mm)	Load	
	(Volts)	(N)		(Volts)	(N)		(Volts)	(N)
0	0	0	0	0	0	0	0	0
0.1	11	107.91	0.1	13	127.53	0.1	7	68.67
0.2	292	2864.5	0.5	101	990.81	0.2	74	725.94
0.3	300	2943	1.2	209	2050.3	0.3	93	912.33
0.6	336	3296.2	1.7	300	2943	0.4	108	1059.5
0.9	372	3649.3	2.4	400	3924	0.6	136	1334.2
1.5	408	4002.5	3.4	482	4728.4	0.8	177	1736.4
2	425	4169.3	4.7	496	4865.8	1	207	2030.7
2.7	432	4237.9	6.3	515	5052.2	1.3	270	2648.7
3.6	442	4336	7.7	526	5160.1	1.6	312	3060.7
4.5	444	4355.6	9.3	538	5277.8	1.8	348	3413.9
5.9	452	4434.1	10.3	546	5356.3	2	382	3747.4
7	454	4453.7	7.6	12	117.72	2.3	418	4100.6
8	467	4581.3	8.1	98	961.38	2.6	443	4345.8
9.3	465	4561.7	9.3	292	2864.5	2.9	466	4571.5
10.5	468	4591.1	9.7	365	3580.7	3.5	481	4718.6
9.5	16	156.96	10.3	448	4394.9	3.8	489	4797.1
10.2	355	3482.6	10.9	495	4856	4.4	495	4856
10.4	391	3835.7	11.7	526	5160.1	5	505	4954.1
10.9	423	4149.6	12.8	544	5336.6	6.1	511	5012.9
11.7	447	4385.1	14.2	556	5454.4	6.7	517	5071.8
12	460	4512.6	15.4	558	5474	7.7	519	5091.4
12.9	467	4581.3	16.8	576	5650.6	8.6	523	5130.6
13.9	472	4630.3	16.1	14	137.34	9.7	535	5248.4
14.8	475	4659.8				10	545	5346.5
16	479	4699				7.8	8	78.48
17.3	482	4728.4				8.2	117	1147.8
18.4	490	4806.9				9.2	325	3188.3
20.8	484	4748				9.4	381	3737.6
19.2	17	166.77				9.9	443	4345.8

Table E3 Continued: Test results for axial compression loading in layered sand

Test 1			Test 2			Test 3		
Pile Head Displacement (mm)	Load		Pile Head Displacement (mm)	Load		Pile Head Displacement (mm)	Load	
	(Volts)	(N)		(Volts)	(N)		(Volts)	(N)
						10.3	480	4708.8
						10.8	504	4944.2
						11.3	522	5120.8
						12.1	530	5199.3
						12.7	544	5336.6
						13.6	547	5366.1
						14.3	555	5444.6
						14.9	565	5542.7
						15.9	562	5513.2
						16.6	575	5640.8
						17.4	577	5660.4
						18.1	580	5689.8
						19	584	5729
						20.1	585	5738.9
						18	14	137.34

Table E4: Test results for oblique compression loading in loose sand

Test 1			Test 2			Test 3		
Pile Head Displacement (mm)	Load		Pile Head Displacement (mm)	Load		Pile Head Displacement (mm)	Load	
	(Volts)	(N)		(Volts)	(N)		(Volts)	(N)
0	0.122	9.2901	0	0.105	3.7612	0	0.118	7.9891
0.5	0.195	33.032	0.5	0.12	8.6396	0.5	0.148	17.746
1	0.245	49.293	1	0.184	29.454	1	0.17	24.901
1.5	0.275	59.05	1.5	0.228	43.764	1.5	0.199	34.333
2	0.29	63.929	2	0.245	49.293	2	0.255	52.546
2.5	0.3	67.181	2.5	0.26	54.172	2.5	0.31	70.433
3	0.335	78.564	3	0.296	65.88	3	0.34	80.19
3.5	0.349	83.117	3.5	0.336	78.889	3.5	0.355	85.069
4	0.362	87.345	4	0.352	84.093	4	0.385	94.826
4.5	0.365	88.321	4.5	0.358	86.044	4.5	0.442	113.36
5	0.372	90.598	5	0.375	91.573	5	0.47	122.47
5.5	0.433	110.44	5.5	0.415	104.58	5.5	0.481	126.05
6	0.443	113.69	6	0.434	110.76	6	0.51	135.48
6.5	0.443	113.69	6.5	0.439	112.39	6.5	0.545	146.86
7	0.45	115.97	7	0.449	115.64	7	0.598	164.1
7.5	0.468	121.82	7.5	0.475	124.1	7.5	0.615	169.63
8	0.501	132.55	8	0.507	134.5	8	0.621	171.58
8.5	0.518	138.08	8.5	0.51	135.48	8.5	0.645	179.39
9	0.522	139.38	9	0.52	138.73	9	0.681	191.09
9.5	0.531	142.31	9.5	0.532	142.63	9.5	0.71	200.53
10	0.543	146.21	10	0.561	152.07	10	0.72	203.78
11	0.571	155.32	11	0.574	156.29	11	0.754	214.84
12	0.582	158.9	12	0.611	168.33	12	0.792	227.19
13	0.64	177.76	13	0.635	176.13	13	0.805	231.42
14	0.672	188.17	14	0.659	183.94	14	0.855	247.68
15	0.695	195.65	15	0.689	193.7	15	0.865	250.94
16	0.71	200.53	16	0.7	197.27	16	0.905	263.95
17	0.733	208.01	17	0.745	211.91	17	0.91	265.57
18	0.74	210.28	18	0.742	210.93	18	0.93	272.08
19	0.761	217.11	19	0.789	226.22	19	0.935	273.7
20	0.776	221.99	20	0.78	223.29	20	0.957	280.86
22.5	0.803	230.77	22.5	0.811	233.37	22.5	0.966	283.78
25	0.822	236.95	25	0.838	242.15	25	0.985	289.96

Table E5: Test results for oblique compression loading in dense sand

Test 1			Test 2			Test 3		
Pile Head Displacement (mm)	Load		Pile Head Displacement (mm)	Load		Pile Head Displacement (mm)	Load	
	(Volts)	(N)		(Volts)	(N)		(Volts)	(N)
0	0.122	9.2901	0	0.159	21.324	0	0.135	13.518
0.5	0.159	21.324	0.5	0.222	41.813	0.5	0.152	19.047
1	0.268	56.774	1	0.329	76.613	1	0.206	36.609
1.5	0.352	84.093	1.5	0.392	97.102	1.5	0.345	81.816
2	0.44	112.71	2	0.476	124.42	2	0.401	100.03
2.5	0.501	132.55	2.5	0.52	138.73	2.5	0.442	113.36
3	0.54	145.24	3	0.564	153.04	3	0.508	134.83
3.5	0.592	162.15	3.5	0.635	176.13	3.5	0.594	162.8
4	0.666	186.22	4	0.7	197.27	4	0.642	178.41
4.5	0.729	206.7	4.5	0.74	210.28	4.5	0.677	189.79
5	0.762	217.44	5	0.771	220.36	5	0.726	205.73
5.5	0.802	230.45	5.5	0.829	239.23	5.5	0.785	224.92
6	0.841	243.13	6	0.881	256.14	6	0.856	248.01
6.5	0.907	264.6	6.5	0.925	270.45	6.5	0.873	253.54
7	0.94	275.33	7	0.95	278.58	7	0.895	260.69
7.5	0.968	284.43	7.5	0.995	293.22	7.5	0.959	281.51
8	1.021	301.67	8	1.045	309.48	8	1.016	300.05
8.5	1.075	319.23	8.5	1.086	322.81	8.5	1.054	312.4
9	1.126	335.82	9	1.14	340.37	9	1.067	316.63
9.5	1.139	340.05	10	1.17	350.13	9.5	1.13	337.12
10	1.169	349.81	11	1.218	365.74	10	1.162	347.53
11	1.273	383.63	12	1.297	391.44	11	1.219	366.07
12	1.305	394.04	13	1.368	414.53	12	1.315	397.29
13	1.406	426.89	14	1.405	426.56	13	1.361	412.25
14	1.419	431.11	15	1.462	445.1	14	1.416	430.14
15	1.45	441.2				15	1.474	449
16	1.513	461.68				16	1.512	461.36
17	1.584	484.78				17	1.568	479.57
18	1.64	502.99				18	1.59	486.73
19	1.656	508.19				19	1.659	509.17
20	1.715	527.38				20	1.657	508.52

Table E6: Test results for oblique compression loading in layered sand

Test 1			Test 2			Test 3		
Pile Head Displacement (mm)	Load		Pile Head Displacement (mm)	Load		Pile Head Displacement (mm)	Load	
	(Volts)	(N)		(Volts)	(N)		(Volts)	(N)
0	0.145	16.77	0	0.104	3.4359	0	0.101	2.4602
0.5	0.215	39.536	0.5	0.17	24.901	0.5	0.122	9.2901
1	0.264	55.473	1	0.219	40.837	1	0.151	18.722
1.5	0.325	75.312	1.5	0.294	65.23	1.5	0.191	31.731
2	0.402	100.35	2	0.361	87.02	2	0.238	47.017
2.5	0.455	117.59	2.5	0.391	96.777	2.5	0.29	63.929
3	0.474	123.77	3	0.403	100.68	3	0.358	86.044
3.5	0.522	139.38	3.5	0.483	126.7	3.5	0.401	100.03
4	0.585	159.87	4	0.53	141.98	4	0.43	109.46
4.5	0.647	180.04	4.5	0.586	160.2	4.5	0.461	119.54
5	0.672	188.17	5	0.594	162.8	5	0.488	128.32
5.5	0.702	197.92	5.5	0.646	179.71	5.5	0.575	156.62
6	0.744	211.58	6	0.713	201.5	6	0.601	165.08
6.5	0.81	233.05	6.5	0.755	215.16	6.5	0.631	174.83
7	0.843	243.78	7	0.766	218.74	7	0.671	187.84
7.5	0.851	246.38	7.5	0.795	228.17	7.5	0.732	207.68
8	0.881	256.14	8	0.84	242.81	8	0.765	218.41
8.5	0.932	272.73	8.5	0.892	259.72	8.5	0.775	221.67
9	0.987	290.61	9	0.928	271.43	9	0.821	236.63
9.5	0.996	293.54	9.5	0.936	274.03	9.5	0.867	251.59
10	1.012	298.74	10	0.975	286.71	10	0.901	262.64
11	1.098	326.71	11	1.047	310.13	11	0.93	272.08
12	1.126	335.82	12	1.075	319.23	12	1.018	300.7
13	1.187	355.66	13	1.16	346.88	13	1.041	308.18
14	1.242	373.55	14	1.18	353.38	14	1.106	329.32
15	1.275	384.28	15	1.246	374.85	15	1.143	341.35
16	1.344	406.72	15.5	1.281	386.23	16	1.178	352.73
17	1.353	409.65	17	1.325	400.54	17	1.226	368.34
18	1.426	433.39	18	1.325	400.54	18	1.225	368.02
19	1.416	430.14	19	1.365	413.55	19	1.282	386.56
20	1.46	444.45	20	1.435	436.32	20	1.267	381.68

Table E7: Test results for lateral loading in loose sand

Test 1			Test 2			Test 3		
Pile Head Displacement (mm)	Load		Pile Head Displacement (mm)	Load		Pile Head Displacement (mm)	Load	
	(Volts)	(N)		(Volts)	(N)		(Volts)	(N)
0	0.005	19	0	0.095	48.243	0	0.065	38.495
0.4	0.053	34.596	0.7	0.142	63.515	1	0.09	46.619
1.1	0.061	37.196	1.2	0.152	66.764	2	0.105	51.493
1.3	0.069	39.795	1.8	0.155	67.739	3	0.12	56.367
1.7	0.077	42.395	3.6	0.17	72.613	4.5	0.128	58.966
2.8	0.088	45.969	5.3	0.179	75.537	5.5	0.143	63.84
3	0.091	46.944	6.5	0.185	77.487	6	0.145	64.49
4	0.103	50.843	8.8	0.193	80.086	8	0.156	68.064
4.4	0.11	53.117	10.1	0.198	81.711	9	0.165	70.988
4.7	0.117	55.392	11.2	0.201	82.686	12	0.177	74.888
5.8	0.12	56.367	13.9	0.207	84.636	13	0.184	77.162
8.1	0.138	62.215	17.5	0.212	86.26	14	0.189	78.787
8.7	0.146	64.815	22.8	0.221	89.185	15	0.195	80.736
9.2	0.149	65.79	24.9	0.227	91.134	16	0.196	81.061
9.6	0.155	67.739	34.6	0.239	95.033	17.5	0.199	82.036
12.3	0.165	70.988	46	0.254	99.907	19	0.2	82.361
13.4	0.172	73.263				22.1	0.207	84.636
16.2	0.18	75.862				22.5	0.21	85.61
19.5	0.188	78.462				23	0.212	86.26
20.1	0.191	79.437				29	0.217	87.885
22.7	0.198	81.711				30	0.22	88.86
23.6	0.199	82.036				35.5	0.227	91.134
25.8	0.205	83.986				45	0.24	95.358
26.8	0.207	84.636						
35	0.214	86.91						
45	0.23	92.109						

Table E8: Test results for lateral loading in dense sand

Test 1			Test 2			Test 3		
Pile Head Displacement (mm)	Load		Pile Head Displacement (mm)	Load		Pile Head Displacement (mm)	Load	
	(Volts)	(N)		(Volts)	(N)		(Volts)	(N)
0	0.036	29.072	0	0.01	20.624	0	0.013	21.599
1.3	0.058	36.221	1.6	0.059	36.546	2.1	0.033	28.098
2.8	0.084	44.669	1.9	0.074	41.42	2.8	0.047	32.647
3.6	0.106	51.818	2.8	0.09	46.619	3.3	0.056	35.571
4	0.128	58.966	3.7	0.12	56.367	3.8	0.063	37.846
5.3	0.152	66.764	4.6	0.14	62.865	4	0.078	42.72
6.1	0.174	73.913	5.8	0.172	73.263	4.7	0.099	49.543
7.1	0.2	82.361	6.8	0.198	81.711	5.7	0.11	53.117
7.7	0.219	88.535	7.6	0.219	88.535	6.1	0.131	59.941
9	0.242	96.008	8.5	0.242	96.008	7.2	0.16	69.364
10.2	0.27	105.11	9.2	0.261	102.18	8.6	0.17	72.613
10.8	0.287	110.63	10.5	0.283	109.33	9.2	0.19	79.112
12.2	0.318	120.7	12.1	0.32	121.35	9.8	0.204	83.661
13.1	0.341	128.18	12.6	0.334	125.9	10.7	0.233	93.084
13.8	0.358	133.7	13.7	0.354	132.4	12	0.257	100.88
15.6	0.391	144.42	15.4	0.381	141.17	13.1	0.28	108.36
16.2	0.415	152.22	15.8	0.389	143.77	13.4	0.3	114.85
17.6	0.438	159.69	16.9	0.412	151.25	15.5	0.32	121.35
20.3	0.464	168.14	18.7	0.438	159.69	16.4	0.334	125.9
20.9	0.49	176.59	20.5	0.462	167.49	17	0.36	134.35
23.4	0.518	185.69	22.8	0.489	176.27	18.5	0.373	138.57
26.5	0.55	196.09	26.4	0.518	185.69	19.9	0.392	144.75
32.7	0.573	203.56				20.4	0.431	157.42
						23.9	0.461	167.17
						26	0.494	177.89
						31	0.54	192.84

Table E9: Test results for lateral loading in layered sand

Test 1			Test 2			Test 3		
Pile Head Displacement (mm)	Load		Pile Head Displacement (mm)	Load		Pile Head Displacement (mm)	Load	
	(Volts)	(N)		(Volts)	(N)		(Volts)	(N)
0	0.064	38.171	0	0.089	46.294	0	0.056	35.571
0.3	0.073	41.095	0.8	0.102	50.518	0.2	0.081	43.694
1.2	0.09	46.619	2.5	0.122	57.016	0.6	0.087	45.644
1.5	0.105	51.493	4	0.156	68.064	1.2	0.101	50.193
1.9	0.115	54.742	6.2	0.185	77.487	2.5	0.112	53.767
2.9	0.141	63.19	6.4	0.2	82.361	3.9	0.133	60.591
3.9	0.157	68.389	6.9	0.205	83.986	4.6	0.144	64.165
4.7	0.165	70.988	8.9	0.222	89.509	5.1	0.156	68.064
5.6	0.18	75.862	11.1	0.24	95.358	6.5	0.17	72.613
6.7	0.191	79.437	12.4	0.251	98.932	7.7	0.187	78.137
7.3	0.199	82.036	13	0.271	105.43	9.2	0.2	82.361
8.1	0.205	83.986	15.6	0.286	110.3	10.7	0.221	89.185
9.6	0.224	90.159	18.1	0.309	117.78	11.3	0.225	90.484
10.7	0.235	93.734	19.1	0.319	121.03	14.3	0.244	96.658
11.4	0.246	97.308	19.6	0.322	122	16.6	0.266	103.81
13.2	0.255	100.23	22.7	0.342	128.47	22.2	0.29	111.6
13.9	0.266	103.81	25.6	0.355	132.86			
14.8	0.274	106.41	29.5	0.369	137.24			
18.2	0.287	110.63	34.6	0.382	141.63			
20	0.3	114.85	41.4	0.396	146.01			
22.3	0.311	118.27						
25.0	0.322	122						
28.1	0.334	125.74						
31.6	0.345	129.51						
35.6	0.357	133.25						

APPENDIX F: Mesh Configuration of Constructed Pile

---oooOOOooo---

This appendix is referred to in Chapter 8. It contains the general pile mesh configuration that was later converted to ABAQUS coding.

The mesh configuration shown in this Appendix is for the mesh adopted for the numerical analysis in Chapter 9.

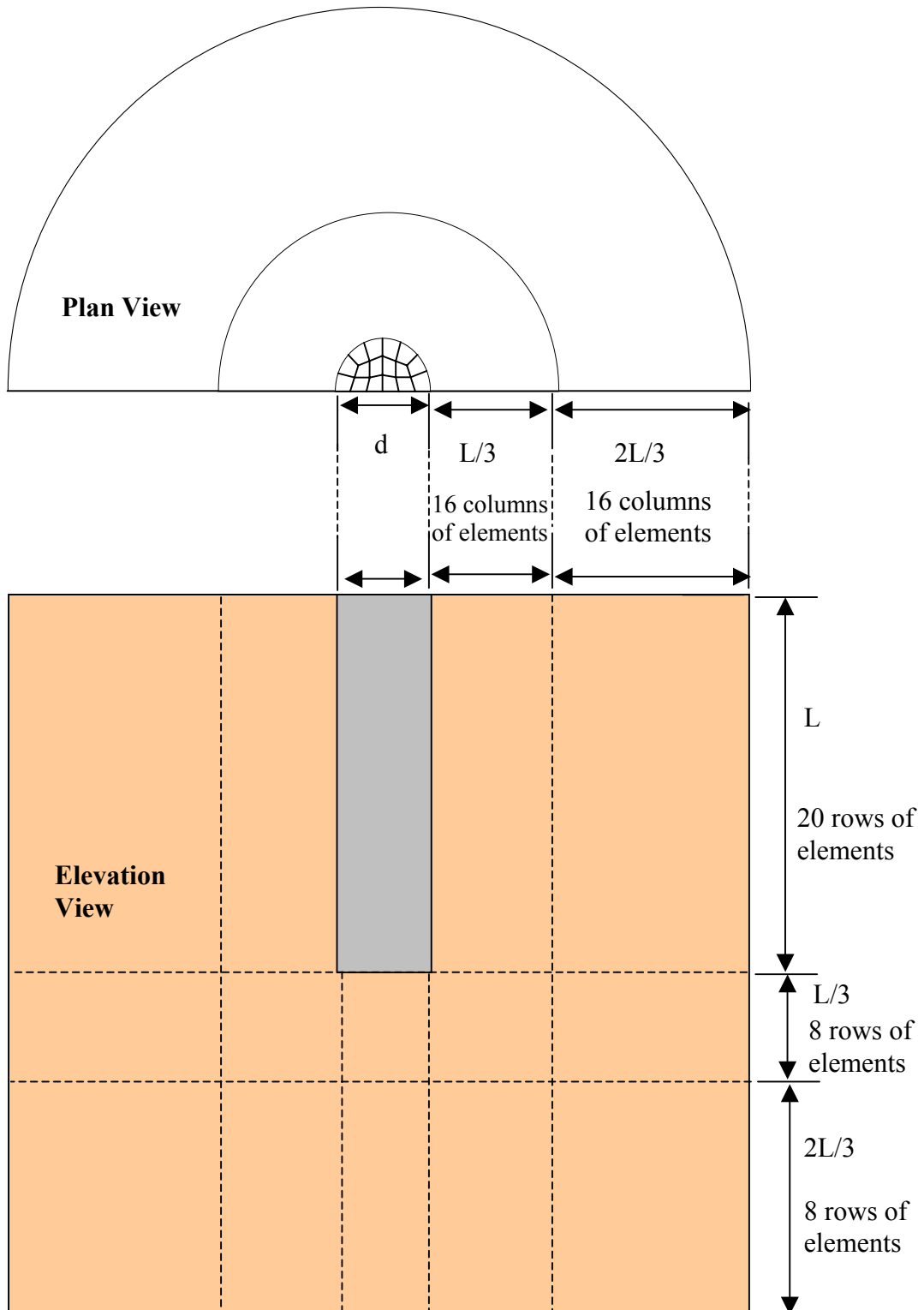


Figure F1: Elevation and plan view of pile model

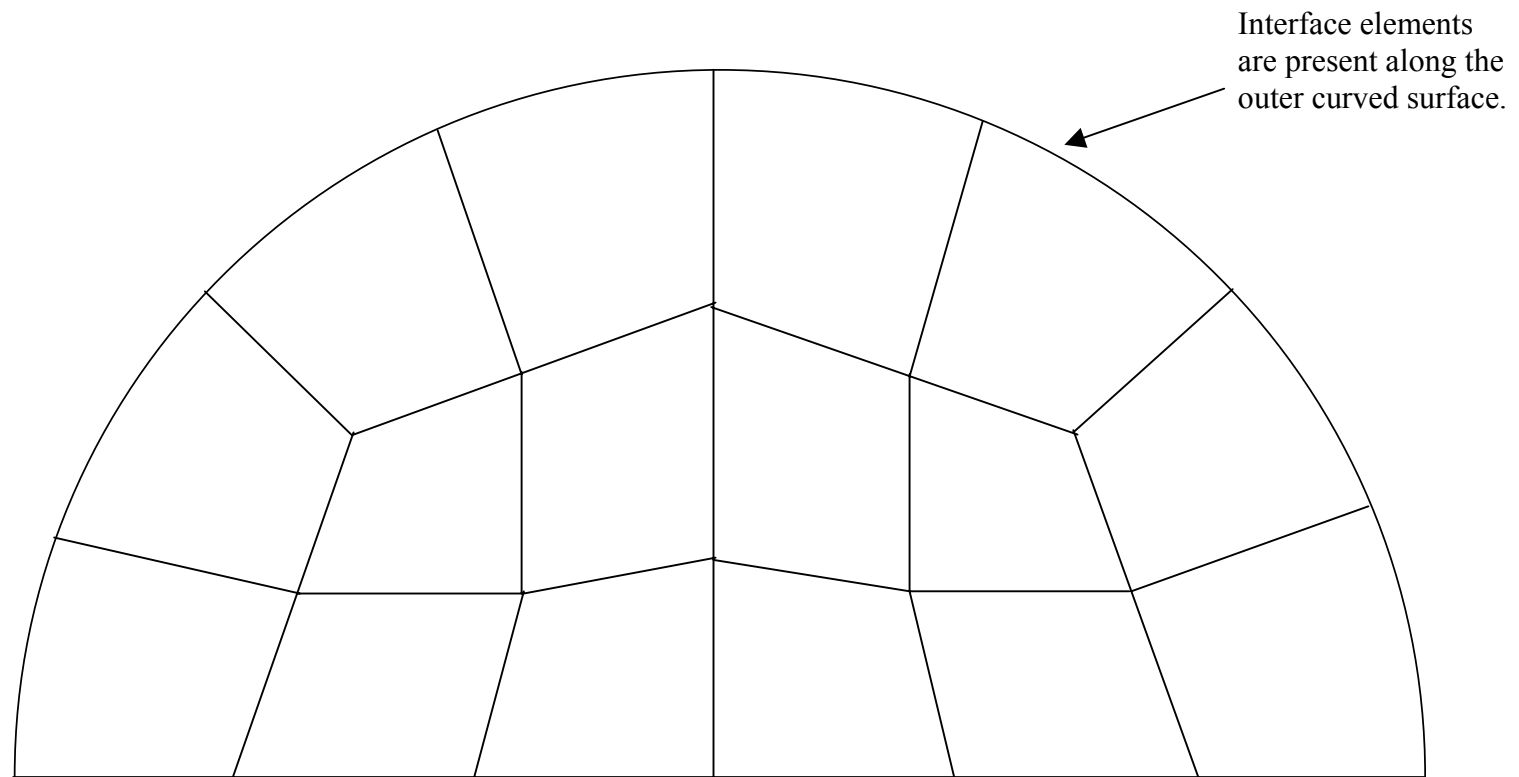


Figure F2: Plan view for the top of the pile

APPENDIX G: ABAQUS Code

---oooOOOooo---

This appendix is referred to in Chapter 8. It contains an example of an input file used for the pile verification Case 7 (see Figure 8.18). The data for Case 7 was obtained from Hage-Chehade et al. (1991), who tested an impact driven pile under horizontal load and subjected to a water table.

*HEADING

Case study 7 - large scale, impact driven, lateral loading (Hage-Chehade et al.,1991)

SI units (m, Pa, N)

1-axis (x), 2-axis (y), 3-axis (z)

**

*NODE

1, -7.392, 0, 0
 17, 7.392, 0, 0
 273, -2.559, 0, 0
 289, 2.559, 0, 0
 545, -0.142, 0, 0
 561, 0.142, 0, 0
 562, -0.118, 0, 0
 578, 0.118, 0, 0
 579, -0.095, 0, 0
 583, -0.067, 0.067, 0
 587, 0.000, 0.095, 0
 591, 0.067, 0.067, 0
 595, 0.095, 0, 0
 596, -0.071, 0, 0
 599, -0.050, 0.050, 0
 602, 0.000, 0.071, 0
 605, 0.050, 0.050, 0
 608, 0.071, 0, 0
 609, -0.047, 0, 0
 611, -0.033, 0.033, 0
 613, 0, 0.047, 0
 615, 0.033, 0.033, 0
 617, 0.047, 0, 0
 618, -0.024, 0, 0
 619, -0.017, 0.017, 0
 620, 0, 0.024, 0
 621, 0.017, 0.017, 0
 622, 0.024, 0, 0
 623, 0, 0, 0
 9969, -7.392, 0, 4.833
 9985, 7.392, 0, 4.833
 10241, -2.559, 0, 4.833
 10257, 2.559, 0, 4.833
 10513, -0.142, 0, 4.833
 10529, 0.142, 0, 4.833
 10530, -0.118, 0, 4.833
 10546, 0.118, 0, 4.833
 10547, -0.095, 0, 4.833
 10551, -0.067, 0.067, 4.833
 10555, 0.000, 0.095, 4.833
 10559, 0.067, 0.067, 4.833
 10563, 0.095, 0, 4.833
 10564, -0.071, 0, 4.833
 10567, -0.050, 0.050, 4.833

10570, 0.000, 0.071, 4.833
10573, 0.050, 0.050, 4.833
10576, 0.071, 0, 4.833
10577, -0.047, 0, 4.833
10579, -0.033, 0.033, 4.833
10581, 0, 0.047, 4.833
10583, 0.033, 0.033, 4.833
10585, 0.047, 0, 4.833
10586, -0.024, 0, 4.833
10587, -0.017, 0.017, 4.833
10588, 0, 0.024, 4.833
10589, 0.017, 0.017, 4.833
10590, 0.024, 0, 4.833
10591, 0, 0, 4.833
19937, -7.392, 0, 7.25
19953, 7.392, 0, 7.25
20209, -2.559, 0, 7.25
20225, 2.559, 0, 7.25
20481, -0.142, 0, 7.25
20497, 0.142, 0, 7.25
20498, -0.118, 0, 7.25
20514, 0.118, 0, 7.25
20515, -0.095, 0, 7.25
20519, -0.067, 0.067, 7.25
20523, 0.000, 0.095, 7.25
20527, 0.067, 0.067, 7.25
20531, 0.095, 0, 7.25
20532, -0.071, 0, 7.25
20535, -0.050, 0.050, 7.25
20538, 0.000, 0.071, 7.25
20541, 0.050, 0.050, 7.25
20544, 0.071, 0, 7.25
20545, -0.047, 0, 7.25
20547, -0.033, 0.033, 7.25
20549, 0, 0.047, 7.25
20551, 0.033, 0.033, 7.25
20553, 0.047, 0, 7.25
20554, -0.024, 0, 7.25
20555, -0.017, 0.017, 7.25
20556, 0, 0.024, 7.25
20557, 0.017, 0.017, 7.25
20558, 0.024, 0, 7.25
20559, 0, 0, 7.25
44857, -7.392, 0, 14.5
44873, 7.392, 0, 14.5
45129, -2.559, 0, 14.5
45145, 2.559, 0, 14.5
45401, -0.142, 0, 14.5
45417, 0.142, 0, 14.5
45418, -0.118, 0, 14.5

45434, 0.118, 0, 14.5
45435, -0.095, 0, 14.5
45439, -0.067, 0.067, 14.5
45443, 0.000, 0.095, 14.5
45447, 0.067, 0.067, 14.5
45451, 0.095, 0, 14.5
45452, -0.071, 0, 14.5
45455, -0.050, 0.050, 14.5
45458, 0.000, 0.071, 14.5
45461, 0.050, 0.050, 14.5
45464, 0.071, 0, 14.5
45465, -0.047, 0, 14.5
45467, -0.033, 0.033, 14.5
45469, 0, 0.047, 14.5
45471, 0.033, 0.033, 14.5
45473, 0.047, 0, 14.5
45474, -0.024, 0, 14.5
45475, -0.017, 0.017, 14.5
45476, 0, 0.024, 14.5
45477, 0.017, 0.017, 14.5
45478, 0.024, 0, 14.5
45479, 0, 0, 14.5
50545, -0.142, 0, 7.25
50561, 0.142, 0, 7.25
50562, -0.118, 0, 7.25
50578, 0.118, 0, 7.25
50579, -0.095, 0, 7.25
50583, -0.067, 0.067, 7.25
50587, 0.000, 0.095, 7.25
50591, 0.067, 0.067, 7.25
50595, 0.095, 0, 7.25
50596, -0.071, 0, 7.25
50599, -0.050, 0.050, 7.25
50602, 0.000, 0.071, 7.25
50605, 0.050, 0.050, 7.25
50608, 0.071, 0, 7.25
50609, -0.047, 0, 7.25
50611, -0.033, 0.033, 7.25
50613, 0, 0.047, 7.25
50615, 0.033, 0.033, 7.25
50617, 0.047, 0, 7.25
50618, -0.024, 0, 7.25
50619, -0.017, 0.017, 7.25
50620, 0, 0.024, 7.25
50621, 0.017, 0.017, 7.25
50622, 0.024, 0, 7.25
50623, 0, 0, 7.25
75465, -0.142, 0, 14.5
75481, 0.142, 0, 14.5
75482, -0.118, 0, 14.5

```

75498, 0.118, 0, 14.5
75499, -0.095, 0, 14.5
75503, -0.067, 0.067, 14.5
75507, 0.000, 0.095, 14.5
75511, 0.067, 0.067, 14.5
75515, 0.095, 0, 14.5
75516, -0.071, 0, 14.5
75519, -0.050, 0.050, 14.5
75522, 0.000, 0.071, 14.5
75525, 0.050, 0.050, 14.5
75528, 0.071, 0, 14.5
75529, -0.047, 0, 14.5
75531, -0.033, 0.033, 14.5
75533, 0, 0.047, 14.5
75535, 0.033, 0.033, 14.5
75537, 0.047, 0, 14.5
75538, -0.024, 0, 14.5
75539, -0.017, 0.017, 14.5
75540, 0, 0.024, 14.5
75541, 0.017, 0.017, 14.5
75542, 0.024, 0, 14.5
75543, 0, 0, 14.5
*NGEN,LINE=C,NSET=BL1
1,17,1,623,0,0,-1,0,0,-1
*NGEN,LINE=C,NSET=BL2
273,289,1,623,0,0,-1,0,0,-1
*NGEN,LINE=C,NSET=BL3
545,561,1,623,0,0,-1,0,0,-1
*NGEN,LINE=C,NSET=BL4
562,578,1,623,0,0,-1,0,0,-1
*NGEN,NSET=BL5
579,583,1
583,587,1
587,591,1
591,595,1
596,599,1
599,602,1
602,605,1
605,608,1
609,611,1
611,613,1
613,615,1
615,617,1
*NFill,NSET=GL
BL1,BL2,16,17
BL2,BL3,16,17
*NSET,NSET=BASEL
GL,BL5,BL4,618,620,622,623
**
*NGEN,LINE=C,NSET=AL1

```

```

9969,9985,1,10591,0,0,-1,0,0,-1
*NGEN,LINE=C,NSET=AL2
10241,10257,1,10591,0,0,-1,0,0,-1
*NGEN,LINE=C,NSET=AL3
10513,10529,1,10591,0,0,-1,0,0,-1
*NGEN,LINE=C,NSET=AL4
10530,10546,1,10591,0,0,-1,0,0,-1
*NGEN,NSET=AL5
10547,10551,1
10551,10555,1
10555,10559,1
10559,10563,1
10564,10567,1
10567,10570,1
10570,10573,1
10573,10576,1
10577,10579,1
10579,10581,1
10581,10583,1
10583,10585,1
*NFill,NSET=AL
AL1,AL2,16,17
AL2,AL3,16,17
*NSET,NSET=LAY A
AL,AL5,AL4,10586,10588,10590,10591
**
*NGEN,LINE=C,NSET=CL1
19937,19953,1,20559,0,0,-1,0,0,-1
*NGEN,LINE=C,NSET=CL2
20209,20225,1,20559,0,0,-1,0,0,-1
*NGEN,LINE=C,NSET=CL3
20481,20497,1,20559,0,0,-1,0,0,-1
*NGEN,LINE=C,NSET=CL4
20498,20514,1,20559,0,0,-1,0,0,-1
*NGEN,NSET=CL5
20515,20519,1
20519,20523,1
20523,20527,1
20527,20531,1
20532,20535,1
20535,20538,1
20538,20541,1
20541,20544,1
20545,20547,1
20547,20549,1
20549,20551,1
20551,20553,1
*NFill,NSET=CL
CL1,CL2,16,17
CL2,CL3,16,17

```



```

*NSET,NSET=LAYC
CL,CL5,CL4,20554,20556,20558,20559
**
*NGEN,LINE=C,NSET=TL1
44857,44873,1,45479,0,0,-1,0,0,-1
*NGEN,LINE=C,NSET=TL2
45129,45145,1,45479,0,0,-1,0,0,-1
*NGEN,LINE=C,NSET=TL3
45401,45417,1,45479,0,0,-1,0,0,-1
*NGEN,LINE=C,NSET=TL4
45418,45434,1,45479,0,0,-1,0,0,-1
*NGEN,NSET=TL5
45435,45439,1
45439,45443,1
45443,45447,1
45447,45451,1
45452,45455,1
45455,45458,1
45458,45461,1
45461,45464,1
45465,45467,1
45467,45469,1
45469,45471,1
45471,45473,1
*NFILL,NSET=TL
TL1,TL2,16,17
TL2,TL3,16,17
*NSET,NSET=LAYT
TL,TL5,TL4,45474,45476,45478,45479
**
*NGEN,LINE=C,NSET=PB1
50545,50561,1,50623,0,0,-1,0,0,-1
*NGEN,NSET=PB2
50579,50583,1
50583,50587,1
50587,50591,1
50591,50595,1
50596,50599,1
50599,50602,1
50602,50605,1
50605,50608,1
50609,50611,1
50611,50613,1
50613,50615,1
50615,50617,1
*NSET,NSET=PILEB
PB1,PB2,50623
**
*NGEN,LINE=C,NSET=PT1
75465,75481,1,75543,0,0,-1,0,0,-1

```

```

*NGEN,NSET=PT2
75499,75503,1
75503,75507,1
75507,75511,1
75511,75515,1
75516,75519,1
75519,75522,1
75522,75525,1
75525,75528,1
75529,75531,1
75531,75533,1
75533,75535,1
75535,75537,1
*NSET,NSET=PILET
PT1,PT2,75543
**
*NFILL,NSET=ALLNODES
BASEL,LAYA,16,623
LAYA,LAYC,16,623
LAYC,LAYT,40,623
PILEB,PILET,40,623
**
*NSET,NSET=PILECORE,GENERATE
50623,75543,623
**
*NFILL,NSET=FIXED1
BL1,AL1,16,623
AL1,CL1,16,623
CL1,TL1,40,623
*NSET,NSET=FIXED
FIXED1,BASEL
**
*NSET,NSET=R1,GENERATE
1,273,17
273,545,17
17,289,17
289,561,17
*NSET,NSET=R2,GENERATE
9969,10241,17
10241,10513,17
9985,10257,17
10257,10529,17
*NSET,NSET=R3,GENERATE
19937,20209,17
20209,20481,17
19953,20225,17
20225,20497,17
*NSET,NSET=R4,GENERATE
44857,45129,17
45129,45401,17

```

```

44873,45145,17
45145,45417,17
*NSET,NSET=RL1
R1, 562, 578, 579, 595, 596, 608, 609, 617, 618,
622, 623
*NSET,NSET=RL2
R2, 10530, 10546, 10547, 10563, 10564, 10576, 10577,
10585, 10586, 10590, 10591
*NSET,NSET=RL3
R3, 20498, 20514, 20515, 20531, 20532, 20544, 20545,
20553, 20554, 20558, 20559
*NSET,NSET=RL4
R4, 45418, 45434, 45435, 45451, 45452, 45464, 45465,
45473, 45474, 45478, 45479
*NSET,NSET=PBR
50562,50578,50579,50595,50596,50608,50609,50617,
50618,50622,50623
*NSET,NSET=PTR
75482,75498,75499,75515,75516,75528,75529,75537,
75538,75542,75543
*NFILL,NSET=ROLLER
RL1,RL2,16,623
RL2,RL3,16,623
RL3,RL4,40,623
PBR,PTR,40,623
**
*NSET,NSET=NP,GENERATE
50623,75543,1246
**
*ELEMENT,TYPE=C3D8,ELSET=BOTTK
1, 1, 35, 37, 3, 1247, 1281, 1283, 1249
129, 545, 579, 581, 547, 1791, 1825, 1827, 1793
137, 579, 609, 611, 581, 1825, 1855, 1857, 1827
138, 581, 611, 585, 583, 1827, 1857, 1831, 1829
139, 585, 611, 613, 587, 1831, 1857, 1859, 1833
140, 587, 613, 615, 589, 1833, 1859, 1861, 1835
141, 589, 615, 593, 591, 1835, 1861, 1839, 1837
142, 593, 615, 617, 595, 1839, 1861, 1863, 1841
143, 609, 623, 613, 611, 1855, 1869, 1859, 1857
144, 613, 623, 617, 615, 1859, 1869, 1863, 1861
*ELGEN,ELSET=BOTTS
1,8,2,1,16,34,8,16,1246,144
129,8,2,1,16,1246,144
137,16,1246,144
138,16,1246,144
139,16,1246,144
140,16,1246,144
141,16,1246,144
142,16,1246,144
143,16,1246,144

```

```

144,16,1246,144
**
*ELEMENT,TYPE=C3D8,ELSET=TOPK
2305, 19937, 19971, 19973, 19939, 21183, 21217, 21219, 21185
2425, 20447, 20481, 20483, 20449, 21693, 21727, 21729, 21695
2569, 21693, 21727, 21729, 21695, 22939, 22973, 22975, 22941
5201, 50545, 50579, 50581, 50547, 51791, 51825, 51827, 51793
5209, 50579, 50609, 50611, 50581, 51825, 51855, 51857, 51827
5210, 50581, 50611, 50585, 50583, 51827, 51857, 51831, 51829
5211, 50585, 50611, 50613, 50587, 51831, 51857, 51859, 51833
5212, 50587, 50613, 50615, 50589, 51833, 51859, 51861, 51835
5213, 50589, 50615, 50593, 50591, 51835, 51861, 51839, 51837
5214, 50593, 50615, 50617, 50595, 51839, 51861, 51863, 51841
5215, 50609, 50623, 50613, 50611, 51855, 51869, 51859, 51857
5216, 50613, 50623, 50617, 50615, 51859, 51869, 51863, 51861
5345, 51791, 51825, 51827, 51793, 53037, 53071, 53073, 53039
**
*ELGEN,ELSET=TOPS1
2305,8,2,1,15,34,8,17,1246,144
*ELGEN,ELSET=TOPS2
2425,8,2,1
*ELGEN,ELSET=TOPSS
2569,8,2,1,16,1246,144
*ELSET,ELSET=TOPSB,GENERATE
2289,2304,1
*ELSET,ELSET=TOPS
TOPSS,TOPS1,TOPS2,TOPSB
*ELGEN,ELSET=PILES
5345,8,2,1,19,1246,144
*ELGEN,ELSET=PILEB1
5201,8,2,1
*ELSET,ELSET=PILEB,GENERATE
5201,5216,1
*ELGEN,ELSET=PILE1
5209,20,1246,144
5210,20,1246,144
5211,20,1246,144
5212,20,1246,144
5213,20,1246,144
5214,20,1246,144
5215,20,1246,144
5216,20,1246,144
*ELSET,ELSET=PILE
PILES,PILE1,PILEB
**
*ELSET,ELSET=ALL
BOTTK,TOPK,BOTTS,TOPS,PILE
**
*SOLID SECTION,ELSET=PILE,MATERIAL=CONC
*MATERIAL,NAME=CONC

```

```

*ELASTIC
47E9,0.15
*DENSITY
10E2
**
*ELSET,ELSET=TOPLAYER,GENERATE
3169,5184,1
*SOLID SECTION,ELSET=TOPLAYER,MATERIAL=SOILTOP
*MATERIAL,NAME=SOILTOP
*ELASTIC
15E6,0.3
*DENSITY
10E2
*MOHR COULOMB
38,5
*MOHR COULOMB HARDENING
0.1
**
*ELSET,ELSET=BOTTLAYER,GENERATE
1,3168,1
*SOLID SECTION,ELSET=BOTTLAYER,MATERIAL=SOILBOTT
*MATERIAL,NAME=SOILBOTT
*ELASTIC
15E6,0.3
*DENSITY
10E2
*MOHR COULOMB
40,7
*MOHR COULOMB HARDENING
0.1
**
**Interface definition
**
*SURFACE,TYPE=ELEMENT,NAME=SURFPILEB
PILEB,S1
*SURFACE,TYPE=ELEMENT,NAME=SURFPILES
PILES,S6
**
*SURFACE,TYPE=ELEMENT,NAME=SURFSOILB
TOPSB,S2
*SURFACE,TYPE=ELEMENT,NAME=SURFSOILS
TOPSS,S4
**
*CONTACT PAIR, INTERACTION=FRICB
SURFSOILB,SURFPILEB
*SURFACE INTERACTION,NAME=FRICB
*FRICTION
0.2
*CONTACT PAIR,INTERACTION=FRICS
SURFSOILS,SURFPILES

```

```

*SURFACE INTERACTION,NAME=FRICS
*FRICTION
0.2
**
*ELSET,ELSET=LOADV,GENERATE
7937,7952,1
*SURFACE,TYPE=ELEMENT,NAME=LOADA
LOADV,S2
**
*NSET,NSET=PTOP
PT1,PT2
*EQUATION
2
PTOP,1,1,75543,1,-1
**
*NSET,NSET=QNODES
75465,75481
*NSET,NSET=HNODES
75467,75469,75471,75473,75475,75477,75479,75499,75515,
75529,75537,75543
*NSET,NSET=FNODES
75501,75503,75505,75507,75509,75511,75513,75531,75533,
75535
**
*INITIAL CONDITIONS, TYPE=STRESS, GEOSTATIC
TOPS,0,13.5,-62.5e3,7.25,0.4,0.4
BOTTS,-62.5e3,7.25,-135e3,0,0.4,0.4
PILE,0,13.5,-62.5e3,7.25,0.4,0.4
**
**
*STEP,UNSYMM=YES,NLGEOM
*STATIC
*BOUNDARY
FIXED,ENCASTRE
ROLLER,2
*DLOAD
TOPS,GRAV,10,0,0,-1
BOTTS,GRAV,10,0,0,-1
PILE,GRAV,10,0,0,-1
*END STEP
**
*STEP,INC=400,NLGEOM=YES,UNSYMM=YES
PRESCRIBE DISPLACEMENT
*STATIC
0.0001,1,1e-20,.1
*CLOAD
QNODES,1,0.08e3
HNODES,1,0.15e3
FNODES,1,0.30e3
*CONTROLS,PARAMETERS=TIME INCREMENTATION

```

```
18,30
*CONTROLS,PARAMETERS=FIELD
3e-2,1e3
*BOUNDARY
FIXED,ENCASTRE
ROLLER,2
*RESTART,WRITE,OVERLAY
*EL PRINT,ELSET=BOTTK
S
*NODE PRINT,NSET=PILECORE
U
*END STEP
**
*STEP,INC=400,NLGEOM=YES,UNSYMM=YES
PRESCRIBE DISPLACEMENT
*STATIC
0.0001,1,1e-20,.1
*LOAD
QNODES,1,0.16e3
HNODES,1,0.30e3
FNODES,1,0.60e3
*CONTROLS,PARAMETERS=TIME INCREMENTATION
18,30
*CONTROLS,PARAMETERS=FIELD
3e-2,1e3
*BOUNDARY
FIXED,ENCASTRE
ROLLER,2
*RESTART,WRITE,OVERLAY
*EL PRINT,ELSET=BOTTK
S
*NODE PRINT,NSET=PILECORE
U
*END STEP
```

APPENDIX H: Verification Results

---oooOOOooo---

This appendix is referred to in Chapter 8. It contains the raw data for the pile verification cases presented in Chapter 8. The constitutive properties based on the raw data are also given for the piles and sand.

The symbols used in this Appendix are as follows:

C_{ER} = hammer efficiency factor

C_N = overburden correction factor

E = Young's modulus

K_o = earth pressure coefficient

N_{60} = blow count corrected for hammer efficiency

N_1 = blow count corrected for overburden

$(N_1)_{60}$ = blow count corrected for hammer efficiency and overburden

Table H1: CASE 1 cast-in-place, compression loading, raw and interpreted data

Soil Characteristics

Homogenous top layer

E (MPa)	24.5
ϕ' (deg)	41
c (kPa)	2
Height (m)	9.6
N(average)	19
Dilation ψ (deg)	8
K_o	0.3

Homogenous bottom layer

E (MPa)	65.2
ϕ' (deg)	50
c (kPa)	0.1
Height (m)	7.46
N(average)	71
Dilation ψ (deg)	17
K_o	0.2

Circle Pile Characteristics

Length(m)	8.53
Diameter (m)	0.406
Area (m ²)	0.129462
E (GPa)	30.0

Raw Soil Data

SPT Blows	C_{er} (assume efficiency=60%)	C_N	N_{60}	N_1	$(N_1)_{60}$	ASTM Code	Depth (m)	Height (m)
0	n/a	n/a	n/a	n/a	n/a	n/a	0	-
13	1.000	1.81	13	24	24	SP-SM	1.62	1.62
15	1.000	1.29	15	19	19	SP	3.2	1.58
23	1.000	1.04	23	24	24	SP	4.88	1.68
31	1.000	0.91	31	28	28	SP	6.4	1.52
14	1.000	0.81	14	11	11	MH	8.08	1.68
71	1.000	0.74	71	53	53	SP	9.6	1.52

N_{60} (layer 1)	19
$(N_1)_{60}$ (layer 1)	21
N_{60} (layer 2)	71
$(N_1)_{60}$ (layer 2)	53

Note: a list of symbols for this appendix is given on the Appendix H title page (pp. 314)

Table H1 Continued: CASE 1 cast-in-place, compression loading, raw and interpreted data

Actual Test Data

Load	pressure	displacement
0	0	0
133.45	1030805	0.51
266.89	2061533	0.76
400.34	3092339	1.52
533.79	4123144	4.06
667.23	5153872	6.6
756.2	5841101	10.67
800.68	6184677	13.72
(kN)	(units N/m ²)	(units mm)

Model Results Circular

	medium mesh	fine mesh
pressure	displacement	displacement
0	0	0
1030805	1.01	1.38
2061533	2.08	
3092339	3.3	4.38
4123144	5.1	
5153872	8.4	
5841101	11.6	13.21
6184677	13.46	22
(units N/m ²)	(units mm)	(units mm)

Table H2: CASE 2 cast-in-place, compression loading, raw and interpreted data

Soil Characteristics

Homogenous top layer

E (MPa)	28.8
ϕ' (deg)	43
c (kPa)	0.1
Height (m)	10.67
N(average)	24
Dilation ψ	10
K_o	0.3

Homogenous bottom layer

E (MPa)	61.3
ϕ' (deg)	50
c (kPa)	0.1
Height (m)	3.97
N(average)	66
Dilation ψ	17
K_o	0.2

Pile Characteristics

Length(m)	7.32
Diameter (m)	0.457
Area (m ²)	0.164030
E (GPa)	30.0

Raw Soil Data

SPT Blows	C_{er} (assume efficiency=60%)	C_N	N_{60}	N_1	$(N_1)_{60}$	ASTM Code	Depth (m)	Height (m)
0	n/a	n/a	n/a	n/a	n/a	n/a	0	-
15	1.000	1.97	15	30	30	SP-SM	1.37	1.37
25	1.000	1.32	25	33	33	SP-SM	3.05	1.68
36	1.000	1.08	36	39	39	MH	4.57	1.52
15	1.000	0.93	15	14	14	SP	6.1	1.53
27	1.000	0.76	27	21	21	SP	9.14	3.04
66	1.000	0.71	66	47	47	SP	10.67	1.53

N_{60} (layer 1)	24
$(N_1)_{60}$ (layer 1)	26
N_{60} (layer 2)	66
$(N_1)_{60}$ (layer 2)	47

Note: a list of symbols for this appendix is given on the Appendix H title page (pp. 314)

Table H2 Continued: CASE 2 cast-in-place, compression loading, raw and interpreted data

Actual Test Data

Load	pressure	displacement
0	0	0
133.45	813573	1.17
266.89	1627084	1.37
400.34	2440657	2.39
533.79	3254229	6.6
667.23	4067741	14.66
(kN)	(units N/m ²)	(units mm)

Model Results Circular

	medium mesh	fine mesh
pressure	displacement	displacement
0	0.00	0.00
813573	0.64	
1627084	1.75	1.56
2440657	3.10	
3254229	5.90	6.60
4067741	11.12	14.19
(units N/m ²)	(units mm)	(units mm)

Table H3: CASE 3 cast-in-place, uplift loading, raw and interpreted data

Soil Characteristics

Homogenous top layer

E (MPa)	32.1
ϕ' (deg)	43
c (kPa)	0.1
Height (m)	15.85
N(average)	29
Dilation ψ	10
K_o	0.3

Homogenous bott layer

E (MPa)	88.0
ϕ' (deg)	50
c (kPa)	0.1
Height (m)	11.59
N(average)	100
Dilation ψ	17
K_o	0.2

Pile Characteristics

Length(m)	13.72
Diameter (m)	0.6096
Area (m^2)	0.291864
E (GPa)	30.0

Raw Soil Data

SPT Blows	C_{er} (assume efficiency=60%)	C_N	N_{60}	N_1	$(N_1)_{60}$	ASTM Code	Depth (m)	Height (m)
0	n/a	n/a	n/a	n/a	n/a	n/a	0	-
16	1.000	1.56	16	25	25	SW	2.19	2.19
25	1.000	1.20	25	30	30	SW	3.66	1.47
20	1.000	1.01	20	20	20	SW	5.18	1.52
38	1.000	0.89	38	34	34	SW	6.71	1.53
55	1.000	0.80	55	44	44	NA	8.23	1.52
42	1.000	0.74	42	31	31	SW	9.75	1.52
21	1.000	0.69	21	14	14	CL-ML	11.28	1.53
17	1.000	0.64	17	11	11	CL-ML	12.8	1.52
86	1.000	0.58	86	50	50	SW	15.85	3.05
42	1.000	0.55	42	23	23	SC	17.37	1.52
120	1.000	0.51	120	61	61	SW	20.27	2.9
120	1.000	0.49	120	59	59	SW	21.79	1.52
130	1.000	0.48	130	62	62	SW	23.29	1.5

N_{60} (layer 1)	29
$(N_1)_{60}$ (layer 1)	26
N_{60} (layer 2)	100
$(N_1)_{60}$ (layer 2)	52

Table H3 Continued: CASE 3 cast-in-place, uplift loading, raw and interpreted data

Actual Test Data

Load	pressure	displacement
0	0	0
322.05	1103427	1.24
426.58	1461574	1.24
667.23	2286103	1.93
853.17	2923181	2.41
862.51	2955183	2.54
939.91	3220375	2.79
1017.31	3485568	3.28
1080.03	3700463	3.3
1148.53	3935161	3.86
1248.17	4276554	4.19
1302.44	4462497	4.92
1334.47	4572240	5.11
(kN)	(units N/m ²)	(units mm)

Model Results Circular

	medium mesh	fine mesh
pressure	displacement	displacement
0	0.00	0.00
1103427	1.30	1.37
1461574		
2286103	2.80	2.93
2923181		
2955183	3.70	3.98
3220375		
3485568	4.50	5.07
3700463		
3935161	5.09	6.14
4276554		
4462497		
4572240	6.00	7.56
(units N/m ²)	(units mm)	(units mm)

Table H4: CASE 4 small scale testing, placed-in-sand, lateral loading, raw and interpreted data

Actual Test Data - Test Pile 2

Load-test 2	Displacement-test2
0	0.00
120	5.03
190	9.04
280	14.49
340	21.14
440	29.11
540	41.39
640	70.94

(N)

(units mm)

Actual Test Data - Test Pile 1

Load test 2	Displacement test2
0	0
60	1.33
90	2.28
180	4.33
210	6.01
240	7
260	9
360	10.98
470	16.53
570	26.14
620	35.78
670	57.69

(N)

(units mm)

Model Results Circular

	medium mesh	fine mesh
pressure	displacement	displacement
0	0	0
120	1.322	1.754
190	3.541	4.624
280	7.978	10.33
340	11.926	15.394
440	20.266	26.074
540	30.806	39.554
640	43.546	55.834

(N)

(units mm)

(units mm)

Soil Characteristics

Homogenous top layer

E (MPa)	11.4
ϕ' (deg)	31
c (kPa)	0.1
Height (m)	0.75
N(average)	2
Dilation ψ	0
K_o	0.5

Circle Pile Characteristics

Length(m)	0.375
Diameter (m)	0.15
Area (m ²)	0.017671
E (GPa)	30.0

Note: a list of symbols for this appendix is given on the Appendix H title page (pp. 314)

Table H5: CASE 5 impact driven, compression loading, raw and interpreted data

Soil Characteristics

Homogenous top layer

E (MPa)	62.9
ϕ' (deg)	40
c (kPa)	0.1
Height (m)	15.85
N(average)	24
Dilation ψ	7
K_o	0.6

Homogenous middle layer

E (MPa)	92.8
ϕ' (deg)	45
c (kPa)	1
Height (m)	13.77
N(average)	54
Dilation ψ	10
K_o	0.3

Circle Pile Characteristics

Length(m)	14.81
Diameter (m)	0.3048
Area (m ²)	0.072966
E (GPa)	30.0

Raw Soil Data

SPT Blows	C_{er} (assume efficiency=60%)	C_N	N_{60}	N_1	$(N_1)_{60}$	ASTM Code	Depth (m)	Height (m)
0	n/a	n/a	n/a	n/a	n/a	n/a	0	-
14	1.000	1.58	14	22	22	SM	2.13	2.13
15	1.000	1.20	15	18	18	SM	3.66	1.53
32	1.000	1.01	32	32	32	SW	5.18	1.52
41	1.000	0.89	41	36	36	SW	6.71	1.53
7	1.000	0.80	7	6	6	MH	8.23	1.52
26	1.000	0.74	26	19	19	SP	9.75	1.52
33	1.000	0.69	33	23	23	SP	11.28	1.53
44	1.000	0.64	44	28	28	SP	12.8	1.52
4	1.000	0.61	4	2	2	SW-SM	14.33	1.53
68	1.000	0.58	68	39	39	SW-SM	15.85	1.52
70	1.000	0.55	70	39	39	SW-SM	17.37	1.52
24	1.000	0.53	24	13	13	SM	18.9	1.53

N_{60} (layer 1)	24
$(N_1)_{60}$ (layer 1)	21
N_{60} (layer 2)	54
$(N_1)_{60}$ (layer 2)	30

Note: a list of symbols for this appendix is given on the Appendix H title page (pp. 314)

Table H5 Continued: CASE 5 impact driven, compression loading, raw and interpreted data

Actual Test Data

Load	pressure	displacement
0	0	0
311.38	4267474.233	0.64
622.75	8534811.416	1.75
934.13	12802285.65	3.1
1245.5	17069622.83	6.78
(kN)	(units N/m^2)	(units mm)

Model Results Circular

	medium mesh	fine mesh
pressure	displacement	displacement
0	0	0
4267474	1.41	1.21
8534811	2.83	3.1
12802286	4.91	5.29
17069623	9.9	10.97
(units N/m^2)	(units mm)	(units mm)

Table H6: CASE 6 impact driven, compression loading, raw and interpreted data

Soil Characteristics

Homogenous top layer

E (MPa)	74.8
ϕ' (deg)	46
c (kPa)	0.1
Height (m)	10.67
N(average)	36
Dilation ψ	13
K_o	0.5

Homogenous middle layer

E (MPa)	89.9
ϕ' (deg)	47
c (kPa)	0.1
Height (m)	14.25
N(average)	51
Dilation ψ	14
K_o	0.5

Pile Characteristics

Length(m)	12.46
Diameter (m)	0.4064
Area (m^2)	0.129717
E (GPa)	30.0

Raw Soil Data

SPT Blows	C_{er} (assume efficiency=60%)	C_N	N_{60}	N_1	$(N_1)_{60}$	ASTM Code	Depth (m)	Height (m)
0	n/a	n/a	n/a	n/a	n/a	n/a	0	-
11	1.000	1.97	11	22	22	SP	1.37	1.52
35	1.000	1.32	35	46	46	SP	3.05	3.05
35	1.000	1.08	35	38	38	SP	4.57	4.57
49	1.000	0.93	49	46	46	SP	6.1	7.62
30	1.000	0.76	30	23	23	SP	9.14	10.67
51	1.000	0.71	51	36	36	SP	10.67	13.72

N_{60} (layer 1)	36
$(N_1)_{60}$ (layer 1)	34
N_{60} (layer 2)	51
$(N_1)_{60}$ (layer 2)	36

Note: a list of symbols for this appendix is given on the Appendix H title page (pp. 314)

Table H6 Continued: CASE 6 impact driven, compression loading, raw and interpreted data

Actual Test Data

Load	pressure	displacement
0	0	0
444.82	3429154	0.61
889.64	6858309	2.13
1334.47	10287540	4.62
1601.36	12345017	6.81
(kN)	(units N/m ²)	(units mm)

Circular Model Results

	medium mesh	fine mesh
pressure	displacement	displacement
0	0.00	0.00
3429154	1.80	1.92
6858309	4.12	5.20
10287540	8.91	10.53
12345017	13.86	15.01
(units N/m ²)	(units mm)	(units mm)

**APPENDIX I: Hypothetical Pile Case Results
Obtained from ABAQUS**

---oooOOOooo---

This appendix is referred to in Chapter 9. It contains the results for the hypothetical pile cases shown in Figure 9.1. The sand and pile characteristics used for each of the pile cases are also given. The oblique interaction charts developed in Chapters 9 and 10 were based on the results shown in this appendix.

Case 1 N=5,L/d=3,d=0.6 m, Axial Compression
Cast-in-place, free Head

Model Results

Load Magnitudes and Combinations

Vertical Load (kN)	Horizontal Load (kN)	Moment (kN.m)	Load Ratio
0	0	0	n/a
100	0	0	n/a
200	0	0	n/a
300	0	0	n/a
400	0	0	n/a
500	0	0	n/a

Pile Head Displacement

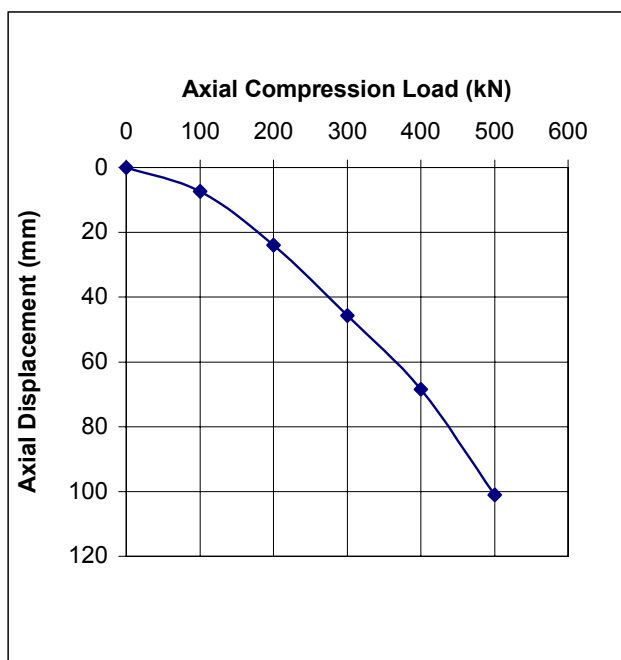
Displacement Magnitude (mm)	Vertical Displacement (mm)	Horizontal Displacement (mm)
0	0	0
7	7.4	0
24	24	0
46	45.7	0
69	68.5	0
101	101	0

Soil Details

E (MPa)	14
phi (deg)	36
c (kPa)	0.1
height (m)	3.6
N _{ave}	5
(N _{1ave})	12
dilation (deg)	3
earth press, K	0.4

Pile Details

Circular	
Length(m)	1.8
Dia (m)	0.6
Area (m ²)	0.283
L/d	3



Ultimate Load

Axial Compression = 220 kN

Case 2 N=5,L/d=3,d=0.6 m, Axial Uplift
Cast-in-place, free Head

Model Results

Load Magnitudes and Combinations

Vertical Load (kN)	Horizontal Load (kN)	Moment (kN.m)	Load Ratio
0	0	0	0
10	0	0	0
14.6	0	0	0
15.2	0	0	0

Pile Head Displacement

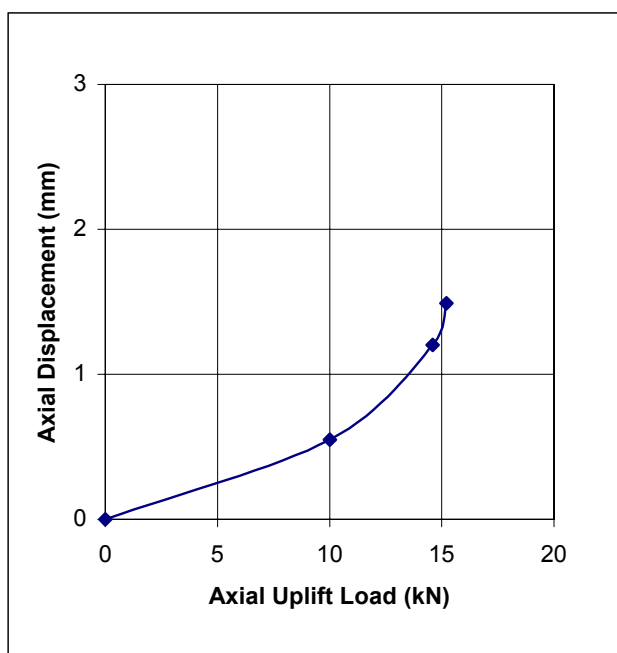
Displacement Magnitude (mm)	Vertical Displacement (mm)	Horizontal Displacement (mm)
0.000	0	0
0.550	0.55	0.000
1.204	1.204	0
1.490	1.49	0

Soil Details

E (MPa)	14
phi (deg)	36
c (kPa)	0.1
height (m)	3.6
N _{ave}	5
(N _{1ave})	12
dilation (deg)	3
earth press, K	0.4

Pile Details

Circular	
Length(m)	1.8
Dia (m)	0.6
Area (m ²)	0.283
L/d	3



Ultimate Load

Axial Uplift = 14 kN

Case 3 N=5,L/d=3,d=0.6 m, Axial Compression + Lateral Load
Cast-in-place, free Head

Model Results

Load Magnitudes and Combinations

Vertical Load (kN)	Horizontal Load (kN)	Moment (kN.m)	Load Ratio
0	0	0	0
43.0	1.07	0	0.203
100.0	2.50	0	0.471
150.0	3.75	0	0.707
207.0	5.18	0	0.976
249.9	6.25	0	1.178

Pile Head Displacement

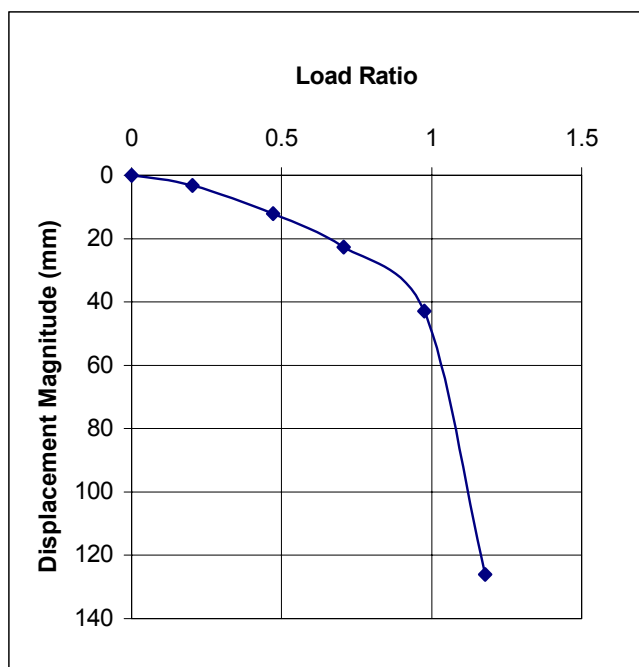
Displacement Magnitude (mm)	Vertical Displacement (mm)	Horizontal Displacement (mm)
0.000	0	0
3.230	3.23	0.04
12.043	12.04	0.25
22.687	22.68	0.57
42.920	42.90	1.31
126.000	114.95	2.21

Soil Details

E (MPa)	14
phi (deg)	36
c (kPa)	0.1
height (m)	3.6
N _{ave}	5
(N _{1ave})	12
dilation (deg)	3
earth press, K	0.4

Pile Details

Circular	
Length(m)	1.8
Dia (m)	0.6
Area (m^2)	0.283
L/d	3



Approximate Ultimate Ratio

Load Ratio = 0.95

Ultimate Load

Axial Compression = 200 kN

Lateral = 5 kN

Moment = 0 kN.m

Case 4 N=5,L/d=3,d=0.6 m, Axial Uplift + Lateral Load
Cast-in-place, free Head

Model Results

Load Magnitudes and Combinations

Vertical Load (kN)	Horizontal Load (kN)	Moment (kN.m)	Load Ratio
0	0	0	0
4.8	1.0	4.90	0.374
9.6	2.0	9.81	0.747
13.2	3.0	13.54	1.030
13.9	3.1	14.24	1.084

Pile Head Displacement

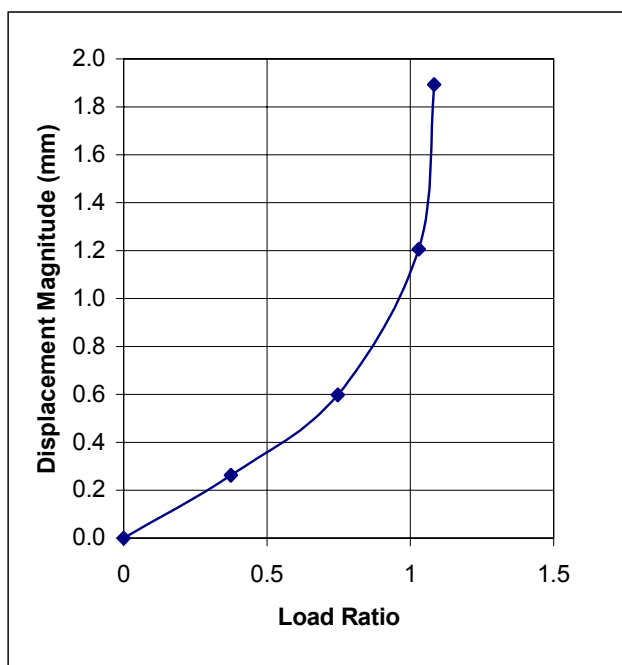
Displacement Magnitude (mm)	Vertical Displacement (mm)	Horizontal Displacement (mm)
0.0	0	0
0.3	0.260	0.030
0.6	0.57	0.18
1.2	1.16	0.33
1.9	1.86	0.35

Soil Details

E (MPa)	14
phi (deg)	36
c (kPa)	0.1
height (m)	3.6
N _{ave}	5
(N _{1ave})	12
dilation (deg)	3
earth press, K	0.4

Pile Details

Circular	
Length(m)	1.8
Dia (m)	0.6
Area (m^2)	0.283
L/d	3



Approximate Ultimate Ratio

Load Ratio = 1.0

Ultimate Load

Axial Uplift =13.2 kN

Lateral = 3 kN

Moment = 0 kN.m

Case 5 N=5,L/d=3,d=0.6 m, Axial Compression + Lateral Load
Cast-in-place, free Head

Model Results

Load Magnitudes and Combinations

Vertical Load (kN)	Horizontal Load (kN)	Moment (kN.m)	Load Ratio
0	0	0	0
39	3	0	0.232
65	10	0	0.581
98	13	0	0.766
110	14	0	0.860
145.85	19.15	0	1.165

Pile Head Displacement

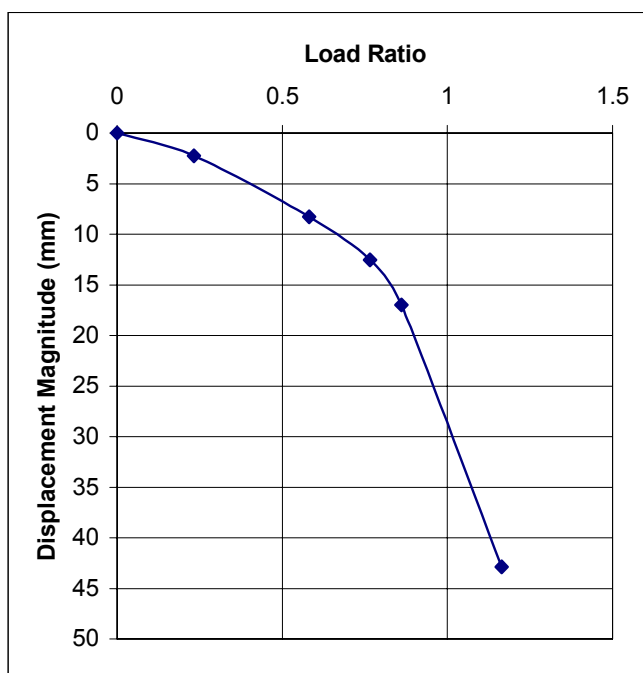
Displacement Magnitude (mm)	Vertical Displacement (mm)	Horizontal Displacement (mm)
0	0	0
2	2.21	0.356
8	8.2	1.150
13	12.4	1.790
17	16.89	2.01
43	42.673	4.272

Soil Details

E (MPa)	14
phi (deg)	36
c (kPa)	0.1
height (m)	3.6
N _{ave}	5
(N _{1ave})	12
dilation (deg)	3
earth press, K	0.4

Pile Details

Circular	
Length(m)	1.8
Dia (m)	0.6
Area (m ²)	0.283
L/d	3



Approximate Ultimate Ratio

Load Ratio = 0.86

Ultimate Load

Axial Compression =110 kN

Lateral = 14 kN

Moment = 0 kN.m

Case 6 N=5,L/d=3,d=0.6 m, Axial Uplift + Lateral Load
Cast-in-place, free Head

Model Results

Load Magnitudes and Combinations

Vertical Load (kN)	Horizontal Load (kN)	Moment (kN.m)	Load Ratio
0	0	0	0
3	2	3.61	0.258
6	4	7.21	0.516
9	6	10.82	0.774
14	8	15.69	1.136
15	10	17.66	1.259

Pile Head Displacement

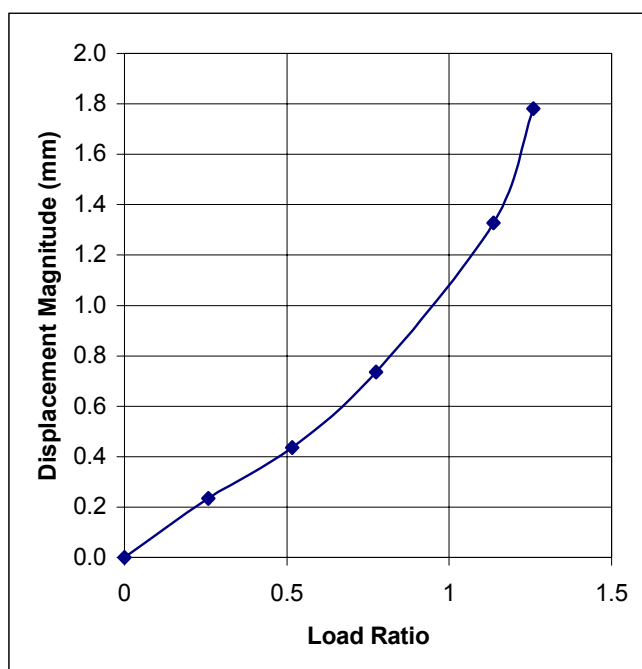
Displacement Magnitude (mm)	Vertical Displacement (mm)	Horizontal Displacement (mm)
0.0	0	0
0.2	0.16	0.170
0.4	0.35	0.26
0.7	0.53	0.51
1.3	1.2	0.57
1.8	1.65	0.67

Soil Details

E (MPa)	14
phi (deg)	36
c (kPa)	0.1
height (m)	3.6
N _{ave}	5
(N _{1ave})	12
dilation (deg)	3
earth press, K	0.4

Pile Details

Circular	
Length(m)	1.8
Dia (m)	0.6
Area (m ²)	0.283
L/d	3



Approximate Ultimate Ratio

Load Ratio = 1.0

Ultimate Load

Axial Uplift = 12 kN

Lateral = 7.5 kN

Moment = 0 kN.m

Case 8 N=5,L/d=3,d=0.6 m, Axial Uplift + Lateral Load
Cast-in-place, free Head

Model Results

Load Magnitudes and Combinations

Vertical Load (kN)	Horizontal Load (kN)	Moment (kN.m)	Load Ratio
0	0	0	0
3	5	0	0.318
6	10	0	0.637
8	15	0	0.955
11	20	0	1.273
14	25	0	1.592

Pile Head Displacement

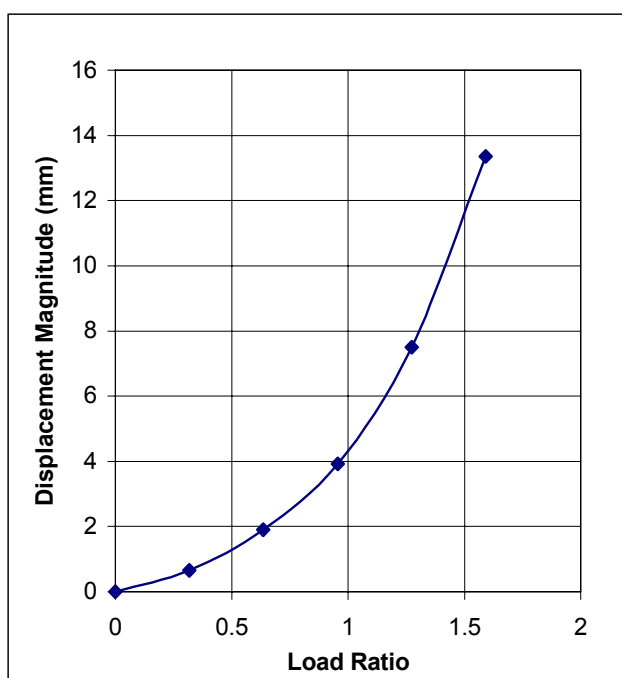
Displacement Magnitude (mm)	Vertical Displacement (mm)	Horizontal Displacement (mm)
0	0	0
1	0.11	0.640
2	0.59	1.81
4	0.87	3.83
7	7.35	1.48
13	13.17	2.19

Soil Details

E (MPa)	14
phi (deg)	36
c (kPa)	0.1
height (m)	3.6
N _{ave}	5
(N _{1ave})	12
dilation (deg)	3
earth press, K	0.4

Pile Details

Circular	
Length(m)	1.8
Dia (m)	0.6
Area (m ²)	0.283
L/d	3



Approximate Ultimate Ratio

Load Ratio = 0.9

Ultimate Load

Axial Uplift = 8 kN

Lateral = 14.5 kN

Moment = 0 kN.m

Case 9 N=5,L/d=3,d=0.6 m, Lateral Load
Cast-in-place, free Head

Model Results

Load Magnitudes and Combinations

Vertical Load (kN)	Horizontal Load (kN)	Moment (kN.m)	Load Ratio
0	0	0	0
0	5	0	n/a
0	10	0	n/a
0	15	0	n/a
0	21.5	0	n/a
0	25	0	n/a

Pile Head Displacement

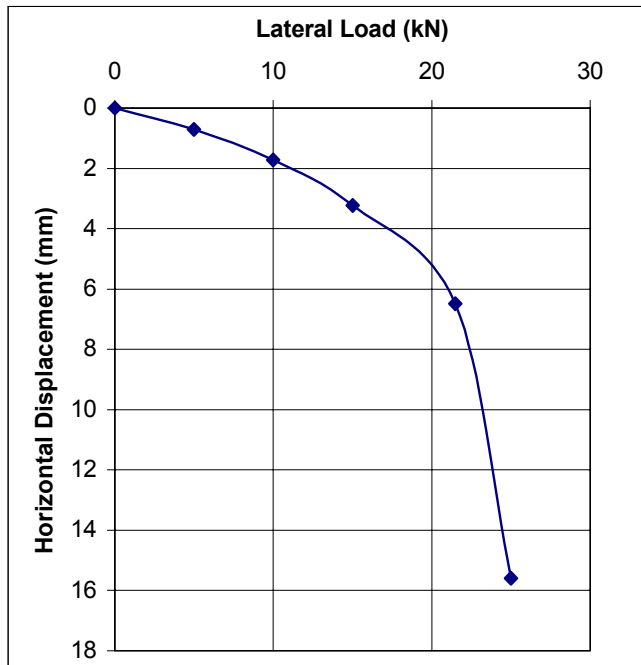
Displacement Magnitude (mm)	Vertical Displacement (mm)	Horizontal Displacement (mm)
0	0	0
1	0.013	0.710
2	0.023	1.71
3	0.106	3.23
6	0.29	6.48
16	0.67	15.57

Soil Details

E (MPa)	14
phi (deg)	36
c (kPa)	0.1
height (m)	3.6
N _{ave}	5
(N _{1ave})	12
dilation (deg)	3
earth press, K	0.4

Pile Details

Circular	
Length(m)	1.8
Dia (m)	0.6
Area (m ²)	0.283
L/d	3



Ultimate Load
Lateral = 20 kN

Case 10 N=5,L/d=3,d=0.6 m, Moment
Cast-in-place, free Head

Model Results

Load Magnitudes and Combinations

Vertical Load (kN)	Horizontal Load (kN)	Moment (kN.m)	Load Ratio
0	0	0	n/a
0	0	10	n/a
0	0	20	n/a
0	0	30	n/a
0	0	40	n/a
0	0	50	n/a

Pile Head Displacement

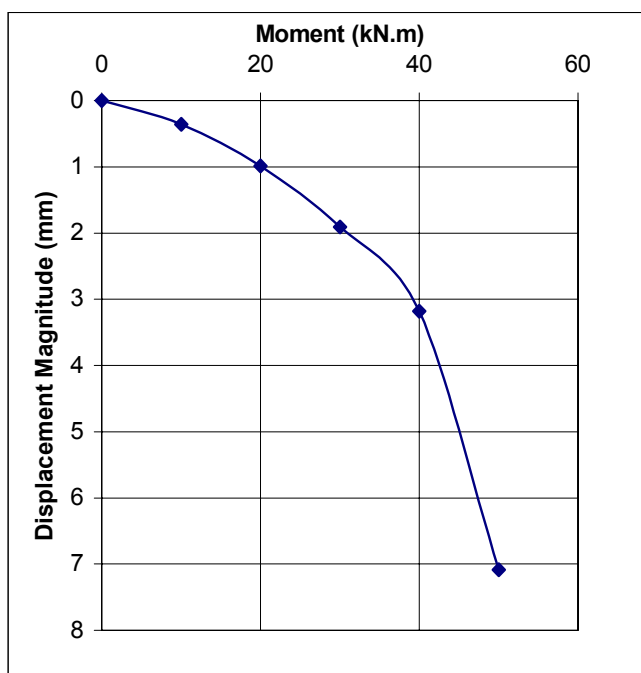
Displacement Magnitude (mm)	Vertical Displacement (mm)	Horizontal Displacement (mm)
0	0	0
0	0.02	0.360
1	0.02	0.99
2	0.084	1.91
3	0.17	3.18
7	0.33	7.08

Soil Details

E (MPa)	14
phi (deg)	36
c (kPa)	0.1
height (m)	3.6
N _{ave}	5
(N _{1ave})	12
dilation (deg)	3
earth press, K	0.4

Pile Details

Circular	
Length(m)	1.8
Dia (m)	0.6
Area (m ²)	0.283
L/d	3



Ultimate Load

Moment = 35 kN.m

Case 11 N=5,L/d=3,d=0.6 m, Axial Compression + Moment
Cast-in-place, free Head

Model Results

Load Magnitudes and Combinations

Vertical Load (kN)	Horizontal Load (kN)	Moment (kN.m)	Load Ratio
0	0	0	0
16	0	4.00	0.135
32	0	8.00	0.271
67	0	18.00	0.598
85	0	21.25	0.720
100	0	25.00	0.847

Pile Head Displacement

Displacement Magnitude (mm)	Vertical Displacement (mm)	Horizontal Displacement (mm)
0	0	0
1.3	1.31	0.050
3.6	3.55	0.122
8.7	8.66	0.34
13.6	13.54	0.53
31.5	31.44	1.87

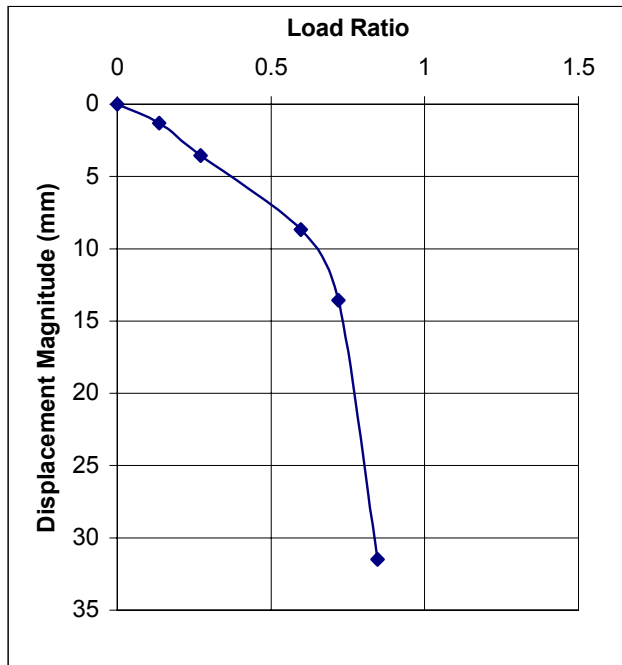
Soil Details

E (MPa)	14
phi (deg)	36
c (kPa)	0.1
height (m)	3.6
N _{ave}	5
(N _{1ave})	12
dilation (deg)	3
earth press, K	0.4

Pile Details

Circular

Length(m)	1.8
Dia (m)	0.6
Area (m ²)	0.283
L/d	3



Approximate Ultimate Ratio

Load Ratio = 0.72

Ultimate Load

Axial Compression = 85 kN

Lateral = 0 kN

Moment = 21 kN.m

Case 12 N=5,L/d=3,d=0.6 m, Axial Uplift + Moment
Cast-in-place, free Head

Model Results

Load Magnitudes and Combinations

Vertical Load (kN)	Horizontal Load (kN)	Moment (kN.m)	Load Ratio
0	0	0	0
4.35	0	10	0.422
8.70	0	20	0.844
13.04	0	30	1.266
14.00	0	32.2	1.359

Pile Head Displacement

Displacement Magnitude (mm)	Vertical Displacement (mm)	Horizontal Displacement (mm)
0	0	0
0	0.28	0.380
1	0.8	1.09
3	1.84	2.72
6	3.47	4.79

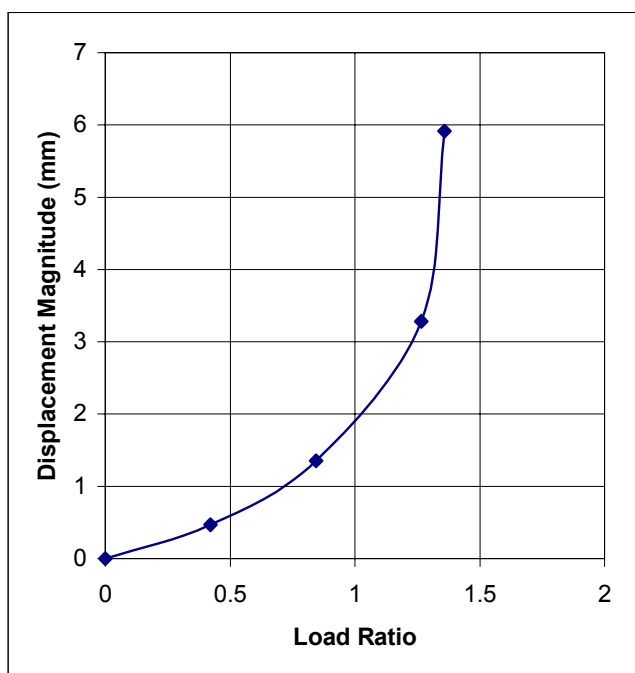
Soil Details

E (MPa)	14
phi (deg)	36
c (kPa)	0.1
height (m)	3.6
N _{ave}	5
(N _{1ave})	12
dilation (deg)	3
earth press, K	0.4

Pile Details

Circular

Length(m)	1.8
Dia (m)	0.6
Area (m^2)	0.283
L/d	3



Approximate Ultimate Ratio

Load Ratio = 0.97

Ultimate Load

Axial Uplift = 10 kN

Lateral = 0 kN

Moment = 23 kN.m

Case 14 N=5,L/d=3,d=0.6 m, Axial Uplift + Moment
Cast-in-place, free Head

Model Results

Load Magnitudes and Combinations

Vertical Load (kN)	Horizontal Load (kN)	Moment (kN.m)	Load Ratio
0	0	0	0
4	0	2	0.291
8	0	4	0.583
10	0	5	0.728
12	0	6	0.874
12.4	0	6.2	0.903

Pile Head Displacement

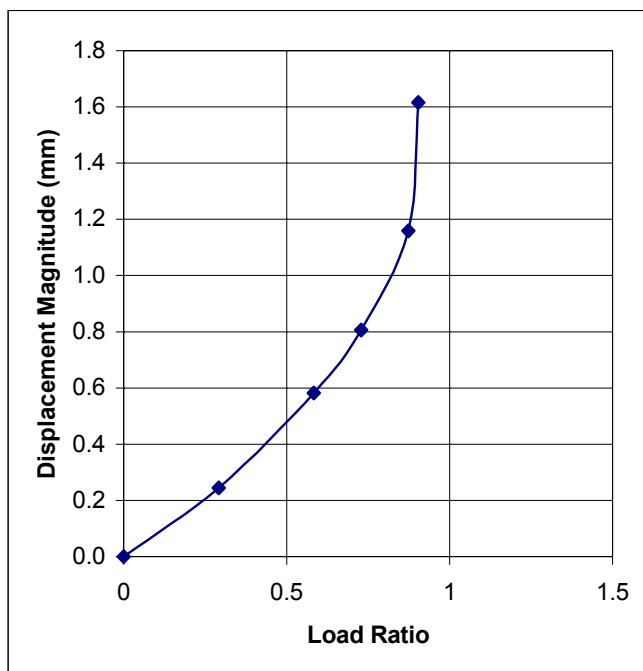
Displacement Magnitude (mm)	Vertical Displacement (mm)	Horizontal Displacement (mm)
0.00	0	0
0.25	0.24	0.050
0.58	0.57	0.12
0.81	0.79	0.16
1.16	1.14	0.21
1.62	1.6	0.23

Soil Details

E (MPa)	14
phi (deg)	36
c (kPa)	0.1
height (m)	3.6
N _{ave}	5
(N _{1ave})	12
dilation (deg)	3
earth press, K	0.4

Pile Details

Circular	
Length(m)	1.8
Dia (m)	0.6
Area (m ²)	0.283
L/d	3



Approximate Ultimate Ratio

Load Ratio = 0.87

Ultimate Load

Axial Uplift = 12 kN

Lateral = 0 kN

Moment = 6 kN.m

Case 15 N=5,L/d=3,d=0.6 m, Lateral Load + Moment
Cast-in-place, free Head

Model Results

Load Magnitudes and Combinations

Vertical Load (kN)	Horizontal Load (kN)	Moment (kN.m)	Load Ratio
0	0	0	0
0	1.7	10	0.298
0	3.3	20	0.595
0	5.0	30	0.893
0	6.7	40	1.190
0	8.3	50	1.488

Pile Head Displacement

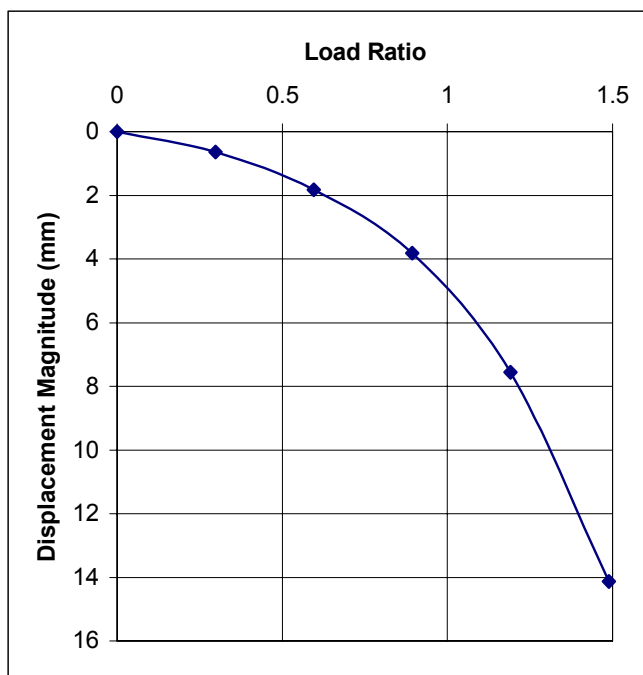
Displacement Magnitude (mm)	Vertical Displacement (mm)	Horizontal Displacement (mm)
0	0	0
0.6	0.01	0.634
1.8	0.06	1.830
3.8	0.18	3.82
7.6	0.45	7.55
14.1	0.923	14.1

Soil Details

E (MPa)	14
phi (deg)	36
c (kPa)	0.1
height (m)	3.6
N _{ave}	5
(N _{1ave})	12
dilation (deg)	3
earth press, K	0.4

Pile Details

Circular	
Length(m)	1.8
Dia (m)	0.6
Area (m ²)	0.283
L/d	3



Approximate Ultimate Ratio

Load Ratio = 0.89

Ultimate Load

Axial Compression = 0 kN

Lateral = 5 kN

Moment = 30 kN.m

Case 16 N=5,L/d=3,d=0.6 m, Lateral Load + Moment
Cast-in-place, free Head

Model Results

Load Magnitudes and Combinations

Vertical Load (kN)	Horizontal Load (kN)	Moment (kN.m)	Load Ratio
0	0	0	0
0	5.7	10	0.404
0	11.4	20	0.808
0	17.1	30	1.212
0	22.9	40	1.616

Pile Head Displacement

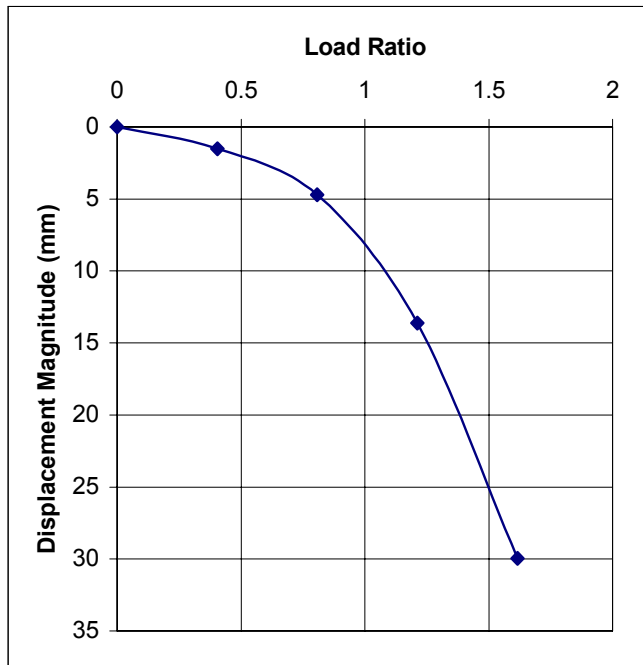
Displacement Magnitude (mm)	Vertical Displacement (mm)	Horizontal Displacement (mm)
0	0	0
2	0.03	1.510
5	0.28	4.71
14	0.92	13.59
30	1.06	29.945

Soil Details

E (MPa)	14
phi (deg)	36
c (kPa)	0.1
height (m)	3.6
N _{ave}	5
(N _{1ave})	12
dilation (deg)	3
earth press, K	0.4

Pile Details

Circular	
Length(m)	1.8
Dia (m)	0.6
Area (m ²)	0.283
L/d	3



Approximate Ultimate Ratio

Load Ratio = 0.85

Ultimate Load

Axial Uplift = 0 kN

Lateral = 12 kN

Moment = 21 kN.m

Case 17 N=5,L/d=3,d=0.6 m, Axial Compression, Lateral Load + Moment
Cast-in-place, free Head

Model Results

Load Magnitudes and Combinations

Vertical Load (kN)	Horizontal Load (kN)	Moment (kN.m)	Load Ratio
0	0	0	0
16	2.8	2	0.168
32	5.6	4	0.336
48	8.4	6	0.503
64	11.2	8	0.671
80	14	10	0.839

Pile Head Displacement

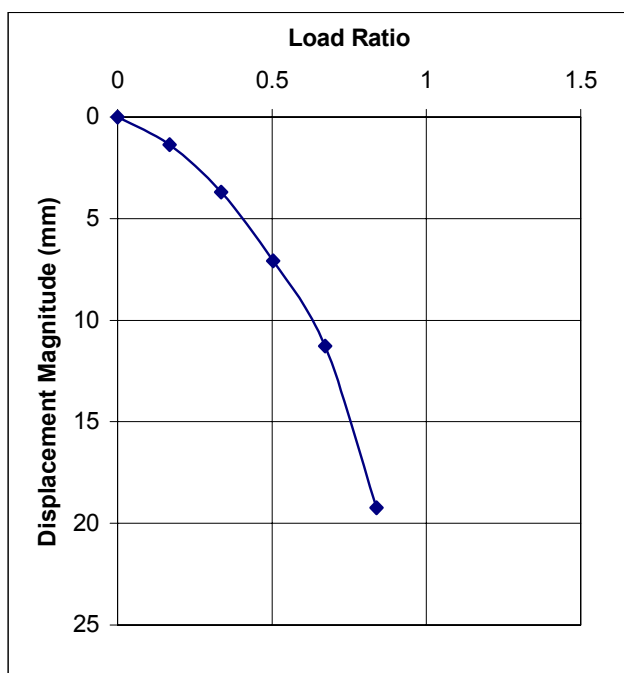
Displacement Magnitude (mm)	Vertical Displacement (mm)	Horizontal Displacement (mm)
0	0	0
1	1.31	0.330
4	3.54	1.02
7	6.7	2.25
11	10.45	4.2
19	17.72	7.45

Soil Details

E (MPa)	14
phi (deg)	36
c (kPa)	0.1
height (m)	3.6
N _{ave}	5
(N _{1ave})	12
dilation (deg)	3
earth press, K	0.4

Pile Details

Circular	
Length(m)	1.8
Dia (m)	0.6
Area (m ²)	0.283
L/d	3



Approximate Ultimate Ratio

Load Ratio = 0.68

Ultimate Load

Axial Compression = 65 kN

Lateral = 12 kN

Moment = 8 kN.m

Case 18 N=5, L/d=3, d=0.6 m, Axial Uplift, Lateral Load + Moment
Cast-in-place, free Head

Model Results

Load Magnitudes and Combinations

Vertical Load (kN)	Horizontal Load (kN)	Moment (kN.m)	Load Ratio
0	0	0	0
2	2.8	2	0.208
4	5.6	4	0.416
6	8.4	6	0.624
8	11.2	8	0.832
10	14	10	1.040

Pile Head Displacement

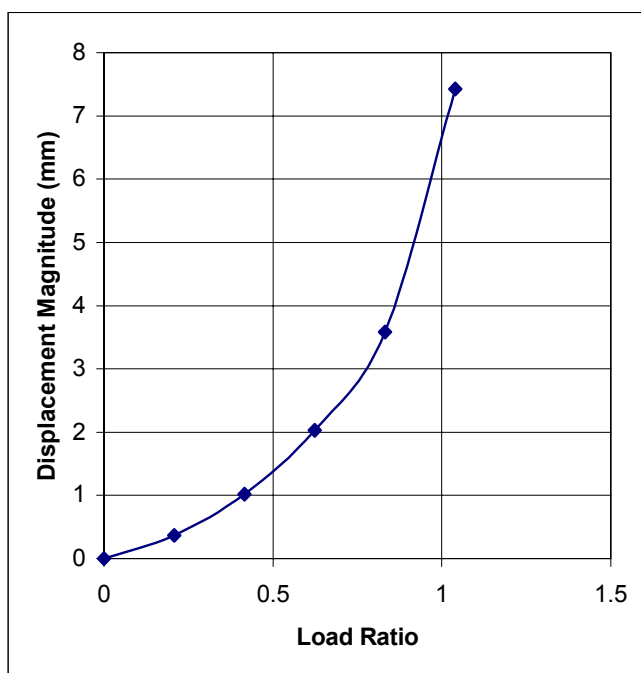
Displacement Magnitude (mm)	Vertical Displacement (mm)	Horizontal Displacement (mm)
0	0	0
0	0.11	0.350
1	0.29	0.98
2	0.56	1.95
4	1.04	3.43
7	2.28	7.07

Soil Details

E (MPa)	14
phi (deg)	36
c (kPa)	0.1
height (m)	3.6
N _{ave}	5
(N _{1ave})	12
dilation (deg)	3
earth press, K	0.4

Pile Details

Circular	
Length(m)	1.8
Dia (m)	0.6
Area (m ²)	0.283
L/d	3



Approximate Ultimate Ratio

Load Ratio = 0.7

Ultimate Load

Axial Uplift = 7 kN

Lateral = 9.5 kN

Moment = 7 kN.m

Case 20 N=5, L/d=3, d=0.6 m, Axial Uplift, Lateral Load + Moment
Cast-in-place, free Head

Model Results

Load Magnitudes and Combinations

Vertical Load (kN)	Horizontal Load (kN)	Moment (kN.m)	Load Ratio
0	0	0	0
4	1	1	0.291
6	1.5	1.5	0.437
8	2	2	0.583
12	3	3	0.874
12.6	3.15	3.15	0.918
(kN)	(kN)	(kPa)	(kN.m)

Pile Head Displacement

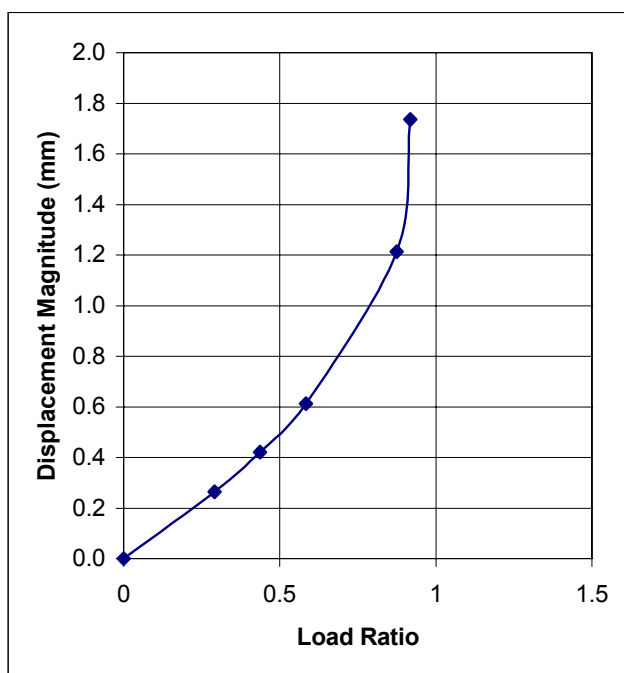
Displacement Magnitude (mm)	Vertical Displacement (mm)	Horizontal Displacement (mm)
0	0	0
0	0.24	0.110
0	0.38	0.18
1	0.55	0.27
1	1.1	0.51
2	1.64	0.57

Soil Details

E (MPa)	14
phi (deg)	36
c (kPa)	0.1
height (m)	3.6
N _{ave}	5
(N _{1ave})	12
dilation (deg)	3
earth press, K	0.4

Pile Details

Circular	
Length(m)	1.8
Dia (m)	0.6
Area (m ²)	0.283
L/d	3



Approximate Ultimate Ratio

Load Ratio = 0.87

Ultimate Load

Axial Uplift = 12 kN

Lateral = 3 kN

Moment = 3 kN.m

Case 42 N=5,L/d=10,d=0.6 m, Axial Uplift
Cast-in-place, free Head

Model Results

Load Magnitudes and Combinations

Vertical Load (kN)	Horizontal Load (kN)	Moment (kN.m)	Load Ratio
0	0	0	0
25	0	25.00	0
50	0	50.00	0
55	0	55.00	0
80	0	80.00	0
90	0	90.00	0

Pile Head Displacement

Displacement Magnitude (mm)	Vertical Displacement (mm)	Horizontal Displacement (mm)
0	0	0
1	1.19	0
3	2.51	0
3	2.81	0
7	6.54	0
12	12.31	0

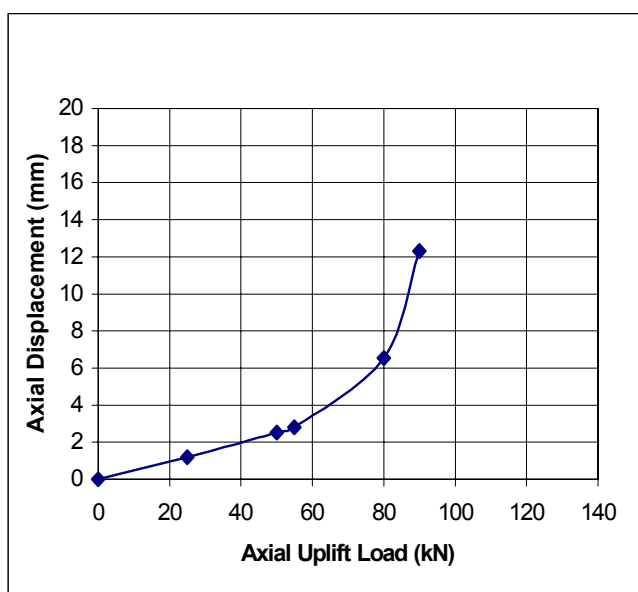
Soil Details

E (MPa)	14
phi (deg)	32
c (kPa)	0.1
height (m)	12
N _{ave}	5
(N _{1ave})	7
dilation (deg)	0
earth press, K	0.5

Pile Details

Circular

Length(m)	6
Dia (m)	0.6
Area (m ²)	0.283
L/d	10



Ultimate Load

Axial Uplift = 75 kN

Case 44 N=5, L/d=10, d=0.6 m, Axial Uplift + Lateral Load

Cast-in-place, free Head

Model Results

Load Magnitudes and Combinations

Vertical Load (kN)	Horizontal Load (kN)	Moment (kN.m)	Load Ratio
0	0	0	0
16	10	0	0.228
32	20	0	0.456
48	30	0	0.684
64	40	0	0.911
80	50	0	1.139

Pile Head Displacement

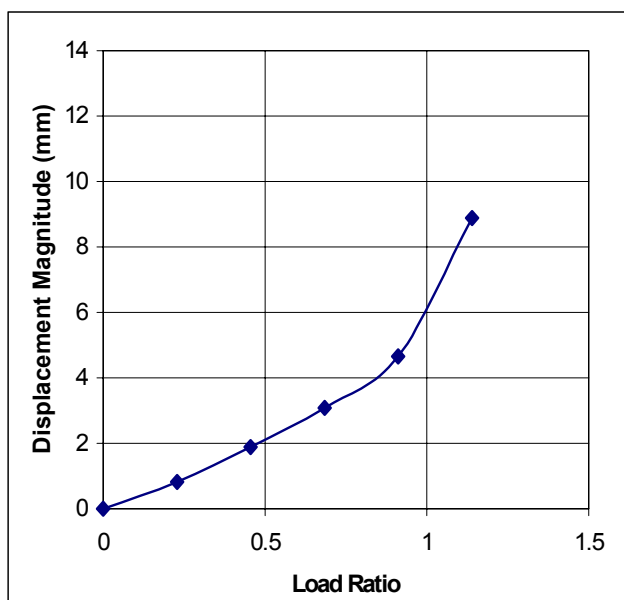
Displacement Magnitude (mm)	Vertical Displacement (mm)	Horizontal Displacement (mm)
0	0	0
1	0.74	0.370
2	1.52	1.12
3	2.41	1.93
5	3.64	2.91
9	7.88	4.12

Soil Details

E (MPa)	14
phi (deg)	32
c (kPa)	0.1
height (m)	12
N _{ave}	5
(N _{1ave})	7
dilation (deg)	0
earth press, K	0.5

Pile Details

Circular	
Length(m)	6
Dia (m)	0.6
Area (m ²)	0.283
L/d	10



Approximate Ultimate Ratio

Load Ratio = 0.91

Ultimate Load

Axial Uplift = 64 kN

Lateral = 40 kN

Moment = 0 kN.m

Case 46 N=5,L/d=10,d=0.6 m, Axial Uplift + Lateral Load
Cast-in-place, free Head

Model Results

Load Magnitudes and Combinations

Vertical Load (kN)	Horizontal Load (kN)	Moment (kN.m)	Load Ratio
0	0	0	0
25	43	0	0.479
50	86	0	0.958
75	129	0	1.437

Pile Head Displacement

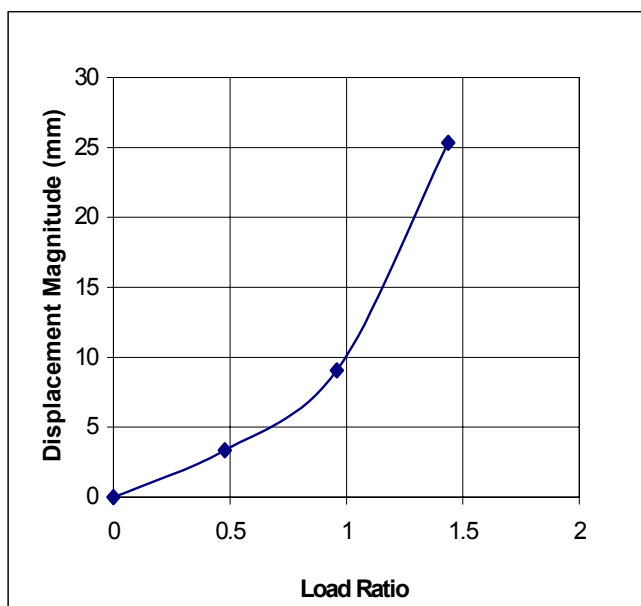
Displacement Magnitude (mm)	Vertical Displacement (mm)	Horizontal Displacement (mm)
0	0	
3	1.01	3.190
9	2.89	8.600
25	10.65	22.97

Soil Details

E (MPa)	14
phi (deg)	32
c (kPa)	0.1
height (m)	12
N _{ave}	5
(N _{1ave})	7
dilation (deg)	0
earth press, K	0.5

Pile Details

Circular	
Length(m)	6
Dia (m)	0.6
Area (m ²)	0.283
L/d	10



Approximate Ultimate Ratio

Load Ratio = 0.96

Ultimate Load

Axial Uplift = 86 kN

Lateral = 50 kN

Moment = 0 kN.m

Case 48 N=5,L/d=10,d=0.6 m, Axial Uplift + Lateral Load

Cast-in-place, free Head

Model Results

Load Magnitudes and Combinations

Vertical Load (kN)	Horizontal Load (kN)	Moment (kN.m)	Load Ratio
0	0	0	0
11	50	0	0.427
22	100	0	0.854
33	150	0	1.280
39	175	0	1.494
44	196	0	1.673

Pile Head Displacement

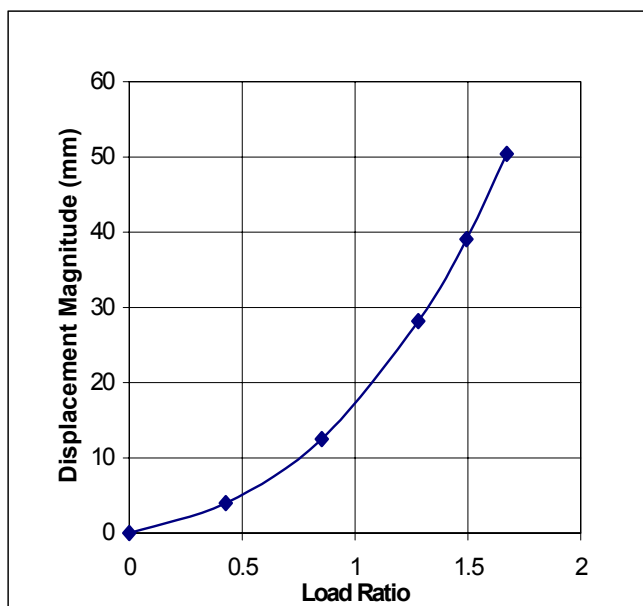
Displacement Magnitude (mm)	Vertical Displacement (mm)	Horizontal Displacement (mm)
0		
4	0.29	3.990
12	1.26	12.43
28	2.69	28.02
39	2.77	38.96
50	3.54	50.29

Soil Details

E (MPa)	14
phi (deg)	32
c (kPa)	0.1
height (m)	12
N _{ave}	5
(N _{1ave})	7
dilation (deg)	0
earth press, K	0.5

Pile Details

Circular	
Length(m)	6
Dia (m)	0.6
Area (m²)	0.283
L/d	10



Approximate Ultimate Ratio

Load Ratio = 0.95

Ultimate Load

Axial Uplift =25 kN

Lateral = 112 kN

Moment = 0 kN.m

Case 49 N=5,L/d=10,d=0.6 m, Lateral Load
Cast-in-place, free Head

Model Results

Load Magnitudes and Combinations

Vertical Load (kN)	Horizontal Load (kN)	Moment (kN.m)	Load Ratio
0	0	0	n/a
0	50	0	n/a
0	100	0	n/a
0	150	0	n/a
0	200	0	n/a
0	204	0	n/a

Pile Head Displacement

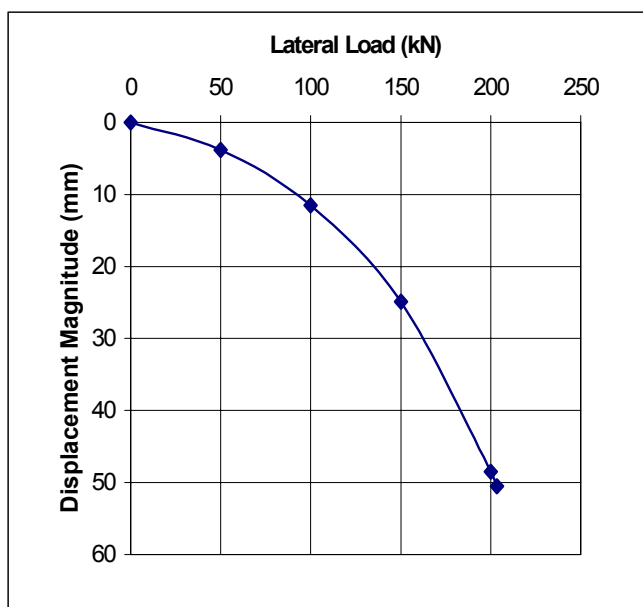
Displacement Magnitude (mm)	Vertical Displacement (mm)	Horizontal Displacement (mm)
0		
4	0.03	3.830
11	0.06	11.48
25	0.48	24.9
49	1.31	48.51
50	1.39	50.47

Soil Details

E (MPa)	14
phi (deg)	32
c (kPa)	0.1
height (m)	12
N _{ave}	5
(N _{1ave})	7
dilation (deg)	0
earth press, K	0.5

Pile Details

Circular	
Length(m)	6
Dia (m)	0.6
Area (m ²)	0.283
L/d	10



Ultimate Load
Lateral = 125 kN

Case 50 N=5,L/d=10,d=0.6 m, Moment
Cast-in-place, free Head

Model Results

Load Magnitudes and Combinations

Vertical Load (kN)	Horizontal Load (kN)	Moment (kN.m)	Load Ratio
0	0	0	n/a
0	0	250	n/a
0	0	500	n/a
0	0	750	n/a
0	0	1000	n/a
0	0	1200	n/a

Pile Head Displacement

Displacement Magnitude (mm)	Vertical Displacement (mm)	Horizontal Displacement (mm)
0	0	0
3	0.04	2.703
7	0.03	6.68
12	0.09	11.9
19	0.3	18.5
27	0.64	27.1

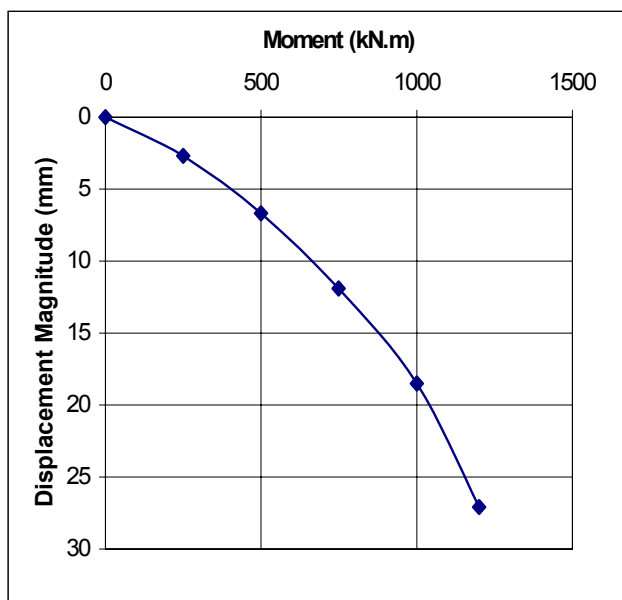
Soil Details

E (MPa)	14
phi (deg)	32
c (kPa)	0.1
height (m)	12
N _{ave}	5
(N _{1ave})	7
dilation (deg)	0
earth press, K	0.5

Pile Details

Circular

Length(m)	6
Dia (m)	0.6
Area (m^2)	0.283
L/d	10



Ultimate Load

Moment = 730 kN.m

Case 52 N=5,L/d=10,d=0.6 m, Axial Uplift + Moment
Cast-in-place, free Head

Model Results

Load Magnitudes and Combinations

Vertical Load (kN)	Horizontal Load (kN)	Moment (kN.m)	Load Ratio
0	0	0	0
4	0	250	0.346
7	0	500	0.692
11	0	750	1.037
14	0	1000	1.383
17	0	1200	1.660

Pile Head Displacement

Displacement Magnitude (mm)	Vertical Displacement (mm)	Horizontal Displacement (mm)
0	0	0
3	0.18	2.760
7	0.41	6.92
12	0.8	12.47
20	1.38	19.68
27	2.02	26.98

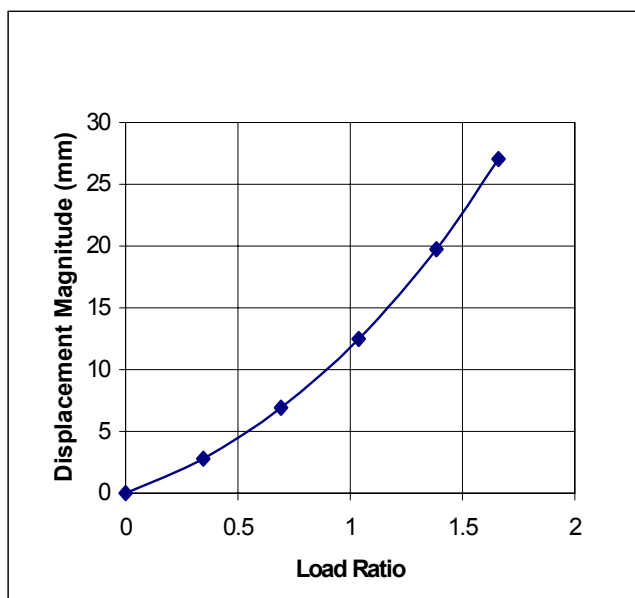
Soil Details

E (MPa)	14
phi (deg)	32
c (kPa)	0.1
height (m)	12
N _{ave}	5
(N _{1ave})	7
dilation (deg)	0
earth press, K	0.5

Pile Details

Circular

Length(m)	6
Dia (m)	0.6
Area (m ²)	0.283
L/d	10



Approximate Ultimate Ratio

Load Ratio = 0.96

Ultimate Load

Axial Uplift =10 kN

Lateral = 0 kN

Moment = 699 kN.m

Case 54 N=5,L/d=10,d=0.6 m, Axial Uplift + Moment
Cast-in-place, free Head

Model Results

Load Magnitudes and Combinations

Vertical Load (kN)	Horizontal Load (kN)	Moment (kN.m)	Load Ratio
0	0	0	0
12.5	0	100	0.216
31.3	0	250	0.539
62.5	0	500	1.079
71.4	0	570	1.231

Pile Head Displacement

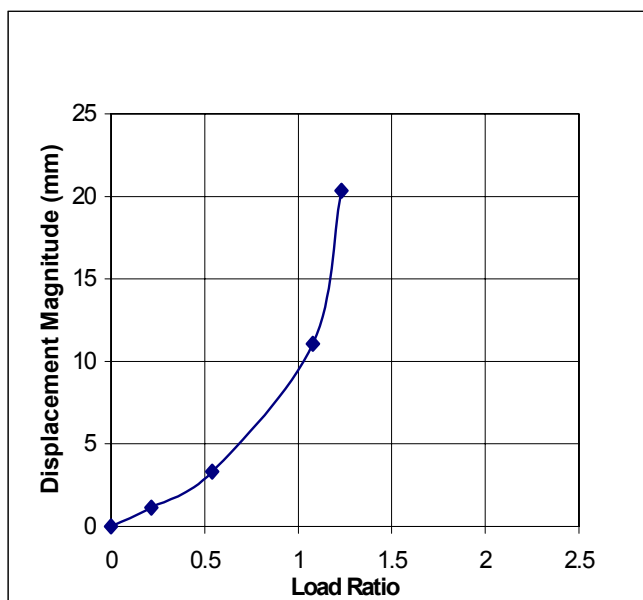
Displacement Magnitude (mm)	Vertical Displacement (mm)	Horizontal Displacement (mm)
0		
1	0.69	0.900
3	1.81	2.780
11	8.49	7.11
20	18.35	8.8

Soil Details

E (MPa)	14
phi (deg)	32
c (kPa)	0.1
height (m)	12
N _{ave}	5
(N _{1ave})	7
dilation (deg)	0
earth press, K	0.5

Pile Details

Circular	
Length(m)	6
Dia (m)	0.6
Area (m^2)	0.283
L/d	10



Approximate Ultimate Ratio

Load Ratio = 1.04

Ultimate Load

Axial Uplift =60 kN

Lateral = 0 kN

Moment = 480 kN.m

Case 55 N=5, L/d=3, d=0.6 m, Lateral Load + Moment
Cast-in-place, free Head

Model Results

Load Magnitudes and Combinations

Vertical Load (kN)	Horizontal Load (kN)	Moment (kN.m)	Load Ratio
0	0	0	0
0	32.5	250	0.430
0	65.0	500	0.860
0	97.5	750	1.290
0	100.0	773	1.327

Pile Head Displacement

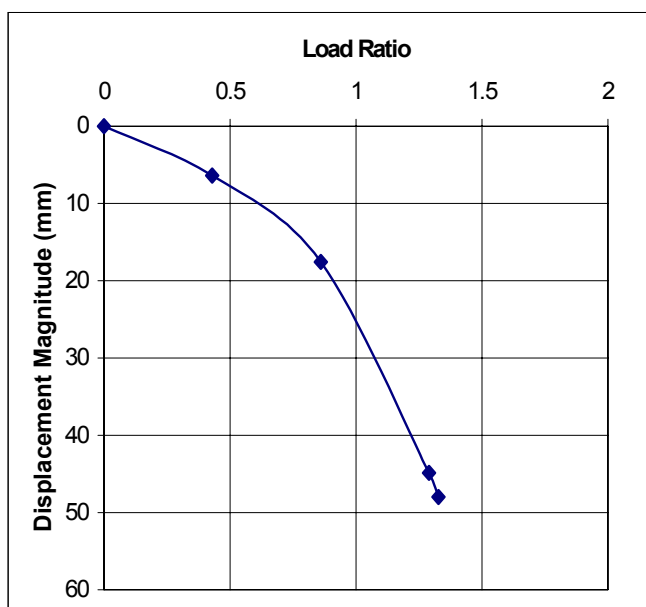
Displacement Magnitude (mm)	Vertical Displacement (mm)	Horizontal Displacement (mm)
0		
6	0.02	6.360
18	0.38	17.59
45	1.41	44.87
48	1.59	47.94

Soil Details

E (MPa)	14
phi (deg)	32
c (kPa)	0.1
height (m)	12
N _{ave}	5
(N _{1ave})	7
dilation (deg)	0
earth press, K	0.5

Pile Details

Circular	
Length(m)	6
Dia (m)	0.6
Area (m ²)	0.283
L/d	10



Approximate Ultimate Ratio

Load Ratio = 0.86

Ultimate Load

Axial Uplift = 0 kN

Lateral = 65 kN

Moment = 500 kN.m

Case 56 N=5, L/d=10, d=0.6 m, Lateral Load + Moment

Cast-in-place, free Head

Model Results

Load Magnitudes and Combinations

Vertical Load (kN)	Horizontal Load (kN)	Moment (kN.m)	Load Ratio
0	0	0	0
0	27.5	50	0.230
0	55.0	100	0.461
0	82.5	150	0.691
0	110.0	200	0.921
0	137.4	250	1.152
(kN)	(kN)	(kPa)	(kN.m)

Pile Head Displacement

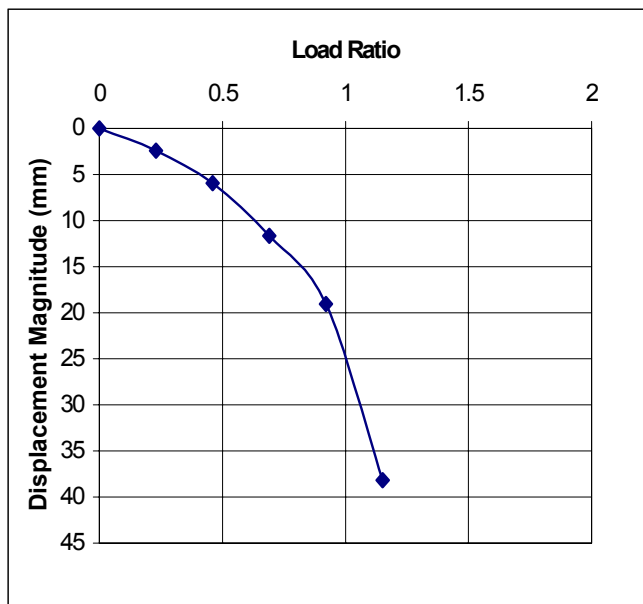
Displacement Magnitude (mm)	Vertical Displacement (mm)	Horizontal Displacement (mm)
0	0	0
2	-0.03	2.400
6	-0.02	5.97
12	0.08	11.65
19	0.35	19.07
38	0.8	38.16

Soil Details

E (MPa)	14
phi (deg)	32
c (kPa)	0.1
height (m)	12
N _{ave}	5
(N _{1ave})	7
dilation (deg)	0
earth press, K	0.5

Pile Details

Circular	
Length(m)	6
Dia (m)	0.6
Area (m ²)	0.283
L/d	10



Approximate Ultimate Ratio

Load Ratio = 0.88

Ultimate Load

Axial Uplift = 0 kN

Lateral = 105 kN

Moment = 191 kN.m

Case 58 N=5, L/d=10, d=0.6 m, Axial Uplift, Lateral Load + Moment

Cast-in-place, free Head

Model Results

Load Magnitudes and Combinations

Vertical Load (kN)	Horizontal Load (kN)	Moment (kN.m)	Load Ratio
0	0	0	0
6	30	50	0.262
12	60	100	0.524
18	80	150	0.714
24	120	200	1.048
30	150	250	1.310
(kN)	(kN)	(kPa)	(kN.m)

Pile Head Displacement

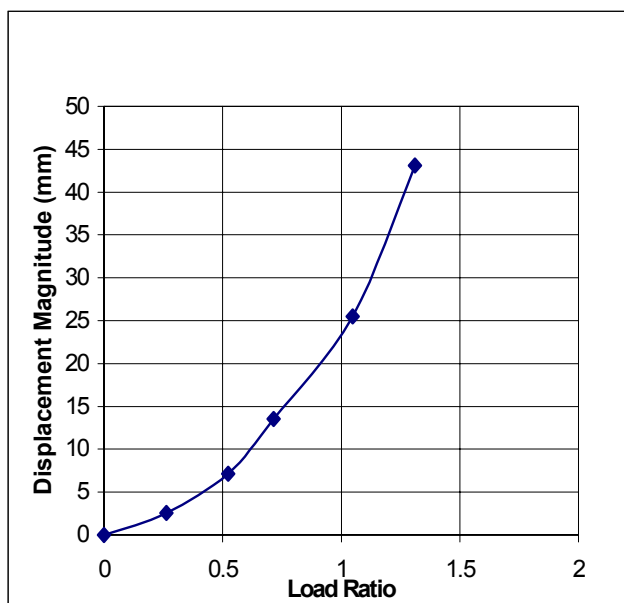
Displacement Magnitude (mm)	Vertical Displacement (mm)	Horizontal Displacement (mm)
0	0	0
3	0.31	2.560
7	0.69	7.14
14	1.28	13.46
25	2.23	25.4
43	3.85	42.93

Soil Details

E (MPa)	14
phi (deg)	32
c (kPa)	0.1
height (m)	12
N _{ave}	5
(N _{1ave})	7
dilation (deg)	0
earth press, K	0.5

Pile Details

Circular	
Length(m)	6
Dia (m)	0.6
Area (m ²)	0.283
L/d	10



Approximate Ultimate Ratio

Load Ratio = 0.86

Ultimate Load

Axial Uplift = 21 kN

Lateral = 98 kN

Moment = 172 kN.m

Case 60 N=5, L/d=10, d=0.6 m, Axial Uplift, Lateral Load + Moment
Cast-in-place, free Head

Model Results

Load Magnitudes and Combinations

Vertical Load (kN)	Horizontal Load (kN)	Moment (kN.m)	Load Ratio
0	0	0	0
15	13	50	0.236
30	26	100	0.471
45	39	150	0.707
60	52	200	0.942
70.5	61.1	235	1.107

Pile Head Displacement

Displacement Magnitude (mm)	Vertical Displacement (mm)	Horizontal Displacement (mm)
0	0	0
1	0.82	1.190
3	1.7	2.96
6	2.79	5.34
10	4.73	8.41
22	18.48	11.48

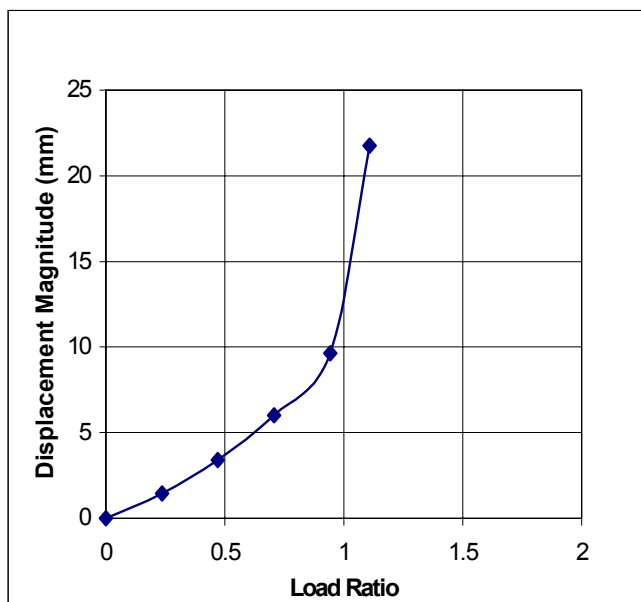
Soil Details

E (MPa)	14
phi (deg)	32
c (kPa)	0.1
height (m)	12
N _{ave}	5
(N _{1ave})	7
dilation (deg)	0
earth press, K	0.5

Pile Details

Circular

Length(m)	6
Dia (m)	0.6
Area (m ²)	0.283
L/d	10



Approximate Ultimate Ratio

Load Ratio = 0.88

Ultimate Load

Axial Uplift = 55 kN

Lateral = 48 kN

Moment = 185 kN.m

Case 61 N=30,L/d=10,d=0.6 m, Axial Compression
Cast-in-place, free Head

Model Results

Load Magnitudes and Combinations

Vertical Load (kN)	Horizontal Load (kN)	Moment (kN.m)	Load Ratio
0	0	0	n/a
500	0	0	n/a
1000	0	0	n/a
1500	0	0	n/a
1750	0	0	n/a
2200	0	0	n/a

Pile Head Displacement

Displacement Magnitude (mm)	Vertical Displacement (mm)	Horizontal Displacement (mm)
0	0	0
20	20	0
45	44.58	0
81	81.27	0
101	101.2	0
161	161.3	0

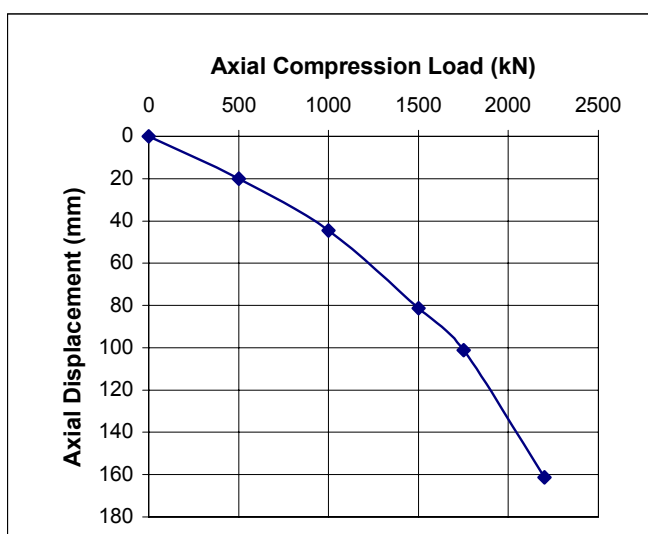
Soil Details

E (MPa)	33
phi (deg)	48
c (kPa)	0.1
height (m)	12
N _{ave}	30
(N _{1ave})	40
dilation (deg)	15
earth press, K	0.3

Pile Details

Circular

Length(m)	6
Dia (m)	0.6
Area (m ²)	0.283
L/d	10



Ultimate Load

Axial Compression = 1200 kN

Case 62 N=30,L/d=10,d=0.6 m, Axial Uplift
Cast-in-place, free Head

Model Results

Load Magnitudes and Combinations

Vertical Load (kN)	Horizontal Load (kN)	Moment (kN.m)	Load Ratio
0	0	0	n/a
100	0	0	n/a
146	0	0	n/a
200	0	0	n/a
246	0	0	n/a
309	0	0	n/a

Pile Head Displacement

Displacement Magnitude (mm)	Vertical Displacement (mm)	Horizontal Displacement (mm)
0	0	0
2	2.28	0
8	7.58	0
17	17.4	0
28	27.8	0
44	44.35	0

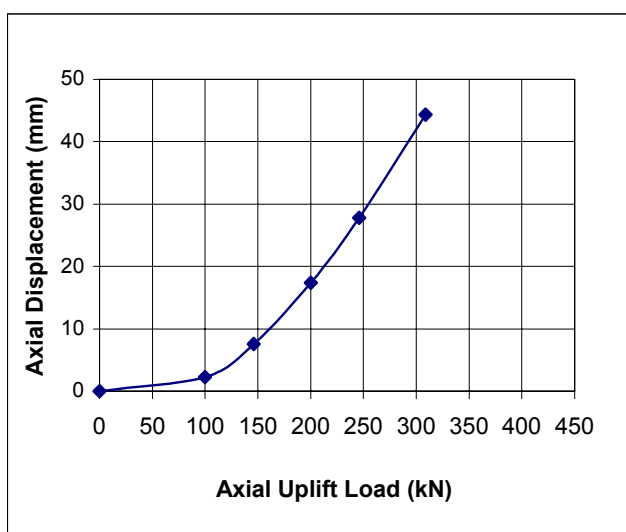
Soil Details

E (MPa)	33
phi (deg)	48
c (kPa)	0.1
height (m)	12
N _{ave}	30
(N _{1ave})	40
dilation (deg)	15
earth press, K	0.3

Pile Details

Circular

Length(m)	6
Dia (m)	0.6
Area (m ²)	0.283
L/d	10



Ultimate Load

Axial Uplift = 160 kN

Case 63 N=30,L/d=10,d=0.6 m, Axial Compression + Lateral Load
Cast-in-place, free Head

Model Results

Load Magnitudes and Combinations

Vertical Load (kN)	Horizontal Load (kN)	Moment (kN.m)	Load Ratio
0	0	0	0
96	30	0	0.131
240	75	0	0.327
480	150	0	0.654
544	170	0	0.741
600	188	0	0.819

Pile Head Displacement

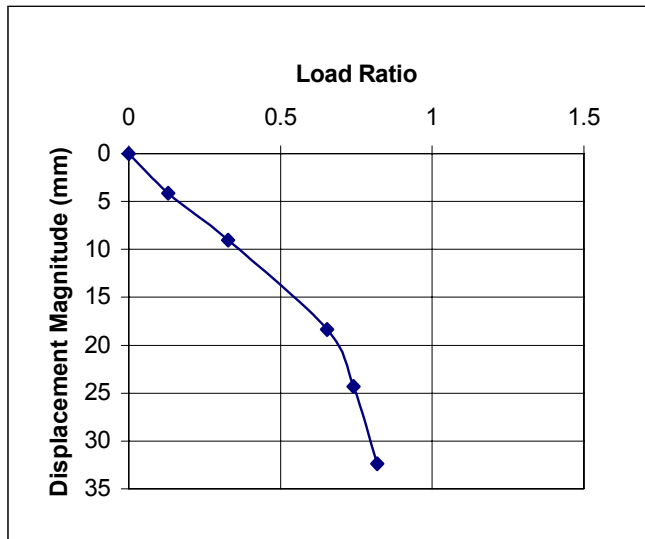
Displacement Magnitude (mm)	Vertical Displacement (mm)	Horizontal Displacement (mm)
0	0.00	0.00
4	4.01	0.96
9	8.57	2.84
18	16.81	7.40
24	22.06	10.18
32	28.86	14.63

Soil Details

E (MPa)	33
phi (deg)	48
c (kPa)	0.1
height (m)	12
N _{ave}	30
(N _{1ave})	40
dilation (deg)	15
earth press, K	0.3

Pile Details

Circular	
Length(m)	6
Dia (m)	0.6
Area (m^2)	0.283
L/d	10



Approximate Ultimate Ratio

Load Ratio = 0.7

Ultimate Load

Axial Compression = 535 kN

Lateral = 161 kN

Moment = 0 kN.m

Case 64 N=30,L/d=10,d=0.6 m, Axial Uplift + Lateral Load
Cast-in-place, free Head

Model Results

Load Magnitudes and Combinations

Vertical Load (kN)	Horizontal Load (kN)	Moment (kN.m)	Load Ratio
0	0	0	0
63	30	0	0.407
126	60	0	0.814
192	92	0	1.242
252	120	0	1.628
287	137	0	1.852

Pile Head Displacement

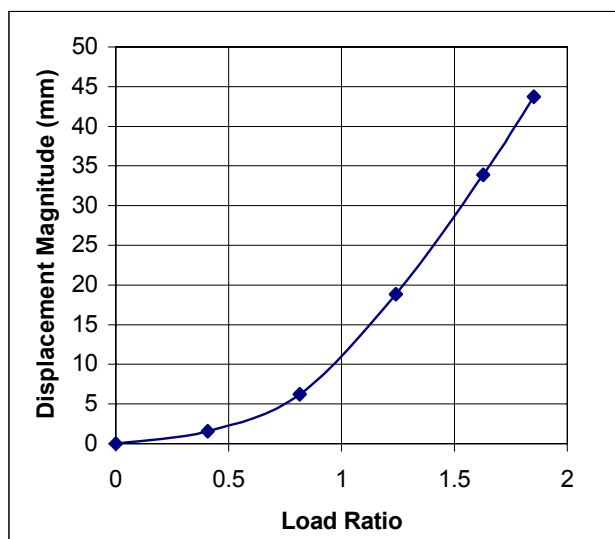
Displacement Magnitude (mm)	Vertical Displacement (mm)	Horizontal Displacement (mm)
0	0	0
2	1.34	0.810
6	5.78	2.26
19	18.41	4.14
34	33.32	6.19
44	43.02	7.63

Soil Details

E (MPa)	33
phi (deg)	48
c (kPa)	0.1
height (m)	12
N _{ave}	30
(N _{1ave})	40
dilation (deg)	15
earth press, K	0.3

Pile Details

Circular	
Length(m)	6
Dia (m)	0.6
Area (m ²)	0.283
L/d	10



Approximate Ultimate Ratio

Load Ratio = 0.94

Ultimate Load

Axial Uplift = 145 kN

Lateral = 71 kN

Moment = 0 kN.m

Case 66 N=30,L/d=10,d=0.6 m, Axial Uplift + Lateral Load
Cast-in-place, free Head

Model Results

Load Magnitudes and Combinations

Vertical Load (kN)	Horizontal Load (kN)	Moment (kN.m)	Load Ratio
0	0	0	0
42	30	0	0.282
84	60	0	0.564
126	90	0	0.846
168	120	0	1.129
210	150	0	1.411

Pile Head Displacement

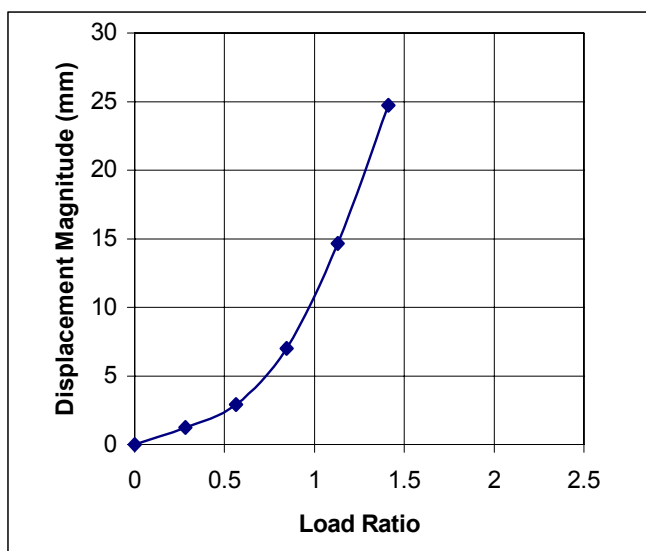
Displacement Magnitude (mm)	Vertical Displacement (mm)	Horizontal Displacement (mm)
0	0.00	0
1	0.87	0.910
3	1.87	2.230
7	5.86	3.870
15	13.45	5.860
25	23.31	8.290

Soil Details

E (MPa)	33
phi (deg)	48
c (kPa)	0.1
height (m)	12
N _{ave}	30
(N _{1ave})	40
dilation (deg)	15
earth press, K	0.3

Pile Details

Circular	
Length(m)	6
Dia (m)	0.6
Area (m ²)	0.283
L/d	10



Approximate Ultimate Ratio

Load Ratio = 0.6

Ultimate Load

Axial Uplift =122 kN

Lateral = 87 kN

Moment = 0 kN.m

Case 68 N=30,L/d=10,d=0.6 m, Axial Uplift + Lateral Load
Cast-in-place, free Head

Model Results

Load Magnitudes and Combinations

Vertical Load (kN)	Horizontal Load (kN)	Moment (kN.m)	Load Ratio
0	0	0	0
67	100	0	0.541
100	150	0	0.811
133	200	0	1.082
147	220	0	1.190

Pile Head Displacement

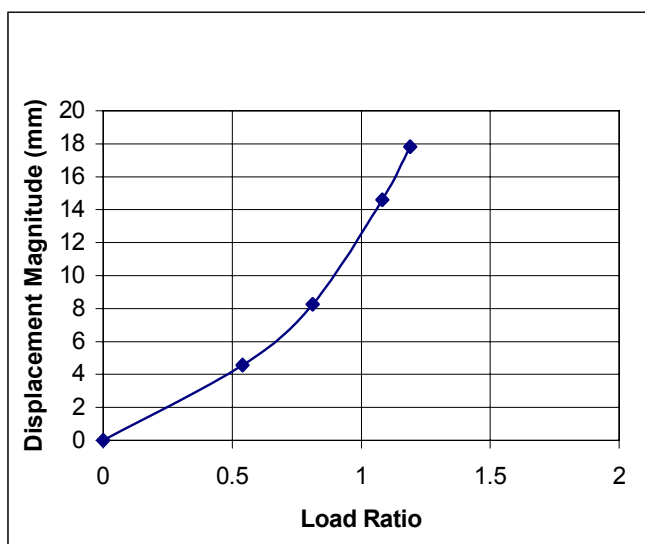
Displacement Magnitude (mm)	Vertical Displacement (mm)	Horizontal Displacement (mm)
0	0	0
5	1.24	4.390
8	2.83	7.76
15	8.31	12
18	11.13	13.92

Soil Details

E (MPa)	33
phi (deg)	48
c (kPa)	0.1
height (m)	12
N _{ave}	30
(N _{1ave})	40
dilation (deg)	15
earth press, K	0.3

Pile Details

Circular	
Length(m)	6
Dia (m)	0.6
Area (m^2)	0.283
L/d	10



Approximate Ultimate Ratio

Load Ratio = 0.81

Ultimate Load

Axial Uplift = 100 kN

Lateral = 150 kN

Moment = 0 kN.m

Case 69 N=30,L/d=10,d=0.6 m, Lateral Load
Cast-in-place, free Head

Model Results

Load Magnitudes and Combinations

Vertical Load (kN)	Horizontal Load (kN)	Moment (kN.m)	Load Ratio
0	0	0	n/a
0	150	0	n/a
0	320	0	n/a
0	400	0	n/a

Pile Head Displacement

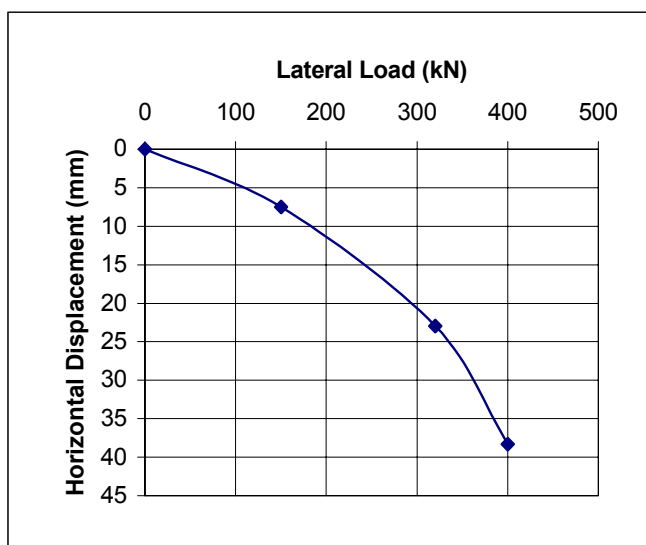
Displacement Magnitude (mm)	Vertical Displacement (mm)	Horizontal Displacement (mm)
0	0	0
8	0.010	7.54
23	0.29	22.95
38	0.56	38.3

Soil Details

E (MPa)	33
phi (deg)	48
c (kPa)	0.1
height (m)	12
N _{ave}	30
(N _{1ave})	40
dilation (deg)	15
earth press, K	0.3

Pile Details

Circular	
Length(m)	6
Dia (m)	0.6
Area (m^2)	0.283
L/d	10



Ultimate Load
Lateral = 290 kN

Case 70 N=30,L/d=10,d=0.6 m, Moment
Cast-in-place, free Head

Model Results

Load Magnitudes and Combinations

Vertical Load (kN)	Horizontal Load (kN)	Moment (kN.m)	Load Ratio
0	0	0	n/a
0	0	500	n/a
0	0	1000	n/a
0	0	1500	n/a
0	0	2000	n/a
0	0	2200	n/a

Pile Head Displacement

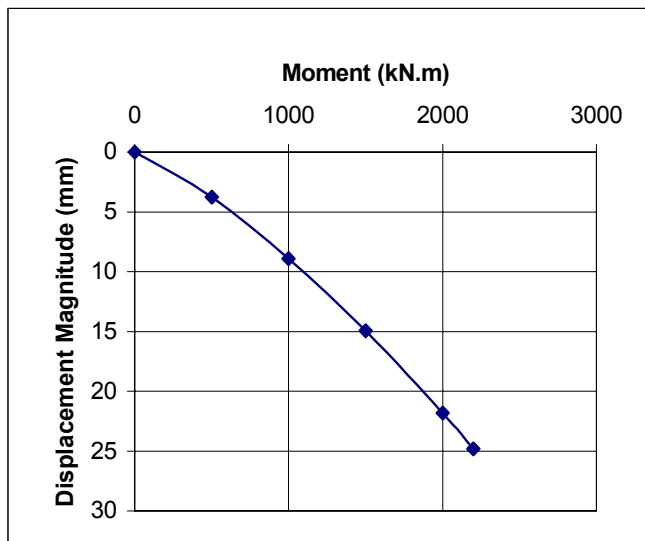
Displacement Magnitude (mm)	Vertical Displacement (mm)	Horizontal Displacement (mm)
0	0	0
4	-3.77	-0.010
9	-8.9	0
15	-14.95	0.05
22	-21.83	0.2
25	-24.82	0.3

Soil Details

E (MPa)	33
phi (deg)	48
c (kPa)	0.1
height (m)	12
N _{ave}	30
(N _{1ave})	40
dilation (deg)	15
earth press, K	0.3

Pile Details

Circular	
Length(m)	6
Dia (m)	0.6
Area (m^2)	0.283
L/d	10



Ultimate Load

Moment = 1250 kN.m

Case 71 N=30,L/d=10,d=0.6 m, Axial Compression + Moment
Cast-in-place, free Head

Model Results

Load Magnitudes and Combinations

Vertical Load (kN)	Horizontal Load (kN)	Moment (kN.m)	Load Ratio
0	0	0	0
231	0	100	0.208
462	0	200	0.417
693	0	300	0.625
924	0	400	0.834
1155	0	500	1.042

Pile Head Displacement

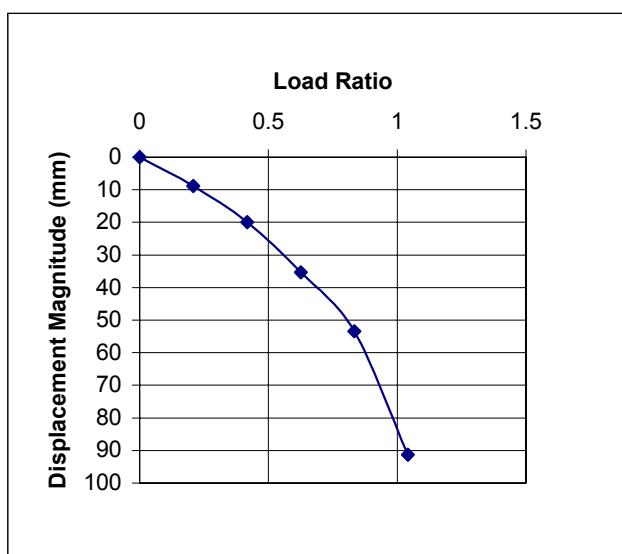
Displacement Magnitude (mm)	Vertical Displacement (mm)	Horizontal Displacement (mm)
0	0	0
9	8.87	0.520
20	19.96	1.16
35	35.29	2
53	53.25	3.77
91	91.09	5.6

Soil Details

E (MPa)	33
phi (deg)	48
c (kPa)	0.1
height (m)	12
N _{ave}	30
(N _{1ave})	40
dilation (deg)	15
earth press, K	0.3

Pile Details

Circular	
Length(m)	6
Dia (m)	0.6
Area (m ²)	0.283
L/d	10



Approximate Ultimate Ratio

Load Ratio = 0.74

Ultimate Load

Axial Compression = 826 kN

Lateral = 0 kN

Moment = 358 kN.m

Case 72 N=30,L/d=10,d=0.6 m, Axial Uplift + Moment
Cast-in-place, free Head

Model Results

Load Magnitudes and Combinations

Vertical Load (kN)	Horizontal Load (kN)	Moment (kN.m)	Load Ratio
0	0	0	0
85	0	500	0.665
123	0	725	0.964
170	0	1000	1.330
187	0	1100	1.463

Pile Head Displacement

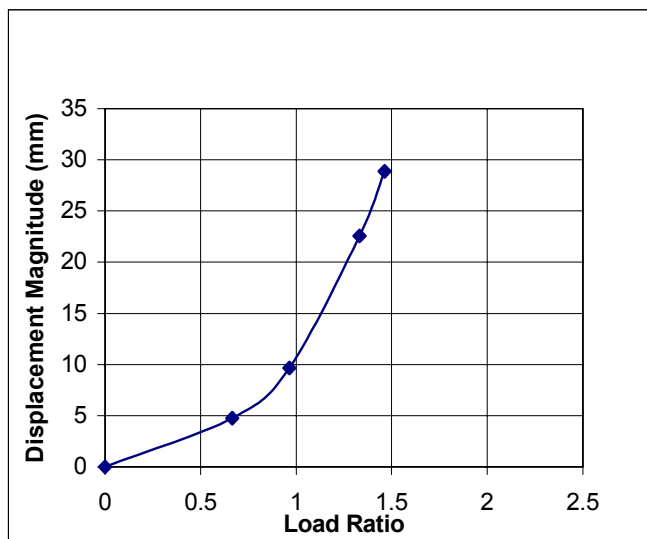
Displacement Magnitude (mm)	Vertical Displacement (mm)	Horizontal Displacement (mm)
0	0	0
5	2.7	3.890
10	7.39	6.22
23	20.4	9.64
29	26.7	11.000

Soil Details

E (MPa)	33
phi (deg)	48
c (kPa)	0.1
height (m)	12
N _{ave}	30
(N _{1ave})	40
dilation (deg)	15
earth press, K	0.3

Pile Details

Circular	
Length(m)	6
Dia (m)	0.6
Area (m ²)	0.283
L/d	10



Approximate Ultimate Ratio

Load Ratio = 0.98

Ultimate Load

Axial Uplift = 125 kN

Lateral = 0 kN

Moment = 735 kN.m

Case 74 N=30,L/d=10,d=0.6 m, Axial Uplift + Moment
Cast-in-place, free Head

Model Results

Load Magnitudes and Combinations

Vertical Load (kN)	Horizontal Load (kN)	Moment (kN.m)	Load Ratio
0	0	0	0
51	0	100	0.329
102	0	200	0.657
153	0	300	0.986
204	0	400	1.315
247.35	0	485	1.594

Pile Head Displacement

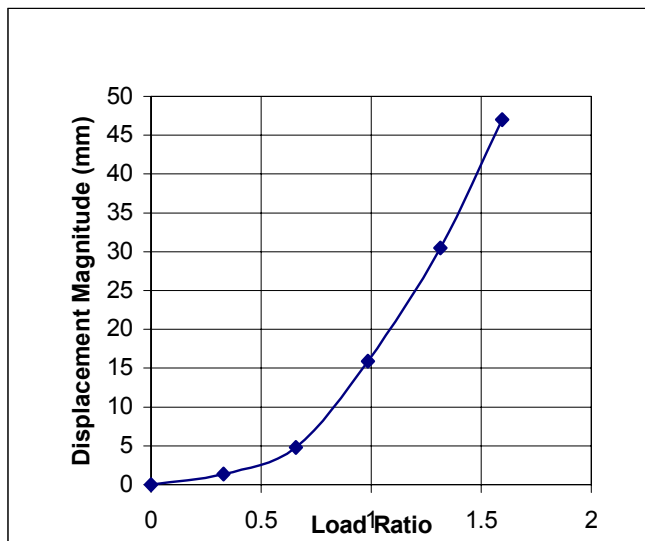
Displacement Magnitude (mm)	Vertical Displacement (mm)	Horizontal Displacement (mm)
0	0	0
1	1.25	0.550
5	4.61	1.28
16	15.74	2.15
31	30.35	3.17
47	46.74	5.11

Soil Details

E (MPa)	33
phi (deg)	48
c (kPa)	0.1
height (m)	12
N _{ave}	30
(N _{1ave})	40
dilation (deg)	15
earth press, K	0.3

Pile Details

Circular	
Length(m)	6
Dia (m)	0.6
Area (m^2)	0.283
L/d	10



Approximate Ultimate Ratio

Load Ratio = 0.9

Ultimate Load

Axial Uplift =140 kN

Lateral = 0 kN

Moment = 276 kN.m

Case 76 N=30,L/d=10,d=0.6 m, Lateral Load + Moment
Cast-in-place, free Head

Model Results

Load Magnitudes and Combinations

Vertical Load (kN)	Horizontal Load (kN)	Moment (kN.m)	Load Ratio
0	0	0	0
0	60	100	0.222
0	117	195	0.433
0	162	270	0.599
0	243	405	0.898
0	300	500	1.109

Pile Head Displacement

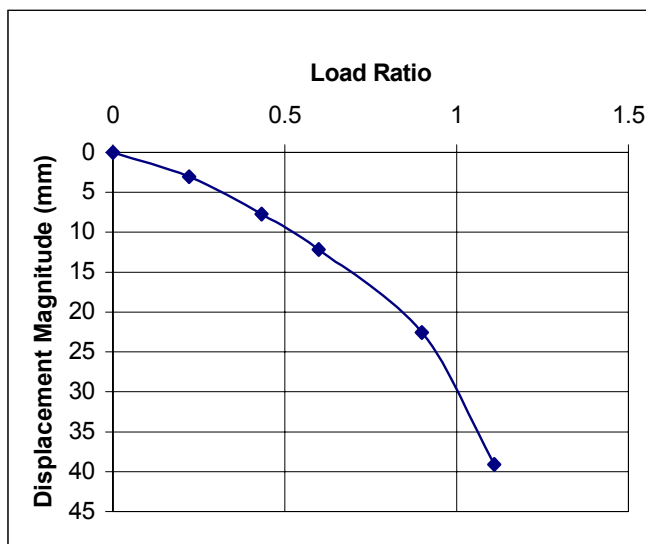
Displacement Magnitude (mm)	Vertical Displacement (mm)	Horizontal Displacement (mm)
0	0	0
3	0	3.060
8	0.01	7.73
12	0.05	12.18
23	0.3	22.57
39	0.5	39.09

Soil Details

E (MPa)	33
phi (deg)	48
c (kPa)	0.1
height (m)	12
N _{ave}	30
(N _{1ave})	40
dilation (deg)	15
earth press, K	0.3

Pile Details

Circular	
Length(m)	6
Dia (m)	0.6
Area (m ²)	0.283
L/d	10



Approximate Ultimate Ratio

Load Ratio = 0.84

Ultimate Load

Axial Uplift = 0 kN

Lateral = 227 kN

Moment = 377 kN.m

Case 77 N=30,L/d=10,d=0.6 m, Axial Compression, Lateral Load + Moment
Cast-in-place, free Head

Model Results

Load Magnitudes and Combinations

Vertical Load (kN)	Horizontal Load (kN)	Moment (kN.m)	Load Ratio
0	0	0	0
115	70	100	0.272
230	140	200	0.543
345	210	300	0.815
460	280	400	1.087
506	308	440	1.196

Pile Head Displacement

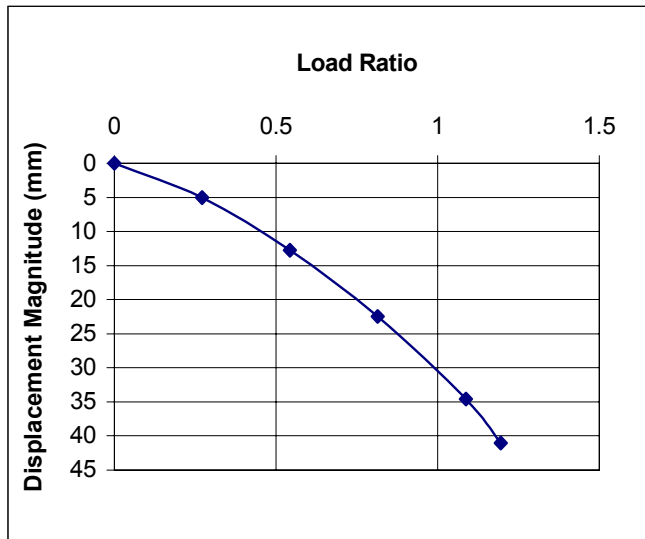
Displacement Magnitude (mm)	Vertical Displacement (mm)	Horizontal Displacement (mm)
0	0	0
5	3.54	3.540
13	8.86	9.18
22	15.07	16.68
35	22.25	26.46
41	27.83	30.14

Soil Details

E (MPa)	33
phi (deg)	48
c (kPa)	0.1
height (m)	12
N _{ave}	30
(N _{1ave})	40
dilation (deg)	15
earth press, K	0.3

Pile Details

Circular	
Length(m)	6
Dia (m)	0.6
Area (m^2)	0.283
L/d	10



Approximate Ultimate Ratio

Load Ratio = 0.73

Ultimate Load

Axial Compression = 309 kN

Lateral = 188 kN

Moment = 268 kN.m

Case 78 N=30,L/d=10,d=0.6 m, Axial Uplift, Lateral Load + Moment
Cast-in-place, free Head

Model Results

Load Magnitudes and Combinations

Vertical Load (kN)	Horizontal Load (kN)	Moment (kN.m)	Load Ratio
0	0	0	0
25	70	100	0.298
50	140	200	0.597
76.25	213.5	300	0.909
97.5	273	400	1.166
125	350	500	1.492

Pile Head Displacement

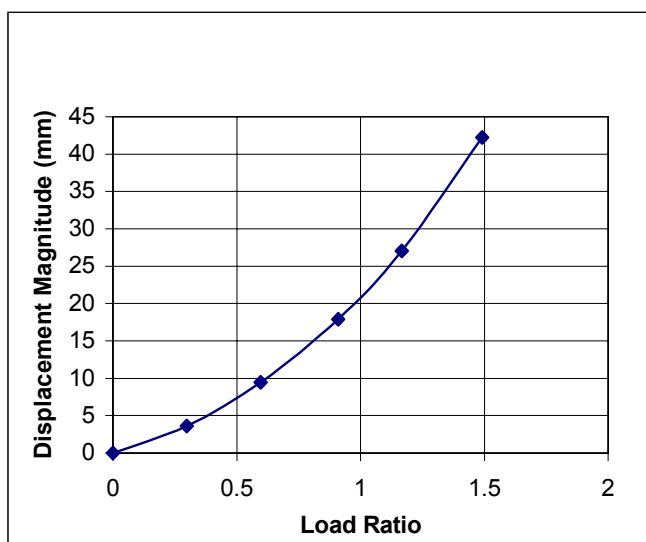
Displacement Magnitude (mm)	Vertical Displacement (mm)	Horizontal Displacement (mm)
0	0	0
4	0.06	3.610
9	1.29	9.35
18	2.88	17.68
27	8.33	25.74
42	18.61	37.92

Soil Details

E (MPa)	33
phi (deg)	48
c (kPa)	0.1
height (m)	12
N _{ave}	30
(N _{1ave})	40
dilation (deg)	15
earth press, K	0.3

Pile Details

Circular	
Length(m)	6
Dia (m)	0.6
Area (m ²)	0.283
L/d	10



Approximate Ultimate Ratio

Load Ratio = 0.85

Ultimate Load

Axial Uplift = 71 kN

Lateral = 198 kN

Moment = 280 kN.m

Case 80 N=30,L/d=10,d=0.6 m, Axial Uplift, Lateral Load + Moment
Cast-in-place, free Head

Model Results

Load Magnitudes and Combinations

Vertical Load (kN)	Horizontal Load (kN)	Moment (kN.m)	Load Ratio
0	0	0	0
59	30	100	0.391
120.95	150	205	0.931
177	61.5	300	1.152

Pile Head Displacement

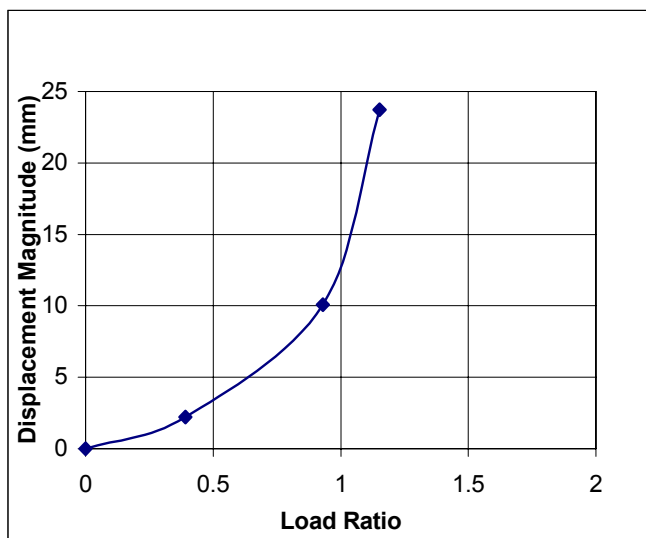
Displacement Magnitude (mm)	Vertical Displacement (mm)	Horizontal Displacement (mm)
0	0	0
2	1.47	1.670
10	9.06	4.42
24	22.51	7.44

Soil Details

E (MPa)	33
phi (deg)	48
c (kPa)	0.1
height (m)	12
N _{ave}	30
(N _{1ave})	40
dilation (deg)	15
earth press, K	0.3

Pile Details

Circular	
Length(m)	6
Dia (m)	0.6
Area (m ²)	0.283
L/d	10



Approximate Ultimate Ratio

Load Ratio = 0.83

Ultimate Load

Axial Uplift = 109 kN
Lateral = 127 kN
Moment = 185 kN.m

Case 81 N=30,L/d=10,d=0.6 m, Axial Compression
Cast-in-place, fixed head

Model Results

Load Magnitudes and Combinations

Vertical Load (kN)	Horizontal Load (kN)	Moment (kN.m)	Load Ratio
0	0	0	0
500	0	0	0
1000	0	0	0
1500	0	0	0
1750	0	0	0
2200	0	0	0

Pile Head Displacement

Displacement Magnitude (mm)	Vertical Displacement (mm)	Horizontal Displacement (mm)
0	0	0
20	20	0
45	44.58	0
81	81.27	0
101	101.2	0
161	161.3	0

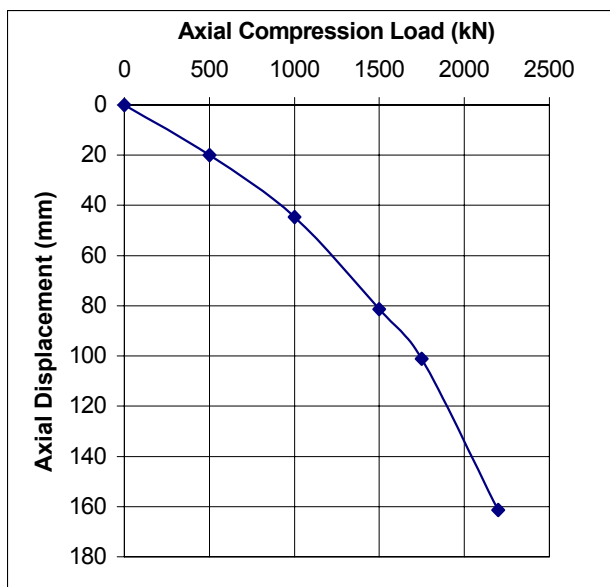
Soil Details

E (MPa)	33
phi (deg)	48
c (kPa)	0.1
height (m)	12
N _{ave}	30
(N _{1ave})	40
dilation (deg)	15
earth press, K	0.3

Pile Details

Circular

Length(m)	6
Dia (m)	0.6
Area (m ²)	0.283
L/d	10



Ultimate Load

Axial Compression = 1200 kN

Case 82 N=30,L/d=10,d=0.6 m, Axial Uplift
Cast-in-place, fixed head

Model Results

Load Magnitudes and Combinations

Vertical Load (kN)	Horizontal Load (kN)	Moment (kN.m)	Load Ratio
0	0	0	0
100	0	0	0
146	0	0	0
200	0	0	0
246	0	0	0
309	0	0	0

Pile Head Displacement

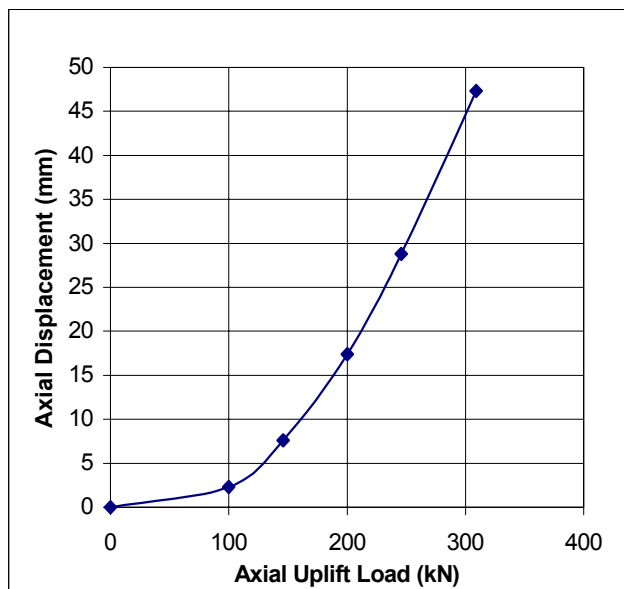
Displacement Magnitude (mm)	Vertical Displacement (mm)	Horizontal Displacement (mm)
0	0	0
2	2.28	0.000
8	7.58	0
17	17.4	0
29	28.8	0
47	47.35	0

Soil Details

E (MPa)	33
phi (deg)	48
c (kPa)	0.1
height (m)	12
N _{ave}	30
(N _{1ave})	40
dilation (deg)	15
earth press, K	0.3

Pile Details

Circular	
Length(m)	6
Dia (m)	0.6
Area (m^2)	0.283
L/d	10



Ultimate Load
Axial Uplift = 160 kN

Case 83 N=30,L/d=10,d=0.6 m, Axial Compression + Lateral Load
Cast-in-place, fixed head

Model Results

Load Magnitudes and Combinations

Vertical Load (kN)	Horizontal Load (kN)	Moment (kN.m)	Load Ratio
0	0	0	0
96	30	0	0.14
192	60	0	0.27
288	90	0	0.41
384	120	0	0.54
480	150	0	0.68
576	180	0	0.81
640	200	0	0.90

Pile Head Displacement

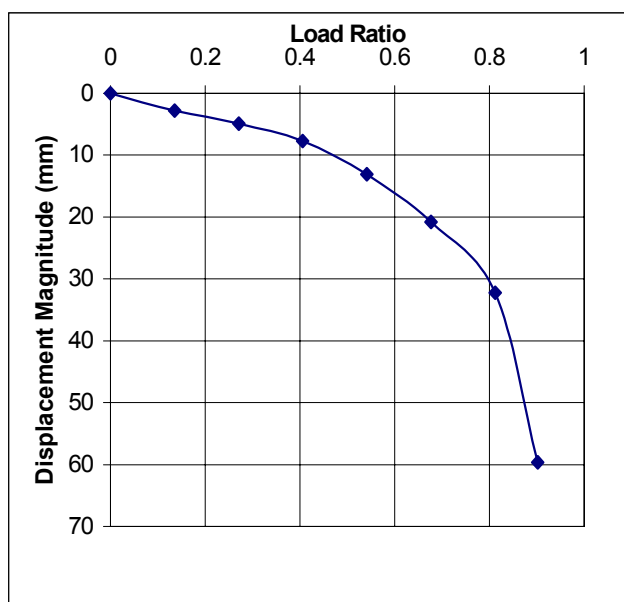
Displacement Magnitude (mm)	Vertical Displacement (mm)	Horizontal Displacement (mm)
0	0	0
3	2.81	0.380
5	4.85	0.85
8	7.58	1.42
13	12.96	2.04
21	18.83	8.74
32	29.711	12.530
60	56.666	18.537

Soil Details

E (MPa)	33
phi (deg)	48
c (kPa)	0.1
height (m)	12
N _{ave}	30
(N _{1ave})	40
dilation (deg)	15
earth press, K	0.3

Pile Details

Circular	
Length(m)	6
Dia (m)	0.6
Area (m ²)	0.283
L/d	10



Approximate Ultimate Ratio

Load Ratio = 0.77

Ultimate Load

Axial Compression = 544 kN

Lateral = 170 kN

Moment = 0 kN.m

Case 84 N=30,L/d=10,d=0.6 m, Axial Uplift + Lateral Load
Cast-in-place, fixed head

Model Results

Load Magnitudes and Combinations

Vertical Load (kN)	Horizontal Load (kN)	Moment (kN.m)	Load Ratio
0	0	0	0
63	30	0	0.41
126	60	0	0.82
189	90	0	1.23
252	120	0	1.63
293	140	0	1.90

Pile Head Displacement

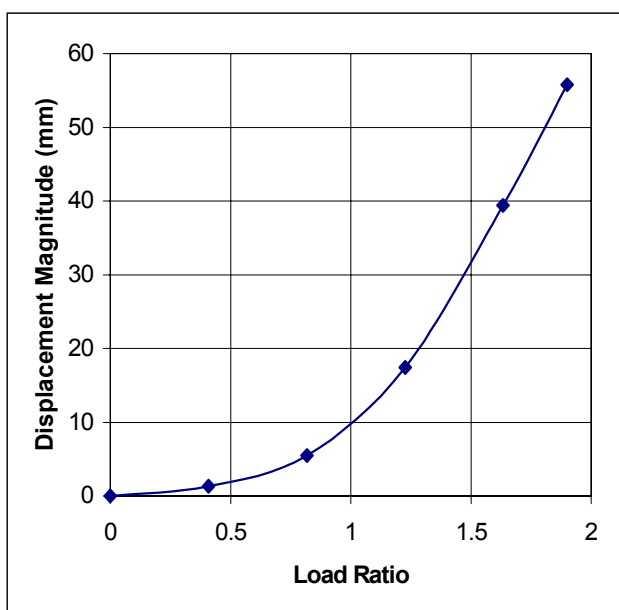
Displacement Magnitude (mm)	Vertical Displacement (mm)	Horizontal Displacement (mm)
0	0	0
1	1.31	0.217
5	5.39	0.9
17	17.34	1.55
39	39.34	2.33
56	55.58	4.85

Soil Details

E (MPa)	33
phi (deg)	48
c (kPa)	0.1
height (m)	12
N _{ave}	30
(N _{1ave})	40
dilation (deg)	15
earth press, K	0.3

Pile Details

Circular	
Length(m)	6
Dia (m)	0.6
Area (m ²)	0.283
L/d	10



Approximate Ultimate Ratio

Load Ratio = 0.94

Ultimate Load

Axial Uplift = 145 kN

Lateral = 69 kN

Moment = 0 kN.m

Case 86 N=30,L/d=10,d=0.6 m, Axial Uplift + Lateral Load
Cast-in-place, fixed head

Model Results

Load Magnitudes and Combinations

Vertical Load (kN)	Horizontal Load (kN)	Moment (kN.m)	Load Ratio
0	0	0	0
42	30	0	0.28
84	60	0	0.57
126	90	0	0.85
168	120	0	1.14
210	150	0	1.42

Pile Head Displacement

Displacement Magnitude (mm)	Vertical Displacement (mm)	Horizontal Displacement (mm)
0		
1	0.85	0.353
2	1.82	0.89
6	5.57	1.5
15	15.17	2.21
31	30.46	6.02

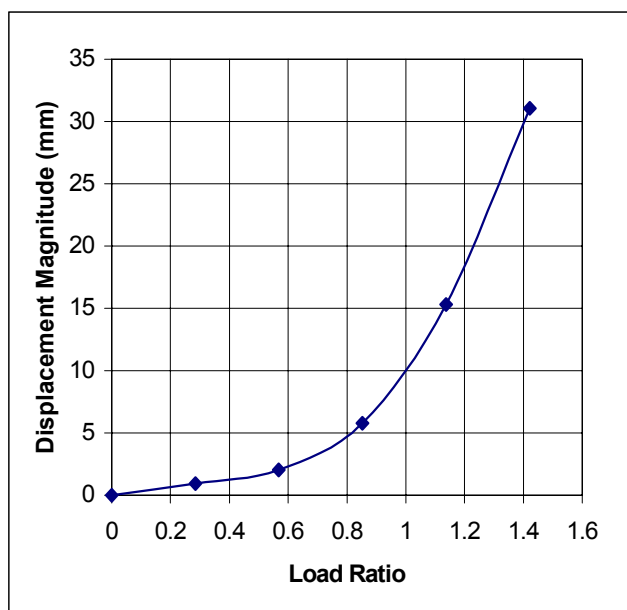
Soil Details

E (MPa)	33
phi (deg)	48
c (kPa)	0.1
height (m)	12
N _{ave}	30
(N _{1ave})	40
dilation (deg)	15
earth press, K	0.3

Pile Details

Circular

Length(m)	6
Dia (m)	0.6
Area (m ²)	0.283
L/d	10



Approximate Ultimate Ratio

Load Ratio = 0.91

Ultimate Load

Axial Uplift = 138 kN

Lateral = 96 kN

Moment = 0 kN.m

Case 88 N=30,L/d=10,d=0.6 m, Axial Uplift + Lateral Load
Cast-in-place, fixed head

Model Results

Load Magnitudes and Combinations

Vertical Load (kN)	Horizontal Load (kN)	Moment (kN.m)	Load Ratio
0	0	0	0
41	75	0	0.37
82	150	0	0.75
109	200	0	1.00
137	250	0	1.25
164	300	0	1.50

Pile Head Displacement

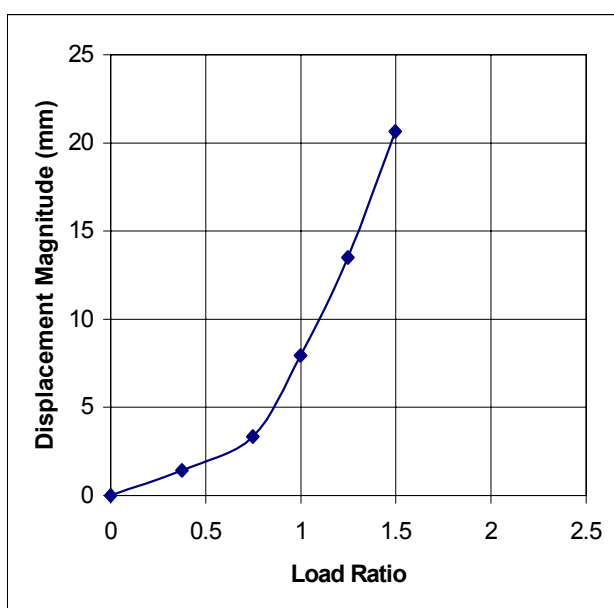
Displacement Magnitude (mm)	Vertical Displacement (mm)	Horizontal Displacement (mm)
0		
1	0.79	1.170
3	1.69	2.890
8	2.99	7.35
13	3.69	12.98
21	4.98	20.05

Soil Details

E (MPa)	33
phi (deg)	48
c (kPa)	0.1
height (m)	12
N _{ave}	30
(N _{1ave})	40
dilation (deg)	15
earth press, K	0.3

Pile Details

Circular	
Length(m)	6
Dia (m)	0.6
Area (m ²)	0.283
L/d	10



Approximate Ultimate Ratio

Load Ratio = 0.92

Ultimate Load

Axial Uplift = 100 kN

Lateral = 183 kN

Moment = 0 kN.m

Case 89 N=30,L/d=10,d=0.6 m, Lateral Load
Cast-in-place, fixed head

Model Results

Load Magnitudes and Combinations

Vertical Load (kN)	Horizontal Load (kN)	Moment (kN.m)	Load Ratio
0	0	0	0
0	150	0	0
0	300	0	0
0	450	0	0
0	500	0	0
0	550	0	0

Pile Head Displacement

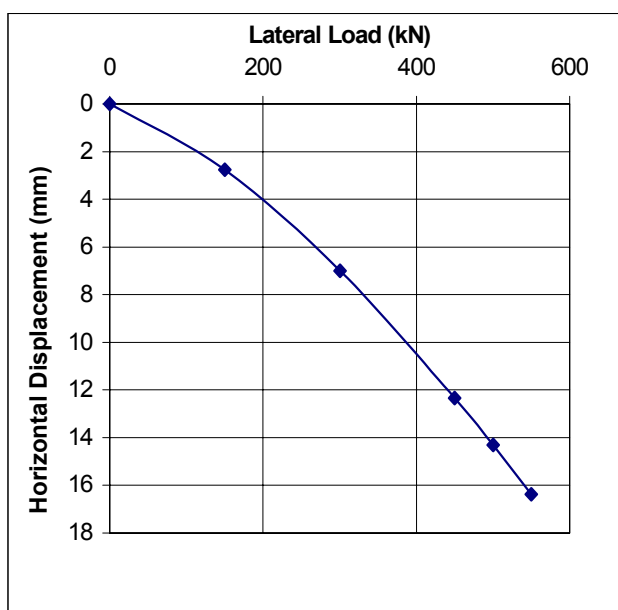
Displacement Magnitude (mm)	Vertical Displacement (mm)	Horizontal Displacement (mm)
0	0	0
3	0	2.770
7	0.04	7
12	0.14	12.34
14	0.19	14.3
16	0.25	16.38

Soil Details

E (MPa)	33
phi (deg)	48
c (kPa)	0.1
height (m)	12
N _{ave}	30
(N _{1ave})	40
dilation (deg)	15
earth press, K	0.3

Pile Details

Circular	
Length(m)	6
Dia (m)	0.6
Area (m ²)	0.283
L/d	10



Ultimate Load
Lateral = 275 kN

Case 101 N=5,L/d=3,d=0.6 m, Axial Compression
Impact Driven, Free Head

Model Results

Load Magnitudes and Combinations

Vertical Load (kN)	Horizontal Load (kN)	Moment (kN.m)	Load Ratio
0	0	0	0
200	0	0	0
400	0	0	0
600	0	0	0
800	0	0	0
1000	0	0	0

Pile Head Displacement

Displacement Magnitude (mm)	Vertical Displacement (mm)	Horizontal Displacement (mm)
0	0	0
7	6.59	0
15	15.25	0
29	29.15	0
45	44.81	0
62	58.75	0

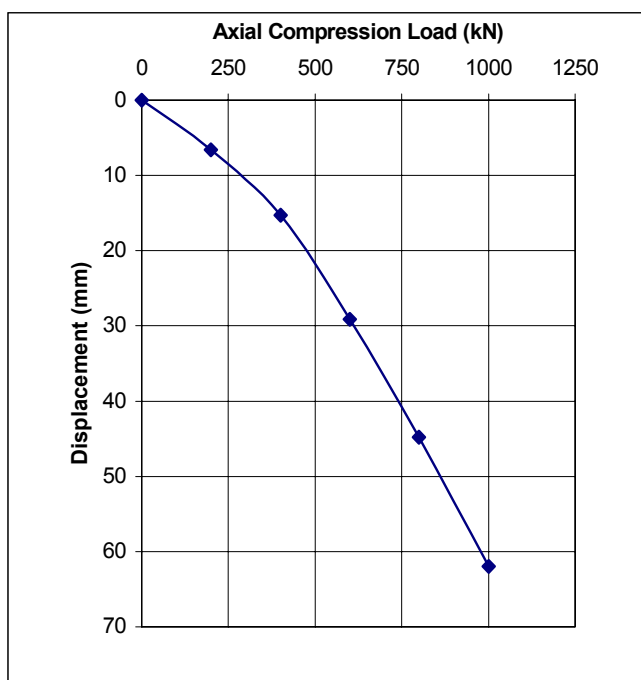
Soil Details

E (MPa)	45
phi (deg)	36
c (kPa)	0.1
height (m)	3.6
N _{ave}	5
(N _{1ave})	12
dilation (deg)	3
earth press, K	0.8

Pile Details

Circular

Length(m)	1.8
Dia (m)	0.6
Area (m ²)	0.283
L/d	3



Ultimate Load

Axial Compression = 300 kN

Case 102 N=5,L/d=3,d=0.6 m, Axial Uplift
Impact Driven, Free Head

Model Results

Load Magnitudes and Combinations

Vertical Load (kN)	Horizontal Load (kN)	Moment (kN.m)	Load Ratio
0	0	0	n/a
3	0	0	n/a
7.5	0	0	n/a
12	0	0	n/a
15	0	0	n/a
18	0	0	n/a

Pile Head Displacement

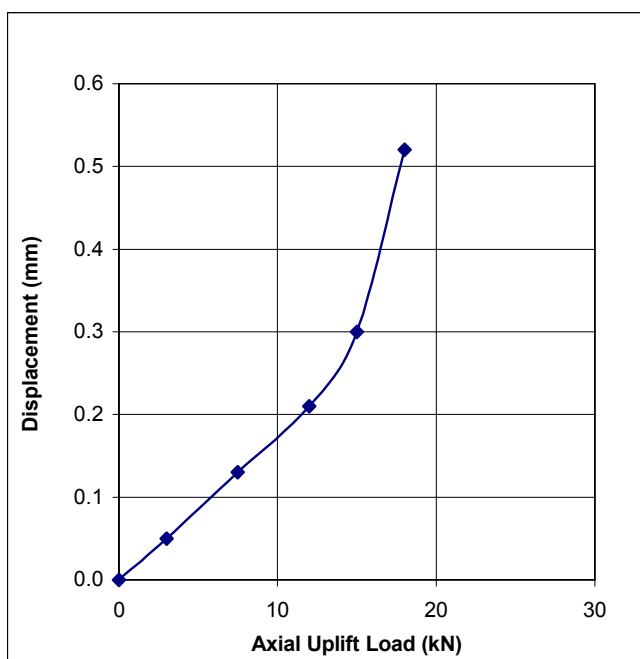
Displacement Magnitude (mm)	Vertical Displacement (mm)	Horizontal Displacement (mm)
0	0	0
0	0.05	0.000
0	0.13	0
0	0.21	0
0	0.3	0
1	0.52	0

Soil Details

E (MPa)	45
phi (deg)	36
c (kPa)	0.1
height (m)	3.6
N _{ave}	5
(N _{1ave})	12
dilation (deg)	3
earth press, K	0.8

Pile Details

Circular	
Length(m)	1.8
Dia (m)	0.6
Area (m^2)	0.283
L/d	3



Ultimate Load

Axial Uplift = 15 kN

Case 103 N=5,L/d=3,d=0.6 m, Axial Compression + Lateral Load
Impact Driven, Free Head

Model Results

Load Magnitudes and Combinations

Vertical Load (kN)	Horizontal Load (kN)	Moment (kN.m)	Load Ratio
0	0	0	0
84	8.4	0	0.369
200	20	0	0.878
250	25	0	1.098
300	30	0	1.317

Pile Head Displacement

Displacement Magnitude (mm)	Vertical Displacement (mm)	Horizontal Displacement (mm)
0		
2	2.110	0.280
10	9.270	3.96
21	16.180	12.68
39	18.923	34.13

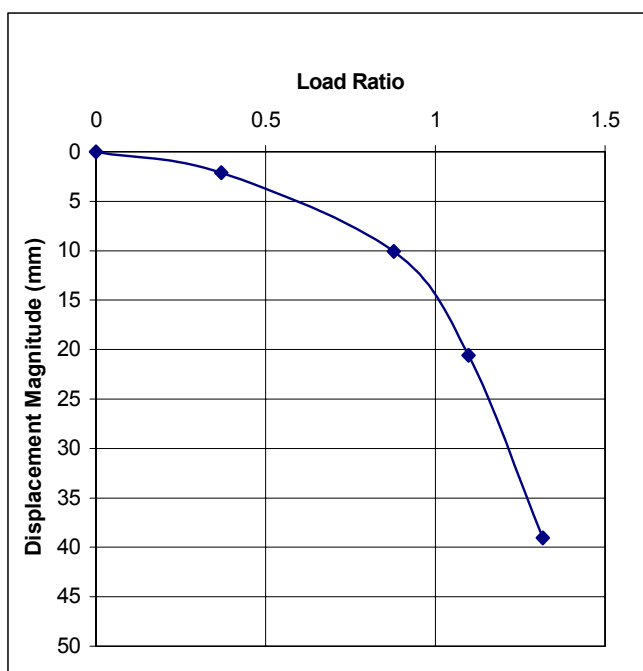
Soil Details

E (MPa)	45
phi (deg)	36
c (kPa)	0.1
height (m)	3.6
N _{ave}	5
(N _{1ave})	12
dilation (deg)	3
earth press, K	0.8

Pile Details

Circular

Length(m)	1.8
Dia (m)	0.6
Area (m^2)	0.283
L/d	3



Approximate Ultimate Ratio

Load Ratio = 0.76

Ultimate Load

Axial Compression = 174 kN

Lateral = 18 kN

Moment = 0 kN.m

Case 104 N=5,L/d=3,d=0.6 m, Axial Uplift + Lateral Load
Impact Driven, Free Head

Model Results

Load Magnitudes and Combinations

Vertical Load (kN)	Horizontal Load (kN)	Moment (kN.m)	Load Ratio
0	0	0	0
2	0.22	0	0.107
3.2	0.44	0	0.214
4.8	0.67	0	0.321
14.4	2.00	0	0.962
14.7	2.04	0	0.983

Pile Head Displacement

Displacement Magnitude (mm)	Vertical Displacement (mm)	Horizontal Displacement (mm)
0.00		
0.02	0.024	0.001
0.04	0.042	0.004
0.07	0.066	0.006
0.21	0.21	0.014
0.38	0.37	0.08

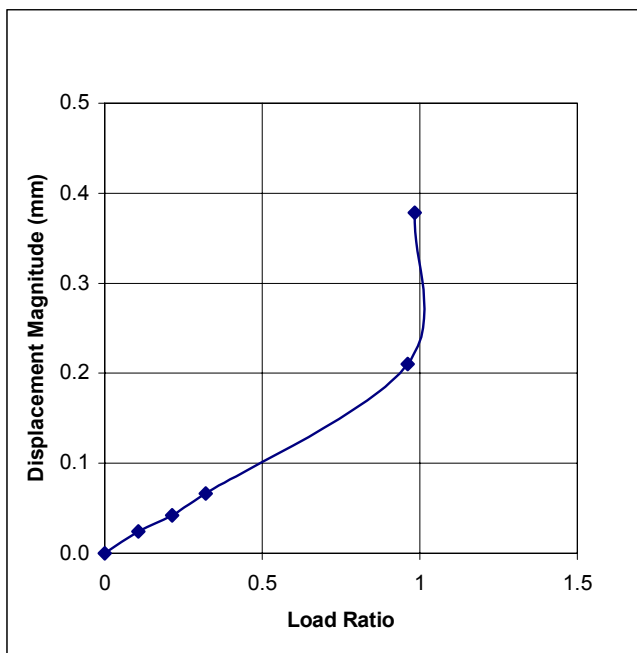
Soil Details

E (MPa)	45
phi (deg)	36
c (kPa)	0.1
height (m)	3.6
N _{ave}	5
(N _{1ave})	12
dilation (deg)	3
earth press, K	0.8

Pile Details

Circular

Length(m)	1.8
Dia (m)	0.6
Area (m^2)	0.283
L/d	3



Approximate Ultimate Ratio

Load Ratio = 0.96

Ultimate Load

Axial Uplift = 14.4 kN

Lateral = 2 kN

Moment = 0 kN.m

Case 109 N=5,L/d=3,d=0.6 m, Lateral Load
Impact Driven, Free Head

Model Results

Load Magnitudes and Combinations

Vertical Load (kN)	Horizontal Load (kN)	Moment (kN.m)	Load Ratio
0	0	0	n/a
0	10.0	0	n/a
0	20.0	0	n/a
0	40.0	0	n/a
0	50.0	0	n/a
0	53.9	0	n/a

Pile Head Displacement

Displacement Magnitude (mm)	Vertical Displacement (mm)	Horizontal Displacement (mm)
0		
1	0.002	0.515
2	0.081	1.92
17	0.94	16.62
38	2.22	37.74
47	2.7	47.23

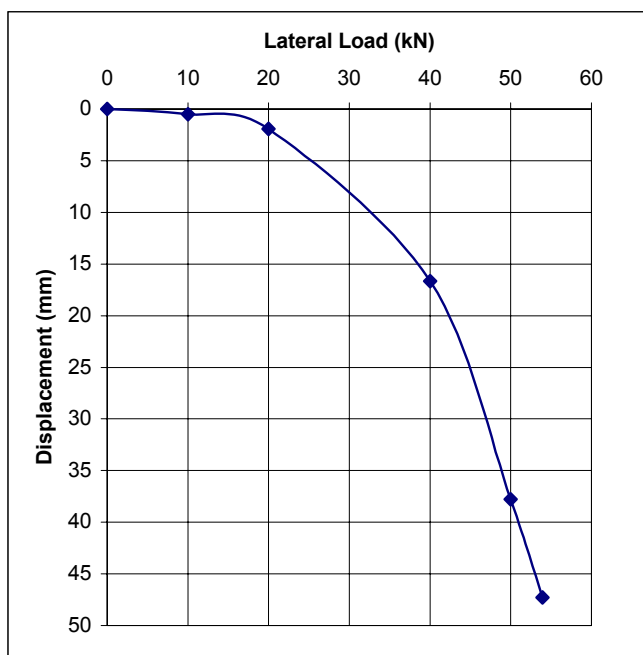
Soil Details

E (MPa)	45
phi (deg)	36
c (kPa)	0.1
height (m)	3.6
N _{ave}	5
(N _{1ave})	12
dilation (deg)	3
earth press, K	0.8

Pile Details

Circular

Length(m)	1.8
Dia (m)	0.6
Area (m^2)	0.283
L/d	3



Ultimate Load
Lateral = 35 kN

Case 110 N=5,L/d=3,d=0.6 m, Moment
Impact Driven, Free Head

Model Results

Load Magnitudes and Combinations

Vertical Load (kN)	Horizontal Load (kN)	Moment (kN.m)	Load Ratio
0	0	0	n/a
0	0	20	n/a
0	0	40	n/a
0	0	60	n/a
0	0	80	n/a
0	0	100	n/a

Pile Head Displacement

Displacement Magnitude (mm)	Vertical Displacement (mm)	Horizontal Displacement (mm)
0		
0	0.06	0.312
1	0.05	0.971
2	0.16	2.37
6	0.37	5.53
11	0.66	10.84

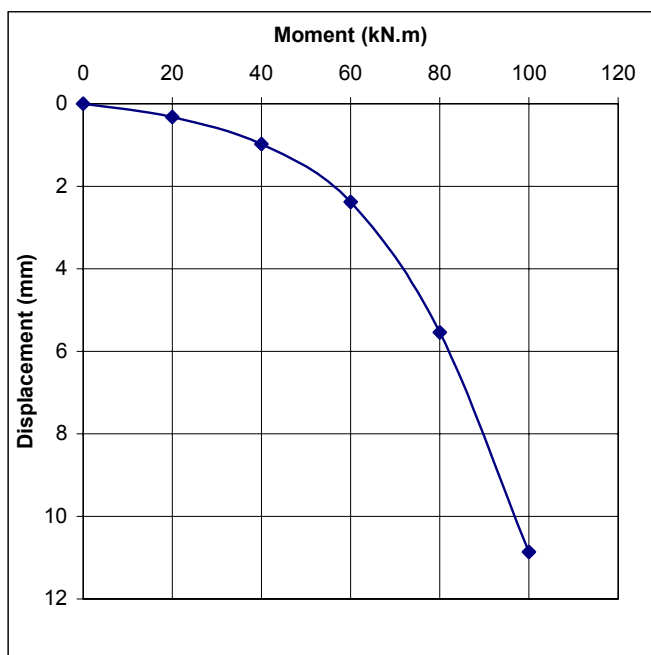
Soil Details

E (MPa)	45
phi (deg)	36
c (kPa)	0.1
height (m)	3.6
N _{ave}	5
(N _{1ave})	12
dilation (deg)	3
earth press, K	0.8

Pile Details

Circular

Length(m)	1.8
Dia (m)	0.6
Area (m^2)	0.283
L/d	3



Ultimate Load
Moment = 60 kN.m

Case 111 N=5,L/d=3,d=0.6 m, Axial Compression + Moment
Impact Driven, Free Head

Model Results

Load Magnitudes and Combinations

Vertical Load (kN)	Horizontal Load (kN)	Moment (kN.m)	Load Ratio
0	0	0	0
50	0	2	0.170
100	0	4	0.340
150	0	6	0.510
250	0	10	0.850
300	0	12	1.020
350	0	14	1.190

Pile Head Displacement

Displacement Magnitude (mm)	Vertical Displacement (mm)	Horizontal Displacement (mm)
0		
2	2.21	0.022
5	5	0.06
8	8.46	0.11
16	16.4	0.616
28	28.025	0.660
42	42.128	0.8432

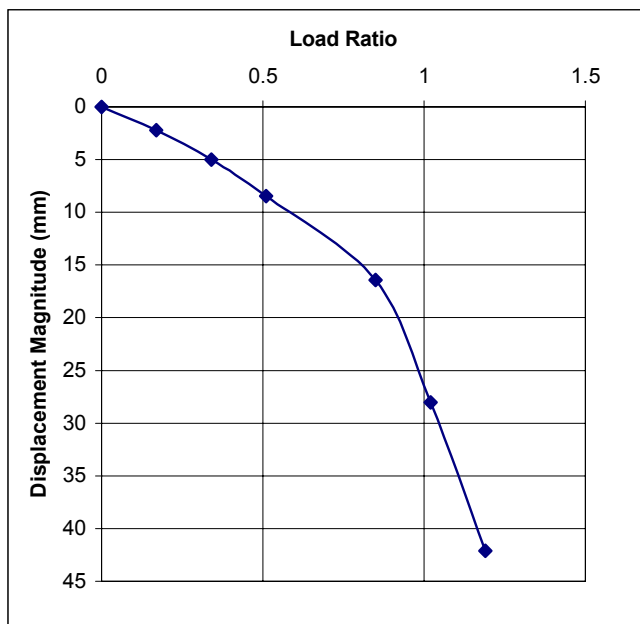
Soil Details

E (MPa)	45
phi (deg)	36
c (kPa)	0.1
height (m)	3.6
N _{ave}	5
(N _{1ave})	12
dilation (deg)	3
earth press, K	0.8

Pile Details

Circular

Length(m)	1.8
Dia (m)	0.6
Area (m^2)	0.283
L/d	3



Approximate Ultimate Ratio

Load Ratio = 0.85

Ultimate Load

Axial Compression = 250 kN

Lateral = 0 kN

Moment = 10 kN.m

Case 112 N=5,L/d=3,d=0.6 m, Axial Uplift + Moment
Impact Driven, Free Head

Model Results

Load Magnitudes and Combinations

Vertical Load (kN)	Horizontal Load (kN)	Moment (kN.m)	Load Ratio
0	0	0	0
3.5	0	0.48	0.233
7	0	0.97	0.467
10.5	0	1.45	0.700
14	0	1.93	0.934
15	0	2.07	1.001
16	0	2.21	1.067

Pile Head Displacement

Displacement Magnitude (mm)	Vertical Displacement (mm)	Horizontal Displacement (mm)
0	0	0
0.03	0.03	0.004
0.09	0.091	0.015
0.19	0.19	0.020
0.30	0.301	0.033
0.40	0.394	0.042
0.57	0.567	0.060

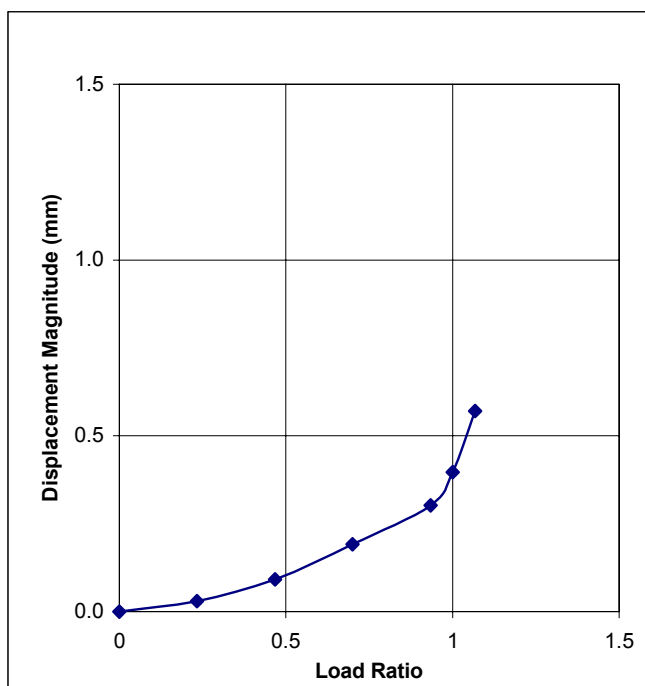
Soil Details

E (MPa)	45
phi (deg)	36
c (kPa)	0.1
height (m)	3.6
N _{ave}	5
(N _{1ave})	12
dilation (deg)	3
earth press, K	0.8

Pile Details

Circular

Length(m)	1.8
Dia (m)	0.6
Area (m^2)	0.283
L/d	3



Approximate Ultimate Ratio

Load Ratio = 0.97

Ultimate Load

Axial Uplift = 14.5 kN

Lateral = 0 kN

Moment = 2 kN.m

Case 115 N=5,L/d=3,d=0.6 m, Lateral Load + Moment
Impact Driven, Free Head

Model Results

Load Magnitudes and Combinations

Vertical Load (kN)	Horizontal Load (kN)	Moment (kN.m)	Load Ratio
0	0.0	0	0
0	5.7	10	0.233
0	11.4	20	0.467
0	20.0	35	0.817
0	22.9	40	0.933
0	25.7	45	1.050

Pile Head Displacement

Displacement Magnitude (mm)	Vertical Displacement (mm)	Horizontal Displacement (mm)
0		
1	0.152	0.920
2	0.25	2.13
4	0.37	4.2
7	0.54	7.14
13	0.75	13.04

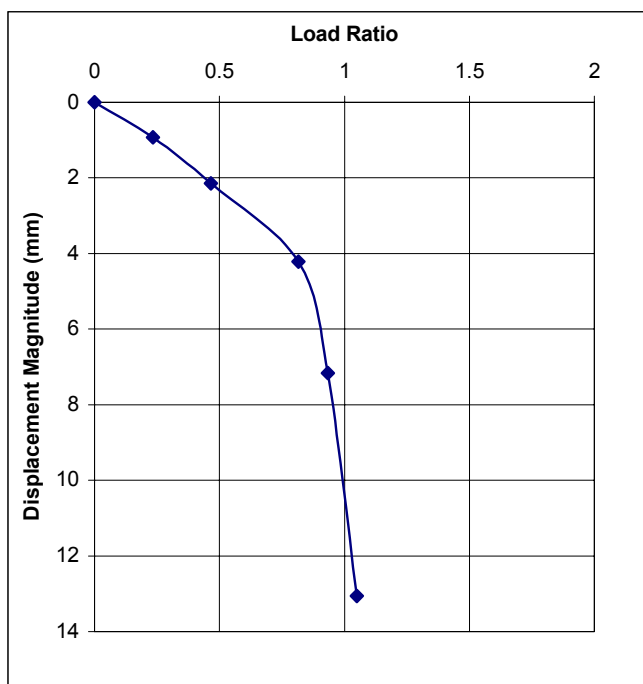
Soil Details

E (MPa)	45
phi (deg)	36
c (kPa)	0.1
height (m)	3.6
N _{ave}	5
(N _{1ave}) =	12
dilation (deg)	3
earth press, K	0.8

Pile Details

Circular

Length(m)	1.8
Dia (m)	0.6
Area (m^2)	0.283
L/d	3



Approximate Ultimate Ratio

Load Ratio = 0.82

Ultimate Load

Axial Uplift = 0 kN

Lateral = 20 kN

Moment = 35 kN.m

Case 117 N=5,L/d=3,d=0.6 m, Axial Compression, Lateral Load + Moment
Impact Driven, Free Head

Model Results

Load Magnitudes and Combinations

Vertical Load (kN)	Horizontal Load (kN)	Moment (kN.m)	Load Ratio
0	0	0	0
20.4	3.2	0.8	0.115
48.45	7.6	1.9	0.272
99.45	15.6	3.9	0.559
153	24	6.0	0.860
198.9	31.2	7.8	1.119

Pile Head Displacement

Displacement Magnitude (mm)	Vertical Displacement (mm)	Horizontal Displacement (mm)
0		
1	0.698	0.134
2	2.04	0.45
6	5.88	2.21
13	10.91	6.46
24	19.43	14.25

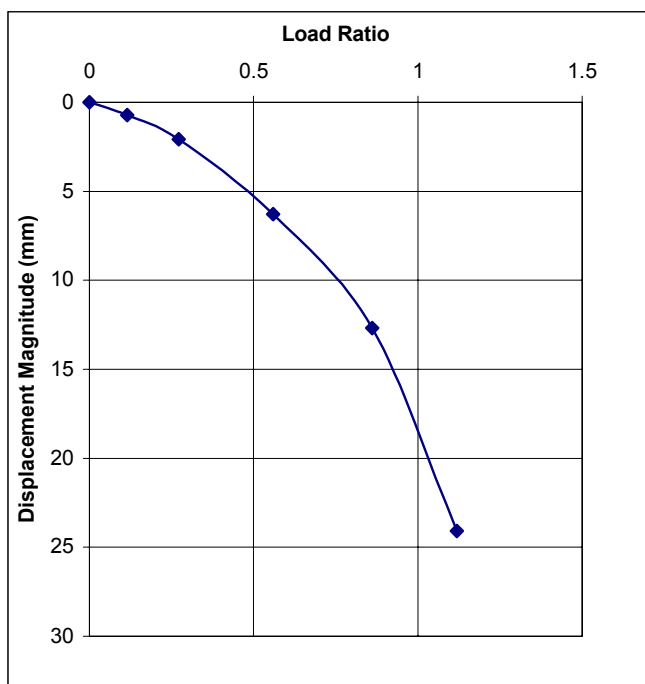
Soil Details

E (MPa)	45
phi (deg)	36
c (kPa)	0.1
height (m)	3.6
N _{ave}	5
(N _{1ave})	12
dilation (deg)	3
earth press, K	0.8

Pile Details

Circular

Length(m)	1.8
Dia (m)	0.6
Area (m^2)	0.283
L/d	3



Approximate Ultimate Ratio

Load Ratio = 0.73

Ultimate Load

Axial Compression = 130 kN

Lateral = 21 kN

Moment = 5 kN.m

Case 118 N=5,L/d=3,d=0.6 m, Axial Uplift, Lateral Load + Moment
Impact Driven, Free Head

Model Results

Load Magnitudes and Combinations

Vertical Load (kN)	Horizontal Load (kN)	Moment (kN.m)	Load Ratio
0	0	0	0
1.9	0.48	0.10	0.127
3.8	0.95	0.19	0.255
5.7	1.43	0.29	0.382
7.6	1.90	0.38	0.510
10	2.50	0.50	0.671
13.3	3.33	0.67	0.892

Pile Head Displacement

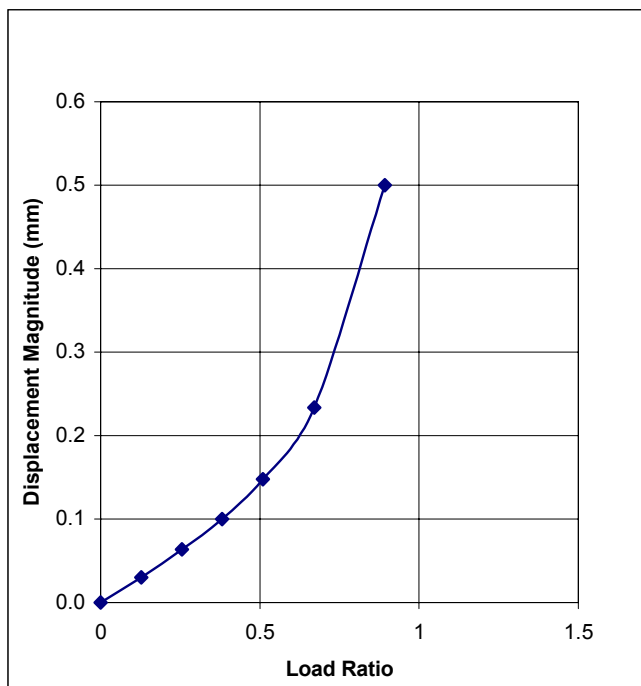
Displacement Magnitude (mm)	Vertical Displacement (mm)	Horizontal Displacement (mm)
0.00		
0.03	0.028	0.012
0.06	0.061	0.0178
0.10	0.096	0.028
0.15	0.14	0.047
0.23	0.224	0.066
0.50	0.49	0.1

Soil Details

E (MPa)	45
phi (deg)	36
c (kPa)	0.1
height (m)	3.6
N _{ave}	5
(N _{1ave})	12
dilation (deg)	3
earth press, K	0.8

Pile Details

Circular	
Length(m)	1.8
Dia (m)	0.6
Area (m^2)	0.283
L/d	3



Approximate Ultimate Ratio

Load Ratio = 0.54

Ultimate Load

Axial Compression = 8 kN

Lateral = 2 kN

Moment = 0.4 kN.m

Case 142 N=5,L/d=3,d=0.6 m, Axial Uplift
Impact Driven, Free Head

Model Results

Load Magnitudes and Combinations

Vertical Load (kN)	Horizontal Load (kN)	Moment (kN.m)	Load Ratio
0	0	0	n/a
30	0	0	n/a
50	0	0	n/a
80	0	0	n/a
100	0	0	n/a
110	0	0	n/a

Pile Head Displacement

Displacement Magnitude (mm)	Vertical Displacement (mm)	Horizontal Displacement (mm)
0		
1	0.51	0
1	0.8	0
1	1.37	0
3	2.95	0
34	34.2	0

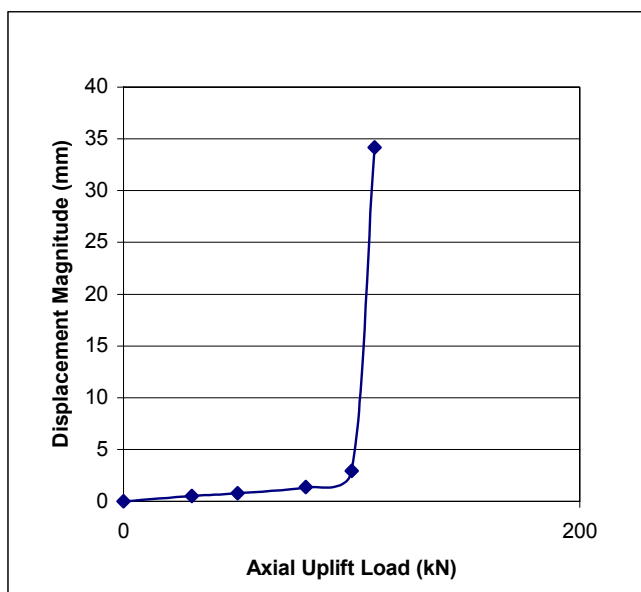
Soil Details

E (MPa)	45
phi (deg)	32
c (kPa)	0.1
height (m)	12
N _{ave}	5
(N _{1ave})	7
dilation (deg)	0
earth press, K	0.9

Pile Details

Circular

Length(m)	6
Dia (m)	0.6
Area (m^2)	0.283
L/d	10



Ultimate Load

Axial Uplift = 100 kN

Case 144 N=5,L/d=3,d=0.6 m, Axial Uplift + Lateral Load
Impact Driven, Free Head

Model Results

Load Magnitudes and Combinations

Vertical Load (kN)	Horizontal Load (kN)	Moment (kN.m)	Load Ratio
0	0	0	0
20	4	0	0.201
45	9	0	0.453
75	15	0	0.755
100	20	0	1.006
105	21	0	1.056

Pile Head Displacement

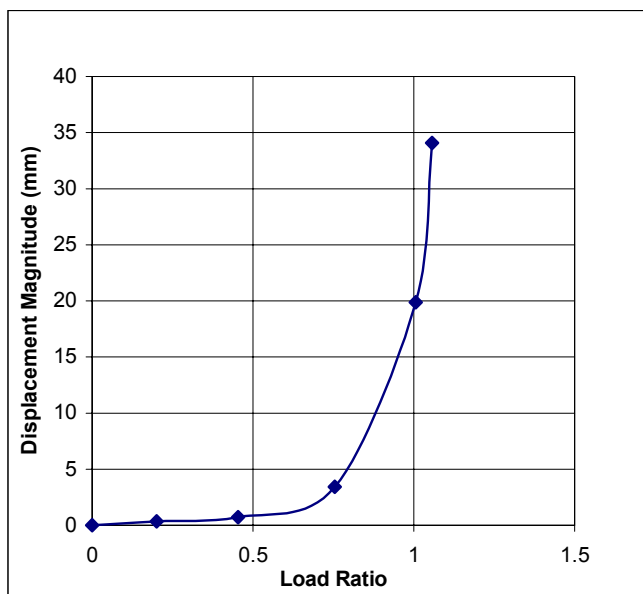
Displacement Magnitude (mm)	Vertical Displacement (mm)	Horizontal Displacement (mm)
0.0		
0.3	0.3	0.050
0.7	0.69	0.17
3.4	3.42	0.33
19.9	19.87	0.49
34.1	34.07	0.54

Soil Details

E (MPa)	45
phi (deg)	32
c (kPa)	0.1
height (m)	12
N _{ave}	5
(N _{1ave})	7
dilation (deg)	0
earth press, K	0.9

Pile Details

Circular	
Length(m)	6
Dia (m)	0.6
Area (m ²)	0.283
L/d	10



Approximate Ultimate Ratio

Load Ratio = 0.97

Ultimate Load

Axial Uplift = 96 kN

Lateral = 20 kN

Moment = 0 kN.m

Case 149 N=5,L/d=3,D=0.6 m, Lateral Load
Impact Driven, Free Head

Model Results

Load Magnitudes and Combinations

Vertical Load (kN)	Horizontal Load (kN)	Moment (kN.m)	Load Ratio
0	0	0	n/a
0	100	0	n/a
0	200	0	n/a
0	300	0	n/a
0	312	0	n/a

Pile Head Displacement

Displacement Magnitude (mm)	Vertical Displacement (mm)	Horizontal Displacement (mm)
0	0	0
5	0	4.980
17	0.23	17.24
43	0.9	42.67
46	1.03	46.1

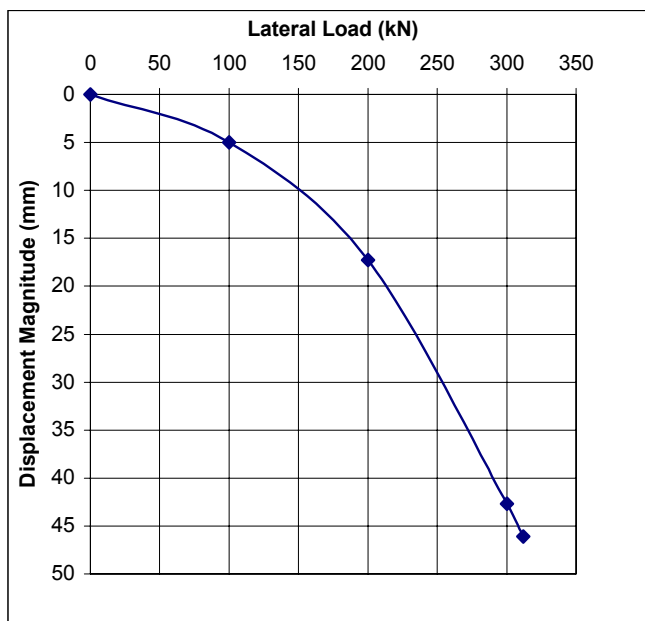
Soil Details

E (MPa)	45
phi (deg)	36
c (kPa)	0.1
height (m)	3.6
N _{ave}	5
(N _{1ave})	12
dilation (deg)	0
earth press, K	0.8

Pile Details

Circular

Length(m)	1.8
Dia (m)	0.6
Area (m^2)	0.283
L/d	3



Ultimate Load
Lateral = 180 kN

Case 150 N=5,L/d=3,D=0.6 m, Moment
Impact Driven, Free Head

Model Results

Load Magnitudes and Combinations

Vertical Load (kN)	Horizontal Load (kN)	Moment (kN.m)	Load Ratio
0	0	0	n/a
0	0	500	n/a
0	0	1000	n/a
0	0	1500	n/a
0	0	2000	n/a
0	0	2315	n/a

Pile Head Displacement

Displacement Magnitude (mm)	Vertical Displacement (mm)	Horizontal Displacement (mm)
0		
4	0.01	4.180
11	0.03	10.85
20	0.2	19.68
31	0.5	31.13
41	0.75	40.76

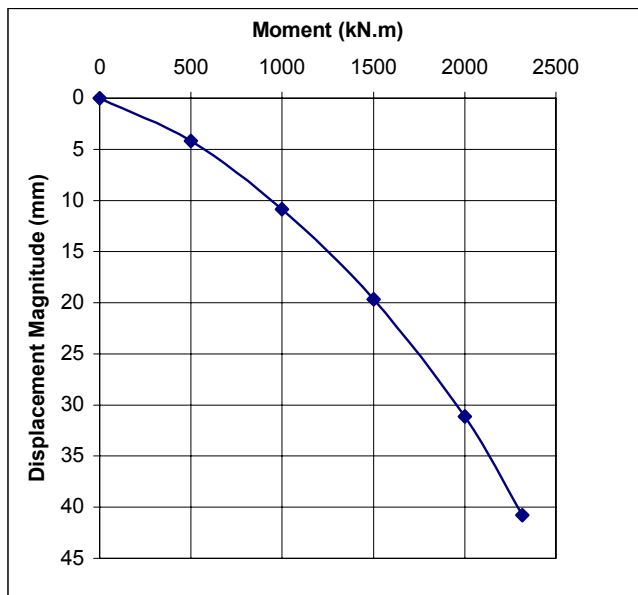
Soil Details

E (MPa)	45
phi (deg)	36
c (kPa)	0.1
height (m)	3.6
N _{ave}	5
(N _{1ave})	12
dilation (deg)	0
earth press, K	0.8

Pile Details

Circular

Length(m)	1.8
Dia (m)	0.6
Area (m ²)	0.283
L/d	3



Ultimate Load

Moment = 1150 kN.m

Case 155 N=5,L/d=3,D=0.6 m, Lateral Load + Moment
Impact Driven, Free Head

Model Results

Load Magnitudes and Combinations

Vertical Load (kN)	Horizontal Load (kN)	Moment (kN.m)	Load Ratio
0	0	0	0
0	56	500	0.535
0	113	1000	1.071
0	169	1500	1.606
0	177	1575	1.687

Pile Head Displacement

Displacement Magnitude (mm)	Vertical Displacement (mm)	Horizontal Displacement (mm)
0		
9	0.1	8.650
20	0.36	19.87
40	0.8	39.78
42	0.85	42.12

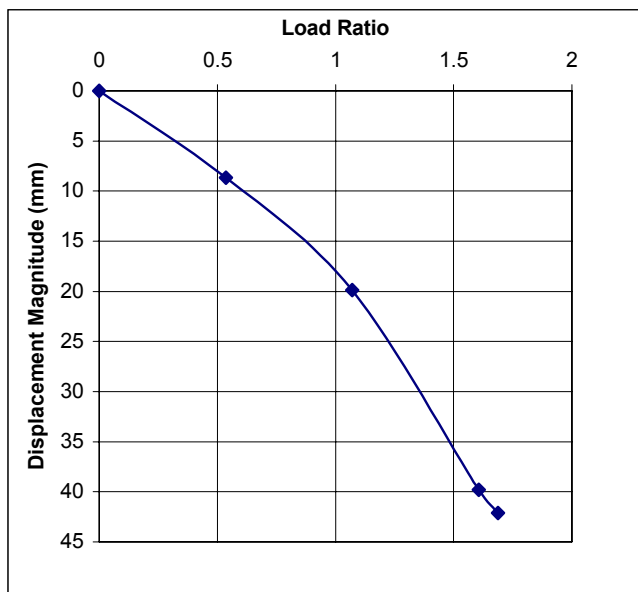
Soil Details

E (MPa)	45
phi (deg)	36
c (kPa)	0.1
height (m)	3.6
N _{ave}	5
(N _{1ave})	12
dilation (deg)	0
earth press, K	0.8

Pile Details

Circular

Length(m)	1.8
Dia (m)	0.6
Area (m^2)	0.283
L/d	3



Approximate Ultimate Ratio

Load Ratio = 0.86

Ultimate Load

Axial Uplift = 0 kN

Lateral = 90 kN

Moment = 800 kN.m

Case 158 N=5,L/d=3,d=0.6 m, Axial Uplift, Lateral Load + Moment
Impact Driven, Free Head

Model Results

Load Magnitudes and Combinations

Vertical Load (kN)	Horizontal Load (kN)	Moment (kN.m)	Load Ratio
0	0	0	0
18	4	10	0.182
36	8	20	0.363
54	12	30	0.545
81	18	45	0.817
99	22	55	0.999

Pile Head Displacement

Displacement Magnitude (mm)	Vertical Displacement (mm)	Horizontal Displacement (mm)
0.0		
0.3	0.28	0.010
0.7	0.65	0.25
1.1	1.04	0.42
2.0	1.92	0.61
4.6	4.59	0.7

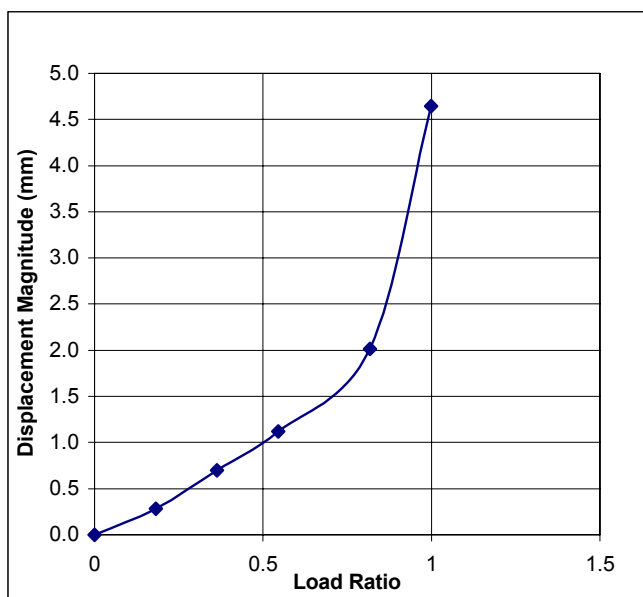
Soil Details

E (MPa)	45
phi (deg)	36
c (kPa)	0.1
height (m)	3.6
N _{ave}	5
(N _{1ave})	12
dilation (deg)	0
earth press, K	0.8

Pile Details

Circular

Length(m)	1.8
Dia (m)	0.6
Area (m^2)	0.283
L/d	3



Approximate Ultimate Ratio

Load Ratio = 0.86

Ultimate Load

Axial Uplift = 90 kN

Lateral = 20 kN

Moment = 50 kN.m

APPENDIX J: Sample Calculations

---oooOOOooo---

This appendix is referred to in Chapter 9. To examine how the pile finite element model developed by the author performed, it was compared to estimates made from the methods of other researchers. The sample calculations using existing methods for one of the cases outlined in Table 9.6 is shown, which is a hypothetical case chosen by the author (see Chapter 9). This allows the validity for the output of the finite element pile model to be checked. It also provides an opportunity to check the output of the hypothetical cases used to form the oblique interaction charts.

The example calculations are for the numerical case where the pile has an $L/d = 3$, $d = 0.6$ m, $L = 1.8$ m, and the sand has a standard field blow count of $N=5$. It is noted that the pile is assumed to be cast-in-place.

The strength and deformation properties of the sand and pile have been discussed in the main body of the thesis, and are shown again in summary form here:

$$\phi = 36^\circ$$

$$E \text{ of soil} = 14 \text{ MPa}$$

$$K=0.4$$

$$E \text{ of pile} = 30 \text{ GPa}$$

J.1 Ultimate Compression Capacity

Poulos and Davies (1980) Method

$$P_u = C \cdot c_a \cdot L + C \cdot \sigma_v \cdot K_s \cdot \tan \phi_a \cdot L + A_b \cdot c \cdot N_c + A_b \cdot \sigma_{vb} \cdot N_q + 0.5 \cdot (A_b \cdot \gamma \cdot d \cdot N_\gamma) - W$$

Where: P_u = ultimate compression capacity based on works by Poulos

C = circumference of pile

c_a = cohesion along the pile shaft = 0kPa for sand

L = length of the pile

σ_v = vertical stress

σ_{vb} = vertical stress at base of pile

A_b = area of pile base

N_c, N_q, N_γ = bearing capacity factors (see discussion below)

W = weight of the pile

$K_s \cdot \tan \phi_a$ = frictional coefficient along pile shaft = 0.2

γ = unit weight of soil (assumed 18 kN/m³)

Meyherhof (1976) stated that the bearing capacity factors reach a maximum value provided the L/d of the pile is higher than 0.5 times the critical ratio.

Using the Meyerhof (1976) method, the critical L/d ratio is equal to 11 for the particular pile being reviewed. Hence according to Meyerhof (1976)

If $L/d > 0.5 \cdot L/d_{\text{critical}}$ is true then the maximum bearing capacity factors will apply. In the case of the pile being reviewed this is not true as the $L/d = 3$, which is less than $0.5 \cdot L/d_{\text{critical}} = (0.5 \cdot 11) = 5.5$. The limiting bearing capacity factors used for shallow foundations should be applied.

Therefore $N_q = 13.97$

$$N_\gamma = 9.41$$

After substituting in the above values $P_u = 153 \text{ kN}$ (this includes shaft and point capacity).

Meyerhof (1976) Method

Point resistance (Q_p) is equal to:

$$Q_p = A_b \cdot \sigma_v \cdot N_q$$

Substitute in the appropriate values $Q_p = 128 \text{ kN}$ without adding skin friction.

The ultimate skin friction (Q_s) may be estimated using a method outlined by Das (1999) where:

$$Q_s = K \cdot \sigma_v \cdot \tan \delta$$

Substitute in the appropriate values $Q_s = 21 \text{ kN}$ without adding skin friction.

Then the total capacity of the pile is approximately equal to 149 kN , which includes both shaft and base bearing capacities.

Vesic (1977) Method

The point resistance (Q_p) is equal to:

$$Q_p = A_b \cdot \sigma_v \cdot N_{\sigma}^*$$

$$N_{\sigma}^* = (3 \cdot N_q) / (1 + 2 \cdot K_0)$$

Substitute in the appropriate values $Q_p = 213$ kN without adding skin friction.

Assume the shaft resistance is approximately 21 kN (see calculations using the method by Meyerhof). The total capacity of the pile is approximately equal to 234 kN, which includes both shaft and base bearing capacities.

Decourt (1995) Method

The point resistance (Q_p) is equal to:

$$Q_p = K_b \cdot N_{60} \cdot A_b$$

where for sand $K_b = 165$

Substitute in the appropriate values $Q_p = 233$ kN without adding skin friction.

The ultimate shaft capacity (Q_s) using the Decourt method is given below:

$$Q_s = a \cdot (2.8 \cdot N_{60} + 10) \cdot C \cdot L$$

where for sand $a = 0.5$

Substitute in the appropriate values $Q_s = 40$ kN without adding skin friction.

J.2 Ultimate Uplift Capacity

From the shaft capacities calculated in the compression cases, and applying Decourt (1995) 20% reduction for uplift capacity, it was calculated that the uplift capacity is in the range of 9 kN to 33 kN.

J.3 Ultimate Lateral Capacity

Broms' Method

$$K_p = \text{Rankine passive pressure} = \tan^2(45 + (\phi/2)) = 2.56$$

From the plots by Brom the ultimate lateral resistance (Q_l):

$$\begin{aligned} Q_l &= 5 \cdot K_p \cdot \gamma \cdot d^3 \\ &= 50 \text{ kN} \end{aligned}$$

Meyerhof (1995) Method

$$Q_l = 0.12 \cdot \gamma \cdot d \cdot L^2 \cdot K_{br}$$

where $K_{br} = 6$ using Meyerhof's plots

Substitute in the appropriate values $Q_l = 25 \text{ kN}$.

Poulos and Davis (1980) Method

$$Q_l = (0.5 \cdot \gamma \cdot d \cdot L^3 \cdot K_p) / (L + e)$$

Assume no load eccentricity (e), and substitute in the appropriate values $Q_l = 45 \text{ kN}$.

APPENDIX K: Influence of Pile Cross-Sectional Shape on Pile Capacity

---oooOOOooo---

As an offshoot to the research in this thesis, the author assisted by Mr Paul Lemcke explored the influence of pile shape on the capacity of a pile, under combined axial and lateral loading. This work was completed using two verified FEM models, one with a square cross-sectional shape and the other with a traditional circular shape. The findings from the study were accepted for publication in a conference and journal. A full reference for the conference publication is shown below, and a copy of the paper is provided in the following pages.

Johnson, K., Lemcke, P., Karunasena, W., and Sivakugan, N. (2003), “Modelling the Response of Deep Foundations under Oblique Loading”, Modsim 2003 Conference Proceeding, Edited by D.A. Post, Townsville, pp. 2048-2053.

The article has also been accepted into an edition of the ‘Environmental Modelling and Software Journal’ due out in the year 2005/2006.

Modelling the Response of Deep Foundations under Oblique Loading

K. Johnson^a, P. Lemcke^a, W. Karunasena^a and N. Sivakugan^a

^aSchool of Engineering, James Cook University, Townsville, Queensland, 4811, Australia.

This article was removed due
to copyright restrictions

This article was removed due
to copyright restrictions

This article was removed due
to copyright restrictions

This article was removed due
to copyright restrictions

This article was removed due
to copyright restrictions

This article was removed due
to copyright restrictions